Luminescent lanthanide architectures for applications in optoelectronics

Eugen S. Andreiadis

École Doctorale Chimie et Sciences du Vivant

THESE

Pour obtenir le grade de

DOCTEUR DE L'UNIVERSITE JOSEPH FOURIER

Discipline : CHIMIE ORGANIQUE

Présentée par

Eugen S. ANDREIADIS

EDIFICES LUMINESCENTS A BASE DE LANTHANIDES POUR L'OPTO-ELECTRONIQUE

Thése soutenue le 28 avril 2009

Composition du jury

Prof. Luisa DE COLA	*Université de Münster*	Rapporteur
Prof. Jean WEISS	*Université de Strasbourg*	Rapporteur
Prof. Muriel HISSLER	*Université de Rennes*	Examinateur
Dr. Guy ROYAL	*Université de Grenoble*	Examinateur
Dr. Marinella MAZZANTI	*CEA Grenoble*	Directeur de thèse
Dr. Renaud DEMADRILLE	*CEA Grenoble*	Co-directeur de thèse

Service de Chimie Inorganique et Biologique
Institut Nanosciences et Cryogénie, CEA Grenoble, France

École Doctorale Chimie et Sciences du Vivant

THESIS

For obtaining the degree of

DOCTOR OF PHILOSOPHY OF THE JOSEPH FOURIER UNIVERSITY

Specialty : ORGANIC CHEMISTRY

Presented by

Eugen S. ANDREIADIS

LUMINESCENT LANTHANIDE ARCHITECTURES FOR APPLICATIONS IN OPTOELECTRONICS

Thesis defended on 28 April 2009

Composition of jury

Prof. Luisa DE COLA	*University of Münster*	Rapporteur
Prof. Jean WEISS	*University of Strasbourg*	Rapporteur
Prof. Muriel HISSLER	*University of Rennes*	Examinator
Dr. Guy ROYAL	*University of Grenoble*	Examinator
Dr. Marinella MAZZANTI	*CEA Grenoble*	Thesis director
Dr. Renaud DEMADRILLE	*CEA Grenoble*	Thesis co-director

Service de Chimie Inorganique et Biologique
Institut Nanosciences et Cryogénie, CEA Grenoble, France

Résumé

Les complexes luminescents de lanthanides font l'objet d'une recherche importante dans le domaine de l'opto-électronique du fait de couleur pure et de rendements quantiques importants. Le développement de nouveaux chelates spécifiquement adaptés pour des applications opto-électroniques reste cependant un domaine moins développé par rapport à d'autres applications.

Le but de ce travail est d'accéder à de nouvelles possibilités de synthèse dans le domaine des émetteurs moléculaires à base de lanthanides pour l'opto-electronique ; ceci, en concevant de nouveaux ligands adaptés à la complexation de ces métaux et l'étude des propriétés optiques des complexes formés.

A cette fin nous avons synthétisés et étudiés une série de ligands basés sur des motifs terpyridine-, bipyridine- et pyridine-tetrazole. Divers substituants ont été ajoutés afin de moduler les propriétés électroniques de ces molécules avec, pour résultats, l'obtention de fortes efficacités lumineuses pour certains de ces complexes tant dans le visible que le proche infrarouge. Les effets induits par l'ajout des divers subtituants sur leurs propriétés photophysiques ont été clairement démontré. De plus, nous avons également synthétisés et testé en couche active de dispositifs OLED une nouvelle classe de complexes neutres complétées par des unités dicétonates.

Nous avons par ailleurs explorés la sensibilisation des ions lanthanides par l'intermédiaire de complexes de métaux de transition d. Pour cela nous avons conçus une nouvelle architecture hétéro-métallique d-f où le complexe d'iridium est employé comme antenne. Finalement, nous avons étudiés les processus de transfert d'énergie par mesures de luminescence.

Mots-clés

lanthanide, opto-électronique, OLED, complexe, tétrazole, luminescence, europium, terbium, néodyme, iridium, hétéronucléaire, héterométallique, greffage.

Discipline

Chimie organique et chimie de coordination

Laboratoire

Laboratoire de Reconnaissance Ionique et Chimie de Coordination
Service de Chimie Inorganique et Biologique, UMR-E3 CEA-UJF
Institut Nanosciences et Cryogénie, CEA Grenoble
17 Rue des Martyrs, 38054 Grenoble Cedex, France

Abstract

Luminescent lanthanide complexes are receiving a large interest for their applications in the field of optoelectronics, as a result of their pure colors and high emission efficiencies. However, the development of new lanthanide chelates for optoelectronic devices has lagged behind that of other applications, and only a limited number of architectures have been tested.

The aim of this work is to access new synthetic possibilities in the area of lanthanide emitters for optoelectronics, by designing specific ligands and studying the properties of their lanthanide complexes, considering their applications for solid state devices.

To achieve this aim, we have designed, synthesized and studied the complexation of lanthanides by a series of ligands based on the terpyridine-, bipyridine- and pyridine-tetrazole motifs, appended with substituents having various electronic effects. The resulting complexes have been characterized by X-ray crystallography, NMR and luminescence studies. The emission efficiencies are very high in some cases, both in the visible and in the NIR region, demonstrating the clear influence of tuning the ligand structure on the photophysical properties of the final lanthanide complexes. Furthermore, we have synthesized, characterized and tested in OLED devices a new class of neutral complexes completed by β-diketonate units.

Finally, in order to explore the sensitization of lanthanide ions by d-metal complexes, we have designed and synthesized, based on our previous studies, a new specific heterometallic architecture containing iridium complexes as lanthanide antennas, and we have investigated by luminescence measurements the energy transfer processes.

Keywords

lanthanide, optoelectronic, OLED, complex, tetrazole, luminescence, europium, terbium, neodymium, iridium, heteronuclear, heterometallic, grafting

Specialty

Organic chemistry and coordination chemistry

Laboratory

Laboratoire de Reconnaissance Ionique et Chimie de Coordination
Service de Chimie Inorganique et Biologique, UMR-E3 CEA-UJF
Institut Nanosciences et Cryogénie, CEA Grenoble
17 Rue des Martyrs, 38054 Grenoble Cedex, France

Acknowledgements

I am very grateful to Dr. Marinella Mazzanti for having given me the opportunity to work on a fascinating and interdisciplinary project and especially for having directed me with clear and useful advices, as well as given me the independence for managing the research details on my own.

I would also like to thank sincerely Dr. Renaud Demadrille as thesis co-director, whose help and support during these three years were essential to me.

I would like to express my gratitude to Professor Luisa De Cola, Professor Jean Weiss, Professor Muriel Hissler and Dr. Guy Royal for accepting to judge the quality of my work.

Particular thanks are addressed to Dr. Daniel Imbert for his help and advices during the preparation of the thesis manuscript and the public defense.

I would like to acknowledge also the following persons for their fundamental contribution to this work:
- Dr. Jacques Pécaut for the X-ray diffraction measurements and the resolution of crystal structures;
- Dr. Daniel Imbert for the photophysical characterization of complexes and for having initiated me in the luminescence measurements;
- Dr. Bruno Jousselme, Professor Alexander Fisyuk, Yann Kervella and Zaireen Yahya for the organic synthesis of some precursors and ligands;
- Adrian Calborean for the DFT calculations on iridium complexes;
- Colette Lebrun for the ES-MS analysis of the compounds;
- Pierre-Alain Bayle for help with the NMR measurements;
- Dr. Pascal Viville for the preliminary testing of the lanthanide complexes in OLED devices.

Many thanks to former and present collaborators at the RICC Laboratory for their practical help, friendly support and encouragement during these years. Last but not least, I would like to thank my family and friends for their long-lasting patience and support.

The European Community through the Marie Curie CHEMtronics programme (MEST-CT-2005-020513) is deeply acknowledged for financial support.

Résumé étendu en français

a) Introduction

Les lanthanides sont les 15 éléments de la première période du bloc f, allant du lanthane (Z = 57) au lutécium (Z = 71). Les orbitales 4f ont une faible extension radiale et sont blindées par les couches externes $5s^2 5p^6$ qui les protègent des perturbations extérieures. Ainsi, les électrons de valence 4f sont peu sensibles à leur environnement chimique et la formation d'une liaison chimique par interaction covalente impliquant des électrons 4f est impossible. L'interaction métal-ligand dans les complexes de Ln(III) est donc décrite par un modèle purement ionique avec une excellente précision. De plus, les ions lanthanides sont des acides durs dans la classification de Pearson. Ils interagissent préférentiellement avec des ligands durs, contenant par exemple des atomes d'oxygène donneurs (eau, carboxylates). Une autre conséquence de l'enfouissement des orbitales f dans le nuage électronique est le faible effet du champ des ligands : environ 500 cm^{-1} contre 5000 à 30 000 cm^{-1} pour les métaux de transition. Ainsi, contrairement aux métaux d, les niveaux d'énergie des complexes de Ln(III) sont très proches de ceux de l'ion libre. Il en est de même pour leurs propriétés spectroscopiques et magnétiques qui sont prévisibles *a priori*.

Le caractère non directionnel de l'interaction métal-ligand se traduit par une faible préférence stéréochimique dans la coordination. En effet, les nombres de coordination ainsi que les géométries associées sont conditionnés essentiellement par les interactions électrostatiques et stériques entre le cation métallique et les ligands. D'un point de vue électrostatique, ces ions très durs vont accommoder un grand nombre (8-9) d'atomes donneurs, de façon à minimiser l'énergie électrostatique. D'un autre côté, minimiser les contraintes stériques est également très important et un ligand multidente donné peut imposer une coordination particulière autour de l'ion.

Tous les ions lanthanides, exceptés le La(III) et le Lu(III) (de configurations respectives $4f^0$ et $4f^{14}$) sont luminescents. Les transitions f-f sont théoriquement interdites

par les règles de sélection électrique dipolaire (règle de Laporte et règle du spin). En pratique, le couplage des états électroniques avec les états vibrationnels et les mélanges de fonctions d'ondes de différents nombres quantiques J ou de différentes parités atténuent cette interdiction. Il en résulte un coefficient d'extinction molaire faible (entre 1 et 10 $L.mol^{-1}.cm^{-1}$) et une durée de vie d'émission de luminescence longue pour certains lanthanides (de l'ordre de la milliseconde pour les ions Eu(III) et Tb(III)).

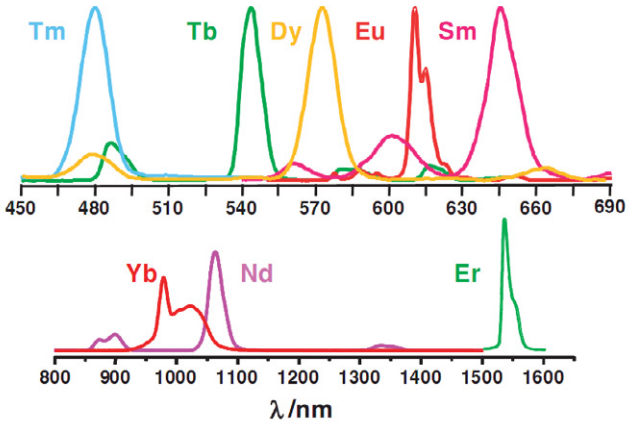

Figure 1. Spectres d'émission de certains complexes de lanthanides

Au cours de la série, différentes efficacités de luminescence des ions Ln(III) sont observées en fonction de la différence d'énergie entre les niveaux excités et le niveau fondamental. Le Tb(III) et l'Eu(III) ont des temps de vie raisonnables et émettent dans le visible (vert λ_{em} = 550 nm et rouge λ_{em} = 620 nm respectivement). Ce sont les ions les plus utilisés pour leur application in optoelectronique et comme sondes luminescentes pour l'analyse et le diagnostic biomédical. L'utilisation des ions émettant dans l'infrarouge (Nd(III) : λ_{em} = 1065 nm, Er(III) : λ_{em} = 1509 nm et Yb(III) : λ_{em} = 978 nm) est en plein essor. Initialement utilisés dans le développement de fibres optiques, de lasers et d'amplificateurs pour les télécommunications, ils suscitent aujourd'hui un intérêt remarquable pour le développement de sondes luminescentes pour l'analyse biomédicale. L'ion Gd(III), en revanche, est peu utilisé car son émission, dans l'ultraviolet, interfère avec les processus d'absorption ou d'émission des composés organiques et biologiques.

Pour résumer, les ions lanthanides s'adaptent à différents environnements. Par conséquent, le contrôle de leur polyhèdre de coordination est difficile et l'étude de leur chimie de coordination a longtemps été délaissée. Cependant, depuis les vingt dernières années, elle connaît un véritable essor motivé par les nombreuses applications en imagerie médicale mais aussi en opto-electronique et la chimie des matériaux et dans le retraitement du combustible nucléaire (séparation actinide/lanthanide).

b) Contexte et objectifs du projet

Les propriétés de luminescence spécifiques des complexes de lanthanide et plus particulièrement, les couleurs pure et efficacités élevées d'émission sont très attractives en raison de leurs applications potentielles pour les dispositifs optoélectroniques. En particulier, des progrès considérables ont été accomplis dans le domaine des diodes luminescentes organiques par l'utilisation de complexes de lanthanide comme matériaux d'émission actifs. Cependant, les rendements quantiques de la plupart de ces dispositifs demeurent plutôt faibles, en partie dus à l'inefficacité des transferts d'énergie et de la faible stabilité des complexes actuellement utilisés qui peuvent se décomposer durant le processus de formation des matériaux ou les conditions opératoires.

En dépit des nombreux dispositifs optoélectroniques étudiés, seuls quelques types de d'architectures de complexes de lanthanide ont été examinés jusque maintenant. Souvent les complexes de lanthanide utilisés ne sont pas correctement caractérisés, rendant difficile de relier leur structure aux propriétés du dispositif final.

Le but de ce travail de dépasser les limitations de conception en ouvrant la voie à de nouvelles possibilités dans le domaine des lanthanides luminescents pour l'optoélectronique. Une étude fondamentale sur le rapport de structure-propriété basée sur une série étendue de complexes de lanthanide a été réalisée, afin de comprendre mieux les facteurs influençant l'efficacité d'émission. Deux approches différentes de sensibilisation de la luminescence des ions lanthanides ont été explorées, liée à l'utilisation

de chromophores organiques dans des architectures comportant des ligands de haute denticité, ou associant des métaux de transition d dans des assemblages polymétaliques.

c) Complexes de lanthanides basés sur des motifs pyridine-tétrazole

Dans la première partie de ce travail, présentée dans le Chapitre II, nous nous sommes intéressés aux relations structure propriétés d'une série de complexes de lanthanides, stables et hautement luminescents, basés sur des motifs chromophores terpyridine, bipyridine, et pyridine tétrazole, modifiés par des substituents induisant différents effets électroniques. En plus de leur influence sur la position des états triplets, les substituents nous ont permis de réaliser sur ces ligands des modifications structurales adaptées pour des applications spécifiques (développement d'assemblages hétéro métalliques, greffage sur des surfaces, etc).

Afin d'éviter les mécanismes de désactivation de la luminescence du lanthanide, les chromophores ont été incorporés dans des architectures polydentates possédant des groupes anioniques présentant une forte capacité de coordination. De ce point de vue, les hétérocycles tétrazoles sont des motifs chélatants versatiles qui peuvent être employés en remplacement des motifs carboxylates. En effet, leurs valeurs de pK_a sont similaires et ils ont déjà été utilisés avec succès en chimie de coordination des métaux de transition. Cependant il apparaît que la sensibilisation de l'émission des lanthanides par des chromophores contenant des tétrazoles est restée inexplorée et pour cette raison nous avons décidé de nous intéresser à l'influence de ce groupe sur les propriétés luminescentes des complexes finaux en les comparants avec celles obtenues avec le motif carboxylate. Le motif tétrazole permet d'obtenir des complexes présentant une très bonne stabilité thermodynamique, tandis que ses effets électroniques sont différents, comparés au motif carboxylate, en effet le motif tétrazole permet de moduler les niveaux énergétiques des chromophores à la fois en terme d'absorption et de propriétés d'émission.

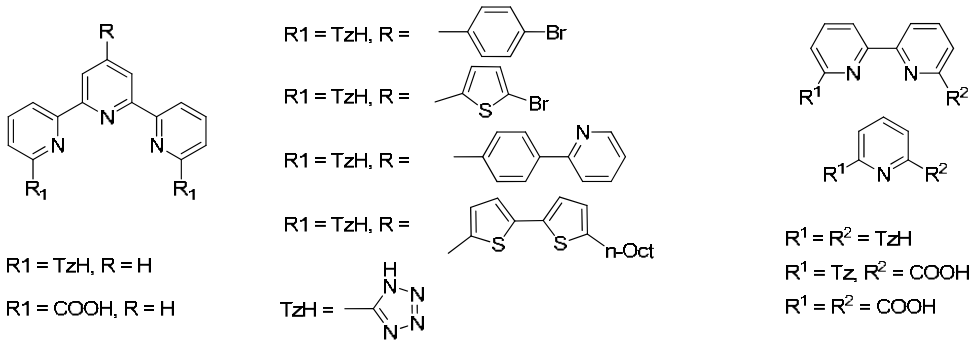

Scheme 1. Séries de ligands basés sur des motifs terpyridines, bipyridines et pyridines étudiés dans ce travail

Dans la série terpyridine, nous avons modifié le synthon principal terpyridine-tétrazole **L1** à l'aide de différents substituents (tels que des motifs bromo-phényle, bromo-thiophène, phenyl-pyridine ou bithiophène) afin de moduler les niveaux énergétiques des états excités des ligands. L'unité terpyridine centrale a été préparée en utilisant différentes stratégies de synthèse en fonction de la molécule cible envisagée (Réaction de Kröhnke ou de Jameson). L'introduction des motifs tétrazoles sur les ligands est basée sur une réaction thermique de cyclo addition de l'azidure de sodium sur le dérivé carbonitrile correspondant dans le DMF en conditions anhydres et en présence de NH_4Cl. Il est à noter que le dérivé carbonitrile précurseur dans cette réaction peut également être hydrolysé pour conduire au dérivé carboxylique offrant ainsi une stratégie de synthèse simple pour accéder à des groupes fonctionnels différents à partir du même synthon. Les substituents sont introduits soit lors de l'étape initiale de synthèse de l'unité terpyridine, soit ultérieurement par le biais de réactions de couplage catalysées au palladium à partir des ligands substitués par des atomes de brome.

Les complexes homoleptiques de lanthanide $[Ln(\mathbf{Li})_2]NHEt_3$ (Ln = Nd, Eu, Tb; i = 1…6) basés sur les ligands précédemment décrits ont été préparés en faisant réagir deux équivalents de ligand avec un équivalent de triflate de lanthanide mis en solution dans le méthanol et en présence de triméthylamine.

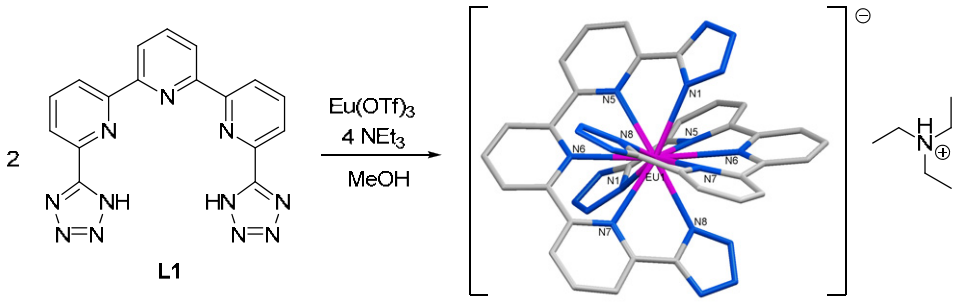

Scheme 2. Synthèse des complexes de lanthanides basés sur des ligands terpyridine-tétrazole

Dans les structures élucidées par diffraction des rayons X des complexes de lanthanides de type $[Ln(\mathbf{Li})_2]^-$, le métal apparaît coordiné dix fois, complètement encapsulé et protégé des interactions avec les molécules de solvant. De plus les études en RMN ^1H, indiquent que la structure pseudo symétrique D_2, observée à l'état solide, est maintenue en solution. Il est à noter qu'une stabilisation cinétique du complexe $[Eu(\mathbf{L1})_2]^-$ est observée par rapport au complexe de formule $[Eu\mathbf{L1}]^+$. Les constantes de stabilité des complexes basés sur les motifs tétrazoles ($\log\beta_2$ = 10.5(5)) sont comparables à celles obtenues dans le cas de l'emploi des analogues carboxylates ($\log\beta_2$ = 11.8(4)).

Les différents complexes obtenus ont révélé des luminescences intenses à la fois dans les régions Visibles et proche Infrarouge du spectre, avec des rendements quantiques de luminescence de 35% pour le complexe $[Eu(\mathbf{L1})_2]^-$ et de 0.29% pour le complexe $[Nd(\mathbf{L4})_2]^-$. L'influence des substituents introduits sur le synthon terpyridine a été discutée en terme d'impact sur les propriétés d'absorption, sur les positions des états triplets et sur les efficacités d'émission. De manière surprenante, nous avons pu observer dans le cas des complexes à base de tétrazole, une extension de la fenêtre d'excitation de 20 nm dans la partie visible du spectre en comparaison avec les complexes analogues contenant les motifs carboxylates. Une extension de pratiquement 100 nm a également été observée dans le cas des complexes basés sur le ligand substitué par un groupe bithiophène.

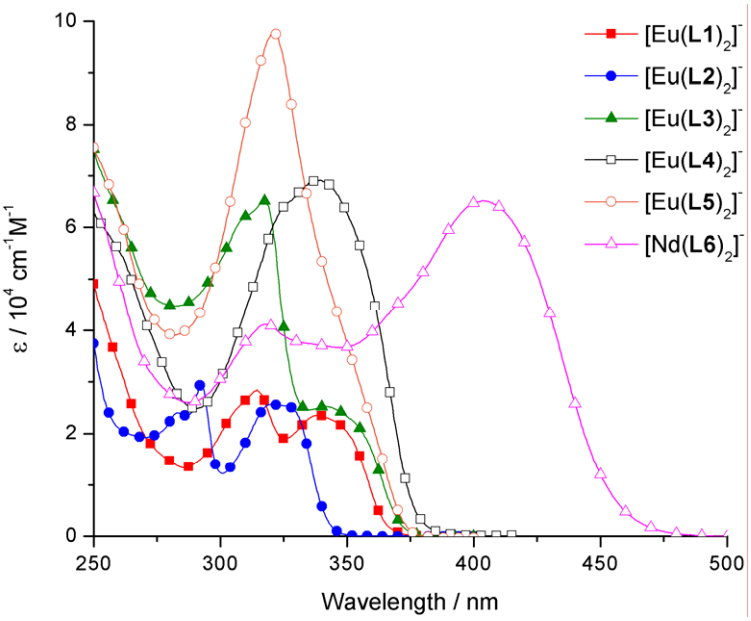

Figure 2. Spectres d'absorption UV-vis des complexes $[Eu(Li)_2]NHEt_3$ (i=1..6)

En séries bi pyridine et pyridine, nous avons étudiés plus en détail l'influence de la présence du groupe tétrazole, en comparaison avec le groupe carboxylique, sur les propriétés de luminescence des complexes de lanthanides. Pour cela nous avons conçu des ligands symétriques et dissymétriques contenant deux groupes anioniques, et nous avons étudié les propriétés structurales et photo physiques des complexes obtenus. Nous avons pu démontrer de manière claire que l'introduction de motifs tétrazoles se manifestait par un décalage bathochromique des spectres d'absorption (approximativement 10 nm par motif tétrazole), permettant ainsi une excitation des ions lanthanides à des longueurs d'ondes de plus basse énergie. De même nous avons observé que la modification de l'état triplet du ligand induite par le motif tétrazole conduisait à une amélioration des rendements quantiques de luminescence des complexes de terbium en série bipyridines par rapport aux analogues contenants des carboxylates (atteignant 27% dans le cas de $[Tb(\mathbf{L9})_2]^-$).

Les efficacités quantiques de luminescence pour les complexes d'Europium, bien que décroissant avec le nombre de motif tétrazole introduit, restent cependant très bonnes (45% dans le cas du complexe $[Eu(\mathbf{L9})_2]^-$). Des rendements quantiques excellents ont par ailleurs été obtenus en série pyridine-tétrazole, pour les complexes $[Eu(\mathbf{L10})_3]^{3-}$ et

[Tb(**L10**)$_3$]$^{3-}$ atteignant 61% et 65% respectivement. Ces rendements placent ces complexes parmi les plus luminescents reportés dans la littérature.

La solubilité des complexes peut être facilement et significativement améliorée, comme il a été démontré dans ce travail, soit par introduction d'une chaîne octyle sur le ligand terpyridine **L6**, soit en remplaçant le contre ion triethyl ammonium par le trioctyl ammonium dans la structure du complexe basé sur la pyridine tétrazole [Eu(**L10**)$_3$]$^{3-}$. L'amélioration de la solubilité permet d'envisager l'emploi de ces complexes fortement luminescents et très solubles dans les milieux organiques, comme émetteurs dans des dispositifs de type diodes électroluminescentes organiques (OLEDs) fabriquées par des techniques de spin-coating.

En perspective, la substitution du ligand terpyridine tétrazole par des groupements électro-attracteurs tels que des motifs cyano ou nitro pourrait permettre de diminuer le niveau d'énergie de l'état triplet et d'améliorer l'efficacité d'émission des complexes de Terbium. D'autre part, la dimérisation du ligand bromo-phenyl-terpyridine-tétrazole par le biais de réactions de couplage pourrait permettre également l'obtention de ligands présentant deux sites de complexation particulièrement adaptés pour la formation de polymères de coordination présentant des propriétés contrôlées.

L'introduction de motifs pyridine tétrazole dans des ligands présentant différentes topologies, comme il a été démontré dans le laboratoire récemment, pourrait permettre d'améliorer la stabilité de ces systèmes dans l'eau et déboucher sur d'éventuelles applications dans le domaine des sondes biologiques à base de lanthanides.

De plus, la modification des complexes à base de tétrazoles pourraient conduire à l'obtention d'architectures luminescentes neutres qui pourraient être utilisées comme constituant de couches émettrices dans des dispositifs électroluminescents organiques mises en œuvre cette fois ci par des procédés de dépôts sous vide.

d) Complexes neutres de lanthanides a base de ligands dicetonates

Dans la seconde partie de ce travail (présentée dans le chapitre III), nous avons conçu une nouvelle classe de complexes de lanthanides construits à partir de l'unité chromophore terpyridine, dont la sphère de coordination est complétée par des unités β-dicétonates. La plupart des complexes de lanthanides utilisés en optoélectronique sont des chélates tris-β-dicétonates renfermant un chromophore supplémentaire, bidentate, avec des azotes comme atomes donneurs telle la 1,10-phénantroline. Cependant, l'utilisation de chromophores anioniques pourrait conférer une stabilité chimique et thermique accrues aux complexes, ce qui conduirait à des systèmes possédant une meilleure efficacité. Par conséquent, nous avons inclus le motif terpyridine dans deux architectures lanthanidiques neutres distinctes : la première, contient un chromophore dissymétrique terpyridine-carboxylate, et est complétée par deux unités β-dicétonate ; la deuxième comporte un chromophore anionique terpyridine-bistétrazole, et est complétée par une unité β-dicétonate.

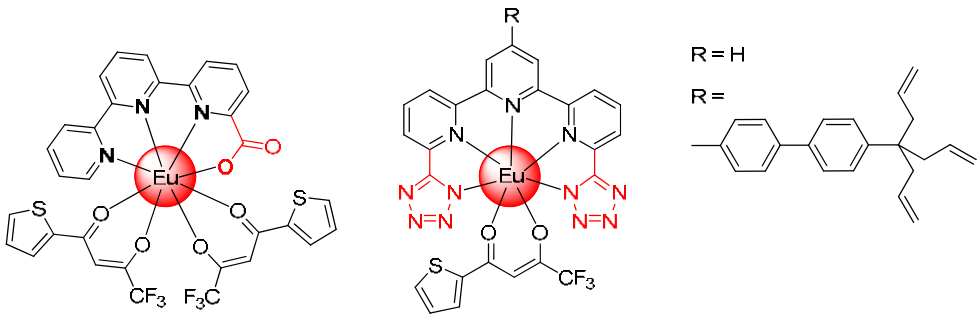

Scheme 3. Complexes neutres de lanthanides renfermant le motif terpyridine.

Les complexes hétéroleptiques ainsi obtenus ont été caractérisés, par diffraction des rayons X, spectroscopie RMN mono et bidimensionnelle, et mesures photophysiques. Le complexe d'europium terpyridine-carboxylate [Eu(**L12**)(TTA)$_2$] présente un très bon rendement quantique de luminescence (41 %). De plus, ce composé conserve cette propriété lorsqu'il est inséré dans une matrice de PVK, déposée sous forme de film. Ceci nous a conduit à tester ce matériau en tant que couche émissive dans des diodes

électroluminescentes organiques (OLEDs). Les études préliminaires sur les complexes d'europium et de terbium ainsi mis en forme ont été réalisées sur des OLEDs présentant la configuration suivante : ITO / PEDOT PH500 / PVK:[Ln(**L12**)(ket)$_2$] / Cs_2CO_3 / Al. Ces cellules présentent un comportement typique de diode, car nous avons pu observer une luminescence intense du matériau, respectivement rouge ou verte, dans chaque cas. Des améliorations dans l'architecture des systèmes sont nécessaires pour conduire à un phénomène d'électroluminescence plus important. Toutefois, ces résultats nous encouragent à envisager tout le potentiel de cette nouvelle classe de complexes dans leur utilisation au sein d'OLEDS.

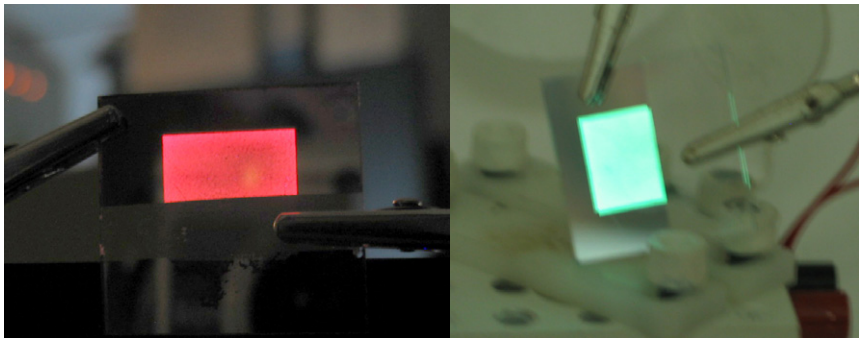

Figure 3. Systèmes OLED construits à partir des complexes d'europium (gauche) et de terbium (droite).

Grâce à la fonctionnalisation aisée du chromophore terpyridine-tétrazole, nous avons introduit, sur ce squelette, un pivot tripode de type acétylénique capable de former des liaisons covalentes Si-C à la surface du silicium, ceci dans le but d'étudier le greffage de complexes de lanthanides sur surface. La « décoration » de différents substrats par des complexes de lanthanides conduit à des propriétés de luminescence très intéressantes et des applications envisageables. Cependant, il n'y a eu jusqu'alors que peu d'exemples décrits de substrats semi-conducteurs, comme le silicium, fonctionnalisés en surface par des complexes de lanthanides. Notre approche a consisté tout d'abord à ancrer sur la surface de silicium un ligand adapté à la complexation des lanthanides. Puis nous avons réalisé la réaction de complexation sur ce ligand greffé.

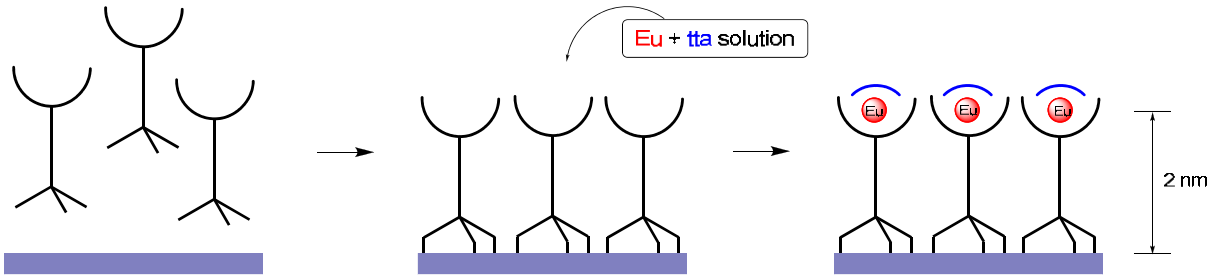

Figure 4. Représentation schématique du processus de complexation à la surface

Les résultats préliminaires attestent de la formation de complexes de lanthanides hétéroleptiques dont le ligand est bien immobilisé à la surface du substrat. Cependant, des études complémentaires doivent être réalisées pour analyser plus en détail la nature de ces substrats fonctionnalisés.

e) Complexes hétérométalliques iridium-lanthanide

Dans la dernière partie de ce travail (présentée au Chapitre IV), en utilisant la deuxième approche pour la sensibilisation des lanthanides, nous avons conçu et synthétisé une architecture hétéropolymétallique modulable renfermant des ions métalliques d et f. Dans cet édifice, les centres métalliques sont reliés entre eux par une architecture organique covalente, ce qui confère une bonne stabilité à l'assemblage final.

De nombreux articles ont été publiés sur des complexes hétérométalliques d-f, qui contiennent des métaux de transition tels le ruthénium, le platine ou l'osmium. En revanche, les exemples présentant la luminescence des lanthanides sensibilisée par l'iridium sont rares. Ceci est assez surprenant étant donné l'intérêt de ces complexes d'iridium dans le domaine des OLEDs et les multiples possibilités de modulation de l'état excité le plus bas en énergie de ces luminophores.

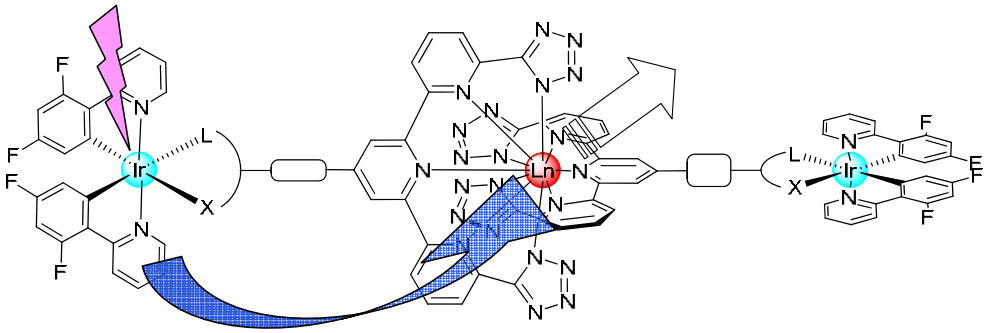

Figure 5. Structure du complexe iridium-lanthanide hétérométallique, montrant la direction du transfert d'énergie.

Nous avons donc connecté un complexe d'iridium cyclométallé (rôle d'antenne) à un motif terpyridine-tetrazole, connu pour former des complexes stables avec les ions lanthanides. Le complexe d'iridium est sensé émettre à une énergie suffisamment élevée pour pouvoir peupler efficacement par transfert d'énergie les niveaux excités émissifs de l'europium. Pour cela, le complexe d'iridium doit être formé à partir d'un ligand cyclométalant avec un niveau HOMO bas en énergie comme la 2,4-difluorophénylpyridine.

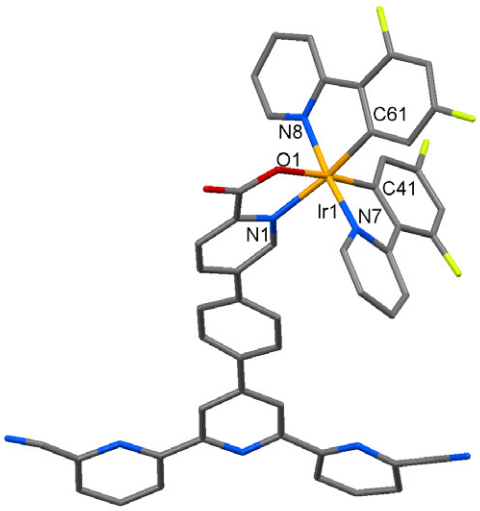

Figure 6. Structure moléculaire du complexe d'iridium **Ir2**

De nombreuses stratégies ont été mises en œuvre pour l'élaboration du "complexe comme ligand" et ont été analysées en détail. Finalement, le ligand a été obtenu par

couplage de Suzuki entre le dérivé bromé du complexe d'iridium et l'ester boronique de la terpyridine. La conversion du groupement nitrile en tétrazole a été réalisée au moyen d'azoture de sodium et de bromure de zinc, selon la procédure décrite par Demko et Sharpless. L'ensemble des complexes d'iridium intermédiaires, ainsi que le ligand final ont été caractérisés par diffraction des rayons X, spectroscopie RMN 1D et 2D et mesures de luminescence. L'origine de l'émission des complexes d'iridium a été attribuée à un état mixte MLCT-LC auquel l'unité ancillaire contribue de façon substantielle.

Les complexes hétérometalliques lanthanide-iridium $[Eu(\mathbf{Ir3})_2]^-$ et $[Nd(\mathbf{Ir3})_2]^-$ ont été obtenus en faisant réagir un équivalent de triflate de lanthanide avec deux équivalents de ligands dans un mélange dichlorométhane-méthanol et en présence de trioctylamine. Des mesures de luminescence ont été réalisées dans le domaine du visible comme dans l'infrarouge pour étudier la sensibilisation de l'émission du lanthanide par le complexe d'iridium. Le transfert d'énergie Ir→Ln a été clairement mis en évidence et son efficacité a été estimée à 85 et 65 % respectivement. Malgré ce transfert intermétallique rapide et efficace, les rendements quantiques de phosphorescence du lanthanide excité au moyen de l'antenne iridium demeurent faibles (1% pour l'émission de l'europium), car le processus global de sensibilisation est peu efficace.

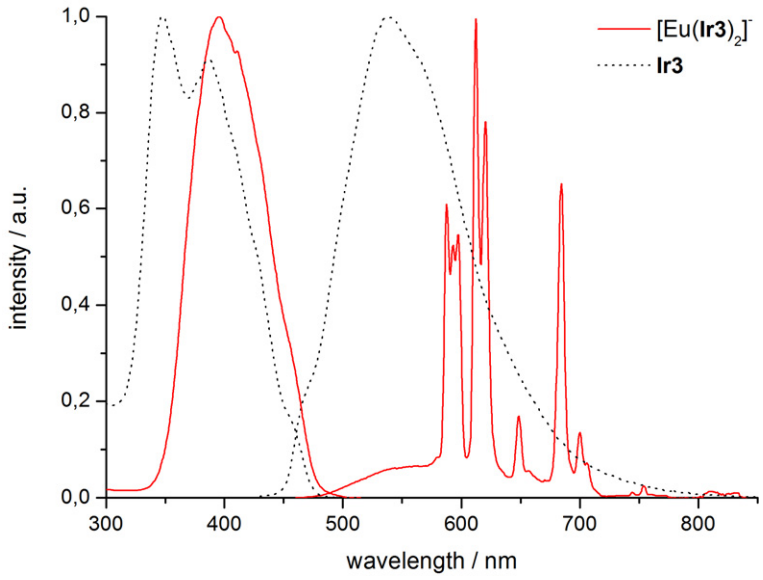

Figure 7. Excitation normalisée et spectres d'émission pour le complexe $[Eu(\mathbf{Ir3})_2]^-$ et le ligand **Ir3.**

Cependant, la modularité de notre approche peut facilement conduire a des efficacités meilleures pour les systèmes, pour peu que l'émission de l'iridium et l'absorption du lanthanide coïncident mieux.Ceci pourrait être atteint en remplaçant le pont phenylene entre le site iridium et le site lanthanide par un groupement ayant un effet électronique différent sur la modulation de l'émission de l'iridium, tel un pont acétylène. Nous pouvons aussi envisager l'utilisation de ligands ancillaires de type acetylacetonates à la place des picolinates. Le déplacement hypsochromique résultant pourrait conduire à une meilleure sensibilisation de l'ion europium. Le remplacement des atomes de fluor par des groupements électro-donneurs sur les ligands cyclométallés pourrait, au contraire, induire un déplacement bathochrome, et ainsi à une meilleure sensibilisation des terres rares émettant dans l'infrarouge.

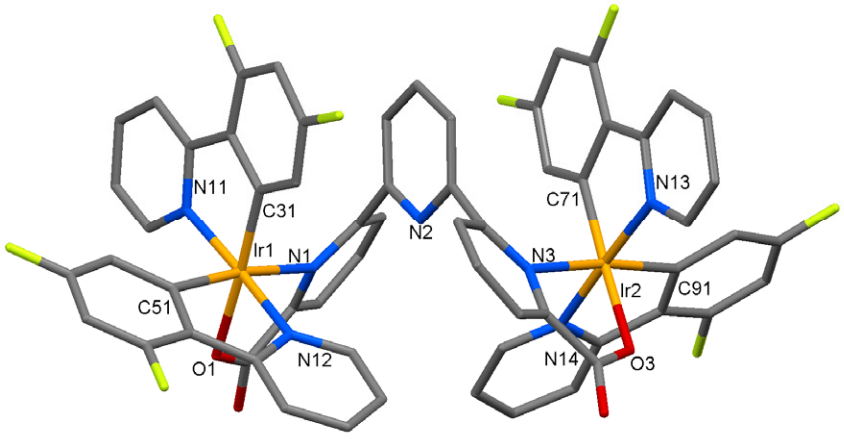

Figure 8. Structure du complexe bis-iridium **Ir5**

Mis à part ces structures d-f hétérométalliques, nous avons aussi synthétisé et étudié des assemblées homopolymétalliques renfermant des complexes bis-iridium liés de façon covalente entre eux et pontés par une unité terpyridine-carboxylate. Grâce à un protocole de synthèse facile et de bonnes propriétés photophysiques (les rendements peuvent atteindre la valeur de 18%), les complexes formés suggèrent l'intérêt de tels édifices dans le développement d'assemblées polymétalliques aux propriétés redox et optiques originales.

Le manuscrit s'organise de la façon suivante : après une courte introduction sur la chimie du groupement tétrazole, nous présentons la synthèse, la structure et les propriétés photophysiques des complexes de lanthanides renfermant des motifs terpyridine-, bipyridine- et pyridine-tétrazole. Par la suite, les complexes neutres de lanthanides contenant des unités β-dicétone seront étudiés ainsi que les toutes premières applications de ces composés pour la formation d'OLEDs et la fonctionnalisation de surfaces. Dans la dernière partie, nous décrirons les stratégies de synthèse pour l'élaboration de complexes polymétalliques à base d'iridium, leurs structures et l'étude de leurs propriétés photophysiques.

Table of contents

Résumé **v**

Abstract **vii**

Acknowledgements **ix**

Résumé étendu en français **xi**

a) Introduction xi
b) Contexte et objectifs du projet xiii
c) Complexes de lanthanides basés sur des motifs pyridine-tétrazole xiv
d) Complexes neutres de lanthanides a base de ligands dicetonates xix
e) Complexes hétérometalliques iridium-lanthanide xxi

Table of contents **xxvii**

Chapter I General introduction to lanthanide complexes **1**

I.1. Fundamental properties of lanthanides *1*
I.1.1. Definition 1
I.1.2. Coordination chemistry 2
I.1.3. Magnetic properties 4
I.1.4. Spectroscopic properties 4
a) Electronic levels 4
b) Electronic transitions 5
c) Luminescence 7

I.2. Sensitization of lanthanide luminescence *9*
I.2.1. The antenna effect 9
I.2.2. Luminescence efficiency and quenching processes 12
I.2.3. Predicting efficient antennas for lanthanides 14
I.2.4. Design of highly luminescent lanthanide complexes 16
I.2.5. Sensitization of lanthanide luminescence by chromophores 18
I.2.6. Sensitization of lanthanide luminescence by other metals 24

I.3. Applications of luminescent lanthanide complexes in optoelectronics *31*
I.3.1. Design and operating principles of OLEDs 31
I.3.2. Lanthanide complexes as emitting layers in OLEDs 35

I.3.3. Other applications of lanthanide complexes in optoelectronics 36

I.4. Context and objectives of the project *38*

Chapter II Lanthanide complexes based on pyridine-tetrazolates **43**

II.1. Introduction *43*

a) General properties of the tetrazoles 43

b) Strategies for the synthesis of 5-substituted tetrazoles 44

c) The tetrazole group in lanthanide coordination chemistry 46

II.2. Lanthanide complexes based on terpyridine-tetrazolates *48*

II.2.1. Synthesis and characterization of ligands 48

a) Ligand design 48

b) Strategies for the synthesis of terpyridines 49

c) Synthesis of terpyridine ligands **L1** - **L6** 51

d) Characterization of terpyridine ligands **L1** - **L6** 54

II.2.2. Synthesis and characterization of the lanthanide complexes 58

a) Molecular and crystal structures 59

b) ^{1}H NMR solution study 67

c) Conditional stability constants 74

II.2.3. Photophysical properties of lanthanide complexes 76

a) Absorption characteristics 76

b) Ligand centered luminescence 78

c) Metal centered luminescence 81

II.3. Lanthanide complexes based on bipyridine-tetrazolates *89*

II.3.1. Synthesis and characterization of ligands 89

a) Ligand design 89

b) Synthesis and characterization of ligands **L7** - **L9** 89

II.3.2. Synthesis and characterization of lanthanide complexes 92

a) Molecular and crystal structures 92

b) ^{1}H NMR solution study 95

II.3.3. Photophysical properties of lanthanide complexes 97

a) Absorption characteristics 97

b) Ligand centered luminescence 98

c) Metal centered luminescence 100

II.4. Lanthanide complexes based on pyridine-tetrazolates *102*

II.4.1. Synthesis and characterization of ligands 102

a) Ligand design 102

b) Synthesis and characterization of ligands **L10** and **L11** 103

II.4.2. Synthesis and characterization of the lanthanide complexes 104

a) Molecular and crystal structures 105

b) ^{1}H NMR solution study 110

II.4.3. Photophysical properties of lanthanide complexes 111

a) Absorption characteristics 111

b) Ligand centered luminescence 113
c) Metal centered luminescence 115

II.5. Conclusions *117*

Chapter III Neutral lanthanide diketonate complexes **121**

III.1. Introduction to lanthanide β-diketonate complexes *121*

III.2. Neutral lanthanide complexes based on terpyridine-monocarboxylate *125*
III.2.1. Ligand and complex design 125
III.2.2. Synthesis and characterization of complexes 126
a) Molecular and crystal structures 127
b) ^{1}H NMR solution study 129
III.2.3. Photophysical properties of lanthanide complexes 131
a) Ligand centered luminescence 131
b) Metal centered luminescence 132
III.2.4. Applications in OLED devices 134

III.3. Neutral lanthanide complexes based on terpyridine-bistetrazolate *137*
III.3.1. Lanthanide complexes for surface functionalization 137
III.3.2. Ligand and complex design 140
III.3.3. Synthesis and characterization of ligands 141
III.3.4. Synthesis and characterization of complexes 144
a) Molecular and crystal structures 145
b) ^{1}H NMR solution study 146
III.3.5. Photophysical properties of complexes 149
III.3.6. Preliminary grafting experiments on silicon surfaces 151

III.4. Conclusions *152*

Chapter IV Heterometallic iridium-lanthanide complexes **155**

IV.1. Coordination and photophysical properties of iridium complexes *155*
IV.1.1. Introduction 155
IV.1.2. Synthesis of cyclometalated iridium complexes 155
IV.1.3. Stereochemistry of cyclometalated iridium complexes 157
IV.1.4. Electronic transitions in octahedral complexes 158
IV.1.5. Emissive excited states in cyclometalated iridium complexes 162

IV.2. Heterometallic iridium-lanthanide complexes *164*
IV.2.1. Literature examples 164
IV.2.2. Design of iridium-lanthanide heterometallic complexes 167
IV.2.3. Synthesis of ligands and iridium complexes 169
a) First synthetic strategy 169
b) Second synthetic strategy 173
c) Third synthetic strategy 175
IV.2.4. Characterization of iridium complexes 181

a) Molecular and crystal structures 181
b) NMR characterization in solution 185
c) Photophysical properties 188
d) DFT calculations 196
IV.2.5. Synthesis of iridium-lanthanide complexes 199
IV.2.6. Characterization of iridium-lanthanide complexes 200
a) ^{1}H NMR solution study 200
b) Photophysical characterization 201

IV.3. Bis-iridium complexes based on terpyridine-carboxylate *210*
IV.3.1. Literature examples 210
IV.3.2. Synthesis of bis-iridium complexes 213
IV.3.3. Characterization of bis-iridium complexes 214
a) Molecular and crystal structure 214
b) NMR characterization in solution 216
c) Photophysical properties 217

IV.4. Conclusions *221*

Chapter V Final conclusions and perspectives **223**

Chapter VI Experimental methods and procedures **227**

VI.1. General *227*
VI.1.1. Solvents and starting materials 227
VI.1.2. Chromatography 227
VI.1.3. Characterization 227

VI.2. Synthesis of ligands *228*
VI.2.1. Ligands based on terpyridine 228
a) Synthesis of 6,6''-bis-(1H-tetrazol-5-yl)-2,2':6',2''-terpyridine (**L1**) 228
b) Synthesis of 2,2':6',2''-terpyridine-6,6''-dicarboxylate (**L2**) 230
c) Synthesis of 4'-(4-bromophenyl)-6,6''-bis-(1H-tetrazol-5-yl)-2,2':6',2''-terpyridine (**L3**) 230
d) Synthesis of 4'-(5-bromothiophen-2-yl)-6,6''-bis-(1H-tetrazol-5-yl)-2,2'-6'-2''-terpyridine (**L4**) 233
e) Synthesis of 4'-(4-(pyridin-2-yl)phenyl)-6,6''-bis-(1H-tetrazol-5-yl)-2,2':6',2''-terpyridine (**L5**) 235
f) Synthesis of 4'-(5''-octyl-2,2'-bithiophen-5-yl)-6,6''-bis-(1H-tetrazol-5-yl)-2,2':6',2''-terpyridine (**L6**) 237
g) Synthesis of 6,2':6',2''-terpyridine-2-carboxylic acid (**L12**) 239
h) Synthesis of 4'-(4'-(4-allylhepta-1,6-dien-4-yl)biphenyl-4-yl)-6,6''-bis-(1H-tetrazol-5-yl)-2,2':6',2''-terpyridine (**L13**) 240
VI.2.2. Ligands based on bipyridine 242
a) Synthesis of 6,6'-bis-(1H-tetrazol-5-yl)-2,2'-bipyridine (**L7**) 242
b) Synthesis of 6'-(1H-tetrazol-5-yl)-2,2'-bipyridine-6-carboxylic acid (**L8**) 243
c) Synthesis of 2,2'-bipyridine-6,6'-dicarboxylic acid (**L9**) 246

VI.2.3. Ligands based on pyridine 246
a) Synthesis of 2,6-bis(1H-tetrazol-5-yl)pyridine (**L10**) 246
b) Synthesis of 6-(1H-tetrazol-5-yl)picolinic acid (**L11**) 247

VI.3. Synthesis of iridium complexes *248*
VI.3.1. Iridium μ-chloro-bridged dimer complexes 248
a) Synthesis of tetrakis(2-(2,4-difluorophenyl)pyridine)bis(μ-ch1oro)diiridium (**31**) 248
b) Synthesis of tetrakis(2-phenylpyridine)bis(μ-ch1oro)diiridium (**44**) 249
VI.3.2. Iridium heteroleptic cyclometallated complexes 250
a) Synthesis of bis(2-(2,4-difluorophenyl)pyridine))(2-picolinic acid)iridium complex (**33**, FIrpic) 250
b) Synthesis of bis(2-(2,4-difluorophenyl)pyridine))(6-bromo-2-picolinic acid)iridium complex (**Ir1a**) 250
c) Synthesis of bis(2-(2,4-difluorophenyl)pyridine))(5-bromo-2-picolinic acid)iridium complex (**Ir1**) 251
d) Synthesis of bis(2-(2,4-difluorophenyl)pyridine))(6-(4-(6,6”-dicyano-terpyridin-4’-yl)phenyl)picolinic acid)iridium complex (**Ir2a**) 252
e) Synthesis of bis(2-(2,4-difluorophenyl)pyridine))(5-(4-(6,6”-dicyano-terpyridin-4’-yl)phenyl)picolinic acid)iridium complex (**Ir2**) 255
f) Synthesis of bis(2-(2,4-difluorophenyl)pyridine))(5-(4-(6,6”-bis-(1H-tetrazol-5-yl)-terpyridin-4’-yl)phenyl)picolinic acid)iridium complex (**Ir3**) 256
VI.3.3. Terpyridine dicarboxylate-diiridium complexes 257
a) Synthesis of tetrakis(2-phenylpyridine)μ-(2,2':6',2''-terpyridine-6,6''-dicarboxylic acid)diiridium complex (**Ir4**) 257
b) Synthesis of tetrakis(2-(2,4-difluorophenyl)pyridine))μ-(2,2':6',2''-terpyridine-6,6''-dicarboxylic acid)diiridium complex (**Ir5**) 258

VI.4. Synthesis of lanthanide complexes *259*
VI.4.1. Lanthanide complexes based on terpyridine ligands 259
a) Synthesis of the [Ln(**L1**)$_2$]NEt$_3$ complexes (Ln = Eu, Tb, Nd) 259
b) Synthesis of the [Ln(**L2**)$_2$]NEt$_3$ complexes (Ln = Eu, Tb, Nd) 260
c) Synthesis of the [Ln(**L3**)$_2$]NEt$_3$ complexes (Ln = Eu, Tb) 261
d) Synthesis of the [Ln(**L4**)$_2$]NEt$_3$ complexes (Ln = Eu, Nd) 262
e) Synthesis of the [Eu(**L5**)$_2$]NEt$_3$ complex 263
f) Synthesis of the [Nd(**L6**)$_2$]NEt$_3$ complex 264
g) Synthesis of the [Eu(**L1**)(TTA)] complex 265
h) Synthesis of the [Eu(**L12**)(TTA)$_2$] complex 265
i) Synthesis of the [Tb(**L12**)(TFAC)$_2$] complex 266
VI.4.2. Lanthanide complexes based on bipyridine ligands 267
a) Synthesis of the [Ln(**L7**)$_2$]NEt$_3$ complexes (Ln = Eu, Tb) 267
b) Synthesis of the [Ln(**L8**)$_2$]NEt$_3$ complexes (Ln = Eu, Tb) 268
c) Synthesis of the [Eu(**L9**)$_2$]NEt$_3$ complex 269
VI.4.3. Lanthanide complexes based on pyridine ligands 269

a) Synthesis of the [Ln(**L10**)$_3$](NHEt$_3$)$_3$ complexes (Ln = Eu, Tb, Nd) 269
b) Synthesis of the [Eu(**L10**)$_3$](NHOct$_3$)$_3$ complex 270
c) Synthesis of the [Eu(**L11**)$_3$](NHEt$_3$)$_3$ complex 271
VI.4.4. Heterometallic iridium-lanthanide complexes 272
a) Synthesis of the [Eu(**Ir3**)$_2$](NHOct)$_3$ complex 272
VI.5. Analytical techniques *272*
Bibliography **277**
Appendix **301**

Chapter I
General introduction to lanthanide complexes

I.1. Fundamental properties of lanthanides

I.1.1. Definition

The lanthanide series is comprised of the 15 elements in the first period of the f block of elements, ranging from lanthanum (Z = 57) to lutetium (Z = 71), as shown in Figure I.1. Lanthanum, with an electronic configuration $[Xe]4f^{0}5d^{1}6s^{2}$, is included by extension. The rest of the lanthanide atoms adopt mainly a configuration of the type $[Xe]4f^{n+1}6s^{2}$, with a progressive filling of the 4f electronic sub-shell along the period. The lanthanide series can be extended with the elements scandium (Z = 21) and yttrium (Z = 39), having similar chemical properties to the lanthanides; the enlarged series is called the *rare earths*.

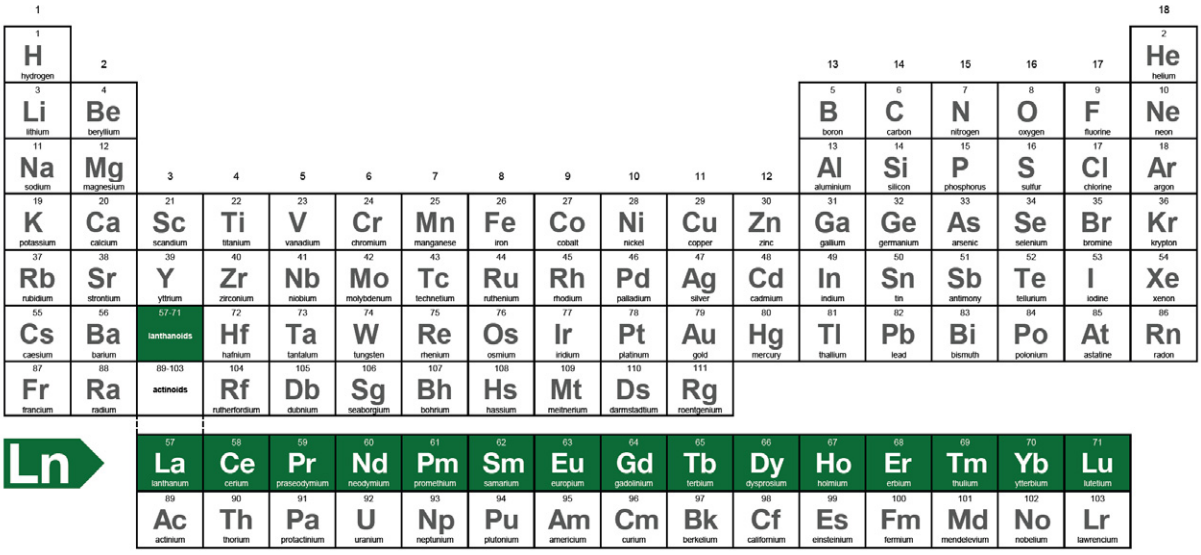

Figure I.1. The lanthanide (Ln) series in the periodic table of elements

Loss of one 4f electron and two 6s electrons results in the formation of trivalent lanthanide ions (Ln^{3+}), which is the oxidation state most stable in the whole series. The only notable exceptions are Ce^{4+} and Eu^{2+} ions. The ground state electronic configuration of the Ln^{3+} ions is $[Xe]4f^n$ (n = 0..14), which is energetically well separated from the $[Xe]4f^{n-1}5d^1$ configuration ($\Delta E > 32\,000$ cm^{-1}). The 4f orbitals are well shielded by the xenon core (54 electrons), due particularly to the large radial expansion of the $5s^25p^6$ sub-shells, transforming the valence 4f orbitals into "inner orbitals." This phenomenon is the key to the chemical and spectroscopic properties of the lanthanide metal ions.

I.1.2. Coordination chemistry

The chemical properties of the lanthanides are similar due to their comparable sizes and shielded valence electron shells, which is also manifested in a lack of preferred coordination geometry. In view of the large sizes of the lanthanide ions and the shielding of the 4f-orbitals within the electron shell, the metal-ligand interaction in the lanthanide complexes can be described with an excellent precision by a purely ionic model. The weak covalent character of these bonds is the result of the minute mixing of 4f metal orbitals and ligand-centered wave functions. The ligand field effect is in the order of hundreds of cm^{-1}, while for the transition metals this ranges from 5 000 to 30 000 cm^{-1}. Also, opposed to the transition metals, the energetic levels in the lanthanide complexes are very close to those in the free ion. Due to this, the spectroscopic and magnetic properties (*vide infra*) are very little influenced by the organic ligand coordinated to the metal.

As the atomic number increases, the lanthanide ionic radii decrease along the series, due to the increase of the effective nuclear charge and the contraction of the 5s and 5p orbitals. The phenomenon is called "lanthanide contraction."

As a consequence of the accentuated ionic character, the Ln^{3+} ions possess weak stereochemical preferences and a labile coordination sphere that leads to variable coordination numbers and geometries.[1] The coordination number is usually high (between 3 and 14) with 8 and 9 being the most common. This results from (a) the large size of the Ln^{3+} ions and (b) the necessity to minimize interligand repulsions leading to

specific geometries. The most common coordination geometries of the Ln^{3+} complexes in solid state are square anti-prismatic and dodecahedral (for a coordination number of 8), tricapped trigonal prismatic and monocapped square anti-prismatic (for a coordination number of 9) and bicapped square antiprismatic and bicapped dodecahedral (for a coordination number of 10), as shown in Figure I.2. Other geometries related to other coordination numbers often show a strong deviation from regular coordination polyhedra, resulting from the non-directional character of the metal-ligand bond.

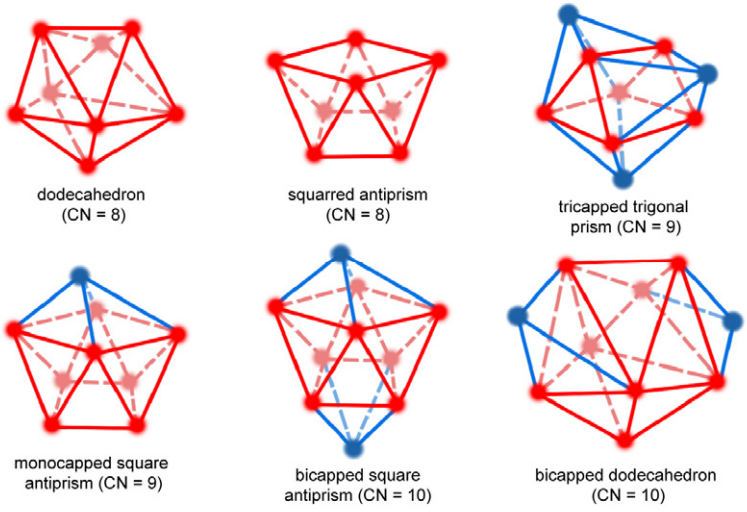

Figure I.2. Usual coordination polyhedra for the lanthanide ions

In solution, the coordination numbers are more difficult to predict.[2] The lanthanide ion is known to complete its coordination sphere with molecules of solvent or anions (water, chloride, hydroxide, etc) if the number of donating atoms in the ligand is too little or their electronic density too low.

The coordination properties of the ligands are determined by the nature of the donor atoms. As the lanthanide ions show a hard acid behavior, according to the classification of Pearson, it is expected (and observed) that they have preference for binding hard bases. Therefore, stronger bonds will be formed with ligands having negatively charged O or N as donor atoms. Both the hard acidic character of Ln^{3+} ions and the predominant ionic nature of bonding interactions lead to a preference for hard bases. Thus water molecules

and hydroxide ions (OH^-) are particularly strong ligands. In water solutions, ligands bearing coordinating moieties possessing negatively charged oxygens (such as carboxylates or phosphonates) generate complexes with large thermodynamic stability, resistant to hydrolysis.[3, 4] Groups containing neutral oxygen or nitrogen atoms generally bind efficiently only in the presence of other donor groups having negatively charged oxygen atoms as part of the same multidentate ligand (e.g. nitrogen of polyaminocarboxylates, for instance EDTA). In anhydrous media, nitrogen donors, even if softer, can coordinate lanthanides more strongly, although they undergo at least partial hydrolysis even in the presence of small amounts of water.[2]

I.1.3. Magnetic properties

All the lanthanide ions possessing unpaired 4f electrons are paramagnetic (with the exception of La^{3+} and Lu^{3+} which have a $4f^0$ and $4f^{14}$ electronic configuration, respectively).[1] Among them, the gadolinium ion, situated in the middle of the series, is particularly interesting. The presence of 7 unpaired electrons (S = 7/2) results in a high magnetic moment, and moreover the electronic relaxation time is long ($T_{1e} > 10^{-9}$ s) compared to the other paramagnetic lanthanide ions ($T_{1e} \approx 10^{-13}$ s for Eu^{3+}, Yb^{3+} and Dy^{3+}), which makes the gadolinium complexes be largely used as contrast agents in Magnetic Resonance Imaging.[3]

I.1.4. Spectroscopic properties

a) Electronic levels

The energy levels of lanthanide ions can be calculated considering the interactions between the 4f electrons. The $4f^6$ and $4f^8$ configurations of the Eu^{3+} and Tb^{3+} species give rise to a large number of states whose relative energy is determined by a combination of inter-electronic repulsion, spin-orbit coupling and the ligand field.[4]

Inter-electronic repulsion splits the conjugate $4f^6$ and $4f^8$ configurations into 119 terms, where Γ = S, P, D and F when the quantum number L = 0, 1, 2 or 3 (see Figure I.3). This electrostatic interaction gives terms which are separated by about 10^4 cm^{-1}. Spin-orbit coupling then splits these terms into J states which are typically separated by 10^3 cm^{-1}.

There are 295 $^{(2S+1)}\Gamma_J$ spectroscopic levels for the f^6 and f^8 configurations whose relative energies are predicted by Hund's rules. For both and Tb^{3+} ions, the 7F term is lowest in energy and the ground state levels are $^7F_6$ for Tb^{3+} and $^7F_0$ for Eu^{3+}.

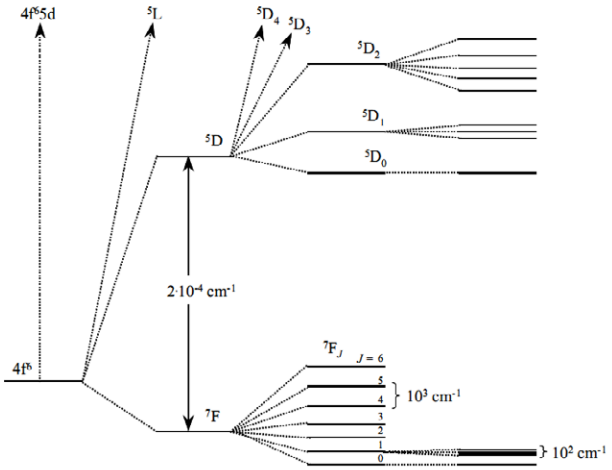

Figure I.3. Schematic energy diagram for the Eu^{3+} ions, showing the splitting of energy levels

b) Electronic transitions

As mentioned above, as a consequence of their relatively small radial extension, the 4f orbitals are effectively shielded from the environment by the $5s^25p^6$ sub-shells and are only minimally involved in bonding. This has two important effects on the lanthanide emission and absorption spectroscopy. First, ligand field splittings are very small, typically between 100 and 250 cm^{-1}. Hence, the $^7F_1$ level of the Eu^{3+} ion lies about 250 cm^{-1} above $^7F_0$. At ambient temperature it is 13% thermally populated[4] ($kT \approx 208$ cm^{-1} at 298K), and this accounts for the magnetic moment of the Eu^{3+} ion in solution. When an f-f transition occurs between the spectroscopic terms with the same $4f^n$ configuration, the spectral bands which arise are very sharp and are similar to the bands observed with the free ions. The second effect concerns the probability of such f-f transitions. Electric dipole transitions are forbidden by the parity (Laporte) selection rule, which not allows transitions among orbitals having the same symmetry.[5] However, when the lanthanide ion is under the influence of a ligand field, non-centrosymmetric interactions somewhat relax the selection rules and the forced (or induced) electric dipole transition becomes

partially allowed (see Figure I.4), resulting in long-lasting emission (lifetimes in the order of milliseconds for europium and terbium). Nonetheless, the weakness of this interaction means that the f-f transitions are characterized by very low extinction coefficients in the absorption spectra, with ε typically less than 1 $cm^{-1}M^{-1}$.

Although magnetic-dipole allowed transitions are permitted by the parity rule, they are weak and their intensity is rather insensitive to the Ln^{3+} ionic environment. This makes then a convenient internal standard when measuring emission (or absorption) intensities, for example the $^5D_0 \leftrightarrow {}^7F_1$ transition in Eu^{3+} complexes.

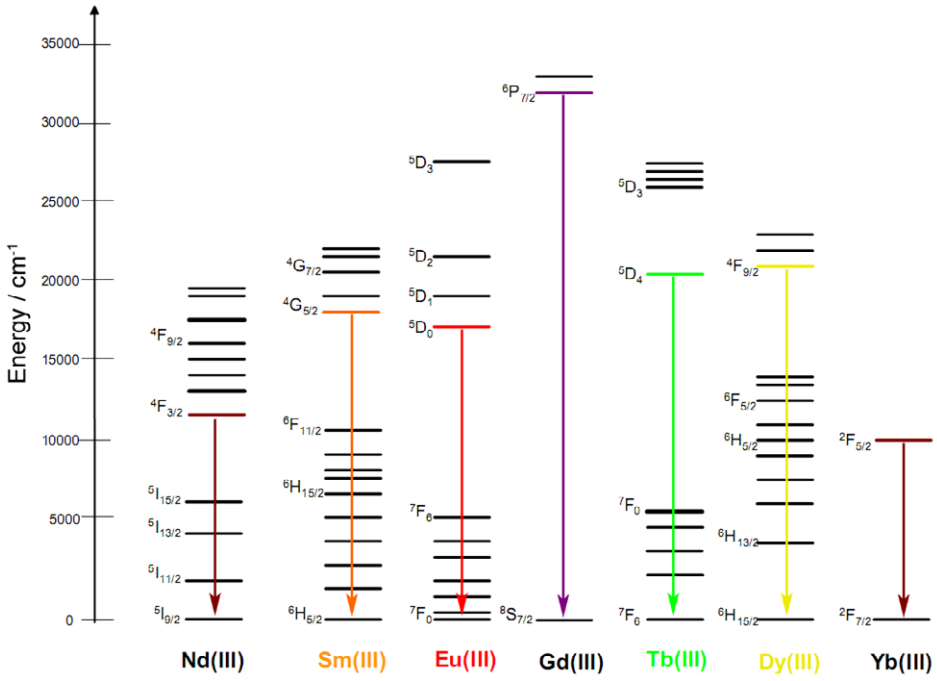

Figure I.4. Partial energy diagram for the Ln(III) ions. The main emitting levels and the transitions to the ground state levels are represented in color.

In addition to parity selection rules, other rules are operative.[5] Furthermore, a transition is only allowed if it conforms to the group theoretical rules appropriate to the site symmetry of the lanthanide ion. This is particularly evident in the case of Eu^{3+} complexes. For example, the $^5D_0 \rightarrow {}^7F_1$ transition is split in two if the complex is axially symmetric and contains a C_3 or C_4 axis. In the case of lower symmetry complexes, a splitting in three components is observed. This behavior provides very important

information regarding the symmetry around the europium ion, only by interpreting the high-resolution f-f emission spectrum.

Aside from the f-f transitions discussed above, other two types of electronic transitions are present in the lanthanide ions: the 4f-5d transitions, and the charge-transfer transitions (metal-to-ligand, MLCT, or ligand-to-metal, LMCT).[5] The promotion of a 4f electron into the 5d sub-shell is parity allowed, and the corresponding transitions are broader than the f-f transitions and their energy depends largely on the metal environment, since the 5d orbitals are external and interact directly with the ligand orbitals. The 4f-5d transitions have high energy and only those of Ce^{3+}, Pr^{3+} and Tb^{3+} are commonly observed below 45 000 cm^{-1}. Charge-transfer transitions, both LMCT and MLCT, are also allowed by the Laporte selection rule. Their energy is usually very large, so that they appear in the UV above 40 000 cm^{-1}, contrary to d-transition metal ions for which this type of transition is widespread (see Chapter IV.1.4.). One exception are the ions which can be relatively easy reduced to their +2 state (Sm^{3+}, Eu^{3+}, Tm^{3+} or Yb^{3+}), or oxidized to their +4 state (Ce^{3+}, Pr^{3+}, Tb^{3+}). In such cases, the broad charge transfer transitions may occur at energies as low as 30 000 cm^{-1} ($\lambda \approx 330$ nm).[6]

c) Luminescence

One of the most interesting features of trivalent lanthanide ions is their luminescence. Luminescence is defined as emission of light from an electronically excited state usually produced by excitation with light (photoluminescence), electric current or electric field (electroluminescence), or by a chemical or biochemical reaction (chemi- or bio-luminescence), to name a few. Depending on the spin of the initial (emitting) and final (usually ground) states, two categories of emission are distinguished: fluorescence for transitions without spin change ($\Delta S = 0$) and phosphorescence for transitions with spin change ($\Delta S \neq 0$). With the exception of La^{3+} and Lu^{3+}, all the trivalent lanthanide ions are luminescent and their f-f emission lines cover the entire spectrum, from UV (Gd^{3+}) to visible (e.g. orange Sm^{3+}, red Eu^{3+}, green Tb^{3+}, yellow Dy^{3+}) and near-infrared (e.g. Nd^{3+},

Yb^{3+}), as seen in Figure I.4 and Figure I.5. Some ions are fluorescent, others are phosphorescent, and some are both.

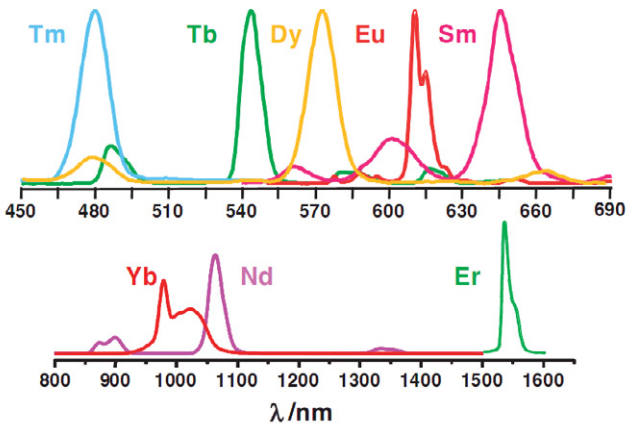

Figure I.5. Emission spectra of some lanthanide complexes (from ref.[7])

The f-f emission lines are sharp because the rearrangement following the promotion of an electron into a 4f orbital of higher energy does not disturb much the excited state geometry. Therefore the inter-nuclear distances remain almost the same, which leads to narrow bands and very small Stokes' shifts. A different situation is observed in organic molecules, where the excitation frequently leads to a lengthening of the bond distances, resulting in large Stokes' shifts and broad emission bands (see Figure I.6).

The resonance energy levels of the europium, terbium and neodymium ions are listed in Table I.1 along with the various luminescence transitions.

Table I.1. Energy levels and luminescence transitions for selected lanthanide ions[3]

	Emissive level	Final levels	Emission wavelength / nm
Eu^{3+}	$^5D_0$ (17 260 cm^{-1})	^7F_J (J = 0..6)	580, 590, 615, 650, 720, 750, 820
Tb^{3+}	$^5D_4$ (20 500 cm^{-1})	^7F_J (J = 6..0)	490, 540, 580, 620, 650, 660, 675
Nd^{3+}	$^4F_{3/2}$ (11 300 cm^{-1})	^4I_J (J = 9/2..13/2)	900, 1060, 1350

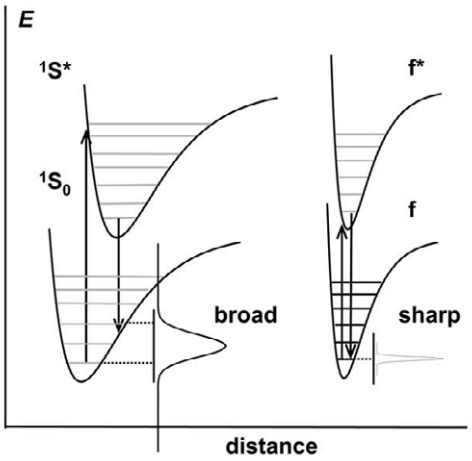

Figure I.6. Configurational coordinate diagram for emission from both an organic chromophore (left) and a lanthanide ion (right); taken from ref.[8]

I.2. Sensitization of lanthanide luminescence

I.2.1. The antenna effect

Since the molar absorption coefficients of the f-f transitions are very low, direct excitation into the 4f excited levels rarely gives highly luminescent materials, even if the intrinsic quantum yield is large, unless considerable excitation power is used, by means of lasers. Fortunately, an alternative path has been developed which is called *luminescence sensitization* or *antenna effect*.

Weissman first noticed[9] that the emission of lanthanide ions could be more easily observed when these ions were coordinated to aromatic carboxylic acids, β-diketones and alcohols. He correctly interpreted this phenomenon as an energy transfer from the ligand to the metal ion, in a sensitization process.

The commonly accepted mechanism of energy transfer from the organic ligand to the lanthanide ion is that of Crosby and Whan,[5] and generally occurs in three steps: (i) light harvesting by the host or ligands, (ii) energy transfer onto the metal ion, and (iii) metal-centered emission. A simplified scheme of these energy transfers is given in Figure I.7. The overall process is quite complex and involves several mechanisms and energy levels. Its optimization is crucial to the overall luminescence yield that can be obtained. In addition to providing an efficient path for the excitation of lanthanide ions, this sensitization

process has also the advantage that now the Stokes' shifts are very large, which allows an easy spectral separation of the remaining matrix luminescence from the metal ion emission.

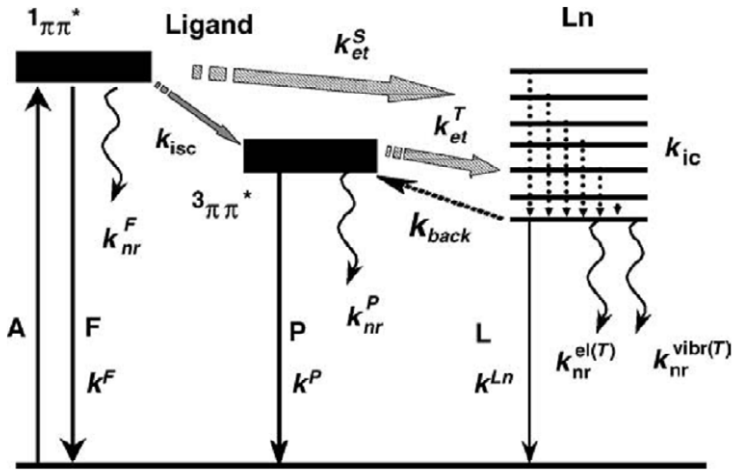

Figure I.7. Simplified diagram showing the sensitization process in a lanthanide complex (from ref.[10])

Upon irradiation with ultraviolet light, the organic ligands of the lanthanide complex are excited to a vibrational level of the first excited singlet state. The molecule undergoes fast internal conversion to lower vibrational levels of the excited singlet state, for instance through interaction with solvent molecules. The excited singlet state can be deactivated radiatively to the ground state (molecular fluorescence), or can undergo non-radiative intersystem crossing (ISC) from the singlet state to the triplet state. The triplet state can be deactivated radiatively to the ground state by a spin-forbidden transition, which results in molecular phosphorescence. Alternatively, the complex may undergo a non-radiative transition from the triplet state to an excited state of the lanthanide ion. After this indirect excitation by energy transfer, the lanthanide ion may undergo a radiative transition to a lower 4f-state by characteristic line-like photoluminescence, or may be deactivated by radiationless processes.

Luminescence by the lanthanide ion is only possible from certain levels, that are termed resonance levels. If the lanthanide ion is excited to a non-emitting level, either directly by excitation in the 4f-levels or indirectly by energy transfer, the excitation energy is dissipated via radiationless processes until a resonance level is reached.

Energy transfer from the antenna to the metal center can in principle take place from both the singlet and triplet states and may be phonon-assisted. However, energy transfer from short-lived singlet state is usually not efficient. Thus classical qualitative considerations on the ligand-to-metal energy transfer take solely the energy of the triplet state into consideration. Two mechanisms[5] are usually invoked for the $^3\pi\pi^*$-to-Ln^{3+} energy transfer: (i) Dexter's (or exchange) mechanism, which involves a double electron transfer, requires a good overlap between the ligand and metal orbitals and thus displays a strong dependence in e^{-r} upon the donor-acceptor distance r; and, (ii) Förster's (or dipole-dipole) mechanism in which the dipole moment associated with the triplet state couples with the dipole moment of the 4f orbitals (Figure I.8). The yield of this transfer is proportional to the overlap integral J between the emission spectrum of the donor (ligand triplet state) and the absorption spectrum of the acceptor (Ln^{3+} center) and operates through space with a r^{-6} distance dependence.

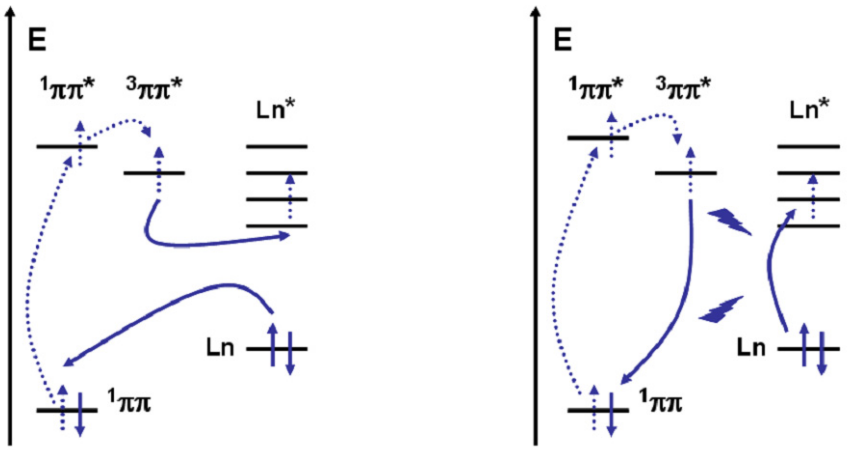

Figure I.8. Schematic representation of the Dexter (left) and Förster (right) energy transfer mechanisms

In addition, dipole-multipole transfers play non-negligible role in the sensitization of lanthanide ions. Due to their respective dependence upon the donor-acceptor distance, Dexter's and the multipolar mechanisms operate at shorter range than the dipole-dipole mechanism. Therefore the preferred mechanisms for energy transfer from the ligands to

the metal ion is by dipole-dipole transfer, which extends over much longer distances (up to 10 Å).

Apart from the sensitization through organic chromophores, energy transfer from d-transition metal levels or MLCT states, or from the excited state of another lanthanide ion may be possible. This strategy is particularly adapted for the sensitization of ions emitting in the near-infrared. Such cases will be discussed later in Chapter I.2.6. Furthermore, in the case of Yb^{3+} excitation, more elaborate mechanisms are operative, involving either a phonon-assisted transfer or a double electron exchange mechanism in which the ytterbium ion is momentarily reduced into its divalent oxidation state.[8]

I.2.2. Luminescence efficiency and quenching processes

The two important parameters characterizing the emission of light from a lanthanide ion are the lifetime of the excited state $\tau_{obs} = 1/k_{obs}$ and the quantum yield Q. The overall quantum yield Q is defined as the ratio between the number of emitted photons over the number of absorbed photons, and is related to the intrinsic quantum yield Q_{Ln}^{Ln}, which depends on the rate at which the excited level is depopulated k_{obs} and on the radiative rate constant k_{rad}

$$Q = \eta_{ISC}\eta_{ET}\, Q_{Ln}^{Ln} = \eta_{sens}\, Q_{Ln}^{Ln} = \eta_{sens}\left(\frac{k^{rad}}{k_{obs}}\right) = \eta_{sens}\left(\frac{\tau_{obs}}{\tau^{rad}}\right) \qquad \text{I.1}$$

The first two contributions (η_{ISC} and η_{ET}) relating the overall and the intrinsic quantum yield depend on the ligand and can be grouped in one term called η_{sens}, namely the overall efficiency of the ligand-to-metal energy transfer. Considering the above equation, it is clear that optimal sensitization of the lanthanide-centered luminescence can only be achieved by maximizing the efficiency of both intersystem crossing (ISC) and energy transfer (see Chapter I.2.3.).

Determination of the overall quantum yields Q is not an easy task. The measurement of *absolute* quantum yields is critical and requires special equipment, because it is necessary to know the amount of excited light received by the sample. These measurements are done by the use of scattering agents and integrating spheres to calibrate the system. For routine

work, one is often satisfied with the determination of *relative* quantum yields. In this case the quantum yield of the unknown sample is compared with that of a reference sample, for which the absolute quantum yield has been previously determined.

The intrinsic quantum yield is the quantum yield of the metal-centered luminescence upon direct excitation into the 4f levels, and its value reflects the extent of non-radiative deactivation processes occurring both in the inner- and outer-coordination spheres of the metal ion. The rate constant k_{obs} is the sum of the rates of the various deactivation processes

$$k_{obs} = k^{rad} + \sum_n k_n^{nr} = k^{rad} + \sum_i k_i^{vibr}(T) + \sum_j k_j^{pet}(T) + \sum_k k'^{nr}_k \qquad \text{I.2}$$

where k^{rad} and k^{nr} are the radiative and nonradiative rate constants, respectively; the superscript *vibr* indicates the vibration-induced processes while *pet* refers to photo-induced electron transfer processes such as those generated by LMCT states. The rate constants *k'* are associated with the remaining deactivation paths. These processes may be divided into two classes: vibration activated and electronic processes.

Deactivation through vibrations is especially effective and represents a major concern in the design of both inorganic and organic edifices.[11] In aqueous solutions, interaction with water, both in the inner and outer coordination spheres of the Ln^{3+} ion, leads to a significant quenching of the metal luminescence via O-H vibrations. The intrinsic quantum yield essentially depends on the energy gap ΔE between the lowest lying excited (emissive) state of the metal ion and the highest sublevel of its ground multiplet.[12] The smaller this gap, the easier non-radiative deactivation processes occur, for example through vibrations of bound ligands, particularly those with high energy vibrations such as O-H, N-H or C-H. This type of non-radiative processes are particularly detrimental to near-infrared (NIR) luminescence.[8]

In a similar way, electronic deactivation processes, such as energy back transfer and photon-induced electron transfer (PET), have to be avoided by an adequate design of the ligand. Indeed, Tb^{3+} luminescence is particularly sensitive to energy back transfer, where the energy is given back to the ligand triplet state by the metal ion. This

phenomenon takes place only when both levels lie in close proximity and is generally assisted by vibrations, being thus strongly temperature-dependent (Arrhenius-type dependence of the lifetime in function of T). There is no easy method to circumvent energy back transfer, except to change the ligand design in a way that the triplet state is sufficiently away from the emissive state. When a molecule is excited, its electron donor or electron acceptor properties are modified, so that an electron transfer, not feasible in the ground state, may become possible upon photo-excitation. PET processes from the ligand to the metal ion thus result in a reduction of Ln^{3+} into Ln^{2+} with a concomitant quenching of the metal-centered luminescence.[13]

I.2.3. Predicting efficient antennas for lanthanides

We have seen in the previous chapters how the weakly-absorbing lanthanide ions can be efficiently excited by coordinated chromophore-containing ligands which, upon irradiation, transfer energy to the metal center, typically via the ligand triplet excited state, and populate the Ln^{3+} emitting levels in a process known as the antenna effect.

It is not obvious whether the energy transfer occurs from an excited $^1\pi\pi^*$ singlet or $^3\pi\pi^*$ triplet state. However, Malta *et al.* have shown with a theoretical model that in several cases the energy transfer from the singlet level of the ligand to the emitting level of Ln^{3+} is not important.[14, 15] The triplet state thus plays a leading role in the intensity of the luminescence, which is also confirmed by experimental evidences. An empirical rule, hereafter called the energy-gap rule, states that the total luminescence quantum yield decreases due to an energy back-transfer when the energy difference between the lowest triplet state of the ligand and the emitting level of the metal is small. This is in particular supported by the extensive study[16] of Latva *et al.* which has clearly shown in the case of terbium complexes a correlation between the lowest $^3\pi\pi^*$ energy level of the ligand and Tb^{3+} luminescence quantum yield. The empirical rule states that a high luminescence quantum yield is unlikely to be observed if the energy gap between the $^3\pi\pi^*$ level of the ligand and the excited Tb($^5D_4$) level is less than about 1 850 cm^{-1}. In the case of europium complexes, the correlation between the energy levels of the $^3\pi\pi^*$ state and the

luminescence quantum yield is less convincing. As a matter of fact, the presence of other ^5D_J resonance levels higher than the emitting $^5D_0$ level is probably responsible for the dispersion of the results. Nonetheless, Latva has concluded that the highest quantum yields are obtained when the energy difference between the first state of the ligand and the emissive Eu($^5D_0$) level is around 2 500 or 4 800 cm^{-1}, the two maxima being situated in between the resonance levels of Eu^{3+}. This observation is also supported by the study of Sato and Wada[17], who have observed that the luminescence quantum yields of the Eu^{3+} β-diketonate chelates decrease when the energy of the ligand triplet state approaches either the Eu($^5D_2$) or Eu($^5D_1$) level. Conversely, the maximum quantum yield was obtained when the $^3\pi\pi^*$ state energy was between these two ^5D_J levels. More recently, Arnaud and Georges[18] have compared the luminescent properties of europium and terbium complexes with the values reported by Latva. They have shown again that the luminescence lifetimes are closely related to the energy gap between the ligand triplet and the resonance energy levels of the metal ion. Archer *et al.* also found results[19] consistent with the triplet state channel since they obtained very low quantum yields for europium complexes with a ligand $^3\pi\pi^*$ energy below the $^5D_0$ level. Guillaumont *et al.* have recently looked at the properties of unsubstituted and substituted tris-bipyridine lanthanide cryptates,[20] both experimentally as well as theoretically, but failed to see significant differences in the photophysical properties of the complexes. In a very recent report,[21] the group of Raymond probed the effect of substitution on 2-hydroxy-isophthalamide ligands for terbium, finding that the energies of the $^1\pi\pi^*$ and $^3\pi\pi^*$ states increase linearly with the π-withdrawing ability of the substituent (delineated by R, the resonance component of the Hammett parameter[22]), in the order OCH_3 < F < CH_3 < Cl < Br < H < SO_3^- < CONHR. Furthermore, the quantum yield of the terbium complexes increased with the $^3\pi\pi^*$ state energy, due to a decrease of non-radiative deactivation. A similar conclusion has been drawn by Corrales *et al.*, who compared the TDDFT-calculated excited state energies of terbium β-diketonates with the experimental quantum yields.[23]

Recently, in a combined experimental/theoretical work on nine-coordinated lanthanide podates published by the Bünzli group,[24] arguments on the $^1\pi\pi^* \rightarrow ^3\pi\pi^*$ ISC

have been given by considering the vertical energy gap calculated in the ground state geometry. As a matter of fact, it is assumed that a large energy gap of 5000 cm^{-1} is required for an efficient ISC.[25]

Although we have underlined the important role of the lowest $^3\pi\pi^*$ state of the chelating ligand, other factors can strongly influence the Ln(III) luminescence and even overcome the triplet state factor. Quenching mechanisms induced by the presence of solvent molecules in the first solvation sphere or by ligand-to-metal charge transfer (LMCT) states are also known to be of great importance.[26] In this latter case, which is very likely to occur for europium complexes, the triplet state is very little populated since there is a competition with the LMCT states. In spite of the presence of other factors influencing the luminescent properties of lanthanide complexes, the antennas should be cautiously designed in order to have a triplet state energy slightly above the emitting level of the lanthanide ion. Although this is not a sufficient condition, it is a necessary one for obtaining efficient luminescent lanthanide complexes.

I.2.4. Design of highly luminescent lanthanide complexes

In designing a convenient chemical environment for a luminescent lanthanide ion, several main requirements have to be taken into account.[6]

The first one is a chemical constraint, related to the coordination cavity which should provide enough donor atoms to saturate the coordination number requirement of the Ln^{3+} ion. Contrary to d transition-metal complexes, coordination numbers are usually large in the absence of sizable sterical hindrance, in the range of 6-12 with a predominance for CN 8-10 (*vide supra*). The ligand must therefore possess an adequate number of donor atoms, otherwise solvent molecules will complete the coordination sphere. Water molecules in the inner coordination sphere deactivate the Ln^{3+} excited states non-radiatively and quench the luminescence. In the same time, the strength of the Ln-ligand interaction has to be maximized, for ensuring a good thermodynamic stability and, when necessary for biological applications, also kinetic inertness. Because lanthanide ions are rather hard cations, with chemical bonds having large electrostatic components, anionic

ligands, which bear either oxygen- or nitrogen-donor atoms, will be preferred. The size of the resulting chelating ring has also an influence, in that five-membered rings result in more stable complexes.[27]

The second requirement is related to the efficiency of the sensitization process. The ligand (or the chromophore connected to it, which acts as an antenna) has to have a strong absorption (high extinction coefficient ε) in the desired spectral region. In the same time, a fast inter-system crossing is necessary to ensure the aromatic triplet is populated efficiently, minimizing ligand fluorescence. Moreover, the energy levels of the ligand should be matched to the emitting levels of the lanthanide ion, considering the phenomenological rules (*vide supra*), in order to maximize the energy transfer mechanism.

The third requirement deals with minimizing non-radiative deactivation processes. This is a delicate problem, which is particularly acute for NIR-emitting ions (small energy gap), since it implies eliminating high-energy vibrations such as O-H, N-H or C-H from the first and the second coordination spheres. Whereas O–H and N–H vibrations can be reasonably well dealt with, for example by replacement of water molecules by non O-H donors in β-diketonate ternary complexes[28] or by substitution of N-H by N-Me demonstrated for quinoline-based podants,[29] C-H vibrations are much more difficult to eliminate. In the case of Er^{3+} luminescence, the chemical environment of the emitting ion must be devoid of C-H vibrators up to a distance of 2 to 3 nm for the radiative rate constant to be larger than the non-radiative one.[8]

Finally, additional requirements may exist depending on the specific applications envisaged, for instance stability in biological fluids if the complex is to be used as an analytical sensor, or evaporability and solubility in chlorinated organic solvents in the case of applications in organic light emitting diodes.

Accordingly, the quest for highly luminescent lanthanide complexes has spurred a large number of studies directed to identify chromophores capable of effectively sensitize the photo- or the electroluminescence of visible and NIR emitting lanthanide ions. The most studied chromophores[30] are N-heterocyclic ligands including pyridine, bipyridine, terpyridine, phenanthroline, benzimidazole, pyrazole, oxazoline, hydroxyquinoline,

azaxanthone, triazophtalazine, tetraazatriphenylene etc. In order to afford highly stable complexes and to prevent non-radiative deactivation, these chromophores have been included in neutral macrocyclic or chelate ligands and associated to β-diketonated ligands in ternary complexes or to carboxylates in polydentate ligands.[12, 31] Excitation of the Ln^{3+} ion by a d-transition metal ion or another f lanthanide ion is an alternative to chromophore-substituted ligands, and proof of principle has been demonstrated for several systems,[32, 33] in which the inter-metallic communication was used as a means to sensitize the luminescence of lanthanide ions. The following two sub-chapters will give a short overview of the most important progress in the field.

I.2.5. Sensitization of lanthanide luminescence by chromophores

One of the simplest chromophoric units is the picolinate, which has been extensively used for the sensitization of lanthanide emitters. The dpa ligand **I** (dpa = 2,6-pyridinedicarboxylic acid) forms a well-studied,[34-37] propeller-shaped complex $[Ln(dpa)_3]^{3-}$ which is 9-coordinate with either Δ or Λ chirality at the metal center. Good luminescence properties have been obtained with the tris-dipicolinate complexes $Cs_3[Eu(dpa)_3]$ and $Cs_3[Tb(dpa)_3]$, proposed as references for the determination of relative quantum yields.[38] In water at pH 7, their quantum yields amount to 24% and 22%, respectively,[39] however the complexes have a rather small stability in solution. In our laboratory, we have described an efficient way of assembling four picolinate chromophores into a tetrapodal multidentate ligand (tpaen, **II**) that yields ten-coordinate, highly luminescent and water-stable lanthanide complexes, with quantum yields of emission of 7% and 45%, respectively, for the Eu^{3+} and Tb^{3+} ions.[40]

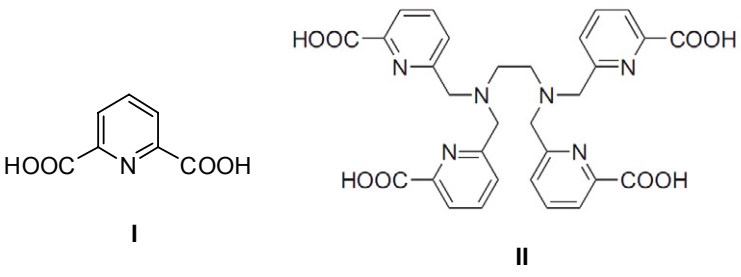

I **II**

Scheme I.1. Picolinate-based ligands

The bidentate ligand bipyridine (bipy) is also an efficient chromophore for the sensitization of visible lanthanide luminescence. The cryptate of Lehn **III** bas been used commercially as a luminescent probe for more than 20 years.[41] Ziessel, Bünzli and their collaborators[42] have studied different ligands **IV** derived from the bipy unit, appended with anionic groups (COOH, PO_3H_2) for increased stability. They have shown that despite an important energy difference between the triplet states of the ligands and the emissive states of the Eu^{3+} and Tb^{3+} ions, the luminescence of the lanthanides is well sensitized, particularly that of terbium, with a quantum yield of 46% in water. However, none of the complexes were isolated in solid state. De Cola has modified the ligand structure with the introduction of a phenyl group in **V**, which resulted in lowering the triplet state of the chromophore and improved luminescence for the Eu^{3+} ion, to the detriment of the Tb^{3+} emission (quantum yields of 60% and 7%, respectively, in acetonitrile).[43]

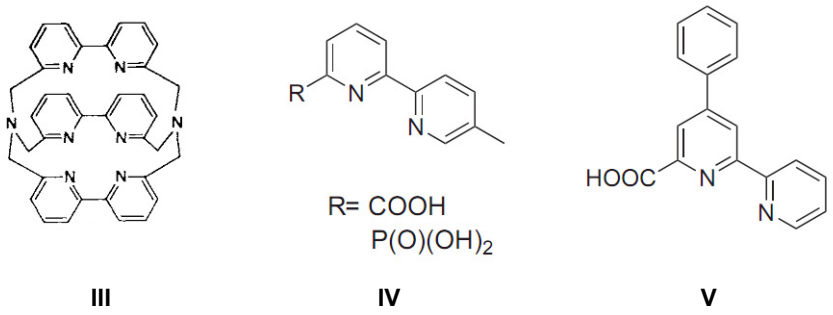

III **IV** **V**

Scheme I.2. Bipyridine-based ligands

Charbonnière and Ziessel have also included the bipyridine-carboxylate chromophore in a series of podating architectures **VI**-**VIII**.[44, 45] The luminescence efficiencies of the lanthanide complexes of **VI** are affected by the presence of one molecule of water (quantum yields of 8% and 31% for the europium and terbium complexes in water solutions, respectively, compared to 35% and 53% in deuterated solvent). The extensive synthetic effort put in the synthesis of various similar architectures with increased denticity (**VII**) has not resulted, however, in improved photophysical properties.

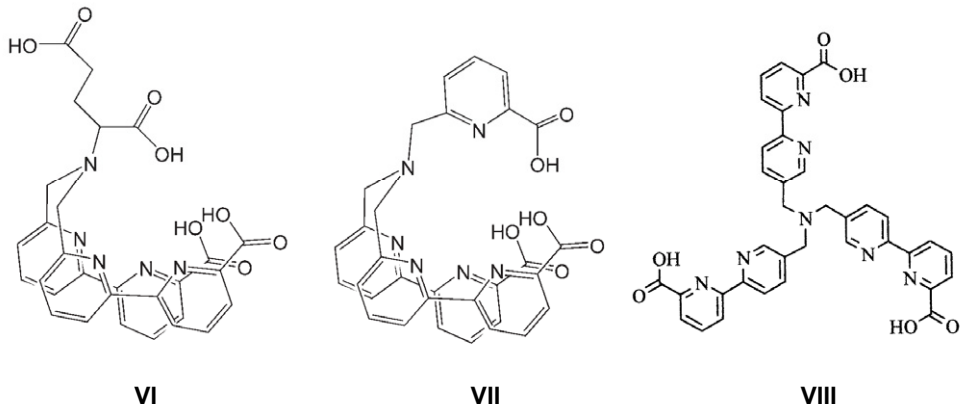

VI VII VIII

Scheme I.3. Bipyridine-carboxylate based podates

The tridentate terpyridine unit (terpy) has also been largely studied and very luminescent systems based on the $[Ln(terpy)_3]^{3+}$ motif have been developed by Bünzli and co-workers.[46] They have shown that 4,4' and 4"-substitution of the terpyridine with electron-donating t-butyl and ethyl groups in **IX** accelerates the inter-system crossing and consequently increases the quantum yields of the complexes, up to 67% in anhydrous acetonitrile in the case of $[Tb(t\text{-}Bu\text{-}terpy)_3]^{3+}$, compared to only 5% for the unsubstituted complex. Replacement of terminal pyridine units by benzimidazole groups in the ligand mbzimpy (**X**) and its $[Ln(mbzimpy)(NO_3)_3(CH_3OH)]$ complexes resulted in luminescent properties measured in acetonitrile similar to those of complexes $[Ln(terpy)_3]^{3+}$.[47, 48]

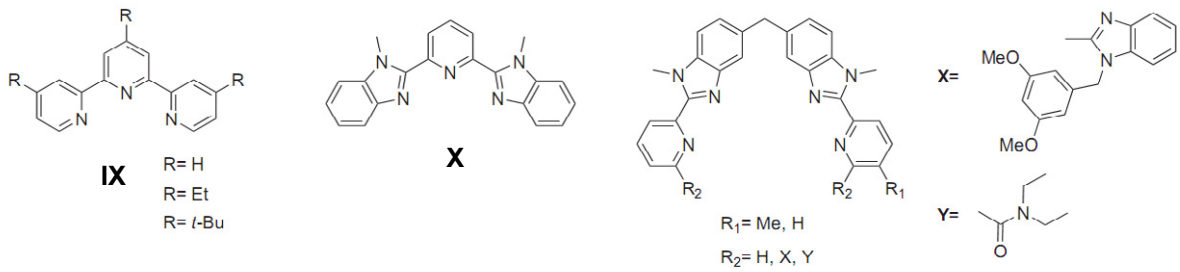

Scheme I.4. Terpyridine and benzimidazole based ligands

One of the big advantages of the pyridine-benzimidazole unit is the versatility of its chemistry. The architecture and geometry of the ligand has been carefully modified to allow the self-assembly of luminescent d-f and f-f helicates.[49] Charbonnière and his

collaborators studied the effect of substitution in the 4' position of the terpyridine chromophore in a series of complexes of the formula [Eu(terpy)(TTA)$_3$] containing β-diketonates (TTA) as secondary ligands.[50] The best results were obtained with a strongly donating dimethylamine substituent, for which the europium emission efficiency is 20% in dichloromethane. Replacement of the terpyridine unit by a bis-pyrazolyl-triazine proved damaging for the photophysical properties, resulting in an europium quantum yield of only 1%.

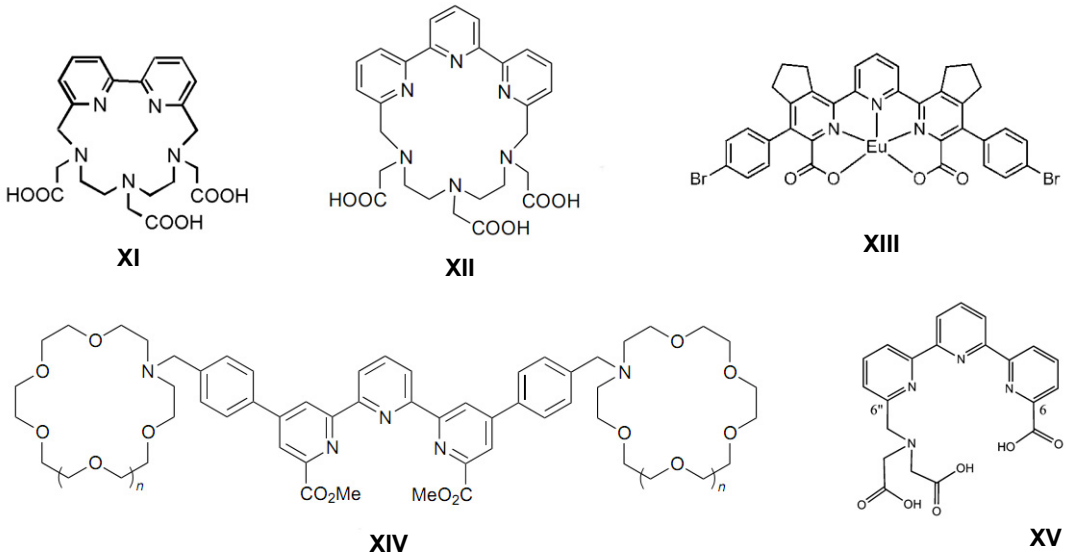

Scheme I.5. Terpyridine-carboxylate based ligands

Various terpyridine and bipyridine ligands with appended with methylenenitrilo-bis-acetic acid groups have been synthesized by Mukkala,[51, 52] which form highly emissive lanthanide chelates with long luminescence lifetimes, particularly useful for the development of bioprobes. Triazamacrocyclic ligands incorporating bipyridine (**XI**) and terpyridine units (**XII**) have been designed and studied by Picard and co-workers,[53, 54] and show very good lanthanide sensitization properties as well as an excellent stability in solution, which makes them suitable for in-vivo use. The bipyridine-based complexes can also be used as bimodal (luminescence and paramagnetic) systems, due to the good relaxivity of the gadolinium chelate. Terpyridine-dicarboxylate based complexes (**XIV**) have been prepared by de Silva *et al.* as sensors for alkaline metals and protons,[13, 55]

however the presence of water molecules in the structures of the 1L:1M species resulted in very low quantum yields (around 3% for the europium complexes). A similar motif was used by Kozhevnikov and his co-workers, who prepared a luminescent europium complex **XIII** containing 4 water molecules in the first coordination sphere of the metal, with a quantum yield of 33% in deuterated water.[56] This complex was later used by De Cola for the formation of a heterometallic iridium-europium assembly,[57] in which the iridium moieties, appended with carboxylate units, displace the water molecules and coordinate to the europium ion (see Chapter IV.2.1.). A dissymmetrical 6,6'-anionic functionalized terpyridine ligand **XV** has been prepared by Charbonnière and Ziessel.[58] The coordination of the lanthanide ion is completed by two water molecules, leading to reduced efficiencies, especially for the europium complex (only 7% compared to 22% for the terbium complex).

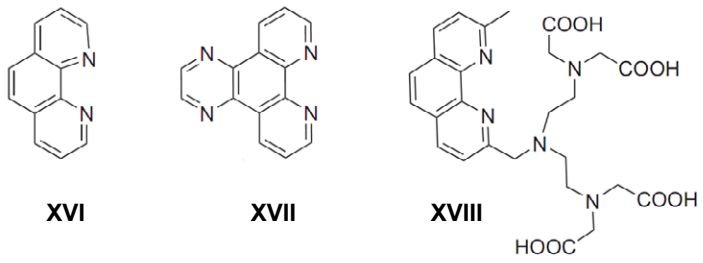

Scheme I.6. Phenantroline-based ligands

The 1,10-phenantroline (phen, **XVI**) chromophore is also a very efficient sensitizer, especially when coupled with the strongly donating β-diketonate ligands in tetradentate complexes,[59] which are particularly used for the development of materials for optoelectronic devices (see Chapter III.1.).[60, 61] Tetraazatriphenylenes ligands **XVII** derived from phenantroline have been synthesized by Reinhoudt, Verhoeven and their collaborators. The ligands form 2:1 complexes with very high quantum yields,[62] reaching 67% and 43% for the terbium and europium ions, respectively, in acetonitrile solutions. Phenantroline was also attached to the macrocyclic platforms DTTA (**XVIII**) or DO3A,[63] giving luminescent, water-soluble chelates with quantum yields in deaerated water

solutions of 24% and 45% for the europium and terbium ions, respectively. Both nitrogens of the phenantroline bind to the metal center, resulting in an overall coordination number of 9. For the near-infrared emitters, the system was less efficient, the best quantum yields being obtained for the ytterbium ion in deuterated water (0.1%).

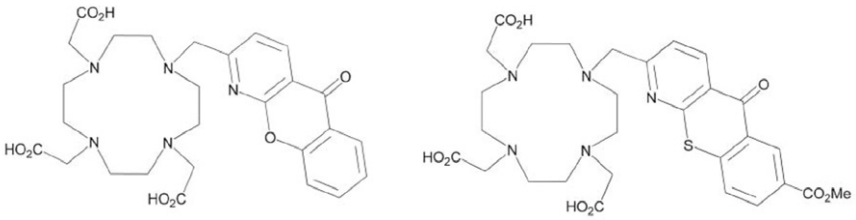

XIX **XX**

Scheme I.7. Azaxanthones and azathioxanthones based macrocycles

Parker and his co-workers studied DO3A-derivatized azaxanthones (**XIX**) and azathioxanthones (**XX**) as sensitizers of Eu^{3+} and Tb^{3+} luminescence.[64, 65] The resulting complexes posses one water molecule, with quantum yields reaching 9% for europium and 24% for terbium. These relatively low values are attributed to reduced ISC efficiency, as indicated by the residual fluorescence of the ligands and the energy mismatch between triplet and emissive states, which results in energy back-transfer in the case of the Tb^{3+} complex.

Podating ligands based on the hydroxyquinoline chromophore substituted with amide substituents (**XXI**) have been developed by Albrecht *et al.* especially for the sensitization of NIR emitters.[66] The tridentate ligands lead to the formation of 3L:1M complexes having high quantum yields, which are increased by a factor of 2.5-3 upon substitution by bromine atoms, reaching 0.40 and 1.40% in solid state for neodymium and ytterbium, respectively. The complexes can be excited in the visible range, up to 550-570 nm. The hydroxyquinoline chromophore has also been introduced in a podating architecture by Imbert and co-workers,[67] which results in large stability constants for the complexes in water. Methylation of the amide hydrogen in **XXII** decreases slightly the stability, however the sensitization abilities are superior, the neodymium and ytterbium

complexes displaying quantum yields of 0.03 and 0.13% in water, respectively. Recently, Petoud and collaborators[68] used the azulene-based ligand **XXIII** for the formation of ML_4 complexes with the NIR-emitting lanthanide ions, which display some of the highest efficiencies in solution (3.8% and 0.45% in acetonitrile for ytterbium and neodymium, respectively).

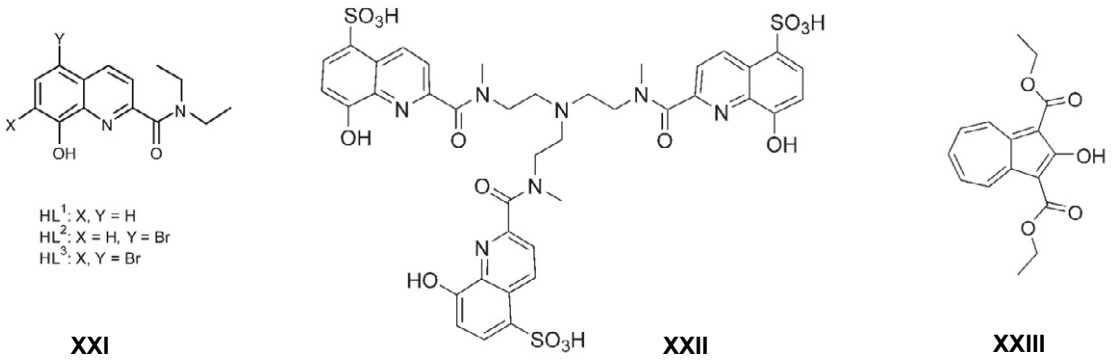

Scheme I.8. Hydroxyquinoline and azulene based ligands

I.2.6. Sensitization of lanthanide luminescence by other metals

The synthesis of hetero-polymetallic d-f complexes is well documented and understood because the two types of metal ions display highly different stereochemical preferences.[8, 12] Valence d-orbitals are external and interact strongly with ligand orbitals, whereas the shielding of 4f-orbitals by the filled $5s^2$ and $5p^6$ sub-shells results in spherical Ln^{3+} ions which bind electrostatically with organic ligands. Hetero-polymetallic d-f molecular edifices are appealing because of several reasons.[33] Transition metal complexes have strong MLCT absorption maxima extending far in the visible region, allowing the sensitization of lanthanide ions (and especially the NIR emitters) by low energy radiation. The heavy d-metal ion effect facilitates the ISC and gives a high triplet quantum yield for the energy donor, while the relatively-long lived excited states facilitate energy-transfer to the lanthanide ion. As lanthanides themselves have poor redox properties, the addition of a redox-active antenna containing d-metal complexes improves the electrical excitation of the f-metal in optoelectronic devices, and could allow the construction of sophisticated redox and optically active edifices.

Three types of inter-metallic interactions have been evidenced: mechanical coupling, interactions based on orbital overlap, and electrostatic communication. Intermolecular mechanical coupling between metallic centers is well established, particularly for Fe^{2+} containing discrete oligomers in which the triggering of the iron spin-crossover properties has been demonstrated in hetero-bimetallic triple-stranded helicates.[69] Orbital overlap (Dexter mechanism) is also route for inter-metallic interaction; when 4f elements are involved though, the distance between the two metal ions must be short because the 4f-nd coupling is very small in view of the limited expansion of the 4f orbitals. This type of interaction is mainly involved in magnetic coupling (e.g., between Cu^{2+} and Gd^{3+}), although it may also influence the flow of energy between the two metal ions.[70] Finally, long-distance energy transfer processes often occur via multipolar (Forster) through-space mechanisms and both 4f→3d and 3d→4f energy transfer processes have been evidenced.[12]

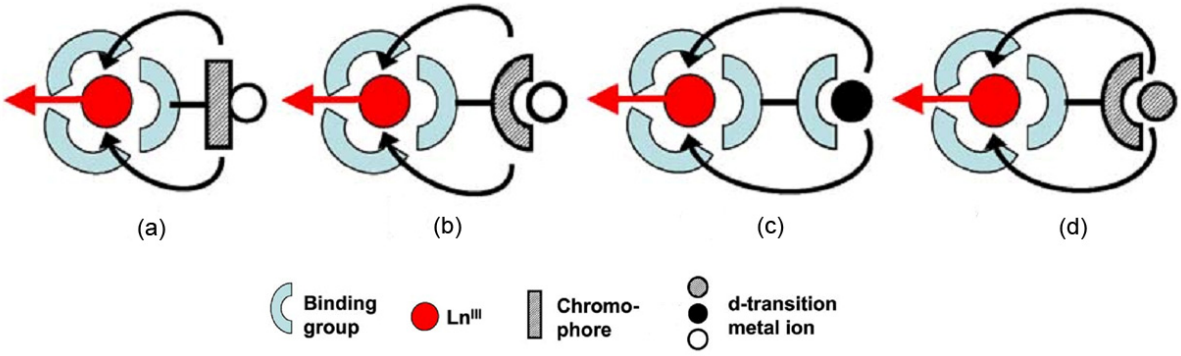

Figure I.9. Various roles of the d metal in d-f heterometallic architectures (from ref.[8])

The various roles of d-transition metal ions in the elaboration of lanthanide-containing luminescent edifices[8] are shown in Figure I.9. In the first case (a), the transition metal ion is a component of the ligand but assumes no essential role, apart from stabilizing and rigidifying the ligand structure. In the second situation (b), transition ion complexation affects the electronic properties of the ligand, allowing a better energy transfer or a more convenient excitation mode. In the third case (c), directional energy transfer from the d-transition metal ion populates the excited state of the 4f ion, therefore

controlling its photophysical properties. The latter two situations can be combined in the last example (d), where complexation of the d-transition metal ion induces ligand-to-metal charge transfer states which will transfer energy to the 4f ion.

Veggel and coworkers published in 2000 a seminal paper in which they described the use of either ferrocene or $[Ru(bipy)_3]^{2+}$ units, covalently attached to Yb^{3+} or Nd^{3+} polycarboxylate complexes.[71] In both cases (Scheme I.9) excitation of the d-block chromophore resulted in the appearance of sensitized NIR luminescence from neodymium or ytterbium, with characteristic lifetimes in the microsecond domain. The low-lying triplet state of ferrocene (ca. 13 300 cm^{-1}) in particular is a good match for the energy-accepting luminescent states of Nd^{3+} (11 300 cm^{-1}) and Yb^{3+} (10 200 cm^{-1}). The ^{3}MLCT state of $[Ru(bipy)_3]^{2+}$ at ca. 17 400 cm^{-1} is quite remote in energy from the Yb^{3+} excited state, but overlaps with many of the higher-lying Nd^{3+} based states which could act as initial energy-acceptors before internal conversion of Nd^{3+} to the emissive $^4F_{3/2}$ state. Consequently, the Ru→Yb energy-transfer was found to be inefficient and at least an order of magnitude slower than Ru→Nd energy-transfer. The relatively slow energy-transfer rates are also a consequence of the high metal-metal distances, and the absence of a conjugated pathway between donor and acceptor, which hinders any energy-transfer that is occurring via a double electron exchange (Dexter) process.

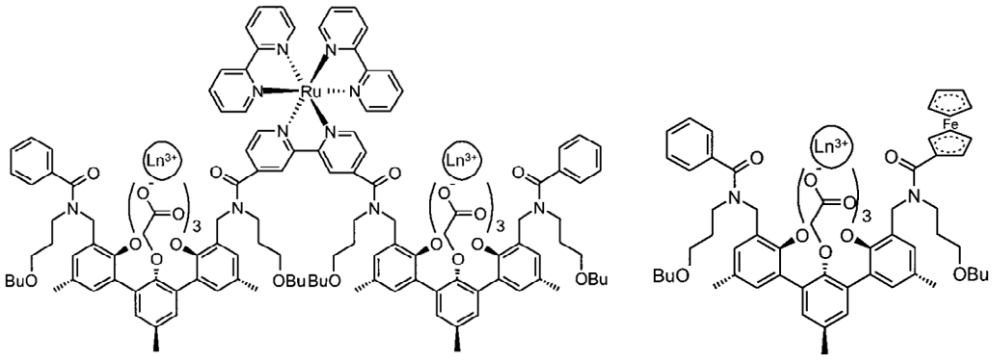

Scheme I.9. Ruthenium tris-bipyridine and ferrocene based complexes studied by Veggel

Faulkner and co-workers have extended this principle to the use of other d^6 polypyridyl complexes of Ru^{2+}, Re^{+} and Os^{2+} as sensitizers in both covalently and non-

covalently linked polynuclear assemblies (Scheme I.10).[72, 73] The presence of the lanthanide ion in the DTPA binding site quenches the emission of the d-block unit as a result of d→f energy-transfer, with a concomitant reduction in the luminescence lifetime. Notably, the $[Os(bipy)_3]^{2+}$ unit allows excitation wavelengths as low as 700 nm, while the Os→Ln energy transfer was faster than the Ru→Ln energy transfer, presumably because the low ^{3}MLCT state of the osmium complex provides a better match with the lanthanide emissive state.

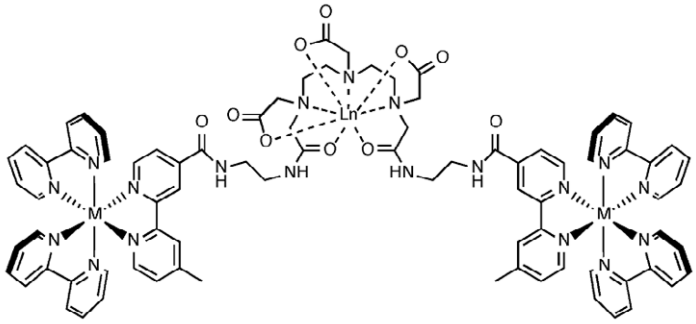

Scheme I.10. Ruthenium, rhenium and osmium complexes with lanthanides studied by Faulkner

Pikramenou and co-workers described a hetero-trimetallic neodymium-platinum complex[74] in which the DTPA binding site is folded around the lanthanide ion, resulting in a 'hairpin' structure (Scheme I.11). The two planar Pt^{2+}-terpyridyl units become oriented on the same side of the complex, and can intercalate into the DNA structure. In addition, the Nd^{3+} ion acts as a luminescent probe, emitting at 1060 nm following excitation from the Pt^{2+} chromophores which have a strong LLCT (thiolate→terpyridyl) band at 515 nm that can sensitize the NIR luminescence.

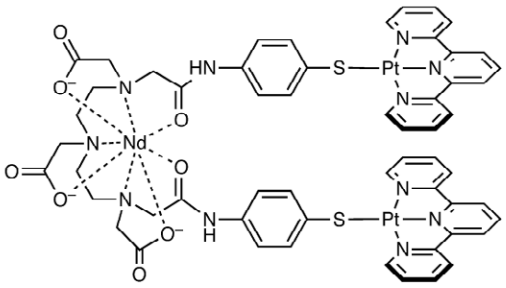

Scheme I.11 Platinum-neodymium heterometallic complex studied by Pikramenou

Lanthanide tris-diketonates can bind two additional monodentate or one bidentate ligand (see Chapter III.1.) to give octa-coordinate ternary adducts. This property has been used as a facile way of assembling d and f metal ions. A square heterometallic complex is formed in the reaction of $[Ru(bipy)_2(4,4'\text{-}bipy)_2]^{2+}$ with lanthanide tris-diketonates, in which excitation of the Ru^{2+} chromophores at 420 nm afforded sensitized NIR luminescence from Nd^{3+} and Yb^{3+} (Scheme I.12).[75] Similarly, coordination of lanthanide tris-β-diketonates to pendant bipyridyl or phenantroline sites in platinum complexes afforded Pt_2Ln_2 and Pt_2Ln_4 assemblies in which the MLCT transition of the platinum complexes at 350-450 nm acts as sensitizer for the emission of europium, neodymium and ytterbium.[76]

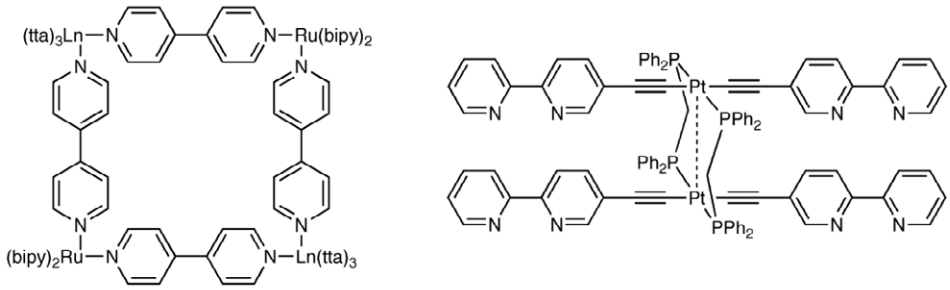

Scheme I.12. Ruthenium and platinum based heterometallic complexes with lanthanides

Ward and his group have studied monovalent rhenium carbonyl complexes with 2,2'-bipyrimidine or 2,3-bis-(2-pyridyl)pyrazine as possible sensitizing groups (Scheme I.13).[77] Similarly to the cases above, the available bidentate coordination unit is simply coupled to a lanthanide β-diketonate complex. The 650-nm emission of the ^{3}MLCT state in the rhenium complexes is quenched in the ternary adducts with Nd^{3+}, Er^{3+}, and Yb^{3+}, demonstrating the energy transfer. The same authors have designed similar chromophores by replacing Re^{+} by Pt^{2+}, the resulting heterometallic complexes displaying improved photophysical properties.[78]

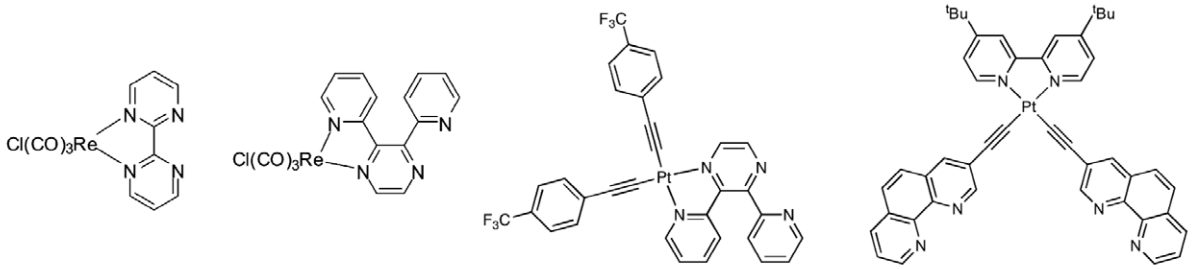

Scheme I.13. Rhenium and platinum complexes with lanthanides studied by Ward

Piguet, Bünzli and their collaborators have prepared d-f dinuclear complexes of chromium or ruthenium with NIR emitting lanthanide ions, having a triple helical architecture (Scheme I.14).[79, 80] Within the helical assembly of three ligands, the d-metal ion is six-coordinated at the bidentate site, while the lanthanide ion is nine-coordinated at the tridentate site. The complexes show d-f energy transfer, but most importantly, they demonstrate the tuning of lanthanide NIR luminescence lifetimes from the micro- to the millisecond range. For example the luminescence lifetime of Yb^{3+} following sensitization by Cr^{3+} can be varied between 23 μs in MeCN solution at 295K, and 2 ms at 10K.

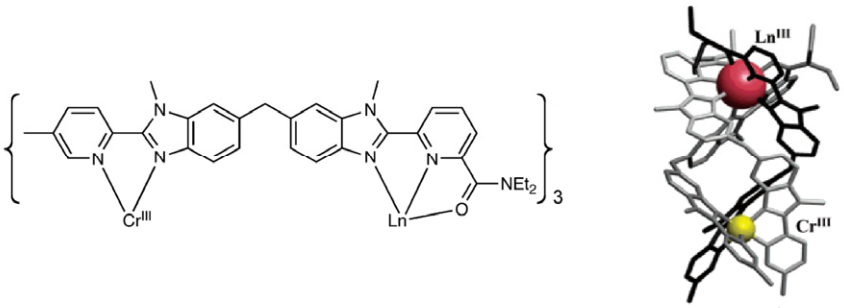

Scheme I.14. Chromium-lanthanide helical heterometallic complexes studied by Piguet and Bünzli

The sensitization of the high-energy emissive states of europium (the $^5D_1$ and $^5D_0$ states at 19000 and 17250 cm^{-1}, respectively) is particularly difficult, as the MLCT levels of most d-metal complexes are too low for an efficient d→f energy transfer. In fact, f→d energy transfer was sometimes observed, leading to a complete quenching of the europium emission.[12] The group of De Cola succeeded in tuning the emission of iridium complexes in the "almost blue" region of the visible spectrum (21 740 cm^{-1}) by employing

fluorinated phenylpyridine cyclometalating ligands (Scheme I.15).[81] The ^{3}MLCT-^{3}LC mixed state of the Ir^{3+} complex acts as a donor in the resulting heterotrimetallic complex,[57] the efficiency of the Ir→Eu energy transfer being 38%. Interestingly, the final Eu-centered red emission combines with the residual broad blue emission of the iridium chromophore to give global white light emission. Further examples of iridium-sensitized lanthanide luminescence are given in Chapter IV.2.1.

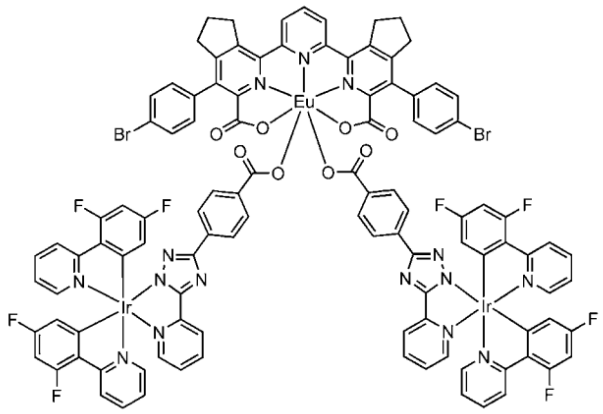

Scheme I.15. Iridium-europium heterometallic complex studied by De Cola

For discrete f–f systems, the lack of suitable synthetic methods for producing pure heterometallic complexes prevented a long time the exploitation of f→f intermetallic energy transfer processes. Faulkner and Pope took advantage of the kinetic inertness of Ln^{3+} cyclen macrocyclic complexes for producing a neutral f-f hetero-trimetallic compound[82] in which convergent directional intramolecular Tb→Yb transfer is responsible for the sensitization of the NIR Yb($^2F_{5/2}$) emission (Scheme I.16).

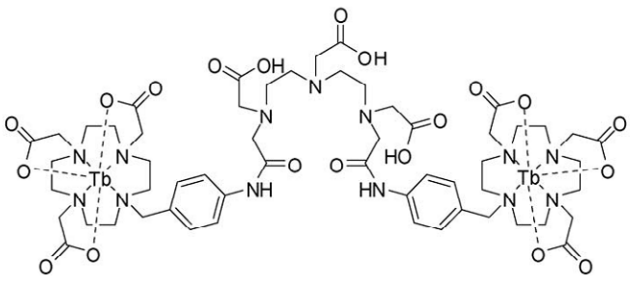

Scheme I.16. Terbium-based ligand for the complexation of ytterbium, studied by Faulkner

I.3. Applications of luminescent lanthanide complexes in optoelectronics

The special spectroscopic, electronic and magnetic properties of the lanthanide ions make them particularly interesting. Potential applications of lanthanide-induced emission essentially lie in two main domains, depending on the emission wavelength: optical and electro-optical devices on one hand, including laser materials, amplifiers, and organic light emitting diodes (OLEDs), and biomedical analysis on the other hand. Ions with transitions in the visible range of the spectrum are used in OLEDs,[60, 61] liquid crystals,[83, 84] as well as in fluoro-immunoassays[11] and in biophysical applications.[7] The ions which emit in the near-infrared have found applications in lasers and are also interesting for telecommunications and optical amplifiers.[6, 85] Moreover, the low energy of the NIR radiation allows extensive tissue penetration, because the biological tissues have little absorption between 700-900 nm, and so *in vivo* applications, such as the imaging of tumors, are becoming increasingly important.[7] Finally, as the auto-fluorescence of biological tissues has a lifetime in the order of nanoseconds, time-resolved techniques can be used with the lanthanide-based probes, which allow excitation of the sample and detection of lanthanide luminescence after the emission from the biological tissue has been quenched.[12, 86]

In the following, we will concentrate on the applications of lanthanide complexes in the optoelectronic field, emphasizing on the organic light emitting diodes.

I.3.1. Design and operating principles of OLEDs

Organic light-emitting diodes (OLEDs) are emerging as the leading technology for the new generation of full-color flat-panel displays. Even if the principle of electroluminescence has been observed in organic semiconductors by Pope *et al.* in 1963, the potential of organometallic compounds has not been realized until 1987, when Tang and VanSlyke[87] demonstrated the bright green emission of the aluminium tris(8-

hydroxyquinolinate) [Al(8-hq)$_3$] complex in thin film organic layers. In their device, the luminance exceeds 1000 cd/m^2 below 10 V with a quantum efficiency of 1% photon/electron. A few years later, another breakthrough came when Friend and his co-workers[88] reported an electro-luminescent device based on a single layer of a π-conjugated organic polymer, poly(phenylene-vinylene) PPV.

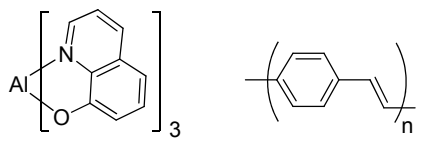

[Al(8-hq)$_3$] PPV

Scheme I.17. Molecules used for the fabrication of the first OLEDs

OLED technology offers many advantages[89] over traditional liquid crystal displays (LCDs). OLED displays are self-luminescent, eliminating the requirement for backlighting and allowing them to be thinner, lighter, and more efficient than LCDs. Light is emitted only from the required pixels rather than the entire panel, reducing the overall power consumption to 20–80% of that of LCDs. OLEDs are extremely robust and may be deposited on most substrates, rigid or flexible, introducing the possibility of many new applications. Finally, OLED displays are aesthetically superior to LCDs, providing truer colors, higher contrast and wider viewing angles.

An OLED consists of very thin layers sandwiched between two electrodes. These layers can be deposited by two main methods: evaporation (vacuum deposition) or various solution techniques (spin coating, inkjet printing etc). The cathode is typically a layer of a metal with a low work function such as Al, Mg, Ca etc., while the anode is typically a transparent layer of indium tin oxide (ITO).

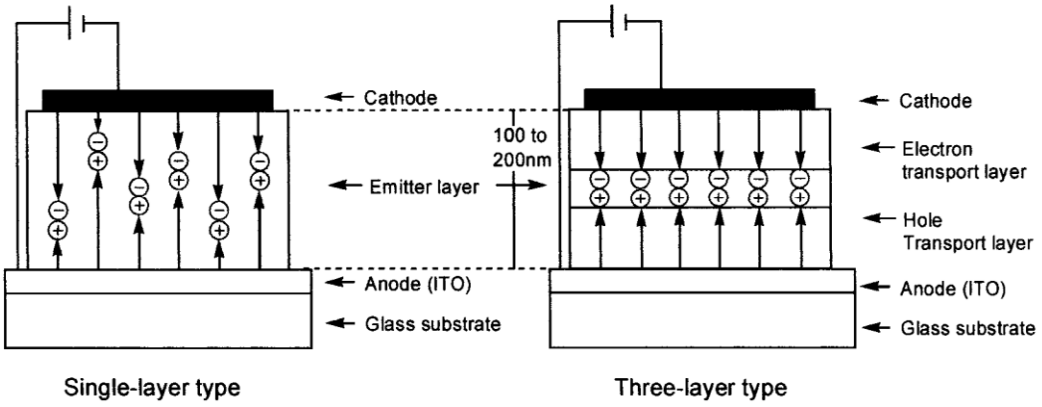

Figure I.10. Schematic configuration of single-layer (left) and three-layer (right) OLEDs (from ref.[60])

Different types of OLEDs have been described, as shown schematically in Figure I.10. Except for the anode and cathode, electroluminescent devices can contain single-layer or multiple-layer structures. The single-layer device consists of only one organic thin film between the anode and cathode. In this case, the organic layer serves as the emitting source for the device and therefore should have a high photoluminescence quantum efficiency, in addition to good bipolar charge-transport properties, which are necessary for the transport of holes and electrons through the device. Instead of using single-layer structures, additional layers can be added to the OLED to improve charge transport and injection. In a multilayer device the layers may consist of the anode, hole-transport layer (HTL), emission layer (EML), electron-transport layer (ETL), and cathode (see Figure I.10).

When the OLED is forward biased, the holes injected from the anode and the electrons injected from the cathode recombine in the emitting layer (ideally) to form roughly 25% singlet and 75% triplet excitons,[90] as shown in Figure I.11. Electron transport will occur through the lowest unoccupied molecular orbital (LUMO), which is analogous to the conduction band in a semiconductor. Holes are transported through the highest occupied molecular orbital (HOMO), which corresponds to the valence band in a semiconductor. The efficiency of electron and hole transport is determined by the mobilities of both of the charge carriers in the organic layer.

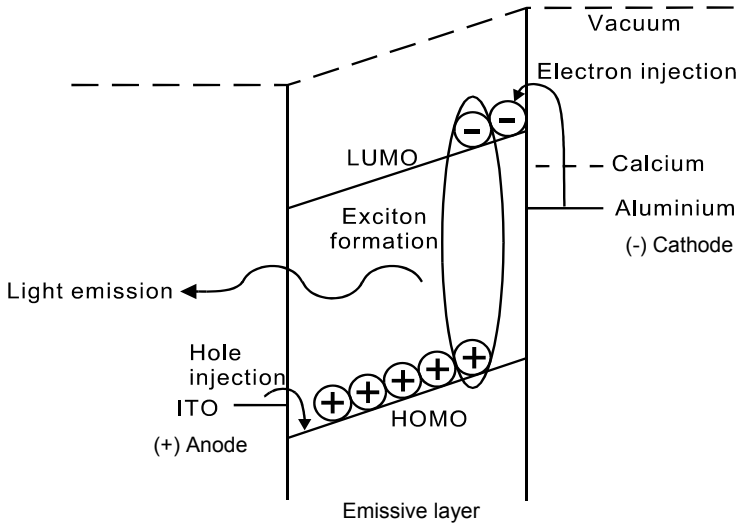

Figure I.11. Recombination of charges in a single-layer OLED

In addition to having very good luminescent properties, the materials used for OLED devices must achieve certain basic requirements,[91] such as suitability for a specific fabrication procedure (solubility in organic solvents for solution deposition techniques, or evaporability for vacuum deposition), good film-forming properties, sufficiently high glass-transition temperature to avoid crystallization in the film, and chemical and photochemical stability. In addition, the hole and electron injection barriers must be low, and the mobilities as well as the HOMO and LUMO energies of the various layers must match those of the neighboring layers. A further requirement is that the lowest triplet state of the host matrix used for the EML layer must be significantly higher (around 0.4 eV, 3 000 cm^{-1}) that the emissive level of the luminescent compound, otherwise quenching may occur.

The performance of OLEDs is tested by measuring the current density–voltage and the luminance–voltage characteristics. The turn-on-voltage (V) is defined as the voltage necessary to have a luminance of 1 cd m^{-2}. Ideally, this value should be as low as possible, but in many lanthanide-based OLEDs the values are between 5 and 10 V.[28] The luminance or brightness (cd m^{-2}) gives the ratio of the light intensity of the light source as perceived by the human eye emitted in a certain direction to the area of the LED in that direction, while the current efficiency (cd A^{-1}) relates the same intensity to the current in the

device. The current density (A cm^{-2}) relates the current flowing through the LED with its area. The luminance increases with increasing voltage up to a maximum value. Increasing the voltage further will then cause a decrease of luminance. The best quantification for the device performance is the external quantum efficiency (η_{ex}), defined as the ratio of the number of emitted photons to the number of electrons injected.

I.3.2. Lanthanide complexes as emitting layers in OLEDs

The incorporation of lanthanide complexes in the emitting layer of OLEDs offers two main advantages, related to improved color saturation and higher efficiency of the OLED. Because of the sharp emission bands of the lanthanide ions, their luminescence is highly monochromatic. This results in a much better color saturation, which is useful for the development of full-color displays based on OLEDs. In addition to the spectral profile of the complexes, the internal efficiencies of the lanthanide based OLEDs can reach in theory 100%, as the heavy metal ion effect facilitates the singlet to triplet ISC process and, subsequently, the energy transfer from the triplet (populated statistically at 75%) to the lanthanide f levels.[90]

The first example of a lanthanide-based OLED was published[92] by Kido *et al.* in 1990. These authors built an electroluminescent device consisting of N,N′-diphenyl-N,N′-(3-methylphenyl)-1,1′-biphenyl-4,4′-diamine (TPD) as the hole injecting layer and [$Tb(acac)_3$] as the emitting and electron transporting layer. The cathode was an aluminum layer and the anode an ITO-coated glass plate. The OLED was made by vacuum deposition. The green emitting OLED had a luminance of 7 cd/m^2, which is very low by the current standards, however the device demonstrated the proof-of-principle. The electroluminescence spectrum was found to be identical with the corresponding photoluminescence spectrum, and the relative intensities of the emission bands were independent of the current density. However, as the [$Tb(acac)_3$] complex described in the paper was not characterized, it is not clear whether the compound under investigation was an hydrate or a partially hydrolyzed compound. Later on, these authors made a red-emitting OLED based on an europium complex.[93] The device consisted of 2-tert-

butylphenyl-5-biphenyl-1,3,4-oxadiazole (PBD) as the electron transporting layer and poly(methylphenylsilane) (PMPS) as the hole transporting layer doped with [Eu(tta)$_3$]. Luminescence started at 12 V, and a maximum luminescence intensity of 0.3 cd/m^2 was obtained at 18 V. By replacing the tris-diketonate [Eu(tta)$_3$] complex with the ternary complex [Eu(dbm)$_3$(phen)] containing phenantroline as secondary ligand, a luminance of 460 cd/m^2 could be achieved.[94] Similarly, the efficiency of the green-emitting OLED could be improved to 90 cd/m^2 by use of [Tb(acac)$_3$(phen)] instead of [Tb(acac)$_3$].

Although most of the lanthanide complexes applied in OLEDs are ternary complexes (Lewis base adducts of tris β-diketonate complexes), there is evidence that the charged tetrakis β-diketonate complexes give a good performance as well. This was illustrated by Yu *et al.*[95] for a series of complexes [Eu(tta)$_4$]$^+$. An advantage of these complexes is their good solubility in organic solvents, which facilitates their processing by spin coating.

Comprehensive reviews on the lanthanide complexes in organic light emitting diodes have been published by Kido[60] and de Bettencourt-Dias,[61] and show the considerable progress achieved in the field. External efficiencies are now in the range of 4%, with very good luminance values.[96] However, these quantum efficiencies are still low compared to other transition metal complexes, such as iridium, and the lifetimes of the devices are not satisfying. This may be due to the inefficiency of the energy transfer and the poor stability of the lanthanide complexes under the fabrication and operation conditions. Therefore, new types of lanthanide architectures need to be developed and studied, in order to better understand the relationship between the complex structure and the device properties.

I.3.3. Other applications of lanthanide complexes in optoelectronics

Lanthanide complexes have found applications in many other optoelectronic devices. The use of rare earths chelates in lasers and amplifiers is known for more than 40 years.[85] More recently, plastic optical fibers have received increasing attention because of their clear technical advantages over glass fibers, such as flexibility and a large core diameter, enabling

efficient connections and therefore reduced costs. Compared to their salts, the utilization of lanthanide complexes containing chromophores has two major advantages: lanthanide ion salts have very limited solubility in organic media and the salts tend to aggregate in these media, resulting in concentration quenching at relatively low concentrations. Encapsulating lanthanide ions with organic ligands makes it possible to incorporate them in organic hosts at higher concentrations. Another feature is that lanthanide ions in chelate systems are pumped more effectively than in the conventional crystal and glass systems because of energy transfer processes occur through the antenna effect.

The lanthanide ions emitting in the NIR are particularly interesting for the development of lasers, amplifiers or optical fibers, as their wavelength of emission is compatible to those commonly used in telecommunications. The Nd^{3+} ion is the most popular in laser applications. In order to avoid the deactivation of neodymium luminescence by O-H and C-H vibrations, fluorinated or deuterated ligands and matrixes have been used.[97] For example, the complexes $[Nd(PMS)_3(DMSO\text{-}d_6)_8]$ and $[Nd(PES)_3(DMSO\text{-}d_6)_8]$ incorporated in the fluorinated matrix P-FiPMA show very high quantum yields of 1.3 and 1.6%, respectively (Scheme I.18).[98]

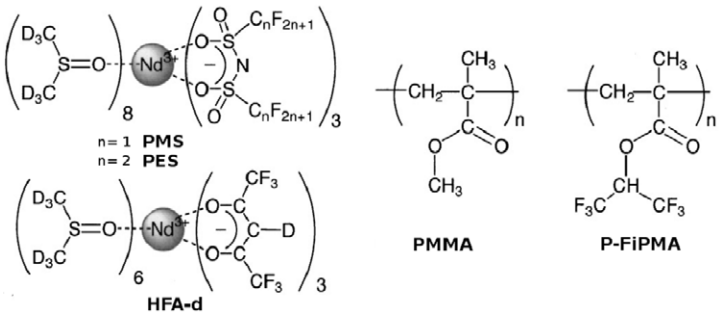

Scheme I.18. Neodymium complexes for applications in optical fibers

The Er^{3+} ion is more interesting for the telecommunications domain. In fact, the silica glass used in the optical fibers is transparent to its wavelength of emission (1550 nm). Recently, Binnemans and his collaborators have shown that the erbium complex $[Er(DBM)_3(Phen)]$ can act as optical amplifier in polymeric waveguides.[99]

I.4. Context and objectives of the project

As we have seen in the preceding introduction, the special luminescent properties of the lanthanide complexes, especially their pure colors and high emission efficiencies, have attracted extensive attention in view of their potential applications in optoelectronic devices. Particularly, considerable progress has been made in the field of organic light emitting diodes utilizing complexes with lanthanide ions as the active emitting materials. However, the quantum efficiencies of most of these devices remain rather low, partly due to the inefficiency of the energy transfer and to the poor stability of the lanthanide complexes currently employed, which can decompose during the materials processing or under the operating conditions.

In spite of the rather large number of optoelectronic devices studied, only few types of lanthanide architectures have been tested so far. Often the lanthanide complexes used are not properly characterized, making it difficult to relate their structure to the properties of the final device.

The aim of this work is to address the current limitation in synthetic design, by accessing new possibilities in the area of lanthanide emitters for optoelectronics. A fundamental study on the structure-property relationship based on an extensive series of lanthanide complexes was performed, in order to better understand the factors influencing the emission efficiency. Two different approaches for the sensitization of lanthanide luminescence have been explored, related to the use of either organic chromophores in high denticity ligand architectures, or transition d-metals in polymetallic assemblies.

For the first part of this work (presented in Chapter II), we have designed several ligands based on the terpyridine-, bipyridine- and pyridine chromophores, appended with substituents having various electronic effects. Aside from their influence on the ligand triplet state, the substituents allow further derivatization to be performed on the system, as required by specific applications (development of heterometallic assemblies, grafting on

surfaces, etc). Increasing the solubility in organic ligands could be easily accomplished by appending long alkyl substituents on the chromophore, or by changing the counterion in the structure of the complexes. To prevent non-radiative deactivation of the lanthanide luminescence, the chromophores were included in polydentate architectures having strongly-coordinating anionic groups. In this respect, tetrazoles are versatile chelating motifs which can be used as replacement of carboxylate groups because of their similar pKa values, and have been used before in the coordination chemistry of transition metals. However, because the sensitization of lanthanide emission by tetrazole-containing chromophores remained unexplored, we have decided to study the influence of this group on the properties of the final complexes, comparing it to the carboxylate motif. The tetrazolate should afford a high thermodynamic stability, while its different electronic effects compared to the carboxylate should allow the modulation of the chromophore energy levels, both in terms of absorption and emission properties.

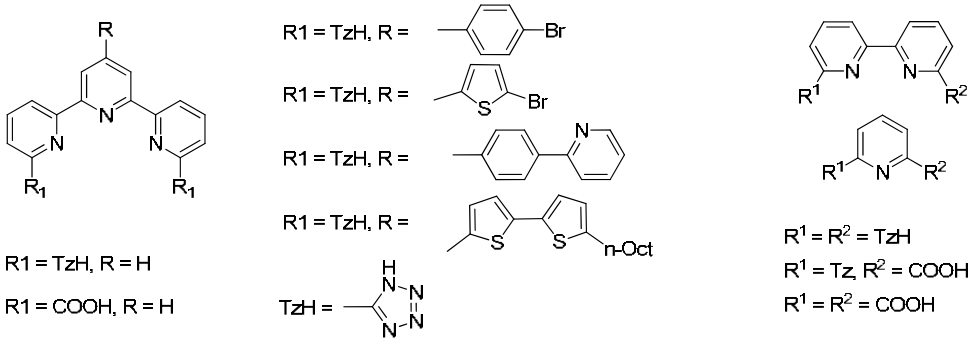

Scheme I.19. The series of terpyridine, bipyridine and pyridine-based ligands studied in this work

The resulting lanthanide complexes will be properly isolated and characterized by X-ray diffraction and NMR spectroscopy, to confirm their solid state and solution structure. Following, a detailed study of the photophysical properties of the complexes will be directed to elucidate the relation between the chromophore structure and the emission efficiency in these new lanthanide systems.

For the second part of this work (presented in Chapter III), we have designed a new class of neutral lanthanide complexes based on the terpyridine chromophore,

completed by additional β-diketonate units. The majority of lanthanide complexes used in optoelectronics are based on tris-β-diketonate chelates, containing a second bidentate N-coordinating chromophore such as 1,10-phenantroline. However, the use of an anionic chromophore would result in improved chemical and thermal stability for the complexes, and would lead to better efficiencies in devices. Therefore, we have included the terpyridine motif in two different neutral lanthanide architectures: one containing a monoanionic asymmetric terpyridine-carboxylate chromophore, completed by two β-diketonate units, and another one containing a dianionic terpyridine-bistetrazole chromophore, completed by one β-diketonate unit.

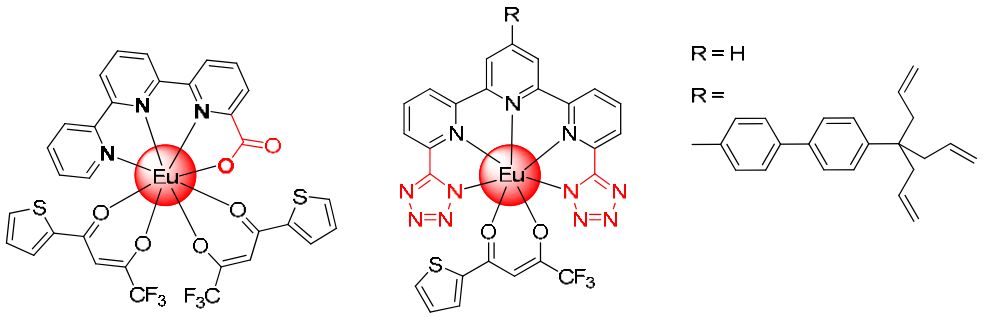

Scheme I.20. Terpyridine-based neutral lanthanide complexes

Benefiting from the facile functionalization of the terpyridine-tetrazole ligands, we have appended a tripodal anchor capable of forming Si-C bonds on the silicon surface, for studying the surface functionalization with lanthanide complexes.

Using the second approach to lanthanide sensitization, we have designed in the last part of this work (presented in Chapter IV) a versatile heteropolymetallic architecture containing d and f metals, in which the metallic centers would be linked by a fully-covalent organic framework, affording a good stability for the final assembly. In spite of the numerous examples of d-f heterometallic complexes containing transition metals such as ruthenium, platinum or osmium, only a few reports of iridium-sensitized lanthanide luminescence have been published. This is surprising considering the popularity of iridium complexes in the field of organic light emitting diodes, and the extended possibilities of modulating the lowest excited states of these emitters.

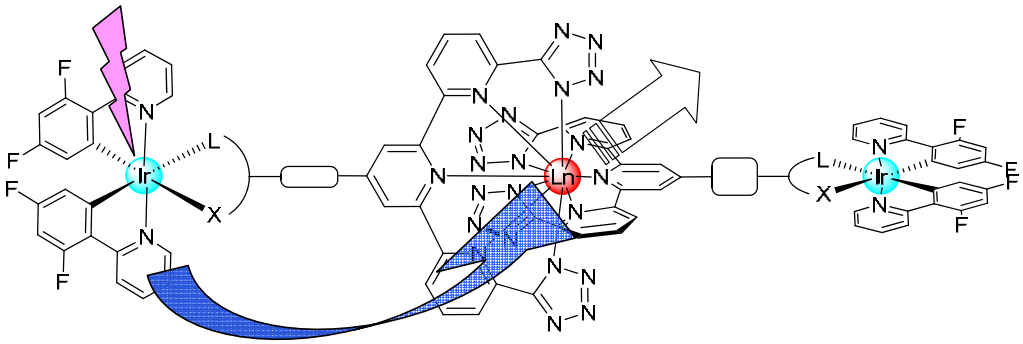

Figure I.12. Structure of the heterometallic iridium-lanthanide complex, showing the direction of energy transfer

Therefore, we have connected a cyclometallated iridium complex functioning as antenna to the terpyridine-tetrazole motif, known to afford stable complexes with the lanthanide ions. Numerous synthetic strategies have been envisaged for the construction of the 'complex as ligand.' In the final heteropolymetallic assembly, the sensitization of lanthanide luminescence by the iridium complex would be studied in both visible and near-infrared regions. The terpyridine motif was also included in homometallic bis-iridium complexes obtained by a facile synthetic protocol, which avoids complicated palladium-coupling reactions. The resulting polymetallic assemblies have increased potential in the development of sophisticated architectures with interesting optical and redox properties.

The rest of the manuscript is organized in the following manner: after a short introduction in the chemistry of the tetrazole group, the syntheses, structures and photophysical properties of the lanthanide complexes based on the terpyridine-, bipyridine- and pyridine-tetrazole motifs will be presented. Following, the neutral lanthanide complexes containing β-diketone units will be discussed, together with the preliminary applications for OLEDs and surface functionalization. In the last part, the synthetic strategies for the construction of the iridium-based polymetallic complexes, as well as their structures and photophysical properties, will be presented.

Chapter II
Lanthanide complexes based on pyridine-tetrazolates

II.1. Introduction

a) General properties of the tetrazoles

5-Substituted tetrazoles that contain a free N–H bond are also frequently referred to as tetrazolic acids, and exist as a nearly 1:1 ratio of 1H- and 2H-tautomeric forms (Scheme II.1). The isomers are essentially different in their chemical and physicochemical characteristics.[100]

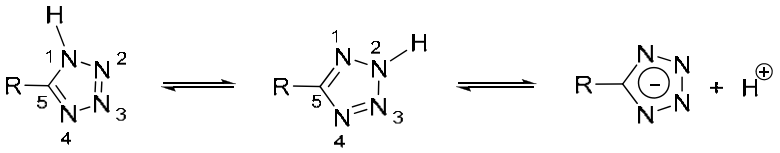

Scheme II.1

The compounds readily lose a proton when treated with a base providing the corresponding tetrazolate anions, which are fairly stable against hydrolysis and exist in water solutions predominantly in a ionic form. The free N–H bond of tetrazoles makes them acidic molecules, and not surprisingly it has been shown that both the aliphatic and aromatic heterocycles have pKa values that are similar to corresponding carboxylic acids (4.5–4.9 vs. 4.2–4.4, respectively),[101] due to the ability of the moiety to stabilize a negative charge by electron delocalization. The characteristic feature of the crystals of all NH-unsubstituted tetrazoles is the presence of strong intermolecular N–H···N hydrogen bonds, which govern mainly the molecular packing of these compounds. In general, tetrazolic acids exhibit physical characteristics similar to carboxylic acids and are strongly

influenced by the effect of substituents at the C_5-position.[100] For example, many 5-aryl tetrazoles are highly soluble in water and are best crystallized from aqueous alcoholic solvents. The corresponding tetrazolate anionic species, which have a higher capacity for hydrogen bonding than the protic species, are easily generated in hot alcohol or aqueous solutions and these intermediates are more reactive than the corresponding neutral species toward a variety of electrophiles and alkylating agents.[100]

b) Strategies for the synthesis of 5-substituted tetrazoles

The most direct method for the preparation of 5-substituted tetrazoles involves the formal [2+3] cycloaddition reaction of azide salts and nitriles, as shown in Scheme II.2. The reaction of hydrazoic acid (HN_3) with organic cyanides has been known since 1932[102]. However, a great disadvantage to this procedure is that hydrazoic acid in organic solution is toxic and extremely explosive. Not many organic solvents are stable at the reaction temperature, and for this reason DMF or DMSO are most commonly used for this purpose.

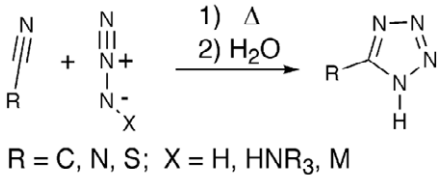

Scheme II.2. Synthesis of 5-substituted tetrazoles

A more practical procedure was developed by Finnegan[103], based on the *in situ* generation of hydrazoic acid from ammonium chloride and sodium azide, avoiding the risks associated with the direct method, and the high-pressure equipment and prolonged heating necessary. A large excess of sodium azide is necessary to maintain a basic pH for preventing the formation of hydrazoic acid. More recently, azide-metal complexes started to be employed[104], in addition to the traditional ammonium chloride-based processes. One of the most notable advances was published by Demko and Sharpless,[105, 106] in which a method was described for the synthesis of tetrazoles in water media. This procedure

utilized a 1:1 ratio of sodium azide and zinc(II) bromide as reagents, and is run at reflux temperatures, minimizing the risk of liberating hydrazoic acid.

Sharpless *et al.* have recently examined the energetics of different mechanisms for the tetrazole formation[107], using the B3LYP density functional theory method. They have concluded that when the azide is bound to an organic substrate, or when NaN_3 is used alone in nonprotic organic solvents, the reaction proceeds by a traditional concerted [2 + 3] mechanism (Scheme II.3).

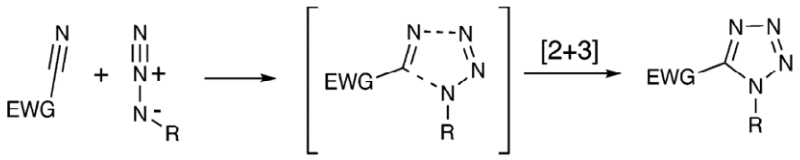

Scheme II.3. [2+3] concerted mechanism for the tetrazole synthesis

If a proton is available in the reaction, the transformation goes via a step-wise reaction involving the protonated intermediate P in Scheme II.4. This pathway is more favorable than [2 + 3] cycloaddition reactions, either neutral or anionic. Experimentally, the proton is provided by the ammonium salt, but other proton sources could play the same role.

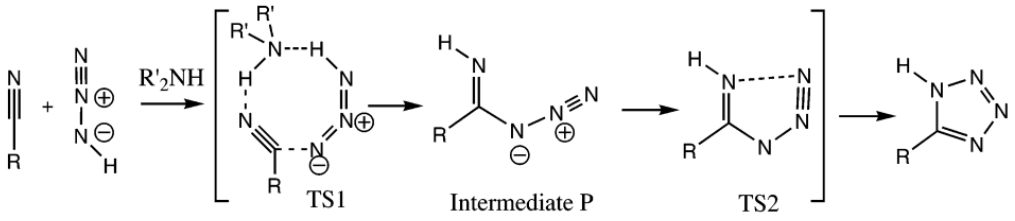

Scheme II.4. Mechanism for the tetrazole synthesis involving protons

The transition state leading to the formation of intermediate P involves the activation of the nitrile by a proton, facilitating the attack of the azide on the carbon of the nitrile. From intermediate P, simple 1,5-cyclization occurs to give the 1H-tetrazole. This mechanism is consistent with the available experimental results and with similar known mechanisms for related reactions involving nucleophilic attack on nitriles.

c) The tetrazole group in lanthanide coordination chemistry

Isosteric replacement of functional groups (e.g. COOH) represents one strategy used in medicinal chemistry for the rational modification of a lead compound to yield safer and more effective agents.[108] Generally, in non-classical isosteres the carboxylate group is replaced by one of the following:

(a) point-charge monoprotic acids (e.g. hydroxamic acids and acylsulphonamides),

(b) tetrahedral oxyacids (e.g. PO_3H_2, SO_3H and derivatives),

(c) charge-distributed monoprotic acids (e.g. tetrazoles and 1,2,4-oxadiazolones).

Over the past two decades, several isosteres of the ligand H_4dota, including phosphonic, phosphinic and sulphonic acids and carboxamides have been evaluated as chelating ligands for lanthanides, especially for applications as MRI agents.[109]

As discussed above, tetrazoles are versatile chelating motifs which can be used in replacement of carboxylate groups because of their similar pKa values. Moreover tetrazolate have attracted considerable interest in coordination chemistry[101] due to their π-acceptor properties and to their ability to form metal complexes and coordination polymers with high thermal stability and displaying interesting luminescence, non-linear optical, electrochemical or H_2 storage properties.[110, 111] Notably tetrazolates based ligands have been shown to afford iridium and ruthenium based electroluminescent devices with improved efficiency with respect to their polypyridine or picolinate analogues.[112, 113]

Surprisingly, in spite of the interesting properties of the tetrazole group, very few examples of tetrazole-based ligands for lanthanides have been reported so far, and their luminescent properties were never studied. Aime *et al.* have synthesized[114] in 2002 the H_4dotetra ligand, a mixed pendant-arm macrocycle embodying a tetrazole subunit. The resulting gadolinium complex exhibited a satisfactory stability and interesting relaxometric properties. A second example came from Facchetti *et al*, who prepared[115] neutral Gd(III) and Zn(II) complexes of pyridine- and (pyridine-1-oxide)tetrazole (Hpytz). The Gd(III) tris-ligand complexes show a large number of coordinated H_2O molecules and hence a high relaxivity, but their stability remains low due to the small denticity of the

ligands. Andrews *et al.* reported[116] the formation of hydrogels using 2-pyridyl-tetrazole in the presence of lanthanum chloride (3L:1M stoichiometry), and later extended the work[117] to other cationic, neutral and hydroxo-bridged lanthanide bis-pyridine-tetrazole complexes.

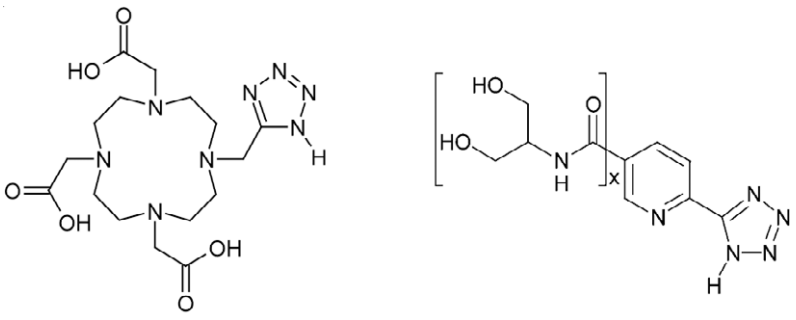

Scheme II.5. Tetrazole-based ligands previously reported in literature[114, 115]

To the best of our knowledge, these are the only reports dealing with the lanthanide coordination chemistry of tetrazole-based ligands, and while they illustrate the potential of these chelating groups for the development of lanthanide chemistry, none of them studied the complexation of emitting lanthanide ions by the tetrazole-based ligands, nor the sensitization of lanthanide emission thereof. Furthermore, in these compounds the presence of water molecules or hydroxo groups coordinated to the metal center is likely to result in the non-radiative deactivation of the lanthanide excited states by O-H oscillators reducing the luminescence emission quantum yield.

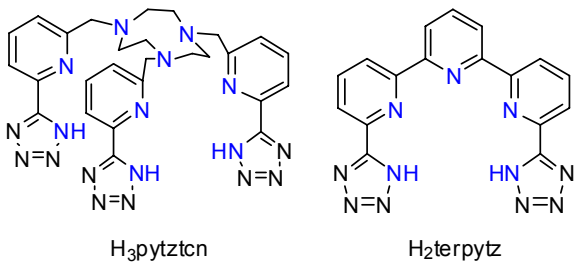

Scheme II.6. Tetrazole-based ligands prepared in our laboratory

In our laboratory, we were the first to report[118] the introduction of the tetrazole moiety in two different high-denticity ligand topologies (a terpyridine-based linear ligand and a triazacyclononane-based tripodal ligand) suitable for lanthanide sensitization (Scheme II.6).

The different geometric and electronic features of these complexes with respect to carboxylate ones[55, 119, 120] resulted in very interesting properties, as highlighted by their very efficient luminescence emission. The quantum yields of the europium and terbium complexes of pytztcn are 20% and 56%, respectively, while those of terpytz are 35% and 6%, respectively. The results prompted us to further explore the rich coordination chemistry of the tetrazole ligands. The following chapters will deal with the synthesis and characterization of a series of emissive lanthanide complexes based on terpyridine-, bipyridine- and pyridine-tetrazole ligands.

II.2. Lanthanide complexes based on terpyridine-tetrazolates

II.2.1. Synthesis and characterization of ligands

a) Ligand design

Considering the similar acidic character of the carboxylate and tetrazolate units, we have decided to incorporate the tetrazole in the terpyridine framework, for obtaining multi-dentate, strongly chelating ligands for lanthanide complexation, featuring a five-site pincer-shaped coordinating pattern. The resulting ligand **L1** (terpytz) being pentadentate, we envisaged the formation of 2L : 1Ln complexes, in which the metal would be fully coordinated and protected by the 10 nitrogen atoms of the ligand, excluding thus the solvent molecules from the first sphere of coordination, with their detrimental effect on the emissive properties of the final chelates (see Chapter I). For having a direct comparison between the properties of tetrazolate- and carboxylate-based lanthanide complexes, the ligand terpyridine-carboxylic acid **L2** (terpyc) was also to be synthesized.

Furthermore, in order to analyze the influence of the ligand electronic structure

on the luminescent properties of the final complexes, we decided to append several substituents (R), having different electronic effects, on the parent terpyridine-tetrazole unit and to compare the photophysical properties of the resulting lanthanide complexes.

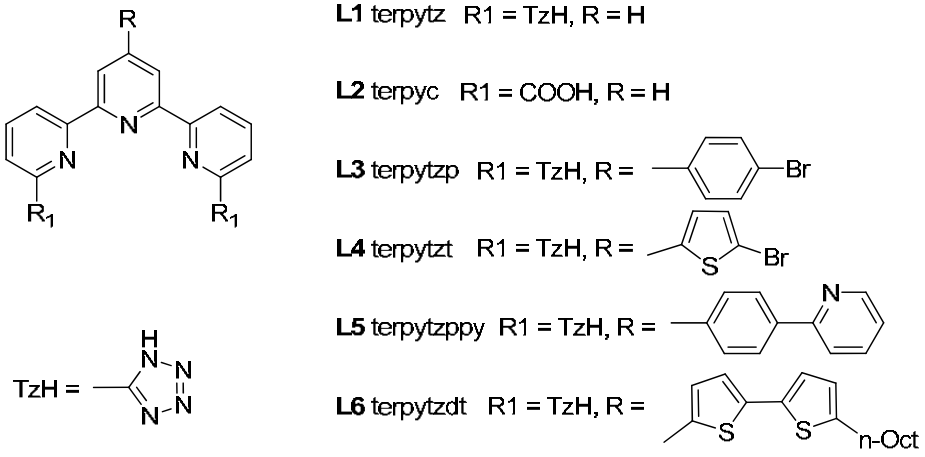

Scheme II.7. Terpyridine-based ligands used in our study

The thiophene substituents were chosen because of their potentially high interest for OLED development (very good charge carriers) and because they can be used to effectively tune the luminescence properties.[121]

Aside from their influence on the ligand triplet state, the substituents would allow further derivatization to be performed, via the bromine groups on the phenyl-substituted **L3** (terpytzp) and the thiophene-substituted **L4** (terpytzt), for introducing for example specific moieties for grafting on surfaces (see Chapter III.3.2.), or for connecting other synthons via palladium-catalysed coupling reactions, as in the synthesis of ligands **L5** (terpytzppy) and **L6** (terpytzdt) (see also Chapter IV for examples). Ligand **L6** would be in turn substituted with a long alkyl chain, which is expected to increase the solubility in non-polar organic solvents, and could ultimately improve the solubility of the final lanthanide complex in the solvents commonly used for optoelectronic device fabrication.

b) Strategies for the synthesis of terpyridines

Since Morgan and Burstall isolated in low yield the terpyridine by the oxidative coupling of pyridine with iron(III) chloride[122], the exciting coordination chemistry of this ligand

promoted the development of various synthetic strategies. A comprehensive review of the different procedures used to obtain unsubstituted or substituted terpyridines has been done by A. Thompson.[123] The two general methodologies commonly used involve either the coupling of pyridine units, or the synthesis of the central pyridine ring. Early attempts utilized mainly the coupling strategy, but tended to lack specificity and consequently required the separation of the numerous reaction products from the mixture. Coupling reactions may involve either the oxidative dehydrogenation of a pyridine,[122] or the reaction of a halogen-substituted pyridine with a metal or a metal complex.[124] More recent examples involve the use of 2-pyridyllithium,[125] with improved yields reaching 65%. However, the most effective and certainly the most widely used general method for the synthesis of terpyridine is the formation of the central pyridine ring (Scheme II.8). This is achieved by the condensation of two ketones with an aldehyde to give a 1,5-diketone, which may be isolated or not. Ring closure is then performed using ammonium acetate, hydroxylamine, formamide or acetamide. In some cases, oxidative dehydrogenation of the intermediate dihydropyridine is necessary.

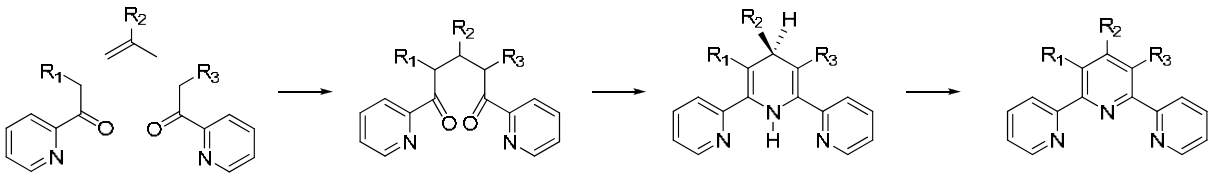

Scheme II.8. General one-pot synthesis of 2,2':6',2"-terpyridines by central ring formation

The desire to improve yields and product specificity led to the development of multistep strategies, a simple representation of which is given in Scheme II.9. The aldol condensation of 2-acetylpyridine (or a derivative) with an aldehyde in basic media gives an α,β-unsaturated ketone (enone). Michael addition of this with an enolate then affords a 1,5-diketone. The potassium enolate of 2-acetylpyridine can, for example, be prepared using potassium *t*-butoxide (Jameson procedure).[126] Ring closure can then be performed with ammonium acetate, giving a dihydropyridine, which undergoes oxidation in air to the final terpyridine.

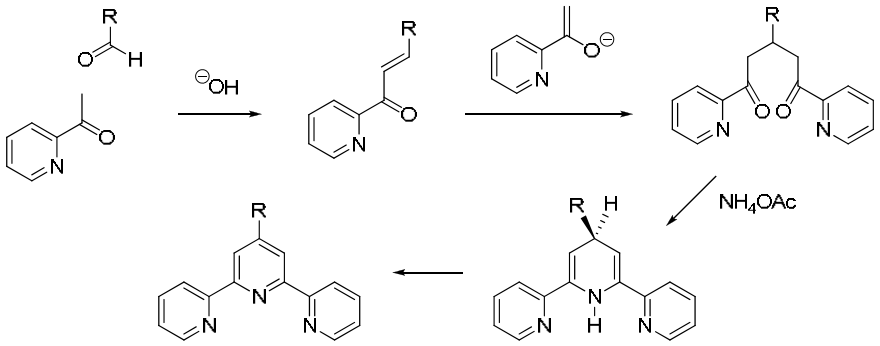

Scheme II.9. Multi-step synthesis of 2,2':6',2"-terpyridines

Mannich bases offer a good synthetic alternative to enones, while acylpyridinium salts are versatile synthetic equivalents of enolates. The latter are easily obtained from the reaction of 2-acetylpyridine with iodine in anhydrous pyridine, furthermore, the pyridinium groups acts as an internal oxidant, performing the last dehydrogenation step in the synthesis of terpyridine (Kröhnke procedure).[127]

Substituted analogues of 2-acetylpyridine can be used instead of the parent compound, allowing substituents to be introduced also on either or both of the two terminal rings of the terpyridine.[128-130] Of course, if an asymmetrically substituted compound is desired,[128] the two acetylpyridine derivatives must be added stepwise, via an enone or other intermediate, and for this reason, as well as its efficiency, the Jameson method is the most popular.

c) Synthesis of terpyridine ligands **L1** - **L6**

We have decided to rely for the synthesis of the ligands in this chapter on the classical procedure for the tetrazole formation, using sodium azide and ammonium chloride in anhydrous DMF.[103, 107] Notably, the carbonitrile precursor can also be hydrolyzed to the corresponding carboxylic acid,[131] offering in this way a simple synthetic strategy for accessing the two functional groups from one synthon. The terpyridine system was prepared using different synthetic strategies from case to case. The terpyridine substituents R were introduced either during the initial synthesis of the terpyridine unit

(**L3** and **L4**), or later via palladium-catalysed coupling reactions of the bromide-substituted ligands (**L5** and **L6**).

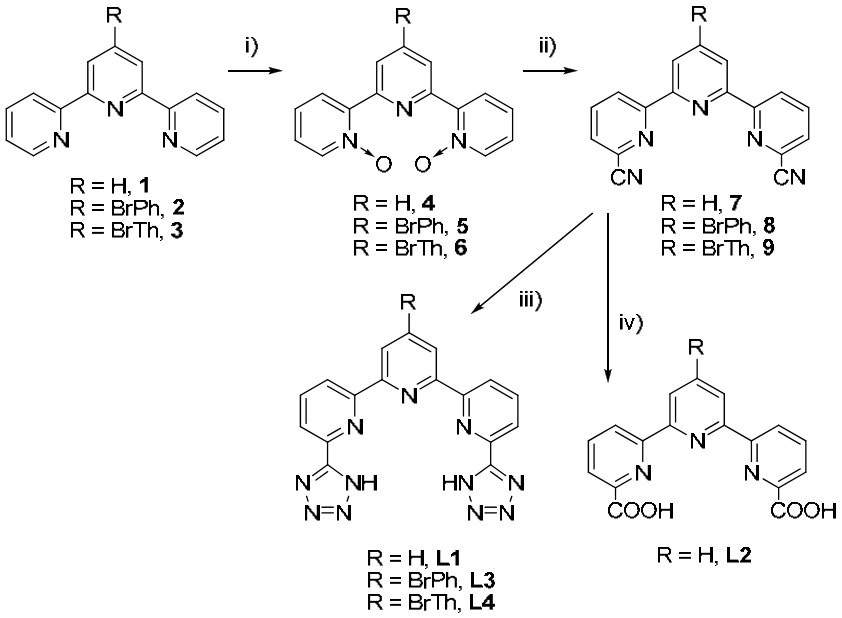

Scheme II.10. Conditions: i) mCPBA, DCM, RT (74% for **4**, 82% for **5**, 60% for **6**); ii) Me_3SiCN, PhCOCl, DCM, RT (83% for **7**, 88% for **8**, 64% for **9**); iii) NaN_3, NH_4Cl, DMF, 125°C (90% for **L1** and **L4**, 87% for **L3**); iv) KOH, EtOH-H_2O, reflux (95%)

Scheme II.10 summarizes the protocols used for the syntheses of ligands **L1**-**L4**. The non-substituted terpyridine **1** was prepared according to the two-step Jameson protocol,[126] starting from 2-acetylpyridine and N,N-dimethylformamide, in 35% overall yield. A modified one-pot Kröhnke procedure[132] based on a sequence of Claisen-Schmidt aldol condensation, 1,4-addition and intramolecular dehydration was used for the synthesis of bromo-phenyl-terpyridine **2**, starting from 2-acetylpyridine and bromo-benzaldehyde. Through this simple, although low-yielding synthesis (42%), the product is obtained as a precipitate, and no chromatographic purification is required. The synthesis of bromo-phenyl-terpyridine **2** was also performed via the classical Kröhnke procedure,[133, 134] but the purification was tedious and this method was abandoned. The Kröhnke procedure was employed for obtaining the bromo-thienyl-terpyridine **3**,[135] starting from 2-acetylpyridine and bromo-thiophencarboxaldehyde (53% yield). Further, the synthesis of the terpyridine carbonitriles **7**-**9** was based on the initial selective activation of the

terminal pyridine rings by N-oxidation with chloroperbenzoic acid,[136] followed by the introduction of cyanide via a modified Reissert-Henze reaction[51, 137] employing trimethylsilane-carbonitrile and benzoyl chloride. The final tetrazole ligands **L1**, **L3** and **L4** were prepared in excellent yields by the thermal cycloaddition reaction of sodium azide with the corresponding terpyridine-dicarbonitrile in anhydrous DMF and in the presence of NH_4Cl, whereas the carboxylate ligand **L2** was obtained via the hydrolysis in basic alcoholic conditions of terpyridine dicarbonitrile.

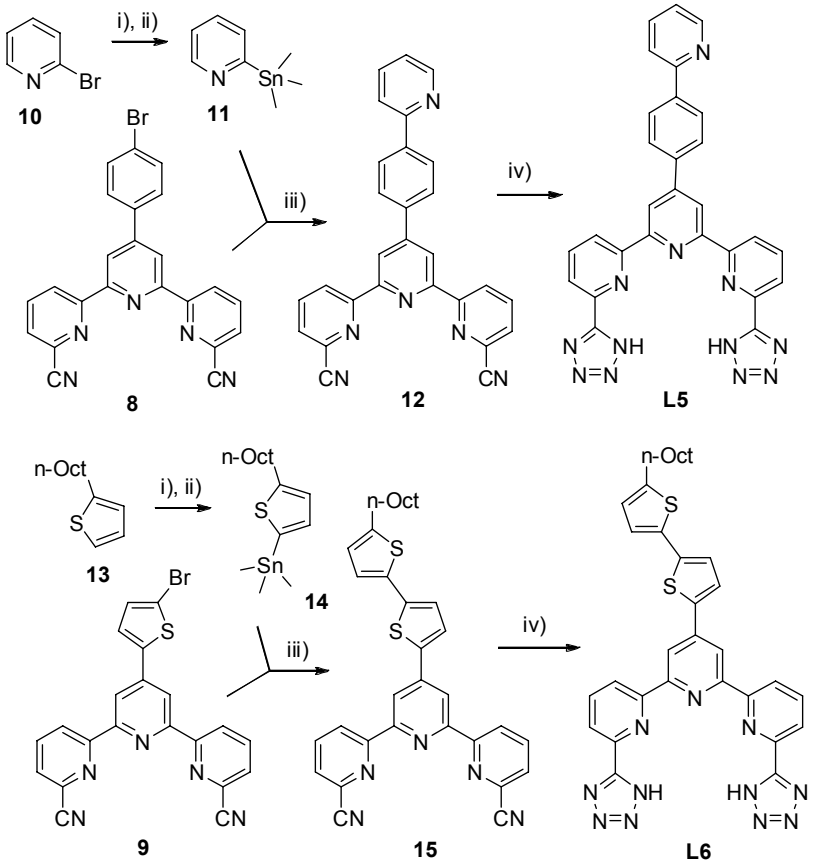

Scheme II.11. Conditions: i) BuLi, THF, -75°C; ii) $SnClMe_3$, THF, -75°C to RT (55% for **11**, 53% for **14**); iii) $Pd(PPh_3)_4$ (cat), DMF, 90°C (30% for **12**, 83% for **15**); iv) NaN_3, NH_4Cl, DMF, 125°C (91% for **L5**, 98% for **L6**)

The essential step for the synthesis of ligands **L5** and **L6** was the Stille coupling[138] of trimethylstannylpyridine **11**[139] or trimethylstannyloctylthiophene **14** with the brominated terpyridine carbonitriles **8** and **9**, respectively, as shown in Scheme II.11. Trimethylstannylpyridine were obtained by lithiation followed by transmetalation with

trimethyltin chloride of bromopyridine **10**, whereas trimethylstannyloctylthiophene was obtained by the same method starting directly from octylthiophene. Finally, the resulting carbonitriles **12** and **15** were converted to their tetrazole analogues using sodium azide.

d) Characterization of terpyridine ligands **L1** - **L6**

All the ligands **L1**-**L6** have been characterized by ^{1}H and ^{13}C NMR spectroscopy and elemental analysis, and the data is available in the Experimental Section. The ligands are insoluble in water or classical organic solvents, with the exception of DMF and DMSO (the NMR spectra were all recorded in DMSO, see Figure II.1). Due to substitution with a long alkyl chain, ligand **L6** is soluble in most organic solvents (dichloromethane, acetone, methanol etc.). Upon deprotonation with inorganic (KOH) or organic (triethylamine) bases, the ligands become soluble in methanol.

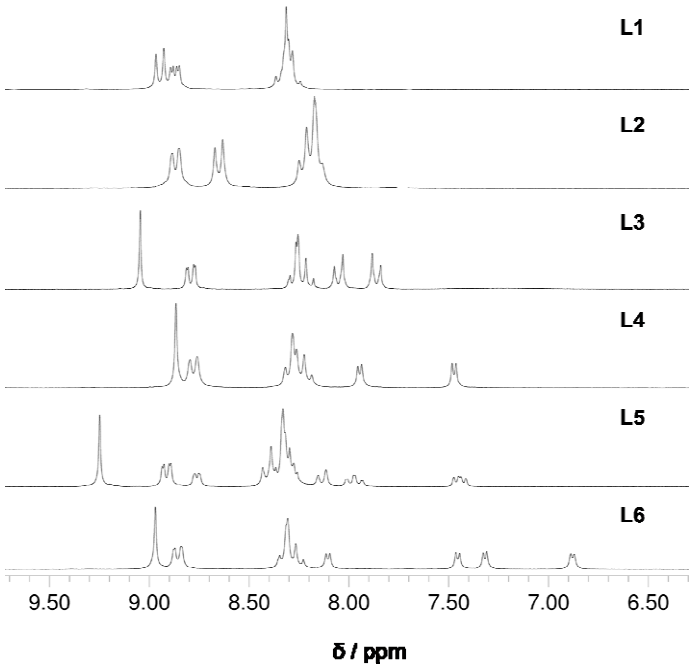

Figure II.1. ^{1}H NMR spectra in DMSO solutions of ligands **L1**-**L6**, showing the aromatic region

The UV-vis absorption spectra of the unsubstituted ligands **L1** and **L2** in methanol solutions after deprotonation with KOH are given in Figure II.2. The absorption spectra of the ligands are characterized by broad overlapping bands, assigned to $n \rightarrow \pi^*$ and $\pi \rightarrow \pi^*$

transitions and their high energy position points to all trans conformations between adjacent pyridyl cycles.[140] The spectrum of **L2** has a narrow maximum at 287 nm, which is typical of the terpyridine carboxylate units.[141] The maximum shifts at lower energy (301 nm) and becomes considerably broader in **L1**, probably as a consequence of the increased conjugation with the aromatic tetrazole ring. Similarly, the small band at 329 nm in **L2** is red-shifted at 344 nm in **L1**.

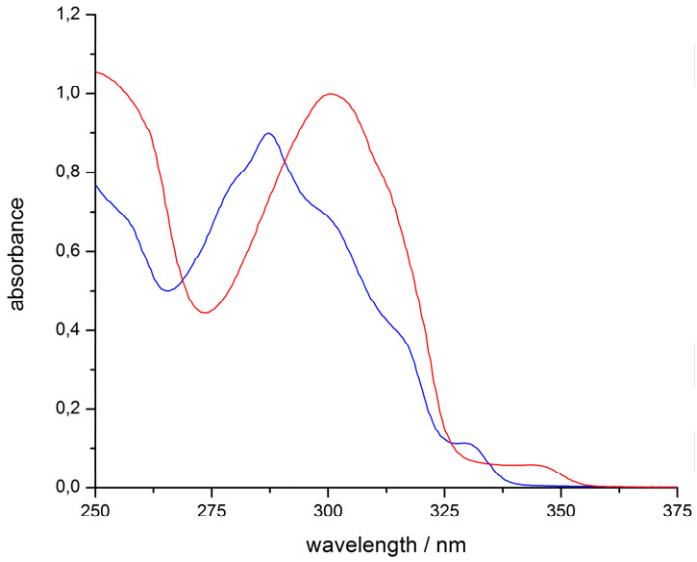

Figure II.2. UV-vis absorption spectra of a $2 \cdot 10^{-4}$ mol·dm^{-3} methanol solution of ligands **L1** (red line) and **L2** (blue line) deprotonated with KOH

Crystal structures has been obtained for the ligand **L1** and **L4** by slow water vapor diffusion in a DMSO solution. Selected distances and angles are given in Table II.1 and Table II.2, while the crystallographic data is presented in the Appendix.

In the structure of ligand **L1** (see Figure II.3), solved in the monoclinic C2/*c* space group, the terpyridine ring system is perfectly planar and adopts a full transoid arrangement about the interannular C-C bonds, which is in agreement with the literature.[142, 143] This configuration minimizes electrostatic interactions between the nitrogen lone pairs and the van der Waals interactions between the meta protons.

Table II.1. Distances (Å) and angles (°) in the structure of ligand **L1**

N1-C1	1.318(2)	C1-N1-N2	105.92(19)
N1-N2	1.351(2)	N3-N2-N1	110.89(16)
N2-N3	1.295(2)	N2-N3-N4	106.16(16)
N3-N4	1.344(2)	C1-N4-N3	108.62(15)
N4-C1	1.334(2)	C2-N5-C6	117.67(15)
N5-C2	1.339(2)	C7-N6-C7A	118.2(2)
N5-C6	1.347(2)	N1-C1-N4	108.40(16)
N6-C7	1.341(2)	N1-C1-C2	125.44(17)
N6-C7A	1.341(2)	N4-C1-C2	126.04(14)
C1-C2	1.468(2)	N5-C2-C3	123.81(15)
C2-C3	1.385(2)	N5-C2-C1	115.56(15)
C3-C4	1.379(3)	C3-C2-C1	120.59(15)
C4-C5	1.379(2)	C4-C3-C2	118.01(16)
C5-C6	1.394(2)	C3-C4-C5	119.38(18)
C6-C7	1.493(2)	C4-C5-C6	119.22(16)
C7-C8	1.393(2)	N5-C6-C5	121.92(15)
C8-C9	1.376(2)	N5-C6-C7	116.28(15)
C9-C8A	1.376(2)	C5-C6-C7	121.80(14)
		N6-C7-C8	122.36(15)
		N6-C7-C6	117.10(16)
		C8-C7-C6	120.55(14)
		C9-C8-C7	119.07(17)
		C8A-C9-C8	118.90(20)

The interannular C-C bond length (1.493 Å) is comparable with those of the 2,2′;6′,2″-terpyridines (1.480-1.498 Å) found in the literature.[142] Bond distances within the NH-tetrazole ring are in good agreement with reported values for the unsubstituted 1H-1,2,3,4-tetrazole,[144] with the shortest bond between the N2-N3 atoms (1.295 Å), consistent with the formulation of a formal double bond between these atoms. The neighboring N3-N4 bond (1.351 Å) is the longest, suggesting there is considerable localization of charge within the ring. The N1-C1 bond is shorter than the C1-N4 distance, although the formal double bond lies between the latter atoms. Each of the two tetrazole substituents is twisted in a different direction at an acute angle of 22.21° from the main plane. Intermolecular π-π interactions occur in the lattice cell between the pyridine rings of different ligands, situated at a distance of 3.466 Å (see Figure II.3). Hydrogen bonds can be observed between the H(N4) of the tetrazole ring and the O1 or O2 of the disordered co-crystallized DMSO molecule with a distance d(N4...O) = 2.623 - 2.772 Å.

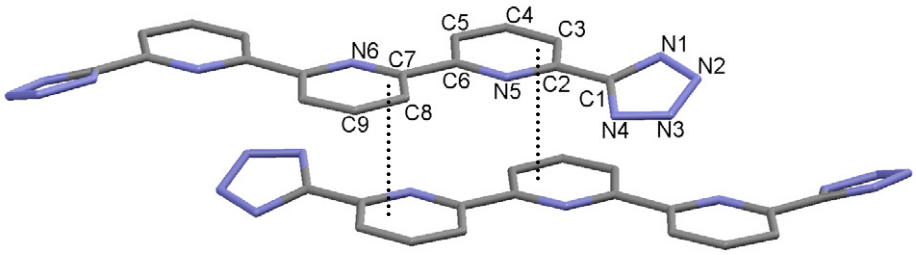

Figure II.3. Packing structure of the ligand **L1** showing the π-π interactions.

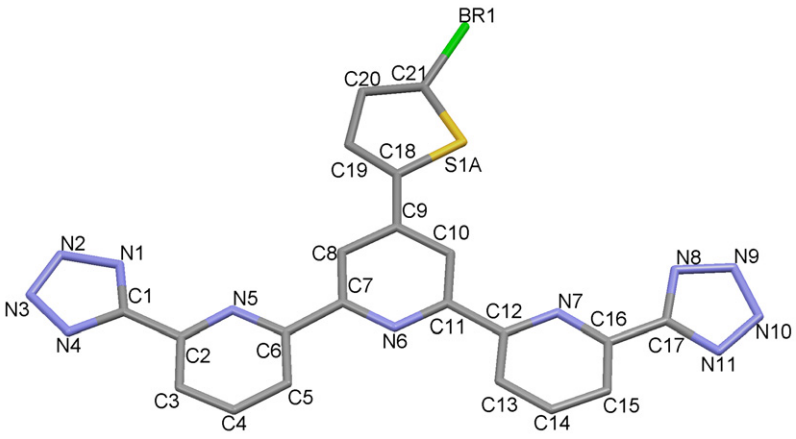

Figure II.4. Structure of the ligand **L4**

In the structure of ligand **L4**, solved in the P2(1)/c space group of the monoclinic system, the terpyridine moiety adopt a similar transoid conformation about the interannular C-C bonds (see Figure II.4), with distances similar to those in ligand **L1**. Bond distances within the NH-tetrazole ring are also similar to **L1** and to the reported values for the unsubstituted 1H- 1,2,3,4-tetrazole,[144] with the shortest bonds between the N2-N3 and N9-N10 atoms (1.295 and 1.288 Å, respectively), and the longest ones between the N3-N4 and N10-N11 atoms (1.360 and 1.345 Å, respectively). The N1-C1 bond is in this case slightly longer than the C1-N4 distance, in agreement with the formal double bond connecting the latter atoms. The terpyridine is almost planar, with the terminal N5 pyridine ring tilted at an angle of 2.21° from the plane of the central N6 ring, and the terminal N7 pyridine ring twisted at 5.02°. Similarly, the N1 and N8 tetrazole rings are tilted and, respectively, twisted from the central pyridine plane at an angle of 3.02° and

16.44°. Hydrogen bonds can be observed between the H(N1) or H(N8) of the tetrazole rings and the O1 or O2 of the disordered co-crystallized DMSO molecule with a distance d(N...O) = 2.702 – 2.708 Å.

Table II.2. Distances (Å) and angles (°) in the structure of ligand **L4**

Br1-C21	1.875(4)	C18-S1A-C21	92.5(2)
Br2-C21B	1.830(3)	C18-S1B-C21B	88.9(14)
S1A-C18	1.711(3)	C1-N1-N2	108.8(3)
S1A-C21	1.723(5)	N3-N2-N1	106.2(3)
S1B-C18	1.624(9)	N2-N3-N4	111.1(3)
S1B-C21B	1.703(10)	C1-N4-N3	105.3(3)
N1-C1	1.327(4)	C2-N5-C6	117.4(3)
N1-N2	1.345(4)	C11-N6-C7	117.8(3)
N2-N3	1.288(4)	C12-N7-C16	116.9(3)
N3-N4	1.360(4)	C17-N8-N9	108.8(3)
N4-C1	1.322(4)	N10-N9-N8	106.3(3)
N5-C2	1.340(4)	N9-N10-N11	110.9(3)
N5-C6	1.341(4)	C17-N11-N10	105.6(3)
N6-C11	1.339(4)		
N6-C7	1.342(4)		
N7-C12	1.339(4)		
N7-C16	1.348(4)		
N8-C17	1.328(5)		
N8-N9	1.345(4)		
N9-N10	1.288(4)		
N10-N11	1.356(5)		
N11-C17	1.325(4)		
C1-C2	1.470(4)		
C11-C12	1.497(4)		

II.2.2. Synthesis and characterization of the lanthanide complexes

Homoleptic lanthanide complexes [Ln(**Li**)$_2$]NHEt$_3$ (Ln = Nd, Eu, Tb; i = 1..6) based on the ligands described above have been prepared by reacting two equivalents of ligand with one equivalent of lanthanide triflate in methanol solution and in the presence of triethylamine, as shown in Scheme II.12 for [Eu(**L1**)$_2$]NHEt$_3$ and [Eu(**L2**)$_2$]NHEt$_3$. The complexes were isolated by crystallization, either by slow evaporation of the methanol solution, or by addition of acetonitrile. The products have been characterized by single crystal X-ray diffraction, 1D and 2D proton NMR spectroscopy (full proton assignment by

COSY correlation spectra and NOESY spectra), mass spectrometry and elemental analysis (full details in the Experimental Section).

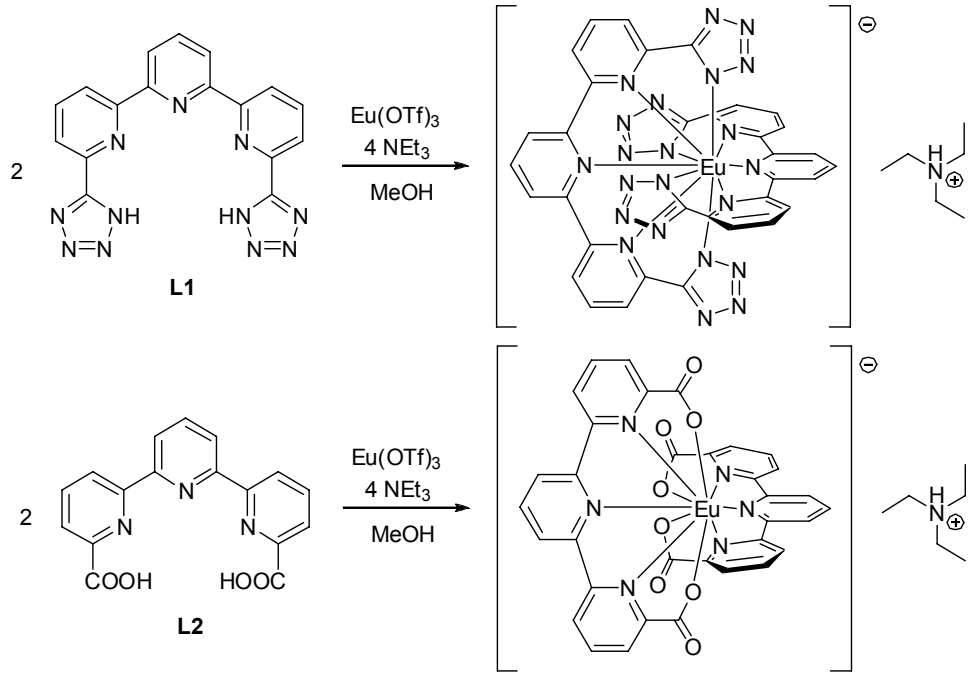

Scheme II.12. Reaction scheme for the synthesis of the [Eu(**L1**)$_2$]NHEt$_3$ and [Eu(**L2**)$_2$]NHEt$_3$ complexes

a) Molecular and crystal structures

Crystals suitable for X-ray diffraction were obtained by slow evaporation of methanol solutions, or by diffusion of diisopropylether in methanol solutions of the complexes, for [Ln(**Li**)$_2$]NHEt$_3$ (Ln = Nd, Eu, Tb for i = 1, 2 and Ln = Eu for i = 3, 4). Selected bond distances and angles for all the complexes are given in Table II.3 - Table II.6, while the crystallographic data is presented in the Appendix.

The complexes [Ln(**L1**)$_2$]NHEt$_3$, Ln = Nd, Eu and Tb, have crystallized in the *C*2/*c* space group of the monoclinic system. The lanthanide ion is surrounded by two fully deprotonated ligands. The two tetrazole-bearing pyridine rings which point outside (trans, trans) in the structure of the free ligand (see Figure II.3) adopted in the complexes a full cisoid conformation, suitable for binding to the metal. The lanthanide is ten coordinated by the three nitrogens of the terpyridine ring and two nitrogens of the pending tetrazoles, for each of the two ligands, giving an all-nitrogen coordination sphere,

as shown in Figure II.5. The charge is balanced by an uncoordinated triethylammonium counter-cation. The coordination polyhedron is best described as a square antiprism capped on the square faces.

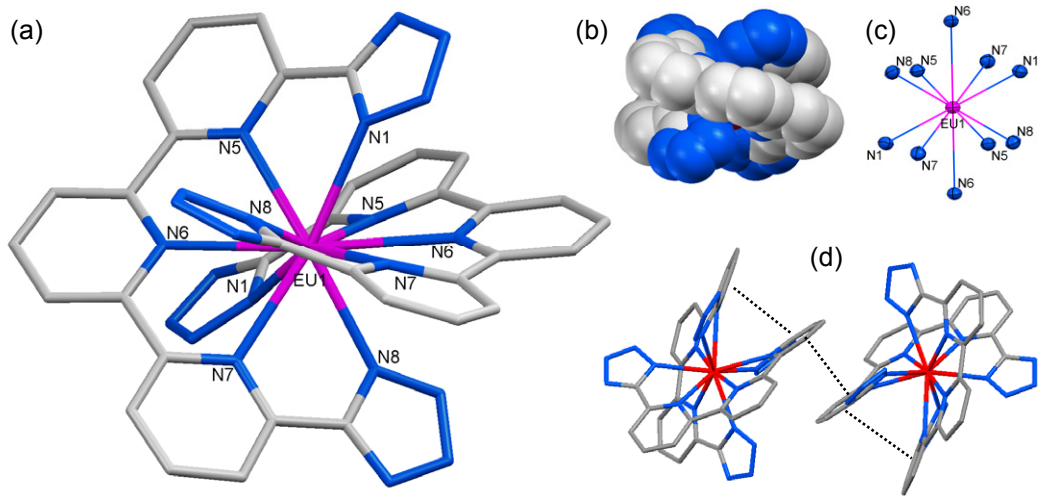

Figure II.5. Structure of the $[Eu(\mathbf{L1})_2]^-$ complex (a). Space-filled model of the structure showing the helical arrangement of the ligands (b) and representation of the coordination polyhedron around the europium atom (c) and of the intra- and intermolecular π-π interactions (d).

The 10 coordinating N atoms interact strongly with the lanthanide ion, with Eu-N distances ranging from 2.569 to 2.704 Å, in line with the distances obtained for other 10-coordinate lanthanide complexes.[40] The longest distance is between the central pyridine nitrogen and the metal, due to steric reasons. The lanthanide-tetrazole distance is similar to previously reported values for pyridine-tetrazole complexes[115]. The decrease in the distance Ln-N1 in the series of Nd, Eu and Tb complexes from 2.635 to 2.602 to 2.577 is correlated to the decrease in ionic radius (the Shannon radius[145] difference $\Delta_{Nd\text{-}Eu}$ = 0.043 Å and $\Delta_{Eu\text{-}Tb}$ = 0.025 Å), in accordance with the absence of steric hindrance influencing the coordination of the lanthanide ions. For the same reason, the bite angle N1-Ln-N5 between the coordinating nitrogen on the tetrazole unit, the metal ion, and the nitrogen of the terminal pyridine increases in the series Nd, Eu and Tb, from 61.14° to 61.66° to 62.04°, as the Ln-N bond decreases.

Table II.3. Selected bond distances (Å) and angles (°) in the [Ln(**L1**)$_2$]NHEt$_3$ complexes (Ln = Eu, Tb and Nd)

	[Eu(**L1**)$_2$]	[Tb(**L1**)$_2$]	[Nd(**L1**)$_2$]
Ln-N1	2.602(3)	2.577(4)	2.635(6)
Ln-N5	2.620(3)	2.598(3)	2.649(5)
Ln-N6	2.704(3)	2.690(3)	2.725(6)
Ln-N7	2.617(3)	2.598(3)	2.653(6)
Ln-N8	2.569(3)	2.546(4)	2.597(6)
π-π distance (inter)[a]	3.551	3.564	3.536
π-π distance (intra)[b]	3.760	3.737	3.797
π-π angle (intra)[c]	35.56	36.53	34.83
N6-Ln-N6A	172.04(12)	172.00(15)	171.9(2)
N1-Ln-N5	61.66(8)	62.04(11)	61.14(18)
N7-Ln-N8	63.10(8)	63.31(11)	62.64(18)
Torsion angle[d]	60.82	62.03	58.32

[a]measured between the N5 pyridine planes of different complexes; [b]measured between the N5 pyridine centroid and the C2A atom; [c]measured between the N5 and N5A pyridine planes; [d]measured between the N1 and N8 tetrazolate planes.

The terpyridine moiety is not planar, the two arms of the ligands being twisted and wrapped around the central metal in a helical manner (P or M), so as to minimize the interaction between the terminal anionic groups. The resulting complexes exhibit ΔΔ or ΛΛ helical chirality (see Figure II.6), with both enantiomers present in the racemic crystals (space group *C*2/*c*).

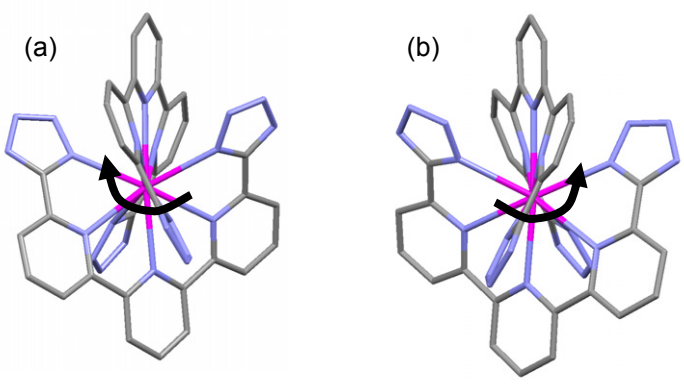

Figure II.6. Helical chirality in the [Eu(**L1**)$_2$]$^-$ complex. (a) P orientation and (b) M orientation of the ligands

The metal ion is situated at an average of 0.06 Å from the plane passing through the central pyridine, being practically coplanar, while the N6-Ln-N6A angle is 172°. The torsion angle between the two tetrazole groups on terpyridine is large and varies in the series of Nd, Eu and Tb complexes, increasing from 58.32° to 60.82° to 62.03°, in

agreement with the size variation of the metal ion. Indeed, as the metal ion is smaller, the Ln-N coordinating bond becomes shorter, bringing the terminal groups closer together and increasing the steric hindrance, resulting in more torsion. The two terpyridine ligands are not perpendicular to each other, the angle between the planes passing through the central pyridine being on average 33°, due to the steric constraints of accommodating the terminal moieties. Weak intramolecular π-π interactions occur between the facing terminal pyridine groups in the complexes. The pyridine rings are offset and situated at an average distance of 3.77 Å and an average angle of 35°, depending on the ionic radius of the metal. Strong π-π interactions (3.55 Å) are present in the lattice between the terminal pyridine units from different complexes, together with hydrogen bonds between the H of the co-crystallized solvent molecules or the triethylammonium counterion on one hand, and the non-coordinating N of the tetrazole group on the other hand.

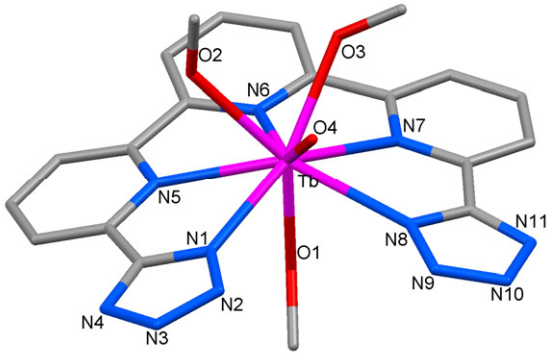

Figure II.7. Structure of the [Tb**L1**$(CH_3OH)_3H_2O]^+$ complex

Table II.4. Selected bond distances (Å) and angles (°) in the [Tb**L1**$(CH_3OH)_3H_2O]^+$ complex

Tb-O4	2.348(3)	O1-Tb-N1	76.73(13)	N1-Tb-N5	64.75(12)
Tb-O3	2.398(4)	O1-Tb-N8	74.72(13)	N8-Tb-N7	63.76(12)
Tb-O1	2.412(4)	O2-Tb-N1	81.32(13)	N1-Tb-N8	92.76(12)
Tb-O2	2.470(3)	O2-Tb-N8	143.15(12)	torsion angle[a]	28.51
Tb-N1	2.510(4)	O3-Tb-N1	143.20(13)		
Tb-N8	2.570(4)	O3-Tb-N8	95.06(14)		
Tb-N5	2.575(3)	O4-Tb-N1	73.00(13)		
Tb-N6	2.577(4)	O4-Tb-N8	71.18(12)		
Tb-N7	2.601(4)				

[a]measured between the N1 and N8 tetrazolate planes.

A crystal has also been obtained for the [Tb**L1**]CF_3SO_3 complex by slow diffusion of diisopropylether in a methanol solution of the 1:1 complex. In the structure solved in the triclinic P1 space group, the metal is nine-coordinated by the 5 nitrogens of the terpyridine-tetrazole ligand, 3 methanol molecules and one water molecule, as represented in Figure II.7. The average distance Tb-N is 2.57 Å, with the strongest bond between the metal and N1 (2.510 Å). The values are smaller than in the case of the bis-ligand complex $[Tb(\mathbf{L1})_2]^-$, and indicate a less sterically hindered arrangement around the metal center. Similarly, the bite angle N1-Tb-N5 is larger than in the case of the $[Tb(\mathbf{L1})_2]^-$ complex. The ligand is not planar, deviations from the plane of the central pyridine ring occurring for both substituents, and for the metal ion (0.808 Å). The N1 tetrazole ring is twisted at an angle of 13.96° compared to the central pyridine, while the N8 tetrazole ring makes a bigger angle at 15.86°, however the distance between the barycenters of the two tetrazole rings and the plane of the central pyridine is 0.338 Å and 0.147 Å, respectively, and the two lay on the same side of the plane. Hydrogen bonds form in the packing structure between the uncoordinated N atoms of the tetrazole rings and the co-crystallized or the coordinated solvent molecules.

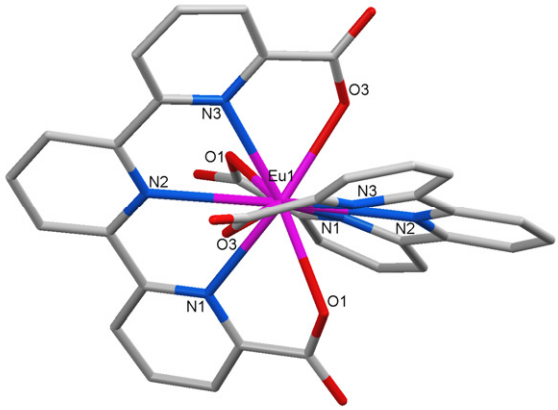

Figure II.8. Structure of the $[Eu(\mathbf{L2})_2]^-$ complex.

In the analogue carboxylate complexes $[Ln(\mathbf{L2})_2]NHEt_3$, Ln = Nd, Eu and Tb, the lanthanide ion is similarly ten coordinated by the three nitrogen atoms of the terpyridine and two oxygen atoms from the carboxylate, for each of the two ligands (see Figure II.8).

The charge is balanced by an uncoordinated triethylammonium counter-cation. The structures were solved in the C2/*c* space group of the monoclinic system. The average Ln-N is slightly longer compared to [Ln(**L1**)$_2$]NHEt$_3$, while the average Eu-O distance of 2.44 Å is similar to previously reported values.[40] The decrease in the Ln-O1 distance from 2.500 to 2.454 to 2.424 Å in the series of Nd, Eu and Tb complexes can be again correlated with the decrease in ionic radius (the Shannon radius[145] difference $\Delta_{Nd\text{-}Eu}$ = 0.043 Å and $\Delta_{Eu\text{-}Tb}$ = 0.025 Å).

Table II.5. Selected bond distances (Å) and angles (°) in the [Ln(**L2**)$_2$]NHEt$_3$ complexes (Ln = Eu, Tb and Nd)

	[Eu(**L2**)$_2$]	[Tb(**L2**)$_2$]	[Nd(**L2**)$_2$]
Ln-O1	2.454(1)	2.424(2)	2.500(2)
Ln-N1	2.642(2)	2.620(2)	2.680(2)
Ln-N2	2.753(2)	2.748(2)	2.779(2)
Ln-N3	2.612(2)	2.588(2)	2.649(2)
Ln-O3	2.430(1)	2.404(2)	2.471(2)
π-π distance (inter)[a]	3.451	3.441	3.465
N2-Ln-N2A	175.84(6)	175.19(7)	176.17(7)
O1-Ln-N1	61.55(5)	62.03(6)	60.87(5)
O3-Ln-N3	62.41(5)	62.98(6)	61.80(5)
Torsion angle[b]	45.13	46.11	42.79

[a]measured between the N3 pyridine planes of different complexes; [b] measured between the C1 and C17 carboxylate planes

The terpyridine ligand is helically wrapped around the metal, the torsion angle between the carboxylate units increasing from Nd to Eu to Tb in the range 42.79° to 45.13° to 46.11°, on average 16° smaller than in the case of the [Ln(**L1**)$_2$]NHEt$_3$ complexes, which are based on the bulkier tetrazole group. The angle between the planes passing through the central pyridine rings is on average 38.5°. No intramolecular π-π interactions can be observed in the crystal structure, as the pyridine rings are too offset from each other. However, strong π-π interactions (3.45 Å) are present in the lattice between the terminal pyridine units from different complexes. Hydrogen bonds occur between the H of the co-crystallized solvent molecules or the triethylammonium counterion on one hand, and the O of the carboxylate group on the other hand.

In the case of the phenyl substituted [Eu(**L3**)$_2$]NHEt$_3$ complex, a similar coordination mode as in the unsubstituted [Ln(**L1**)$_2$]NHEt$_3$ complexes is observed (see Figure II.9). The Eu-N bonding distances are in the same range, whereas the torsion angle between the tetrazolate groups is reduced to 54.00°.

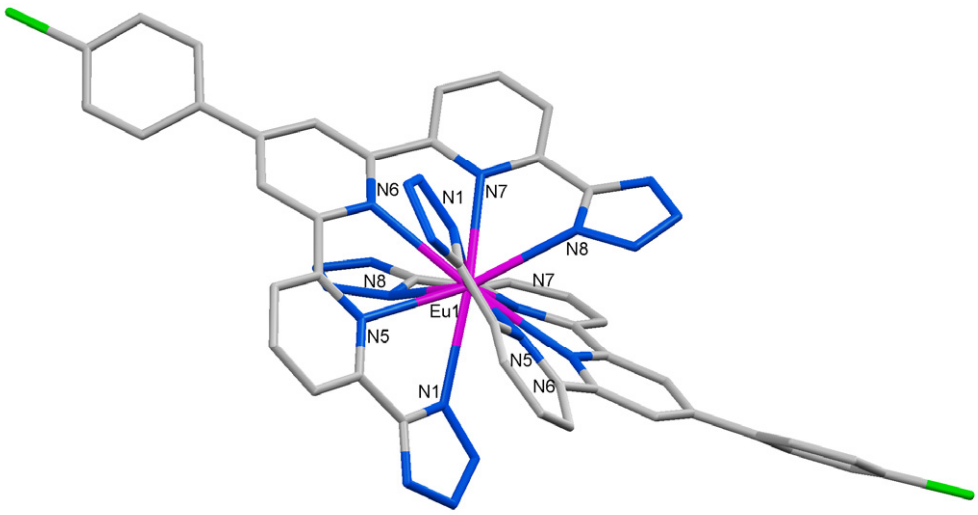

Figure II.9. Structure of the [Eu(**L3**)$_2$]$^-$ complex.

Table II.6. Selected bond distances (Å) and angles (°) in [Eu(**Li**)$_2$]NHEt$_3$ complexes (i = 3, 4)

	[Eu(**L3**)$_2$]	[Eu(**L4**)$_2$]
Eu-N1	2.586(12)	2.564(7)
Eu-N5	2.622(10)	2.614(7)
Eu-N6	2.691(11)	2.692(7)
Eu-N7	2.627(11)	2.615(7)
Eu-N8	2.604(11)	2.589(7)
π-π distance (inter)	3.748[a]	3.510[b]
π-π distance (intra)	3.586[c]	3.513[d]
π-π angle (intra)	32.36[e]	30.36[f]
N6-Eu-N6A	170.5(4)	175.7(2)[g]
N1-Eu-N5	62.5(3)	61.5(2)
N7-Eu-N8	61.8(3)	62.5(2)
Torsion angle[h]	54.00	65.84

[a]measured between the C18 phenyl centroid and the N7 pyridine centroid of different complexes; [b]measured between the N5 and N35 pyridine centroids of different complexes; [c]measured between the N5 pyridine centroid and the C1A atom; [d]measured between the N5 pyridine centroid and the C31 atom; [e]measured between the N1 tetrazolate plane and the N5A pyridine plane; [f]measured between the N31 tetrazolate plane and the N5 pyridine plane; [g]due to the non-symmetric positions, corresponds to N6-Eu-N36; [h]measured between the N1 and N8 tetrazolate planes.

Intramolecular π-π interactions (3.586 Å, 32.36°) occur between the facing tetrazole and terminal pyridine rings. π-π bonding involving the tetrazole unit has been reported before.[23, 146] Weak intermolecular π-π interactions (3.748 Å, 15.75°) also occur in the lattice cell between the phenyl ring of one complex, and the terminal pyridine ring of another complex, resulting in a twisting of the phenyl with respect to the central pyridine of 23.9°, and a tilting of 5.0°. (The tilting angle is measured between the C_2 axes of the aromatic rings.) To preserve conjugation with the phenyl group, the pyridine ring is itself tilted in the same direction. Accordingly, the europium ion is no longer coplanar to the central pyridine ring plane, being situated at a distance of 0.54 Å, while the axial angle N6-Eu-N6A is less affected at 170.5°.

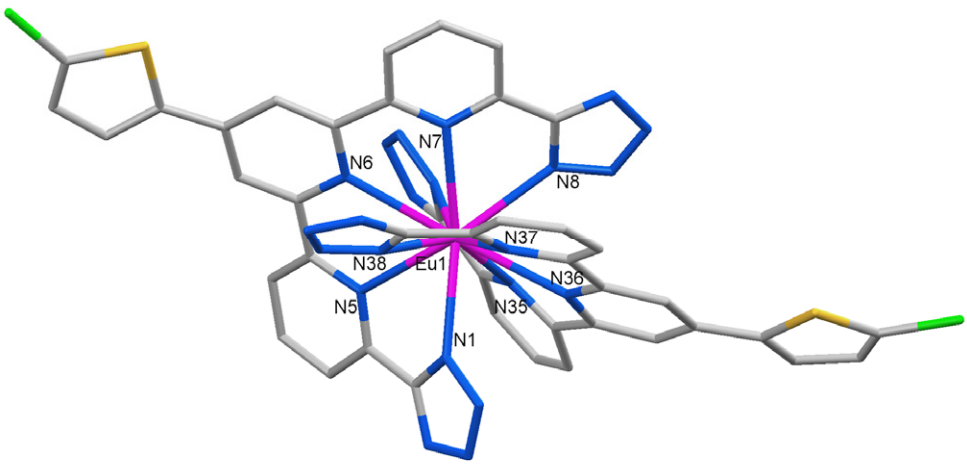

Figure II.10. Structure of the $[Eu(\mathbf{L4})_2]^-$ complex.

The thienyl substituted $[Eu(\mathbf{L4})_2]NHEt_3$ complex has crystallized in the P2(1)/c space group of the monoclinic system, and it has a similar structure to the unsubstituted $[Ln(\mathbf{L1})_2]NHEt_3$ complexes (see Figure II.10). The Eu-N bonding distances are in the same range, whereas the torsion angle between the tetrazolate groups is increased to 65.8° and 57.1°, respectively, for the two non-symmetric ligands in the complex. Intramolecular π-π interactions (3.513 Å, 30.36°) occur between the facing tetrazole and terminal pyridine rings. Sterical hindrance occuring in the lattice cell between the bromo-thienyl substituents of two complexes brings in this case a 12.9° average twist and a 7.1° average

tilting of the thienyl with respect to the central pyridine. The smaller twist of the thiophene compared to the phenyl in the [Eu(**L3**)$_2$]NHEt$_3$ complex can also be correlated with less H-H hindrance in the case of the five-membered ring, as well as with an increased conjugation steaming from the electro-releasing effect of thiophene. The europium atom is no longer coplanar to the central pyridine ring plane, being situated at a distance of 0.72 and 0.54 Å from the central pyridine planes, respectively, while the axial angle N6-Eu-N36 is very obtuse at 175.7°, comparable to the [Eu(**L2**)$_2$]NHEt$_3$ complex.

The crystal structures presented above prove that the terpyridine tetrazole ligands are well-adapted and able to coordinate the lanthanide ions with the formation of architectures in which the metal is completely encapsulated and protected from interaction with the solvent molecules. While triple helical mononuclear complexes have been reported before[147, 148], the complexes described here are the first examples of double-helical mononuclear lanthanide architectures.

b) ^{1}H NMR solution study

The ^{1}H NMR spectra of the [Ln(**L1**)$_2$]NHEt$_3$ (Ln = Nd, Eu, Tb) complexes in a MeOD solution at 298K show the presence of only one set of signals, with 5 resonances for the 18 protons in the two terpyridine ligands, and 2 resonances for the 15 ethyl protons in the ammonium counterion. These features are consistent with the presence of stable, D_2 symmetric [Ln(**L1**)$_2$]$^-$ solution species, in agreement with the X-ray structures. The chemical shift equivalence of the ethyl protons indicates a fast conformational mobility of the C_3 symmetric ammonium species. The solutions of the Eu and Nd complexes show sharp peaks at room temperature, spread over less than 16 ppm, while the spectrum of the Tb complex is broad due to the strong characteristic paramagnetic effect of the metal and extends over 240 ppm. All the protons have been assigned by 2D ^{1}H-^{1}H COSY and NOESY experiments. Varying the temperature range of an [Eu(**L1**)$_2$]$^-$ solution in MeOD does not result in a broadening of the ^{1}H NMR signals, indicative of a high rigidity of the structure in solution, although the paramagnetic shift increases with lower temperature (Figure II.11).

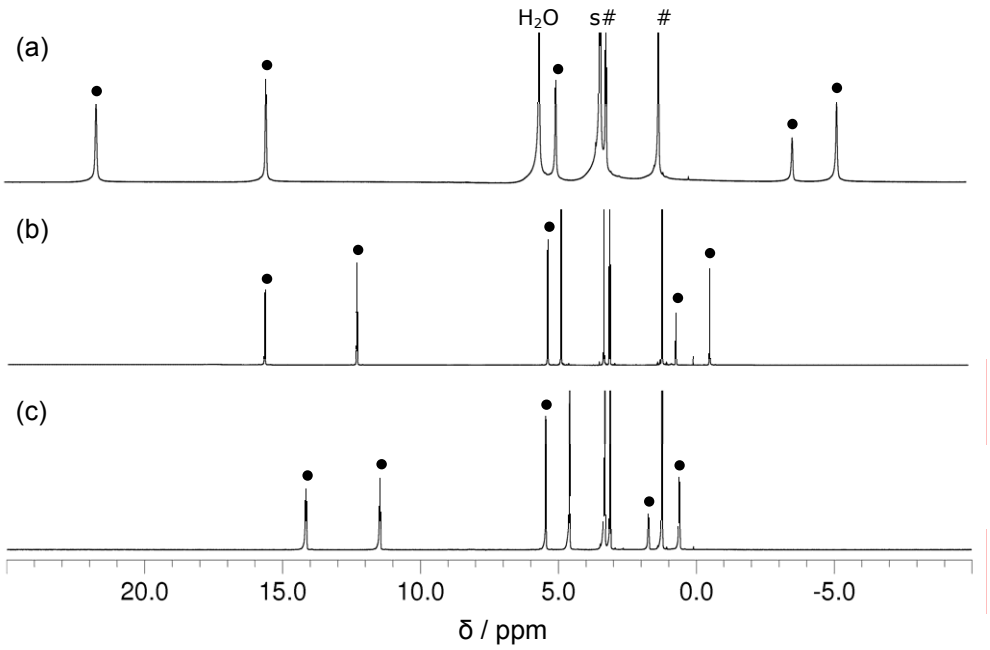

Figure II.11. Variable temperature ^{1}H NMR spectra of a solution of [Eu(**L1**)$_2$]NHEt$_3$ in CD$_3$OD at (a) 223K, (b) 298K and (c) 323K (● = [Eu(**L1**)$_2$]$^-$, # = Et$_3$NH$^+$)

The addition of an excess of europium triflate to a solution of the [Eu(**L1**)$_2$]NHEt$_3$ complex up to a 1:1 ligand-to-metal stoechiometry does not result, surprisingly, in the complete formation of the [Eu**L1**]$^+$ complex, but in a mixture of [Eu**L1**]$^+$ and [Eu(**L1**)$_2$]$^-$ species, even after equilibration for 10 minutes. Increasing the amount of metal results in further formation of the 1:1 and the consequent dissociation of the 2:1 species, up to a tri-fold excess of metal with respect to the ligand, when only the 1:1 complex can be observed, as shown in Figure II.12. Heating a directly prepared 1:1 ligand-to-metal solution at 318K for a week also results in the complete formation of [Eu**L1**]$^+$. The same effect has been observed in the case of terbium. The 5 proton resonances of the [Eu**L1**]$^+$ complex are sharp in the temperature range 273-323K, however going to low temperatures (223K) results in a large broadening of the signals, indicating the presence of a fast exchanging C_2-symmetrical specie at 273K which slows down upon decreasing temperature (see Figure II.13).

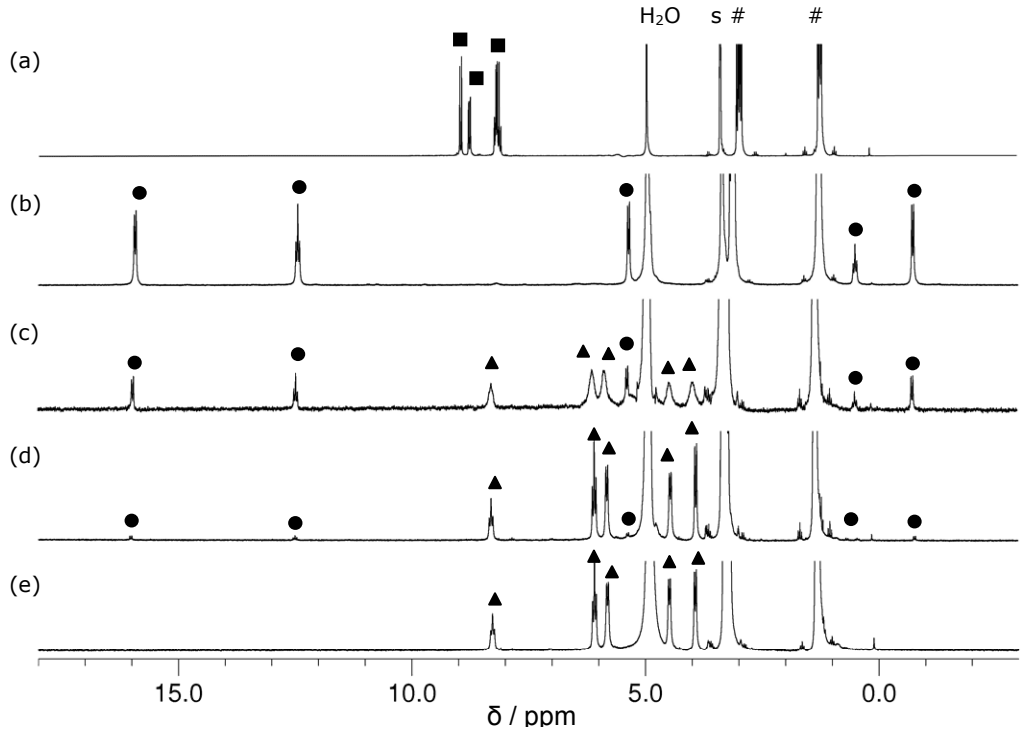

Figure II.12. Titration of **L1** with europium triflate in methanol solution, followed ^{1}H NMR at (a) $5 \cdot 10^{-3}$ mol·dm^{-3} ligand concentration and (b) 2:1, (c) 1:1, (d) 1:2 and (e) 1:3 ligand:metal ratio. (■ = **L1**$^{2-}$, ● = [Eu(**L1**)$_2$]$^-$, ▲= [Eu**L1**]$^+$, # = Et_3NH^+)

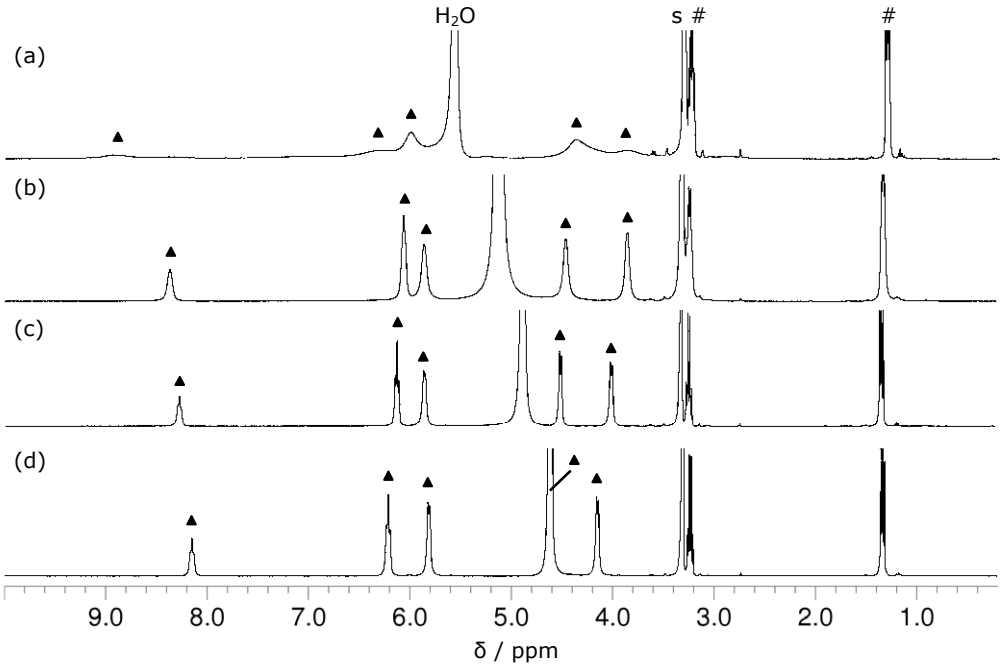

Figure II.13. Variable temperature ^{1}H NMR spectra of a solution of [Eu**L1**]OTf in CD_3OD at (a) 223K, (b) 273K, (c) 298K and (d) 323K (▲= [Eu**L1**]$^+$, # = Et_3NH^+)

Upon the addition of small amounts of water to a methanol solution containing $[Eu(\mathbf{L1})_2]^-$, the 2:1 complex slowly dissociates into the 1:1 complex and the free ligand. Due to its insolubility, the stability of the $[Eu(\mathbf{L1})_2]^-$ complex in water cannot be directly determined. However, in strongly coordinating solvents such as DMF or DMSO, the dissociation is clearly evidenced. While at $5{\cdot}10^{-3}$ mol·dm^{-3} in DMF there is an equilibrium between the 2:1 and 1:1 complexes and the free ligand (26%, 37%, 37%, respectively), in DMSO the dissociation is practically total (2%, 49%, 49%, respectively).

The particular kinetic stabilization of the $[Eu(\mathbf{L1})_2]^-$ complex with respect to the $[Eu\mathbf{L1}]^+$ could be assigned to hydrophobic[149] or π-π interactions[150] favoring the bis-**L1** complex. To gain more insight, the bipyridine bis-tetrazole ligand **L7** (see Chapter II.3) was investigated as well, however at 1:1 ligand-to-metal stoichiometry, the major specie (>95%) was $[Eu\mathbf{L7}]^+$ (Figure II.14). Heating this solution at 318K for 48h resulted indeed in the disappearance of the bis-ligand complex traces, but the small kinetic stabilization of the 2:1 complex in this case indicates that the major responsible effect is related to the structural difference between the complexes $[Eu(\mathbf{L1})_2]^-$ and $[Eu(\mathbf{L7})_2]^-$.

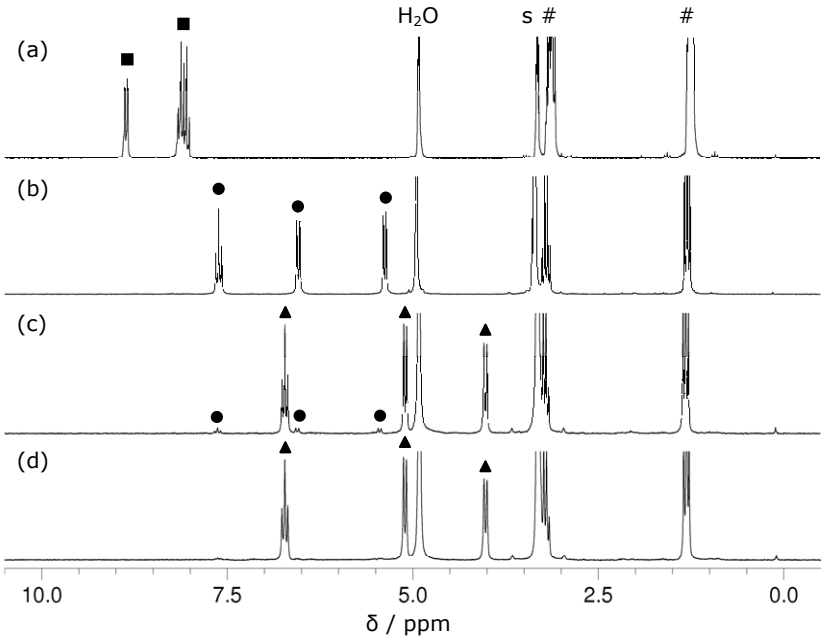

Figure II.14. Titration of **L7** with europium triflate in methanol solution, followed ^{1}H NMR at (a) $5{\cdot}10^{-3}$ mol·dm^{-3} ligand concentration and (b) 2:1, (c) 1:1 ligand:metal ratio, and (d) 1:1 after thermodynamic equilibration (■ = $\mathbf{L7}^{2-}$, ● = $[Eu(\mathbf{L7})_2]^-$, ▲= $[Eu\mathbf{L7}]^+$, # = Et_3NH^+)

The ^{1}H NMR spectra of the other terpyridine-tetrazole-based complexes [Ln(**Li**)$_2$]NHEt$_3$ (i = 3..6) in MeOD solutions at 298K show the presence of only one set of signals, with different number of resonances depending on the nature of the substituent. These features are consistent with the presence of stable, rigid, *D*$_2$ symmetric [Ln(**Li**)$_2$]$^-$ solution species, similarly to the parent [Ln(**L1**)$_2$]$^-$ and in agreement with the X-ray structures.

The ^{1}H NMR spectra of the [Ln(**L2**)$_2$]NHEt$_3$ (Ln = Nd, Eu, Tb) complexes in a MeOD solution at 298K show the presence of only one set of signals, with 5 resonances for the 18 protons in the two terpyridine ligands, and 2 resonances for the 15 ethyl protons in the ammonium counterion, similarly to the [Ln(**L1**)$_2$]NHEt$_3$ complexes. These features correspond to the presence of stable, *D*$_2$ symmetric [Ln(**L2**)$_2$]$^-$ solution species, in agreement with the X-ray structures. Decreasing the temperature of a methanol solution of [Eu(**L2**)$_2$]$^-$ down to 223K results in a broadening of the ^{1}H NMR signals, although they remain sharp at 298K and 323K (see Figure II.15), indicating the presence of a fluxional specie at room temperature which becomes more rigid upon decreasing temperature.

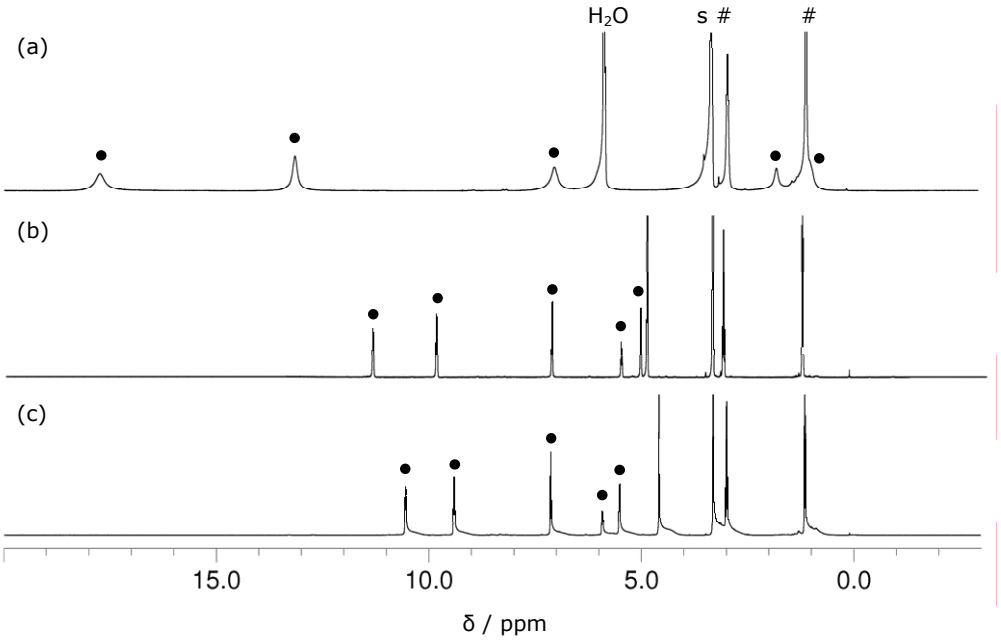

Figure II.15. Variable temperature ^{1}H NMR spectra of a solution of [Eu(**L2**)$_2$]NHEt$_3$ in CD$_3$OD at (a) 223K, (b) 298K and (c) 323K (● = [Eu(**L2**)$_2$]$^-$, # = Et$_3$NH$^+$)

Adding an europium triflate solution up to a 1:1 ligand-to-metal stoichiometry results in the fast and complete formation of [Eu**L2**]$^{+}$, as shown in Figure II.16, demonstrating that the effect responsible for the stabilization of [Eu(**L1**)$_2$]$^{-}$ is not present here. The proton resonances of the 1:1 species are broad at 298K and 328K, and become even broader at 223K, indicating an exchange equilibrium.

For comparison, in Figure II.17 are given the ^{1}H NMR spectra of the whole series of europium complexes [Eu(**Li**)$_2$]NHEt$_3$ (i = 1..5), in MeOD solutions at 298K. Note the similar proton resonances of the terpyridine-tetrazole-based complexes, resulting from the similar coordination environment around the europium ion, and different from those of the [Eu(**L2**)$_2$]$^{-}$ complex.

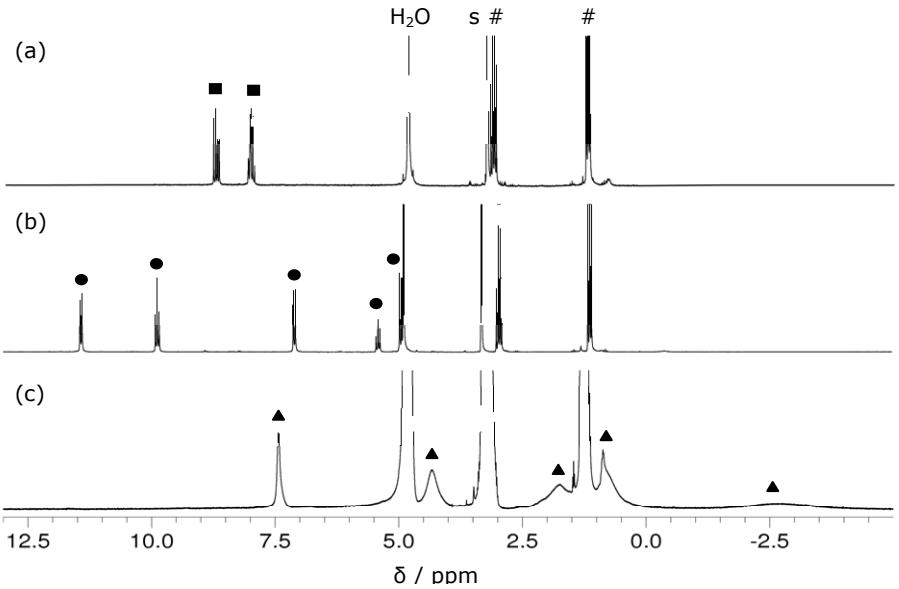

Figure II.16. Titration of **L2** with europium triflate in methanol solution, followed ^{1}H NMR at (a) 5·10^{-3} mol·dm^{-3} ligand concentration and (b) 2:1 and (c) 1:1 ligand:metal ratio. (■ = **L2**$^{2-}$, ● = [Eu(**L2**)$_2$]$^{-}$, ▲= [Eu**L2**]$^{+}$, # = Et$_3$NH^{+})

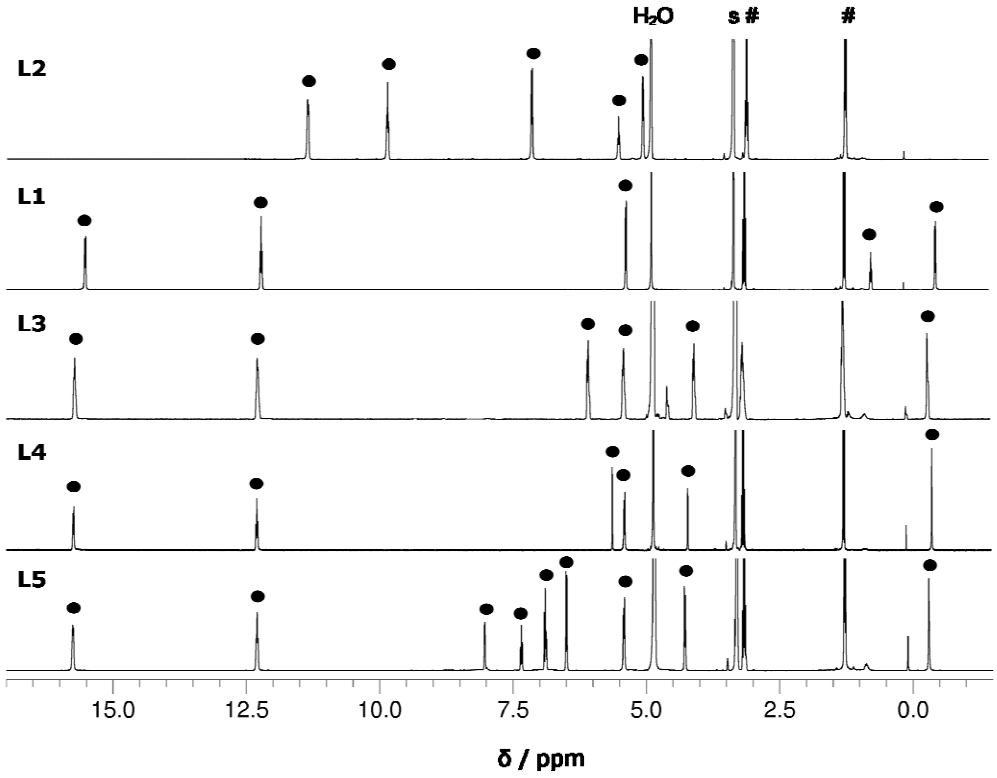

Figure II.17. ^{1}H NMR spectra of the [Eu(**Li**)$_2$]NHEt$_3$ (i = 1..5) complexes in MeOD solutions at 298K

To gain insight concerning the relative stability of the [Eu(**L1**)$_2$]$^-$ and [Eu(**L2**)$_2$]$^-$ complexes in methanol, solutions containing 2 equivalents of both ligands ($5\cdot10^{-3}$ mol·dm^{-3}) deprotonated with triethylamine and 1 equivalent of europium triflate have been prepared and analyzed by ^{1}H NMR. When the order of addition is **L1**, Eu, **L2**, both 2:1 complexes and the free ligands can be observed in the first minutes (the amount of [Eu(**L1**)$_2$]$^-$ is approximately double compared to [Eu(**L2**)$_2$]$^-$). However, after reaching thermodynamic equilibrium (318K, 24h), only the signals of [Eu(**L2**)$_2$]$^-$ can be observed, together with free **L1**. Identical results have been obtained when using NaOD for ligand deprotonation. Adding another 2 equivalents of deprotonated **L1** and allowing for thermodynamic equilibrium still does not result in the formation of [Eu(**L1**)$_2$]$^-$. When the order of addition is different (**L1**, **L2**, Eu or **L2**, Eu, **L1**), only the formation of the [Eu(**L2**)$_2$]$^-$ complex can be observed, together with free **L1**, and the situation does not change after thermodynamic equilibration. The experiments confirm the existence of a

kinetic stabilization effect in the case of the $[Eu(\mathbf{L1})_2]^-$ complex, whereas at equilibrium the $[Eu(\mathbf{L2})_2]^-$ complex exhibits a greater stability and forms preferentially.

c) Conditional stability constants

To obtain a quantitative description for the stability of $[Ln(\mathbf{L1})_2]^-$ and $[Ln(\mathbf{L2})_2]^-$ complexes, we have turned to UV-vis spectrophotometric titrations. Due to the insolubility of the complexes in water, the measurements have been performed in methanol. Increasing amounts of europium triflate were added to solutions of the ligands ($2 \cdot 10^{-4}$ mol·dm^{-3}) deprotonated with a stoichiometric quantity of KOH, up to a ratio $R = [Eu]_t/[L]_t = 3$. The europium ion was chosen as a typical example because it lies in the middle part of the lanthanide series. Whereas **L2** gave clear and distinct curves in the continuous titrations (equilibration time 5 minutes), indicating the fast formation of the 2:1 and 1:1 species (Figure II.18c), ligand **L1** did not behave similarly, as expected from the NMR experiments, due to the kinetic stabilization of the 2:1 complex which inhibited the complete formation of the 1:1 species at R = 1 (Figure II.18a). Changing the metal salt to europium chloride or lutetium triflate, or changing the order of addition (titration of metal with ligand aliquots) did not have any effect. Therefore, we had to resort to batch titrations for ligand **L1**, measuring discreet solutions of different ligand-to-metal stoichiometries which have been previously equilibrated for 60h at 45°C (Figure II.18b).

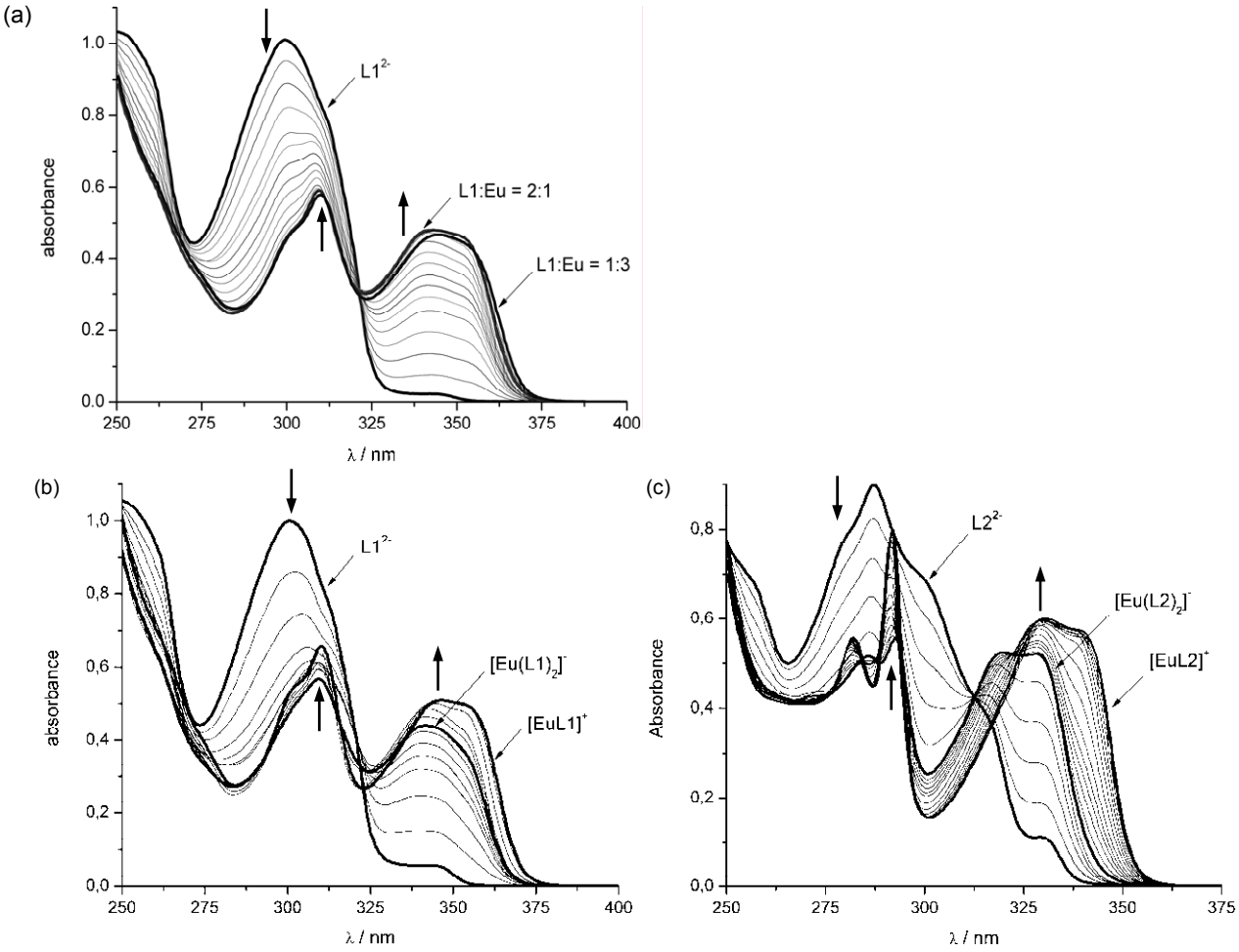

Figure II.18. UV-vis absorption spectra of a $2 \cdot 10^{-4}$ mol·dm^{-3} methanol solution of **L1** in (a) continuous or (b) batch titration and (c) **L2** upon addition of increasing amounts of europium triflate, from 0 to 3 equivalents

The absorption spectra of the ligands are characterized by broad overlapping bands, assigned to n→π* and π→π* transitions, which are affected by complexation. Factor analysis performed with the Specfit software indicated the presence of two new absorbing species during the titration, in line with the formation of 1:1 and 2:1 complexes. The data could be satisfyingly fitted to the following model (i = 1, 2; charges have been omitted for simplicity):

$$Eu + \mathbf{Li} \leftrightarrows Eu\mathbf{Li} \qquad \log\beta_1 = [Eu\mathbf{Li}] / [Eu][\mathbf{Li}] \qquad (II.1)$$

$$Eu + 2\mathbf{Li} \leftrightarrows Eu(\mathbf{Li})_2 \qquad \log\beta_2 = [Eu(\mathbf{Li})_2] / [Eu][\mathbf{Li}]^2 \qquad (II.2)$$

The conditional stability constants β extracted from this data for ligand **L1** are $\log\beta_1^{\mathbf{L1}}$ = 6.1(4) and $\log\beta_2^{\mathbf{L1}}$ = 10.5(5), which are slightly smaller, but in the same order of magnitude

as those corresponding to ligand **L2** with $\log\beta_1^{L2}$ = 6.9(3) and $\log\beta_2^{L2}$ = 11.8(4), and in line with values of related lanthanide complexes. The results obtained compare reasonably well with the distribution of species observed in the NMR experiments.

II.2.3. Photophysical properties of lanthanide complexes

a) Absorption characteristics

The UV-vis absorption spectra of the complexes [Ln(**Li**)$_2$]NHEt$_3$ (i=1..6) in methanol solutions at 298K are represented in Figure II.19. The maximum absorption wavelengths and their corresponding molar extinction coefficients are given in Table II.7

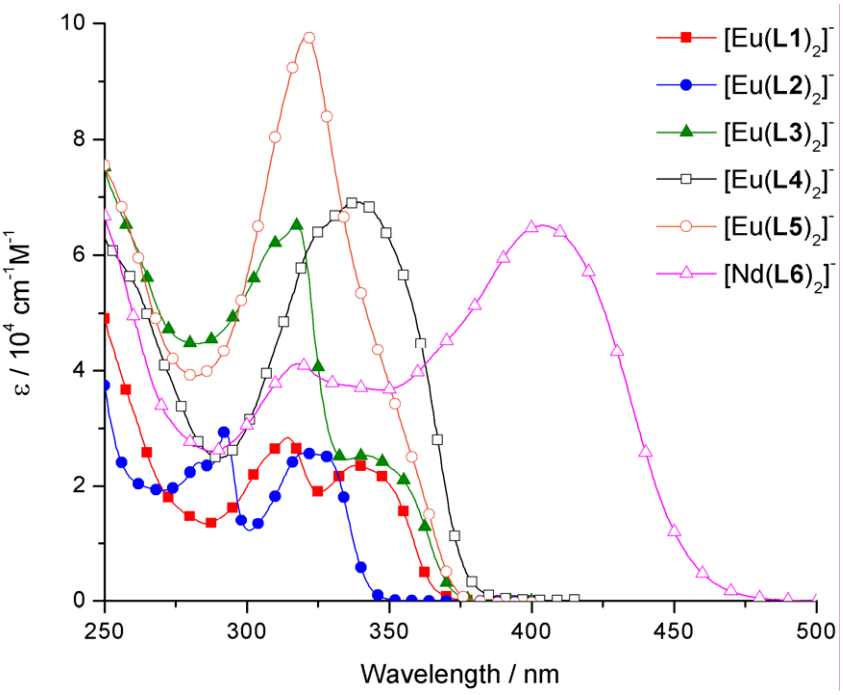

Figure II.19. UV-vis absorption spectra of the complexes [Ln(**Li**)$_2$]NHEt$_3$ (i=1..6) in methanol solutions at 298K

The terpyridine-carboxylate complex [Eu(**L2**)$_2$]NHEt$_3$ shows a strong absorption band split into two components at 283 and 292 nm (ε = 24 050 and 29 550 cm^{-1}M^{-1}, respectively), associated with the pyridine-carboxylate unit.[40, 141] A second broader band appears at 320 nm (ε = 25 700 cm^{-1}M^{-1}), characteristic of the coordinated terpyridine unit,[141] which is greatly increased in intensity compared to the free ligand **L2** (see Figure

II.2, page 55), as a result of the conformational changes associated to the complex formation. In the terpyridine-tetrazole complex [Eu(**L1**)$_2$]NHEt$_3$, the bands are bathochromically shifted with about 20 nm compared to the carboxylate analogue, probably due to the increased conjugation of the terpyridine with the aromatic tetrazole ring. Thus, the spectrum of [Eu(**L1**)$_2$]NHEt$_3$ shows a strong absorption band at 314 nm (ε = 28 300 $cm^{-1}M^{-1}$), and a broader structure centered at 338 nm (ε = 23 500 $cm^{-1}M^{-1}$). Excitation can be performed with a good molar extinction coefficient (ε = 20 300 $cm^{-1}M^{-1}$) even at 350 nm. This difference in absorption between the carboxylate and tetrazole-based complexes can be very useful for extending the excitation window towards the visible region, with important applications in the biomedical analysis and optoelectronic devices.

The substitution of the terpyridine system with various groups in the series of ligands **L3**-**L6** has a very large effect on the absorption spectra of their lanthanide complexes. In the case of [Eu(**L3**)$_2$]NHEt$_3$, the bromophenyl substituent increases the conjugation effect in the system and accordingly the band at 317 nm becomes more intense (ε = 65 100 $cm^{-1}M^{-1}$), while low energy band at 341 nm is less affected (ε = 25 300 $cm^{-1}M^{-1}$). This effect is even more pronounced for the [Eu(**L5**)$_2$]NHEt$_3$ complex, where the terpyridine is substituted with a phenyl-pyridine unit, the spectrum showing a very intense band at 321 nm (ε = 97 750 $cm^{-1}M^{-1}$) and a shoulder in the region 350 nm (ε = 37 350 $cm^{-1}M^{-1}$). Substitution with the bromothiophene unit has also a pronounced effect on the shape of the absorption spectrum of [Eu(**L4**)$_2$]NHEt$_3$, which displays a strong maximum at 339 nm (ε = 69 100 $cm^{-1}M^{-1}$) with a faint shoulder around 325 nm. Excitation can be performed with a very good molar extinction coefficient (ε = 56 500 $cm^{-1}M^{-1}$) even at 355 nm. However, by far the greatest effect is caused by adding a second thiophene unit in the structure of the [Nd(**L6**)$_2$]NHEt$_3$ complex. Here, the absorption spectrum extends in the visible region, with a maximum low-energy band at 405 nm (ε = 65 100 $cm^{-1}M^{-1}$) and a second, less intense band at 318 nm (ε = 41 100 $cm^{-1}M^{-1}$). Excitation can be performed with a good molar extinction coefficient (ε = 25 800 $cm^{-1}M^{-1}$) even at 440 nm.

Table II.7. Absorption wavelengths (λ_{max}) and their corresponding molar extinction coefficients (ε) for the complexes [Ln(**Li**)$_2$]NHEt$_3$ (i = 1..6).

[Ln(**Li**)$_2$]NHEt$_3$	λ_{max} / nm (ε / cm^{-1}M^{-1})
i = 1	308 (25 600), 314 (28 300), 338 (23 500), 350 (20 300)
i = 2	283 (24 050), 292 (29 550), 320 (25 700), 328 (25 100)
i = 3	311 (62 400), 317 (65 100), 341 (25 300), 355 (21 000)
i = 4	326 (64 400), 339 (69 100), 355 (56 500)
i = 5	321 (97 750), 350 (37 350)
i = 6	318 (41 100), 405 (65 100), 440 (25 800)

b) Ligand centered luminescence

Further insights into the spectroscopic characterization of the complexes in water solution were obtained by luminescence spectroscopy. The emission spectra of the ligand **L1** and its complexes with non-luminescent lanthanide ions (Gd, La) in methanol at 298K are presented in Figure II.20. UV excitation at 35 700 cm^{-1} and at the maximum in the excitation spectra results in a ligand-centred emission displaying one broad band assigned to the $^1\pi\pi^*$ state with maximum at 28 2500, 26 670 and 26 600 cm^{-1} for **L1**, [Gd(**L1**)$_2$]$^-$ and [La(**L1**)$_2$]$^-$, respectively. At 77K (methanol glass) and upon enforcement of a time delay (0.2 ms), the singlet state emission disappears with concomitant appearance of a broad and structured band arising from the $^3\pi\pi^*$ state emission. The 0-phonon transition is located at 22 570, 22 170 and 21 830 cm^{-1}, respectively, whereas the triplet state maximum is at 21 230, 20 790 and 20 700 cm^{-1}, respectively. The energy gap between the 0-phonon transitions of the singlet and triplet states is large (7 150 cm^{-1} for the free ligand and 5 230 cm^{-1} for its Gd complex) while a value higher than 5 000 cm^{-1} is commonly considered as optimum for efficient intersystem crossing.[25] Excitation spectra measured at the maximum of the $^3\pi\pi^*$ state display the lowest energy peak at 31 800, 30 200 and 28 570 cm^{-1}, for **L1**, [Gd(**L1**)$_2$]$^-$ and [La(**L1**)$_2$]$^-$, respectively.

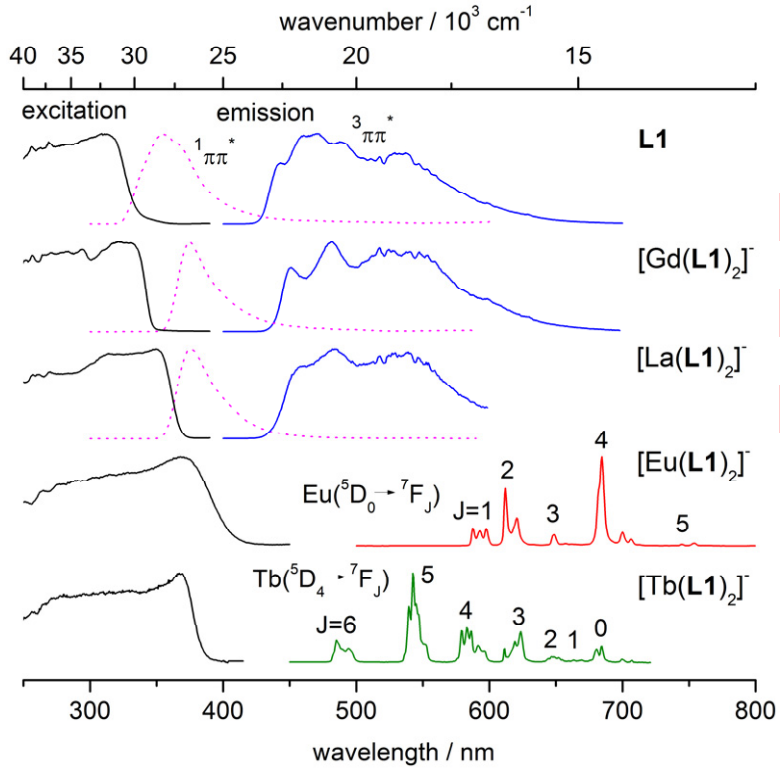

Figure II.20. Normalized excitation and emission spectra of the ligand **L1** and its $[Ln(\mathbf{L1})_2]^-$ complexes (Ln=Gd, La, Eu and Tb). Singlet and triplet state levels are measured in methanol solutions at 298K and 77K, respectively, upon excitation at 35 700 cm^{-1}. Eu and Tb luminescence spectra are recorded in solid state at 298K (excitation at 27 100 and 26 800 cm^{-1}, respectively). Excitation spectra are measured at the maximum of emission.

The $^3\pi\pi^*$ state 0-phonon transition for the Gd complexes of all the ligands are listed in Table II.8. Whereas there is only little difference (300 cm^{-1}) between the phenyl-substituted ligand **L3** and the unsubstituted **L1**, both being situated in the optimal range at about 5 000 cm^{-1} above the $^5D_0$ emissive level of Eu^{3+}, the first $^3\pi\pi^*$ state of the thienyl-substituted ligand **L4** is red-shifted at 18 450 cm^{-1} (3 725 cm^{-1} difference from the parent **L1**), due to the electro-releasing effect of the thiophene substituent which increases the electronic density and the conjugation in the terpyridine system. Similarly, the first $^3\pi\pi^*$ state of the phenylpyridine-substituted ligand **L5** is lowered at 20 080 cm^{-1}. A further decrease in the energy of the $^3\pi\pi^*$ state is found in the ligand **L6**, where the strongly electro-releasing bis-thiophene substituent lowers the triplet state down to 15 000 cm^{-1}.

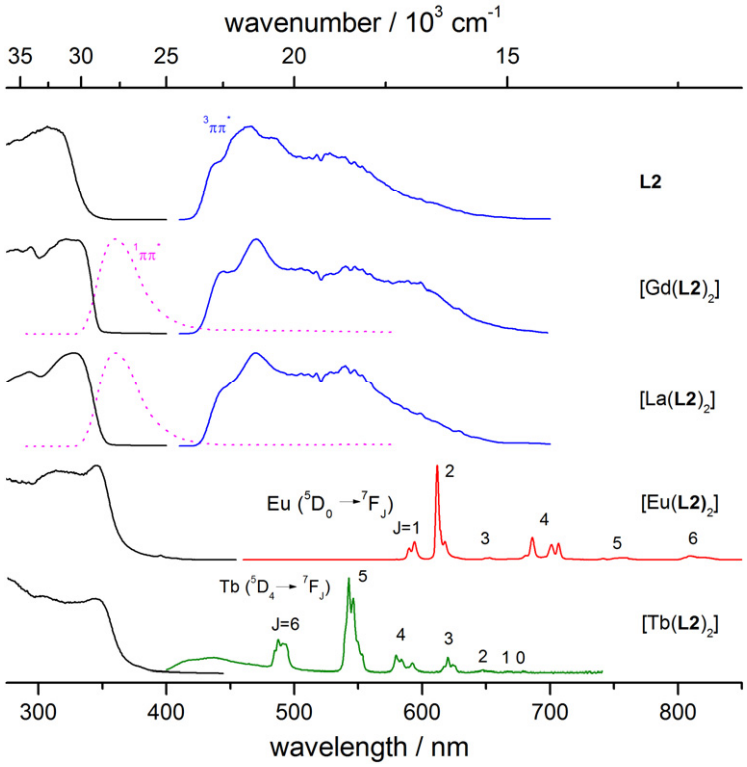

Figure II.21. Normalized excitation and emission spectra of the ligand **L2** and its $[Ln(\mathbf{L2})_2]^-$ complexes (Ln=Gd, La, Eu and Tb). Singlet and triplet state levels are measured in methanol solutions at 298K and 77K, respectively, upon excitation at 35 700 cm^{-1}. Eu and Tb luminescence spectra are recorded in solid state at 298K (excitation at 29 000 cm^{-1}). Excitation spectra are measured at the maximum of emission.

In the case of the terpyridine carboxylate ligand **L2**, no room temperature emission was observed in methanol solution (see Figure II.21). Only its Gd and La complexes shown a broad $^1\pi\pi^*$ state with a maximum at 27 780 cm^{-1}, higher in energy with 1 100 cm^{-1} compared to the **L1**. This is correlated with the π-electro-withdrawing effect of the carboxylate group (the resonance component of the Hammett substituent[22] R = +0.11) which is known to increase the energy of the ligand levels[21, 151], in contrast with the tetrazole group which has a π-electro-releasing effect (R = -0.09) and leads to a decrease in the energy. At 77K in methanol glass, the $^3\pi\pi^*$ state emission is observed in time-resolved mode, with the 0-phonon transition at 22 680 and 22 520 cm^{-1}, and maxima at 21 550 and 21 280 cm^{-1}, for free **L2** and its complexes, respectively, again higher in energy (with 350 cm^{-1}) compared to **L1**. Excitation spectra measured at this maximum of the $^3\pi\pi^*$ state show the lowest energy peak at 31 800 and 30 400 cm^{-1}, respectively, similarly to **L1**.

Table II.8. Summary of photophysical properties for the [Ln(**Li**)$_2$]NHEt$_3$ complexes (i = 1..6). Singlet ($^1\pi\pi^*$) and lowest triplet state ($^3\pi\pi^*$) energies of the Gd chelates are measured in methanol solutions at 298K and 77K, respectively. The energy difference (ΔE) is calculated between the $^3\pi\pi^*$ and the emissive lanthanide level. Excitation maxima ($\tilde{\upsilon}_{max}$) are given from solid state excitation spectra. Lifetimes (τ) and absolute quantum yields (Φ) are measured for solid state samples at 298K.

L	$^1\pi\pi^*$/cm^{-1}	$^3\pi\pi^*$/cm^{-1}	Ln	ΔE/cm^{-1}	$\tilde{\upsilon}_{max}$/cm^{-1}	τ/ms	Φ/%
L1	26 670	22 170	Eu	4 910	27 100	2.500(7)	35.3(2)
			Tb	1 670	26 800	0.179(4)	6.1(3)
			Nd	10 870	27 030	$1.61\cdot10^{-3}$ (10^{-5})	0.22(1)
L2	27 780	22 520	Eu	5 260	29 000	2.11(2)	35.9(4)
			Tb	2 020	29 000	2.03(2)	34.9(2)
			Nd	11 220	29 500	$1.0\cdot10^{-3}$ ($2\cdot10^{-4}$)	0.09(1)
L3	26 390	21 980	Eu	4 720	27 030	2.465(5)	29.4(6)
			Tb	1 480	26 950	$2.81\cdot10^{-2}$ ($2\cdot10^{-3}$)	0.085(5)
L4	23 530	18 450	Eu	1 190	26 040	0.502(3)	5.4(2)
			Nd	7 150	26 450	$2.22\cdot10^{-3}$ (10^{-5})	0.29(2)
L5	26 250	20 080	Eu	2 820	26 530	2.47(3)	27.8(2)
L6	20 040	15 000	Nd	3 700	20 700	$2.07\cdot10^{-3}$ (10^{-5})	0.19(1)

c) Metal centered luminescence

All the Eu, Tb and Nd complexes prepared with the ligands presented in this study show metal-centred luminescence. The luminescence spectrum of [Eu(**L1**)$_2$]$^-$ in solid state at 298K is given in Figure II.20. The ligand-centred $^1\pi\pi^*$ emission is not detected, pointing to an efficient ligand to metal energy transfer process. Upon broadband excitation, the Eu emission exhibits the characteristic $^5D_0\rightarrow{}^7F_J$ transitions and is dominated by the $^7F_4$ transition, same as all the series of terpyridine-tetrazole Eu complexes, opposed to the carboxylate analogue (see Figure II.22).

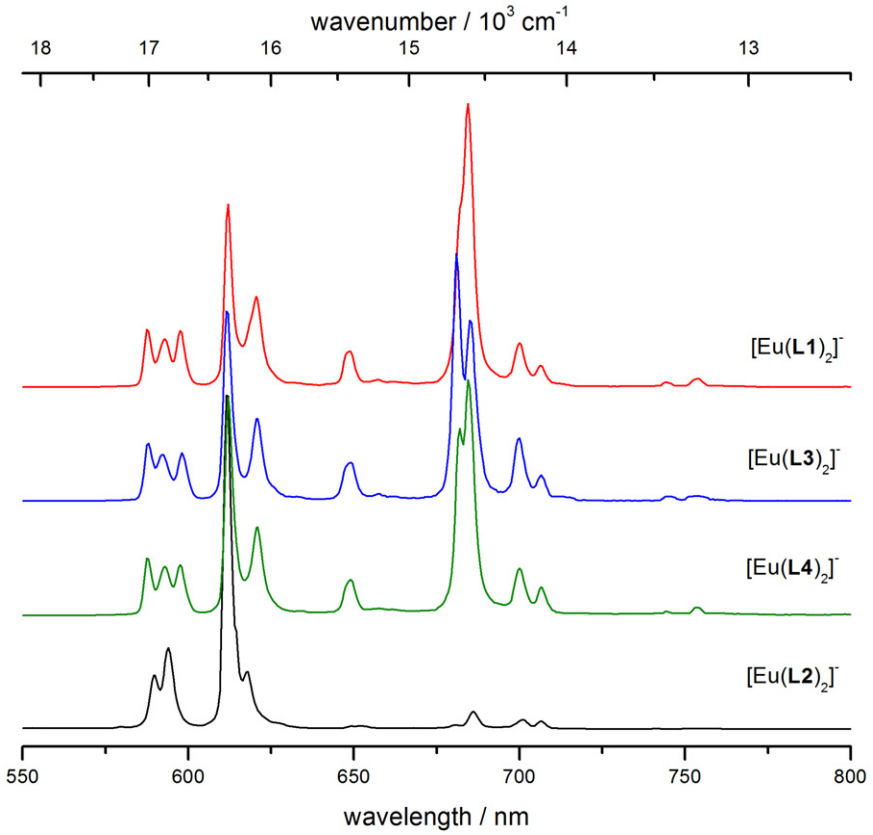

Figure II.22. Solid state emission spectra measured at 298K for $[Eu(\mathbf{Li})_2]^-$ where i = 1, 2, 3 and 4 upon ligand excitation at the maximum of the excitation spectrum. Spectra are normalized for the $^7F_1$ band.

The crystal field splitting of the $[Eu(\mathbf{L1})_2]^-$ emission spectra can be interpreted in terms of a low D_2 symmetry point group, with two C_2 axes perpendicular to a third one, as shown by the X-ray structure. The $^5D_0 \rightarrow {}^7F_0$ transition occurs at 17 240 cm^{-1} and is very faint, consistent with the fact that it is symmetry forbidden in the D_2 symmetry group. The $^7F_1$ level presents three main components of the same intensity at 17 020, 16 870 and 16 735 cm^{-1}, assigned to the allowed magnetic dipole transitions $A \rightarrow B_1$, B_2, B_3 in D_2 symmetry, while the $^5D_0 \rightarrow {}^7F_4$ transition displays a strong band at 14 610 cm^{-1} and two smaller ones at 14 290 and 14 155 cm^{-1}, attributed to the electric dipole transitions $A \rightarrow B_1$, B_2, B_3. The typical $^5D_0 \rightarrow {}^7F_2$ transition appears only as two bands (instead of three) at 16 340 and 16 115 cm^{-1} due to the low resolution of the spectrum. For the same reason, the fine structure of the $^5D_0 \rightarrow {}^7F_4$ transition cannot be seen. The same crystal field splitting is observed when recording the emission spectrum of a methanol solution ($5 \cdot 10^{-3}$ $mol \cdot dm^{-3}$) of $[Eu(\mathbf{L1})_2]^-$, implying the preservation of the solid state symmetry in solution (see Figure

II.23). The europium complex of **L2** shows a solid state emission dominated by the $^7F_2$ transition, with only two components at the $^7F_1$ band and a very weak $^7F_4$ transition, indicating a somewhat different symmetry of the complex (Figure II.22 and Table II.9)

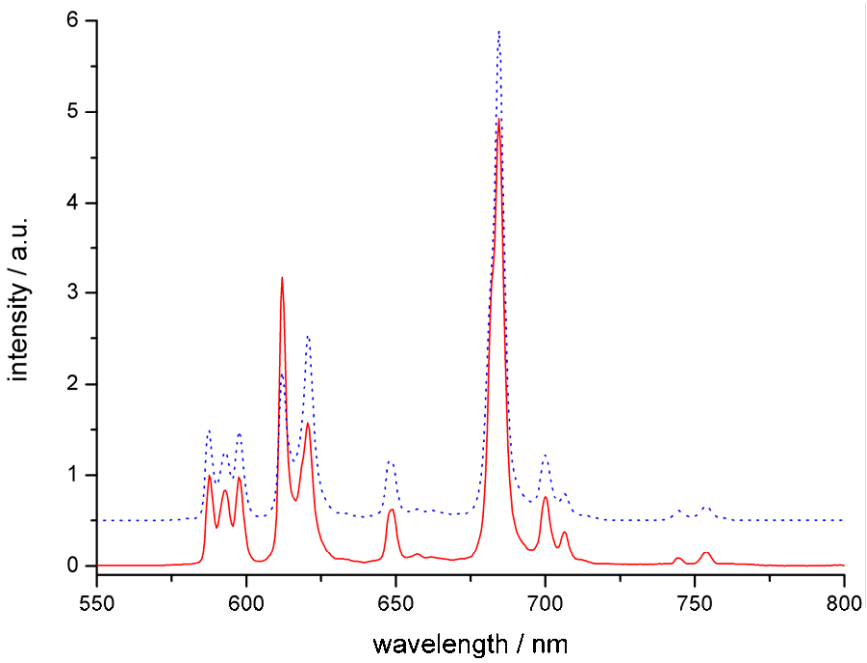

Figure II.23. Emission spectra of the $[Eu(\mathbf{L1})_2]^-$ complex in solid state (continuous red line) and in $5{\cdot}10^{-3}$ mol·dm^{-3} methanol solution (dotted blue line).

Table II.9. Energy (cm^{-1}) of the identified crystal-field sublevels of the Eu (^7F_J) manifold (J = 1-5) as determined from the solid state emission spectra at 298K[a]

	$[Eu(\mathbf{L1})_2]^-$	$[Eu(\mathbf{L2})_2]^-$
$\tilde{\upsilon}_{ex}$ / cm^{-1}	27100	28985
$^5D_0$	17240	17250
$^7F_1$	220, 370, 505	290, 415
$^7F_2$	900, 1125	905, 1065
$^7F_3$	1820, 2030, 2140	15400, 15330
$^7F_4$	2630, 2950, 3085	1850, 2670, 2985, 3095
$^7F_5$	3805, 3975	-

[a] $^5D_0$ is taken as the origin

The excitation spectra of $[Eu(\mathbf{L1})_2]^-$, recorded in solid state or methanol solutions ($5{\cdot}10^{-3}$ mol·dm^{-3}) at the $^7F_2$ site, show a maximum displaced at 27 100 cm^{-1} compared to the excitation spectra of $[Gd(\mathbf{L1})_2]^-$ recorded at the $^3\pi\pi^*$ state maximum. The shifted band has

been assigned to the $^1\pi\pi^*$ state of the ligand, visible as a result of the efficient $^1\pi\pi^* \rightarrow {}^5D_0$ energy transfer. The excitation maximum of $[Eu(\mathbf{L1})_2]^-$ is red-shifted (by 1 900 cm^{-1}) with respect to the carboxylate analogue $[Eu(\mathbf{L2})_2]^-$. The excitation spectra of $[Eu(\mathbf{L1})_2]^-$ recorded in dilute methanol solutions ($2 \cdot 10^{-5}$ mol·dm^{-3}) have a maximum at higher energy (28 570 cm^{-1}) compared to the solid state, and they reproduce the shape of the components of the absorption spectra recorded at the same concentration (see Figure II.24), indicating again an efficient intramolecular energy transfer process from the ligand to the europium emissive levels.

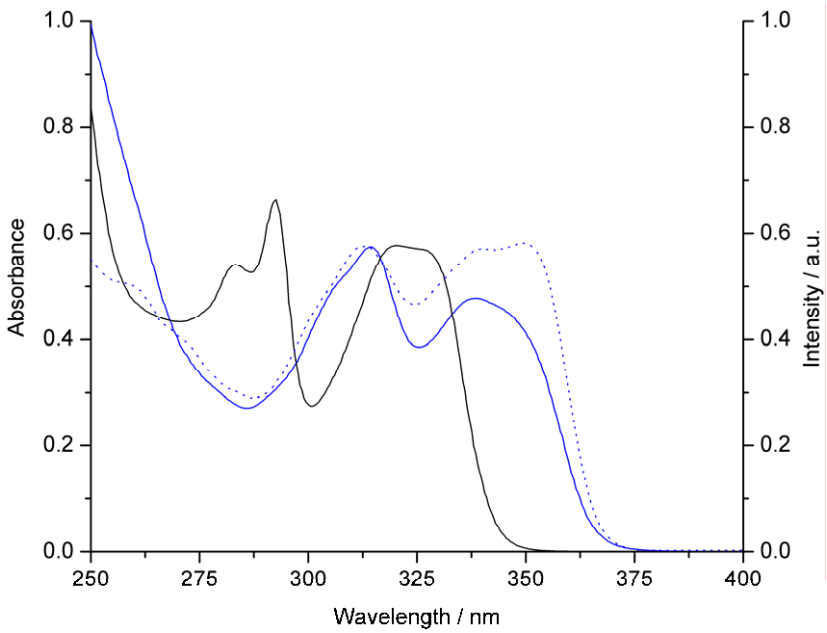

Figure II.24. UV absorption spectra of the $[Eu(\mathbf{L1})_2]^-$ complex (blue line) compared to its carboxylate analogue $[Eu(\mathbf{L2})_2]^-$ (black line) in methanol solution ($2 \cdot 10^{-5}$ mol dm^{-3}) at 298K. The normalized excitation spectrum of the $[Eu(\mathbf{L1})_2]^-$ complex (dotted blue line) in the same concentration is also represented.

The luminescence decay of the $[Eu(\mathbf{L1})_2]^-$ emission, measured at the $^7F_2$ site upon ligand excitation, can be fitted as a monoexponential function and corresponds to a 2.50 ms lifetime in solid state at 298K. Methanol solutions ($5 \cdot 10^{-3}$ mol·dm^{-3}) in both protonated and deuterated solvent shown similar long lifetimes of 3.34 and 4.00 ms, respectively, confirming the absence of OH oscillators in the inner coordination sphere of the metal ion, as implied by the X-ray structure. The number of solvent molecules q can be calculated using the empirical equation of Horrocks:

$$q = A\,(\tau_H^{-1} - \tau_D^{-1} - B) \qquad \text{(II.3)}$$

For methanol, A = 2.1 and B = 0,[152] and thus q = 0.105 ≈ 0. Lifetimes over 2 ms have also been obtained in solid state for the Eu complexes of **L2**, **L3** and **L5**, while only 0.50 ms was obtained for the complex of **L4**. In view of the first $^3\pi\pi^*$ state energy of this ligand, situated only 1 185 cm^{-1} above the emissive Eu($^5D_0$) energetic level, and assuming that no solvent molecules are present in the first sphere of coordination (according to the X-ray structure), such a low lifetime can be correlated with a strong de-exciting back-energy transfer from the metal ion to the triplet state of the ligand, or perhaps a charge transfer mechanism.

At 298 K in solid state and upon ligand excitation, the [Tb(**L1**)$_2$]$^-$ complex displays a typical emission spectrum dominated by the $^5D_4 \rightarrow {}^7F_5$ transition (Figure II.20). The relative intensities of the $^7F_{6\text{-}0}$ bands are 1, 2.37, 1.23, 0.70, 0.16, 0.07, 0.25, respectively, while in the case of the [Tb(**L2**)$_2$]$^-$ complex, the ratio is 1, 2.03, 0.43, 0.20, 0.06, 0.05, 0, with smaller intensities for the low-energy bands. The luminescence decay, measured for the [Tb(**L1**)$_2$]$^-$ complex at the maximum of emission, is monoexponential but corresponds to a short lifetime of 0.18 ms in solid state at 298K, compared to the value of 2.03 ms for the [Tb(**L2**)$_2$]$^-$ complex, although the $^3\pi\pi^*$ state energies of the two ligands are only 350 cm^{-1} apart. This apparent contradiction will be explained later when considering the quantum yield determination.

NIR luminescence measurements have also been performed on the [Nd(**Li**)$_2$]$^-$ complexes, where i = 1, 2, 4 and 6 (see Figure II.25). The luminescence spectra, measured in solid state at 298 K upon broad band excitation through the ligand levels, display three bands in the spectral ranges 845-940, 1010-1130 and 1275-1430 cm^{-1}, which are assigned to transitions from the $^4F_{3/2}$ level to the $^4I_{9/2}$, $^4I_{11/2}$ and $^4I_{13/2}$ sublevels, respectively. For the tetrazole-based complexes, the components of the bands are very similar, showing 2, 2 and 4 peaks, respectively (at 11430, 11000, 9480, 9285, 7720, 7550, 7350 and 7130 cm^{-1}), whereas the complex of **L2** shows a different splitting pattern. The lifetimes of the neodymium emission, measured at the 1 μm transition, are characteristically small, with the longest value (2.22 μs) obtained for the [Nd(**L4**)$_2$]$^-$ complex.

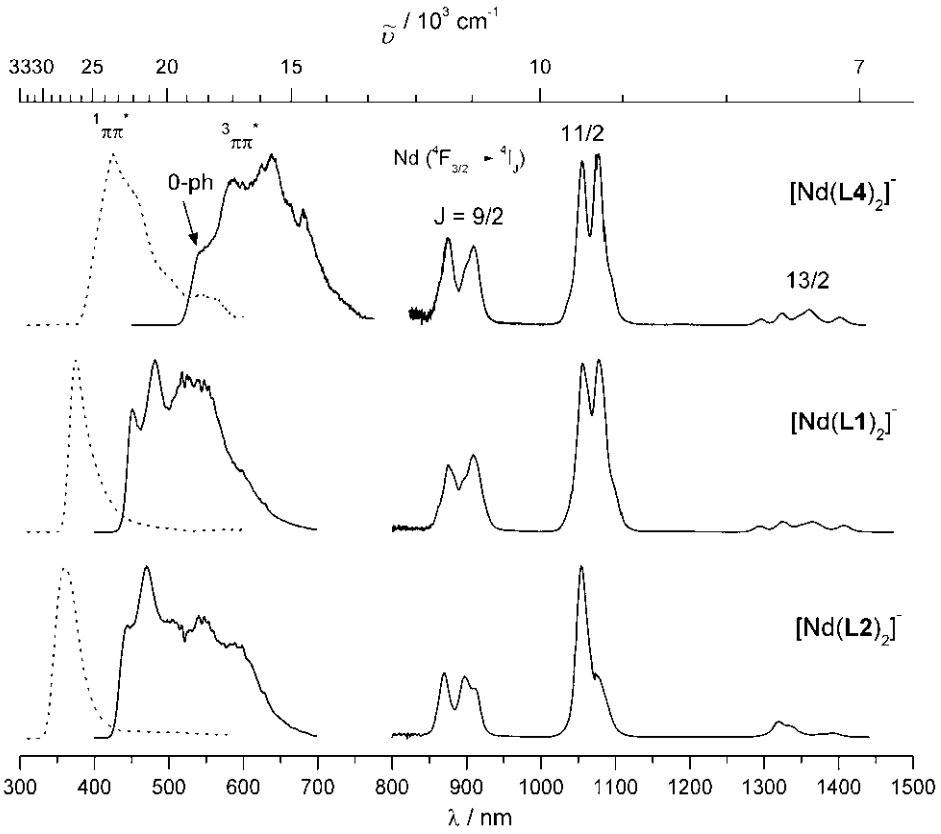

Figure II.25. Fluorescence, phosphorescence (recorded in solution at 298K and 77K, respectively, for the Gd complexes upon excitation at 280 nm) and near-IR emission spectra for [Nd(**Li**)$_2$]$^-$ complexes, i = 1, 2 and 4 (measured at 298K in solid state upon excitation at 378, 370 and 343 nm, respectively). Spectra are normalized and not drawn on the same vertical scale.

To quantify the ability of the ligands prepared to sensitize the luminescence of lanthanides, and to draw conclusions concerning the relationship between structure and properties, the absolute quantum yields of the complexes have been determined upon ligand excitation (see Table II.8). In solid state, the [Eu(**L1**)$_2$]$^-$ complex shows a high value (35.3%), similar to that of [Eu(**L2**)$_2$]$^-$ (35.9%) and one of the highest reported for europium complexes. The europium quantum yields have also been measured in methanol solutions using the tris(dipicolinate) [Eu(dpa)$_3$]$^{3-}$ complex as reference,[38, 39] the values obtained being close to the solid state measurements (28.0% and 37.2%, respectively). In the terpyridine tetrazole series, the phenyl-substituted [Eu(**L3**)$_2$]$^-$ complex displays a comparable quantum yield (29.4%), similar to that of [Eu(**L5**)$_2$]$^-$ (27.8%), whereas the thienyl-substituted [Eu(**L4**)$_2$]$^-$ complex has a much lower value (5.4%).

To better understand these results, one must take into account the $^3\pi\pi^*$ state energies of the ligands. In Figure II.26a, we have re-plotted the dependency of the europium quantum yields upon the triplet state, as originally done by Latva[16], including also our results. In the original paper, the authors have concluded that the highest quantum yields are obtained when the energy difference between the first $^3\pi\pi^*$ state of the ligand and the emissive $^5D_0$ level of europium is around 2 500 or 4 800 cm^{-1}, the two maxima being situated in between the resonance levels of Eu^{3+}. While the energy difference in the case of ligands **L1**, **L2** and **L3** is situated in the latter range, and accordingly their Eu complexes exhibit strong luminescence, the first $^3\pi\pi^*$ state of **L4** is much too close to the emissive $^5D_0$ level and so the europium luminescence is quenched by a back-energy transfer process, as suggested from the lifetime measurement. Interestingly, the quantum yield of the $[Eu(\mathbf{L5})_2]^-$ complex is also high, as the first $^3\pi\pi^*$ state of **L5** is conveniently situated at 2 800 cm^{-1} above the $Eu(^5D_0)$ level (first maximum).

In the case of terbium luminescence, solid state measurements gave a quantum yield of only 6.1% for the $[Tb(\mathbf{L1})_2]^-$ complex, compared with 34.9% for $[Tb(\mathbf{L2})_2]^-$. The value obtained for the tetrazole-substituted complex has also been checked in methanol solution, giving 5.1 % in this case. The triplet state energies and the structures of the two ligands being similar, one could also expect a similar quantum yield. It is not until we plot the dependency of the terbium quantum yields upon the lowest $^3\pi\pi^*$ state (see Figure II.26b) that we see a sharp decrease in luminescence starting around 22 000 cm^{-1}, as the $^3\pi\pi^*$ state energy approaches the emissive $^5D_4$ level of Tb^{3+}. On this region, very small changes of triplet state energy cause strong modification in emissive quantum yield. Ligand **L1**, with the first $^3\pi\pi^*$ state at 22 170 cm^{-1}, is situated on the descending slope and thus the emission of its terbium complex is strongly decreased via an energy back transfer mechanism from the $Tb(^5D_4)$ level to the ligand triplet state. A lifetime of 0.18 ms and the absence of OH oscillators in the inner sphere of coordination also point to this de-excitation pathway. Ligand **L3**, with a first $^3\pi\pi^*$ state even lower in energy, practically quenches the emission of terbium (quantum yield 0.085%).

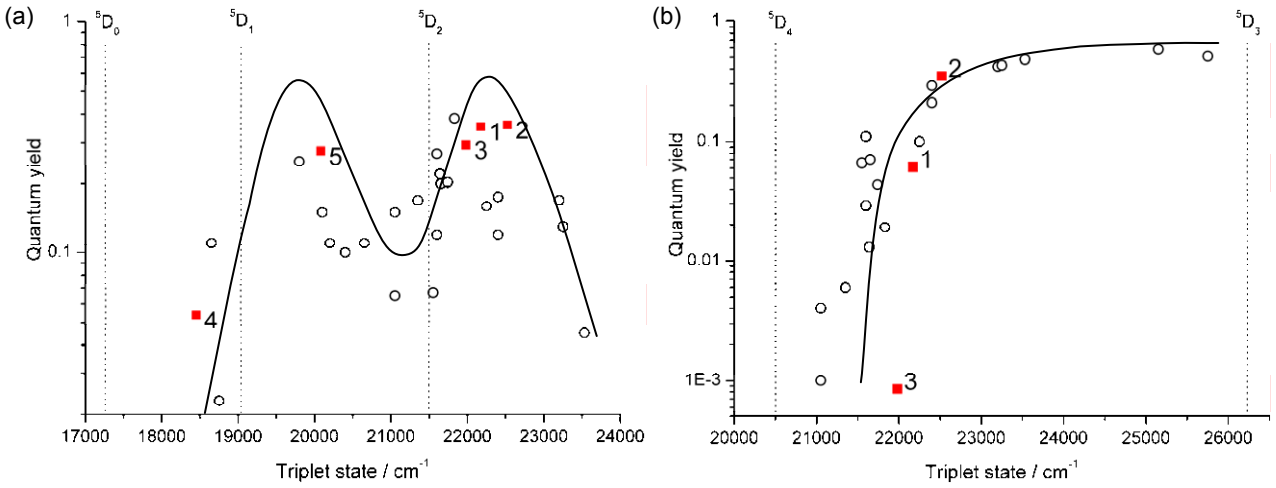

Figure II.26. Luminescence solid state quantum yields of (a) Eu and (b) Tb complexes (■) as a function of the lowest triplet state energy of the ligands **Li** (i = 1..5). Values obtained by Latva[16] in solution (○) are also plotted for comparison. The curves are a coarse tendency drawn from average values.

The absolute quantum yields in the NIR have been measured in solid state for the $[Nd(\mathbf{Li})_2]^-$complexes (i = 1, 2, 4 and 6). While the carboxylate-based complex $[Nd(\mathbf{L2})_2]^-$ shown average values (0.09%), the tetrazole-based complexes $[Nd(\mathbf{L1})_2]^-$, $[Nd(\mathbf{L4})_2]^-$ and $[Nd(\mathbf{L6})_2]^-$ exhibited high quantum yields (0.22%, 0.29% and 0.19%, respectively). In fact, to our knowledge, the thienyl-substituted complex $[Nd(\mathbf{L4})_2]^-$ displays one of the highest absolute quantum yields for an organic neodymium complex, similar to the ones measured for a dansyl-based dendrimer in acetonitrile (0.27%)[153] and a phthalexon S derivative in D_2O (0.23%).[154] It should be stressed here that the intrinsic quantum yield of Nd rarely exceeds 2–4%, so that the sensitization process is not the limiting factor.[8] Typical quantum yields for Nd, obtained using for example 8-hydroxyquinolinates, amount to 0.10% in D_2O,[155] while the use of fluorescein dyes gives only 0.03% in MeOD.[156] It is interesting to note that lowering the $^3\pi\pi^*$ state by strongly electro-donating groups in the thienyl-substituted ligand **L4**, albeit a problem for europium sensitization, proved to be very useful for exciting the low-lying $^4F_{3/2}$ emissive level of Nd^{3+}. However, further lowering of the $^3\pi\pi^*$ state in **L6** did not result in improved emission efficiencies for the neodymium complex.

II.3. Lanthanide complexes based on bipyridine-tetrazolates

II.3.1. Synthesis and characterization of ligands

a) Ligand design

After looking at the influence of different ligand substituents on the properties of the resulting lanthanide complexes in the terpyridine series, we have decided to incorporate the tetrazole moiety in the bipyridine framework as well, for obtaining strongly chelating ligands for lanthanides, featuring a four-site pincer-shaped coordinating pattern. We have focused in this study on the influence of the tetrazole group, compared to the carboxylic acid, on the photophysical properties of the visible lanthanide emitters. For this, we planned the synthesis of three ligands: two symmetrical ones containing the tetrazole (**L7**, bipytz) and the carboxylic acid group (**L9**, bipyc), respectively, and one asymmetric ligand containing both substituents (**L8**, bipytzc). The resulting ligands being tetradentate, we envisaged the formation of 2L : 1Ln complexes, in which the metal would be octa-coordinated. As the bipyridine-carboxylate is a very used motif in lanthanide coordination chemistry,[44, 52, 157] studying the effects of tetrazole substitution in a coherent series would prove beneficial for the further development of efficient lanthanide chelates.

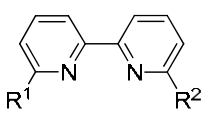

L7 bipytz $R^1 = R^2 = TzH$
L8 bipytzc $R^1 = Tz$, $R^2 = COOH$
L9 bipyc $R^1 = R^2 = COOH$

TzH = 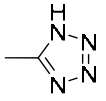

b) Synthesis and characterization of ligands **L7** - **L9**

The symmetric bipyridine-tetrazole ligand **L7** was prepared according to a protocol similar to that employed for the terpyridine-based ligands, starting with the initial activation of the bipyridine **16** by N-oxidation with chloroperbenzoic acid[136] to give **17**,

followed by the introduction of cyanide via a modified Reissert-Henze reaction[52, 137] employing trimethylsilane-carbonitrile and benzoyl chloride (Scheme II.13), yielding the symmetric bipyridine dicarbonitrile **18**. The final ligand was prepared in good yield by the thermal cycloaddition reaction of sodium azide with **18** in anhydrous DMF and in the presence of NH_4Cl. The analogous symmetric bipyridine-carboxylic ligand **L9** was obtained via the hydrolysis in strong acidic conditions of the same bipyridine-dicarbonitrile **18**. The ligand **L9** has been reported before,[157] however the synthetic strategy in that case was the oxidation of 6,6'-dimethyl-bipyridine with CrO_3 in concentrated sulfuric acid.

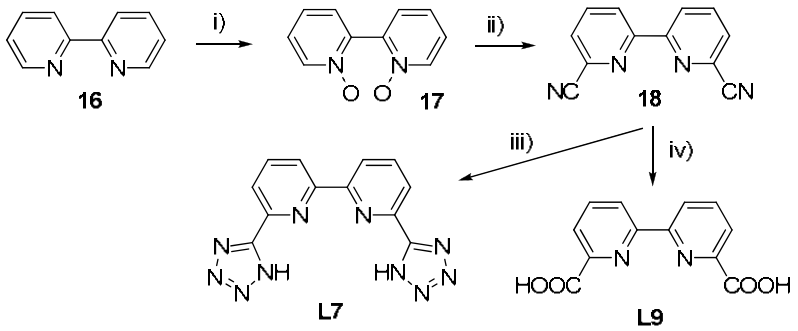

Scheme II.13. Conditions: i) mCPBA, DCM, RT (87%); ii) Me_3SiCN, PhCOCl, DCM, RT (79%); iii) NaN_3, NH_4Cl, DMF, 125°C (77%); iv) H_2SO_4, HOAc, RT (99%)

The asymmetric bipyridine ligand **L8** was synthesized according to a different procedure, as shown in Scheme II.14. The bromo-methyl-bipyridine **22**[158] was prepared by the Stille coupling of 2-methyl-6-trimethylstannylpyridine **20** with 2,6-dibromopyridine **21**. Attempts at synthesizing directly the bromo-bipyridine-carboxylate **24** by the Stille coupling of methyl trimethylstannylpicolinate with dibromopyridine failed in our hands, probably due to the instability of the stannylpicolinate. After oxidation of the methyl group with CrO_3 in concentrated H_2SO_4, the resulting bromo-bipyridine-carboxylic acid **23** was protected by esterification and the bromine group converted into cyanide using CuCN in DMF under microwave irradiation. The thermal cycloaddition reaction of sodium azide with the ethyl cyano-bipyridine-carboxylate **25** in anhydrous DMF, followed by deprotection of the ester group, gave finally the asymmetric ligand **L8**.

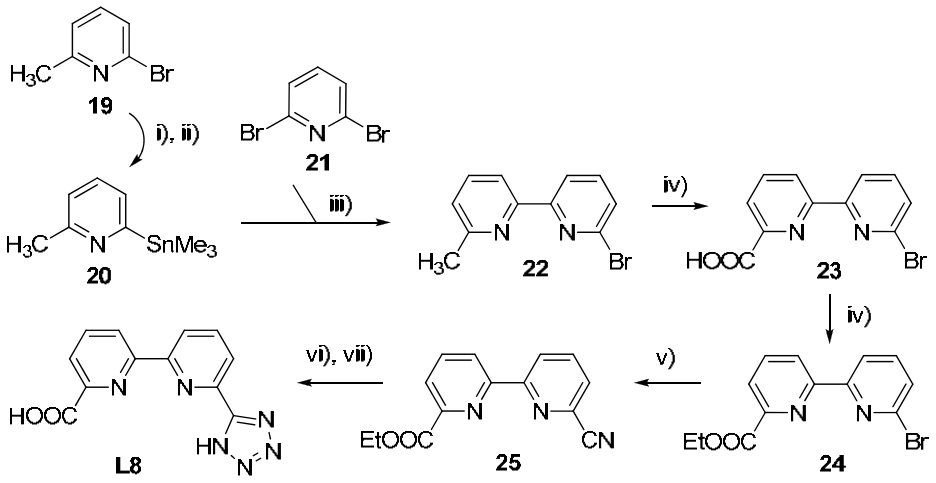

Scheme II.14. Conditions: i) BuLi, THF, -75°C; ii) $SnClMe_3$, THF, -75°C to RT (92%); iii) $Pd(PPh_3)_4$ (cat), toluene, reflux (74%); iv) CrO_3, H_2SO_4, 0°C to RT (87%); iv) EtOH, H_2SO_4, microwave (80%); v) CuCN, DMF, microwave (87%); vi) NaN_3, NH_4Cl, DMF, 135°C; vii) KOH, H_2O, reflux (59%)

The ligands **L7**-**L9** have been characterized by ^{1}H and ^{13}C NMR spectroscopy and elemental analysis, and the data is available in the Experimental part. The ^{1}H NMR spectra in DMSO solution are given in Figure II.27.

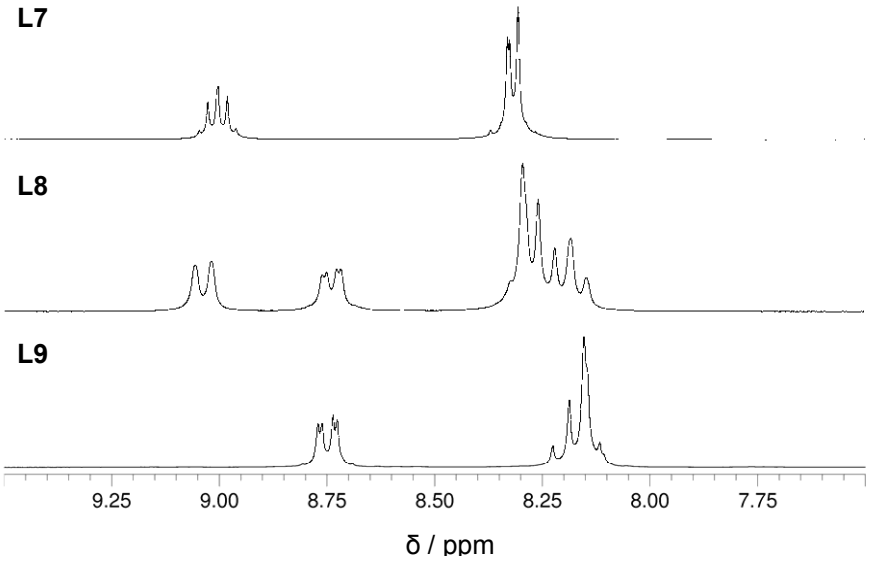

Figure II.27. ^{1}H NMR spectra in DMSO solutions of ligands **L7**-**L9**, showing the aromatic region

II.3.2. Synthesis and characterization of lanthanide complexes

Homoleptic lanthanide complexes [Ln(**Li**)$_2$]NHEt$_3$ (Ln = Eu, Tb; i = 7, 8 and Ln = Eu; i = 9) based on the ligands described above have been prepared by reacting two equivalents of ligand with one equivalent of lanthanide triflate in methanol solution and in the presence of triethylamine, as shown in Scheme II.15 for [Eu(**L7**)$_2$]NHEt$_3$. The complexes were isolated by crystallization, after addition of acetonitrile. The products have been characterized by single crystal X-ray diffraction, proton NMR spectroscopy and elemental analysis (full details in the Experimental Section).

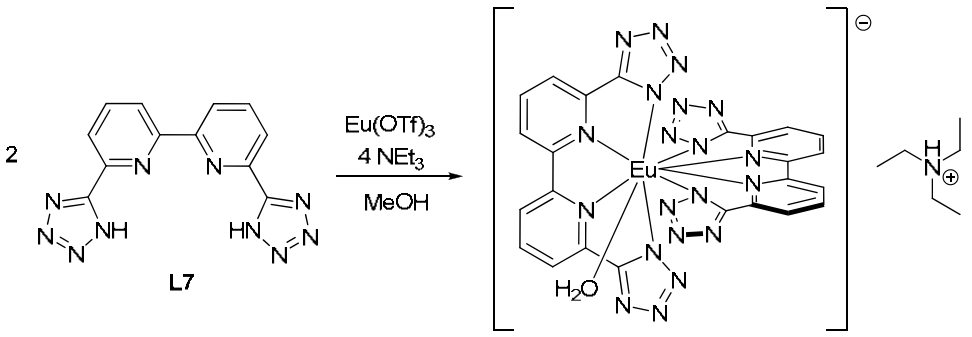

Scheme II.15. Reaction scheme for the synthesis of the [Eu(**L7**)$_2$]NHEt$_3$ complex

a) Molecular and crystal structures

A crystal suitable for X-ray diffraction has been obtained for the [Eu(**L7**)$_2$H$_2$O]NHEt$_3$ complex, by diffusion of diisopropylether in a methanol solution of the complex. Selected bond distances and angles are given in Table II.10, while the crystallographic data is presented in the Appendix.

In the monoclinic P2(1)/*n* structure, the nine-coordinated metal is surrounded by two deprotonated ligands. The metal is coordinated by the bipyridine nitrogens and the two charged nitrogens of the terminal tetrazole groups, for each of the two ligands, and by the oxygen of one water molecule (see Figure II.28). The Eu-N distances range from 2.511 to 2.583 Å, being slightly shorter than in the case of the more sterically hindered [Eu(**L1**)$_2$]NHEt$_3$. The two practically planar ligands are situated at an angle of 71.9°, at which no intramolecular π-π interactions can occur. The deviation from orthogonally is

caused by one water molecule (Eu-O(1) distance of 2.442 Å and N(7)-Eu-O(1) angle of 69.42°) which completes the coordination sphere of the metal. The lanthanide ion is situated at an average distance of 0.7 Å from the planes of the ligands, and an angle N(1)-Eu-N(7) between the tetrazolate nitrogens of 147.26°.

Table II.10. Selected bond distances (Å) and angles (°) in the [Eu(**L7**)$_2$ H_2O]$NHEt_3$ complex

Eu-O(1)	2.442(2)	O(1)-Eu-N(17)	138.25(8)	N(1)-Eu-N(16)	78.73(7)
Eu-N(17)	2.511(2)	O(1)-Eu-N(7)	69.42(8)	N(11)-Eu-N(16)	123.80(7)
Eu-N(7)	2.518(2)	N(17)-Eu-N(7)	73.14(8)	N(5)-Eu-N(16)	132.49(7)
Eu-N(1)	2.536(2)	O(1)-Eu-N(1)	140.91(8)	O(1)-Eu-N(15)	80.19(7)
Eu-N(11)	2.547(2)	N(17)-Eu-N(1)	80.31(8)	N(17)-Eu-N(15)	126.29(7)
Eu-N(5)	2.552(2)	N(7)-Eu-N(1)	147.26(8)	N(7)-Eu-N(15)	102.53(7)
Eu-N(16)	2.562(2)	O(1)-Eu-N(11)	68.72(8)	N(1)-Eu-N(15)	78.02(7)
Eu-N(15)	2.564(2)	N(17)-Eu-N(11)	147.94(7)	N(11)-Eu-N(15)	64.70(7)
Eu-N(6)	2.583(2)	N(7)-Eu-N(11)	137.74(7)	N(5)-Eu-N(15)	131.97(7)
π-π distance[a]	3.408	N(1)-Eu-N(11)	72.68(8)	N(16)-Eu-N(15)	62.61(7)
		O(1)-Eu-N(5)	109.06(8)	O(1)-Eu-N(6)	74.56(7)
		N(17)-Eu-N(5)	78.31(7)	N(17)-Eu-N(6)	73.34(7)
		N(7)-Eu-N(5)	125.13(7)	N(7)-Eu-N(6)	64.90(7)
		N(1)-Eu-N(5)	65.51(7)	N(1)-Eu-N(6)	125.02(7)
		N(11)-Eu-N(5)	74.99(7)	N(11)-Eu-N(6)	108.54(7)
		O(1)-Eu-N(16)	118.39(8)	N(5)-Eu-N(6)	62.41(7)
		N(17)-Eu-N(16)	65.24(7)	N(16)-Eu-N(6)	127.44(7)
		N(7)-Eu-N(16)	72.99(7)	N(15)-Eu-N(6)	154.44(7)

[a] measured between N(7) tetrazolate centroid and the N(13) atom of different complexes

Intermolecular π-π interactions (3.408, 3.12°) occur in the packing structure between the N(7) and N(11) tetrazole rings of different complexes. A comparison of the structures of terpyridine and bipyridine-tetrazole based complexes shows that the [Eu(**L7**)$_2$$H_2O$]$NHEt_3$ complex displays stronger metal coordinative bonds, however one molecule of solvent is present in the first coordinative sphere of the lanthanide. The Eu-N distances involving the tetrazole nitrogens are on average 2.528 Å in [Eu(**L7**)$_2$$H_2O$]$NHEt_3$, compared to 2.586 Å in [Eu(**L1**)$_2$]$NHEt_3$. Furthermore, the bipyridine-based complex no longer displays helical chirality, as the ligands are practically planar.

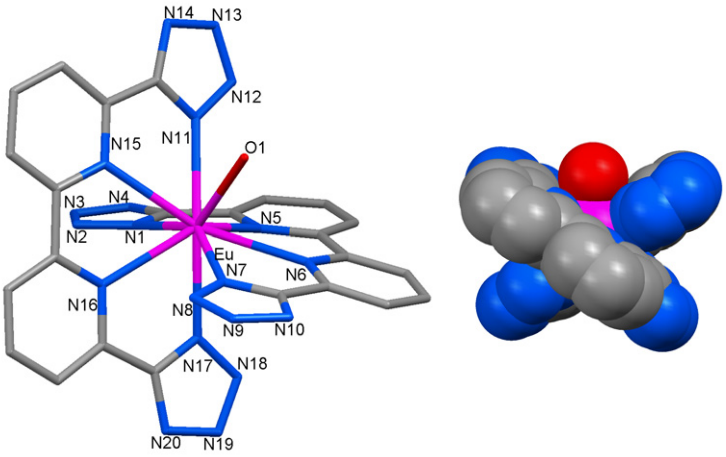

Figure II.28. Stick structure of the [Eu(**L7**)$_2$H$_2$O]$^-$ complex (left) and spacefill model along the axis *a* (right)

A structure has also been obtained for the dissymmetric [Tb(**L8**)$_2$]Na complex, shown in Figure II.29, however with a high residue (12.5%). In this case, due to the change in counterion and the bidentate nature of the carboxylate, two complexes are bridged by the sodium ion via the free oxygens of the carboxylate groups. The intermetallic distance between the two terbium atoms is large (11.8 Å). The two perfectly planar ligands around the terbium ion are practically perpendicular to each other, and no solvent molecule coordinates the metal center. The sodium ion lies on the axis defined by the two terbium atoms, and is six-coordinated by two bridging carboxylate units, and 4 methanol molecules. Intermolecular π-π interactions (3.43 Å) occur in the lattice between the bipyridine moieties.

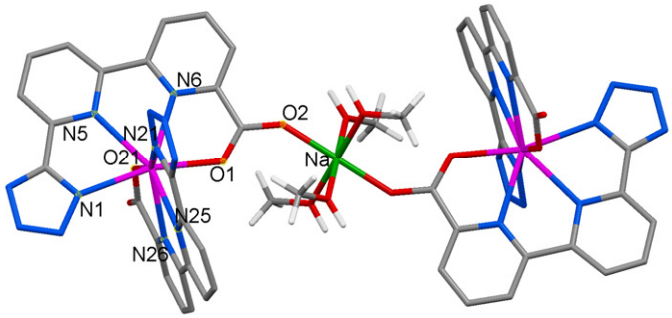

Figure II.29. Structure of the [Eu(**L8**)$_2$]$^-$ complex

b) ^{1}H NMR solution study

The ^{1}H NMR spectra of the [Ln(**L7**)$_2$]NHEt$_3$ (Ln = Eu, Tb) complexes in methanol solutions at 298K show the presence of only one set of signals, with 3 resonances for the 12 protons in the two bipyridine ligands, and 2 resonances for the 15 ethyl protons in the ammonium counterion. These features are consistent with the presence of D_2 symmetric [Ln(**L7**)$_2$]$^-$ solution species on the NMR timescale, in agreement with a fast exchange of the coordinated water molecule. The solution of the [Eu(**L7**)$_2$]$^-$ complex shows sharp peaks at room temperature (see Figure II.30), shifted upfield compared to the free ligand, while the spectrum of the Tb complex is broad due to the strong characteristic paramagnetic effect of the metal and extends over 46 ppm. Full assignment of the protons could not be made because of the equivalence of H_1 and H_3 in 1D and 2D (^{1}H-^{1}H COSY or NOESY) NMR experiments. Upon addition of an europium triflate solution up to 1:1 ligand-to-metal stoichiometry, the major specie observed (>95%) was [Eu**L7**]$^+$. Heating this solution at 318K for 48h resulted in the disappearance of the bis-ligand complex traces, as mentioned in Chapter II.2.2. b) (Figure II.14), indicating that the effect responsible for the kinetic stabilization of [Eu(**L1**)$_2$]$^-$ is related to the structural difference between the terpyridine and bipyridine-based chelates. Indeed, as one water molecule coordinates the europium ion in the [Eu(**L7**)$_2$]$^-$ complex, the hydrophobic interactions which could stabilize the bis-ligand species are greatly diminished. Moreover, as seen from the crystal structure, the orthogonality of the two ligands excluded any intramolecular π-π interactions which could as well stabilize the 2:1 species.

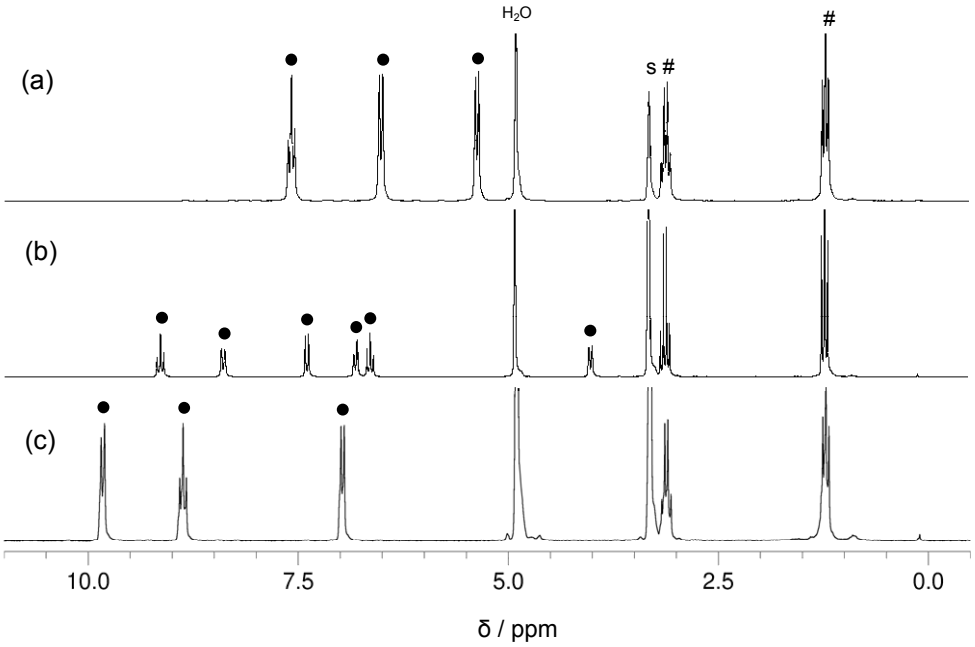

Figure II.30. ^{1}H NMR spectra of the (a) [Eu(**L7**)$_2$]NHEt$_3$, (b) [Eu(**L8**)$_2$]NHEt$_3$ and (c) [Eu(**L9**)$_2$]NHEt$_3$ complexes in MeOD solutions at 298K (# = Et$_3$NH$^+$)

The ^{1}H NMR spectra of the [Eu(**L9**)$_2$]NHEt$_3$ complex[157] in methanol solutions has not been reported before, and shows the presence of only one set of signals, with 3 resonances for the 12 protons in the two equivalent bipyridine ligands, and 2 resonances for the 15 ethyl protons in the ammonium counterion, consistent with the presence of a D_2 symmetric solution specie on the NMR timescale (Figure II.30).

The ^{1}H NMR spectra of the [Ln(**L8**)$_2$]NHEt$_3$ (Ln = Eu, Tb) complexes in methanol solutions at 298K show also the presence of only one set of signals, with 6 resonances for the 12 protons in the two asymmetric bipyridine ligands, and 2 resonances for the 15 ethyl protons in the ammonium counterion. These features are consistent with the presence of C_2 symmetric [Ln(**L8**)$_2$]$^-$ solution species. The [Eu(**L8**)$_2$]$^-$ complex shows sharp peaks at room temperature (see Figure II.30), while the spectrum of the Tb complex is broad due to the strong characteristic paramagnetic effect of the metal and extends over more than 90 ppm.

II.3.3. Photophysical properties of lanthanide complexes

a) Absorption characteristics

The absorption spectra of the complexes [Ln(**Li**)$_2$]NHEt$_3$ (i=7..9) in methanol solutions at 298K are represented in Figure II.31, while the maximum absorption wavelengths and their corresponding molar extinction coefficients are given in Table II.11.

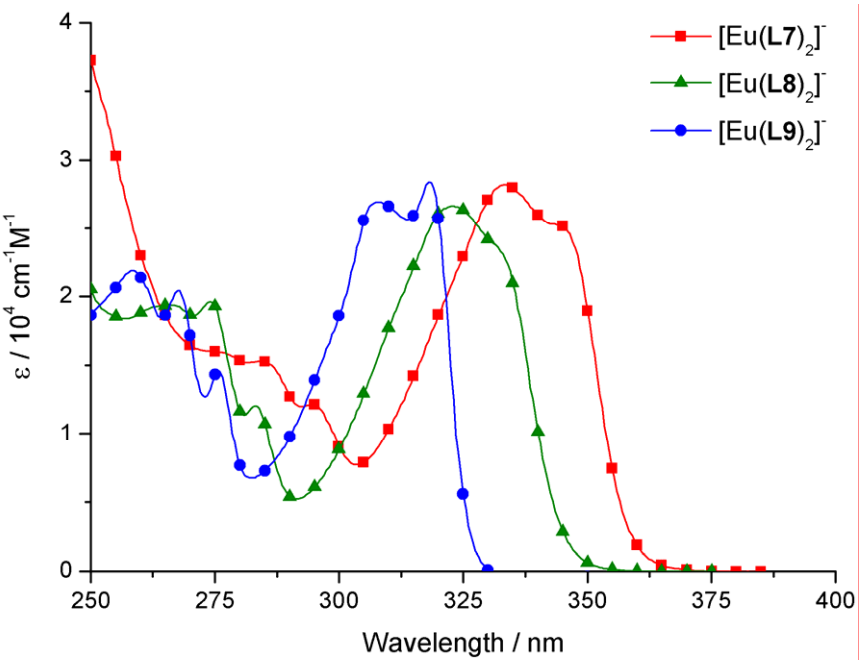

Figure II.31. UV absorption spectra of the complexes [Eu(**Li**)$_2$]NHEt$_3$ (i=7..9) in methanol solutions at 298K

The influence of the tetrazole groups in extending the absorption spectrum of the corresponding lanthanide complexes is clearly evidenced. While the bipyridine-carboxylate complex [Eu(**L9**)$_2$]NHEt$_3$ shows two main bands in its absorption spectrum at 308 and 318 nm (ε = 26 900 and 28 400 cm^{-1}M^{-1}, respectively), in agreement with previous reports,[157] substitution of one of the carboxylate group by a tetrazole in the structure of [Eu(**L8**)$_2$]NHEt$_3$ leads to a bathochromic shift of about 15 nm, the bands appearing at 323 and 332 nm, respectively (ε = 26 650 and 23 600 cm^{-1}M^{-1}, respectively). The fine structure in the region below 300 nm follows the same bathochromic shift. In the case of the bipyridine-tetrazole complex [Eu(**L7**)$_2$]NHEt$_3$, further displacement of the bands towards

the visible region can be observed. The maxima are situated at 333 and 345 nm (ε = 28 200 and 25 150 $cm^{-1}M^{-1}$, respectively), with an overall bathochromic shift compared to the carboxylate analogue [Eu(**L9**)$_2$]NHEt$_3$ of 25 nm, similar to the one observed in the terpyridine series (20 nm).

Table II.11. Absorption wavelengths (λ_{max}) and their corresponding molar absorptivity coefficients (ε) for the complexes [Eu(**Li**)$_2$]NHEt$_3$ (i = 7..9).

[Eu(**Li**)$_2$]NHEt$_3$	λ_{max} / nm (ε / $cm^{-1}M^{-1}$)
i = 7	276 (16 000), 285 (15 300), 295 (12 100), 333 (28 200), 345 (25 150)
i = 8	266 (19 300), 274 (19 600), 283 (12 000), 323 (26 650), 332 (23 600)
i = 9	258 (21 900), 268 (20 400), 276 (14 600), 308 (26 900), 318 (28 400)

b) Ligand centered luminescence

Further insights into the spectroscopic characterization of the complexes in water solution were obtained by luminescence spectroscopy. The emission spectra of the ligand **L7** and its complexes with the non-luminescent gadolinium ion in methanol at 298K are presented in Figure II.32. UV excitation at 35 700 cm^{-1} and at the maximum in the excitation spectra results in a ligand-centred emission displaying one asymmetric broad band assigned to the $^1\pi\pi^*$ state with maximum 28 400 and 26 670 cm^{-1} for the free ligand and the [Gd(**L7**)$_2$]$^-$ complex, respectively. At 77K (methanol glass) and upon enforcement of a time delay (0.2 ms), the singlet state emission disappears with concomitant appearance of a broad and structured band arising from the $^3\pi\pi^*$ state emission, with a 0-phonon transition at 22 830 and 22 270 cm^{-1}, respectively. The energy gap between the 0-phonon transitions of the singlet and triplet states is large (7 100 cm^{-1} for the free ligand and 5 580 cm^{-1} for its Gd complex) while a value higher than 5 000 cm^{-1} is commonly considered as optimum for efficient intersystem crossing[25]. The values are very similar to those obtained for the terpyridine-tetrazole ligand **L1**, in agreement with the extent of conjugation between the pyridine rings.

The dissymmetric ligand **L8** shows equivalent emission characteristics (see Figure II.32), with the $^1\pi\pi^*$ state of [Gd(**L8**)$_2$]$^-$ at 26 810 cm^{-1} and the first $^3\pi\pi^*$ state at 22 620 cm^{-1}.

The ligand **L9** was previously characterized by Bünzli[157], who obtained values of 25 575 and 20 325 cm^{-1} for the $^1\pi\pi^*$ maximum and the $^3\pi\pi^*$ 0-phonon transition in the Gd complex, respectively. Curiously, while there is little difference in the first $^3\pi\pi^*$ states of the terpyridine-tetrazole **L1** and terpyridine-carboxyl **L2** ligands, the bipyridine analogues **L7** and **L9** differ by almost 2 000 cm^{-1}.

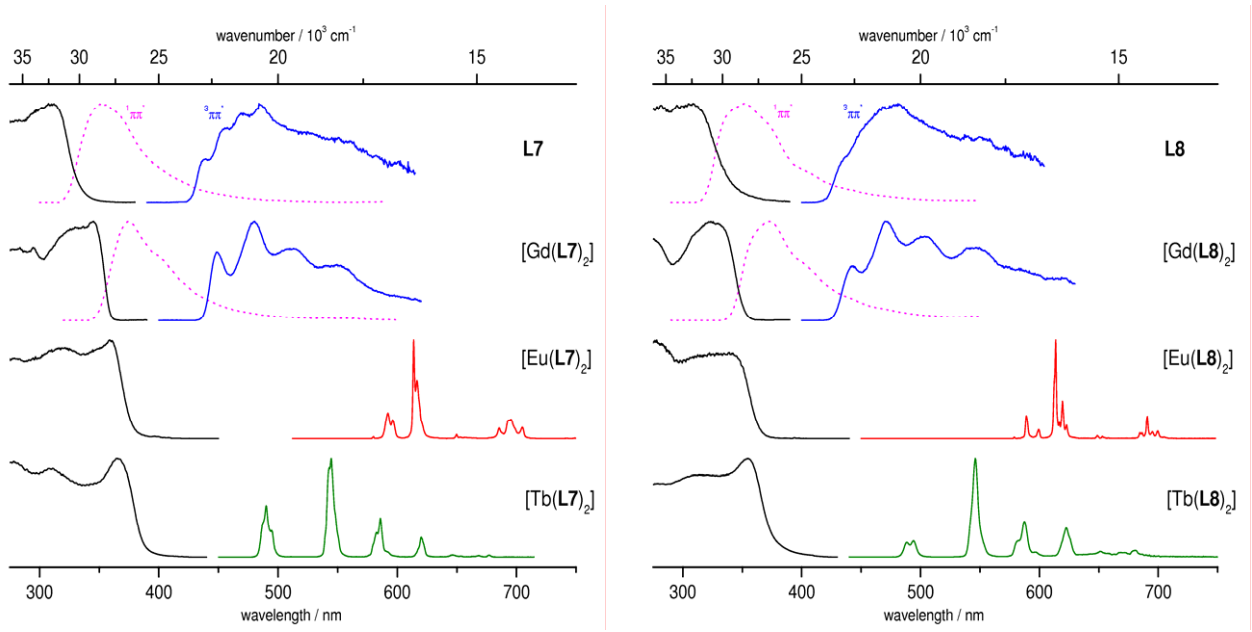

Figure II.32. Normalized excitation and emission spectra of the ligand **L7** (left) and ligand **L8** (right) and their $[Ln(\mathbf{L})_2]^-$ complexes (Ln=Gd, Eu and Tb). Singlet and triplet state levels are measured in methanol solutions at 298K and 77K, respectively, upon excitation at 35 700 cm^{-1}. Eu and Tb luminescence spectra are recorded in solid state at 298K. Excitation spectra are measured at the maximum of emission.

Table II.12. Summary of photophysical properties for the $[Ln(\mathbf{Li})_2]NHEt_3$ complexes (i = 7..9). Singlet ($^1\pi\pi^*$) and triplet state ($^3\pi\pi^*$) energies of the Gd chelates are measured in methanol solutions at 298K and 77K, respectively. Excitation maxima ($\tilde{\upsilon}_{max}$) are given from solid state excitation spectra. Lifetimes (τ) and absolute quantum yields (Φ) are measured for solid state samples at 298K.

L	$^1\pi\pi^*/cm^{-1}$	$^3\pi\pi^*/cm^{-1}$	Ln	$\tilde{\upsilon}_{max}/cm^{-1}$	τ/ms	Φ/%
L7	26 670	22 270	Eu	27 780	0.87(2)[a]	45.4(2)[a]
					0.53(9)	20.4(1)
			Tb	27 320	0.54(2)[a]	26.6(1)[a]
L8	26 810	22 620	Eu	29 070	2.06(1)[a]	53.6(4)[a]
			Tb	28 170	0.41(1)[a]	12.6(1)[a]
L9	25 575[157]	20 325[157]	Eu	29 940	1.64(1)[a]	63.0(2)[a]
					0.86(2)[157,b]	11.5(2.3)[157,b]
			Tb	30 300[157,b]	0.21(1)[157,b]	6.3(1.3)[157,b]

[a] samples dried for one week at 150°C under high vacuum (the measurements have been performed in anhydrous conditions); [b] measured in water solution.

c) Metal centered luminescence

All the lanthanide complexes prepared with the bipyridine ligands presented above show metal-centred luminescence. Both europium complexes of ligands **L7** and **L8** show similar emission characteristics upon ligand excitation, with a dominating $^5D_0 \rightarrow {}^7F_2$ transition, that could be ascribed perhaps to a low C_{2v} symmetry group. The lifetime of $[Eu(\mathbf{L7})_2]^-$ measured in solid state at 298K is 0.53 ms, indicating that probably one water molecule is coordinated to the metal centre, in accordance with the X-ray structure. After drying at 150°C under high vacuum, the lifetime increases at 0.87 ms. However, another deactivation pathway is still maybe present, as the lifetime of $[Eu(\mathbf{L8})_2]^-$ is much longer (2.06 ms). To eliminate the negative influence of coordinated solvent molecules on the emissive properties of the bipyridine complexes, all the measurements have been performed after drying, and the values are given in Table II.12. The previously reported $[Eu(\mathbf{L9})_2]^-$ complex[157] was also synthesized, dried and measured for comparison, showing a lifetime of 1.64 ms. The dried terbium complexes display short lifetimes, decreasing from 0.54 ms ($[Tb(\mathbf{L7})_2]^-$) to 0.41 ms ($[Tb(\mathbf{L8})_2]^-$) while the measurements made in solution for the $[Tb(\mathbf{L9})_2]^-$ complex[157] indicate an even shorter lifetime of 0.21 ms. Apparently, as the number of tetrazole groups decreases, the lifetimes of the terbium complexes are strongly decreased.

To quantify the ability of the ligands prepared to sensitize the luminescence of lanthanides, and to draw conclusions concerning the relationship between structure and properties, the absolute quantum yields of the complexes have been determined upon ligand excitation. For $[Eu(\mathbf{L7})_2]^-$, measurements have been performed for both normal and dried samples, while for the rest of the complexes, only the dried samples have been recorded. All the europium complexes are highly luminescent, their quantum yields increasing in the order $[Eu(\mathbf{L7})_2]^-$ (45.4%), $[Eu(\mathbf{L8})_2]^-$ (53.6%) and $[Eu(\mathbf{L9})_2]^-$ (63.0%) with the decrease of appended tetrazole groups. Reversely, the quantum yields of the terbium complexes decreases in the same order, from 26.6% to 12.6% to 6.3% (the last value being measured in solution[157]).

For a better understanding of these results, we took into account the triplet state energies of the ligands, and we have re-plotted again the dependency of the quantum yields upon the triplet state, as originally done by Latva[16], including also the bipyridine complexes (Figure II.33).

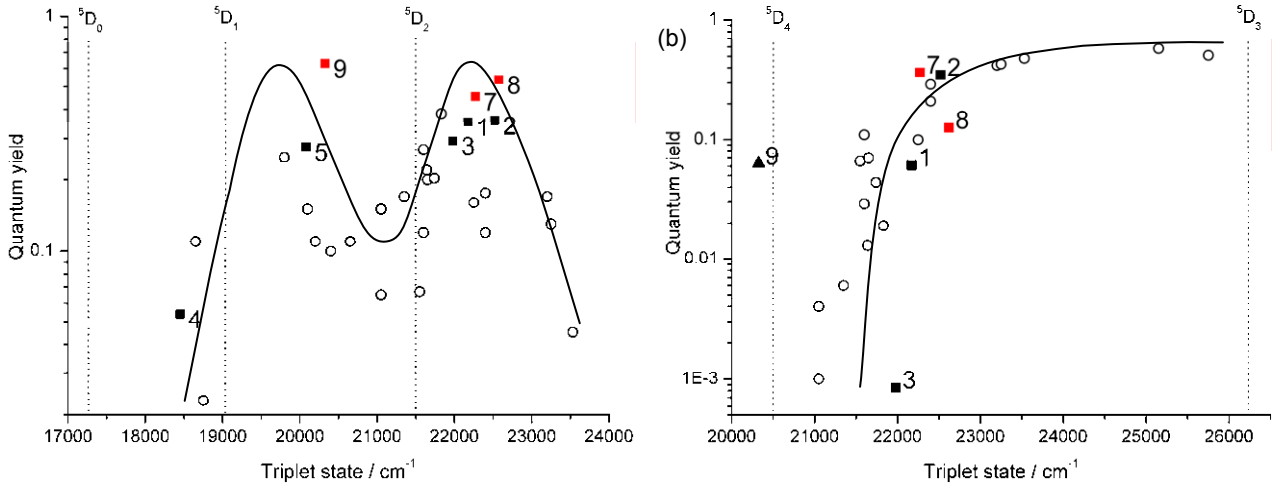

Figure II.33. Luminescence solid state quantum yields of (a) Eu and (b) Tb complexes (■) as a function of the lowest triplet state energy of the ligands **Li** (i = 7..9). Values obtained for terpyridine-based ligands **Li** (i = 1..6) are also plotted for comparison (■), as well as the values of Latva[16] in solution (○) and the value for $[Tb(\mathbf{L9})_2]^-$ in solution[157] (▲).The curves are a coarse tendency drawn from average values.

The energy difference between the first $^3\pi\pi^*$ state of the ligands **L7** and **L8** and the emissive $^5D_0$ level of europium is situated around the maximum of 4 800 cm^{-1}, and accordingly their Eu complexes exhibit strong luminescence. In fact, the tetrazole-based ligands **L1**, **L3**, **L7** and **L8** show an almost linear dependence of the first $^3\pi\pi^*$ state with their $[Eu(\mathbf{L})_2]^-$ quantum yields. Interestingly, the quantum yield of the $[Eu(\mathbf{L9})_2]^-$ complex is very high, as the first $^3\pi\pi^*$ state of **L9** is conveniently situated at 3 070 cm^{-1} above the Eu($^5D_0$) level (first maximum)

In the case of the terbium complex $[Tb(\mathbf{L9})_2]^-$, with a first $^3\pi\pi^*$ state energy of the ligand below the emissive Tb($^5D_4$) level, a back-transfer energy process lowers the quantum yield to only 6.3% in aqueous solutions, as reported before[157]. By contrast, the tetrazole-based bipyridine ligands **L7** and **L8** are better at sensitizing terbium in view of their higher energy $^3\pi\pi^*$ states (quantum yields of 20.4% and 12.6%, respectively).

However, considering their short lifetimes, some non-radiative deactivation due to the proximity of the Tb($^5D_4$) level is probably still present. Curiously, although ligand **L8** has a $^3\pi\pi^*$ state energy higher than **L7**, its quantum yield and its lifetime are smaller, indicating that, in the case of bipyridine ligands, an all-tetrazole structure is better at sensitizing the luminescence of terbium.

In view of the above discussion, one can see that, for obtaining both strong europium and terbium luminescence, a delicate balance of factors has to be considered, while a high energy $^3\pi\pi^*$ state around 22 500 - 23 000 cm^{-1} is probably essential.

II.4. Lanthanide complexes based on pyridine-tetrazolates

II.4.1. Synthesis and characterization of ligands

a) Ligand design

After looking at the influence of the tetrazole group, compared to the carboxylic acid, on the properties of the resulting lanthanide complexes in the bipyridine series, we have decided to incorporate the tetrazole moiety in the pyridine framework as well, for obtaining tridentate ligands for lanthanides. For this, we planned the synthesis of two ligands, one symmetric containing two tetrazole groups (**L10**, pytz) and one asymmetric containing both the tetrazole and the carboxyl substituents (**L11**, pytzc), for obtaining 3L : 1Ln lanthanide complexes, in which the metal would be nine-coordinated. The photophysical properties of the resulting complexes will be compared to those of the already described tris-dipicolinate complexes[16, 38, 39], containing only carboxylate groups.

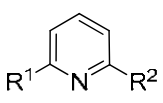

L10 pytz $R^1 = R^2 = TzH$
L11 pytzc $R^1 = Tz$, $R^2 = COOH$
dpa $R^1 = R^2 = COOH$

b) Synthesis and characterization of ligands **L10** and **L11**

The ligand **L10** was synthesized in quantitative yield by the thermal cycloaddition reaction of sodium azide with the commercial pyridine-dicarbonitrile **26** in anhydrous DMF in the presence of ammonium chloride, as shown in Scheme II.16.

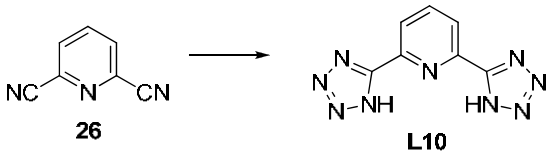

Scheme II.16. Conditions: NaN_3, NH_4Cl, DMF, 125°C (98%)

The ligand **L11** was synthesized in good yield by the same cycloaddition reaction of sodium azide and ammonium chloride with methyl 6-cyanopicolinate **28** (Scheme II.17). The cyanated precursor was obtained from the commercially available methyl 6-bromopicolinate **27** in presence of CuCN in DMF under microwave irradiation, similarly to compound **25** in the bipyridine series.

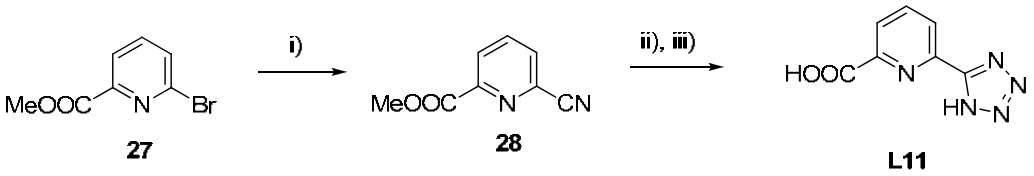

Scheme II.17. Conditions: i) CuCN, DMF, microwave (51%); ii) NaN_3, NH_4Cl, DMF, 135°C; iii) KOH, H_2O, reflux (71%).

The ligands **L10** and **L11** have been characterized by ^1H and ^{13}C NMR spectroscopy and elemental analysis, and the data is available in the Experimental part. In the ^1H NMR spectrum of **L10** in a DMSO solution, only one broad singlet at 8.34 ppm can be seen, however recording the spectrum in MeOD in the presence of triethylamine leads to the resolution of the proton resonances.

II.4.2. Synthesis and characterization of the lanthanide complexes

Homoleptic lanthanide complexes [Ln(**Li**)$_3$](NHEt$_3$)$_3$ (Ln = Nd, Eu, Tb for i = 10 and Ln = Eu for i = 11) based on the ligands described above have been prepared by reacting three equivalents of ligand with one equivalent of lanthanide triflate in methanol solution and in the presence of triethylamine, as shown in Scheme II.18 for [Eu(**L10**)$_3$](NHEt$_3$)$_3$. The complexes were isolated by crystallization after addition of acetonitrile. The products have been characterized by single crystal X-ray diffraction, proton NMR spectroscopy and elemental analysis (full details in the Experimental Section).

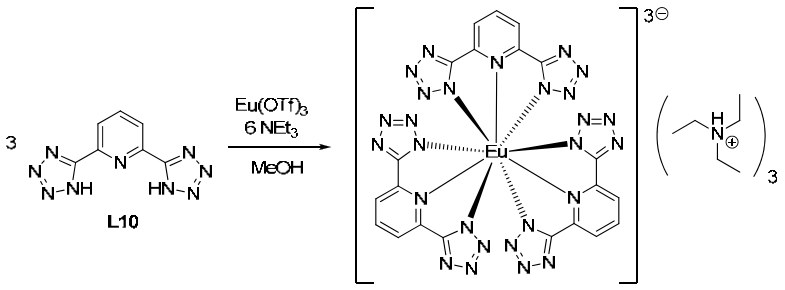

Scheme II.18. Reaction scheme for the synthesis of the [Eu(**L10**)$_3$](NHEt$_3$)$_3$ complex

In a second synthetic strategy, in order to improve the solubility of the complex in the chlorinated solvents normally used for thin film preparation in optoelectronic devices, we have changed the amine used for deprotonation of **L10** from triethylamine to trioctylamine. Counterions with long alkyl chains have been used before for this purpose, as reported by the group of Ziessel[159] who prepared solution-processable liquid crystals of luminescent aluminum-hydroxyquinoline complexes.

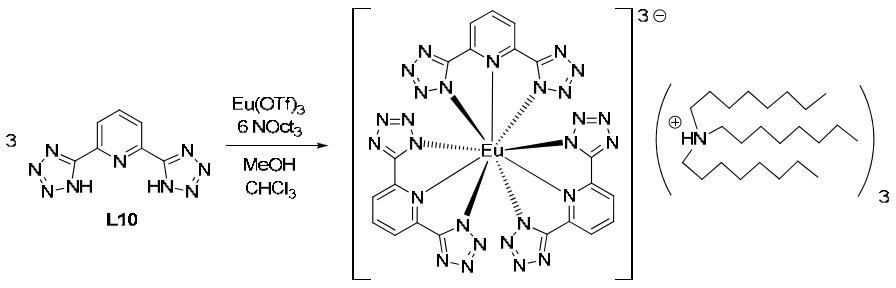

Scheme II.19. Reaction scheme for the synthesis of the [Eu(**L10**)$_3$](NHOct$_3$)$_3$ complex

Due to the 9 octyl chains present in the structure of our final [Eu(**L10**)$_3$](NHOct$_3$)$_3$ complex, it was impossible to isolate the product by crystallization. Accordingly, size-exclusion chromatography on a column packed with Sephadex LH-20 in methanol was used for the purification process. The complex elutes rapidly and its advancement through the column can be visualized easily with an UV lamp, while the salts are retarded by the gel. The pure complex was obtained in good yield as a highly viscous transparent oil and characterized by proton NMR spectroscopy and elemental analysis.

a) Molecular and crystal structures

Crystals suitable for X-ray diffraction have been obtained for the complexes [Eu(**L10**)$_3$]K$_3$ and [Eu(**L11**)$_3$](NHEt$_3$)$_3$, by slow diffusion of diisopropylether in methanol solutions.

Due to its similarity to the structures obtained so far, we will describe first the complex [Eu(**L11**)$_3$](NHEt$_3$)$_3$. The structure was solved in the P2(1)/c space group of the monoclinic system. The metal is nine-coordinated by the nitrogen of the tetrazole group, the oxygen of the carboxylate group, and the neutral nitrogen of the pyridine ring, for each of the three ligands surrounding the metal, as shown in Figure II.34. The negative charge is balanced by three triethylammonium counter-cations. Selected distances and angles are given in Table II.13, while the crystallographic data is presented in the Appendix.

The Eu-O bonding distances (average 2.40 Å) are shorter but in the same range to those found in the [Eu(**L2**)$_2$]$^-$ complex (average 2.44 Å). Similarly, the Eu-N distances (average 2.56 Å) are shorter compared to those found in the [Eu(**L1**)$_2$]$^-$ complex (average 2.62 Å) but similar to those found in the [Eu(**L7**)$_2$]$^-$ complex (average 2.55 Å). The smallest Eu-N distances are between the metal and the anionic nitrogen atoms of the tetrazole, as expected. The bite angle O1-Eu-N1 (63.52°) is very similar to the bite angle N2-Eu-N1 (63.72°), and both are larger than the analogue angles obtained in the complexes [Eu(**L2**)$_2$]$^-$ and [Eu(**L1**)$_2$]$^-$, as a result of the shorter Eu-N distance.

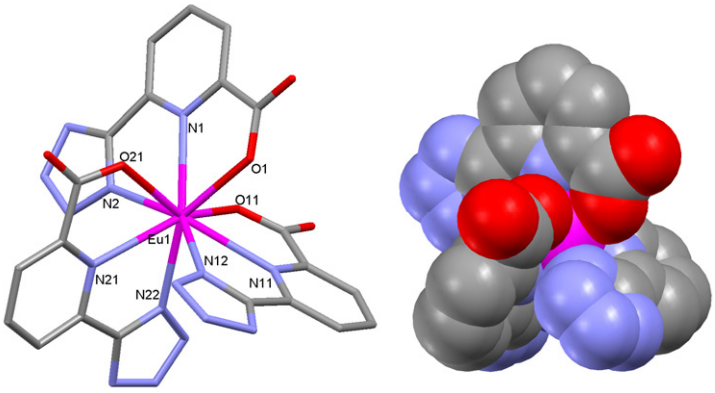

Figure II.34. Stick structure of the $[Eu(\mathbf{L11})_3]^{3-}$ complex (left) and spacefill model along the axis *c* (right)

Table II.13. Selected bond distances (Å) and angles (°) in the $[Eu(\mathbf{L11})_3](NHEt_3)_3$ complex

Eu1-O11	2.390(4)	O11-Eu1-O1	85.32(13)	N22-Eu1-N21	63.61(14)
Eu1-O1	2.399(4)	O11-Eu1-O21	143.59(13)	N2-Eu1-N21	75.78(13)
Eu1-O21	2.407(4)	O1-Eu1-O21	81.55(13)	N12-Eu1-N21	71.18(14)
Eu1-N22	2.547(4)	O11-Eu1-N22	79.62(14)	O11-Eu1-N1	71.37(13)
Eu1-N2	2.551(4)	O1-Eu1-N22	145.97(14)	O1-Eu1-N1	63.52(13)
Eu1-N12	2.567(5)	O21-Eu1-N22	127.10(14)	O21-Eu1-N1	72.37(13)
Eu1-N21	2.570(4)	O11-Eu1-N2	78.12(13)	N22-Eu1-N1	136.43(14)
Eu1-N1	2.578(4)	O1-Eu1-N2	127.24(13)	N2-Eu1-N1	63.72(14)
Eu1-N11	2.584(5)	O21-Eu1-N2	83.19(13)	N12-Eu1-N1	139.01(14)
		N22-Eu1-N2	79.20(14)	N21-Eu1-N1	122.68(13)
		O11-Eu1-N12	127.00(15)	O11-Eu1-N11	63.58(14)
		O1-Eu1-N12	80.52(14)	O1-Eu1-N11	72.62(13)
		O21-Eu1-N12	84.03(15)	O21-Eu1-N11	140.90(14)
		N22-Eu1-N12	84.51(15)	N22-Eu1-N11	73.35(14)
		N2-Eu1-N12	146.90(15)	N2-Eu1-N11	135.88(14)
		O11-Eu1-N21	138.00(13)	N12-Eu1-N11	63.44(16)
		O1-Eu1-N21	136.65(13)	N21-Eu1-N11	119.06(14)
		O21-Eu1-N21	63.78(13)	N1-Eu1-N11	118.26(14)

The three, almost planar ligands wrap around the lanthanide ion in a helical manner, resulting in Δ or Λ chirality at the metal center, similarly to the $[Ln(dpa)_3]^{3-}$ complexes,[36, 37] with both enantiomers present in the racemic crystal. The metal ion lies in the equatorial plane defined by the N atoms of the pyridine rings. The pitch angle between this plane and the pyridine rings is on average 48.33°, while the angle between the nitrogen atoms of two pyridine rings and the metal center (for example, N1-Eu-N11) is on average 120.00°. As the ligands are dissymmetric, two types of conformations around the metal ion are possible (*syn* and *anti*); in our case, the complex has crystallized as the

anti stereoisomer. Hydrogen bonds occur in the crystal cell between the non-coordinated O of the carboxylate group and the H of the triethylammonium counterion or the H of the co-crystallized water molecules.

In contrast with the previous case, the crystals obtained for the pyridine-tetrazole-based complex [Eu(**L10**)$_3$](NHEt$_3$)$_3$ were of bad quality, in spite of repeated crystallization attempts, and the positions of several atoms in the pyridine rings had to be constrained during the structure resolution; even so, the residue was rather large (9.0%). We have decided to change the counter-cation to potassium, suspecting an increased disorder introduced in the crystal by the three triethylammonium moieties, and in this case we obtained a crystal suitable for X-ray analysis.

In the structure of [Eu(**L10**)$_3$]K$_3$, solved in the C2/c space group of the monoclinic system, the lanthanide ion is nine-coordinated by the two nitrogen atoms of the tetrazole groups and the nitrogen of the pyridine rings, for each of the three ligands surrounding the metal, as shown in Figure II.35. Selected distances and angles are given in Table II.14, while the crystallographic data is presented in the Appendix.

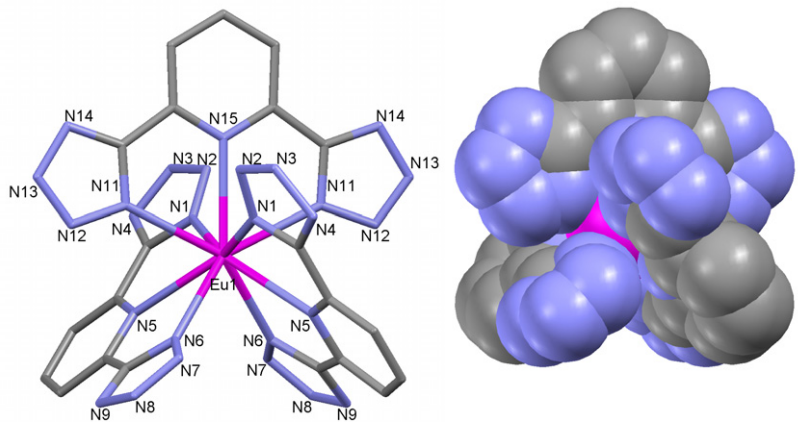

Figure II.35. Stick structure (left) and space-fill model (right) along the axis *c* for the lanthanide coordination sphere in complex [Eu(**L10**)$_3$]K$_3$

The Eu-N bonds (between 2.5089 Å and 2.6095 Å) are comparable to those obtained for the dissymmetric complex [Eu(**L11**)$_3$]$^{3-}$ and the bipyridine-based complex [Eu(**L7**)$_2$]$^-$ and are shorter than those found in the terpyridine-based complex [Eu(**L1**)$_2$]$^-$, as expected

with the decrease of the ligand size, which allows a better arrangement around the metal center. The Eu-N5 and Eu-N15 bonds involving the neutral nitrogen of the pyridine are longer than the average. The bite angles N1-Eu-N5, N6-Eu-N5 and N11-Eu-N15 (on average 63.74°) are very similar to the ones measured in $[Eu(\mathbf{L11})_3]^{3-}$.

Table II.14. Selected bond distances (Å) and angles (°) in the $[Eu(\mathbf{L10})_3]K_3$ complex

Eu1-N1	2.5089(16)	N1A-Eu1-N1	142.47(7)	N11-Eu1-N15	64.20(4)
Eu1-N5	2.6095(15)	N1A-Eu1-N11	84.60(5)	N6-Eu1-N15	137.99(4)
Eu1-N6	2.5326(16)	N1-Eu1-N11	79.29(5)	N1-Eu1-N5	63.39(5)
Eu1-N11	2.5193(16)	N1-Eu1-N11A	84.59(5)	N11-Eu1-N5	135.43(5)
Eu1-N15	2.5830(20)	N11-Eu1-N11A	128.40(8)	N6-Eu1-N5	63.63(5)
		N1A-Eu1-N6	82.90(5)	N6A-Eu1-N5	73.17(5)
		N1-Eu1-N6	126.99(5)	N15-Eu1-N5	119.59(3)
		N11-Eu1-N6	146.65(5)	N1-Eu1-N5A	139.96(5)
		N11A-Eu1-N6	79.13(5)	N11-Eu1-N5A	73.58(5)
		N6-Eu1-N6A	84.01(7)	N6-Eu1-N5A	73.16(5)
		N1-Eu1-N15	71.23(4)	N5-Eu1-N5A	120.83(7)

The ligand containing the N15 pyridine ring is practically planar, while the other two ligands deviate from planarity, the angle between the terminal tetrazole groups and the central pyridine ring being on average 10.71°. The ligands wrap around the europium ion, inducing a helical chirality at the metal center, similarly to $[Eu(\mathbf{L11})_3]^{3-}$ and the $[Ln(dpa)_3]^{3-}$ complexes.[36, 37] Both Δ and Λ enantiomers are present in the racemic crystal. The metal ion lies in the equatorial plane defined by the N atoms of the pyridine rings, and the pitch angle between this plane and the pyridine rings is on average 48.74°, almost identical to the one calculated for the structure of $[Eu(\mathbf{L11})_3]^{3-}$ complex.

The charge is balanced by 3 potassium counterions, displaying two different coordination environments. Potassium K1 is coordinated by two tetrazole nitrogens (N9 and N12) belonging to two different ligands of one complex, and one tetrazole nitrogen (N8) from another complex unit. The rest of the coordination sphere is occupied by five methanol molecules, resulting in a coordination number of 8, as can be seen in Figure II.36. Methanol molecules bridge the potassium atoms K1 and K2, the latter being hexa-coordinate. The potassium ions form a chain along the direction *a+b* of the unit cell. The equivalent nitrogen atoms N8A, N9A and N12A of the complex unit coordinate the

potassium ion K1A, which forms, together with K2A, a second chain in the global structure, along the direction *a*-*b*. The final structure consists of a 3-dimensional network of europium complexes linked by the potassium ions via the K-N bonds (see Figure II.37).

Metal-metal separations are significant with regard to electronic interactions affecting luminescence behavior; the shortest K···Eu separation is 6.005 Å, while the shortest Eu···Eu separation is 11.045 Å. Hydrogen bonds occur in the unit cell between the nitrogen atoms of the tetrazolate groups and the methanol molecules coordinating the potassium ions.

A similar structure has already been described[37] for $[Eu(dpa)_3]Cs_3$, in which two types of cesium ions, bridged by carboxylate and water oxygen atoms, are found part of a single chain extending throughout the crystal.

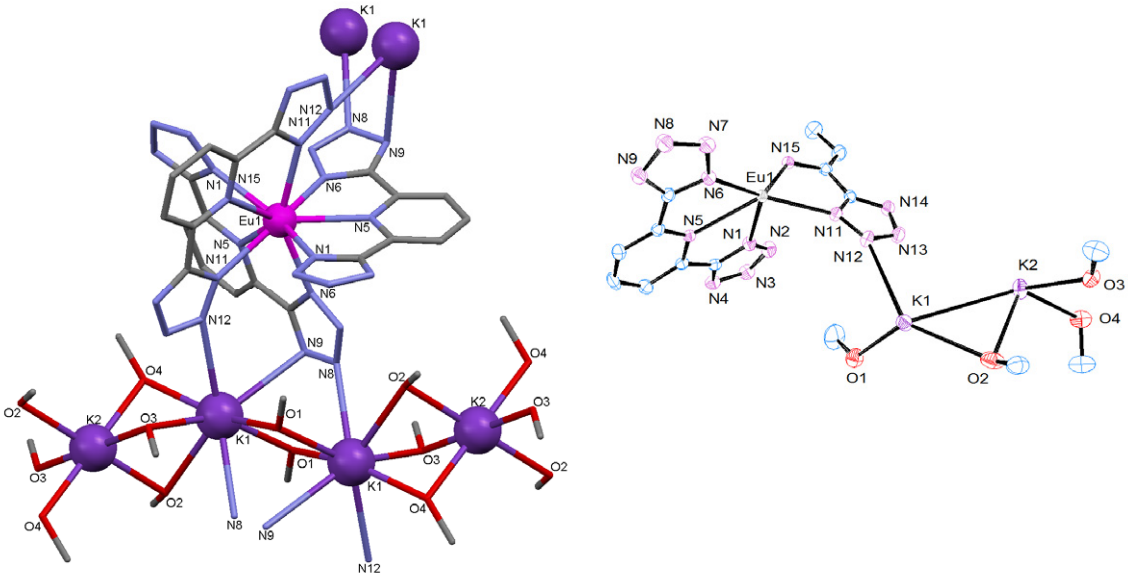

Figure II.36. Selected view of the $[Eu(\mathbf{L10})_3]K_3$ structure (left) and the asymmetric unit cell (right)

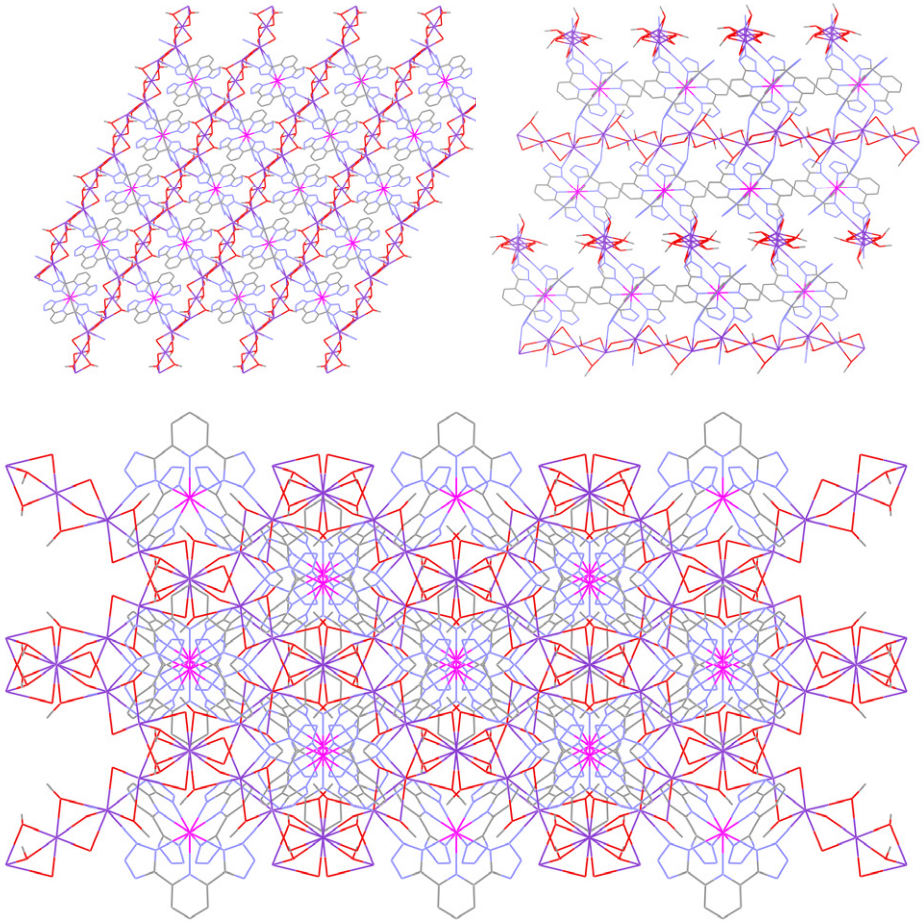

Figure II.37. Full 3D structure of the [Eu(**L10**)$_3$]K$_3$ complex, viewed along the *b* (top left), *a*+*b* (top right) and *c* (bottom) directions

b) ^{1}H NMR solution study

The ^{1}H NMR spectra of the [Ln(**L10**)$_3$](NHEt$_3$)$_3$ (Ln = Nd, Eu, Tb) complexes in methanol solutions at 298K show the presence of only one set of signals, with 2 resonances for the 9 protons in the three pyridine-tetrazole ligands, and 2 resonances for the 45 ethyl protons in the three ammonium counterions. These features are consistent with the presence of D$_3$ symmetric [Ln(**L10**)$_3$]$^{3-}$ solution species on the NMR timescale. The solutions of the europium (see Figure II.38a) and neodymium complexes shows sharp peaks at room temperature, shifted upfield and, respectively, downfield, compared to the free ligand, while the spectrum of the Tb complex is broad due to the strong characteristic paramagnetic effect of the metal, but the resonances remain in the normal field region.

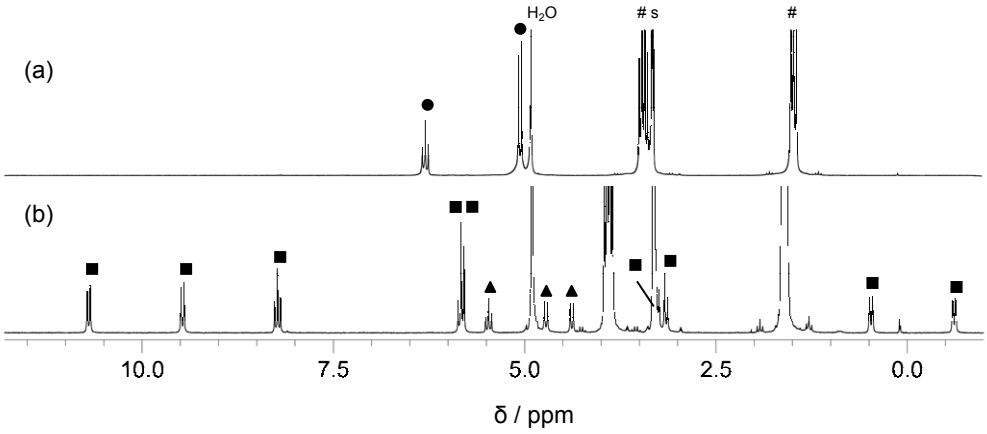

Figure II.38. ^{1}H NMR spectra of the (a) [Eu(**L10**)$_3$](NHEt$_3$)$_3$ complex (●) and (b) [Eu(**L11**)$_3$](NHEt$_3$)$_3$ complexes (▲ for *syn* and ■ for *anti* conformations) in MeOD solutions at 298K (# = Et$_3$NH$^+$)

The ^{1}H NMR spectra of the isolated [Eu(**L11**)$_3$](NHEt$_3$)$_3$ complex in methanol solution at 298K shows the presence of two sets of signals, one corresponding to the dissymmetric *anti* isomer (9 resonances), and another one corresponding to the C_3 symmetric *syn* isomer (3 resonances), as can be seen in Figure II.38b. The presence of all the expected resonances has been confirmed by measuring the spectrum at variable temperatures, when the position of the signal underneath the solvent peak is shifted.

The integration of the signals of the two species observed in NMR corresponds to the expected statistical distribution (75% *anti*, 25% *syn*) when recording the spectrum of the isolated complex. The solution prepared in situ shows however a higher amount of *anti* isomer (85%), which is probably thermodynamically more favored due to a lower steric hindrance compared to the *syn* isomer, where all the bulkier tetrazole groups are on the same side.

II.4.3. Photophysical properties of lanthanide complexes

a) Absorption characteristics

The absorption spectra of the complexes [Eu(**Li**)$_3$](NHEt$_3$)$_3$ (i=10, 11) in methanol solutions and [Eu(dpa)$_3$]$^{3-}$ in TRIS buffer (0.1 M) at 298K are represented in Figure II.39, while the maximum absorption wavelengths and their corresponding molar extinction coefficients are given in Table II.15.

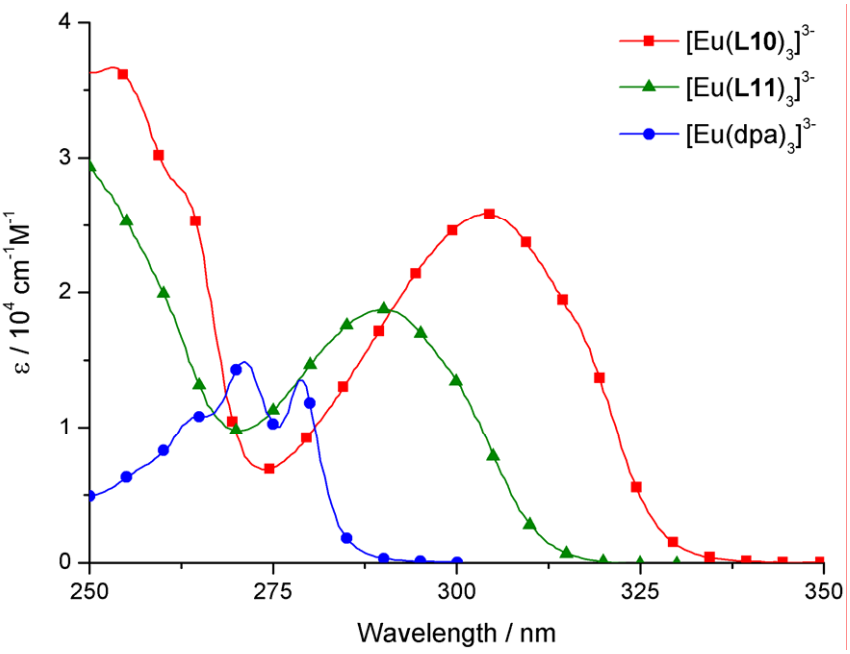

Figure II.39. UV absorption spectra of the complexes [Eu(**Li**)$_3$](NHEt$_3$)$_3$ (i=10, 11) in methanol solutions and [Eu(dpa)$_3$]$^{3-}$ in TRIS buffer (0.1 M) at 298K

The influence of the tetrazole groups in extending the absorption spectrum of the corresponding lanthanide complexes is again clearly evidenced. While the absorption spectrum of the europium tris-dipicolinate complex shows two main maxima at 271 and 279 nm with a rather low extinction coefficient (ε = 14 900 and 13 500 cm^{-1}M^{-1}, respectively), replacement of one carboxylate group by a tetrazolate in the structure of the complex [Eu(**L11**)$_3$](NHEt$_3$)$_3$ leads to a bathochromic shift of around 25 nm, as also observed in the case of the bipyridine complex [Eu(**L18**)$_2$]NHEt$_3$, and a broadening of the spectral features, together with an increase in the molar extinction coefficients. Only one broad band with a maximum at 290 nm (ε = 18 700 cm^{-1}M^{-1}) and a shoulder around 300 nm (ε = 13 400 cm^{-1}M^{-1}) appear in the low-energy region. The effect becomes even more pronounced in the pyridine-tetrazolate complex [Eu(**L9**)$_3$](NHEt$_3$)$_3$, having a maximum absorption at 304 nm with a shoulder around 316 nm (ε = 25 800 and 18 000 cm^{-1}M^{-1}, respectively), accompanied by another increase in the molar extinction coefficients.

Table II.15. Absorption wavelengths (λ_{max}) and their corresponding molar absorptivity coefficient (ε) for the complexes $[Eu(\mathbf{Li})_3](NHEt_3)_3$ (i=10, 11) and $[Eu(dpa)_3]^{3-}$

	λ_{max} / nm (ε / $cm^{-1}M^{-1}$)
$[Eu(\mathbf{L10})_3]^{3-}$	263 (27 300), 304 (25 800), 316 (18 000)
$[Eu(\mathbf{L11})_3]^{3-}$	290 (18 700), 300 (13 400)
$[Eu(dpa)_3]^{3-}$	264 (10 700), 271 (14 900), 279 (13 500)

b) Ligand centered luminescence

Further insights into the spectroscopic characterization of the complexes in water solution were obtained by luminescence spectroscopy. The emission spectra of the ligand **L10** and its complexes with the non-luminescent gadolinium ion in methanol at 298K are presented in Figure II.40. UV excitation at 35 700 cm^{-1} and at the maximum in the excitation spectra results in a ligand-centred emission displaying one asymmetric broad band assigned to the $^1\pi\pi^*$ state with maximum 30 075 and 29 630 cm^{-1} for the free ligand and the $[Gd(\mathbf{L10})_3]^{3-}$ complex, respectively. At 77K (methanol glass) and upon enforcement of a time delay (0.2 ms), the singlet state emission disappears with concomitant appearance of a broad and structured band arising from the $^3\pi\pi^*$ state emission, with a 0-phonon transition at 24 750 and 24 640 cm^{-1}, respectively. The energy gap between the 0-phonon transitions of the singlet and triplet states is in the optimal range for efficient intersystem crossing[25] (5 700 cm^{-1} for the Gd complex). The values for the energies of singlet and triplet states are much higher than in the case of tetrazole-based ligands **L1** (terpytz) and **L7** (bipytz), and indicate a reduced extent of conjugation, which involves now only one pyridine ring.

The dissymmetric ligand **L11** shows states located at even higher energies, with the $^1\pi\pi^*$ level of $[Gd(\mathbf{L11})_3]^{3-}$ at 31 250 cm^{-1} and the first $^3\pi\pi^*$ state at 25 500 cm^{-1}. The symmetrical carboxylate ligand dpa has been studied before,[37] and the values of its singlet and triplet states have been measured to be 32 900 and 26 700 cm^{-1}, respectively. We observe here the same trend as in the case of terpyridine ligands, with the energies of the ligand levels decreasing with the degree of substitution of the carboxylate groups by the tetrazolate. This is in agreement with the π-electro-withdrawing effect of the carboxylate

group[22] which is known to increase the energy of the ligand levels[21, 151], in contrast with the tetrazole group which has a π-electro-releasing effect[22] and leads to a decrease in the energy. In fact, in the case of pyridine ligands, this relationship is almost linear, for both the singlet and the triplet states.

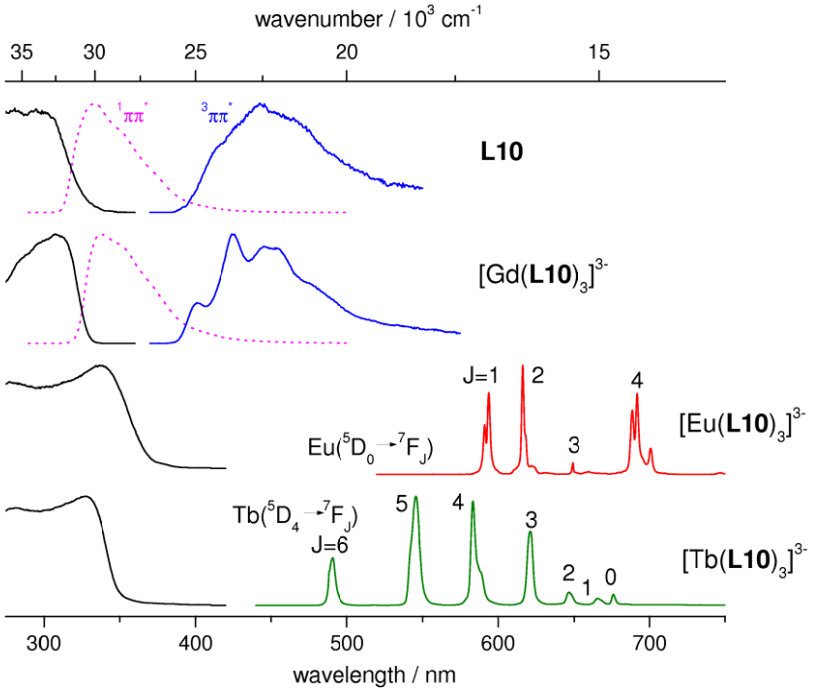

Figure II.40. Normalized excitation and emission spectra of the ligand **L10** and its $[Ln(\mathbf{L10})_3]^{3-}$ complexes (Ln=Gd, Eu and Tb). Singlet and triplet state levels are measured in methanol solutions at 298K and 77K, respectively, upon excitation at 35 700 cm^{-1}. Eu and Tb luminescence spectra are recorded in solid state at 298K. Excitation spectra are measured at the maximum of emission.

Table II.16. Summary of photophysical properties for the $[Ln(\mathbf{Li})_3]^{3-}$ and $[Ln(dpa)_3]^{3-}$ complexes (i = 10, 11). Singlet ($^1\pi\pi^*$) and triplet state ($^3\pi\pi^*$) energies of the Gd chelates are measured in methanol solutions at 298K and 77K, respectively. Excitation maxima ($\tilde{\upsilon}_{max}$) are given from solid state excitation spectra. Lifetimes (τ) and absolute quantum yields (Φ) are measured for solid state samples at 298K.

L	$^1\pi\pi^*/cm^{-1}$	$^3\pi\pi^*/cm^{-1}$	Ln	$\tilde{\upsilon}_{max}/cm^{-1}$	τ/ms	Φ/%
L10	29 630	24 640	Eu	29 590	3.11(4)	61.1(3)
			Tb	30 490	1.54(2)	64.5(1.1)
			Nd	28 250	$1.701(7)\cdot10^{-3}$	0.214(3)
L11	31 250	25 500	Eu	31 850	2.39(1)	38.5(3)
dpa	32 900[37]	26 700[37]	Eu	35 800	2.02(4)[37]	24.0(2.5)[39,[a]]
			Tb	35 800		22.0(2.5)[39,[b]]

[a] measured in Tris buffer aqueous solution at $7.5\cdot10^{-5}$ mol·dm^{-3}; [b] measured in Tris buffer aqueous solution at $6.5\cdot10^{-5}$ mol·dm^{-3}

c) Metal centered luminescence

The visible luminescence spectra of the [Ln(**L10**)$_3$]$^{3-}$ complexes (Ln = Eu, Tb) recorded in solid state at 298K are shown in Figure II.40. The ligand centered emission is not detected, suggesting an efficient ligand to metal energy transfer process. Upon broadband excitation through the ligand levels, the Eu emission exhibits the characteristic $^5D_0 \rightarrow {}^7F_J$ transitions, and is dominated by the $^7F_2$ band. Both $^7F_1$ and $^7F_4$ band are also very intense. In spite of the low resolution of the emission spectrum, the very faint $^7F_0$ transition suggests that the crystal field splitting can be interpreted in terms of a D_3 symmetry point group (in which $^7F_0$ is forbidden), as implied from the X-ray structure and the ^{1}H NMR spectrum. The $^7F_1$ band presents two main components of different intensities at 16 915 and 16 840 cm^{-1}, assigned to the magnetic dipole transitions $A_1 \rightarrow A_2$ and $A_1 \rightarrow E$, while the $^7F_4$ band presents four main components (one as a shoulder), attributed to the electric dipole transitions $A_1 \rightarrow A_2$ and $A_1 \rightarrow E$ (three) in the D_3 symmetry. Due to the low resolution, the splitting in two of the main $^7F_2$ band (corresponding to the electric dipole transition $A_1 \rightarrow E$) cannot be observed.

The excitation spectrum of [Eu(**L10**)$_3$]$^{3-}$ recorded in solid state at the $^7F_2$ site shows a maximum displaced at 29 590 cm^{-1} compared to the excitation spectrum of [Gd(**L10**)$_3$]$^{3-}$ recorded at the $^3\pi\pi^*$ state maximum (32 260 cm^{-1}). We have seen this effect already in the case of the **L1** terpytz ligand, and we have assigned the shifted band to the $^1\pi\pi^*$ state of the ligand, visible as a result of the efficient $^1\pi\pi^* \rightarrow {}^5D_0$ energy transfer. The luminescence decay of the [Eu(**L10**)$_3$]$^{3-}$ emission, measured at the $^7F_2$ site upon ligand excitation, can be fitted as a monoexponential function and corresponds to a 3.11 ms lifetime in solid state at 298K, in agreement with the absence of solvent molecules from the first sphere of coordination. The absolute quantum yield measured in solid state at 298K amounts to 61.1%, being the highest yield among the europium complexes presented in this work, and among the highest reported in the literature. Recently the group of De Cola reported a neutral europium complex[43] showing a similarly high quantum yield (60%) in dichloromethane, and de Bettencourt-Dias *et al.* claim an efficiency of 76% for their pyridine-bis(oxazoline) europium complex[121] measured in situ in acetonitrile.

The size of the gap between the ligand feeding level and the Eu ($^5D_0$) emitting level at 17 260 cm^{-1} shows that a resonance condition is not essential for an efficient ligand-to-metal energy transfer as long as adequate vibronic couplings are at hand.[37] In addition, the location of ligand states at high energy prevents both a mixing of these states with the 4f states and a back-transfer from the excited metal to the ligand, as often observed for Tb(III) compounds[43, 48, 157] ($[Tb(\mathbf{L1})_2]^-$ or $[Tb(\mathbf{L3})_2]^-$) or in $[Eu(\mathbf{L4})_2]^-$, and favors high quantum yields.

The $[Tb(\mathbf{L10})_3]^{3-}$ complex, measured in solid state at room temperature, displays a typical emission spectrum dominated by the $^5D_4 \rightarrow {}^7F_J$ (J = 5, 4 and 3) transitions. The $^7F_6$ band is moderate in intensity, and the ^7F_J (J = 2, 1 and 0) bands are low. The luminescence decay, measured at the maximum of the $^7F_5$ transition, is monoexponential and corresponds to a lifetime of 1.54 ms, while the absolute quantum yield amounts to 64.5%, being by far the highest yield among the terbium complexes presented in this work, and among the highest reported in the literature. Recently in our laboratory, a tripodal ligand based on pyridine-tetrazole[118] afforded a terbium complex with a quantum yield in solid state of 56.1%.

The luminescence spectrum of the $[Nd(\mathbf{L10})_3]^{3-}$ complex, measured in solid state at 298 K upon broad band excitation through the ligand levels, displays three bands in the spectral ranges 865-925, 1045-1110 and 1315-1400 cm^{-1}, which are assigned to transitions from the $^4F_{3/2}$ level to the $^4I_{9/2}$, $^4I_{11/2}$ and $^4I_{13/2}$ sublevels, respectively. The bands are each split into 2 components, located respectively at 880 and 910, 1071 and 1080, 1339 and 1373 nm. The emission decay is characteristically short, and corresponds to a lifetime of $1.701(7)\cdot10^{-3}$ ms, while the absolute quantum yield amounts to 0.21%, similar to the one obtained for the $[Nd(\mathbf{L1})_2]^-$ complex. Although the triplet state of ligand **L10** is positioned high in energy compared to the Nd($^4F_{3/2}$) emissive level, the rigidity of the complex, together with the absence of OH and CH oscillators in the vicinity of the lanthanide ion, result in a very good NIR quantum yield.

The luminescence spectrum of the $[Eu(\mathbf{L11})_3]^{3-}$ complex, recorded upon broadband excitation through the ligand levels, exhibits the characteristic $^5D_0 \rightarrow {}^7F_J$ transitions, and is dominated by the $^7F_2$ band, with an intense secondary band from the $^7F_4$ level. The $^7F_0$

transition is present, albeit not intense, suggesting that the crystal field splitting could be interpreted in terms of a low symmetry point group such as C_1 (in which $^7F_0$ would be allowed), as implied from the X-ray structure (*anti* conformation). The maximum of the excitation spectrum of the $[Eu(\mathbf{L11})_3]^{3-}$ complex measured at the $^7F_2$ site shows a shift compared to the spectrum of the gadolinium complex, as observed also for the $[Eu(\mathbf{L10})_3]^{3-}$ complex, due to the appearance of the ligand $^1\pi\pi^*$ state. The luminescence lifetime of the $[Eu(\mathbf{L11})_3]^{3-}$ complex, calculated in solid state at room temperature, is 2.39 ms, shorter than in the symmetric $[Eu(\mathbf{L10})_3]^{3-}$ complex, but still indicative of the absence of solvent molecules coordinated to the metal center. The quantum yield, measured in the same conditions, amounts to 38.5%. This value, albeit lower than for $[Eu(\mathbf{L10})_3]^{3-}$, is above the average recorded for europium complexes in literature, and compares to the values obtained for the unsubstituted terpyridine complexes.

The quantum yields for the $[Ln(dpa)_3]^{3-}$ complexes (Ln = Eu, Tb) have been previously determined in aqueous solutions[39], giving 24.0% and 22.0%, respectively, and although a comparison between these values and the ones measured for our pyridine-tetrazole complexes in solid state is not easy to make, we could say that the influence of the tetrazole groups in slightly lowering the triplet states of the ligands proves to be beneficial for the emissive properties of their lanthanide chelates.

II.5. Conclusions

In this chapter, we have looked at the structure-property relationship in a series of stable, highly luminescent lanthanide complexes based on the terpyridine-, bipyridine- and pyridine-tetrazole chromophores. Comparison with the isostructural carboxylate complexes clearly demonstrated the positive effect of the tetrazolate motif on the absorption and emissive properties of the lanthanide complexes.

In the terpyridine series, we have appended the parent terpyridine-tetrazole ligand **L1** with various substituents (such as bromo-phenyl, bromo-thiophene, phenyl-pyridine or bis-thiophene) in order to modulate the energies of the ligand excited states. In the X-

ray structures of the resulting $[Ln(\mathbf{Li})_2]^-$ lanthanide complexes, the metal is ten-coordinated by the two ligands and is fully encapsulated and protected from interaction with the solvent molecules. Furthermore, ^1H NMR studies indicate that the solid state structure is maintained in solution. Notably, a particular kinetic stabilization of the $[Eu(\mathbf{L1})_2]^-$ complex with respect to the $[Eu\mathbf{L1}]^+$ was observed. The conditional stability constants of the tetrazolate-based complexes are comparable to those of the carboxylate analogues. Accordingly, all the complexes displayed intense luminescence in both visible and near-infrared regions, with quantum yields reaching 35% for the $[Eu(\mathbf{L1})_2]^-$ complex and 0.29% for the $[Nd(\mathbf{L4})_2]^-$ complex. The influence of the appended substituents was discussed in terms of absorption maxima, triplet states and emission efficiencies. Strikingly, we have observed in the case of the parent tetrazole complex an increase with 20 nm in the excitation window towards the visible region, compared to the carboxylate analogue, and a further increase with almost 100 nm upon substitution with the bis-thiophene group.

In the bipyridine and pyridine series, we have looked in more detail at the influence of the tetrazolate compared to the carboxylate motif on the luminescence properties of the lanthanide complexes. For this, we have designed symmetrical and dissymmetrical ligands containing the two anionic groups, and we have studied the structural and photophysical properties of the complexes. We have clearly shown that the introduction of tetrazole moieties results in a bathochromic shift in the absorption spectra (roughly 10 nm / tetrazole group), allowing excitation of the lanthanide ions at lower energies. In the same time, modification in the ligand triplet states results in improved quantum yields for the bipyridine terbium complexes (reaching 27% in the case of $[Tb(\mathbf{L9})_2]^-$), compared to the carboxylate analogues. The europium efficiency, although decreasing with number of tetrazole groups, remains still very good (45% in the $[Eu(\mathbf{L9})_2]^-$ complex). Excellent quantum yields have been obtained in the pyridine-tetrazole series, reaching 61% and 65% for the $[Eu(\mathbf{L10})_3]^{3-}$ and $[Tb(\mathbf{L10})_3]^{3-}$ complexes, respectively, being among the highest reported in literature.

The solubility of the complexes in organic solvents can be easily but dramatically increased, as demonstrated by introducing an octyl chain in the terpyridine-based ligand **L6**, or by replacing triethy- with trioctyl-ammonium as the counterion in the structure of the pyridine-based complex $[Eu(\mathbf{L10})_3]^{3-}$. This points to the possible use of such highly luminescent, highly soluble complexes as emitters in OLEDs prepared by the spin-coating technique.

In summary, we have investigated in this chapter the relationship between the chromophore structure and the lanthanide emission efficiency in a series of tetrazole-based complexes, showing in the same time the versatility of the tetrazole motif for the coordination and sensitization of lanthanide ions.

Chapter III
Neutral lanthanide diketonate complexes

III.1. Introduction to lanthanide ß-diketonate complexes

The lanthanide β-diketonates were first prepared at the end of the 19th century, more than 100 years ago by one of the pioneers of rare earth research, G. Urbain. The β-diketonate complexes are probably the most extensively investigated lanthanide coordination compounds. This popularity is due to the fact that they are easily synthesized, readily available from commercial sources, and have many applications. In his comprehensive review,[28] Binnemans points out that there have been four periods of active research: the late 1950s – early 1960s, the mid 1960s, the 1970s -1985 (which he calls the Golden Years of β-diketonate research) and the 1990s. In the first period these compounds were studied as extractants for the solvent-solvent extraction processes used to separate the individual rare earth elements. In the 1960s they were studied for their potential as laser materials, *i.e.* chelate lasers and liquid lasers. In the Gold Years, the β-diketonates were used as NMR shift reagents. The latest period of active research focuses on their electroluminescent properties for organic light emitting diodes (OLEDs), their high vapor pressures as volatile reagents for chemical deposition, and their utilization as catalysts for organic reactions.

Three main types of lanthanide β-diketonate complexes are most studied: tris complexes, Lewis base adducts of the tris complexes (ternary lanthanide β-diketonates) and tetrakis complexes.

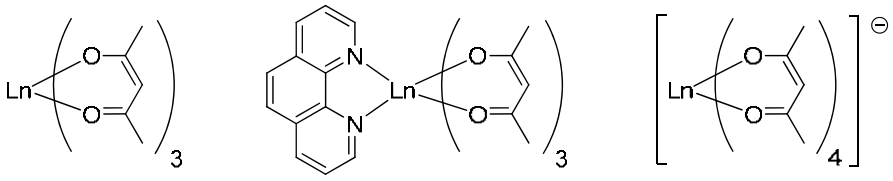

Scheme III.1. The main types of lanthanide β-diketonate complexes

The neutral tris complexes or tris(β-diketonates) have three β-diketonate ligands for each lanthanide ion and they can be represented by the general formula [Ln(β-diketonate)$_3$]. Because the coordination sphere of the rare-earth ion is unsaturated in these six-coordinate complexes, unless a sterically encumbering β-diketonate ligand is used, the lanthanide ion can expand its coordination sphere by oligomer formation (with bridging β-diketonates ligands), but also by adduct formation with Lewis bases, such as water, 1,10-phenanthroline, 2,2′-bipyridine or tri-n-octylphosphine oxide. It is also possible to arrange four β-diketonate ligands around a single lanthanide ion and in this way tetrakis complexes or tetrakis(β-diketonates) with the general formula [Ln(β-diketonate)$_4$]$^-$ are formed. These complexes are anionic and the electric neutrality is achieved by a counter cation. The cation can be an alkali-metal ion, but more often it is a protonated organic base (pyridinium, piperidinium, isoquinolinium, etc) or a quaternary ammonium ion.

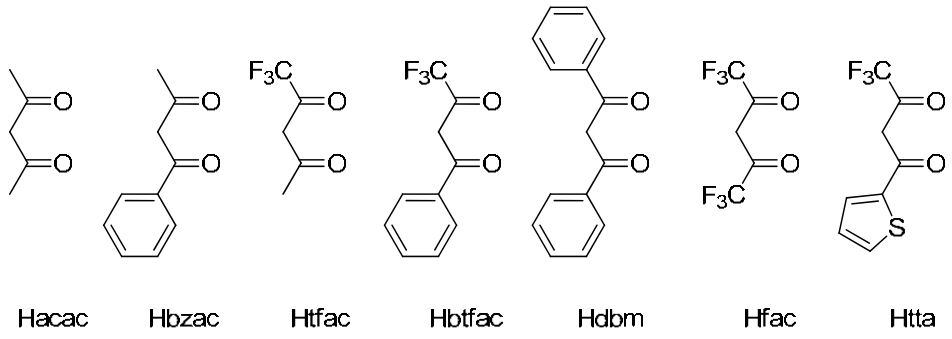

Scheme III.2. Typical structures of β-diketonates used in lanthanide complexes

The β-diketones bear two carbonyl groups that are separated by one carbon atom. The substituent on the carbonyl function can be an alkyl group, a fluorinated alkyl group, an aromatic or an heteroaromatic group, as shown in Scheme III.2. The simplest β-

diketone is acetylacetone (Hacac), were the substituents on both carbonyl groups are methyl groups. All other β-diketones can be considered as derived from acetylacetone by substitution of the methyl groups by other moieties.

The choice of the substituents on the β-diketones influences the properties of the corresponding lanthanide complexes, as we have also seen in Chapter II.2. for the terpyridine-tetrazole complexes. Long alkyl chains increase the solubility in organic solvents and the film-forming properties of the complexes,[160] while fluorinated alkyl groups increase increasing the volatility of the complexes, thus facilitating thin-film fabrication by evaporation, and leading to improved thermal and oxidative stability and reduced concentration quenching of the luminescence.[161] The β-diketones with aromatic substituents have a stronger light absorption than the β-diketones with only aliphatic substituents. The substituents have also an influence on the position of the energy levels of the ligand (singlet and triplet states), which is essential in determining the luminescent properties of the complexes, as well as of the optoelectronic devices in which they are incorporated.

The β-diketones exhibit keto–enol tautomerism, with the equilibrium depending on a variety of factors such as the substituents on the β-dicarbonyl system, the solvent, the temperature and the presence of other species in solution that are capable of forming hydrogen bonds.[28] Because of the presence of the two carbonyl groups, the β-diketones are quite acidic and can be deprotonated by relatively weak bases (ammonia, triethylamine, pyridine, etc).

Ternary lanthanide β-diketonates are by far the most used in device fabrication, due to the coordination of a forth neutral ligand which eliminates the molecules of solvent normally present in the structure of tris(β-diketonate) complexes, and increases in this way the emission efficiency of the complex. Because the trivalent lanthanide ions are hard Lewis acids, the tris β-diketonate complexes form preferentially complexes with oxygen-donor or nitrogen-donor ligands which act as Lewis bases. An overview of the neutral ligands commonly used in the ternary β-diketonate complexes is given in Scheme III.3. The most popular ligands are based on the N-coordinating 1,10-phenanthroline (phen),

substituted with various aromatic groups, because the resulting europium complexes often show an intense luminescence. Numerous examples of such lanthanide complexes are given in Chapter I.3.2. , together with their applications in optoelectronic devices.

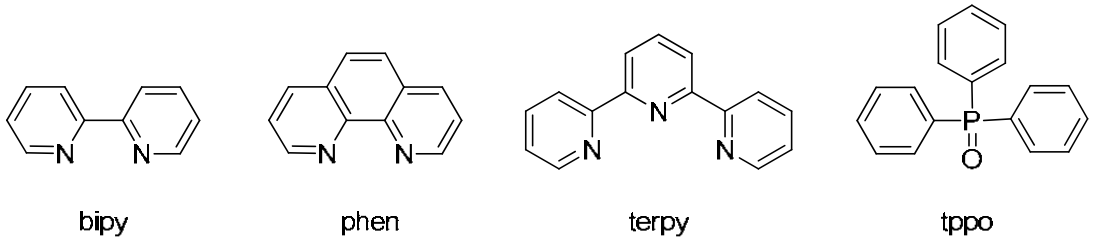

Scheme III.3. Typical structures of secondary ligands used in ternary lanthanide complexes

As a direct consequence of the labile nature of the complexes, an equilibrium of various mono-, bis- and tetrakis- diketonate species exists in solution.[28] Because of the preference of lanthanide ions for hard, oxygen-donor ligands, the interaction between N-coordinating secondary ligands (such as phen) and the metal is very weak in aqueous solution, and accordingly the complexes are not stable in water. Moreover, the complexes are often unstable upon long UV irradiation[162] (such as employed in optoelectronic device processing, *e.g.*, UV curing of polymers, UV pumping of chelate lasers), or upon thermal treatment for vacuum evaporation,[163] and thus they can decompose under the conditions required for materials processing or under the operating conditions.

Therefore, up to now, the electroluminescence performance of the lanthanide β-diketonate complexes is lower than expected, although the achieved external efficiencies increased in the last years. The luminescent properties of these complexes have been explored to test their applicability in laser amplifiers, organic light emitting diodes and optical waveguides,[60, 61, 85] but it is unlikely that the lanthanide β-diketonate complexes will be used soon in real commercial devices, because of their low chemical and thermal stability.[28] Accordingly, new types of lanthanide β-diketonate complexes need to be investigated, with the final aim of developing more stable, highly emissive materials.

III.2. Neutral lanthanide complexes based on terpyridine-monocarboxylate

III.2.1. Ligand and complex design

All the ternary lanthanide β-diketonate complexes used in optoelectronic devices employ a neutral secondary ligand, most often a 1,10-phenantroline derivative. Due to the preference of lanthanide ions for hard donor atoms, such N,N-coordinating ligands are rather labile and could dissociate in solution or upon thermal treatment (*vide supra*).

In view of the low stability of previously described β-diketonate chelates, we have decided to improve the molecular design of such complexes by the use of an anionic secondary ligand, which could bind strongly to the lanthanide ions. Terpyridine monocarboxylic acid **L12** is known to efficiently sensitize the luminescence of europium and terbium metals, and was previously studied in our laboratory.[120, 164] Being monoanionic and tetradentate, the ligand could allow the additional coordination to the metal center of two β-diketonate units, to give an overall neutral complex suitable for vacuum processing in OLED devices, where the lanthanide metal would be octa-coordinated.

We have planned to use the terpyridine-monocarboxylic acid **L12** for the complexation of visible-emitting lanthanide ions, europium and terbium. For the europium complexes, we have chosen to complete the coordination sphere of the metal with 2-thenoyltrifluoroacetone units (TTA) as β-diketone, which is known to give highly luminescent europium complexes.[28] In the case of terbium however, the low triplet state of TTA[165] is situated at the same energy (20 490 cm^{-1}) to the $Tb(^5D_4)$ emissive level and consequently the luminescence of the metal is completely quenched. Therefore, we have resorted to TFAC (trifluoroacetylacetone) with a triplet state at an optimum value around 23 800 cm^{-1}, which was reported before[166] to give more luminescent complexes than the analogous unsubstituted acetylacetonate.

III.2.2. Synthesis and characterization of complexes

The 6,2':6',2"-terpyridine-2-carboxylic acid **L12** was synthesized according to the reported procedure,[120] by oxidation of the 6-methyl-2,2':6'-2"-terpyridine precursor **45** with selenium dioxide in pyridine.

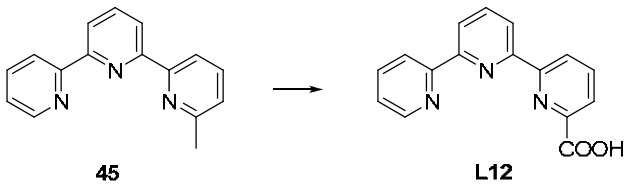

Scheme III.4. Conditions: SeO_2, pyridine 120°C, 58%

The heteroleptic complexes [Eu(**L12**)(TTA)$_2$] and [Tb(**L12**)(TFAC)$_2$] were synthesized by reacting one equivalent of **L12** and two equivalents of the corresponding β-diketone, in a methanol solution and in the presence of a stoichiometric amount of KOH, with one equivalent of metal triflate, as shown in Scheme III.5. After solvent evaporation, the complexes were extracted in dichloromethane, washed with water, dried using sodium sulfate and finally obtained as pale-yellow powders (yield 78-97%) after removal of dichloromethane.

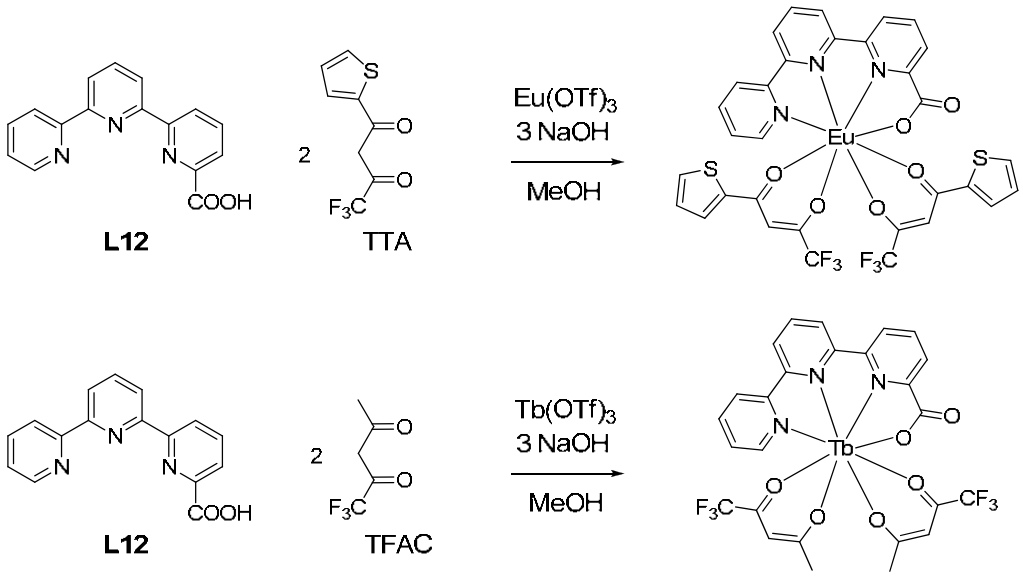

Scheme III.5. Reaction scheme for the synthesis of the [Eu(**L12**)(TTA)$_2$] and [Tb(**L12**)(TFAC)$_2$] complexes

The complexes have been characterized by single crystal X-ray diffraction, 1D and 2D proton NMR spectroscopy, mass spectrometry and elemental analysis (full details are given in the Experimental part).

a) Molecular and crystal structures

Crystals suitable for X-ray diffraction were obtained for both complexes [Eu(**L12**)$(TTA)_2$] and [Tb(**L12**)$(TFAC)_2$] by slow evaporation of their methanol solutions. Selected bond distances and angles are given in Table III.1, while the full crystallographic data is presented in the Appendix.

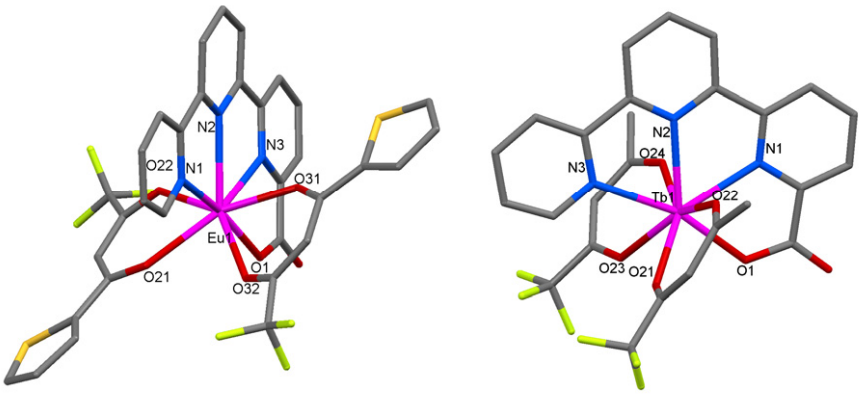

Figure III.1. Structures of the complexes [Eu(**L12**)$(TTA)_2$] (left) and [Tb(**L12**)$(TFAC)_2$] (right)

The structures of the complexes were solved in the $P2_1/n$ space group of the monoclinic system. The lanthanide ion is surrounded by one terpyridine-carboxylate and two β-diketonate units, and is octa-coordinated by the three nitrogens and one oxygen of the terpyridine-carboxylate, and by the two oxygens of the two β-diketonates. The overall structures are neutral. No solvent molecule is found in the first coordination sphere of the metal ion.

The Eu-O bond distances of the β-diketonate units in [Eu(**L12**)$(TTA)_2$] are slightly longer (2.374 Å) than in other octa-coordinated tris-β-diketonate complexes containing phenantroline as secondary ligand[167] (2.352 Å), but the Eu-O1 distance with the oxygen of the carboxylate moiety on terpyridine is much shorter (2.304 Å). The Eu-N1 and Eu-N2 distances (average 2.564 Å) are within normal ranges, similar but slightly shorter to those

found in coordinated phenantroline units[167] (average 2.578 Å), whereas the Eu-N3 bond is even shorter (2.514 Å), due to the vicinity of the strongly coordinating carboxylate moiety. The middle N atom of the terpyridine unit is situated at a longer distance than the terminal N atoms, similar to what was observed previously for coordinated terpyridine molecules[120] (see also Chapter II.2.2. a).

The distances in the analogous complex [Tb(**L12**)(TFAC)$_2$] present the same features, with a short Tb-O1 bond (2.295 Å) of the carboxylate moiety, and a shorter than average Tb-N1 bond (2.455 Å) due to proximity with the same carboxylate unit. Overall, the bond distances are slightly smaller in the [Tb(**L12**)(TFAC)$_2$] complex, compared to [Eu(**L12**)(TTA)$_2$], reflecting the reduced size of the terbium ion.

Table III.1. Selected bond distances (Å) and angles (°) in the complexes [Eu(**L12**)(TTA)$_2$] and [Tb(**L12**)(TFAC)$_2$]

[Eu(**L12**)(TTA)$_2$]		[Tb(**L12**)(TFAC)$_2$]	
Eu1-O1	2.304(2)	Tb1-O1	2.295(5)
Eu1-O31	2.352(2)	Tb1-O23	2.337(5)
Eu1-O22	2.368(2)	Tb1-O22	2.337(5)
Eu1-O32	2.368(2)	Tb1-O21	2.341(5)
Eu1-O21	2.408(2)	Tb1-O24	2.353(5)
Eu1-N3	2.514(2)	Tb1-N1	2.455(6)
Eu1-N1	2.538(2)	Tb1-N2	2.540(5)
Eu1-N2	2.589(2)	Tb1-N3	2.515(6)
N1-Eu1-N2	63.35(5)	N1-Tb1-N2	64.36(18)
N2-Eu1-N3	63.17(6)	N2-Tb1-N3	63.96(19)
O1-Eu1-N3	66.34(5)	O1-Tb1-N1	67.07(17)
O21-Eu1-O22	70.47(5)	O21-Tb1-O22	72.25(17)
O31-Eu1-O32	71.90(5)	O23-Tb1-O24	72.04(17)

The terpyridine ring system is practically planar in both cases, with a small deviation of the pyridine-carboxylate part in the [Eu(**L12**)(TTA)$_2$] complex (deviation angle 6.29°), and the lanthanide ion is located within this plane. The β-diketonate ligands are found on the opposite sides of the plane defined by the terpyridine-carboxylate ligand. In the structure of [Eu(**L12**)(TTA)$_2$], due to the larger size of the thiophene ring, the two β-diketonates are arranged anti-symmetrically, with the heterocycles pointing in opposite directions, whereas in [Tb(**L12**)(TFAC)$_2$], the arrangement of the two β-diketonates is

symmetrical. The angle between the planes of the two diketonate ligands and the plane of the terpyridine-carboxylate is on average 68° and 79° for [Eu(**L12**)(TTA)$_2$] and [Tb(**L12**)(TFAC)$_2$], respectively.

The crystal structures presented above show that the lanthanide ions are fully coordinated by the terpyridine-carboxylate and two β-diketonates ligands, being protected from interactions with the solvent molecules (detrimental to the emissive properties). Therefore, we could expect good luminescence efficiencies for this new type of heteroleptic architectures, as well as an improved stability, as a result of the strongly coordinating ligands.

b) ^{1}H NMR solution study

The ^{1}H NMR spectrum of the [Eu(**L12**)(TTA)$_2$]complex in methanol at room temperature shows 10 resonances which integrate for the 18 protons in the structure of the complex. Because some of the terpyridine signals are overlapped at 298K, we have run a variable temperature experiment (see Figure III.2) for finding the optimal temperature range at which the NMR spectrum is properly resolved. The two resonances situated in the downfield and upfield extremities of the spectrum are heavily affected by the temperature variation, while the rest of the signals are less influenced. However, between 273-263K, the signals in the aromatic region become more differentiated, and the spectrum shows a number of 14 resonances which integrate for 18 protons (10 signals with integral 1, assigned to the terpyridine ligand, and 4 signals with integral 2, assigned to the β-diketonate ligands). These features are in agreement with a Cs symmetrical specie in solution, having a symmetry plane passing through the terpyridine ligand, in which the two TTA units are equivalent. Going to even lower temperatures results in a large broadening of the signals, indicating that the fast exchange between the equivalent β-diketonate ligands slows down with the decreasing of the temperature. All the protons have been assigned by 2D ^{1}H-^{1}H COSY and NOESY experiments run in methanol solutions at 268K (see Figure III.3).

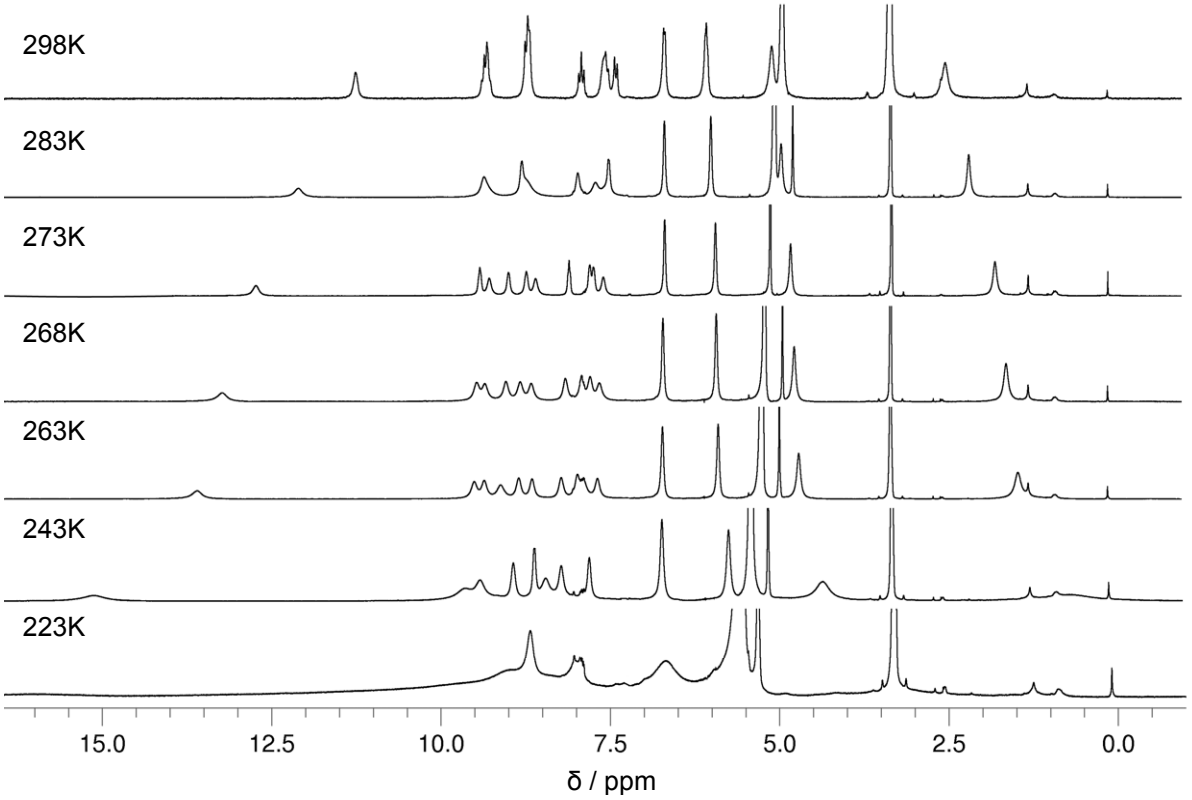

Figure III.2. Variable temperature ^{1}H NMR spectra of the [Eu(**L12**)(TTA)$_2$] complex in MeOD solution

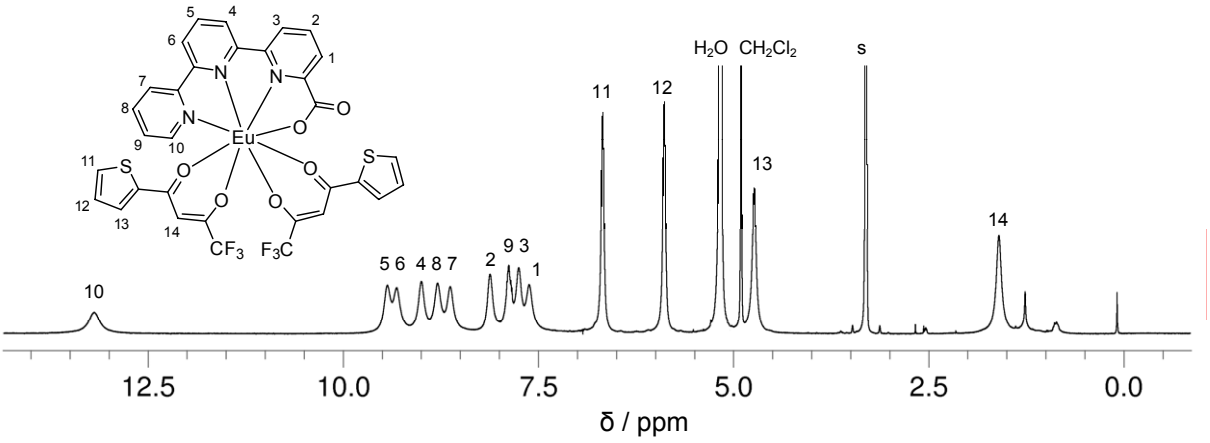

Figure III.3. ^{1}H NMR spectrum of the [Eu(**L12**)(TTA)$_2$] complex in MeOD solution at 268K

The ^{1}H NMR spectrum of the [Tb(**L12**)(TFAC)$_2$] complex is best resolved in chloroform at room temperature, and it shows 12 resonances which correspond to the 18 protons in the structure of the complex, as shown in Figure III.4. Ten signals with integral 1 are attributed to the terpyridine ligand, and four signals with integral 2 are attributed to

the β-diketonate ligands. This result is in agreement with the presence in solution of a Cs symmetrical specie with two equivalent β-diketonate ligands, similarly to the [Eu(**L12**)(TTA)$_2$] complex. Due to the large characteristic paramagnetic effect of terbium, the spectrum extends over 250 ppm, and therefore clear assignment by 2D NMR was not attempted.

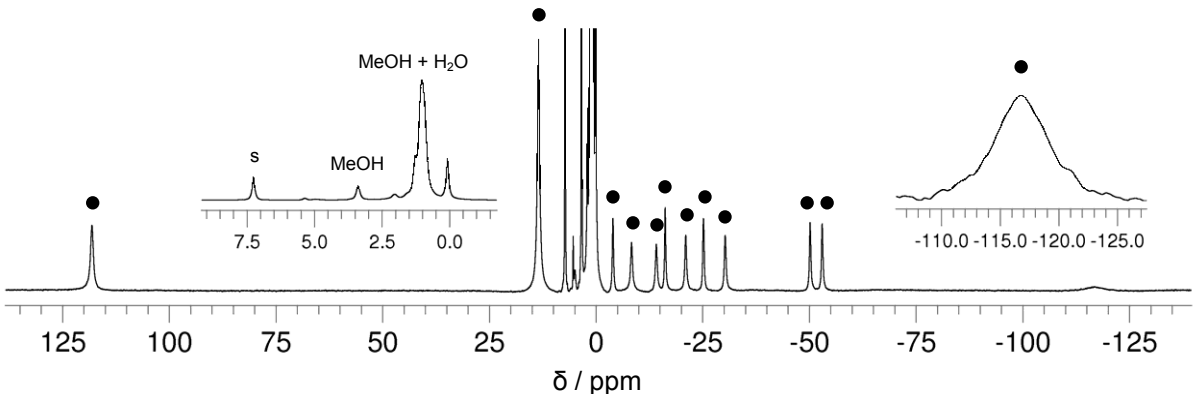

Figure III.4. ^{1}H NMR spectrum of the [Tb(**L12**)(TFAC)$_2$] complex in $CDCl_3$ solution at 298K

The proton NMR spectra show that the heteroleptic species are stable and do not dissociate in methanol or chlorinated solvents, indicating that the solid state structures of the two complexes obtained by X-ray diffraction are maintained in solution.

III.2.3. Photophysical properties of lanthanide complexes

a) Ligand centered luminescence

The lowest triplet states of the 2-thenoyltrifluoroacetone (TTA) and trifluoroacetylacetone (TFAC) ligands have been previously reported[165, 166] and correspond to 20 490 cm^{-1} (488 nm) and 23 800 cm^{-1} (420 nm), respectively. The emission spectra of the ligand **L12** and its complexes with the non-luminescent gadolinium ion have been measured in methanol solutions at 298K (see Figure III.5). UV excitation at 35 700 cm^{-1} and at the maximum in the excitation spectra results in a ligand-centered emission displaying one asymmetric broad band assigned to the singlet state, with a maximum at 28 570 cm^{-1} and 27 780 cm^{-1} for the free ligand and its [Gd(**L12**)$_2$]$^-$ complex, respectively. At 77K in methanol glass and

upon enforcement of a time delay (0.2 ms), the singlet state emission disappears with concomitant appearance of a broad and structured band arising from the triplet state emission. The 0-phonon transition is located at 22 730 and 22 520 cm^{-1} for the free ligand and its $[Gd(\mathbf{L12})_2]^-$ complex, respectively. The energy gap between the 0-phonon transitions of the singlet and triplet states is 6 000 cm^{-1} in the case of the gadolinium chelate, which would indicate an effective intersystem crossing. Moreover, the values obtained for the singlet and triplet state energies of the ligand **L12** are identical to those measured before for the terpyridine dicarboxylic acid **L2**, and are optimal for the sensitization of europium or terbium emission, as seen in Chapter II.2.3. c).

b) Metal centered luminescence

The visible luminescence spectra of the $[Eu(\mathbf{L12})(TTA)_2]$ and $[Tb(\mathbf{L12})(TFAC)_2]$ complexes recorded in solid state at 298K are shown in Figure III.5. The ligand centered emission is not detected, pointing to an efficient ligand to metal energy transfer process in both cases.

Upon broadband excitation of the $[Eu(\mathbf{L12})(TTA)_2]$ complex through the ligand levels, the Eu^{3+} emission exhibits the characteristic $^5D_0 \rightarrow {}^7F_J$ transitions and is dominated by a very intense $^7F_2$ band, in agreement with the low symmetry of the complex. The excitation spectrum recorded in similar conditions upon monitoring the $^7F_2$ band shows a broad maximum at 365 nm (27 400 cm^{-1}) which has been assigned to the singlet state of the ligand **L12**, visible as a result of the efficient $^1\pi\pi^* \rightarrow {}^5D_0$ energy transfer.

The $[Tb(\mathbf{L12})(TFAC)_2]$ complex displays a typical emission spectrum dominated by the $^5D_4 \rightarrow {}^7F_5$ transition, while the corresponding excitation spectrum shows a broad maximum at 380 nm (26 300 cm^{-1}) which has been similarly assigned to the singlet state of the ligand **L12**.

The luminescence decay of the $[Eu(\mathbf{L12})(TTA)_2]$ emission, measured at the $^7F_2$ site upon ligand excitation, can be fitted to a monoexponential function and corresponds to a 0.95 ms lifetime in solid state at 298K, indicating the absence of solvent molecules in the first coordination sphere of the metal, in agreement with the X-ray structure. The absolute quantum yield shows a very high value of 40.8%, which suggests the complex

could be used successfully in the emitting layer of an OLED. The [Tb(**L12**)(TFAC)$_2$] complex is characterized by a shorter lifetime (0.34 ms) and a lower quantum yield (12.9%). As the X-ray structure points to the absence of solvent molecules from the coordination sphere of the metal, the reduced lifetime could be explained by a partial back-energy transfer from the triplet state of the ligand **L12** to the Tb(^{5}D$_4$) emissive state, which would also lead to a lower quantum yield.

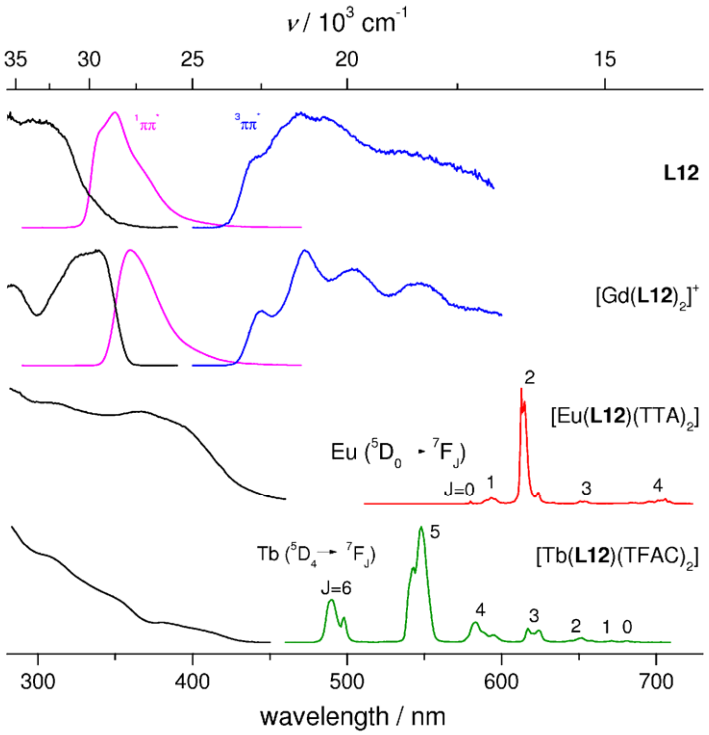

Figure III.5. Normalized excitation and emission spectra of the ligand **L12** and its [Eu(**L12**)(TTA)$_2$] and [Tb(**L12**)(TFAC)$_2$] complexes. Singlet and triplet state levels are measured in methanol solutions at 298K and 77K, respectively, upon excitation at 35 700 cm^{-1}. Eu and Tb luminescence spectra are recorded in solid state at 298K. Excitation spectra are measured at the maximum of emission.

Summary of photophysical properties for the [Eu(**L12**)(TTA)$_2$] and [Tb(**L12**)(TFAC)$_2$] complexes. Singlet (^{1}ππ*) and lowest triplet state (^{3}ππ*) energies are measured in methanol solutions at 298K and 77K, respectively. Excitation maxima ($\tilde{\upsilon}_{max}$) are given from solid state excitation spectra. Lifetimes (τ) and absolute quantum yields (Φ) are measured for solid state samples at 298K.

	^{1}ππ*/cm^{-1}	^{3}ππ*/cm^{-1}	Ln	$\tilde{\upsilon}_{max}$/cm^{-1}	τ/ms	Φ/%
L12	27 780	22 520	Eu	27 400	0.95(2)	40.8(4)
			Tb	26 300	0.344(4)	12.9(2)

III.2.4. Applications in OLED devices

In an organic light emitting diode, the ligands are typically excited by absorbing energy, through dipole–dipole interactions (Förster transfer), from an electrically excited host polymer whose emission spectrum overlaps the absorption spectrum of the ligand. Following energy absorption by the ligand, intersystem crossing to a triplet state occurs which, if the energy of the triplet level is higher than that of the emission level of the lanthanide ion, is followed by energy retransfer to the metal. The excited ion subsequently emits the characteristic sharp bands from the f-f transitions (see Chapter I.3.2.).

The very good photophysical properties of our [Eu(**L12**)(TTA)$_2$] and [Tb(**L12**)(TFAC)$_2$] complexes, combined with their overall neutrality and good solubility in chlorinated solvents, prompted us to investigate the potential applications of such architectures as emitting layers in organic light emitting diodes.

For this, we have first looked at the thermal stability of the europium complex, in view of the possibility to prepare OLED devices by vacuum deposition techniques. While the free ligand **L12** melts at 489K (216°C), the [Eu(**L12**)(TTA)$_2$] complex remains solid up to 573K (300°C), after which it decomposes to a black solid. However, a slight change in color towards brown starts to become visible around 473K (200°C), which intensifies with further increase in temperature. Sublimation tests carried out by heating the complex at 473K under medium vacuum ($5 \cdot 10^{-5}$ torr, 7 mPa) shown however that the compound does not undergo evaporation in the conditions used.

We have then investigated the film-forming properties of the europium complex dispersed in a polymer matrix, in order to asses the suitability of the complexes for spin-coating device-processing techniques. Poly(N-vinylcarbazole) or PVK is widely used in many studies on OLED devices because of its good hole-transporting and film-forming properties. Thin films of [Eu(**L12**)(TTA)$_2$] dissolved in a PVK (MW = 42 000 g/mol) solution at 0, 2.5 and 5% w/w doping in chlorobenzene were obtained by spin coating on 2.4×2.4 cm^2 glass surfaces, using the following program: 40s at 1500 rpm, then 40s at 2000 rpm. The films were dried in air for 1h, then under vacuum, and their surface morphology analyzed by atomic force microscopy technique in tapping mode (5 μm × 5 μm scans). In all

the cases, the films obtained were smooth, with only a few spots that may be caused by dust or surface defects. The best results have been obtained from solutions of the complex doped at 2.5% w/w in the PVK matrix (see Figure III.6). No regions with high phase contrast were observed, indicating that the complex dissolved without substantial aggregation into the PVK host and was evenly distributed throughout the film such that the surface appeared to be quite homogeneous.

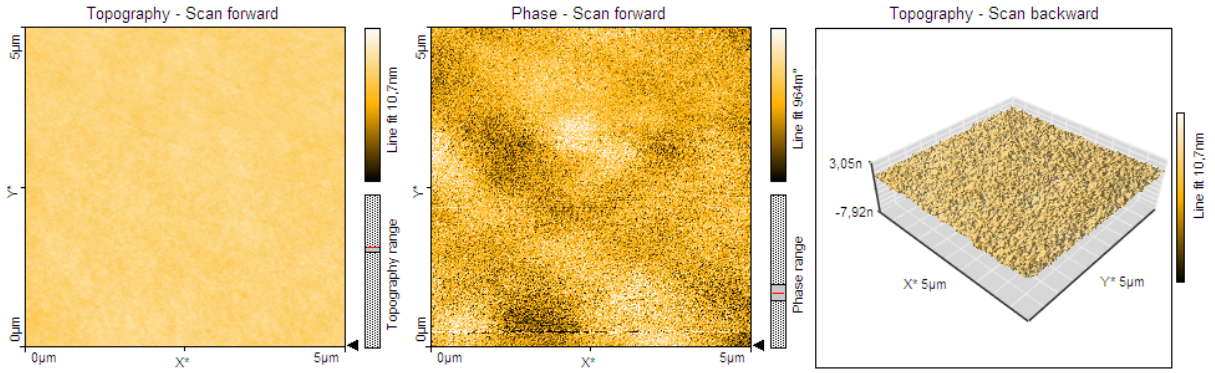

Figure III.6. Tapping mode AFM images of the thin films obtained from [Eu(**L12**)(TTA)$_2$] - PVK (2.5 % w/w doping) solutions in chlorobenzene

To obtain preliminary information regarding the optoelectronic properties of the [Eu(**L12**)(TTA)$_2$] and [Tb(**L12**)(TFAC)$_2$] complexes, OLED devices were prepared in collaboration with Materia Nova, Belgium. The devices were fabricated using polymer solution spin casting techniques, and have the following configuration: ITO / PEDOT PH500 / PVK:[Eu(**L12**)(TTA)$_2$] / Cs_2CO_3 / Al for the europium complex, and ITO / PEDOT PH500 / PVK:[Tb(**L12**)(TFAC)$_2$] / Cs_2CO_3 / Al for the terbium complex (see Figure III.7).

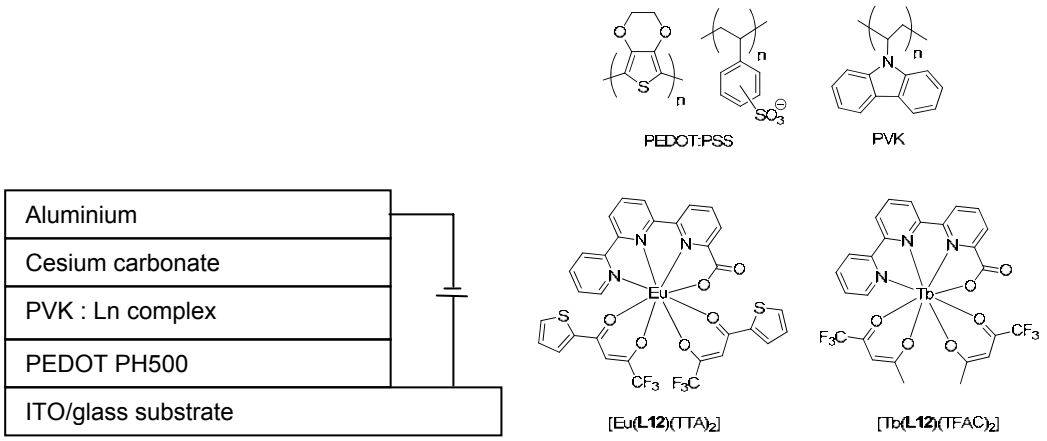

Figure III.7. Schematic configuration of the OLED devices and molecular structures of the materials used

The OLEDs comprised an emissive layer of PVK doped at 5% w/w with the corresponding lanthanide complex, on a glass/indium tin oxide (ITO) surface coated with a special blend of 3,4-polyethylene-dioxythiophene-polystyrene sulfonate (PEDOT-PSS) denoted as PH500. Incorporating PEDOT into the device structure presents a number of benefits. Concerning the quality of ITO electrodes, which is known to be very variable, PEDOT planarizes the ITO layer and also has a higher work function (5.3 eV) compared to ITO (4.8 eV), resulting in a 0.5 V reduction in the hole injection barrier at the PVK/ anode interface (the highest occupied molecular orbital of PVK is 5.8 eV). Also, use of orthogonal solvents eliminates device degradation associated with interlayer dissolution and mixing.

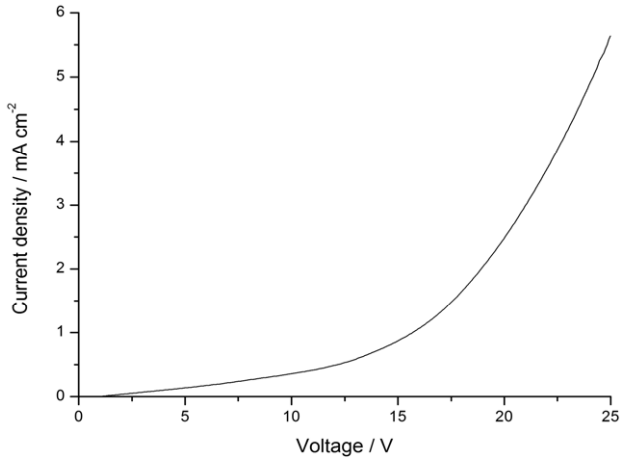

Figure III.8. Current density-voltage curve for an ITO/PEDOT/PVK:[Eu(**L12**)$(TTA)_2$]/Cs_2CO_3/Al device

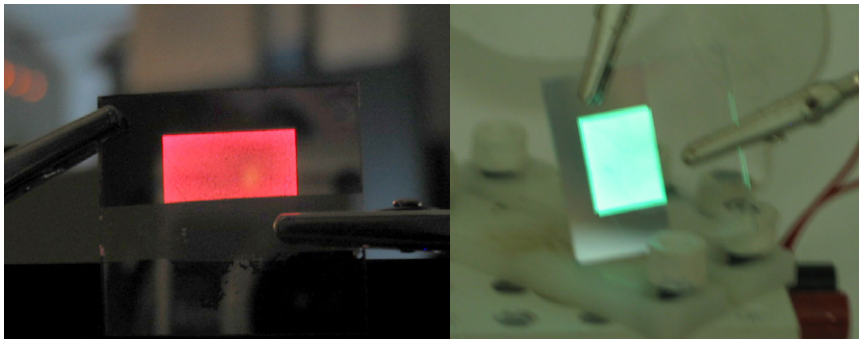

Figure III.9 OLED devices constructed using the europium (left) and terbium (right) complexes

The devices exhibited typical diode behavior, with a turn on voltage of cca. 2 V for the europium-based OLED (see Figure III.8). Characteristic bright red or green luminescence was observed in both cases, as shown in Figure III.9. However, the current intensity measured was rather low for the europium-based OLED, with only 5.4 mA/cm^2 at 25V, but better in the case of the terbium-based OLED, with 45 mA/cm^2 at 20V. These preliminary results suggest that the lanthanide complexes [Eu(**L12**)(TTA)$_2$] and [Tb(**L12**)(TFAC)$_2$] have potential for use as active layers in organic light emitting diodes, however the device architecture needs to be improved, by using perhaps a different host matrix,[168] with better electron-transporting properties (such as a blend of PVK and PBD, [2-(4-biphenyl)-5-(4-*tert*-butylphenyl)-1,3,4-oxadiazole]), and the addition of a hole-blocking layer (which could also be PBD).

III.3. Neutral lanthanide complexes based on terpyridine-bistetrazolate

III.3.1. Lanthanide complexes for surface functionalization

Surface functionalization of solid substrates by appropriate chemical compounds has opened very exciting potential applications[169, 170] in the field of micro and nanoelectronics, optoelectronics or thin-film technology.

As discussed in Chapter I.3.2. , lanthanide complexes have been often used in optoelectronic devices because of their very interesting photophysical properties (strong

and sharp emission, long lifetimes, etc). A lot of effort has been also dedicated to introduce the lanthanide complexes onto various solid surfaces, such as silica matrixes.[171, 172] The functionalization of the silica with lanthanide complexes results into attractive luminescent properties and potential applications. However, there are still very few reports concerning the surface functionalization with lanthanide complexes of semiconductor substrates, such as silicon wafers. So far, the complexes have been incorporated in solid substrates by the Langmuir-Bloggett or self-assembly techniques.[173] However, because the films obtained by these methods do not have a long-term stability,[174] their potential applications in the field of organic optoelectronic devices is rather limited.

Recently, a method to covalently introduce an europium complex onto silicon and ITO substrates through the use of an organosilane as molecular bridge has been reported[175] by Duan *et al*. The strong Si-O covalent bonding provides a high stability of the resulting monolayers on the surface. The authors grafted silicon and ITO glass surfaces with 3-aminopropyltriethoxysilane (APTES), which they further reacted with a bromoheptyl-methyl-bipyridine. Finally, the europium complex was integrated onto the substrates via coordination of the appended bipyridine unit to the [Eu(TTA)$_3$] complex, to give the assembly illustrated in Figure III.10 (left).

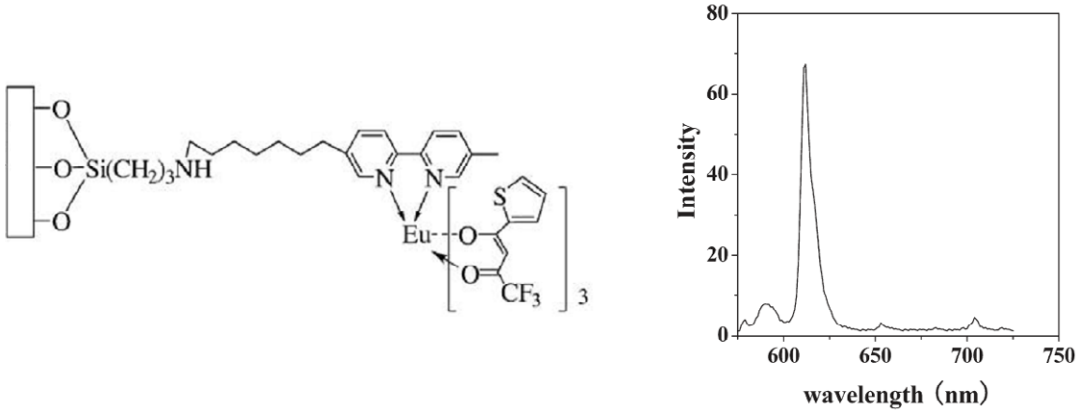

Figure III.10. Chemical structure of the grafted assembly (left) and photoluminescence spectra of the europium complex on ITO glass substrate (right) taken from ref.[175]

The grafted surfaces were analyzed by X-ray photoelectron spectroscopy (XPS), atomic force microscopy (AFM), cyclic voltammetry and fluorescence microscopy. XPS indicated the presence of Eu ions on the surface, which was further confirmed by the luminescence measurements on ITO substrates (Figure III.10, right), which shown the characteristic emission of europium. However, no luminescence measurements have been performed on the grafted silicon surfaces.

Apart from this publication, to the best of our knowledge, no other attempts at covalently grafting lanthanide complexes on silicon surfaces have been undertaken. Therefore, we set out to investigate this possibility by designing a ligand appended with a tripodal anchor capable of forming Si-C bonds on a silicon wafer.

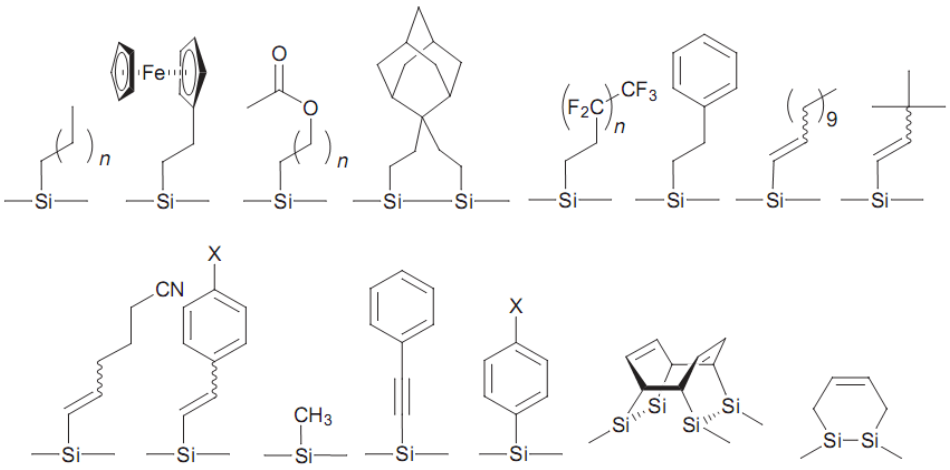

Figure III.11. Examples of organic monolayers formed on silicon surfaces through Si–C bonds (from ref.[176])

Strong covalent Si-C bonds form the basis of covalently bound monolayers of 1-alkenes containing molecules on H-terminated Si surfaces. These monolayers have been investigated extensively both experimentally and theoretically. However, most of the previous studies reported in the literature concerning the preparation of monolayers utilised molecules that were functionalized for tethering to the surface via a single anchor atom,[176, 177] as shown in Figure III.11. Bocian and co-workers,[178, 179] followed by other groups, performed limited studies of molecules functionalized for tethering via multiple anchor groups, in particular tripodal linkers. The reasons for preparing tripode-based molecules to

produce active monolayers are two-fold. First, it can be anticipate that this type of multiple attachments to a surface via three versus one anchor atom might result in a more robust architecture. Second, it is believed that the symmetrical tripodal motif might result in higher packing densities in the monolayers.

III.3.2. Ligand and complex design

Due to the easy functionalization and strong coordinating abilities of the terpyridine-tetrazolate ligands presented in Chapter II.2.1. we have decided to use this moiety in the construction of grafted complex assemblies. For anchoring on the silicon surface, tripodal anchoring groups have particular advantages (*vide supra*). The connection between the anchoring group and the terpyridine chromophore was done through a bis-phenylene bridge. The structure of the final ligand is shown in Scheme III.6.

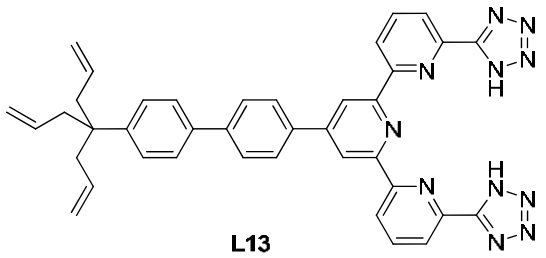

L13

Scheme III.6. Structure of the ligand **L13** with appended surface anchoring group

This type of ligand architecture could allow the formation of both homoleptic or heteroleptic lanthanide complexes. For the purpose of this study, we planned the coordination of a second ligand containing chemical moieties which could be easily detected by surface analysis techniques, allowing us to confirm the formation of a lanthanide complexes on the surface. As seen before in Chapter III.2.2. , β-diketonate units act as excellent secondary ligands in the case of terpyridine-monocarboxylate, leading to stable, strongly luminescent heteroleptic lanthanide complexes. Similarly, we can anticipate that terpyridine-bistetrazolate ligands can also form heteroleptic complexes with β-diketones, perhaps with a different stoichiometry.

The final grafted assembly will comprise thus the terpyridine ligand anchored on the surface via the tripodal unit and coordinated to an europium ion. β-diketonate secondary ligands (such as 2-thenoyltrifluoroacetone, TTA) will complete the coordination sphere of the lanthanide metal. The estimated non-bonding distance between the silicon substrate and the europium ion will be around 2 nm, which should be sufficiently long so that quenching of europium luminescence mediated by the silicon surface is minimized.

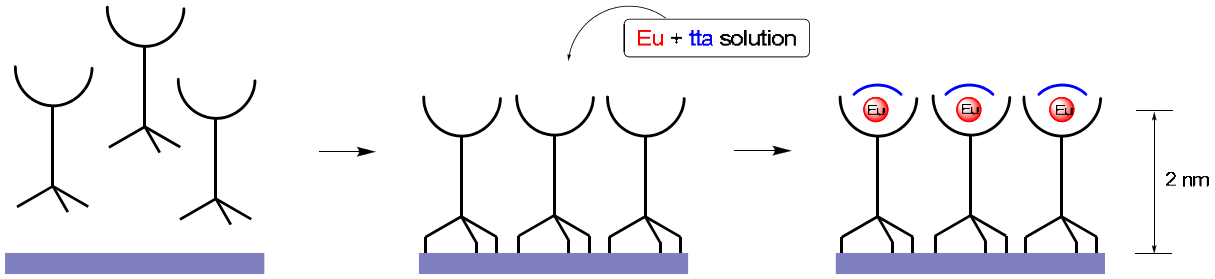

Figure III.12. Schematic representation of the surface complexation process

The grafting will take place in two steps, as depicted schematically in Figure III.12. The terpyridine-tetrazolate ligand will be first anchored to the surface by the methods previously developed in our laboratory for other allylic tripods. Following, the grafted surface will be immersed in a solution containing the europium salt and the β-diketonate ligand, leading to the formation of the heteroleptic complex on the surface. Analysis of the grafted substrate by IR (C=O signature) or XPS (specific binding energies for Eu or S) could then confirm the formation of a complex.

III.3.3. Synthesis and characterization of ligands

The synthesis of the ligand **L13** (see Scheme III.7) begins with commercially available 4-(trifluoromethyl) aniline **46**, which upon reaction with allylmagnesium chloride **47** provides the triallyl-aniline **48**. The reaction requires excess of allylmagnesium chloride and involves repetition of fluoride elimination followed by addition of the Grignard reagent to the resulting quinone-imine.[179] The synthesis can be carried out at the gram scale in THF. The conversion of the triallyl-aniline to the triallyliodobenzene **49** was

achieved via the Sandmeyer reaction, by diazotization of amine in the presence of hydrochloric acid with sodium nitrite at 0-5 °C followed by treatment with potassium iodide.[179] The Suzuki coupling reaction of the iodinated derivative **49** with the previously prepared boronic ester **40** (see Scheme IV.15) afforded the cyanated precursor **50**, from which the classical thermal cycloaddition with gave the final ligand **L13**.

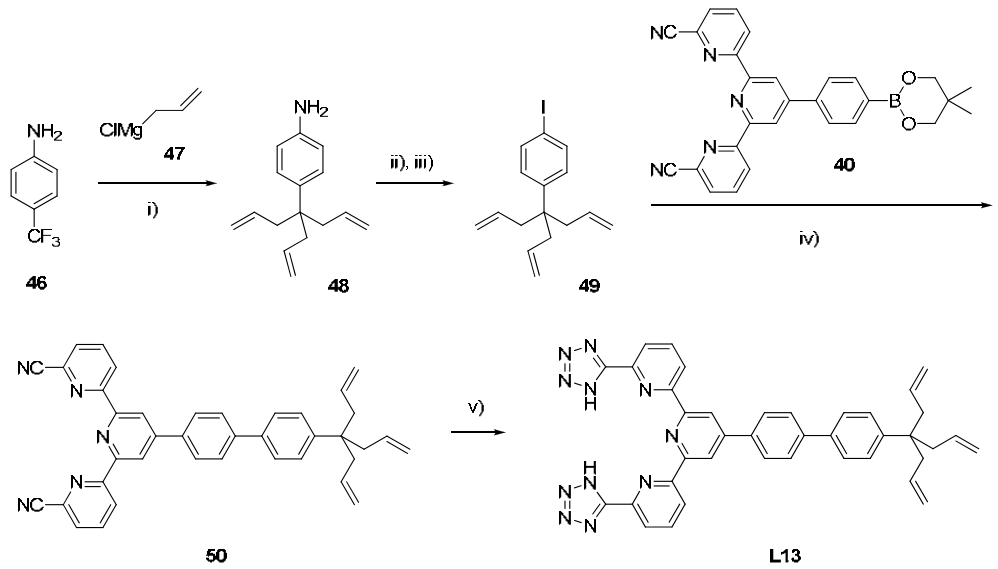

Scheme III.7. Conditions: i) THF, -50°C to reflux (87%); ii) $NaNO_2$, HCl; iii) KI (30%); iv) $Pd(dppf)Cl_2$, NaOAc, DMSO (60%); v) NaN_3, NH_4Cl. DMF (88%).

The ligand **L13** has been characterized by ^1H and ^{13}C NMR spectroscopy and elemental analysis, and the data is available in the Experimental part. The ligand is insoluble in classical organic solvents with the exception of DMF and DMSO, but it becomes soluble in MeOH after addition of inorganic (KOH) or organic (triethylamine) bases. The DMSO ^1H NMR spectrum is given in Figure III.13.

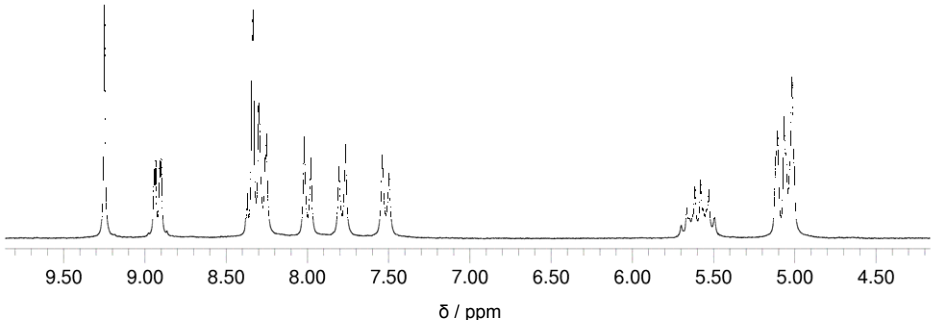

Figure III.13. ^{1}H NMR spectrum of ligand **L13** in DMSO solution at 298K

A crystal structure has been obtained for the intermediate **50** by slow evaporation of a chloroform solution of the product. The structure has been solved in the P1 space group of the triclinic system (see Figure III.14). Selected information is given in Table III.2, while the full crystallographic data is available in the Appendix. The bond distances and angles are within the normal ranges expected for similar compounds.

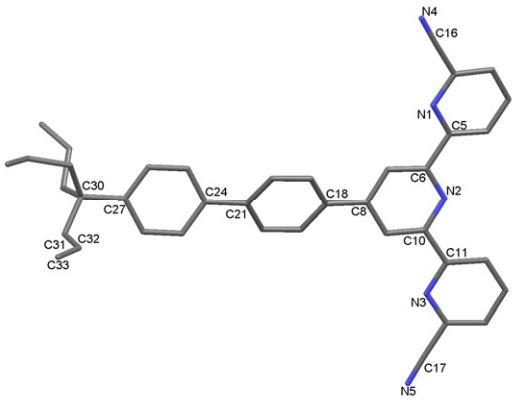

Figure III.14. Molecular structure of the intermediate **50**

Table III.2. Selected bond distances (Å) and angles (°) in the structure of intermediate **50**

N1-C5	1.3420(16)	C8-C18	1.4876(17)	N1-C5-C6	116.04(11)
N2-C6	1.3411(16)	C21-C24	1.4912(17)	C6-N2-C10	117.35(11)
N2-C10	1.3434(17)	C27-C30	1.5441(17)	N3-C11-C10	116.80(11)
N3-C11	1.3385(17)	C30-C31	1.5450(20)	C27-C30-C31	111.95(11)
N4-C16	1.1453(18)	C31-C32	1.4940(20)	C31-C32-C33	125.90(19)
N5-C17	1.1420(20)	C32-C33	1.3160(30)		

III.3.4. Synthesis and characterization of complexes

The initial studies on the formation of heteroleptic complexes of lanthanides with terpyridine-tetrazolate and β-diketonate ligands have been carried out using the unsubstituted terpyridine ligand **L1**, previously described in Chapter II.2.1. c).

The complex [Eu(**L1**)(TTA)] containing one coordinated 2-thenoyltrifluoroacetone molecule was synthesized by reacting equimolar quantities of **L1,** TTA and europium triflate in a methanol solution and in the presence of triethylamine, as shown in Scheme III.8. The complex started to crystallize immediately, and was isolated by filtration as a yellowish powder (yield 75%). Characterization was performed by single crystal X-ray crystallography, 1D and 2D proton NMR spectroscopy and elemental analysis (full details in the Experimental section). The complex is insoluble in water, methanol, chloroform or acetonitrile, but it is soluble in DMSO.

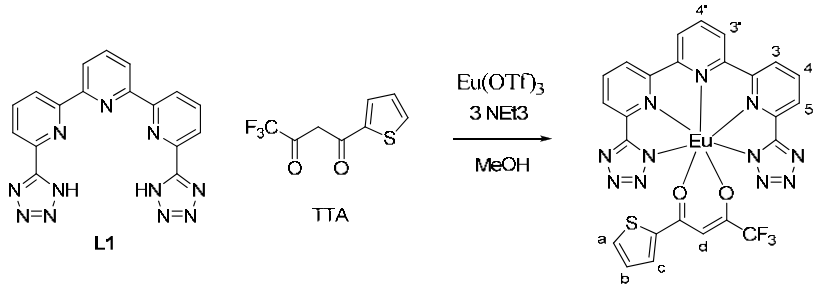

Scheme III.8. Reaction scheme for the synthesis of the [Eu(**L1**)(TTA)] complex

The complex [Eu(**L13**)(TTA)] containing the substituted terpyridine-bistetrazole ligand **L13** and one coordinated 2-thenoyltrifluoroacetone molecule was synthesized according to the reaction Scheme III.9 and characterized in situ by 1D and 2D proton NMR spectroscopy.

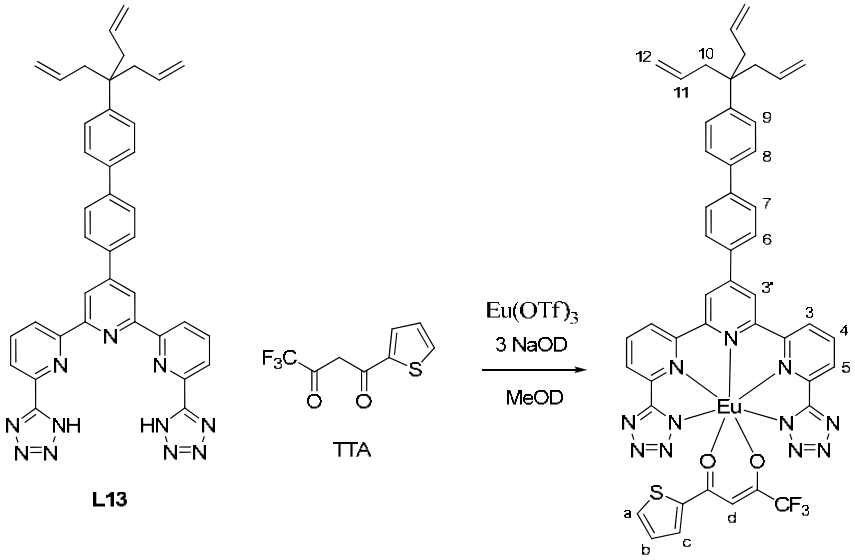

Scheme III.9. Reaction scheme for the synthesis of the [Eu(**L13**)(TTA)] complex

a) Molecular and crystal structures

A crystal suitable for X-ray diffraction has been obtained for [Eu(**L1**)(TTA)] by slow water vapor diffusion in a DMSO solution of the complex. Selected bond distances and angles are given in Table III.3, while the full crystallographic data is presented in the Appendix.

In the structure solved in the P1 space group of the triclinic system, the metal is nine-coordinated by the 5 nitrogens of the terpyridine-tetrazolate ligand, the 2 oxygens of the β-diketonate ligand, and the oxygen atoms of one coordinated DMSO and one coordinated water molecule, respectively (see Figure III.15). The average distance Eu-N is 2.5784 Å, with the strongest bond between the metal and N1 (2.5246 Å). The values are smaller than in the case of the bis-ligand complex $[Eu(\mathbf{L1})_2]^-$, and indicate a less sterically hindered arrangement around the metal center. Similarly, the bite angle N1-Eu-N5 is larger than in the case of the $[Eu(\mathbf{L1})_2]^-$ complex.

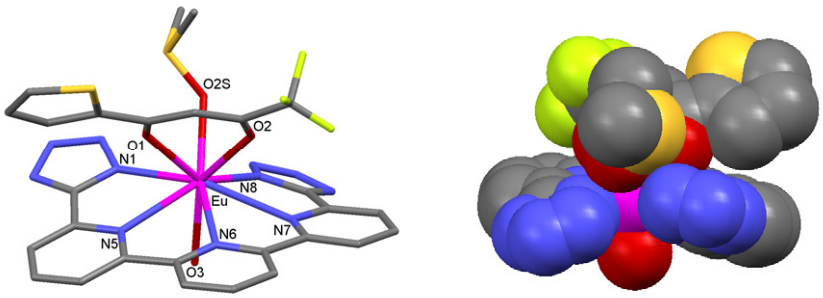

Figure III.15. Molecular structure of the complex [Eu(**L1**)(TTA)(dmso)(H_2O)]

Table III.3. Selected bond distances (Å) and angles (°) in the structure of [Eu(**L1**)(TTA)(dmso)(H_2O)]

Eu-O2S	2.3824(16)	O2S-Eu-O3	130.06(6)
Eu-O3	2.4239(17)	O2S-Eu-O1	77.76(6)
Eu-O1	2.4270(16)	O2S-Eu-O2	77.01(6)
Eu-O2	2.4542(16)	O1-Eu-O2	68.53(6)
Eu-N1	2.5246(18)	N1-Eu-N8	95.90(6)
Eu-N8	2.5697(18)	N8-Eu-N7	63.53(6)
Eu-N6	2.5824(18)	N6-Eu-N7	62.04(6)
Eu-N7	2.5994(18)	N1-Eu-N5	64.15(6)
Eu-N5	2.6161(18)	N6-Eu-N5	62.30(6)

The terpyridine-tetrazolate unit is not planar, the two arms of the ligand being twisted in a helical manner (P and M), with an angle between the N1 or N8 tetrazole groups and the central pyridine ring of 15.37° and 25.40°, respectively. The non-bonding distance between the europium ion and the plane of the central pyridine is of 0.715 Å. The 2-thenoyltrifluoroacetone moiety is planar, with the fluorine and sulfur atoms disordered, as usually observed in the lanthanide complexes of this ligand.[167] The average Eu-O distance from the diketonate unit is 2.441 Å, which is longer than the average Eu-O distance in the complex [Eu(**L12**)$(TTA)_2$] (2.374 Å, see Table III.1).

Hydrogen bonds form in the packing structure between the uncoordinated N atoms of the tetrazole rings and the coordinated water molecules.

b) ^{1}H NMR solution study

The ^{1}H NMR spectrum of the isolated [Eu(**L1**)(TTA)] complex in a DMSO solution at 298K shows the presence of only one set of signals, with 9 resonances for the 13 protons in the structure of the complex, as seen in Figure III.16. These features are consistent with the

presence of a stable species showing C_2 symmetry on the NMR time scale, in agreement with the fast exchange of the coordinated β-diketonate ligand, which renders equivalent the symmetric protons of the terpyridine unit. Signals corresponding to coordinated methanol molecules appear in the DMSO spectrum even after prolonged drying of the isolated complex, in agreement with the elemental analysis. All the protons have been assigned by 2D COSY and NOESY experiments.

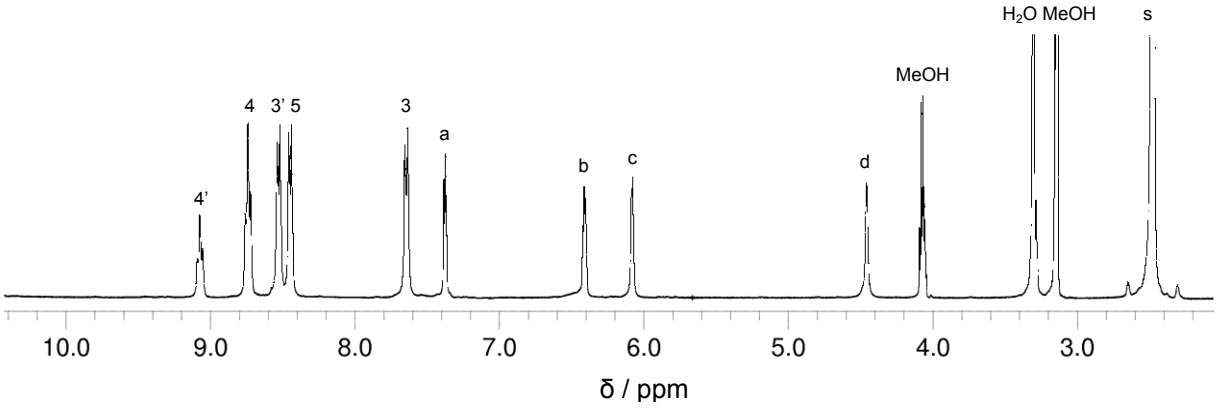

Figure III.16. ^{1}H NMR spectrum of the complex [Eu(**L1**)(TTA)] in DMSO solution at 298K

The formation of the [Eu(**L1**)(TTA)] complex can be followed by ^{1}H NMR titration, as shown in Figure III.17. Addition of one equivalent of 2-thenoyltrifluoroacetone deprotonated with triethylamine to a methanol solution of $[Eu(\mathbf{L1})]^+$ prepared in situ results in the complete disappearance of the mono-chelate signals and the appearance of a new set of resonances, corresponding to the [Eu(**L1**)(TTA)] complex. The heteroleptic complex crystallizes very rapidly from the solution. The chemical shift is slightly different in MeOD compared to DMSO-D_6, and two of the TTA resonances are hidden beneath the water peak.

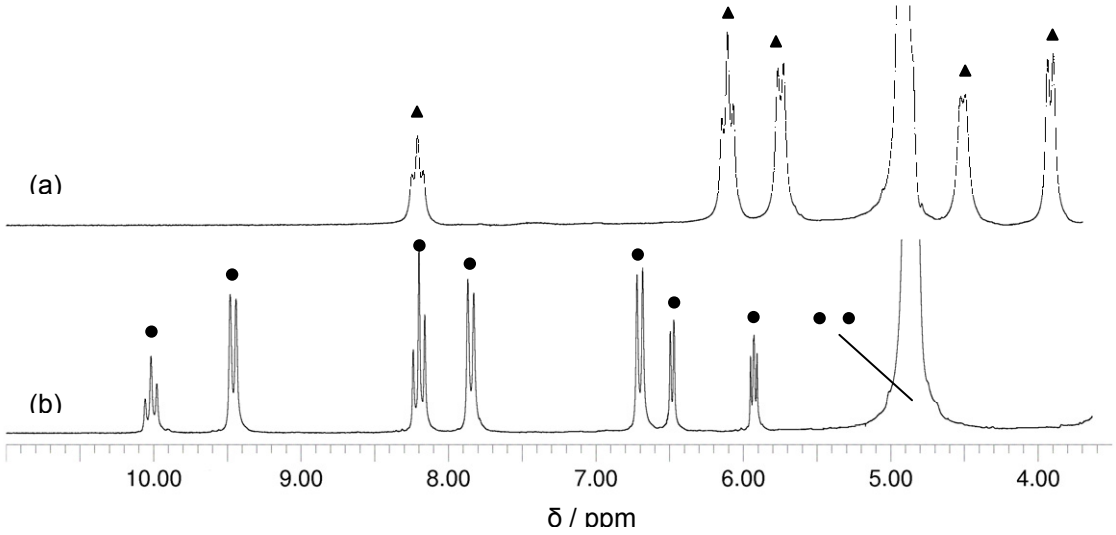

Figure III.17. ^{1}H NMR spectra in MeOD solution of the [Eu(**L1**)]$^{+}$ species (a) before and (b) after addition of an equimolar amount of TTA, showing the formation of [Eu(**L1**)(TTA)]

Addition of 2 equivalents of TTA to a methanol solution of the [Eu(**L1**)]$^{+}$ complex, or addition of one equivalent of **L1** to a methanol solution of [Eu(TTA)$_3$] resulted in the crystallization of the same [Eu(**L1**)(TTA)] species, as confirmed by proton NMR and X-ray diffraction of the isolated crystals.

In the case of ligand **L13**, appended with the allylic tripod, the formation of the [Eu(**L13**)(TTA)] complex has been studied in situ and was concluded to proceed similarly. Addition of one equivalent of 2-thenoyltrifluoroacetone deprotonated with NaOD to a deuterated methanol solution of [Eu(**L13**)]$^{+}$ results in the formation of the [Eu(**L13**)(TTA)] species. The ^{1}H NMR spectrum of [Eu(**L13**)(TTA)] in MeOD at 298K shows the presence of 15 resonances (one hidden underneath the water peak but visible upon increasing temperature) which have been assigned by 2D NMR to the 35 protons in the structure of the complex (see Figure III.18). The spectrum is in agreement with the presence of a stable species showing C_2 symmetry on the NMR time scale. The coordinated β-diketonate ligand is in fast exchange, rendering equivalent the protons on the two sides of the terpyridine-based ligand.

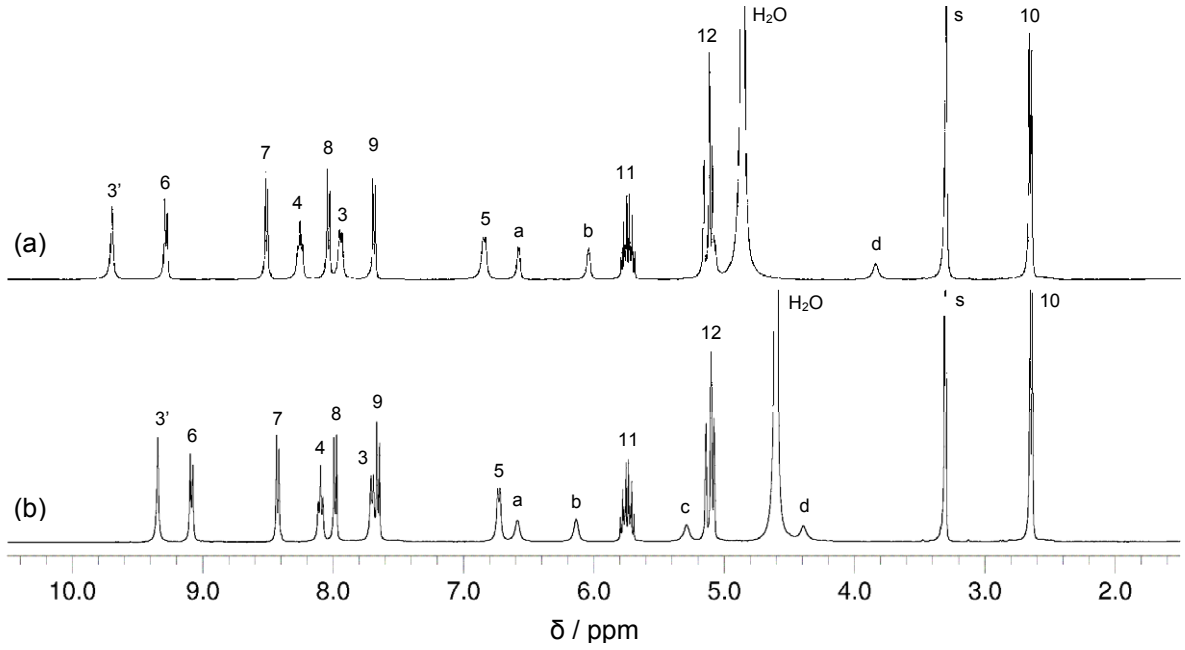

Figure III.18. ^{1}H NMR spectra in MeOD solution of the [Eu(**L13**)(TTA)] complex at (a) 298K and (b) 323K

Due to the presence of the allylic tripod, the solubility in methanol of the [Eu(**L13**)(TTA)] complex compared to [Eu(**L1**)(TTA)] is markedly increased, and the product no longer crystallizes from the solution.

The NMR studies performed on the two complexes, together with the solid state information obtained by single crystal X-ray diffraction, indicated that the terpyridine-bis-tetrazole ligand **L13** is capable of forming neutral heteroleptic lanthanide complexes incorporating one 2-thenoyltrifluoroacetone secondary ligand. The coordination sphere of the metal is completed by solvent molecules. Such a system could be successfully used for the incorporation of lanthanide complexes on a silicon surface.

III.3.5. Photophysical properties of complexes

The luminescence spectrum of the [Eu(**L1**)(TTA)] complex in solid state at 298K is given in Figure III.19. The lowest triplet state of the 2-thenoyltrifluoroacetone (TTA) ligand has been previously reported[165] and corresponds to 20 490 cm^{-1} (488 nm), while the lowest triplet state of ligand **L1** is 22 170 cm^{-1} (451 nm). The ligand centered singlet emission is not detected, pointing to an efficient ligand to metal energy transfer. Upon broadband

excitation, the europium emission exhibits the characteristic $^5D_0 \rightarrow {}^7F_J$ transitions and is dominated by the very intense $^7F_2$ transition, in agreement with the low symmetry of the complex.

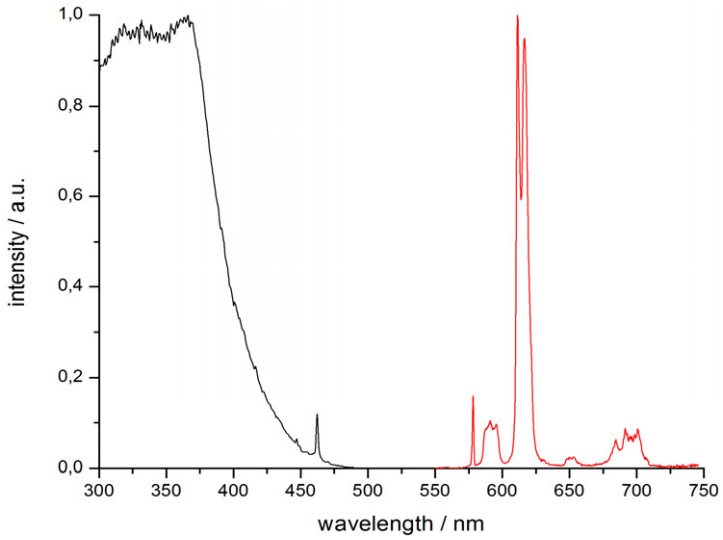

Figure III.19. Normalized solid state excitation (left) and emission (right) spectra of [Eu(**L1**)(TTA)]

The excitation spectrum recorded in similar conditions upon monitoring the $^7F_2$ band shows a maximum at 365 nm (27 400 cm^{-1}) which has been assigned to the singlet state of the ligand **L1**, visible as a result of the efficient $^1\pi\pi^* \rightarrow {}^5D_0$ energy transfer. A similar attribution has been made in the case of the homoleptic $[Eu(\mathbf{L1})_2]^-$ complex.

The luminescence decay of the [Eu(**L1**)(TTA)] emission, measured at the $^7F_2$ site upon ligand excitation, can be fitted to a monoexponential function and corresponds to a 0.374(17) ms lifetime in solid state at 298K, indicating the presence of coordinated solvent molecules in the first coordination sphere of the metal, in agreement with the X-ray structure. The absolute quantum yield shows a relatively low value of 11.6(9)%, which is normal considering the vibrational deactivation promoted by the solvent molecules.

These results show that the terpyridine-tetrazolate and β-diketonate architecture is capable of sensitizing the luminescence of europium, in spite of the reduced coordination sites which allow the presence of solvent molecules in the vicinity of the metal. Similar results, with perhaps a variation in the value of the quantum yield due to the different

triplet state of the ligand, are expected for the [Eu(**L13**)(TTA)] complex. The measurements are currently in progress.

III.3.6. Preliminary grafting experiments on silicon surfaces

Having seen that the ligand **L13** is capable of forming neutral heteroleptic lanthanide complexes of the formula [Eu(**L13**)(TTA)], stable in solid state and methanol solutions, we have decided to test the complexation reaction on a silicon surface of the type Si(100).

The process involved several steps, as shown in Figure III.20: preparation of the silicon surface, grafting of the ligand, and finally the lanthanide complexation reaction.

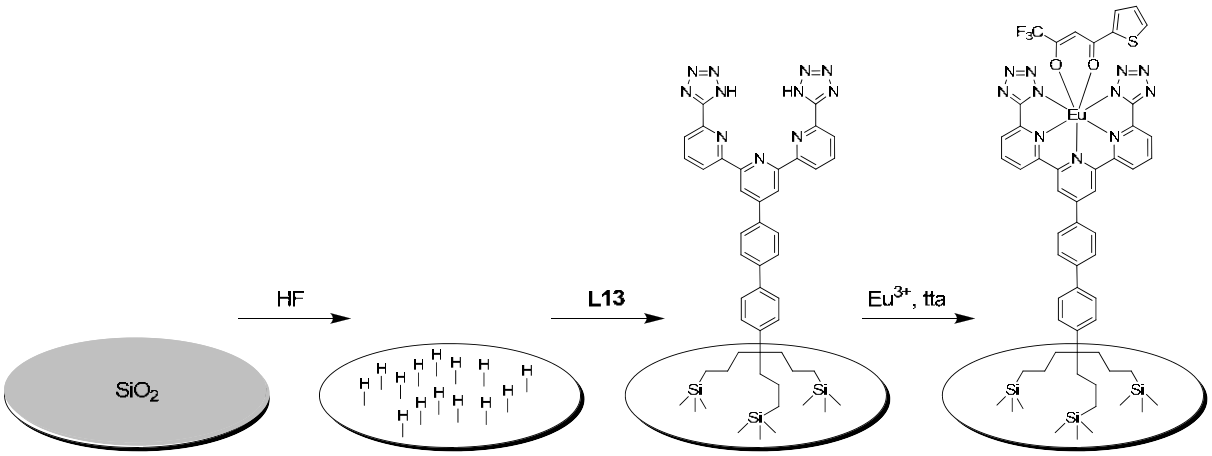

Figure III.20. Schematic representation of the grafting process

Preparation of hydrogenated silicon surface is the key step for obtain a high quality, densely packed monolayer. To remove the possible organic residues on the surface, the silicon substrate was washed in a "piranha" solution (concentrated H_2SO_4 / H_2O_2 (2:1)). After rinsing with copious amounts of water, the silicon substrate was dried with argon and then deoxidized by immersion in 1% hydrofluoric acid solution. The hydrogenated silicon surface was washed three times in water and used immediately in the next step. Previous experiments performed in the laboratory demonstrated that this technique gives highly activated surfaces from which the silicon oxide layer has been completely removed.

The grafting of the ligand **L13** on the activated silicon surface was performed by the thermal hydrosylilation reaction, refluxing for 2 hours a diluted mesitylene solution of the ligand together with the silicon wafer. The reaction conditions have been previously optimized in the laboratory on different other molecules, and resulted in the formation of homogeneous, densely packed monolayers. Two samples have been grafted, one acting as a reference and the other for performing the lanthanide complexation. The grafted substrates were thoroughly washed and dried with argon.

The lanthanide complexation step was performed by immersing the grafted silicon wafer in a dilute equimolar solution of europium triflate and 2-thenoyltrifluoroacetone in the presence of an excess of triethylamine, at 323K. After 2 hours, the substrate was thoroughly washed with methanol and dried with argon.

Preliminary characterization of the grafted surfaces has been performed by IR spectroscopy in internal multi-reflection mode, and shows the characteristic stretching vibration absorption peak of C=O in the TTA molecule shifted from 1 662 and 1 645 cm^{-1} to 1 608 cm^{-1}, indicating that the oxygen atoms in the β-diketonate coordinate to the europium atom.[180] Further analysis of the substrates by the XPS technique is in progress.

However, the luminescence measurements performed on the grafted surfaces using a spectrofluorimeter failed to show the characteristic emission of europium. While this can be caused by the reduced luminescence of the [Eu(**L13**)(TTA)] monolayer, quenching of the europium luminescence due to proximity to the silicon surface may also be involved.

III.4. Conclusions

In this chapter, we have shown that the terpyridine chromophore can be included in stable, neutral lanthanide complexes containing additional β-diketonate units. Compared to the majority of lanthanide complexes used in optoelectronics, which are based on tris-β-diketonate chelates containing a second neutral bidentate chromophore, the use of a strongly-coordinating anionic terpyridine chromophore would lead to better stability and efficiency. Accordingly, we have synthesized and characterized by X-ray diffraction, ^{1}H

NMR and luminescence measurements two different neutral heteroleptic lanthanide architectures. The first one is based on a monoanionic asymmetric terpyridine-carboxylate chromophore, completed by two β-diketonate units, and the second one is based on a dianionic terpyridine-bistetrazole chromophore, completed by one β-diketonate unit.

A very good emission efficiency (41%) was obtained for the terpyridine-carboxylate europium complex [Eu(**L12**)(TTA)$_2$]. Furthermore, the film-forming properties of the complex embedded in a PVK matrix were excellent, prompting us to test the materials as emitting layers in organic light emitting diodes. Preliminary studies on the europium and terbium complexes were performed on OLEDs having the configuration ITO / PEDOT PH500 / PVK:[Ln(**L12**)(ket)$_2$] / Cs_2CO_3 / Al. The devices exhibited typical diode behavior, the characteristic bright red or green luminescence being observed in both cases. Further improvements in device architecture may be required to afford better electroluminescence efficiencies, however the results indicate that this new class of neutral lanthanide complexes has potential for applications in OLEDs.

Benefiting from the facile functionalization of the terpyridine-tetrazole chromophore, we have appended to this ligand a tripodal anchor capable of forming Si-C bonds on the silicon surface, for studying the surface functionalization with lanthanide complexes. Preliminary results suggest the formation of heteroleptic lanthanide complexes with ligands grafted on the surface, although further studies need to be performed to analyze the functionalized substrates.

Chapter IV
Heterometallic iridium-lanthanide complexes

IV.1. Coordination and photophysical properties of iridium complexes

IV.1.1. Introduction

Iridium was usually regarded, more than ten tears ago, as a very useful metal center for reactivity and model studies related to homogeneous catalysis,[181] and the optical properties of very few Ir(III) complexes were know. Back then, ruthenium, osmium and rhenium-based polyimine complexes, for instance, were comparatively much more popular especially in the field of interconversion between light and chemical energy.[182] The iridium complexes proved to be more difficult to synthesize, and they were generally characterized after the similar complexes of ruthenium, for example, were already known (such as the case of iridium tris-bipyridine).[181] Furthermore, the diimine complexes of Ir(III) have high-energy emitting states, and were less interesting for photochemical applications. However, the use of cyclometalating ligands for the coordination of iridium results in very interesting photophysical properties[183] (*vide infra*) which are distinct from those of the N-coordinated bipyridine or phenantroline analogues. Recently, the cyclometalated iridium complexes have emerged also as great materials for emissive optoelectronic devices, and especially OLEDs,[89, 184] due to their high phosphorescence efficiencies and remarkable color tuning.

IV.1.2. Synthesis of cyclometalated iridium complexes

As a third-row transition metal, iridium(III) is characterized by the great inertness of its coordination sphere, requiring harsh reaction conditions to substitute the classical chlorine

ligands of the starting iridium salts. It is noteworthy that iridium(III) is capable of forming a large range of complexes, including mono-, bis- and tris-cyclometalated complexes, the last being a unique feature among all polyimine complexes of transition metals.[181] The tris-cyclometalated complexes exhibit the most interesting photophysical characteristics and consequently have been the most studied. However, obtaining homoleptic tris-chelate [Ir(C^N)$_3$] complexes is not straightforward, and often mixtures of facial and meridional isomers are obtained.[185] Furthermore, some cyclometalating ligands do not form iridium tris-chelate complexes by the reported synthetic methods,[186] probably due to steric hindrance. Replacement of the third cyclometalating ligand by a bidentate anionic species (denoted as ancillary ligand L^X) leads to bis-cyclometalated heteroleptic complexes which generally exhibit similar properties to those of the tris-cyclometalated homoleptic complexes,[186] and have the advantage of being easier to synthesize.

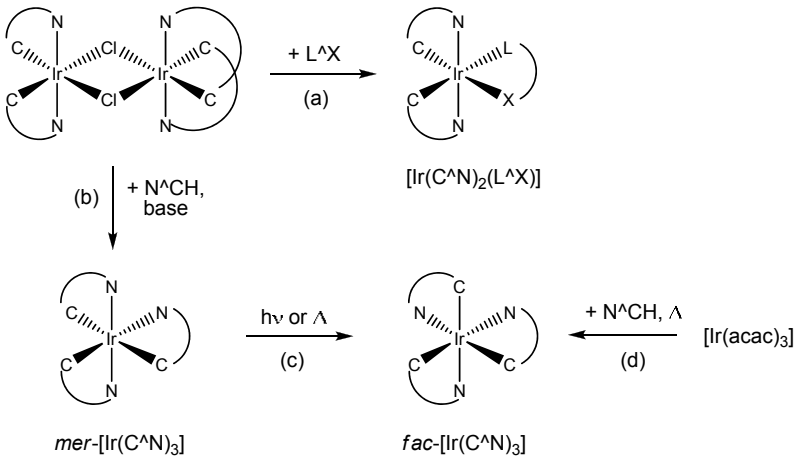

Scheme IV.1. Synthetic methods for the preparation of cyclometalated iridium complexes. The cyclometalating ligands (usually abbreviated as C^N) are illustrated by arcs, terminated with C and N atoms. The "C" atom represents an anionic moiety (phenyl), and the "N" atom a neutral group (pyridyl).

Schematically, the various synthetic strategies[187] used to prepare the bis- and tris-cyclometalated iridium complexes are summarized in Scheme IV.1. A μ-dichloro bridged dimer complex with *bis*-cyclometalated Ir centers can be readily obtained in good yield[186, 188] from a reaction of the ligand precursor with $IrCl_3 \cdot xH_2O$. Typical cyclometalating ligands such as phenylpyridines are shown in Figure IV.1.

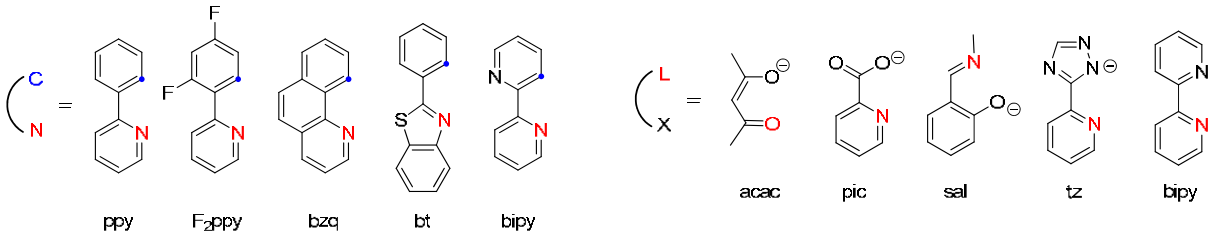

Figure IV.1. Typical examples of cyclometalating (C^N) and ancillary (L^X) ligands

The chloro ligands can be subsequently replaced with a different L^X ancillary ligands (path a) which leads to a heteroleptic complex with a *trans*-N,N configuration of the C^N ligands. L^X ligands are chelating units such as β-diketonates, picolinates, salicylanilides (Figure IV.1). Alternatively, a third C^N ligand can be added to form a homoleptic tris-cyclometalated complex (path b). Through a careful control of the reaction conditions (and especially the use of low temperature) is possible to obtain nearly pure meridional isomers of tris-cyclometalates of Ir(III), including both homoleptic[185, 189] and heteroleptic[190-192] tris-chelates. A significant kinetic barrier in these reactions is the breakage of the final Ir-Cl bond.[193] Several of the isolated samples of *mer*-[Ir(C^N)$_3$] complexes can be converted to facial forms in solution either by thermal or photochemical means[194] (path c), indicating that the meridional isomers are the kinetically-favored products. The lower thermodynamic stabilities of the meridional isomers are likely related to the structural features of these complexes, containing strongly trans influencing aryl groups opposite to each other, whereas in the facial isomers all three aryl groups are opposite pyridyl or other neutral donor groups. For some C^N ligands, typically ppy and its derivatives, the facial isomer can also be directly prepared by a thermal reaction between the ligand precursor and [Ir(acac)$_3$] (acac = acetylacetonate) (path d),[191] but the yields are rather poor in this case.

IV.1.3. Stereochemistry of cyclometalated iridium complexes

The homoleptic cyclometalated iridium complexes [Ir(C^N)$_3$] have two stereochemical forms: meridional (*mer*) and facial (*fac*), as shown in Scheme IV.2. The *mer* isomers

possess three nitrogens around the equator of the molecule with two nitrogens trans to each other and the third nitrogen trans to an aromatic carbon. In the *fac*-isomer all nitrogen atoms are trans to a carbon atom. In the case of heteroleptic complexes $[Ir(C^N)_2(L^X)]$, similar stereoisomers can be defined, plus in addition various *cis* and *trans* isomers for the meridional complexes,[195] as depicted in Scheme IV.2. Nevertheless, it is well-established[196] that the cyclometalating carbons of the $[Ir(C^N)_2(L^X)]$ complexes occupy mutually *cis* positions, which are in turn *trans* to the atoms of the (L^X) ancillary ligand, configuration *N,N-trans-mer*.

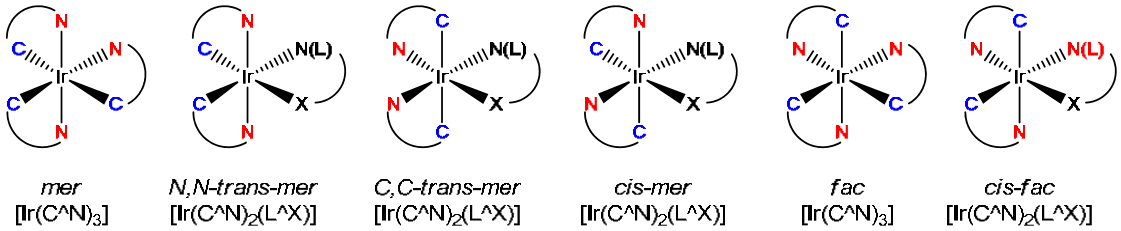

Scheme IV.2. Facial and meridional isomerism in homoleptic $[Ir(C^N)_3]$ and heteroleptic $[Ir(C^N)_2(L^X)]$ cyclometalated iridium complexes

Because of the different *trans* influence of phenyl and pyridyl ligands, the meridional and facial isomers exhibit slightly different structural properties: in a *fac* isomer the Ir-C and Ir-N bonds have nearly identical length, while for the corresponding *mer* isomer, the bonds *trans* to the Ir-C bond are slightly longer than those *trans* to the Ir-N bonds.[185, 190] A practical consequence is that facial and meridional isomers may show different photophysical and spectroscopic properties.[197] Generally the *fac* isomer has an order of magnitude longer emission lifetime (τ) than the *mer*. Similarly, the quantum yield of emission (Φ) in the *fac* tends to be an order of magnitude greater than that of the *mer* isomer.

IV.1.4. Electronic transitions in octahedral complexes

The Ir(III) cation is a $5d^6$ center and the electronic properties of its complexes share several features with those of other well-studied octahedral (O_h) complexes of Fe(II),

Ru(II) or Os(II) ($3d^6$, $4d^6$ and $5d^6$ configurations, respectively). The degenerate *d* orbitals of these cations are destabilized and split in an octahedral field by an amount Δ, as shown in Figure IV.2. Because of the different spatial extension for 3d (Fe), 4d (Ru) and 5d (Os and Ir) orbitals, this effect is smallest for the 3d orbitals and increases with the quantum number. The amount of the splitting also depends on the field strength exerted by the ligands, which can be ordered along a "spectrochemical series."[198] In this series, a cyclometalating ligand such as phenylpyridine (ppy) occupies a position among those causing the strongest effect.

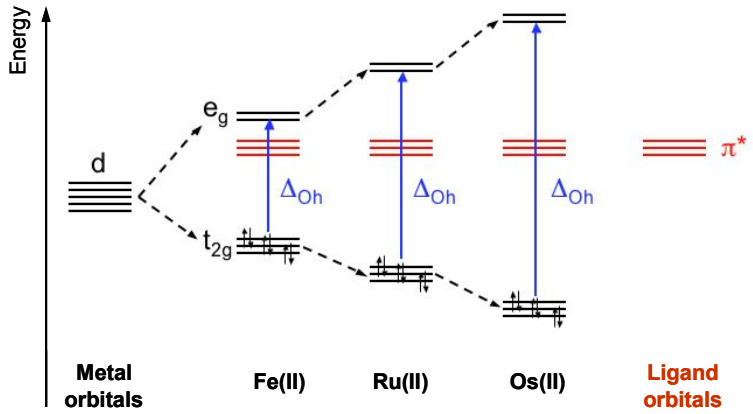

Figure IV.2. Diagram of *d* orbital splitting in an octahedral field

In such *d* metal complexes, light absorption is associated with electronic transitions from the ground state to, mostly, singlet levels of various nature and electronic localization: ligand-centered (^{1}LC), metal-centered (^{1}MC), and metal-to-ligand charge transfer (^{1}MLCT). In principle, ligand-to-metal transitions (^{1}LMCT) can also be involved. On the contrary, emission is always from triplet levels, ^{3}MLCT or ^{3}LC in nature, as a consequence of the high spin-orbit coupling constants of the metal centers.[90]

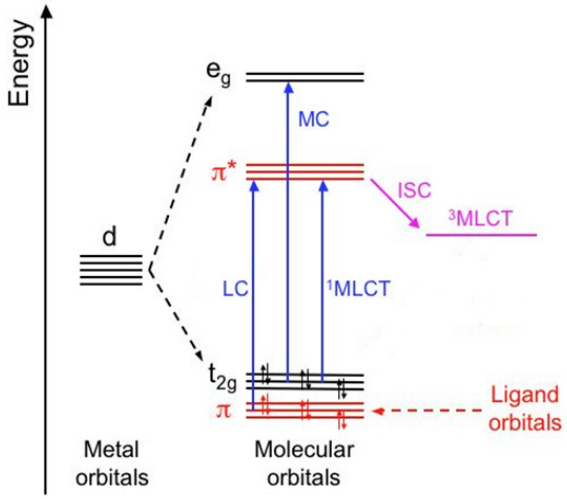

Figure IV.3. Orbital description of MC, MLCT and LC(π-π*) transitions in an octahedral complex

The metal-centered MC states are low-energy excitation states arising from electron hopping between the nonbonding and antibonding d orbitals. These d-d transitions are Laporte-forbidden, although certain vibrations may relax this restriction. Due to the small splitting of the d metal orbitals for the first-row transition metals, the lowest excited state is most likely MC in nature, and thus not emissive (Figure IV.4). Due to its low energy, population of the MC state may be thermally accessible. For the second- and/or third-row transition-metal complexes with strong-field ligands in the spectrochemical series (such as the cyclometalating ligands), the anticipated MC transitions are destabilized to the higher-energy region, such that the population to these states becomes less accessible. Accordingly, the interference of the MC states in quenching of the lowest-energy electronic transition is significantly diminished. Finally, spin-selection rules are not strictly obeyed for these second- and third-row transition-metal complexes, for which the singlet-to-triplet intersystem crossing (ISC) is facilitated by the heavy-atom enhanced spin–orbit coupling. As a consequence, many of them have exhibited highly efficient, room-temperature phosphorescence in both fluid and solid states.

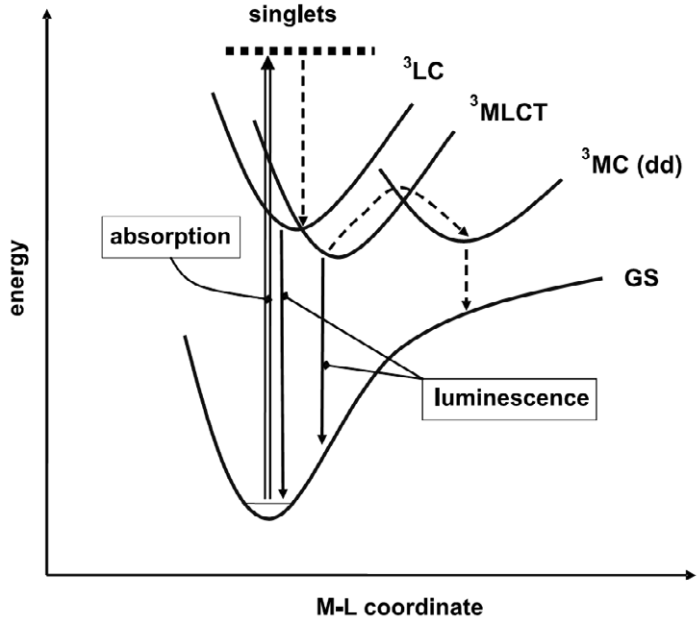

Figure IV.4. Electronic transitions involving MC, MLCT, and LC excited states (from ref.[182])

Metal-to-ligand charge-transfer (MLCT) states involve electronic transitions from a metal-based d orbital to a ligand-based delocalized π* antibonding orbital (Figure IV.4). In a classical sense, the corresponding excitation results in metal oxidation and concomitant ligand reduction. These transitions are commonly observed in the 2nd and 3rd row transition-metal complexes possessing relatively low oxidation potentials. Since the π* ligand orbital is usually delocalized over the acceptor ligand, the population to MLCT states usually causes only minimum structural distortion, facilitating its radiative recombination, which proceeds with remarkable efficiency. The MLCT states of the 1st row transition-metal complexes are quite reactive, but they become stable and highly luminescent upon shifting the metal to its 2nd and 3rd row counterparts. This results from a systematical increase in metal-ligand bonding strengths, accompanied by destabilizing the aforementioned MC excited states, and consequently the reduction of the radiationless deactivation. Moreover, MLCT transitions are strongly allowed processes, manifested by intense absorption bands in the visible or near UV spectral regions, characteristic for symmetry-allowed electronic transitions.

Ligand-centered (LC) ππ* excited states originate from electronic transitions between π orbitals that are mainly localized on the ligand chromophore (Figure IV.4). As

such, if the metal perturbation upon coordination is minimized, the luminescent complex may exhibit a transition that has spectral properties closely resembling the free ligand states, and the LC character of the complex emission can be evaluated by comparing it to the free ligand emission.

IV.1.5. Emissive excited states in cyclometalated iridium complexes

As mentioned above, in the cyclometalated complexes, the strong ligand effect of the ligands raises the energy of the MC excited states to very high levels, and in the same time favors the low-energy MLCT states via enhancement of formal oxidation at the metal center. This combination of effects leads to cyclometalated complexes which, relative to their N-coordinated analogues (bipy, phen), have superior visible light absorption properties and low-energy excited states well-suited for their use in optoelectronic applications.

It is generally established[199] that luminescence from the cyclometalated iridium complexes originates from a lowest excited state that is best described as a ligand centered triplet (^{3}LC) with triplet metal-to-ligand charge transfer (^{3}MLCT) character mixed in through the spin-orbit coupling. An assessment of the MLCT or LC nature of the phosphorescence is afforded by the photophysical properties, based on the following equation:

$$\Phi = \frac{k_r}{k_r + k_{nr}} \qquad \text{(IV.1)}$$

where k_r and k_{nr} are the radiative and non-radiative rate constants, respectively, for deactivation of the emitting level, with $\tau = (k_r + k_{nr})^{-1}$. In the absence of non-radiative contributions, as happens at low temperature (77K or lower), only the radiative lifetime can be considered, $\tau_r = 1/k_r$. In the case of iridium complexes with bidentate cyclometalating ligands like [Ir(ppy)$_3$], a typical MLCT emission would have a radiative constant $k_r \sim 2 \cdot 10^5$ s^{-1}, while a typical LC emission would have a much smaller $k_r \sim 0.2 \cdot 10^5$ s^{-1}, corresponding to a longer radiative lifetime.[182] The profile of the luminescence

spectrum, which is structured for LC emissions and broad, less-featured for MLCT ones, provides additional indications, as well does the rigidochromic effect, based on the fact that charge transfer levels undergo blue-shifting on passing from fluid to frozen polar solvent, while the ligand centered levels are either unaffected or slightly red-shifted under the same conditions.[182] Further information can be derived from the Stokes shifts observed between the absorption and emission bands.[200] Thus, emission from a predominantly ^{3}MLCT state would be expected to have a small Stokes shift between the ^{3}MLCT absorption and emission bands, whereas emission from a predominantly ligand-based excited state would give a large Stokes shift between the ^{3}MLCT absorption and emission bands.

Iridium complexes, like some other transition metal complexes,[201] are very interesting due to the possibility of tuning their emission energy (and their electrochemical behavior) by playing with the ligand levels. In the case of heteroleptic complexes based on 2-phenylpyridine (ppy), the highest occupied molecular orbital (HOMO) comprises mainly the iridium *d* orbitals and the phenyl π orbitals on the ppy ligand, whereas the lowest occupied molecular orbital (LUMO) is mainly located on the π* orbitals of the pyridyl rings, with little metal character.[202] Similar molecular orbital descriptions are found for other Ir organometallic complexes with related cyclometalating ligands. The HOMO principally comprises orbitals on the metal-aryl linkage, whereas the LUMO is ligand-localized.[203] The photophysical properties of [Ir(C^N)$_2$(L^X)] and [Ir(C^N)$_3$] complexes are determined primarily by the C^N ligand, while the ancillary ligand L^X (when present) has only a secondary role, with few exceptions.[203-207] The ancillary ligand is expected only to affect the ground state energies by direct interaction with the metal center, as long as it has a higher triplet energy than the cyclometalating fragment.

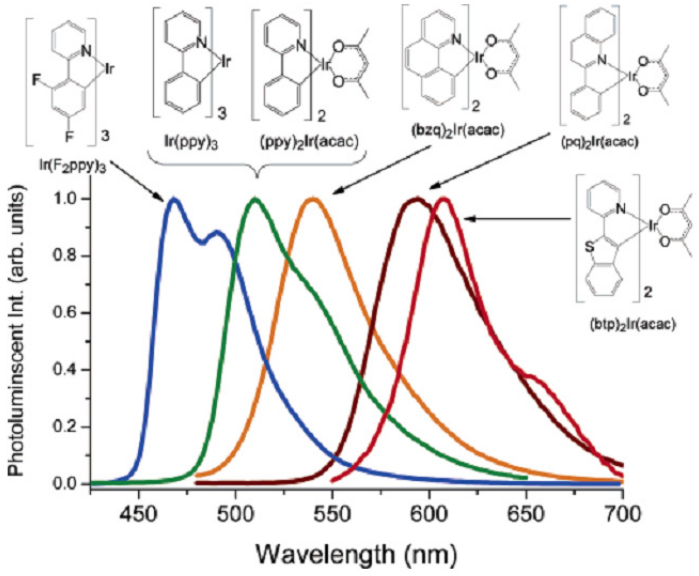

Figure IV.5. Tuning the emission color of iridium complexes (from ref.[202])

Therefore, changes in the HOMO-LUMO energy gap, based on the appropriate design of the chemical structure of the cyclometalating and/or ancillary ligands, or on the systematic control of the nature and position of substituents in these ligands, result in a fine-tuning of the emission energy of iridium complexes[182, 201] (for an example see Figure IV.5).

IV.2. Heterometallic iridium-lanthanide complexes

IV.2.1. Literature examples

While there are numerous studies on d-f heterometallic complexes containing transition metals such as Ru, Pt, Re, Os, Pd, and Cr acting as antennae for the sensitization of the lanthanide ion (see Chapter I.2.6. for literature examples), just a handful of reports concerning iridium-sensitized lanthanide luminescence have been published, and only two groups have been active in this field. This is surprising considering the popularity of iridium complexes in the field of organic light emitting diodes,[184] and the extended possibilities of modulating the lowest exciting states of these complexes by modifying the cyclometalating or ancillary ligands[201] (*vide supra*).

The sensitization of the high-energy emissive states of europium (the $^5D_1$ and $^5D_0$ states are found at 19000 and 17250 cm^{-1}, respectively) is particularly difficult, as the MLCT levels of most d-metal complexes are too low for an efficient d→f energy transfer. In fact, f→d energy transfer was sometimes observed, leading to a complete quenching of the europium emission.[12] The group of De Cola succeeded in tuning the emission of iridium complexes in the "almost blue" region of the visible spectrum (21 740 cm^{-1}) by employing fluorinated phenylpyridine cyclometalating ligands[81] and consequently published in 2005 the first example of an iridium-europium heterotrimetallic complex[57] in which the emission of europium was sensitized by the ^{3}MLCT-^{3}LC mixed state of the iridium complex (Scheme IV.3). The europium ion is five coordinated by a terpyridine-dicarboxylate ligand,[56] and the remaining sites are occupied by two benzolates each linked to a pyridine-1,2,4-triazole. This latter unit plays the role of the ancillary ligand for the iridium ion, further coordinated by two fluorinated phenylpyridine cyclometalating ligands. Inducing a significant separation between the two metals, by the use of the phenyl spacer, led to only a partial d→f energy transfer (estimated at 38%) and the simultaneous emission from both the europium levels (red color) and the iridium ^{3}MLCT-^{3}LC mixed state (blue color), the combination of which resulted in an apparent white-light emission. The quantum yield of the overall emission is however rather weak (7% in deuterated methanol).

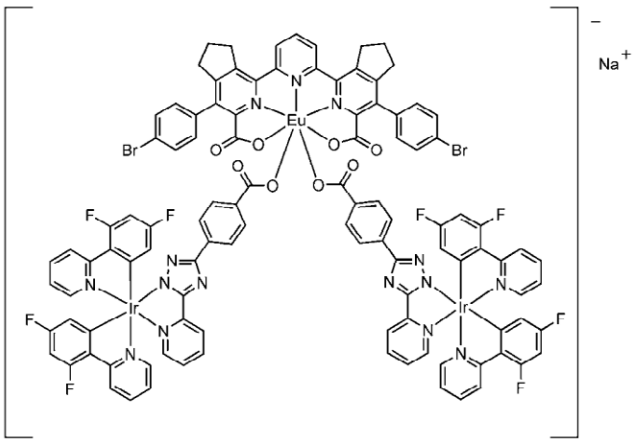

Scheme IV.3. Example of heterometallic iridium-europium complex (from ref.[57])

A second example[208] of an Ir-Eu heterometallic assembly came during our work from Chen *et al.* in 2008. Here, a dual-site phenantroline-diketonate-based ligand allows the successive coordination of iridium and europium (Scheme IV.4). The same fluorinated phenylpyridine cyclometalating ligand as in the complex of De Cola has been used to drive the emission of iridium in the blue region, however the low-lying ^{3}LC state of the phenantroline ligand quenches the room temperature emission of the iridium complex. Nonetheless, energy transfer from Ir to Eu in the final heterometallic complex was evidenced, presumably from the iridium→F_2ppy ^{3}MLCT state, resulting in red luminescence (18% quantum yield in water). Using a similar design, the same group extended this work[209] to near-infrared emitting lanthanide ions (Nd, Er and Yb).

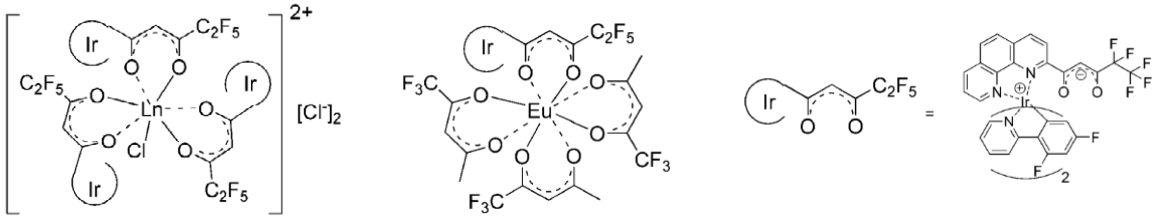

Scheme IV.4. Examples of heterometallic iridium-europium complexes (Ln=Eu, Gd; from ref.[208])

Also in 2008, another example of ytterbium sensitized luminescence through energy transfer from an iridium complex was reported by De Cola *et al.*[210] (Scheme IV.5). The iridium metal is coordinated by two non-substituted cyclometalating phenylpyridine ligands and a pyridine-1,2,4-triazole ancillary unit,[81, 211] connected by two phenyl bridges to a bipyridine-carboxylate ligand for the complexation of the lanthanide ion.[43] In the final neutral heterotetrametallic complex, three iridium complexes surround and sensitize the ytterbium emission, however a non-radiative deactivation pathway (accounting for cca. 35% of energy transfer) is believed to be present, due to the large energy gap between the donor and acceptor levels. The quantum yield (0.7%) measured by excitation through the ligand levels (300 nm) is relatively good for ytterbium organic complexes.

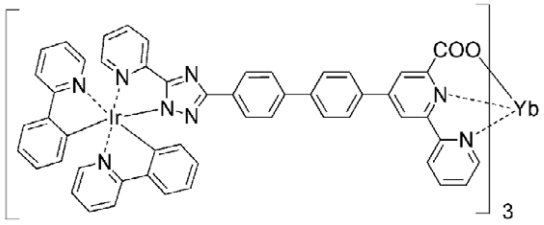

Scheme IV.5. Example of heterometallic iridium-ytterbium complex (from ref.[210])

In spite of these considerable advances in the field of iridium-sensitized lanthanide luminescence in heterometallic complexes, there is still a strong interest for synthesizing new types of architectures and studying the fundamentals of the Ir→Ln energy transfer for a better understanding of the factors influencing the efficiency of lanthanide emission.

IV.2.2. Design of iridium-lanthanide heterometallic complexes

We have decided to study the sensitization of lanthanide ions emitting in the visible and near-infrared regions (europium and neodymium) by means of a phosphorescent iridium complex, incorporated in a heterometallic assembly. For affording a good stability of the final d-f complex, the two metallic centers should be linked by a fully-covalent organic framework. Benefiting from our previous studies on the coordination of lanthanide ions by terpyridine-tetrazole-based ligands (see Chapter II.2.), we have decided to use this unit for the complexation of the f metal. The iridium complex should emit a sufficiently high energy as to be able to sensitize effectively the emitting levels of the europium ion, and as such it should include a cyclometalating ligand with a low-lying HOMO level, e.g. 2,4-difluorophenylpyridine (F_2ppy).[81] In according to these criteria, the proposed structure of the heterometallic complex is represented in Figure IV.6 (bottom).

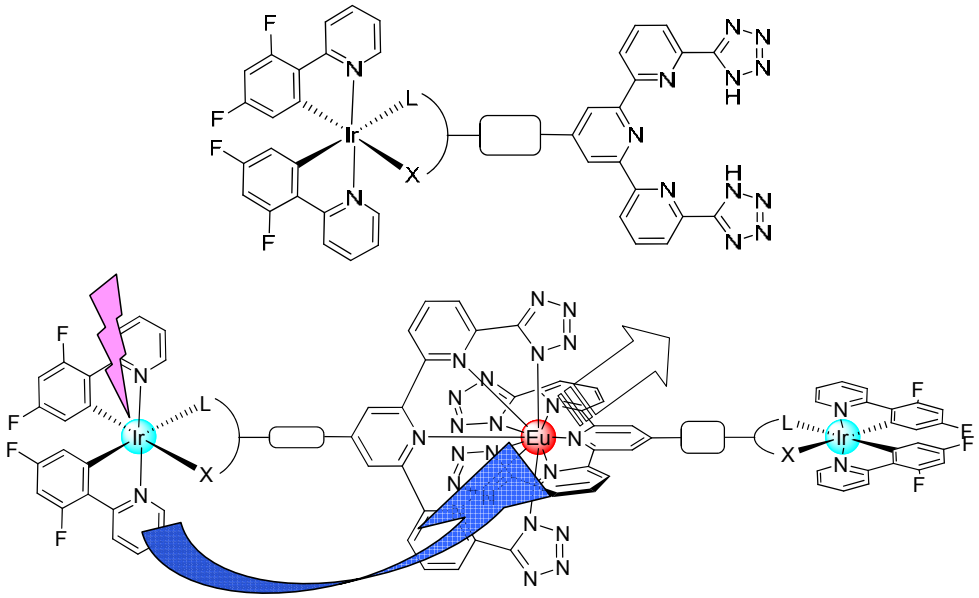

Figure IV.6. Proposed structure for an iridium complex as ligand for lanthanides (top) and the expected heterotrimetallic complex with europium (bottom). The arrows indicate the probable direction of energy transfer.

In principle, the synthesis of such heterometallic complexes could be done in two ways, by reacting either a pre-synthesized lanthanide complex of terpyridine-tetrazole with the diiridium precursor (path I in Scheme IV.6) or by reacting a pre-synthesized iridium complex containing the terpyridine-tetrazolate with a lanthanide salt (path II). However, it was observed that in the reaction conditions used (ethoxyethanol, room temperature), the diiridium precursor displaces the europium ion from its bis-terpyridine-tetrazole complex, as expected from the labile electrostatic bonding of lanthanide ions. Accordingly, the only practical synthetic strategy is the second pathway, where the iridium "complex-as-ligand" is synthesized before the lanthanide complexation step. Due to the relative inertness of the iridium compounds in the conditions normally used for lanthanide complexation (due to the strong covalent bonding in the iridium coordination sphere), displacement of iridium by the lanthanide ion is not a practical possibility, and the selective coordination of the f metal to the terpyridine-tetrazolate site is expected to take place unimpeded.

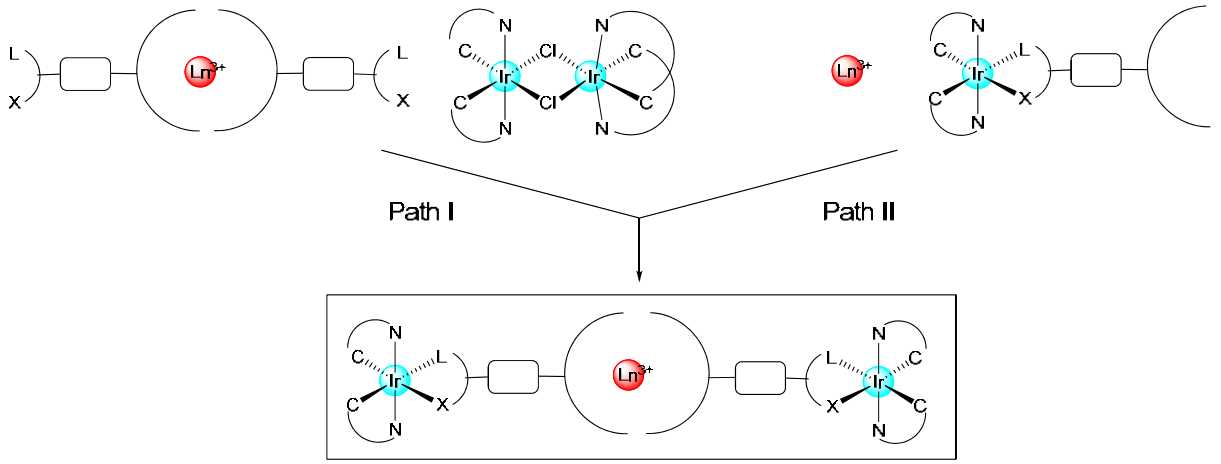

Scheme IV.6. Synthetic pathways for the formation of heterometallic iridium-lanthanide complexes. The large arcs of circle symbolize the terpyridine-tetrazolate unit.

In conclusion, we set out to synthesize a terpyridine-tetrazole ligand, covalently bonded to an iridium complex able to emit high-energy radiation (Figure IV.6 top). Following, the coordination of two of these ligands to the lanthanide ion would allow us to isolate the heterotrimetallic complex.

IV.2.3. Synthesis of ligands and iridium complexes

a) First synthetic strategy

The key step in the synthesis of our iridium "complex-as-ligand" for lanthanides is the formation of a precursor containing terpyridine-dicarbonitrile, covalently linked to the iridium complex part. From this, conversion to the tetrazole derivative by one of the methods presented in Chapter II.1. b) can be envisaged. Due to the difficult chemistry of the tetrazole compounds (low solubility, difficulty in column chromatography purification), the tetrazole formation should be the last organic synthetic step before the final complexation of the lanthanide ions. The retrosynthetic strategy is given in Scheme IV.7.

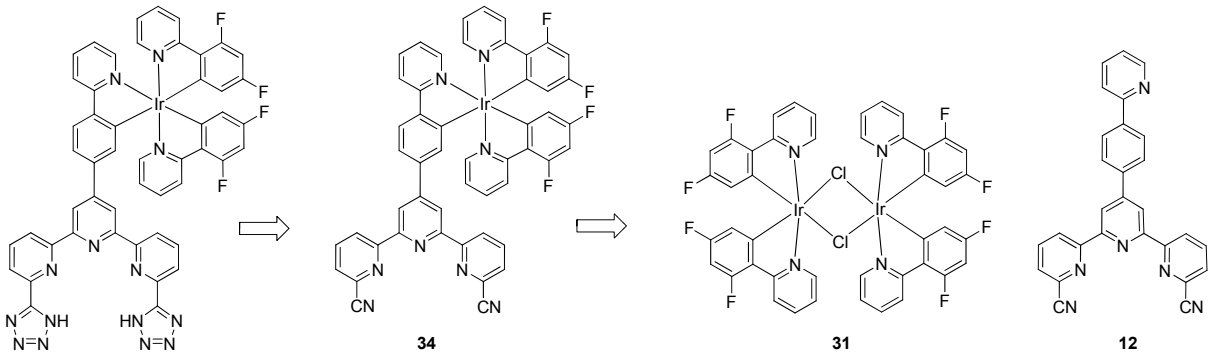

Scheme IV.7. Retrosynthetic scheme for the first strategy

Our initial strategy aimed at the synthesis of the heteroleptic complex **34**, starting from the previously-described 4'-(4-(pyridin-2-yl)phenyl)terpyridine-6,6"-dicarbonitrile **12**, which contained the ppy cyclometalating moiety. Previous reports have mentioned[212] that the ease of coordination of bidentate ligands to the iridium center increases in the order N,N-bipyridine < C,N-bipyridine < C,N-phenyl-pyridine. This result appears to indicate a reduced activity of the pyridine ring in bipy towards metalation in comparison to the phenyl ring in ppy, due to the presence of an electro-withdrawing N atom in the pyridine ring, which disfavors the electrophilic attack of the metal on the aromatic ring. Therefore, in spite of the presence in **12** of two cyclometalating sites for the coordination of iridium (the appended phenyl-pyridine group, and the C,N-bipyridine site as part of the terpyridine moiety), we had reasons to believe that the major reaction product would be the expected phenyl-pyridine complex **34**.

As iridium source was used the cyclometalated Ir(III) μ-chloro-bridged dimer **31**, prepared by adapting the method reported by Nonoyama[81, 188] which involved heating $IrCl_3 \cdot H_2O$ with a small excess of cyclometalating ligand **30** in a mixture of 2-ethoxyethanol and water (see Scheme IV.8). The fluorinated phenyl-pyridine **30** (F_2ppy) was obtained by the Suzuki coupling[213] of bromo-pyridine **10** and difluorophenylboronic acid **29**.[81, 214]

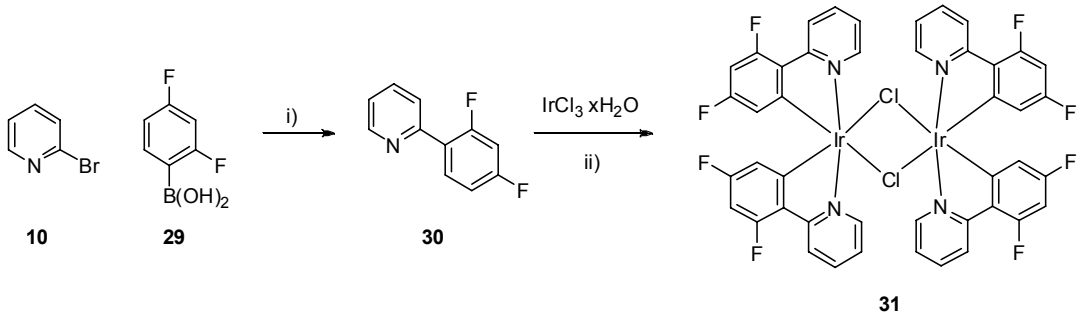

Scheme IV.8. Conditions: i) $Pd(PPh_3)_4$ (cat), K_2CO_3, THF-EtOH-H_2O, 80°C (89%); ii) ethoxyethanol-H_2O, 120°C (81%)

The reaction of the Ir(III) μ-chloro-bridged dimer **31** with the terpyridine-dicarbonitrile **12** was carried out in 2-ethoxyethanol at 100°C and in the presence of potassium carbonate, according to the classical literature method for tris-cyclometalated iridium complexes.[185, 197] However, the discrimination between the two bidentate coordination sites in **12** was not sufficiently good in the reaction conditions employed, and perhaps due to the rather high temperature used, an intricate mixture of products was obtained. From this, the desired complex **34** could not be separated even after column chromatography (alumina, dichloromethane : methanol gradient) and several recrystallization attempts from various solvent mixtures. ES-MS analysis shown no indication of the desired compound, and ^{1}H NMR spectra were too complicated to be assigned.

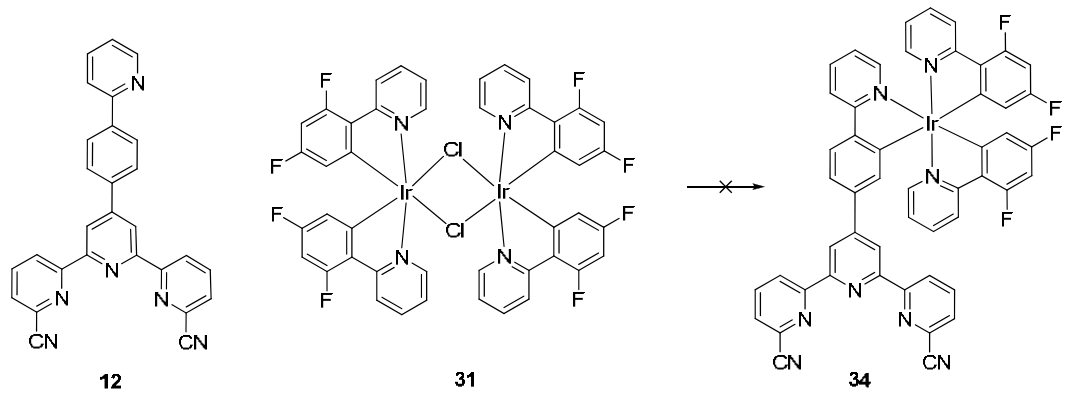

Scheme IV.9. Conditions: K_2CO_3, ethoxyethanol, 100°C

Fortunately, a rather low-quality crystal was obtained from one of the separated fractions, which was solved by X-ray diffraction to give the structure in Figure IV.7,

however with a large residue. In this surprising bimetallic heteroleptic complex, two iridium atoms are each hexa-coordinated by two F_2ppy cyclometalating ligands and the terminal pyridine-carboxylate part of the terpyridine ligand, and are situated at an intermetallic distance of 7.4 Å. Aside from its novelty, which we further explored in Chapter IV.3. , the structure indicated us that in the reaction conditions, due perhaps to traces of water and the basic environment provided by K_2CO_3, a part of the terpyridine-dicarbonitrile hydrolyzed to the corresponding carboxylic acid, which further reacted with the iridium μ-chloro-bridged dimer.

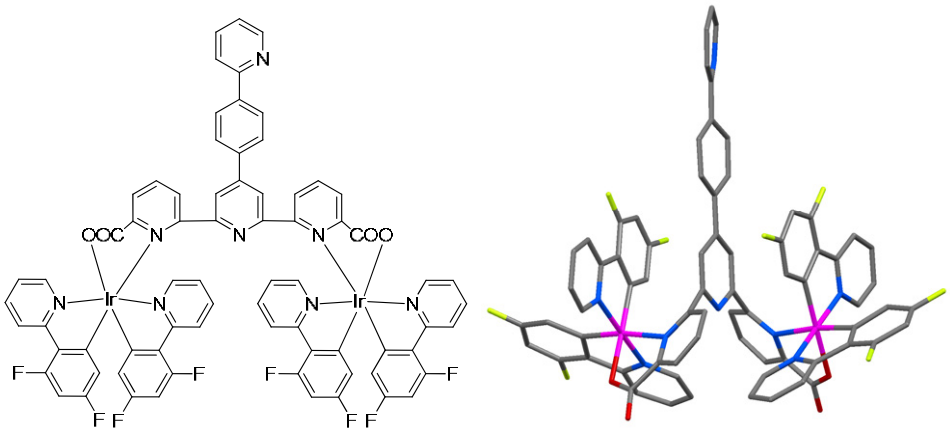

Figure IV.7. Terpyridine-dicarboxylate diiridium complex obtained as side-product

Whereas most of the chemistry of tris-cyclometalated iridium complexes involves harsh reaction conditions similar to the one we tried,[185, 197] alternative synthetic strategies, employing lower reaction temperatures and different solvent systems, have also been published. A procedure that utilized silver triflate as a reagent in 2-ethoxyethanol at 95 °C was reported to give low yields of the *fac* isomer of a heteroleptic complex.[215] Relatively high yields of *mer* isomers have also been reported by treatment of the iridium μ-chloro-bridged dimer with a silver salt and triethylamine as a base.[215, 216] In a recent contribution,[193] the iridium chloro-bridged dimers were cleaved in coordinating solvents like acetonitrile to give neutral $[Ir(C^N)_2(NCCH_3)Cl]$ species which in turn were reacted with $AgPF_6$ to give hexafluorophosphate salts of the bis-acetonitrile species $[Ir(C^N)_2(NCCH3)_2]PF_6$. The use of bis-acetonitrile complexes as the source of Ir(III) instead of the μ-chloro-bridged dimer

eliminates the activation of Ir-Cl bonds in the rate-limiting step, and allows a lower temperature to be used.

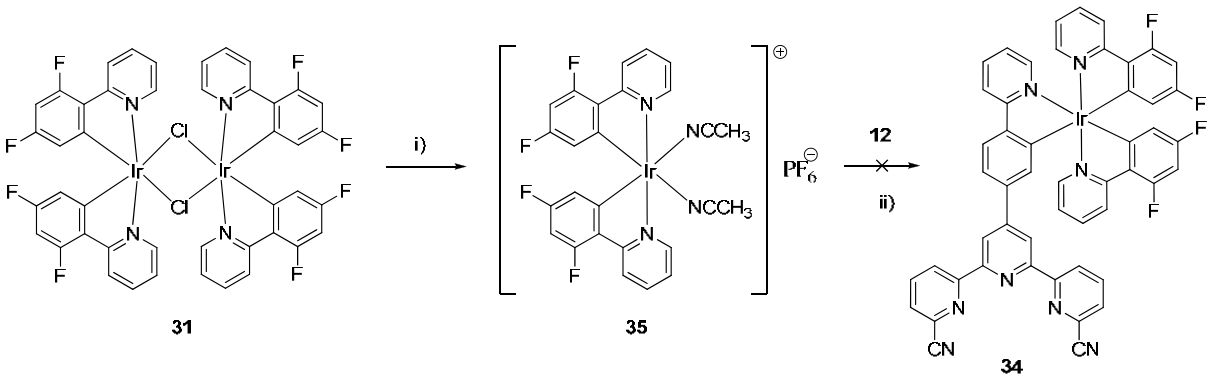

Scheme IV.10. Conditions: i) $AgPF_6$, CH_3CN, 80°C (60%); ii) chlorobenzene, 70°C.

Following the last synthetic procedure,[193] the iridium bis-acetonitrile complex **35** was prepared and reacted with the terpyridine-dicarbonitrile **12** in chlorobenzene at 70°C, according to Scheme IV.10, however a mixture of products was again obtained from which the desired complex could not be separated.

b) Second synthetic strategy

At this point, we have decided to change our synthetic strategy and to connect the bis-cyclometalated iridium moiety to a negatively charged ancillary ligand linked to the terpyridine unit, with the formation of a heteroleptic complex of the formula $[Ir(F_2ppy)_2(LX)]$. The retrosynthetic strategy is given in Scheme IV.11.

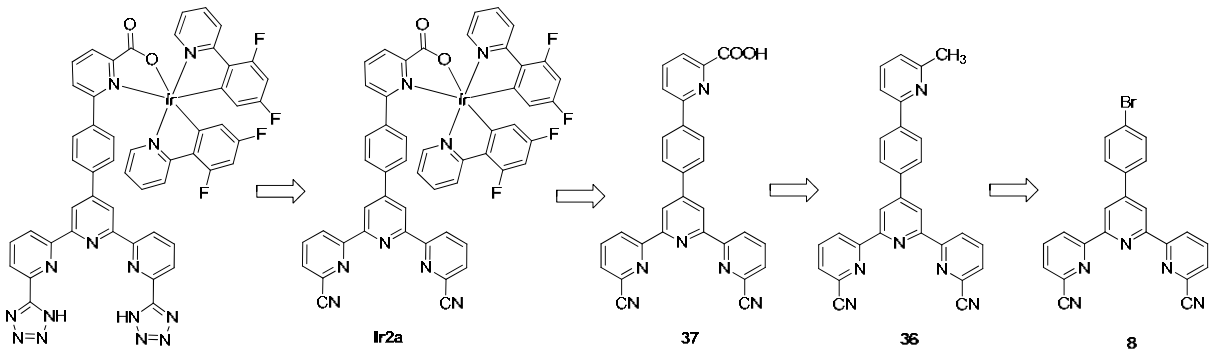

Scheme IV.11. Retrosynthetic scheme for the second strategy

Similar iridium complexes, containing bipyridine,[217] triazolyl-pyridine,[81] or picolinate[218] units as ancillary ligands, for example, have been previously obtained in mild conditions, avoiding scrambling of the ligands and the formation of undesired iridium(III) tris-phenylpyridine derivatives. According to this strategy, our new target compound was 6-(4-(6,6"-dicyano-terpyridin-4'-yl)phenyl)picolinic acid **37**.

As mentioned before in Chapter II.3.1. b), the direct Stille coupling of trimethyl-stannylpicolinates with brominated aryl compounds does not work, probably due to the instability of the stannylpicolinates. Consequently, we have decided to prepare first the 4'-(4-(6-methylpyridin-2-yl)phenyl)terpyridine-6,6"-dicarbonitrile precursor **36** by the Stille coupling of the previously synthesized methyl-trimethylstannylpyridine **20** with the bromo-phenyl-terpyridine-dicarbonitrile **8**, as shown in Scheme IV.12. Special reaction conditions have been chosen, employing DMF as solvent and cesium fluoride as well as catalytic amounts of cuprous iodide for improved reactivity,[219, 220] in order to facilitate the coupling of the deactivated terpyridine-dicarbonitrile substrate.[132] The product was obtained in 42% yield, which is still rather low, but however better than the one obtained in the synthesis of the analogous non-methylated terpyridine dicarbonitrile **12** (30%) described in Chapter II.2.1. c).

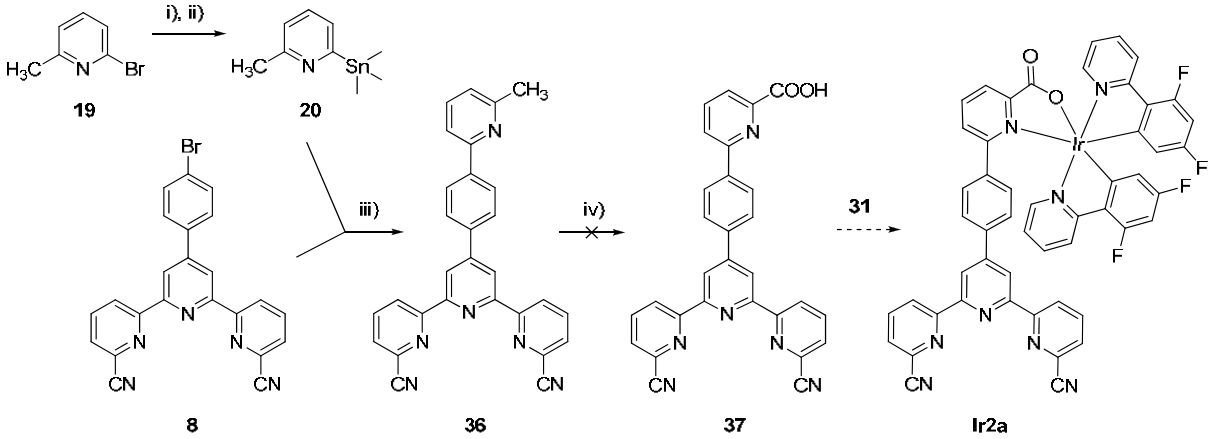

Scheme IV.12. Conditions: i) BuLi, THF, -75°C; ii) $SnClMe_3$, THF, -75°C to RT (92%); iii) $Pd(PPh_3)_4$ and CuI (cat), CsF, DMF, 70°C (42%); iv) SeO_2, pyridine, 120°C.

Conversion of the methyl group in **36** to the corresponding carboxylic acid has to be performed in the absence of basic or acidic conditions, which could catalyze the hydrolysis of the two carbonitrile groups. Among the existing oxidation procedures, we have found only two that match these requirements: the oxidation with selenium dioxide in pyridine,[24] and the oxidation with potassium permanganate in water.[221] Due to previous successful experiences with selenium dioxide reactions in our laboratory,[120] we have decided to follow this synthetic route. Accordingly, the methyl-derivative **36** was reacted with a large (9 equivalents) excess of selenium dioxide in pyridine at reflux for one week. Some starting product was still unreacted after this prolonged reaction time, however the reaction was stopped fearing side-oxidation products. After laborious treatment and column chromatography on silica with a gradient ethanol-DMF-acetic acid solvent mixture, we have isolated a mixture of products containing (as confirmed by mass analysis) the expected compound together with higher molecular weight species. These can be attributed to the conversion products of one or two of the carbonitrile groups into the corresponding carboxylates, as well as to other unidentified oxidation compounds. It appears that, in the slightly basic reaction conditions (pyridine), and due to the formation of water as a result of selenium dioxide reduction, the carbonitrile functions have been partially hydrolyzed. As further purification of the product mixture proved inefficient, we have decided to change again our synthetic strategy.

c) Third synthetic strategy

Due to the apparent difficulty in preparing a ligand having specific sites for the coordination of iridium (picolinate unit) and lanthanide ions (terpyridine-ditetrazolate), we have decided to synthesize first a heteroleptic cyclometallated iridium complex containing the picolinate ancillary ligand and having a suitable group for further linking to the phenyl-terpyridine system. The key idea is to complete the iridium coordination sphere before the entire ligand is assembled via coupling through covalent bonding. The retrosynthetic strategy is shown in Scheme IV.13.

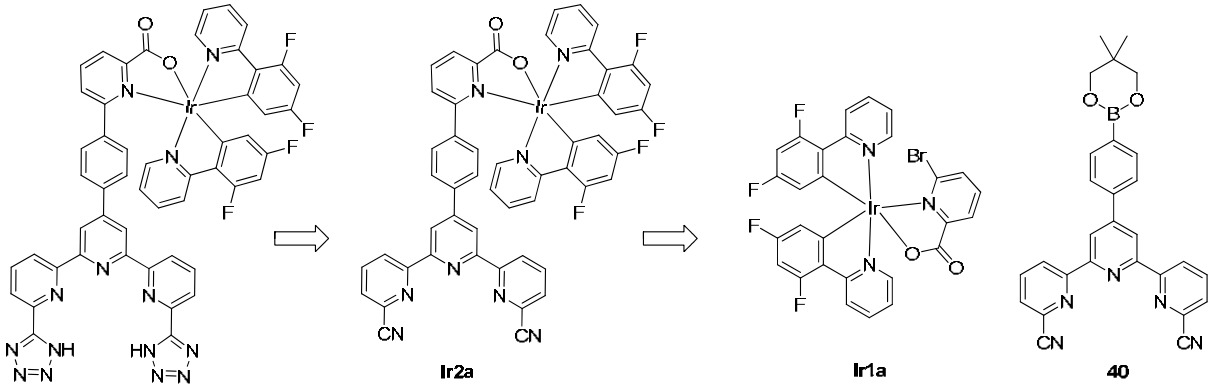

Scheme IV.13. Retrosynthetic scheme for the third strategy

Therefore, we have prepared the bromo-substituted iridium complex **Ir1a**, by the reaction of the μ-chloro-bridged dimer precursor **31** with the commercially-available 6-bromo-picolinic acid **38** in dichloromethane at reflux and in the presence of an excess of potassium carbonate (Scheme IV.14). Note that in this case, compared to the synthesis of FIrpic (Scheme IV.17, *vide infra*), the presence of base was necessary; in the absence of it the reaction does not proceed. Presumably, the base has the effect of abstracting the chloride ions released from the coordination sphere of iridium, with the formation of dichloromethane-insoluble KCl. The low temperature used prevented the formation of byproducts, and the pure complex was easily isolated in very good yield without column chromatography purification.

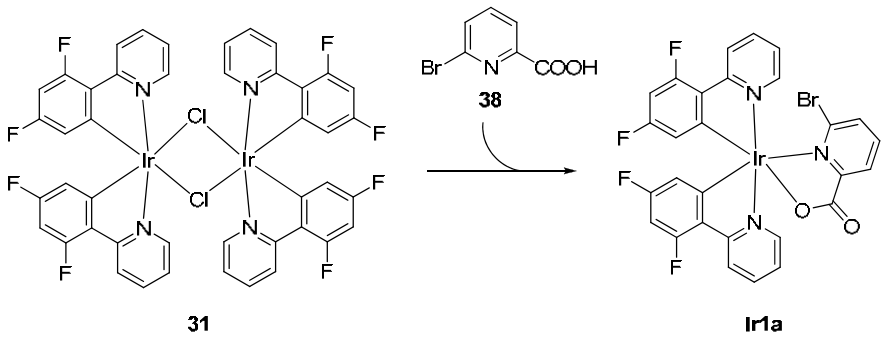

Scheme IV.14. Conditions: K_2CO_3, CH_2Cl_2, 45°C (77%)

For the coupling of the bromo-substituted complex **Ir1a** to the terpyridine system, we have resorted to the palladium-catalyzed Suzuki cross-coupling reaction, requiring

milder conditions compared to the Stille protocol.[213] In the field of coordination chemistry, the procedure has been applied to the synthesis of new ligands, but there are few instances of the use of pre-formed metal complexes themselves as substrates in Suzuki couplings. The notable examples are the formation of dinuclear homometallic complexes with aryl spacers by cross-coupling of appropriate bromo-functionalized complexes with 1,4-benzene-diboronic acid: originally demonstrated for cyclometallated ruthenium complexes with terdentate ligands in the group of J.-P. Sauvage,[222] this approach has also been applied more recently to bis-cyclometalated iridium(III) complexes by the groups of L. De Cola[217] and J.A.G. Williams.[223, 224] Towards the end of our work, a similar strategy for the synthesis of an iridium-ytterbium heterometallic complex[210] through a Suzuki cross-coupling reaction involving the iridium complex has been published by De Cola *et al.*

The conventional route to arylboronic acids proceeds via the formation of the analogous aryllithium compound, usually obtained by lithiation of the parent aryl bromide with n-butyllithium, similarly to the arylstannyl derivatives. The aryllithium compound then reacts rapidly with electrophilic trimethylborate to generate the dimethyl ester of the boronic acid, which is readily hydrolyzed to the acid during work-up. However, Aspley *et al.* have failed[225] to prepare in this way the corresponding boronic acid from 4'-(4-bromophenyl)-2,2' :6',2"-terpyridine **2**, and have resorted to the Miyaura reaction[226] involving the palladium catalyzed coupling of the aryl halide with bis(neopentylglycolato)diboron **39**. Accordingly, we have employed the same procedure for the synthesis of the terpyridine-dicarbonitrile boronic ester **40**, starting from the previously-described bromo-derivative **8** (Scheme IV.15). The most effective catalyst here is reported to be $Pd(dppf)Cl_2$, and the presence of a mild base such as sodium acetate is necessary, as stronger bases promote further reaction of the product with the brominated starting material. The desired boronic ester **40** was finally obtained in a rather good yield after chromatographic purification and recrystallization.

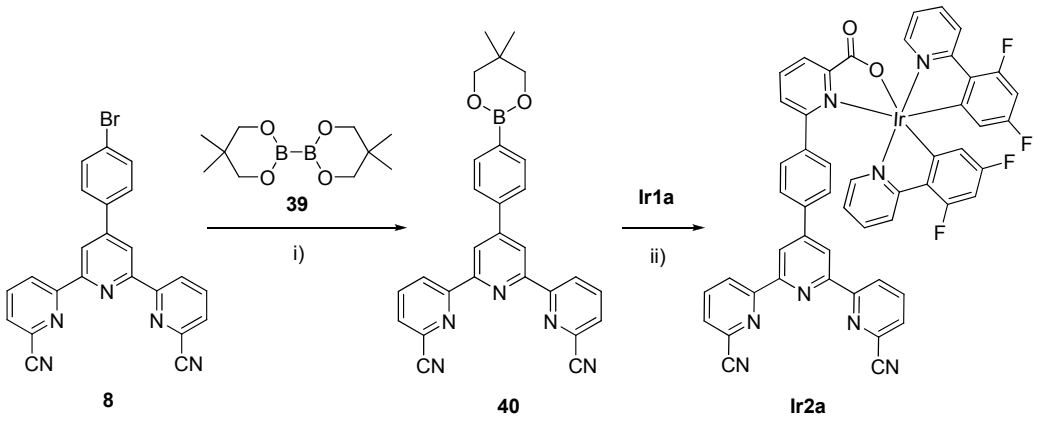

Scheme IV.15. Conditions: i) $Pd(dppf)Cl_2 \cdot CH_2Cl_2$, NaOAc, DMSO, 70°C (58%); ii) $Pd(PPh_3)_4$ (cat), K_2CO_3, DMSO, 80°C (1%)

The Suzuki coupling reaction of the boronic ester **40** with the bromo-substituted iridium complex **Ir1a** was carried out in standard conditions using DMSO at 80°C as solvent and $Pd(PPh_3)_4$ as catalyst. The reaction was quenched after 24h in spite of the presence of unreacted **Ir1a** complex, due to the formation of numerous reaction by-products, as evidenced from the mass analysis. After treatment and extensive column chromatography purifications and recrystallizations (see the Experimental part), a very small amount of the desired coupling product was isolated and characterized by ^1H NMR and ES-MS. We can conclude that the coupling of the boronic ester to the brominated iridium compound proceeded with difficultly, in part due to the reaction conditions used, which should be further optimized, and in part due to the sterical hindrance at the site of the bromine atom in **Ir1a** (see the crystallographic structure in Chapter IV.2.4. a)), which prevented the efficient formation of the palladium complex intermediate.[213]

To eliminate both of these factors, we have decided to change the position of the bromide atom in the iridium starting complex, from ortho to meta with respect to the pyridine nitrogen, and to optimize the palladium-catalyzed coupling reaction conditions. For this, we have synthesized the 5-bromopicolinic acid **42** by the hydrolysis in concentrated chlorhydric acid[227] of the corresponding carbonitrile **41** (see Scheme IV.16). The heteroleptic cyclometalated iridium complex **Ir1** was prepared with excellent yield in refluxing dichloromethane, similarly to **Ir1a**, starting from the μ-chloro-bridged dimer

precursor **31** and the bromopicolinate **42**. The Suzuki-Miyaura coupling reaction of **Ir1** and **40** was carried out in a heterogeneous solvent mixture of toluene : water : ethanol (10:2:1) at 80°C using $Pd(PPh_3)_4$ as catalyst and potassium carbonate as base. The choice of the solvent is particularly important, as toluene solubilizes the starting brominated iridium complex **Ir1** and various other possible side-products, but not the coupling product **Ir2** (as previously verified with **Ir2a**). We believed this behavior would drive the equilibrium towards the formation of the desired product, and indeed, after 48h, a yellow precipitate was obtained, from which, after several recrystallizations, the pure complex **Ir2** was isolated in a very good yield, without the need for chromatographic purification.

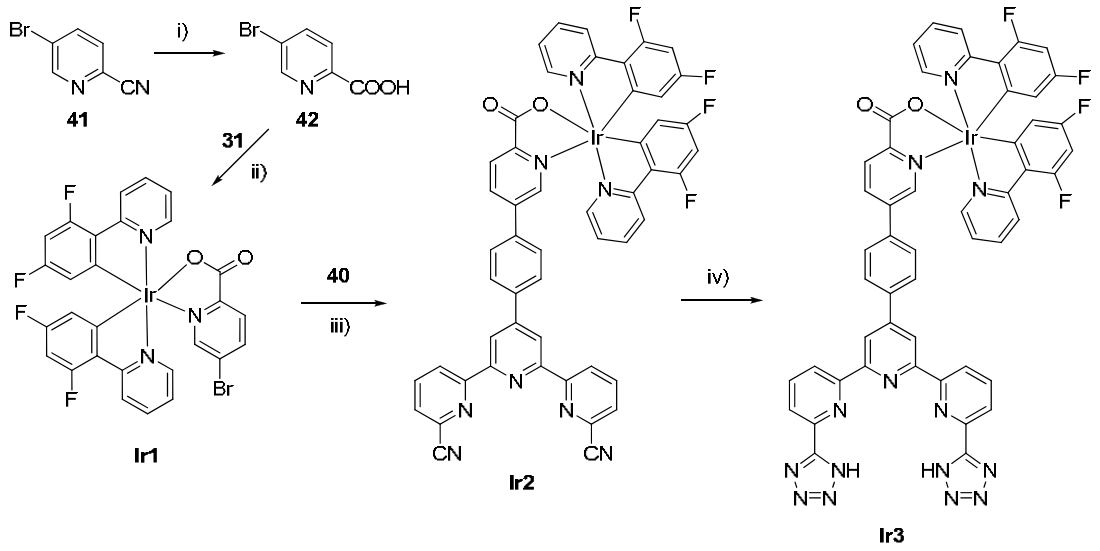

Scheme IV.16. Conditions: i) HCl conc, 110°C (66%); ii) K_2CO_3, CH_2Cl_2, 45°C (93%); iii) $Pd(PPh_3)_4$ (cat), K_2CO_3, toluene/water/ethanol, 80°C (67%); iv) NaN_3, $ZnBr_2$, CH_2Cl_2/MeOH/H_2O, 35°C (62%).

For the conversion of the iridium-terpyridine-dicarbonitrile complex **Ir2** into its tetrazole analogue **Ir3**, numerous reactions (summarized in Table IV.1) have been tried on milligram quantities in order to find the optimal conditions.

Surprisingly, the classical procedure with sodium azide and ammonium chloride in anhydrous DMF, which have been used extensively for the preparation of tetrazole-based ligands in the previous chapters, proved to be unsuccessful, and changing the solvent to chloroform had no effect. Similarly, when we tried the new conditions described by

Demko and Sharpless,[105, 106] using sodium azide and zinc salts in aqueous medium, we had no success. However, as the aqueous mixture was heterogeneous and the solubility of complex **Ir2** in water is probably minimal, we tried employing DMSO and water for obtaining a homogeneous solution, but the reaction was again unsuccessful. Only when using ethoxyethanol and water, the classical solvent for Ir(III) chemistry, we obtained a complicated mixture of products, indicating that the conversion of the carbonitrile took place. Changing the ethoxyethanol/water solvent with a homogeneous mixture of dichloroethane, ethanol and water gave us the first evidence of the formation of **Ir3**, however unpurified with other iridium complexes by-products. Finally, running the reaction at a lower temperature (35°C) to reduce the activity of the $NaN_3/ZnBr_2$ system and prevent ligand scrambling, and using as solvent a homogeneous mixture of dichloromethane, methanol and water, gave the desired iridium complex **Ir3** as a yellow precipitate in the reaction medium, allowing us to easily isolate the pure product in good yield (62%) without the need for column chromatography.

Table IV.1. Optimization of tetrazole synthesis conditions for the conversion of complex **Ir2** into **Ir3**

Reactants	Solvent	Conditions	Outcome[a]
NaN_3, NH_4Cl	DMF anhydrous	100°C, 60h	no reaction
NaN_3, NH_4Cl	$CHCl_3$	60°C, 24h	no reaction
NaN_3, $ZnBr_2$	H_2O	60°C, 48h	no reaction
NaN_3, $ZnBr_2$	DMSO + H_2O	70°C, 90h	no reaction
NaN_3, $ZnCl_2$	ethoxyethanol + H_2O	110°C, 42h	complicated mixture
NaN_3, $ZnBr_2$	dichloroethane + EtOH + H_2O	75°C, 24h	mixture **Ir3** + side-products
NaN_3, $ZnBr_2$	dichloromethane + MeOH + H_2O	35°C, 24h	**Ir3** precipitated

[a] as determined by ^1H and ^{13}H NMR and ES-MS

As reference compound for comparing the properties of our iridium complexes, we have synthesized the complex **33** (non-brominated analogue of **Ir1a** and **Ir1**), previously known as FIrpic.[228] From the Ir(III) μ-chloro-bridged dimer **31**, the complex FIrpic was prepared in very good yield by an adapted literature procedure[218] using dichloromethane as solvent at reflux (Scheme IV.17). The low temperature prevented the formation of

byproducts, and the complex was easily isolated without column chromatography purification.

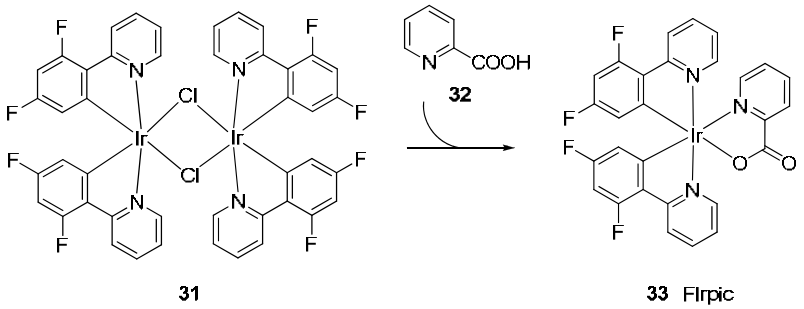

Scheme IV.17. Conditions: CH_2Cl_2, 45°C (84%).

Characterization of the iridium complexes **Ir1** - **Ir3** has been performed by 1D and 2D (COSY, NOESY) proton NMR, mass spectrometry and elemental analysis.

IV.2.4. Characterization of iridium complexes

a) Molecular and crystal structures

Single crystals of the iridium complexes **Ir1a**, **Ir1** and **Ir2**, as well as of the diiridium precursor **31**, were obtained by slow evaporation of chloroform solutions of the complexes or by slow diffusion of diisopropylether or ethanol non-solvents in dichloromethane solutions of the complexes. The crystals were characterized by X-ray diffraction to confirm the mode of coordination of the difluorophenylpyridine and picolinate ligands.

Somewhat surprisingly, the crystal structure of the μ-chloro bridged diiridium complex **31** has not been previously reported, according to our search in the Cambridge Crystallographic Database, although the compound is rather well-known.[81] The structure was solved in the P2(1)/c space group of the monoclinic system. Selected distances and angles are given in Table IV.2, while the full crystallographic data is given in the Appendix.

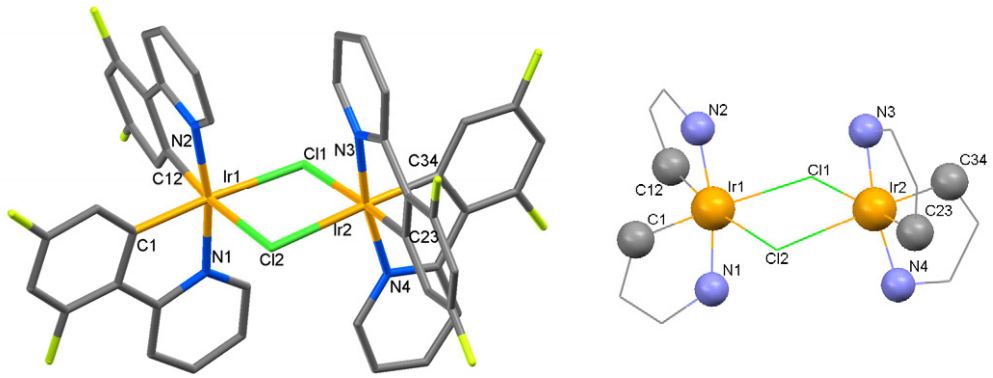

Figure IV.8. Structure of the iridium complex **31** (left) and the N-trans arrangement of the coordination ligands around the iridium atoms (right)

Each iridium atom is hexa-coordinated in a distorted octahedral mode by two cyclometalating difluorophenylpyridine ligands (via the C and N atoms) and two chlorine atoms, which also bridge the two iridium centers, as seen in Figure IV.8. The intermetallic distance is 3.769 Å. The Ir-C (1.982 - 1.995 Å) and Ir-N (2.050 - 2.057 Å) bond distances are within the normal ranges for such cyclometalated complexes.[186, 229] The Ir-Cl bonds are longer (2.500 - 2.529 Å), as can be expected with the higher radius of the chloride ion. The C-Ir-N bite angles are on the average 80.8°, similar to the Cl1-Ir-Cl2 angles of 82.6°. The planes of two cyclometalating ligands and the plane defined by the Cl1-Ir-Cl2 atoms are practically orthogonal with respect to each other. As a result of the strong *trans*-effect of the M-C bonds found in cyclometalated complexes, the formation of the Ir-Cl bridges takes place in the opposite direction of the Ir-C bonds. The coordinating nitrogen atoms are found in a typical *trans* arrangement (Figure IV.8 right), as previously reported,[186, 212, 229] although recently a mutually-cis disposition has been proven by NMR studies.[192] The N1-Ir1-N2 and N3-Ir2-N4 angles are on average 170.1°. In principle, three configurations for the N-trans arrangement can be possible,[212] one in which the two iridium centers are symmetric with respect to one another (ΔΛ meso form, achiral compound), and another two pair of enantiomers lacking a symmetry plane (ΔΔ, ΛΛ). Steric interactions in the meso form favor however the formation of a (ΔΔ, ΛΛ) racemate, as also found in our case. No π-π interactions or H-bonds form in the crystal structure.

Table IV.2. Selected bond distances (Å) and angles (°) in the structure of diiridium complex **31**

Ir1-C12	1.985(6)	C12-Ir1-C1	90.4(2)	C34-Ir2-N3	91.5(3)
Ir1-C1	1.995(7)	C12-Ir1-N2	80.8(3)	C23-Ir2-N3	80.9(3)
Ir1-N2	2.054(5)	C1-Ir1-N2	90.4(2)	C34-Ir2-N4	80.3(3)
Ir1-N1	2.057(5)	C12-Ir1-N1	93.7(2)	C23-Ir2-N4	94.7(3)
Ir1-Cl2	2.509(2)	C1-Ir1-N1	80.8(3)	N3-Ir2-N4	170.5(2)
Ir1-Cl1	2.515(2)	N2-Ir1-N1	169.7(2)	C34-Ir2-Cl1	93.98(18)
Ir2-C34	1.982(7)	C12-Ir1-Cl2	171.94(19)	C23-Ir2-Cl1	172.01(19)
Ir2-C23	1.994(7)	C1-Ir1-Cl2	96.70(18)	N3-Ir2-Cl1	94.72(17)
Ir2-N3	2.050(6)	N2-Ir1-Cl2	95.22(17)	N4-Ir2-Cl1	90.63(16)
Ir2-N4	2.051(6)	N1-Ir1-Cl2	91.21(16)	C34-Ir2-Cl2	174.2(2)
Ir2-Cl1	2.500(2)	C12-Ir1-Cl1	90.55(18)	C23-Ir2-Cl2	91.00(19)
Ir2-Cl2	2.529(2)	C1-Ir1-Cl1	175.8(2)	N3-Ir2-Cl2	93.47(16)
		N2-Ir1-Cl1	93.84(15)	N4-Ir2-Cl2	95.0(2)
		N1-Ir1-Cl1	95.00(17)	Cl1-Ir2-Cl2	82.57(5)
		Cl2-Ir1-Cl1	82.67(5)	Ir2-Cl1-Ir1	97.44(6)
		C34-Ir2-C23	92.8(3)	Ir1-Cl2-Ir2	96.85(6)

The structures of the heteroleptic complexes **Ir1a** and **Ir1** have been solved in the monoclinic system (space group C2/c for **Ir1a** and P 1 21/c 1 for **Ir1**). Selected bond distances and angles are given in Table IV.3, while the full crystallographic details can be found in the Appendix. The complexes have an octahedral coordination geometry around central iridium atom, retaining the cis-C,C trans-N,N chelate disposition of the chloride-bridged precursor complex **31**. For the cyclometalating ligands, the Ir-C bond distances (on average 2.004 Å) are slightly shorter than the Ir-N bond distances (on average 2.038 Å), and the values are similar to those found in the dimer complex **31** and to those previously reported in the literature.[186, 212, 229] The average Ir-O1 bond length of 2.145 Å is longer than the mean Ir-O value of 2.088 Å reported in the Cambridge Crystallographic Database and reflects the large *trans* influence of the phenyl groups (due to the sigma donation of the cyclometalating carbons). The same effect is observed when comparing the longer Ir-N1 bond distance (affected by the *trans* effect) to the average Ir-N distance in the cyclometalating ligands. The difference between the Ir-N1 bond distance in **Ir1a** and **Ir1** (2.222 vs. 2.140 Å, respectively) can be attributed to the steric hindrance caused by the Br atom in the 6 position of the picolinate ligand in **Ir1a**, which elongates the corresponding Ir-N1 bond, whereas in complex **Ir1** the Br atom in the 5 position induces no steric hindrance.

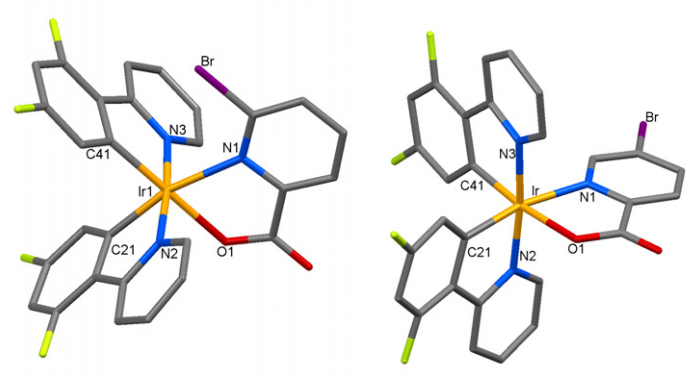

Figure IV.9. Structures of the iridium complexes **Ir1a** (left) and **Ir1** (right)

Table IV.3. Selected bond distances (Å) and angles (°) in the structures of iridium complexes **Ir1a** and **Ir1**

	Ir1a	**Ir1**
Ir1-C21	2.004(6)	2.000(5)
Ir1-C41	2.011(6)	2.002(5)
Ir1-N3	2.041(5)	2.025(4)
Ir1-N2	2.042(5)	2.042(4)
Ir1-O1	2.147(4)	2.142(3)
Ir1-N1	2.222(5)	2.140(4)
C21-Ir1-C41	86.6(2)	92.59(19)
C21-Ir1-N3	95.2(2)	94.30(18)
C41-Ir1-N3	80.4(2)	80.81(19)
C21-Ir1-N2	80.5(2)	80.50(19)
C41-Ir1-N2	96.4(2)	96.09(19)
N3-Ir1-N2	174.86(19)	173.86(16)
C21-Ir1-O1	91.6(2)	92.22(16)
C41-Ir1-O1	175.7(2)	173.09(17)
N3-Ir1-O1	95.89(19)	93.89(16)
N2-Ir1-O1	87.09(19)	89.59(15)
C21-Ir1-N1	166.8(2)	167.97(18)
C41-Ir1-N1	106.1(2)	98.59(17)
N3-Ir1-N1	90.85(18)	91.88(16)
N2-Ir1-N1	93.94(18)	93.83(16)
O1-Ir1-N1	75.99(17)	77.05(14)

The structure of the complex **Ir2** was obtained in the I2/a space group of the monoclinic system, however the crystals were of poorer quality compared to the previous ones. Selected bond distances and angles are given in Table IV.4, while the full crystallographic details can be found in the Appendix. The complex has the same octahedral coordination geometry around central iridium atom, retaining the cis-C,C trans-N,N arrangement found in its precursors **31** and **Ir1** (see Figure IV.10). Similar bond distances and angles compared to the previous structures have been obtained.

Interestingly, the phenyl ring and the pyridine ring of the picolinate ancillary ligand are not coplanar, being twisted at an angle of 33.08°. The terpyridine ring system adopts a full transoid arrangement about the interannular C-C bonds, which is in agreement with the literature[142, 143] and the previously determined structures of the ligands **L1** and **L4** (see Chapter II.2.1. d)). This configuration minimizes electrostatic interactions between the nitrogen lone pairs and the van der Waals interactions between the meta protons. π-π interactions occur in the crystal between the pyridine groups in the terpyridine ring system, situated at an average distance of 3.50 Å.

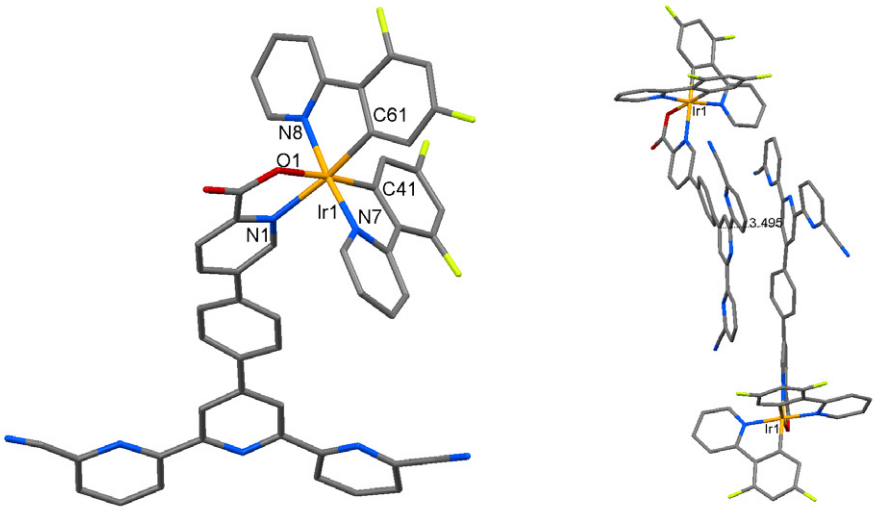

Figure IV.10. Molecular structure of the iridium complex **Ir2** (left) and π-π interactions in the packing structure (right)

Table IV.4. Selected bond distances (Å) and angles (°) in the structure of iridium complex **Ir2**

Ir1-C41	2.051(14)	N7-Ir1-C61	96.0(5)	N8-Ir1-O1	88.5(5)
Ir1-C61	1.996(12)	N7-Ir1-N8	173.9(4)	C41-Ir1-O1	175.4(5)
Ir1-N7	1.909(17)	C61-Ir1-N8	79.3(6)	N7-Ir1-N1	88.0(4)
Ir1-N8	2.009(16)	N7-Ir1-C41	80.1(6)	C61-Ir1-N1	172.1(5)
Ir1-O1	2.148(9)	C61-Ir1-C41	87.3(5)	N8-Ir1-N1	97.1(5)
Ir1-N1	2.154(10)	N8-Ir1-C41	95.7(6)	C41-Ir1-N1	100.0(5)
		N7-Ir1-O1	95.8(5)	O1-Ir1-N1	77.4(4)
		C61-Ir1-O1	95.4(4)		

b) NMR characterization in solution

The ^{1}H NMR spectrum of the diiridium complex **31** in a $CDCl_3$ solution at 298K indicates the presence of one set of signals, with 6 well-resolved resonances for the 24 protons in

the four 2,4-difluorophenylpyridine units, as previously reported,[81] indicating the equivalence of the four cyclometalating ligands in *trans*-N,N arrangement, as shown in the X-ray molecular structure (having three C_2 axes, Figure IV.8).

Substitution with the bromo-picolinate ancillary ligands in **Ir1a** and **Ir1** results in a non-equivalence of the two difluorophenylpyridine ligands (C_1 symmetry), as shown by the X-ray analysis, and accordingly the ^{1}H NMR spectra of the complexes in $CDCl_3$ solution at 298K show the presence of 15 resonances (overlapping in the aromatic region), which have been assigned to the 15 protons in the structure of the complexes (see Figure IV.11a and Figure IV.12a) by 2D COSY and NOESY experiments. The high-field resonances (two doublets at around 5.4 and 5.8 ppm, and two triplets at around 6.4 ppm) have been attributed to the protons situated ortho and, respectively, para to the cyclometalating carbon, known to experience the largest shielding of any of the ligand protons.[212] The ^{13}C NMR spectrum of **Ir1** shows the presence of only 17 resonances (Figure IV.13a), indicating that on the NMR resolution used (50 MHz), the carbon signals of the two cyclometalating ligands are superposed.

The ^{1}H NMR spectra of the complexes **Ir2a** and **Ir2** show the presence of 21 resonances (overlapping in the aromatic region), assigned to the 27 protons in the structures of the complexes (see Figure IV.11b and Figure IV.12b) by 2D COSY and NOESY experiments. The number of signals is in agreement with the presence of two non-equivalent cyclometalating ligands, as in the case of **Ir1a** and **Ir1**, and with the free rotation in solution of the phenyl-terpyridine system, even in the case of the more sterically-hindered complex **Ir2a**. The ^{13}C NMR spectrum of **Ir2** shows the presence of 30 resonances (Figure IV.13b), due to the superposition of the carbon signals of the two cyclometalating ligands. Comparison of the ^{13}C NMR spectra of **Ir1** and **Ir2**, together with empirical estimations using the ACD software,[230] allowed us to attribute the carbon signals in both cases.

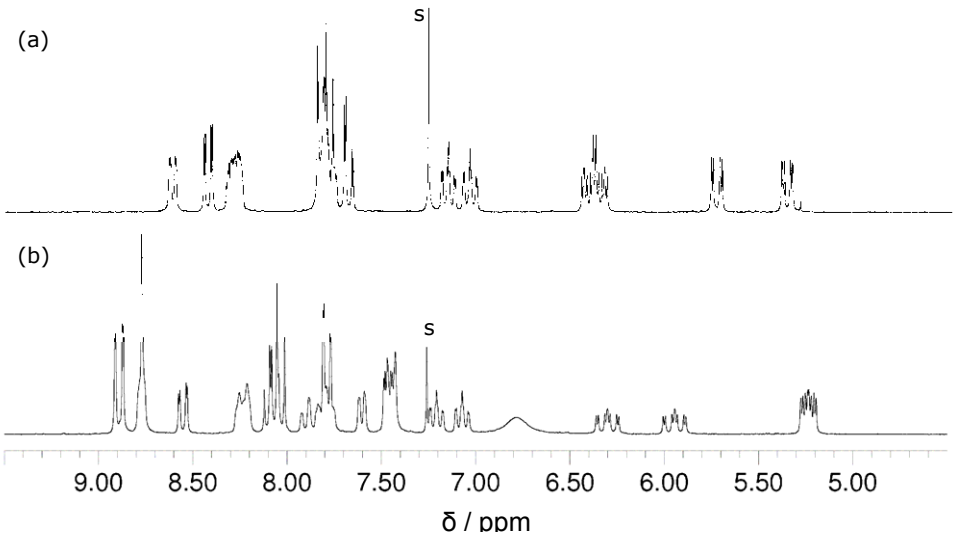

Figure IV.11. ^{1}H NMR spectra of iridium complexes **Ir1a** (a) and **Ir2a** (b) in $CDCl_3$ solutions at 298K

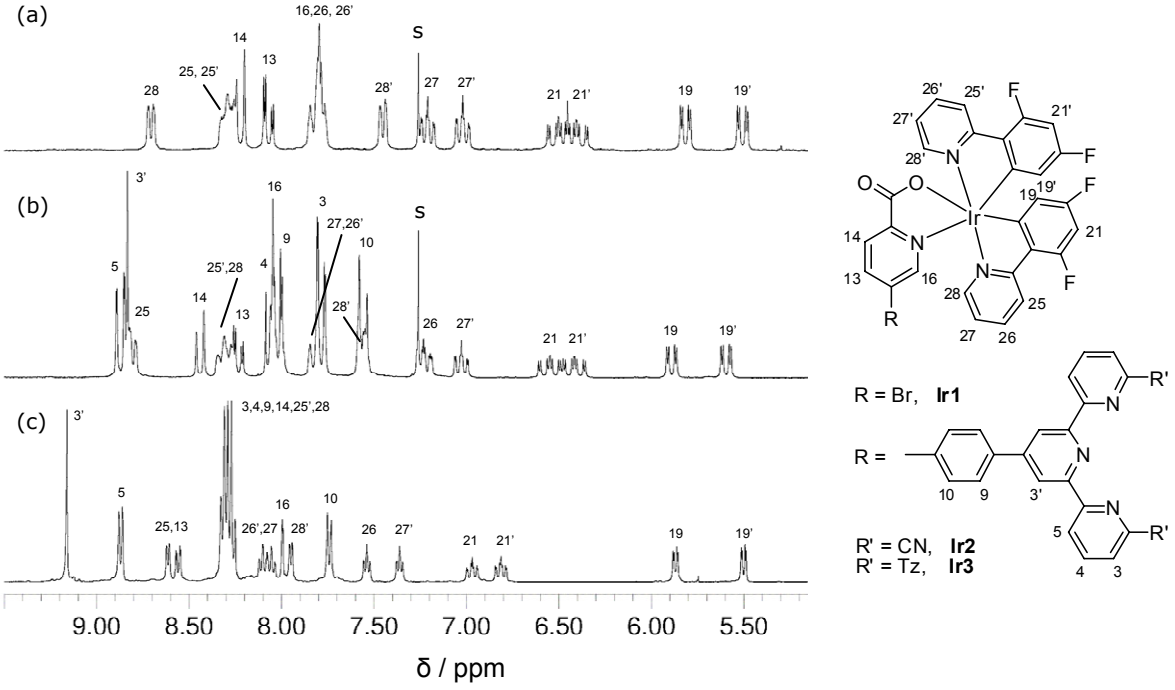

Figure IV.12. ^{1}H NMR spectra with complete assignment for the iridium complexes **Ir1** (a) and **Ir2** (b) in $CDCl_3$ solutions and of **Ir3** (c) in DMSO solution at 298K

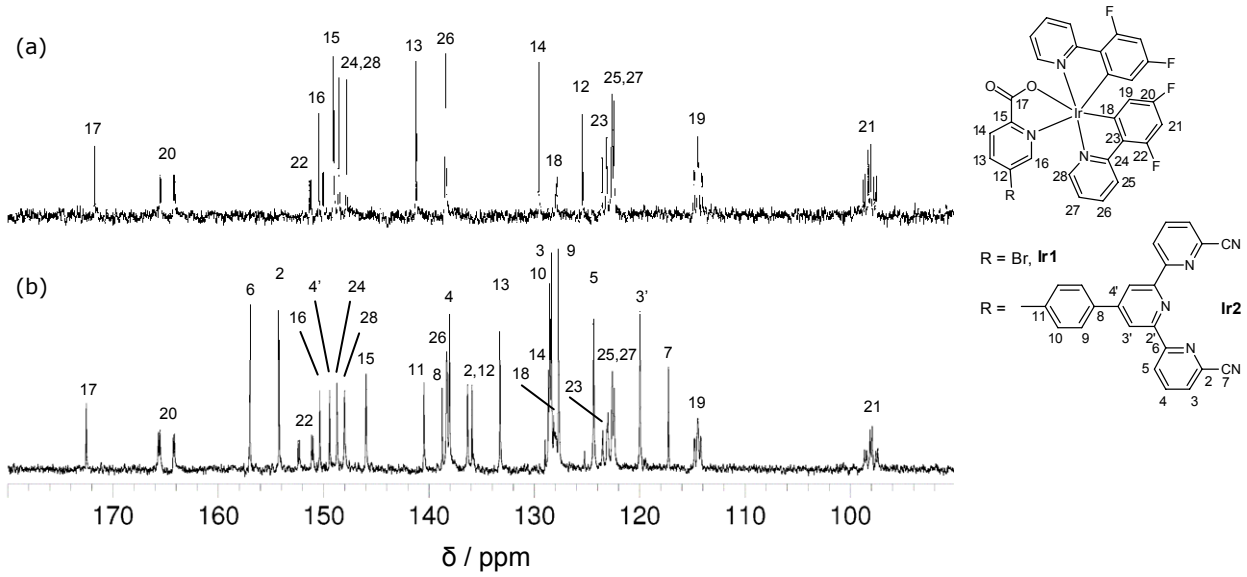

Figure IV.13. ^{13}C NMR spectra with complete assignment for the iridium complexes **Ir1** (a) and **Ir2** (b) in $CDCl_3$ solutions at 298K

In the case of the tetrazole complex **Ir3**, due to its low solubility in chlorinated solvents, the ^{1}H NMR spectrum has been recorded in d_6-DMSO (see Figure IV.12c). It shows the presence of 21 resonances (6 signals at 8.3 ppm being superposed), which have been assigned to the 27 protons of the complex, similarly to **Ir2**.

The NMR solution spectra prove the retention of the iridium complex conformation during the Suzuki coupling of **Ir1** (confirmed by the X-ray crystal structures of **Ir1** and **Ir2**), as well as during the tetrazole synthesis giving the final ligand **Ir3**.

c) Photophysical properties

The absorption spectra of the complexes **Ir1**-**Ir3** (and the already-known complex FIrpic[228] for comparison) in a dichloromethane solution at room temperature are characteristic of (C^N)-cyclometalated iridium complexes[185, 186, 200] (see Figure IV.14). Intense bands are observed in the ultraviolet part of the spectra, between 250 and 350 nm, which can be assigned to the allowed $^{1}(\pi\text{-}\pi^*)$ ligand-centered (LC) transitions. While the complex **Ir1** shows a very similar spectrum to the un-brominated analogue FIrpic ($\varepsilon \approx 1.5\text{-}5\cdot10^4$ $M^{-1}\cdot cm^{-1}$), with the highest energy maximum at 254 and 256 nm, respectively, the terpyridine-substituted complexes **Ir2** and **Ir3** display more intense bands at high energy ($\varepsilon_{max} = 7\cdot10^4$

$M^{-1}\cdot cm^{-1}$), with an additional characteristic maximum of similar intensity around 290 and 298 nm, respectively, due to the terpyridine system.[141] Furthermore, the spectra of all the complexes exhibit weaker ($\varepsilon \approx 0.5\text{-}5\cdot10^3$ $M^{-1}\cdot cm^{-1}$) absorption tails towards lower energy regions (360-475 nm), which can be assigned to singlet $d\pi(Ir)\rightarrow\pi(F_2ppy)$ and triplet $d\pi(Ir)\rightarrow\pi^*(F_2ppy)$ MLCT transitions, as reported for similar cyclometalated complexes.[186, 231] The formally spin forbidden ^{3}MLCT at 453 nm (shown in inset in Figure IV.14) gains intensity by mixing with the higher lying ^{1}MLCT transition through the strong spin-orbit coupling of iridium.

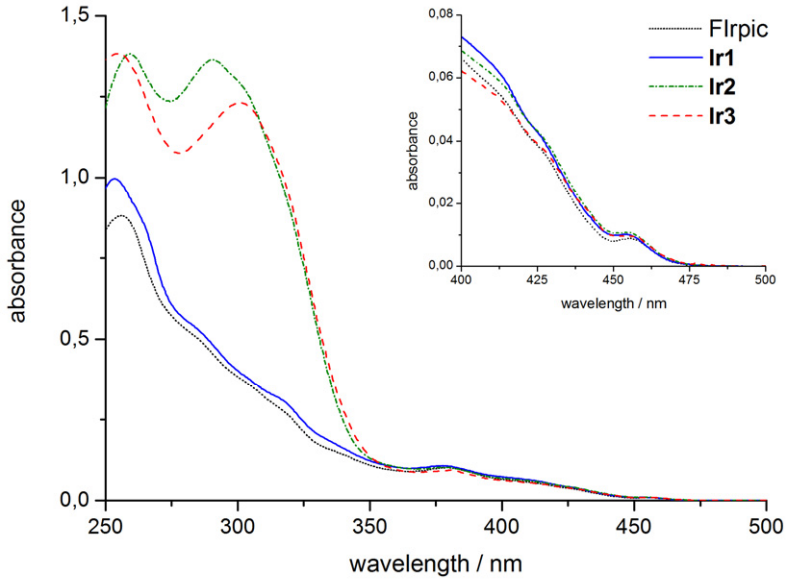

Figure IV.14. UV-vis absorption spectra of the complexes **Ir1** - **Ir3** and FIrpic in a 10^{-4} $mol\cdot dm^{-3}$ CH_2Cl_2 solution at RT. For solubility reasons, the solution of **Ir3** was measured in the presence of triethylamine (2 equivalents). The inset shows a magnified view of the spectra between λ = 400-500 nm.

Practically all the complexes **Ir1**-**Ir3** and FIrpic display similar absorption features in the low energy region (360-475 nm), suggesting that the ancillary ligands make only a small contribution to the absorption process in these systems, and that the MLCT states are located on the cyclometalating F_2ppy ligands.

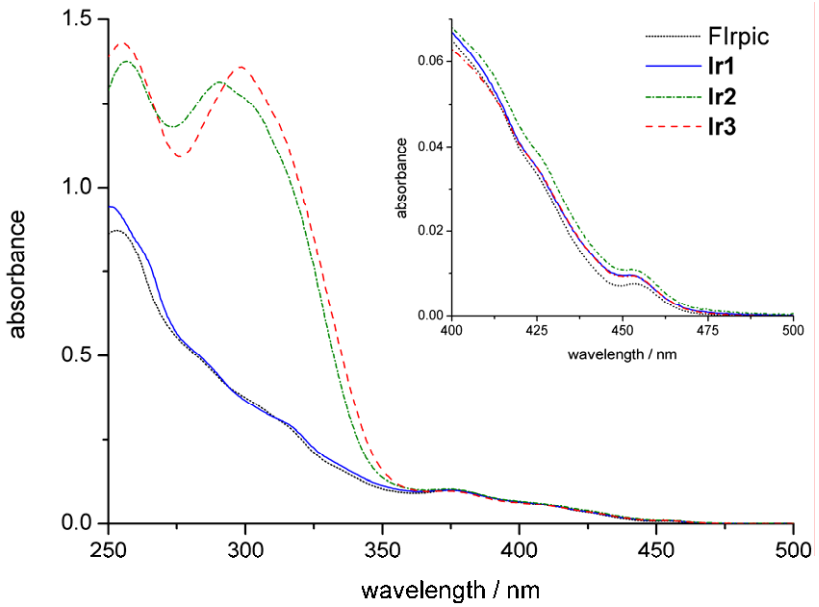

Figure IV.15. UV-vis absorption spectra of the complexes **Ir1** - **Ir3** and FIrpic in a 10^{-4} mol·dm^{-3} CH_2Cl_2 and MeOH (1:1) solution at 298K. The inset shows a magnified view of the spectra between λ = 400-500 nm.

The same absorption spectra have been recorded for the more polar dichloromethane-methanol (1:1) solutions of the complexes (Figure IV.15). The MLCT transitions have similar energies and seem not to be affected by solvatochromism, undergoing only a small 2-3 nm blue-shift. There is no change in the shape of the absorption bands of the **Ir3** solution (in the dichloromethane-methanol mixture) before and after addition of an excess of triethylamine, however the deprotonated complex shows a highly increased solubility in pure dichloromethane, and for this reason the dichloromethane solution of **Ir3** was measured in the presence of triethylamine (2 equivalents).

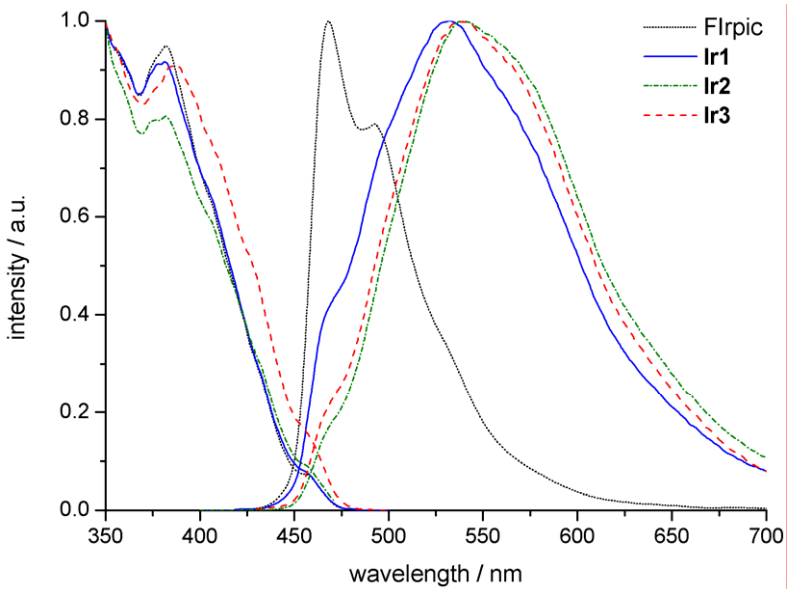

Figure IV.16. Normalized excitation(left) and emission (right) spectra of the complexes **Ir1**- **Ir3** and FIrpic in a 10^{-4} mol·dm^{-3} CH_2Cl_2 solution at 298K. For solubility reasons, the solution of **Ir3** was measured in the presence of triethylamine (2 equivalents).

The emission and excitation spectra of the complexes **Ir1**-**Ir3** (and FIrpic for comparison) in dichloromethane solutions at room temperature are given in Figure IV.16. Surprisingly, although they have similar MLCT absorption profiles and energies, there is considerable difference between the emission spectra of the bromo-substituted complex **Ir1** and the parent FIrpic. While the spectrum of the latter displays the characteristic blue-range emission with vibronic progressions, with one intense band at 468 nm, a second less intense at 492 nm and a shoulder around 530 nm, the broader, less featured emission spectrum of the **Ir1** complex is yellow-shifted with a maximum at 531 nm, and only a shoulder at 470 nm and a second faint one at 495 nm. Apparently, the low-energy transition appearing as a shoulder in FIrpic has become the major emissive pathway in **Ir1**, while conversely, the two high-energy maxima in FIrpic appear in **Ir1** only as secondary transitions. The vibronic structure of the emission bands of FIrpic indicates a large amount of ^{3}LC character, and the excited state is believed[200] to be a mixture of predominantly ^{3}LC (F_2ppy) as well as ^{3}MLCT states, as also confirmed by theoretical studies.[232] In the case of **Ir1**, the broad emission would suggest however a more prevalent MLCT character for the excited state. The emission spectra of **Ir2** and **Ir3** are similar to

Ir1, only slightly red-shifted, with a maximum at 538 nm, while the relative intensity of the shoulder at 470 nm is diminished compared to **Ir1**. The lifetime of the **Ir1** complex was measured in degassed (three freeze-thaw-pump cycles) dichloromethane solution at room temperature, and corresponds to 0.12 μs, while the absolute quantum yield measured in the same conditions is 5.3%. A similar quantum yield of 3.7% has been obtained for the **Ir3** complex. The small quantum yields point to a substantial contribution of the ^{3}LC state.

The excitation spectra of all the complexes are however similar to each other, and they reproduce the shape of the components of the absorption spectra recorded at the same concentration, with the maximum of the ^{1}MLCT state around 380-385 nm and the spin forbidden ^{3}MLCT transition appearing as a shoulder at 453 nm.

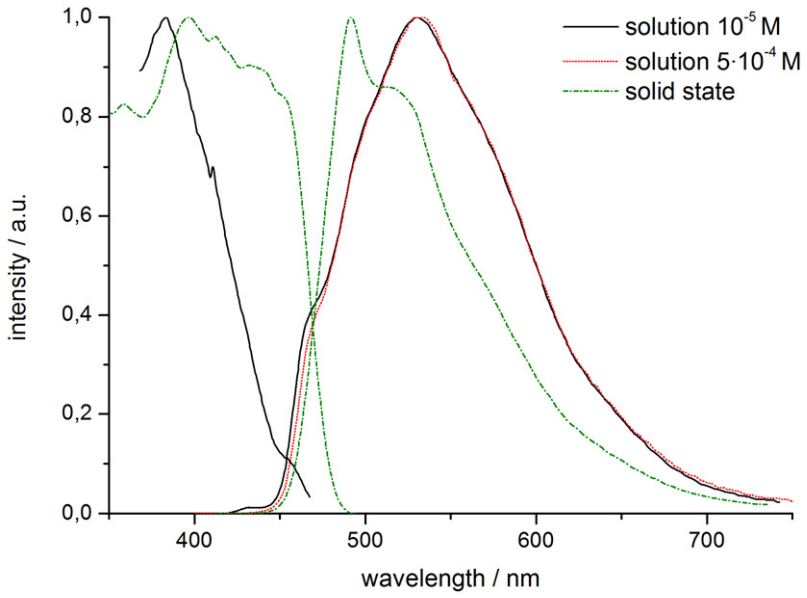

Figure IV.17. Normalized excitation and emission spectra of the complex **Ir1** in CH_2Cl_2 solution (concentration 10^{-5} and $5{\cdot}10^{-4}$ mol·dm^{-3}) and in solid state at 298K

One possible reason for the difference observed in the emission spectra of **Ir1** and FIrpic could be related to the formation of aggregates in solution, due to the relatively high concentration used, leading to an emission from the excimer species, which is characteristically red-shifted.[233] However, the emission spectra of a dilute and a concentrated dichloromethane solution of **Ir1** are virtually identical (see Figure IV.17),

whereas the solid state emission spectrum is in fact blue-shifted, indicating a rigidochromic effect. Consequently, we can exclude the formation of excimers in the case of the **Ir1** complex.

To gain more insight into the nature of the emissive excited state, the emission spectra of all the complexes **Ir1**-**Ir3** (and FIrpic for comparison) were measured at 77K in a dichloromethane glass matrix (see Figure IV.18).

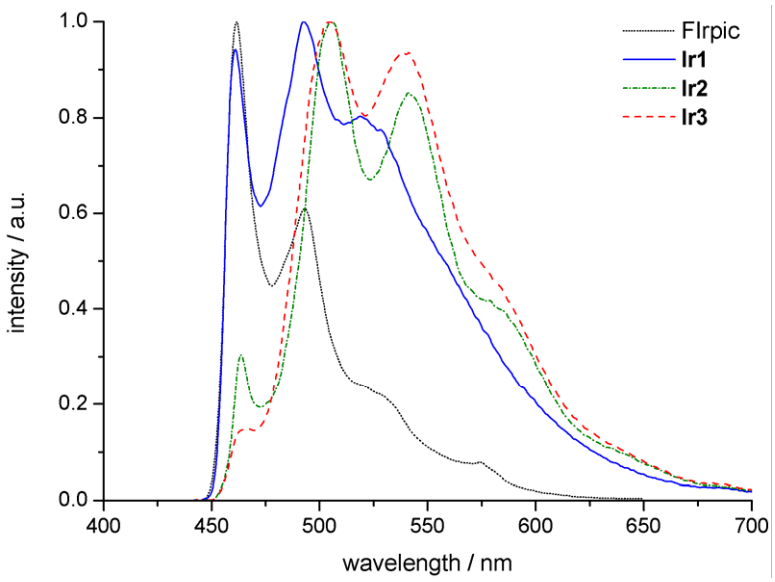

Figure IV.18. Normalized emission spectra of the complexes **Ir1**- **Ir3** and FIrpic in CH_2Cl_2 glass (77K) at $8.5 \cdot 10^{-5}$ mol·dm^{-3} concentration.

All the complexes display a rigidochromic shift towards the blue region when frozen in glass. The high energy band of FIrpic is displaced to 461.5 nm (from 468 nm at room temperature), accompanied by a decrease in intensity of the second band and a more structured tail towards the lower energies, but the overall spectrum remains the same. By contrast, the **Ir1** complex is much more affected by low temperature, compared to the rather featureless emission at room temperature. The complex displays a highly vibronic emission with two strong bands at 461 and 493 nm and a shoulder at lower energy (around 520 nm). The shoulder becomes the dominating band in the room temperature spectrum. The positions of the two high energy maxima are the same in FIrpic and **Ir1**, only differing in their relative intensities. In the case of the complexes **Ir2** and **Ir3**, a

similar hypsochromically-shifted vibronic structure can be observed. The high energy band which dominates the emission of FIrpic (and to some extent that of **Ir1**) is however heavily decreased, and the emission is dominated by two strong maxima at 505 and 540 nm, the latter being the dominating band in the room temperature spectra. In addition, a shoulder around 583 nm can be observed. The rigidochromic effect which characterizes the emission of the complexes **Ir1**-**Ir3** at low temperature can be thought to be associated with the motional relaxation of the excited-state geometry, which is prone to be affected by the rigidity of the matrix, or to the solvent-stabilization of the emissive state in solution (*vide infra*), which is no longer possible in frozen state. Furthermore, the vibronic character of the emission spectra is indicative of a pronounced ligand-centered character in the emissive excited state at low temperature. The lifetimes measured at 77K for the **Ir1** and **Ir3** complexes are 3.77 and 3.48 μs, respectively, more than one order of magnitude larger compared to the room temperature values. From these data, the radiative rate constants can be calculated as $k_r = \tau^{-1}$ and amount to $2.65 \cdot 10^5$ and $2.87 \cdot 10^5$ s^{-1}, for the two complexes, respectively.

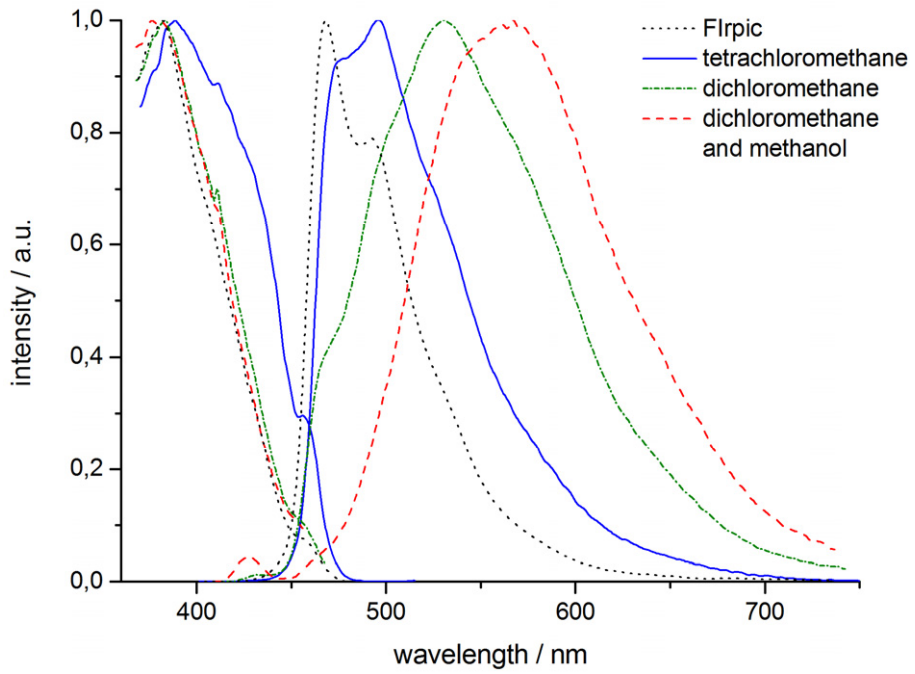

Figure IV.19. Normalized excitation and emission spectra of the complex **Ir1** in different solvents of increasing polarity (CCl_4, CH_2Cl_2 and a 1:1 mixture of CH_2Cl_2 and MeOH) and of the complex FIrpic in CH_2Cl_2 at room temperature

Table IV.5. Summary of photophysical properties for the complexes **Ir1** and **Ir3** measured in degassed dichloromethane solutions at 298K (RT) and 77K (LT).

	λ_{ex}/nm	λ_{em}/nm	τ^{RT}/μs	τ^{LT}/μs	$k_r/10^5$ s^{-1}	Φ/%
Ir1	375	518	0.117(2)	3.77(3)	2.65	5.33(16)
Ir3	379	535	-	3.48(3)	2.87	3.74(12)

To investigate further the causes of the emission spectral difference between **Ir1** and FIrpic at room temperature in solution, we have recorded the excitation and emission spectra of **Ir1** in solvents of increasing polarity (tetrachloromethane, dichloromethane, and a 1:1 mixture of dichloromethane and methanol), as shown in Figure IV.19. We have observed a strong positive solvatochromic effect in the phosphorescence spectra, while the excitation spectra (as well as the absorption spectra, *vide supra*) are not affected. In fact, the high energy band in the emission spectrum of **Ir1** in tetrachloromethane (the least polar solvent) is only slightly bathochromically shifted compared to FIrpic in dichloromethane, and appears as a well-defined peak at 476 nm, whereas the emission maximum of **Ir1** in dichloromethane at 531 nm appears only as a shoulder in tetrachloromethane solution.

FIrpic is known not to be affected by solvatochromism, both in its absorption and emission spectra,[234] indicating that there is no significant charge-rearrangement during its phosphorescence and that the dominant emission process is most-likely from the cyclometalating LC state with only a small contribution from the MLCT state, as reported earlier.[200] By contrast, the solvatochromic effect observed for the emission spectra of **Ir1** suggests the presence of a polar lowest excited state. This could be located either on the ancillary bromo-picolinic acid, which is highly affected by solvent polarity,[204, 234] or on the Ir→F_2ppy MLCT state, which is also affected by solvatochromism. However, the vibronic structure of the low temperature emission in **Ir1**-**Ir3** suggests a major contribution from a ligand-centered level. This hypothesis is also in agreement with the abovementioned rigidochromism, which indicated that the phosphorescent emissive state is affected by dipole-dipole relaxation. Similar observations have been made before in the case of substituted iridium complexes based on picolinic acids,[234] and the group of Park suggested[204] and recently verified[235] a mechanism based on inter-ligand energy transfer

(ILET) from the cyclometalating ligand (F_2ppy) to the emitting ancillary ligand (pic) which has a lower excited state due to substitution with electron-active groups.

d) DFT calculations

In order to estimate the energy levels of the ancillary ligands in our iridium complexes, we have performed DFT-based quantum chemical calculations using the ADF software on the molecular geometry and electronic structure of the complexes **Ir1**, **Ir3** and FIrpic (for comparison) in dichloromethane solvent (see Table IV.6). While the electron density in the HOMOs of the complexes resides significantly on the phenyl part of the cyclometalating ligand (F_2ppy) as well as the core Ir(III) atom (~40%), the electron density in the LUMOs depends on the ancillary ligand (see Figure IV.20). In the case of the FIrpic complex, a large electron density is localized on the pyridine of the cyclometalating ligand, and only a small electron density on the ancillary (pic) ligand, in agreement with previous calculations.[232] The ancillary ligand has major electronic contribution only in the LUMO+2 level. However, in the case of **Ir1** the LUMO is mainly located on the ancillary bromo-picolinate ligand with small electronic contributions from the cyclometalating ligands, which increase in the higher levels LUMO+1 and LUMO+2, the latter containing mainly electronic densities located on the pyridine of F_2ppy. The complex **Ir3** shows a similar electronic configuration with LUMO levels located on the ancillary terpyridine-substituted picolinate ligand, although in this case there are no substantial contributions from the cyclometalating ligands up to the level LUMO+4. In all cases, the excitation from the HOMO greatly decreases the charge density in the iridium center and increases it in the ligands, indicating that the emissions of all of the complexes have some MLCT character.

Table IV.6. Calculated energies of selected MOs of the iridium complexes **Ir1** and **Ir3** (and FIrpic for comparison) obtained from DFT calculations and the experimental emission wavelengths measured in solution

	HOMO / eV	LUMO / eV	LUMO+1 / eV	LUMO+2 / eV	HL gap / nm	λ_{em} / nm
FIrpic	-5.80	-3.15	-3.08	-3.01	468	468[a]
Ir1	-5.86	-3.24	-3.14	-3.12	473	476[a]
Ir3	-5.84	-3.68	-3.42	-3.31	574	538[a]

[a]measured in dichloromethane; [b]measured in tetrachloromethane.

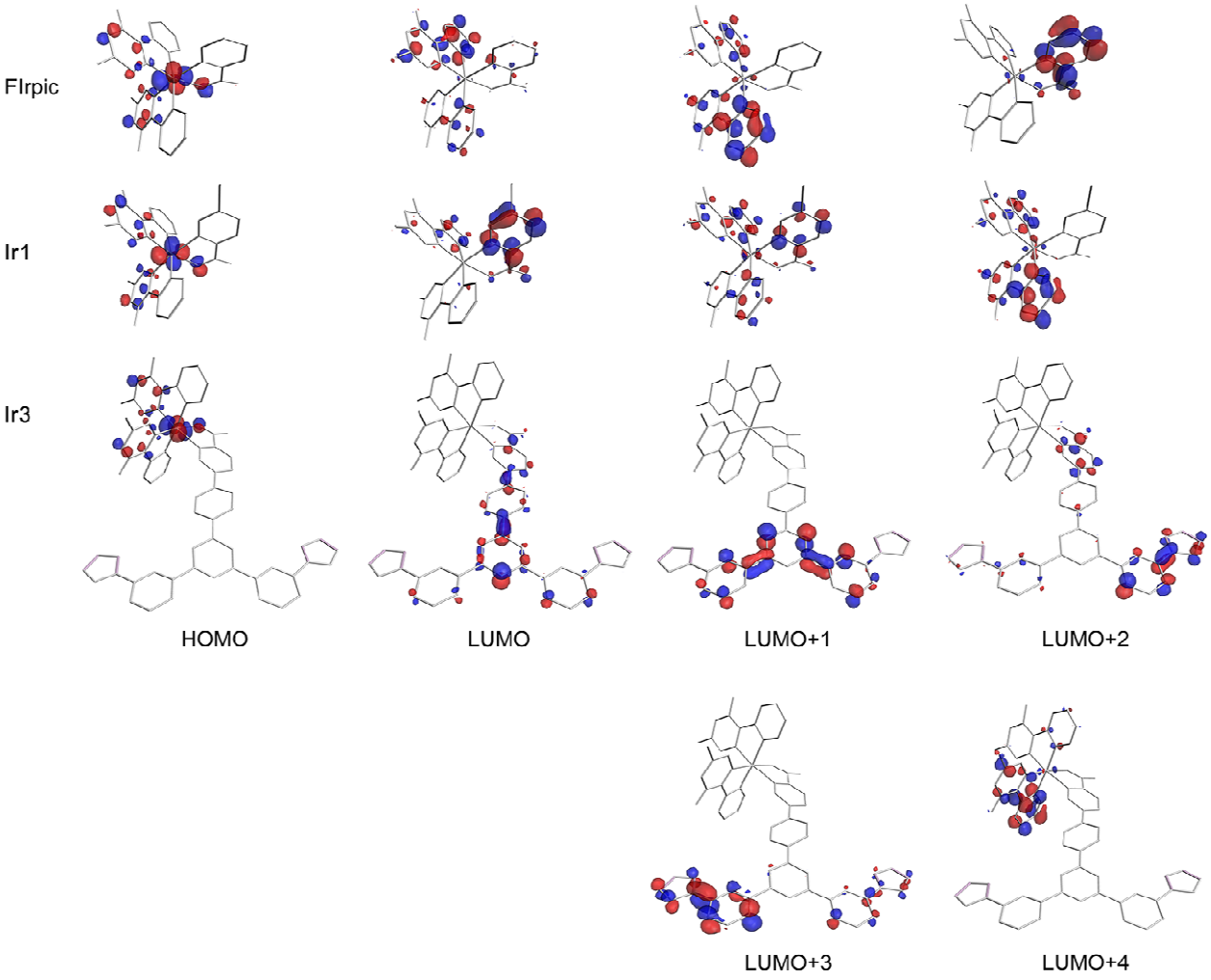

Figure IV.20. Contour plots of selected MOs of the iridium complexes **Ir1** and **Ir3** (and FIrpic for comparison) obtained from DFT calculations. The color and size of the lobes reflect the sign and amplitude of the LCAO coefficients, respectively. The hydrogen atoms are omitted for clarity.

The calculated contributions agree with the pattern observed in the phosphorescence spectra of the complexes, and explain the decrease in intensity of the 468 nm band going from FIrpic to **Ir1** to **Ir3**, as well as the shift of the emission maximum towards the yellow region in the case of **Ir1** and **Ir3**. Furthermore, the calculated energy differences between the HOMO and the LUMO levels of FIrpic correlate very well with the phosphorescence emission wavelengths. However, the excited state stabilization by polar solvents in the case of **Ir1** and **Ir3** (put in evidence by the solvatochromic effect) is probably not fully taken into account in our calculations, in spite of introducing the solvent parameter, leading to a discrepancy between the calculated and the observed transition wavelength.

In fact, the calculated value for **Ir1** agrees well with the experimental one measured in tetrachloromethane, where the solvatochromic effect is minimized. A new set of TD-DFT calculations of the excited states in **Ir1** and **Ir3** would probably be necessary for properly evaluating the solvatochromic effect and providing a more exact description for the energies of various transitions.

In spite of this, the DFT calculations allowed us to clearly identify the ancillary ligand as having a major contribution to the emissive excited state in complexes **Ir1** and **Ir3** (and, by analogy, **Ir2**). The stabilization effect of the electron-active substituents attached to the picolinate ancillary ligand decreases the energy of its excited state below that of the ^{3}MLCT state. Following the ^{1}MLCT excitation from iridium to F$_2$ppy in the singlet manifold, highly efficient inter-system crossing to ^{3}MLCT occurs due to the strong spin-orbit coupling of iridium. This excitation process is similar for all the complexes, as evidenced by their resembling MLCT absorption and excitation bands.

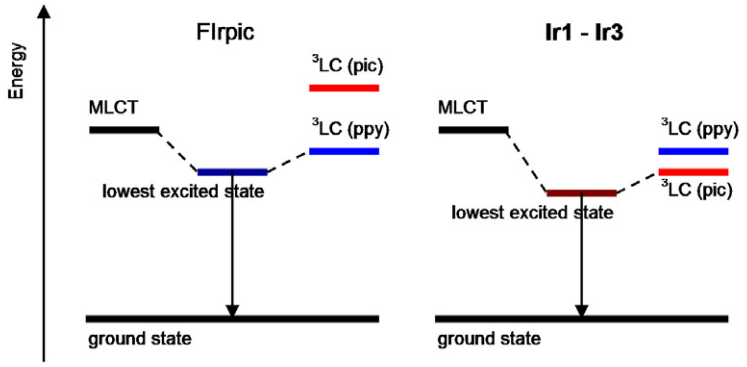

Figure IV.21. Simplified energy state model showing the difference between the emissive states in FIrpic (left) and the **Ir1**-**Ir3** complexes (right)

In the case of FIrpic, the emission originates from a lowest excited state containing the F$_2$ppy ^{3}LC with some ^{1,3}MLCT character mixed in through the spin-orbit coupling (see Figure IV.21). However, due to the low-lying ^{3}LC state of the substituted ancillary ligands in **Ir1**-**Ir3**, the emissive state in these cases is most probably a mixture of ^{3}MLCT and picolinate ^{3}LC states, with some contributions from the F$_2$ppy ^{3}LC (especially in the case of **Ir1**), the degree of mixing depending on the relative energies of the levels involved, which

are also affected by the surroundings (solvatochromic or rigidochromic effects). Due to the smaller energy gap to the singlet ground state, the phosphorescence wavelength is shifted bathochromically compared to FIrpic. Inter-ligand energy transfer[204, 235] from the F_2ppy ^{3}LC could be involved in the population of the picolinate ^{3}LC state. An emission originating from a triplet metal-ligand-to-ligand ^{3}MLLCT state, as described[236] by Tamayo *et al.,* can probably be excluded, since the absorption spectra of **Ir1**-**Ir3** do not show the low energy bands (>475 nm) characteristic of the MLLCT transitions, and furthermore, the low energy region of their spectra is similar to that of FIrpic (see Figure IV.14), which is known not to display MLLCT transitions.

IV.2.5. Synthesis of iridium-lanthanide complexes

Homoleptic heterotrimetallic lanthanide-iridium complexes of the general formula [Ln(**Ir3**)$_2$]NHOct$_3$ (Ln = Nd, Eu) have been prepared by reacting two equivalents of iridium complex **Ir3** with one equivalent of lanthanide triflate in a 1:1 dichloromethane-methanol solvent mixture and in the presence of trioctylamine. The conditions were adjusted to favor the formation of the bis-ligand complexes, due to the high insolubility of the mono-species [Ln(**Ir3**)]$^+$, which instantly precipitate from the reaction mixture if present. To avoid precipitation, dilute lanthanide solutions were added slowly under vigorous stirring to more concentrated iridium complex solutions. The long alkyl chain organic base was chosen to increase the solubility of the final bis-ligand complex. Only the [Eu(**Ir3**)$_2$]$^-$ complex has been isolated so far, while the [Nd(**Ir3**)$_2$]$^-$ complex has been prepared in situ for photophysical studies. Size-exclusion chromatography on a column packed with Sephadex LH-20 in dichloromethane-methanol was used for the purification process of [Eu(**Ir3**)$_2$]$^-$, the elution of the europium complex being easily visualized with an UV lamp. The complex has been characterized by proton NMR spectroscopy. Further characterization is still in progress.

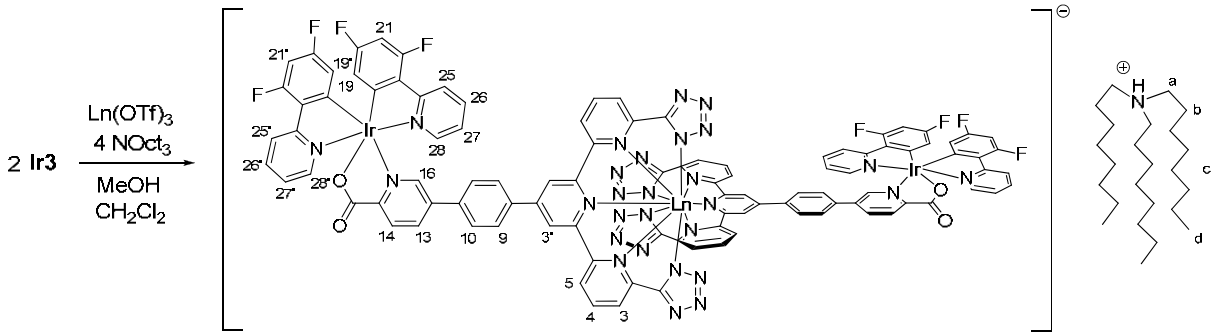

Scheme IV.18. Reaction scheme for the synthesis of [Ln(**Ir3**)$_2$]NHOct$_3$ (Ln = Nd, Eu) complexes

IV.2.6. Characterization of iridium-lanthanide complexes

a) ^{1}H NMR solution study

Due to the same lanthanide coordination motif (terpyridine-tetrazolate) in the complexes [Ln(**Ir3**)$_2$]$^-$ and [Ln(**Li**)$_2$]$^-$ (i = 1..6), a similar solution structure is to be expected. Indeed, the ^{1}H NMR spectrum of the [Eu(**Ir3**)$_2$]$^-$ complex in a MeOD-CD_2Cl_4 solvent mixture at 298K shows the presence of one set of sharp signals, with 21 resonances for the 54 protons in the structure of the iridium ligand, and 8 resonances for the 24 n-octyl protons in the ammonium counterion (see Figure IV.22). Due to its particular chemical structure, the complex can only be solubilized in a solvent mixture of an alcohol and a chlorinated solvent (such as dichloromethane, chloroform, tetrachloroethane etc).

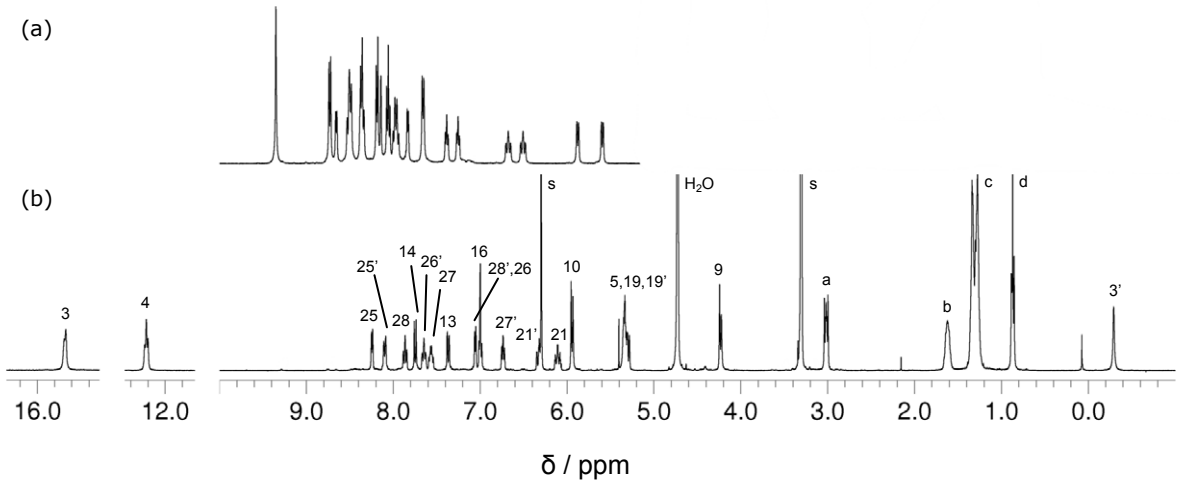

Figure IV.22. ^{1}H NMR spectra of (a) **Ir3** (deprotonated with NOct$_3$) in MeOD-$CDCl_3$ solution and of (b) the isolated [Eu(**Ir3**)$_2$]NHOct$_3$ complex in MeOD-CD_2Cl_4 solution at 298K

These features are in agreement with the presence of a stable, rigid, D_2 symmetric species, in which the two cyclometalating ligands of each iridium complex are non-equivalent, as indicated also by the crystal and solution structure of **Ir2**. Free rotation along the C-C bond between the picolinate pyridine ring and the adjacent phenyl ring induces the equivalence on the NMR time-scale of the two iridium complexes in the trimetallic assembly. The proton signals of the $[Eu(\mathbf{Ir3})_2]^-$ specie are clearly resolved at room temperature and are shifted compared to the free ligand **Ir3** due to the paramagnetic effect of the lanthanide ion. The signals have been assigned by 2D ^1H-^1H COSY and NOESY experiments. The position of the terpyridine-phenyl proton NMR signals (H_3-H_5, $H_{3'}$, H_9 and H_{10}) are identical for the complexes $[Eu(\mathbf{Ir3})_2]^-$ and the previously studied $[Eu(\mathbf{L3})_2]^-$, further confirming the solution structure of the heterometallic assembly.

b) Photophysical characterization

For solubility reasons, all the measurements of the heterometallic complexes in solution have been performed in a dichloromethane-methanol (1:1 v/v) solvent mixture. The absorption spectrum of the trimetallic $[Eu(\mathbf{Ir3})_2]^-$ complex in solution at room temperature is similar to that of the iridium complex **Ir3** alone (deprotonated with triethylamine), while the molar absorptivity is about two times higher, as expected with the formation of a bis-**Ir3** species (see Figure IV.23). The intense bands observed in the ultraviolet part of the $[Eu(\mathbf{Ir3})_2]^-$ spectrum, between 250 and 350 nm, are assigned to the allowed $^1(\pi\text{-}\pi^*)$ ligand-centered (LC) transitions. The maximum at 323 nm, attributed to the absorption of the conjugated terpyridine system,[141] is shifted at lower energy (with 23 nm) compared to the spectrum of the **Ir3** complex alone. The weaker transitions in absorption tail towards lower energy regions (360-475 nm), which are assigned to singlet $d\pi(Ir)\rightarrow\pi(F_2ppy)$ and triplet $d\pi(Ir)\rightarrow\pi^*(F_2ppy)$ MLCT transitions,[186, 231] are similar to those found in the iridium complex **Ir3**. For comparing the influence of the iridium complex on the absorption properties of the whole trimetallic assembly, we have recorded the absorption spectrum of the $[Eu(\mathbf{L3})_2]^-$ complex (having the same phenyl-substituted terpyridine-tetrazolate

lanthanide coordination motif, see Chapter II.2.1. a)) in a methanol solution at room temperature (Figure IV.23). The low energy absorption maximum of the $[Eu(\mathbf{L3})_2]^-$ complex is centered around 350 nm, with a tail extending up to 375 nm. Consequently, the absorption features of the $[Eu(\mathbf{Ir3})_2]^-$ trimetallic assembly in the range 375 – 475 nm are due exclusively to the iridium complex part, and selective excitation of the iridium moiety can be performed in this region.

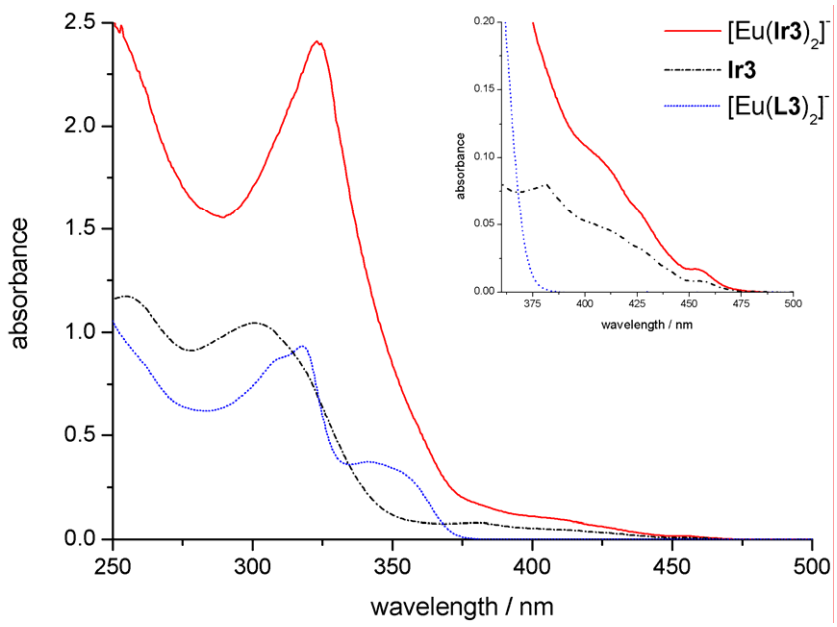

Figure IV.23. UV-vis absorption spectra of the complexes $[Eu(\mathbf{Ir3})_2]^-$ and **Ir3** in CH_2Cl_2 and MeOH (1:1) solutions and of the complex $[Eu(\mathbf{L3})_2]^-$ in MeOH solution at $8.5 \cdot 10^{-5}$ mol·dm^{-3} at 298K. The inset shows a magnified view of the spectra between λ = 360-500 nm.

The emission spectrum of the $[Eu(\mathbf{Ir3})_2]^-$ complex, recorded upon selective excitation of the iridium center at 440 nm (well beyond the absorption bands of the phenyl-terpyridine chromophore, and in between the weak f-f transitions of the Eu^{3+} ion), displays the characteristic $^5D_0 \rightarrow {}^7F_J$ transitions of the europium, and is dominated by the $^7F_2$ band, as shown in Figure IV.24. A small residual emission from the iridium ^{3}LC-^{3}MLCT mixed state can also be detected, indicating that the Ir→Eu energy transfer is not complete. This residual emission matches the emission of the **Ir3** complex in a similar CH_2Cl_2-MeOH solvent mixture and in the presence of triethylamine, which is also represented in Figure IV.24.

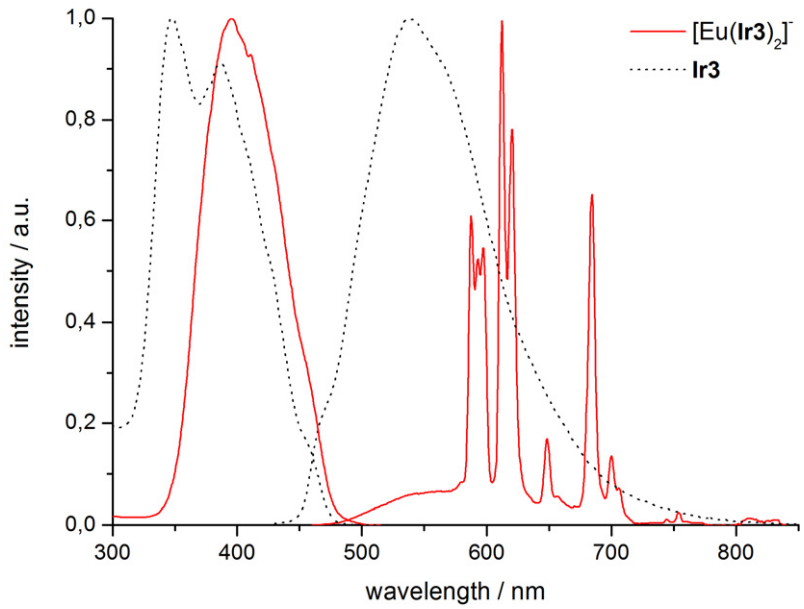

Figure IV.24. Normalized excitation and emission spectra of the complexes $[Eu(\mathbf{Ir3})_2]^-$ and **Ir3** in $8.5 \cdot 10^{-5}$ mol·dm^{-3} CH_2Cl_2 - MeOH (1:1) solutions at room temperature.

The excitation spectrum of the $[Eu(\mathbf{Ir3})_2]^-$ complex, obtained while monitoring the $^5D_0 \rightarrow {}^7F_2$ transition at 612 nm, shows a maximum centered at 395 nm, which can be attributed to the singlet $d\pi(Ir) \rightarrow \pi(F_2ppy)$ MLCT transition in the iridium complex, and a faint shoulder around 455 nm, which can be assigned to the corresponding triplet $d\pi \rightarrow \pi^*$ MLCT transition (Figure IV.24). Recording the excitation upon monitoring the 810 nm $^5D_0 \rightarrow {}^7F_6$ transition (where only the europium ion emits), or the 530 nm region (where only the iridium complex emits) gave the same spectra. This clearly indicates that the sensitization of europium emission is due to an energy transfer from the iridium MLCT states to the $^5D_0$ emissive excited state of the europium ion. For comparison, the excitation spectrum of the **Ir3** complex in solution is also represented in Figure IV.24. The peak at 387 nm and the shoulder at 455 nm were assigned to the singlet and triplet MLCT transitions, respectively, while the higher-energy peak at 348 nm is characteristic of the conjugated terpyridine-tetrazole ring system. The absence of bands in the 300-350 nm region from the excitation spectrum of the heterometallic complex $[Eu(\mathbf{Ir3})_2]^-$ confirms that the sensitization of europium emission is due exclusively to the iridium center.

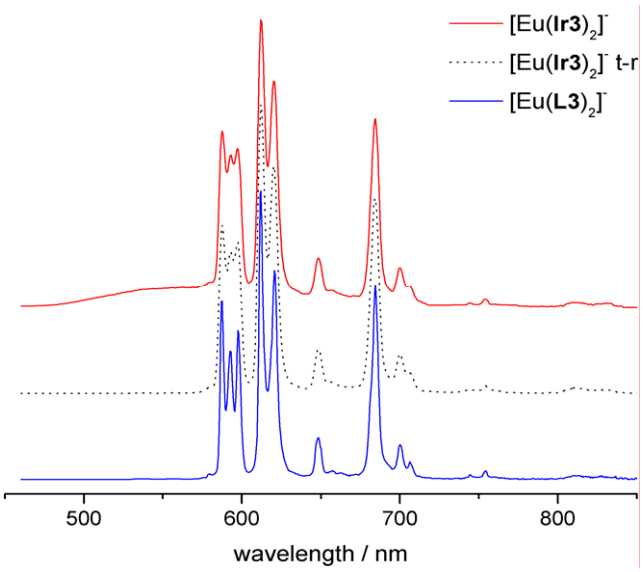

Figure IV.25. Emission spectra of the complex [Eu(**Ir3**)$_2$ in CH_2Cl_2 - MeOH (1:1) solution in fluorescence mode (red line) and time-resolved phosphorescence mode (delay 0.05 ms, black line) and of the complex [Eu(**L3**)$_2$]$^-$ in MeOH solution at $8.5 \cdot 10^{-5}$ mol·dm^{-3} and 298K. Spectra are normalized for the $^7F_2$ band.

Upon enforcement of a short time delay (0.05 ms), the residual emission of the iridium complex disappears, and only the europium-centered emission can be observed. The crystal field splitting in the [Eu(**Ir3**)$_2$]$^-$ emission spectrum is practically identical to that in the [Eu(**L3**)$_2$]$^-$ emission (see Figure IV.25). This clearly confirms that the iridium moiety can act as a sensitizer of europium luminescence in the same way as do directly coordinated ligands, following energy transfer from the iridium MLCT states to the emissive excited state of the europium ion. The europium emission of the heterometallic assembly can be interpreted in terms of a low D_2 symmetry point group, with two C_2 axes perpendicular to a third one, as also shown by the ^{1}H NMR study. The $^5D_0 \rightarrow {}^7F_0$ transition occurs at 580 nm (17 240 cm^{-1}) and is very faint, consistent with the fact that it is symmetry forbidden in the D_2 symmetry group. The $^7F_1$ level presents three main components of the same intensity at 587.5, 593 and 597.5 nm (17 020, 16 870 and 16 735 cm^{-1}), assigned to the allowed magnetic dipole transitions $A \rightarrow B_1$, B_2, B_3 in D_2 symmetry, while the $^5D_0 \rightarrow {}^7F_4$ transition displays a strong band at 684.5 nm (14 610 cm^{-1}) and two smaller ones at 700 and 706.5 nm (14 290 and 14 155 cm^{-1}), attributed to the electric dipole transitions $A \rightarrow B_1$, B_2, B_3. The typical $^5D_0 \rightarrow {}^7F_2$ transition appears only as two bands

(instead of three) at 612 and 620.5 nm (16 340 and 16 115 cm^{-1}) due to the low resolution of the spectrum. For the same reason, the fine structure of the $^5D_0 \rightarrow {}^7F_4$ transition cannot be seen. The same spectrum has been recorded for a solid sample of the $[Eu(\mathbf{Ir3})_2]^-$ complex.

Table IV.7. Summary of the photophysical properties of the heterometallic complexes $[Ln(\mathbf{Ir3})_2]^-$ (Ln = Eu, Nd) in degassed dichloromethane-methanol solutions (at 298K, RT and 77K, LT) and solid state

	τ^{RT}/μs, λ_{em}/nm	τ^{LT}/μs, λ_{em}/nm	Φ_{Ir}/%, λ_{ex}/nm	Φ_{Ln}/%, λ_{ex}/nm	η_{IrLn}/%
$[Eu(\mathbf{Ir3})_2]^-$	0.154(3), 559 $1.87(2)\cdot10^3$, 612	0.500(2), 559 $3.18(6)\cdot10^3$, 612	0.15(02), 350 0.34(02), 375	2.27(02), 350 0.96(01), 375	85-90
$[Eu(\mathbf{Ir3})_2]^-$ solid	$1.94(2)\cdot10^3$, 612	-	0.60(4), 375	10.33(3), 375	
$[Nd(\mathbf{Ir3})_2]^-$	0.200(7), 559 1.52(4), 1077	1.22(3), 559	1.1(7), 350 2.65(5), 375	0.021(1), 350 0.015(1), 375	30-65

To quantify the energy transfer process occurring in the heterometallic complex, lifetime measurements (at room temperature and at 77K) as well as quantum yield measurements have been performed. Due to the sensitivity of iridium emission towards oxygen, all the solution samples have been degassed by three freeze-thaw-pump cycles, while the solid state sample has been conditioned under argon. The values obtained are summarized in Table IV.7. At room temperature in solution, the luminescence decay of the iridium emission in the $[Eu(\mathbf{Ir3})_2]^-$ complex, measured at 559 nm, can be fitted as a monoexponential function and corresponds to a lifetime of 0.154 μs. The europium-centered luminescence, measured at 612 nm, decays monoexponentially with a lifetime of 1.87 ms (more than 3 orders of magnitude longer), indicating the absence of OH oscillators in the inner coordination sphere of the lanthanide ion. The absolute quantum yields of emission, determined upon selective excitation through the iridium levels (375 nm), correspond to 0.34% and 0.96% for the iridium- and europium-centered luminescence, respectively. Comparing with the quantum yield of the **Ir3** complex alone (3.74%) measured in similar conditions, it is evident that the iridium emission is partially quenched in the presence of europium.

In view of the long intermetallic Ir-Eu distance (estimated at 15.0 Å from the crystal structures of the **Ir2** and $[Eu(\mathbf{L3})_2]^-$ complexes), we can assume a dipole-dipole mechanism for the Ir→Eu intermetallic energy transfer. If we consider that the inter-

metallic transfer is the only additional non-radiative process affecting the deactivation of the iridium excited state, its efficiency η_{ET} can be estimated by the formula[79]

$$\eta_{ET} = 1 - \frac{\Phi_{IrEu}}{\Phi_{Ir}} = 1 - \frac{\tau_{IrEu}}{\tau_{Ir}} = \frac{1}{1 + \left(\frac{R}{R_0}\right)^6} \qquad \text{(IV.1)}$$

where Φ_{IrEu} and τ_{IrEu} are the iridium quantum yield and lifetime, respectively, in the heterometallic complex, and Φ_{Ir} and τ_{Ir} are the iridium quantum yield and lifetime in the **Ir3** complex alone; R is the donor acceptor distance (15.0 Å) and R_0 is the distance for 50% transfer. From the quantum yield data above, we calculate η_{IrEu} = 90% at room temperature, which indicates a very good energy transfer. However, the emission of europium remains faint, probably due to the small quantum yield of the iridium sensitizer, as well as to additional radiationless processes involved in the decay of europium luminescence. Measuring the absolute quantum yields upon excitation at 350 nm, where the terpyridine-based organic chromophore absorbs as well, results in a better value for the europium efficiency (2.27%). The R_0 distance for 50% transfer can be estimated at 20 Å, implying that for a quantitative Ir→Eu energy transfer, the distance between the two metals should be less than 9 Å.

At 77K in a rigid matrix, the luminescence decay of the iridium and europium centered emissions have been recorded and can be fitted to monoexponential functions corresponding to lifetimes of 0.500 μs and 3.18 ms, respectively. From this, the efficiency of the intermetallic Ir→Eu transfer at low temperature can be estimated using the above equation, giving 85%, in very good agreement with the value obtained at room temperature. The rate constant k_{ET} associated with the energy transfer process may be obtained from the equations $\tau_{IrEu} = (k_r + k_{nr} + k_{ET})^{-1}$ and $\tau_{Ir} = (k_r + k_{nr})^{-1}$, where k_r and k_{nr} are the radiative and non-radiative deactivation rates, giving

$$k_{ET} = \frac{1}{\tau_{IrEu}} - \frac{1}{\tau_{Ir}} \qquad \text{(IV.2)}$$

Thus, we calculate $k_{ET} = 1.71 \cdot 10^6\ s^{-1}$ which indicates a very fast energy transfer.

The overall sensitization efficiency η_{sens} relating the absolute quantum yield Q with the intrinsic quantum yield of the lanthanide ion Q_{Ln}^{Ln} is given by the formula

$$Q = \eta_{sens}\, Q_{Ln}^{Ln} = \eta_{sens}\left(\frac{\tau_{obs}}{\tau^{rad}}\right) \qquad \text{(IV.3)}$$

The sensitization efficiency groups all the factors influencing the antenna mechanism: absorption of light by the antenna, transfer of energy to the antenna emissive level (for example ILET in the iridium complex), transfer of energy to the lanthanide levels, as well as the non-radiative deactivation processes associated. If we assume that the dipole strength of the magnetic dipole Eu($^5D_0 \rightarrow {}^7F_1$) transition is constant, the radiative lifetime τ^{rad} of the Eu($^5D_0$) level is given by the equation below,[5] in which $A_{MD,0}$ = 14.65 s^{-1} is the spontaneous emission probability of the Eu($^5D_0 \rightarrow {}^7F_1$) transition, n is the refractive index of the solvent (n = 1.378) and I_{MD}/I_{tot} is the ratio of the area of the Eu($^5D_0 \rightarrow {}^7F_1$) transition to the area of the $^5D_0 \rightarrow {}^7F_J$ transitions (J = 0-6) in the [Eu(**Ir3**)$_2$]$^-$ complex.

$$\tau^{rad} = \frac{1}{A_{\mathrm{MD},0} \cdot n^3} \cdot \left(\frac{I_{\mathrm{MD}}}{I_{\mathrm{tot}}}\right) \qquad \text{(IV.4)}$$

Experimentally, the ratio I_{MD}/I_{tot} = 0.163 is determined from the solution emission spectrum of [Eu(**Ir3**)$_2$]$^-$ at room temperature, and so the radiative lifetime τ^{rad} = 4.25 ms. The intrinsic quantum yield Q_{Ln}^{Ln} = 44%, and so the sensitization efficiency η_{sens} = 2%, which is very inefficient.

In solid state, the luminescence decay of the europium centered emission (612 nm) in the [Eu(**Ir3**)$_2$]$^-$ complex corresponds to a lifetime of 1.94 ms, in very good agreement with the value obtained in solution (1.87 ms), considering the experimental errors. However, the absolute quantum yield of the europium emission, determined upon selective excitation through the iridium levels (375 nm), is more than one order of magnitude larger (10.33%) compared to the value obtained in solution. This difference could be ascribed to an improved emission efficiency of the **Ir3** antenna in solid state, however the quantum yield of **Ir3** has not yet been determined to confirm this hypothesis.

The photophysical properties of the [Nd(**Ir3**)$_2$]$^-$ complex have been measured in situ in a dichloromethane-methanol solution. The luminescence spectrum recorded

through selective excitation at the iridium levels (375 nm) exhibits both the iridium and neodymium luminescence, as shown in Figure IV.26. As the visible and NIR emission was recorded on different detectors, the intensity of the bands has been normalized and are not related. Quantum yield determination *(vide infra*) allows however the quantitative estimation of the emission efficiencies.

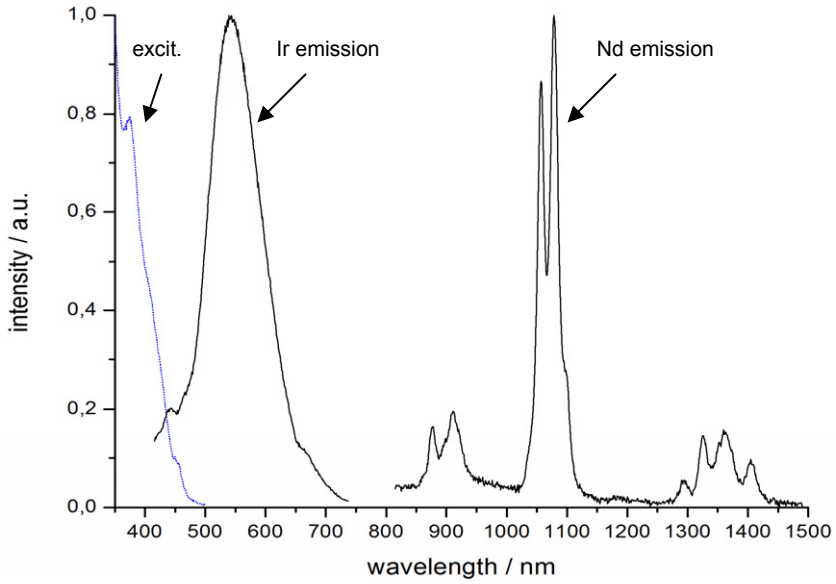

Figure IV.26. Normalized excitation (blue dotted line) and emission spectra (black continuous line) of the complex $[Nd(\mathbf{Ir3})_2]^-$ in $4.5 \cdot 10^{-5}$ mol·dm^{-3} CH_2Cl_2 - MeOH (1:1) solution at room temperature.

The iridium emission in the $[Nd(\mathbf{Ir3})_2]^-$ complex is centered at 543 nm and is similar to that of the **Ir3** complex alone, originating from a mixed ^{3}MLCT-^{3}LC state. The neodymium emission displays three main bands in the spectral ranges 850-950, 1025-1125 and 1275-1450 nm, which are assigned to the transitions from the $^4F_{3/2}$ level to the $^4I_{9/2}$, $^4I_{11/2}$ and $^4I_{13/2}$ sublevels, respectively. The components are very similar to those of the other terpyridine-tetrazole based complexes previously studied (see Chapter II.2.3. c)), and they show 2, 2, and 4 peaks, respectively (at 877, 911, 1057, 1078, 1294, 1326, 1360 and 1404 nm) for the three bands.

The excitation spectra of the $[Nd(\mathbf{Ir3})_2]^-$ complex, obtained while monitoring the $^4F_{3/2} \rightarrow {}^4I_{11/2}$ neodymium transition at 1077 nm or the iridium emission at 559 nm, are identical and show a low energy maximum at 375 nm, which can be attributed to the

singlet dπ(Ir)→π(F_2ppy) MLCT transition in the iridium complex, and a faint shoulder around 450 nm, which can be assigned to the corresponding triplet dπ→π* MLCT transition (Figure IV.26). This clearly indicates that the sensitization of neodymium emission is due to an energy transfer from the iridium MLCT states to the $^4F_{3/2}$ emissive excited state of the neodymium ion.

Lifetime measurements (at room temperature and at 77K), as well as quantum yield measurements have been performed in situ, and the values obtained are also summarized in Table IV.7. At room temperature in solution, the luminescence decay of the iridium emission in the [Nd(**Ir3**)$_2$]$^-$ complex, measured at 559 nm, can be fitted as a monoexponential function and corresponds to a lifetime of 0.200 μs, slightly longer than in the [Eu(**Ir3**)$_2$]$^-$ complex. The neodymium-centered luminescence, measured at 1077 nm, decays monoexponentially with a lifetime of 1.52 μs, similar to the one obtained before through terpyridine-based sensitization in the complex [Nd(**L1**)$_2$]$^-$. At 77K in a rigid matrix, the luminescence decay of the iridium centered emission can be fitted to monoexponential functions corresponding to a lifetime of 1.22 μs, which is longer than in the case of the [Eu(**Ir3**)$_2$]$^-$ complex, but shorter compared to the **Ir3** complex alone. This indicates that the Ir→Nd energy transfer occurring at low temperature has a reduced efficiency (estimated at 65%) compared to the Ir→Eu transfer (85%). The absolute quantum yields of emission, determined at room temperature upon selective excitation through the iridium levels (375 nm), correspond to 2.65% and 0.015% for the iridium- and neodymium-centered luminescence, respectively. Taking into account the quantum yield of the **Ir3** complex alone (3.74%) measured in similar conditions, the efficiency of the Ir→Nd energy transfer at room temperature can be estimated at only 30%, which is roughly half compared to the low temperature value. The variation could be attributed to the difference in the **Ir3** emission properties in the rigid matrix, compared to the solution (see Figure IV.18), which could result in a different sensitization mechanism. Measuring the absolute quantum yield upon excitation at 350 nm, where the terpyridine-based organic chromophore absorbs as well, results in a better value for the neodymium

efficiency (0.021%), which is identical, within the experimental error, to the one obtained in solid state for the complex $[Nd(\mathbf{L1})_2]^-$.

IV.3. Bis-iridium complexes based on terpyridine-carboxylate

IV.3.1. Literature examples

Covalently linked bimetallic complexes of second and third row d^6 transition metals are of particular interest for the study of photo-induced electron and energy transfers. In the same time, they are promising precursors for more sophisticated molecular materials and devices with applications in electronics and light energy conversion.[237] A suitable choice of mononuclear building blocks and bridging ligands can lead to the construction of bi- or polynuclear metal complexes with supramolecular structure, which can exhibit an excited state nature significantly different from that of simple mononuclear complexes. In the polynuclear complexes, polyimine ligands used as bridging ligands have been widely studied, in particular with Ru(II) and Os(II) as metal centers. The photochemistry and photophysics of such complexes have been recently reviewed.[238, 239]

However up to now, binuclear complexes containing cyclometalated Ir(III) centers bridged by polyimine ligands have not been much investigated (probably due to the synthetic difficulties), in spite of the interest associated with iridium complexes, as a result of their exciting luminescence properties (see Chapter IV.1.5. and references therein).

One of the first examples has been published[217] by the group of De Cola, who synthesized and studied phenyl-pyridine cyclometalated heteroleptic bis-iridium complexes bridged by phenylene units (see Figure IV.27). The use of a substituted bipyridine ancillary ligands renders the final assembly positively charged. The bimetallic complexes were synthesized by Suzuki coupling of the individual iridium units. The mixed ^{3}MLCT - ^{3}LC lowest excited state involves the substituted bipyridine ligand, and is significantly delocalized over the phenylene units. Using time-resolved emission and

transient absorption spectroscopy, the equilibrium between the two states and the exact nature of the lowest emitting level was investigated, and it was found that the properties strongly depend on the number of phenylene units attached on the bipyridine since the excited state energy of the ^{3}LC decreases with increasing of the conjugation and thus an inversion of states (^{3}MLCT and ^{3}LC) becomes possible. The quantum yields measured in de-aerated solutions range from 9% (n=1) to 18% (n=2). The work was later extended to the analogue difluoro-substituted phenylpyridine cyclometalated complexes,[240] which show similar characteristics (quantum yield 12% in de-aerated conditions for n=2).

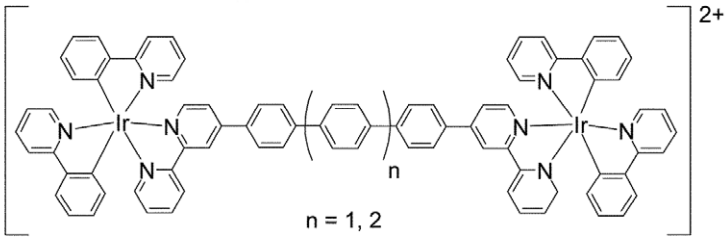

Figure IV.27. Example of a bimetallic iridium complex (from ref.[217])

Another contribution came from Tsuboyama *et al.*, who reported[241] a bis-iridium complex based on a dipyridinylbenzene bridging ligand (Figure IV.28). The one-pot synthetic yield was however very low (3%), characteristic of heteroleptic tris-cyclometalated iridium complexes where little ligand specificity is involved. The rest of the iridium complexes obtained in the reaction were not identified. A crystal structure was however obtained, proving the *fac*-*fac* octahedral coordination of the iridium moieties. The emission of the complex was red-shifted by about 150 nm compared to the homoleptic tris-cyclometalated *fac*-Ir(ppy)$_3$ complex, and was ascribed to an ^{3}MLCT state localized on the central ligand, however the quantum yield is one order of magnitude smaller than in the *fac*-Ir(ppy)$_3$ complex (4% versus 40%, respectively).

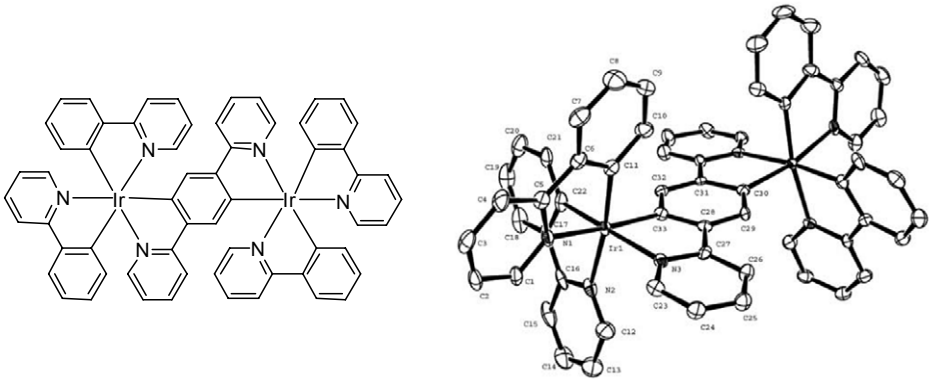

Figure IV.28. Example of a bimetallic iridium complex and its crystal structure (from ref.[241])

In a more recent report, Auffrant *et al.* described[242] a charged bis-iridium complex similar to the one reported earlier by De Cola, consisting of phenylpyridine cyclometalated complexes bridged by a dipyridyl-phenantroline ancillary ligand (see Figure IV.29). The high-yield synthesis involved direct mixing of the chloro-bridged bis-iridium precursor with the tetradentate dipyridyl-phenantroline ligand. The complex was obtained as a mixture of three stereoisomers (a meso form and a racemic pair), which were separated by ion-pair chromatography with a chiral resolving anion. The crystal structure of the meso form was also reported, showing the location of the two iridium moieties above and below the medial plane of the bridging ligand. The absorption and emission spectra of the three isomers show very small variations, and the emission was assigned to a MLCT state. The quantum yields have been measured only in aerated conditions, and they show characteristic low values (0.6 %), due to the quenching of the triplet excited state by molecular oxygen.[182]

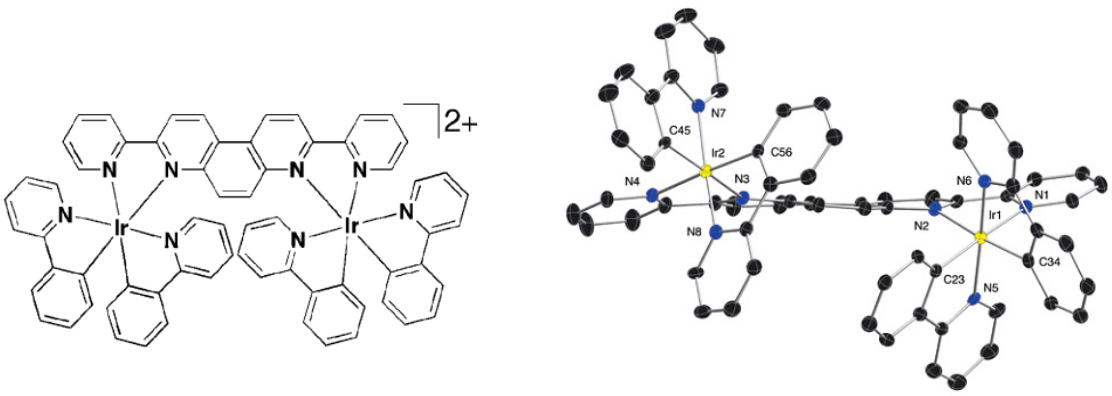

Figure IV.29. Example of a bimetallic iridium complex and its crystal structure (from ref.[242])

In spite of these very interesting reports, there is still a strong interest for synthesizing new types of bis-iridium architectures and studying the emission properties of such complexes. Particularly, an efficient synthetic route for obtaining neutral bimetallic iridium complexes for possible applications in the optoelectronics is still to be reported.

During the course of our synthetic effort directed at the formation of heterometallic iridium-lanthanide complexes, we have isolated a homo-bimetallic heteroleptic complex containing two iridium centers, each hexa-coordinated by two phenylpyridine cyclometalating ligands and the terminal pyridine-carboxylate part of a terpyridine unit which acts as bridging moiety (see Figure IV.7, page 172). Therefore, we set out to optimize the synthetic conditions for the formation of such assemblies, and to study their photophysical properties.

IV.3.2. Synthesis of bis-iridium complexes

To evaluate the properties of bimetallic iridium complexes containing both fluorine-substituted as well as unsubstituted phenylpyridine cyclometalating ligands, we have prepared (see Scheme IV.19) the Ir(III) μ-chloro-bridged dimer **44**, using a similar procedure[188] to that employed for the fluorinated analogue **31** which was described above.

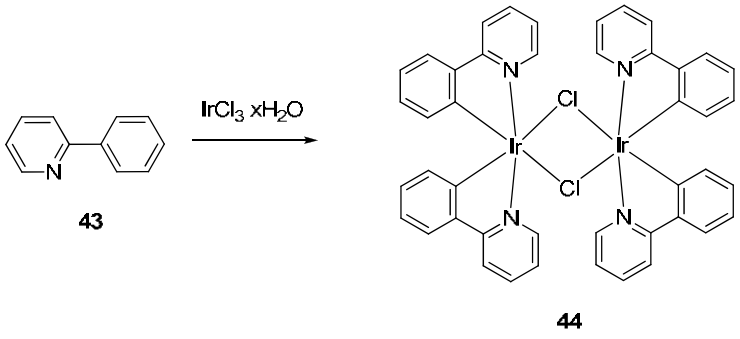

Scheme IV.19. Conditions: ethoxyethanol-water, 120°C (75%)

Our strategy for the formation of neutral bis-iridium complexes bridged by a polyimine ligand is rather simple and does not require complicated palladium-catalyzed coupling procedures as in the case of other bis-iridium complexes. From the iridium

precursor **44**, reaction with the potassium salt of terpyridine carboxylate **L2** in ethoxyethanol at 60°C lead to the formation of the desired bis-iridium complex **Ir4**, according to Scheme IV.20. The resulting potassium chloride precipitated from the reaction mixture. A similar procedure employing the fluorinated μ-chloro-bridged precursor **31** resulted in the formation of the bis-iridium complex **Ir5**. The yield of the synthesis of **Ir4** is very good (86%), however the fluorinated analogue **Ir5** proved to be more difficult to isolate due to a difference in solubility, leading to a lower yield (25%). The reaction conditions in this case need to be further optimized.

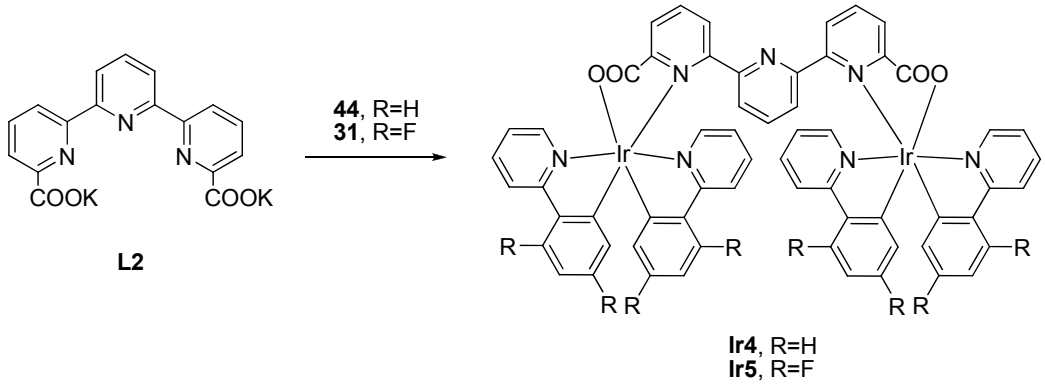

Scheme IV.20. Conditions: ethoxyethanol, 60°C (86% for **Ir4**, 25% for **Ir5**)

The bis-iridium complexes **Ir4** and **Ir5** were fully characterized by ^{1}H NMR spectroscopy, mass spectrometry and elemental analysis (see the Experimental part).

IV.3.3. Characterization of bis-iridium complexes

a) Molecular and crystal structure

Single crystals suitable for X-ray analysis were obtained for the complex **Ir5** by slow evaporation of a dichloromethane solution. The structure was solved in the P1 space group of the triclinic system. Selected distances and angles are given in Table IV.8, while the full crystallographic data is available in the Appendix.

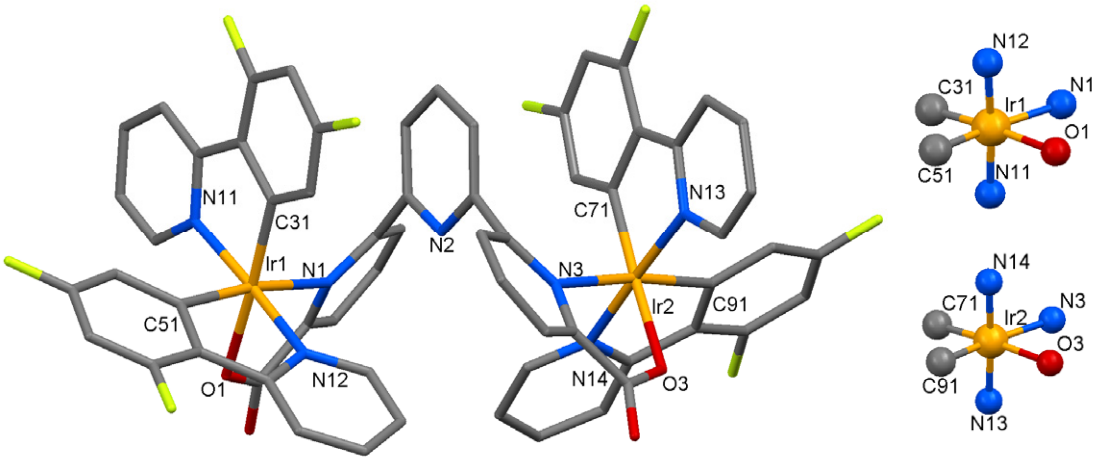

Figure IV.30. Structure of the iridium complex **Ir5** (left)
and the N-*trans* arrangement of the coordination ligands around the iridium atoms (right)

Table IV.8. Selected bond distances (Å) and angles (°) in the structure of bis-iridium complex **Ir5**

Ir1-C31	1.997(8)	C31-Ir1-C51	87.0(3)	C71-Ir2-C91	86.3(3)
Ir1-C51	1.997(8)	C31-Ir1-N12	98.8(3)	C71-Ir2-N14	99.2(3)
Ir1-N12	2.036(6)	C51-Ir1-N12	80.0(3)	C91-Ir2-N14	80.8(3)
Ir1-N11	2.043(6)	C31-Ir1-N11	80.4(3)	C71-Ir2-N13	79.8(3)
Ir1-O1	2.132(6)	C51-Ir1-N11	96.0(3)	C91-Ir2-N13	95.9(3)
Ir1-N1	2.216(7)	N12-Ir1-N11	175.9(3)	N14-Ir2-N13	176.7(3)
Ir2-C71	1.983(8)	C31-Ir1-O1	175.2(3)	C71-Ir2-O3	174.8(3)
Ir2-C91	2.002(8)	C51-Ir1-O1	94.2(3)	C91-Ir2-O3	95.5(3)
Ir2-N14	2.039(7)	N12-Ir1-O1	86.0(2)	N14-Ir2-O3	85.9(2)
Ir2-N13	2.050(7)	N11-Ir1-O1	94.9(2)	N13-Ir2-O3	95.2(3)
Ir2-O3	2.139(6)	C31-Ir1-N1	101.4(3)	C71-Ir2-N3	100.8(3)
Ir2-N3	2.205(7)	C51-Ir1-N1	171.6(3)	C91-Ir2-N3	172.9(3)
		N12-Ir1-N1	97.9(2)	N14-Ir2-N3	97.7(2)
		N11-Ir1-N1	86.1(2)	N13-Ir2-N3	85.6(3)
		O1-Ir1-N1	77.6(3)	O3-Ir2-N3	77.4(2)

In the structure, each iridium atom is hexa-coordinated by the carbon and nitrogen atoms of two cyclometalating difluorophenylpyridine ligands and the nitrogen and oxygen atoms of the terminal picolinate moiety of the terpyridine carboxylate ligand, as seen in Figure IV.30 (left). The two iridium centers have a distorted octahedral coordination geometry, retaining the *cis*-C,C *trans*-N,N chelate disposition of the chloride-bridged precursor **31** (see Figure IV.30, right). The Ir-C bond distances (on average 1.995 Å) are slightly shorter than the Ir-N bond distances (on average 2.042 Å) in the cyclometalating ligands, and the values are similar to those found in the literature[186, 212, 229]

and in our previous iridium complexes **31**, **Ir1** and **Ir2**. The Ir-O bond length (mean 2.136 Å) and the Ir-N1 and Ir-N3 bond lengths (mean 2.211 Å) are longer than the usual values and reflect the large *trans* influence of the phenyl groups. The N12-Ir1-N11 and N14-Ir2-N13 angles are on average 176.3°, similar to the C31-Ir1-O1 and C71-Ir2-O3 angles (average 175.0°), and reflect the orthogonality of the ligands. Due to steric hindrance, the terminal pyridine unit is tilted, decreasing the C51-Ir1-N1 and C91-Ir2-N3 angles to an average of 172.3°.

The largely distorted terpyridine unit acts as a bridge between the two iridium centers, bringing them at a non-bonding intermetallic distance of 7.467. Due to the constraints of accommodating the iridium complexes, the terminal pyridine ring planes are twisted with 61.9° compared to the central ring plane.

Intramolecular π-π interactions occur between the central pyridine and the cyclometalating phenyl rings, situated at a distance of 3.225 and 3.241 Å, respectively, as seen in Figure IV.31.

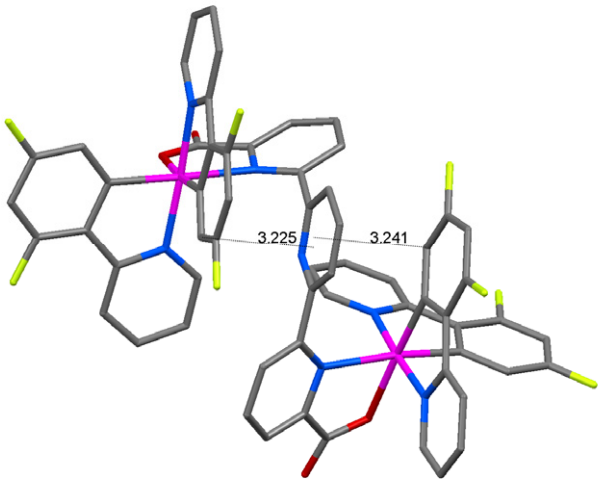

Figure IV.31. Intramolecular π-π interactions in the structure of the iridium complex **Ir5**

b) NMR characterization in solution

The ^{1}H NMR spectrum of the bis-iridium complex **Ir4** in a deuterated tetrachloroethane solution at 298K indicates the presence of one set of signals, with 21 resonances for the 41 protons in the structure of the complex, in the range 8.7-5.3 ppm, as shown in Figure

IV.32a. This indicates the equivalence in solution of the two iridium centers on the NMR timeline, due to the presence of a C_2 axis passing through the central pyridine ring, as seen in the crystal structure of **Ir5**. Within each iridium coordination sphere, the two cyclometalating ligand are non-equivalent, as observed for the other picolinate-based iridium complexes **Ir1**-**Ir3**. The high-field resonances (two doublets at 5.70 and 5.34 ppm) have been attributed to the protons situated ortho to the cyclometalating carbon, known to experience the largest shielding of any of the ligand protons.[212]

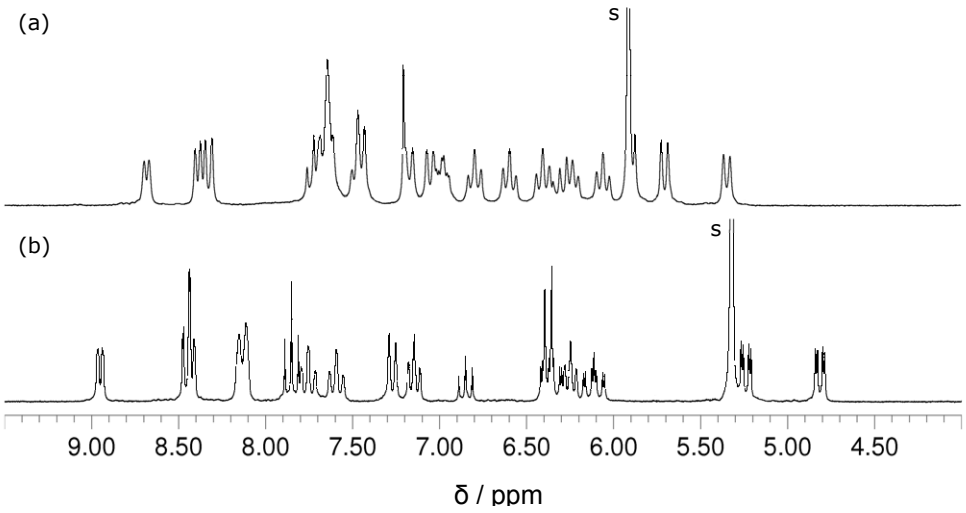

Figure IV.32. ^{1}H NMR spectra of iridium complexes **Ir4** in $C_2D_2Cl_4$ solution (a) and **Ir5** in CD_2Cl_2 solution (b) at room temperature

A similar ^{1}H NMR spectrum has been obtained for the fluorinated bis-iridium complex **Ir5**, in a deuterated dichloromethane solution at 298K (see Figure IV.32b). The complex shows 17 resonances for the 33 protons in the structure, in the range 9.0-4.8 ppm. This agrees with the equivalence of the two iridium centers, due to the presence of a C_2 axis along the central pyridine ring, as in the previous case of **Ir4**.

c) Photophysical properties

The absorption spectra of the complexes **Ir4** and **Ir5** (and the already-known complex FIrpic[228] for comparison) in a dichloromethane solution at room temperature are given in Figure IV.33, and are characteristic of the (C^N)-cyclometalated iridium complexes.[185, 186, 200]

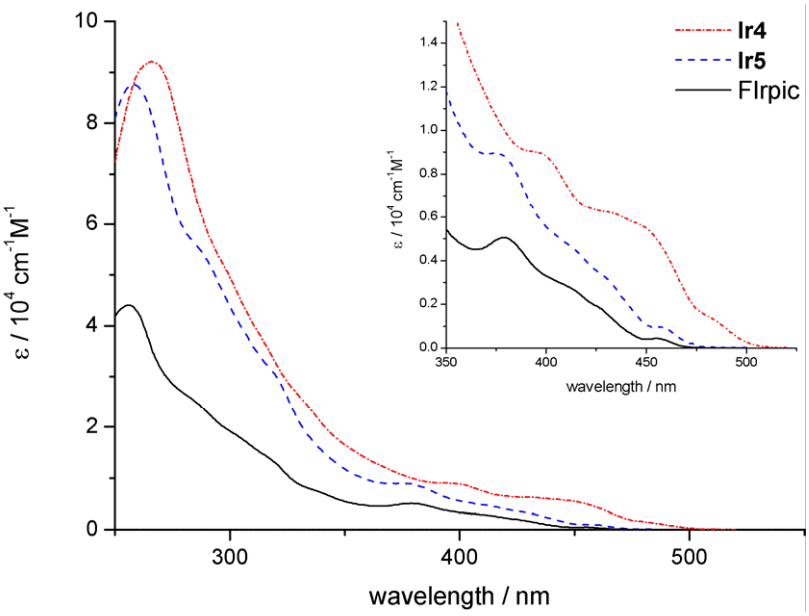

Figure IV.33. UV-vis absorption spectra of the complexes **Ir4** and **Ir5** and FIrpic in a 10^{-4} mol·dm^{-3} CH_2Cl_2 solution at 298K. The inset shows a magnified view of the spectra between λ = 350-550 nm.

The bis-nuclear compounds show intense bands in the region 250 - 350 nm which can be assigned to the spin allowed $^1(\pi\text{-}\pi^*)$ ligand-centered (LC) transitions. The high energy maximum of **Ir4** at 266 nm (ε ≈ $9.2\cdot10^4$ M^{-1}·cm^{-1}) is shifted hypsochromically to 258 nm (ε ≈ $8.8\cdot10^4$ M^{-1}·cm^{-1}) in **Ir5**. Compared to the mononuclear complex FIrpic, the molar extinction coefficient is roughly doubled in the bis-complex **Ir5**. In the lower energy region (360-500 nm), the spectra of the complexes exhibit weaker (ε ≈ 5-$9\cdot10^3$ M^{-1}·cm^{-1}) absorption tails (shown in inset in Figure IV.33), which can be assigned to the singlet dπ(Ir)→π(ppy) MLCT transitions, as reported for similar cyclometalated complexes.[186, 231] In the case of **Ir5**, these bands are blue-shifted with cca. 20 nm compared to the non-fluorinated analogue **Ir4**. The formally spin forbidden triplet dπ(Ir)→π*(ppy) MLCT transitions gain intensity by mixing with the higher lying ^{1}MLCT transition through the strong spin-orbit coupling of iridium and appear as weak shoulders at 480 and 457 nm in **Ir4** and **Ir5**, respectively (ε ≈ 1-1.5·10^3 M^{-1}·cm^{-1}).

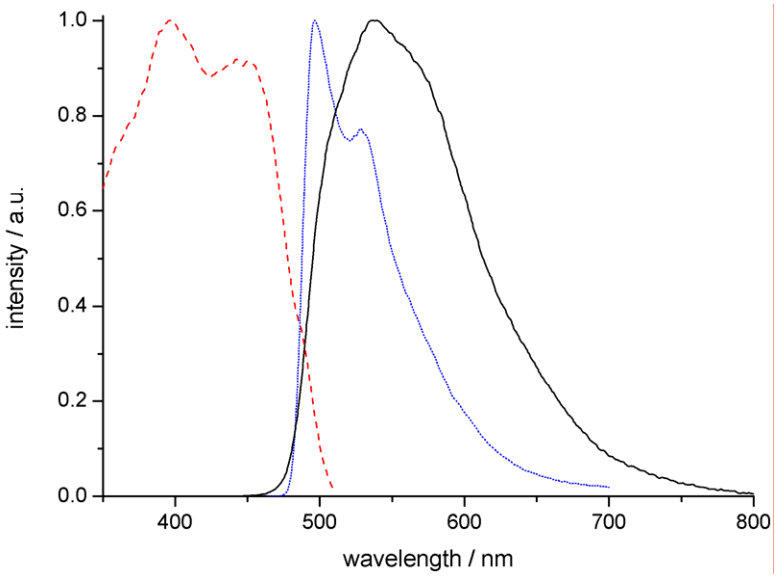

Figure IV.34. Normalized excitation(dashed red line) and emission spectra of the complex **Ir4** in a 10^{-4} mol·dm^{-3} CH_2Cl_2 solution at 298 K (continuous black line) and 77K (dotted blue line).

The emission and excitation spectra of the **Ir4** complex in dichloromethane solution at room (298K) and low (77K) temperature are compared in Figure IV.34. The emission spectrum is dominated by a broad, featureless band centered at 538 nm, displaying two faint shoulders, at higher (508 nm) and respectively lower (570 nm) energy, which indicates a prevalent ^{3}MLCT character, as described before for monometallic complexes coordinated by similar ligands.[200] Compared to those, a red-shift of 24 nm is observed when passing to the bi-metallic specie **Ir4** (as mentioned in previous reports[240]), but the shape of the spectrum remains the same. Upon freezing the solution at 77K, the emission becomes structured, with two bands at 496 and 529 nm, the first being more intense. Compared to the room temperature spectrum, a hypsochromic shift of 9 nm (measured between the equivalent bands) occurs in glass matrix. Such a structured emission is characteristic of the phenyl-pyridine ligand-centered states, and seems to indicate that the overall emission is due to a mixing of ^{3}MLCT and ^{3}LC levels. Upon freezing the solution, the charge-transfer state is known to display a characteristic rigidochromic effect[182] and its energy level rises (due to the lack of solvent stabilization), while the ligand centered state located on the pheny-pyridine ligands is less affected by the solvation. Therefore, due to the possible inversion of energetic levels occurring in the glass matrix, the emission may

be dominated in such cases by the ^{3}LC(ppy) state, as observed before,[199, 240] and we believe a similar situation is present in our system. The excitation spectrum reproduces the shape of the components of the absorption spectrum recorded at the same concentration, with two main bands corresponding to the ^{1}MLCT state at 397 and 450 nm and the spin forbidden ^{3}MLCT transition appearing as a shoulder at 485 nm.

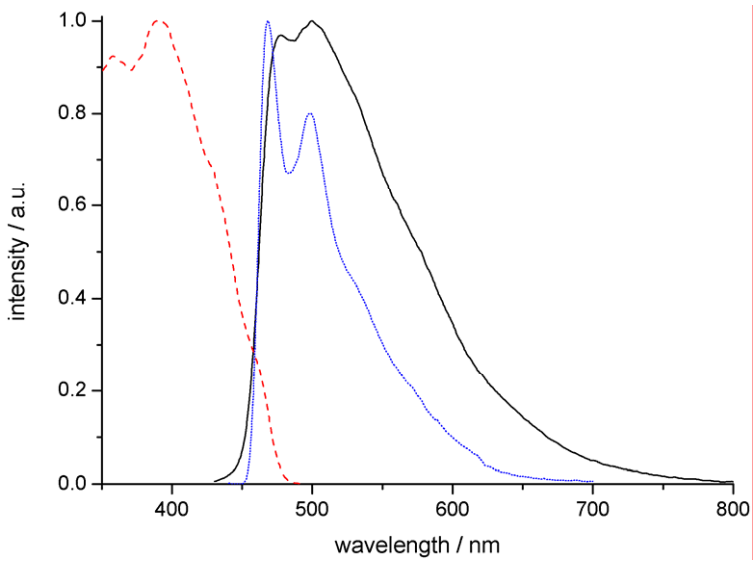

Figure IV.35. Normalized excitation(dashed red line) and emission spectra of the complex **Ir5** in a 10^{-4} mol·dm^{-3} CH_2Cl_2 solution at 298 K (continuous black line) and 77K (dotted blue line).

For the fluorinated analogue **Ir5** complex, the emission and excitation spectra in dichloromethane solution at room (298K) and low (77K) temperature are compared in Figure IV.35. The emission is characterized by a broad band displaying a finer structure, with two components at 477 and 500 nm. In agreement with previous assignments on the monometallic specie FIrpic, the emission of **Ir5** could be ascribed to a mixed ^{3}MLCT-^{3}LC state. Compared to the monometallic complex, a red-shift of 10 nm and broadened spectral features indicate however a more prevalent charge-transfer character. Upon freezing the solution at 77K, the emission becomes more structured, and the two bands are hypsochromically shifted by 10 nm, appearing now at 468 and 499 nm. In fact, the low temperature emission spectrum of **Ir5** and the solution spectrum of FIrpic are virtually identical. The same destabilization of the ^{3}MLCT state in rigid matrixes, evoked for **Ir4**

(*vide supra*), is expected to influence the emissive properties of the **Ir5** complex, resulting in a mainly ^{3}LC emission from the fluorinated phenyl-pyridine unit at low temperatures.

Table IV.9. Summary of photophysical properties for the complexes **Ir4** and **Ir5** measured in dichloromethane solutions at 298K (RT) and 77K (LT).

	λ_{ex}/nm	λ_{em}/nm	τ^{RT}/μs	τ^{LT}/μs	$k_r/10^5$ s^{-1}	Φ/%
Ir4	375	533	0.09(1)	5.81(2)	1.72	17.73(27)
Ir5	375	533	0.155(6)	3.193(2)	3.13	4.84(09)

The lifetimes and the absolute quantum yields determined for the complexes **Ir4** and **Ir5** in degassed dichloromethane solutions are given in Table IV.9. The room temperature emission has a short monoexponential decay which corresponds to lifetimes of 0.09 and 0.155 μs for the complexes **Ir4** and **Ir5**, respectively, while the low temperature emission is much longer, corresponding to lifetimes of 5.81 and 3.19 μs, respectively. The radiative rate constants can be calculated as $k_r = \tau^{-1}$ and amount to $1.72 \cdot 10^5$ and $3.13 \cdot 10^5$ s^{-1}, for the two complexes, respectively. The absolute emission quantum yields are sizeable, the non-fluorinated complex **Ir4** showing a larger value (17.7%) than the fluorinated one (4.8%), comparable with similar bis-iridium complexes.[217, 240]

IV.4. Conclusions

In this chapter, we have presented new types of polymetallic architectures based on iridium complexes, which can be potentially used for the sensitization of lanthanide emission, in both visible and near-infrared regions. Numerous examples of other d-f polymetallic complexes have been published, however the role of iridium as antenna for lanthanides has been less investigated, probably due to its difficult chemistry. This is surprising considering the popularity of iridium complexes in the field of organic light emitting diodes, and the extended possibilities of modulating the lowest excited states of these complexes.

We have proven this concept by constructing a heterometallic assembly containing an iridium antenna covalently linked to a lanthanide complex based on the terpyridine-tetrazole ligand. The detailed strategies for the synthesis of the iridium 'complex as ligand' have been presented, together with the characterization of the intermediate iridium complexes. The emission in the final ligand iridium **Ir3** was assigned to a mixed MLCT-LC state containing a substantial contribution from the ancillary unit. In the final heterometallic complexes $[Eu(\mathbf{Ir3})_2]^-$ and $[Nd(\mathbf{Ir3})_2]^-$, the Ir→Ln energy transfer was clearly evidenced, and its efficiency was estimated at 85% and 65%, respectively. In spite of this fast and efficient intermetallic transfer, the lanthanide quantum yields upon excitation of the iridium antenna remain low (1% for the europium emission), due to a low overall sensitization efficiency.

In addition, we have also presented homopolymetallic architectures containing covalently-linked bis-iridium complexes bridged by a terpyridine-carboxylate unit. The facile synthetic protocol, which avoids complicated palladium-coupling reactions, together with the good photophysical properties of the resulting complexes (quantum yields up to 18%), suggest the potential of such architectures for the development of polymetallic assemblies with interesting optical and redox properties.

Chapter V
Final conclusions and perspectives

The main objective of this work was related to a better understanding of the structure-property relationship in emissive lanthanide complexes with potential applications in optoelectronics. We have achieved this by a careful design of lanthanide antennas based on either organic chromophores or transition metals as ligands, followed by a study of the structural and photophysical properties of the resulting complexes, in order to estimate and further predict the sensitization efficiencies.

In the first line of research, we have designed and synthesized an extensive series of ligands based on terpyridine-, bipyridine- and pyridine-tetrazole organic chromophores, which proved to be very efficient in sensitizing the luminescence of lanthanide ions, both in the visible and the NIR region. We have shown that the resulting complexes are stable in solid state as well as in solution, due to the high acidity of the tetrazole group, the conditional stability constants of the tetrazolate-based complexes being comparable to those of the carboxylate analogues. Furthermore, the different electronic effects of the tetrazolate, compared to the carboxylate, result in increased absorption towards the visible region, with potential benefits for the development of biolabels. The luminescence efficiencies of the complexes are very high, reaching 61% and 65% for the $[Eu(\mathbf{L10})_3]^{3-}$ and $[Tb(\mathbf{L10})_3]^{3-}$ complexes, respectively, among the highest values reported in literature.

Modulation of the ligand triplet state was achieved both by an interplay of the tetrazolate and carboxylate group, which allows a fine tuning, but also by the use of various substituents appended to the terpyridine chromophore. The resulting complexes show markedly different spectroscopic and photophysical properties. Absorption wavelengths were increased towards the visible region, the complex $[Nd(\mathbf{L6})_2]^-$ having good absorption properties even at 450 nm. The values of the quantum yields were

especially influenced, and were discussed in terms of ligand energy levels. Particularly, very good emission for neodymium (0.29%) was obtained by lowering the ligand triplet state in the $[Nd(\mathbf{L4})_2]^-$ complex.

In addition to modifying the energy levels of the chromophores, the appended substituents allow facile functionalization for various applications. Additional substituents, as well as solubilizing groups, can be added with ease, resulting in a modification of the energy levels and of the physico-chemical properties of the complexes. Furthermore, as the complexes are charged, their solubility can be strongly modified by simply changing the counterions, as demonstrated with the trioctylammonium salt of $[Eu(\mathbf{L10})_3]^{3-}$, which now becomes a candidate for the development of solution-processed optoelectronic devices.

In perspective, the substitution of the terpyridine-tetrazole ligand with electro-withdrawing groups such as cyano or nitro could decrease the triplet state energy and improve the emission efficiency of the terbium complexes. Dimerization of the bromophenyl-terpyridine-tetrazole ligand via coupling reactions would easily give dual-site ligands suitable for the formation of coordination polymers with controlled properties. The introduction of the pyridine-tetrazole chromophore in different ligand topologies, as recently demonstrated in our laboratory,[118] would lead to improved stabilities in water, with potential applications in the development of lanthanide probes. Moreover, further modification of the tetrazole-based complexes would result in neutral architectures which could be used as emitting layers in vacuum-processed organic light emitting diodes.

In the second line of research, we have introduced an anionic terpyridine chromophore in a series of stable, neutral lanthanide complexes containing additional β-diketonate units. This lead to improved stabilities compared to the majority of lanthanide complexes used in optoelectronics, which are based on neutral bidentate chromophores such as phenantroline. Two different neutral heteroleptic lanthanide architectures were synthesized and fully characterized, one based on a monoanionic asymmetric terpyridine-carboxylate chromophore, completed by two β-diketonate units, and the second one based on a dianionic terpyridine-bistetrazole chromophore, completed by one β-diketonate unit.

Good emission efficiencies were obtained for all the complexes (reaching 41% for the europium complex of terpyridine-carboxylate) which led us to testing the materials as emitting layers in organic light emitting diodes. Preliminary studies have shown that the devices exhibit typical diode behavior, the characteristic bright red or green luminescence of europium or terbium being observed. Further improvements in device architecture would lead to better electroluminescence efficiencies, however the results indicate the high potential of this class of neutral lanthanide complexes for applications in OLEDs.

Benefiting from the facile functionalization of the terpyridine-tetrazole chromophore, we have also appended to this ligand a tripodal anchor capable of forming Si-C bonds on the silicon surface, for studying the surface functionalization with lanthanide complexes. Preliminary results suggested the formation of heteroleptic lanthanide complexes with the ligands grafted on the surface, although further studies need to be performed for analyzing the functionalized substrates.

In the third line of research, we have designed new types of polymetallic architectures based on iridium complexes for the sensitization of lanthanide emission. Numerous examples of other d-f polymetallic complexes have been published, however the role of iridium as lanthanide antenna has been less investigated. In this work, we have proven this concept by constructing a heterometallic assembly containing a cyclometallated iridium antenna covalently linked to a lanthanide complex based on the terpyridine-tetrazole ligand. In the final heterometallic complexes, the iridium to lanthanide energy transfer was clearly evidenced, and its efficiency was estimated at 85% and 65% for europium and neodymium, respectively. In spite of this fast and efficient intermetallic transfer, the lanthanide quantum yields upon excitation of the iridium antenna remain modest, due to a overall low sensitization efficiency.

However, the versatility of our approach could easily lead to better efficiencies, provided that a better matching the iridium emission and lanthanide absorption spectra is achieved. This could be done by replacing the phenylene bridge between the iridium and lanthanide complexes by one having a different electronic effect on the modulation of

iridium emission, for example the alkyne group, or the use of acetylacetonate ancillary ligands instead of picolinates. This would lead to a hypsochromic effect in the iridium emission, which could provide a better sensitization for the europium ion. Replacement of the fluorine atoms in the iridium cyclometalating ligands with electro-donating groups could conversely lead to a bathochromic effect, allowing a better sensitization of the NIR lanthanide emitters.

In addition to heterometallic d-f architectures, we have also synthesized and investigated homopolymetallic assemblies containing covalently-linked bis-iridium complexes bridged by a terpyridine-carboxylate unit. The facile synthetic protocol and the good photophysical properties of the resulting complexes (quantum yields up to 18%), suggest the potential of such architectures for the development of polymetallic assemblies with interesting optical and redox properties.

Chapter VI
Experimental methods and procedures

VI.1. General

VI.1.1. Solvents and starting materials

Solvents and starting materials were purchased from Aldrich, Fluka or Acros and used without further purification, unless otherwise stated. Lanthanide triflate salts were purchased from Aldrich and titrated for metal content before use, in the presence of EDTA and xylene orange. Tetrahydrofuran (THF) was distilled immediately prior use from potassium / benzophenone and triethylamine was distilled from potassium hydroxide. The water used in the syntheses was obtained from a Millipore MilliQ Academic A10 purification system. When necessary, the glassware was systematically oven dried at 130˚C overnight followed by 3 vacuum/ argon cycles.

VI.1.2. Chromatography

Analytical thin layer chromatography (TLC) was performed on aluminium sheets pre-coated with silica gel or neutral aluminium oxide (Merck 60 F_{254}). Visualization was accomplished by UV light (254 or 360 nm). Flash column chromatography were carried out on silica gel (Merck Kieselgel 60, 40-63 μm) or on neutral activated aluminium oxide 90 (Merck, 4.9% water/wt, 63-200μm).

VI.1.3. Characterization

Proton (^{1}H) and carbon (^{13}C) NMR spectra were recorded either on a Bruker Advance DMX 200 or a Varian Unity 400 spectrometers. Chemical shifts are reported in ppm and were referenced internally to the residual solvent resonance. Abbreviations used to described multiplicity of the NMR signals are: s (singlet), d (doublet), dd (doublet of

doublet), t (triplet), dt (doublet of triplet), q (quadruplet), m (multiplet) and br (broad). Mass spectra were recorded on a Thermo Scientific LXQ mass spectrometer equipped with an electrospray source. Elemental analyses were performed by the Service Central d'Analyses of CNRS (Vernaison, France). In the case of previously reported compounds, only the ^{1}H NMR spectra are presented, to confirm the consistency with the reference data.

VI.2. Synthesis of ligands

VI.2.1. Ligands based on terpyridine

a) Synthesis of 6,6''-bis-(1H-tetrazol-5-yl)-2,2':6',2''-terpyridine (**L1**)

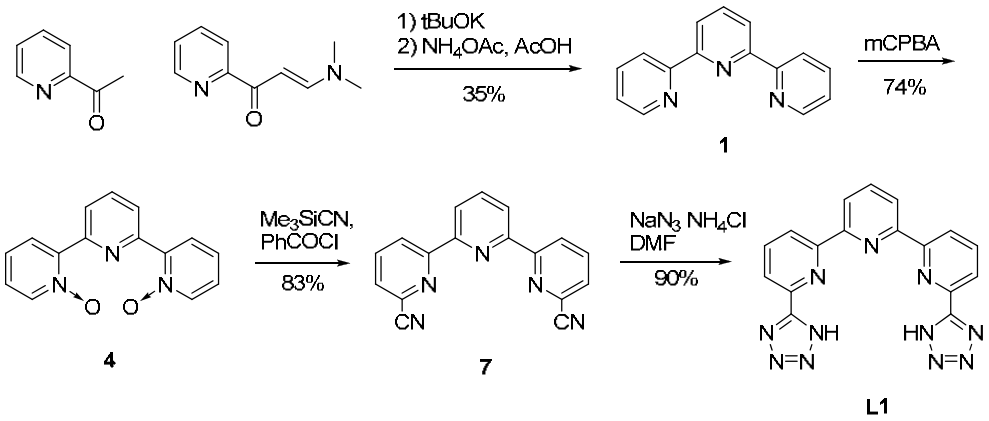

2,2':6',2''-terpyridine (**1**)

The compound was prepared in 35% yield using the Jameson procedure[126] starting from 2-acetylpyridine and N,N-dimethylformamide.

^{1}H NMR (200 MHz, $CDCl_3$): δ ppm 8.70 (ddd, *J* = 4.8, 1.7, 0.9 Hz, 2H), 8.62 (td, *J* = 8.0, 0.9, 0.9 Hz, 2H), 8.45 (d, *J* = 7.8 Hz, 2H), 7.96 (t, *J* = 7.8, 7.8 Hz, 1H), 7.86 (dt, *J* = 7.8, 7.8, 1.8 Hz, 2H), 7.33 (ddd, *J* = 7.5, 4.80, 1.2 Hz, 2H).

2,2':6',2''-terpyridine-1,1''-dioxide (**4**)

The compound was synthesized in 74% yield according to the literature procedure[136] by N-oxidation with chloroperbenzoic acid in dichloromethane at room temperature.

^{1}H NMR (200 MHz, $CDCl_3$): δ ppm 8.93 (d, *J* = 8.0 Hz, 2H), 8.34 (dd, *J* = 6.3, 1.4 Hz, 2H), 8.19 (dd, *J* = 7.8, 2.4 Hz, 2H), 7.97 (t, *J* = 8.0, 8.0 Hz, 1H), 7.38 (td, *J* = 7.8, 7.7, 1.5 Hz, 2H), 7.30 (td, *J* = 6.3, 6.3, 2.4 Hz, 2H).

2,2':6',2''-terpyridine-6,6"-dicarbonitrile (**7**)

The compound was prepared in 83% yield via a modified Reissert-Henze reaction, according to the literature procedure,[51, 137] employing trimethylsilane-carbonitrile and benzoyl chloride in dichloromethane at room temperature.

^{1}H NMR (200 MHz, $CDCl_3$): δ ppm 8.81 (d, *J* = 8.1 Hz, 2H), 8.57 (d, *J* = 7.9 Hz, 2H), 8.04 (t, *J* = 7.1, 7.1 Hz, 1H), 8.01 (t, *J* = 7.8, 7.8 Hz, 2H) 7.75 (d, *J* = 7.6 Hz, 2H)

6,6''-bis-(1H-tetrazol-5-yl)-2,2':6',2''-terpyridine (**L1**)

A mixture of 2,2':6',2''-terpyridine-6,6''-dicarbonitrile (1.133 g, 4.51 mmol), sodium azide (1.300 g, 20 mmol) and ammonium chloride (1.07 g, 20 mmol) in anhydrous DMF (36 ml) was stirred under argon at 125-130ºC for 16 h. After cooling, the inorganic salts were filtrated and the solvent removed under reduced pressure. After addition of dilute HCl (0.1 M, pH=2), the resulting suspension was stirred for 1h. The precipitate was filtered, washed thoroughly with cold water and dried under vacuum, to yield 1.50 g (90%) of white powder.

^{1}H NMR (200 MHz, dmso-d_6): δ ppm 8.94 (d, *J* = 7.8 Hz, 2H), 8.87 (dd, *J* = 6.3, 2.6 Hz, 2H), 8.36-8.24 (m, 5H).

^{13}C NMR (50 MHz, dmso-d_6): δ ppm 155.70, 155.29, 153.94, 144.42, 139.20, 138.60, 122.62, 122.04, 121.97.

Elemental analysis calcd. (%) for $C_{17}H_{11}N_{11} \cdot 1.9\ H_2O$: C 50.66, H 3.69, N 38.23;
found: C 51.03, H 3.87, N 37.86.

b) Synthesis of 2,2':6',2''-terpyridine-6,6''-dicarboxylate (**L2**)

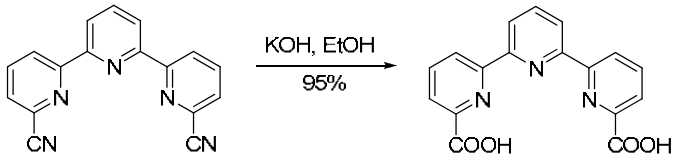

7 **L2**

The ligand was synthesized in 95% yield via the hydrolysis of 2,2':6',2''-terpyridine-6,6"-dicarbonitrile **7**, using KOH in ethanol/water, according to the literature method.[131]

^{1}H NMR (200 MHz, dmso-d_6): δ ppm 13.05 (sbr, 2H), 8.87 (dd, *J* = 7.6, 1.4 Hz, 2H), 8.64 (d, *J* = 7.6 Hz, 2H), 8.21 (t, *J* = 7.6, 7.6 Hz, 3H), 8.16 (dd, *J* = 7.6, 1.4 Hz, 2H).

Elemental analysis calcd. (%) for $C_{17}H_{11}N_3O_4 \cdot 2.5\ H_2O$: C 55.74, H 4.40, N 11.47; found: C 55.55, H 4.31, N 11.62.

c) Synthesis of 4'-(4-bromophenyl)-6,6''-bis-(1H-tetrazol-5-yl)-2,2':6',2''-terpyridine (**L3**)

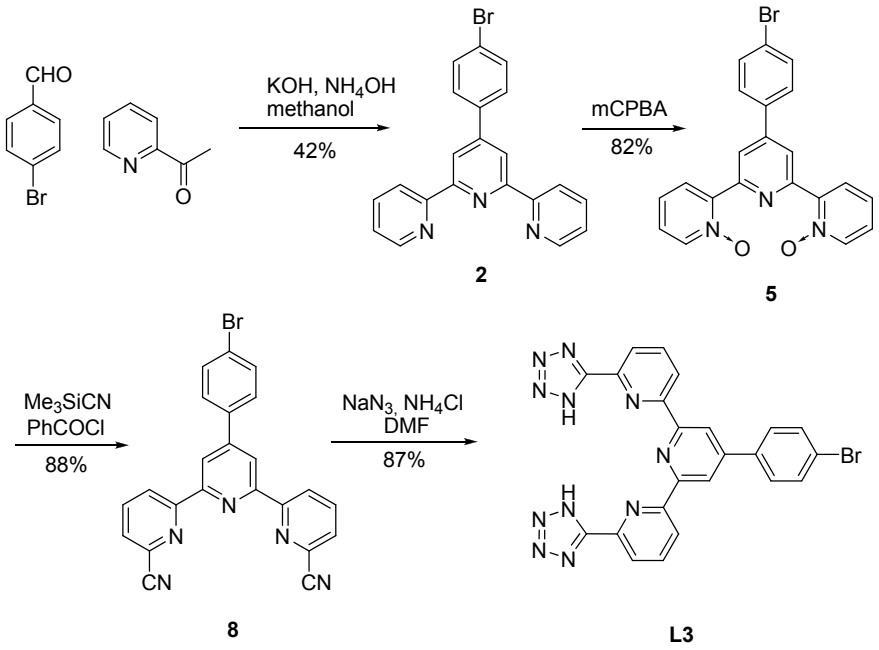

2 **5** **8** **L3**

4'-(4-bromophenyl)-2,2':6',2''-terpyridine (**2**)

The compound was prepared in 42% yield starting from 2-acetylpyridine and bromo-benzaldehyde by modified one-pot Kröhnke procedure[132] based on a sequence of Claisen-

Schmidt aldol condensation, 1,4-addition and intramolecular dehydration, using KOH and ammonia in methanol.

^{1}H NMR (200 MHz, $CDCl_3$): δ ppm 8.73 (ddd, *J* = 4.8, 1.8, 0.9 Hz, 2H), 8.69 (s, 2H), 8.66 (dt, *J* = 7.9, 1.1, 1.0 Hz, 2H), 7.89 (ddd, *J* = 8.0, 7.5, 1.8 Hz, 2H), 7.79 (dt, *J* = 8.8, 2.2, 2.2 Hz, 2H), 7.64 (dt, *J* = 8.8, 2.2, 2.2, 2H), 7.37 (ddd, *J* = 7.5, 4.8, 1.2 Hz, 2H)

4'-(4-bromophenyl)-2,2':6',2"-terpyridine-1,1"-dioxide (**5**) was prepared using a literature adapted procedure.[243]

To a solution of 4'-(4-bromophenyl)-2,2':6',2"-terpyridine (2.0 g, 5.15 mmol) in chloroform (40 mL) was slowly added a slurry of m-chloro-perbenzoic acid (3.5 g, 20.3 mmol) in chloroform. The reaction mixture was stirred at room temperature for 18 h, then washed with a solution of sodium carbonate, separated and the organic phase washed with water. The combined aqueous phases were extracted with chloroform and then all the organic phases were dried over sodium sulfate, filtered and concentrated. Purification on a plug chromatography column (neutral alumina / chloroform, then ethyl acetate and finally ethyl acetate : ethanol 1:1) gave 1.78 g (82%) off-white product.

^{1}H NMR (200 MHz, $CDCl_3$): δ ppm 9.19 (s, 2H), 8.35 (dd, *J* = 6.2, 1.0 Hz, 2H), 8.22 (dd, *J* = 7.7, 2.5 Hz, 2H), 7.70 (dt, *J* = 8.8, 2.2, 2.0 Hz, 2H), 7.60 (dt, *J* = 8.8, 2.2, 2.0 Hz, 2H), 7.40 (td, *J* = 7.9, 7.7, 1.5 Hz, 2H), 7.31 (td, *J* = 7.5, 6.2, 2.3 Hz, 2H).

^{13}C NMR (50 MHz, $CDCl_3$): δ ppm 149.90, 147.78, 146.96, 140.70, 136.63, 132.15, 129.03, 128.04, 125.93, 125.50, 123.78, 123.65.

4'-(p-bromophenyl)-2,2':6',2"-terpyridine-6,6"-dicarbonitrile (**8**) was prepared using a literature adapted procedure.[243]

A suspension of 4'-(p-bromophenyl)-2,2':6',2"-terpyridine-1,1"-di-oxide (1.307 g, 3.11 mmol) in dichloromethane (50 mL) was sonicated and treated with trimethylsilylcyanide (4 mL, 30 mmol). To the resulting clear solution, benzoyl chloride (1.45 mL, 12.44 mmol) was slowly added and the reaction mixture stirred at room temperature for 24h. The mixture was washed with sodium carbonate (50 mL 10% solution), and the aqueous phase

extracted with dichloromethane (5 x 50 mL). The combined organic phases were dried over sodium sulfate and evaporated. The product was crystallized from ether, filtered and washed with ether and acetonitrile giving 1.200 g (88%) white crystals.

^{1}H NMR (200 MHz, dmso-d_6): δ ppm 8.87 (dd, *J* = 7.9, 1.2 Hz, 2H), 8.56 (s, 2H), 8.25 (t, *J* = 7.8, 7.8 Hz, 2H), 8.14 (dd, *J* = 7.7, 1.2 Hz, 2H), 7.87 (d, *J* = 8.6 Hz, 2H), 7.74 (d, *J* = 8.6 Hz, 2H)

^{13}C NMR (50 MHz, $CDCl_3$): δ ppm 157.15, 154.20, 149.86, 141.45, 137.99, 136.44, 133.33, 132.43, 128.83, 128.50, 124.35, 119.98, 117.29.

4'-(p-bromophenyl)- 6,6''-bis-(1H-tetrazol-5-yl)-2,2':6',2''-terpyridine (**L3**)

A mixture of 4'-(p-bromophenyl)-2,2':6',2"-terpyridine-6,6"-dicarbonitrile (0.435 g, 0.99 mmol), sodium azide (0.325 g, 5 mmol) and ammonium chloride (0.267 g, 5 mmol) in anhydrous DMF (20 mL) was reacted under argon for 20 h at 130°C. After cooling and filtering, the precipitate was treated with dilute HCl, stirred for 1 h and refrigerated. Filtration, washing with cold water and drying finally afforded 0.454 g (87%) light-yellow powder.

^{1}H NMR (200 MHz, dmso-d_6): δ ppm 9.04 (s, 2H), 8.79 (dd, *J* = 7.2, 1.5 Hz, 2H), 8.27 (dd, *J* = 7.9, 1.9 Hz, 2H), 8.21 (t, *J* = 7.6, 7.6 Hz, 2H), 8.05 (d, *J* = 8.5 Hz, 2H), 7.86 (d, *J* = 8.4 Hz, 2H).

^{13}C NMR (50 MHz, dmso-d_6): δ ppm 156.62, 154.89, 148.60, 145.56, 138.96, 136.42, 132.09, 129.32, 123.12, 122.52, 121.84, 118.73.

Elemental analysis calcd (%) for $C_{23}H_{14}BrN_{11} \cdot 2.8\ H_2O$: C 48.06, H 3.44, N 26.81;
found: C 47.90, H 3.09, N 26.71.

d) Synthesis of 4'-(5-bromothiophen-2-yl)-6,6''-bis-(1H-tetrazol-5-yl)-2,2'-6'-2"-terpyridine (**L4**)

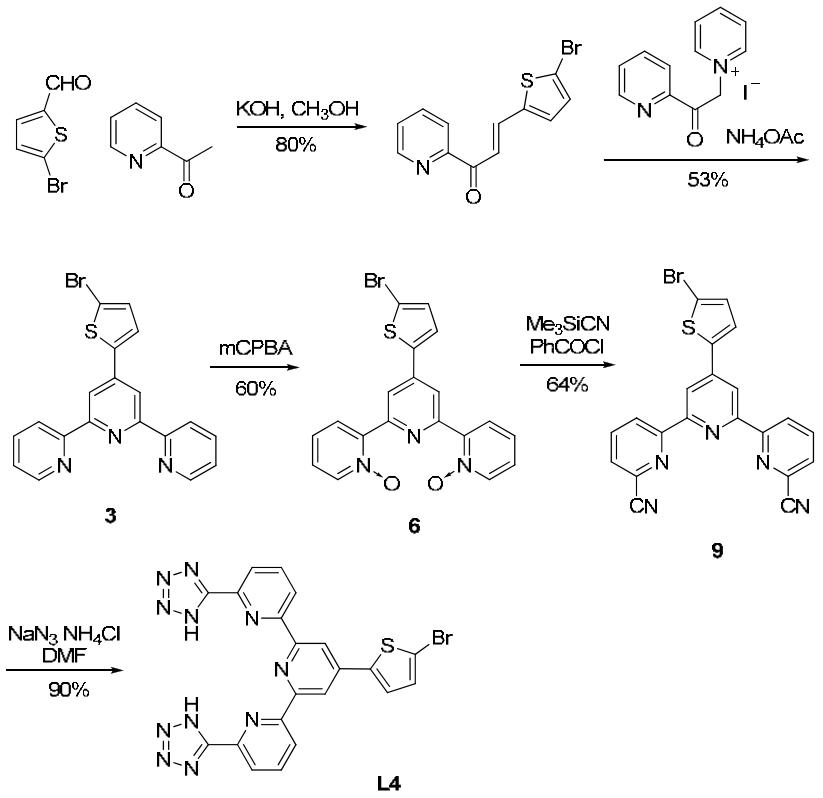

4'-(5-bromothiophen-2-yl)-2,2'-6'-2"-terpyridine (**3**)

The compound was synthesized in 53% yield by the classical Kröhnke procedure,[135] starting from 2-acetylpyridine and bromo-thiophencarboxaldehyde.

^{1}H NMR (200 MHz, $CDCl_3$): δ ppm 8.72 (dd, *J* = 4.9, 1.5 Hz, 2H), 8.62 (dd, *J* = 8.0, 1.0 Hz, 2H), 8.59 (s, 2H), 7.87 (ddd, *J* = 8.0, 7.5, 1.5 Hz, 2H), 7.52 (d, *J* = 3.7 Hz, 1H), 7.36 (ddd, *J* = 8.0, 4.9, 1.0 Hz, 2H), 7.12 (d, *J* = 3.7 Hz, 1H)

4'-(5-bromothiophen-2-yl)-2,2'-6'-2"-terpyridine-1,1"-dioxide (**6**)

A slurry of 3-chloroperbenzoic acid (5.62 g 70%, 22.8 mmol) in dichloromethane was slowly added to a solution of 4'-(5-bromothiophen-2-yl)-2,2'-6'-2"-terpyridine (2.40 g, 6.09 mmol) in dichloromethane (50 mL) and the resulting reaction mixture was stirred at room temperature for 18 h. The mixture was then washed with a sodium carbonate 10% solution, dried over sodium sulfate and concentrated. Purification by column

chromatography on alumina with an ethyl acetate : ethanol gradient eluent gave after solvent evaporation 1.55 g white powder (60%).

^{1}H NMR (200 MHz, $CDCl_3$): δ ppm 9.14 (s, 2H), 8.35 (dd, *J* = 6.1, 1.3 Hz, 2H), 8.23 (dd, *J* = 7.8, 2.4 Hz, 2H), 7.44 (d, *J* = 3.4 Hz, 1H), 7.36 (td, *J* = 7.7, 1.4 Hz, 2H), 7.32 (td, *J* = 7.5, 2.3 Hz, 2H), 7.10 (d, *J* = 3.9, 1H)

^{13}C NMR (50 MHz, $CDCl_3$): δ ppm 149.96, 146.77, 142.47, 141.50, 140.79, 131.31, 127.97, 126.51, 125.79, 125.53, 121.70, 114.89

4'-(5-bromothiophen-2-yl)-2,2'-6'-2"-terpyridine-6,6"-dicarbonitrile (**9**)

A suspension of 4'-(5-bromothiophen-2-yl)-2,2'-6'-2"-terpyridine-1,1"-dioxide (3.00 g, 7.04 mmol) and trimethylsilanecarbonitrile (6.98 g, 70.4 mmol) in dichloromethane (100 mL) was stirred at room temperature until solubilisation (20 min). Benzoyl chloride (3.95 g, 28.1 mmol) was added dropwise and the solution stirred at room temperature for 20h. The precipitate obtained was filtered, washed with water and methanol and then dried, to afford 2.00 g white-yellowish solid (64%).

^{1}H NMR (200 MHz, dmso-d_6, 80°C): δ ppm 8.80 (dd, *J* = 8.1, 1.0 Hz, 2H), 8.59 (s, 2H), 8.01 (t, *J* = 7.9, 7.9 Hz, 2H), 7.76 (dd, *J* = 7.6, 1.0 Hz, 2H), 7.55 (d, *J* = 3.9 Hz, 1H), 7.16 (d, *J* = 3.9 Hz, 1H)

^{13}C NMR (50 MHz, $CDCl_3$): δ ppm 156.87, 154.22, 143.18, 142.09, 137.95, 133.30, 131.47, 128.55, 126.69, 124.27, 117.81, 117.22, 115.32

4'-(5-bromothiophen-2-yl)-6,6''-bis-(1H-tetrazol-5-yl)-2,2'-6'-2"-terpyridine (**L4**)

A mixture of 4'-(5-bromo-2-thienyl)-2,2'-6'-2"-terpyridine-6,6"-dicarbonitrile (0.633 g, 1.425 mmol), sodium azide (0.463 g, 7.12 mmol) and ammonium chloride (0.381 g, 7.12 mmol) in anhydrous DMF (15 mL) was stirred under argon at 140°C for 20h. After cooling and filtering, the precipitate was treated with dilute HCl and stirred for 1 h. The organic phase was evaporated and the residue taken with dilute HCl, sonicated and stirred for 1h. The combined acidic suspensions were filtered, washed with cold water and dried under vacuum to give 0.630 g yellow-brown powder (90%).

^{1}H NMR (200 MHz, dmso-d_6): δ ppm 8.86 (s, 2H), 8.77 (d, *J* = 7.2 Hz, 2H), 8.30 (d, *J* = 6.9 Hz, 2H), 8.22 (t, *J* = 7.6 Hz, 7.6 Hz, 2H), 7.94 (d, *J* = 3.8 Hz, 1H), 7.47 (d, *J* = 3.8 Hz, 1H)

^{13}C NMR (50 MHz, dmso-d_6): δ ppm 154.84, 154.46, 143.02, 142.38, 142.02, 139.36, 131.91, 127.98, 122.91, 122.83, 116.90, 114.46

Elemental analysis calcd (%) for $C_{21}H_{12}BrN_{11}S \cdot 3.5\ H_2O \cdot 0.2$ HCl: C 41.99, H 3.22, N 25.65; found: C 41.85, H 2.84, N 25.35.

e) Synthesis of 4'-(4-(pyridin-2-yl)phenyl)-6,6''-bis-(1H-tetrazol-5-yl)-2,2':6',2''-terpyridine (**L5**)

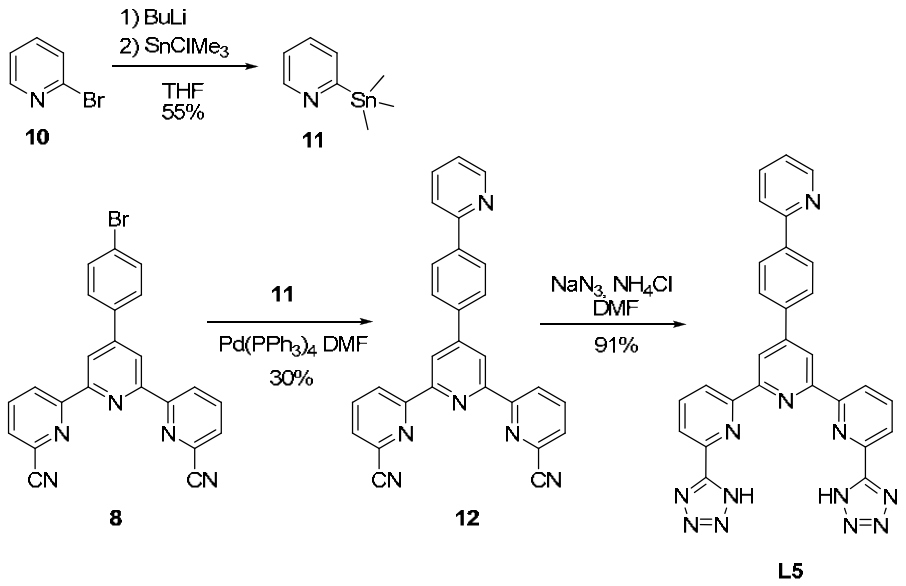

2-(trimethylstannyl)pyridine (**11**) was prepared using an adapted procedure.[139] 2-bromopyridine (0.076 mL, 0.126 mg, 0.8 mmol) dissolved in freshly distilled THF (1.5 mL) under argon was cooled at -75°C. *n*-BuLi (2.1 M in hexane, 0.46 mL, 0.96 mmol) was added dropwise via a syringe during 10 min, and the resulting red reaction mixture was stirred at -75°C for 1 hour. Next, trimethylstannyl chloride (167 mg, 0.84 mmol) in THF (0.5 mL) was added dropwise and the resulting deep yellow solution was allowed to reach room temperature overnight. Diethylether (10 mL) and saturated ammonium chloride solution (10 mL) were added to the mixture and the organic phase separated. The aqueous phase was extracted with diethylether (2 x 10 mL) and the reunited organic phases

washed with saturated ammonium chloride solution (20 mL) and dried over sodium sulfate. Filtration and solvent evaporation gave 107 mg (55%) orange oil.

^{1}H NMR (200 MHz, $CDCl_3$): δ ppm 8.74 (d, J = 4.6 Hz, 1H), 7.52 (td, J = 7.4, 1.7 Hz, 1H), 7.45 (d, J = 6.8 Hz, 1H), 7.14 (ddd, J = 6.9, 4.8, 1.7 Hz, 1H), 0.34 (s, J_{SnH} = 27 Hz, 9H).

4'-(4-(pyridin-2-yl)phenyl)-2,2':6',2"-terpyridine-6,6"-dicarbonitrile (**12**)

To a solution of 4'-(4-bromophenyl)-2,2':6',2"-terpyridine-6,6"-dicarbonitrile (194 mg, 0.44 mmol) in anhydrous DMF (3 mL) under argon was added 2-trimethylstannylpyridine (107 mg, 0.44 mmol) obtained as above and tetrakis(triphenylphosphine)palladium catalyst (25 mg, 5% mol) suspended in anhydrous DMF (1 mL). The reaction mixture was stirred at 90°C under argon atmosphere for 24 h, and the solvent evaporated under reduced pressure. Purification by column chromatography (alumina, dichloromethane) afforded after solvent evaporation 59 mg (30%) white powder.

^{1}H NMR (200 MHz, $CDCl_3$): δ ppm 8.87 (s, 2H), 8.86 (dd, J = 8.1, 1.0 Hz, 2H), 8.77 (td, J = 4.8, 1.5, 1.5 Hz, 1H), 8.22 (d, J = 8.6 Hz, 2H), 8.03 (d, J = 8.6 Hz, 2H), 8.03 (t, J = 7.9, 7.9 Hz, 2H), 7.86-7.82 (m, 2H), 7.77 (dd, J = 7.6, 1.0 Hz, 2H), 7.31 (ddd, J = 6.0, 4.9, 2.3 Hz, 1H).

Elemental analysis calcd (%) for $C_{28}H_{16}N_6$: C 77.05, H 3.69, N 19.25;
found: C 76.88, H 3.70, N 19.21.

4'-(4-(pyridin-2-yl)phenyl)-6,6''-bis-(1H-tetrazol-5-yl)-2,2'-6'-2"-terpyridine (**L5**)

A mixture of 4'-(*4-(pyridin-2-yl)phenyl*)-2,2'-6'-2"-terpyridine-6,6"-dicarbonitrile (61 mg, 0.14 mmol), sodium azide (46 mg, 0.7 mmol) and ammonium chloride (38 mg, 0.7 mmol) in anhydrous DMF (3 mL) was stirred under argon at 120°C for 18h. After cooling, the inorganic salts were filtrated and the solvent removed under reduced pressure. The precipitate was washed with dilute HCl (0.1 M) and combined with the previously evaporated residue. After addition of dilute HCl, the resulting suspension was stirred for 1h. The precipitate was filtered, washed thoroughly with cold water and dried under vacuum to yield 66 mg (91%) of cream-white powder. The compound was recrystallized from water-ethanol.

^{1}H NMR (200 MHz, dmso-d_6): δ ppm 9.25 (s, 2H), 8.91 (dd, *J* = 6.9, 1.8 Hz, 2H), 8.76 (d, *J* = 4.3 Hz, 1H), 8.47-8.22 (m, 8H), 8.13 (d, *J* = 7.7 Hz, 1H), 7.97 (dt, *J* = 7.9, 7.8, 1.7 Hz, 1H), 7.44 (dd, *J* = 6.9, 5.0 Hz, 1H)

^{13}C NMR (50 MHz, dmso-d_6): δ ppm 155.28, 155.11, 154.45, 154.33, 149.63, 149.36, 143.00, 139.51, 139.28, 137.64, 137.28, 127.79, 127.05, 122.93, 122.76, 122.65, 120.43, 119.09

Elemental analysis calcd (%) for $C_{28}H_{18}N_{12} \cdot 2.8\ H_2O \cdot 0.2\ C_2H_5OH$: C 58.59, H 4.29, N 28.87; found: C 58.60, H 4.06, N 28.63.

f) Synthesis of 4'-(5'-octyl-2,2'-bithiophen-5-yl)-6,6''-bis-(1H-tetrazol-5-yl)-2,2':6',2''-terpyridine (**L6**)

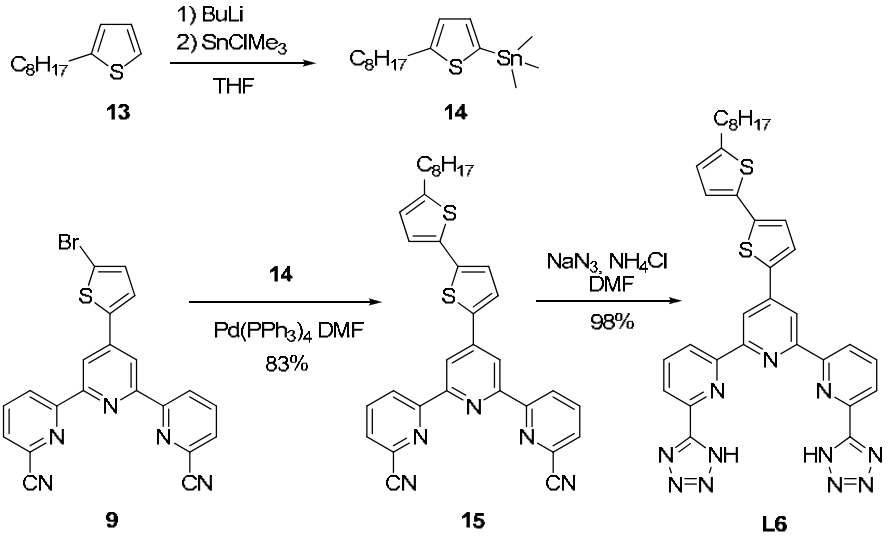

trimethyl(5-octylthiophen-2-yl)stannane (**14**)

A solution of *n*-BuLi (2 M in hexane, 0.6 mL, 1.22 mmol) was added drop wise to a solution of 2-*n*-octylthiophene (200 mg, 1.02 mmol) in freshly distilled THF (10 mL) under argon at -75°C. After 20 min of stirring, trimethylstannyl chloride (223 mg, 1.12 mmol) was added drop wise to the mixture at -75°C. The reaction mixture was allowed to warm at room temperature and stirred for a couple of hours. Then a saturated aqueous solution of ammonium chloride was added and the stannane extracted with dichloromethane. The organic phase was dried over sodium sulfate and the solvent evaporated to give 195 mg (53%) colourless oil which was used in the following step without further purification.

^{1}H NMR (200 MHz, $CDCl_3$): δ ppm 7.02 (d, J = 3.2 Hz, 1H), 6.90 (d, J = 3.2 Hz, 1H), 2.86 (t, *J* = 7.5, 7.5 Hz, 2H), 1.75-1.61 (m, 2H), 1.56 (s, 2H), 1.40-1.27 (m, 8H), 0.89 (t, *J* = 6.7 Hz, 6.7 Hz, 3H), 0.34 (s, J_{SnH} = 27 Hz, 9H).

4'-(5''-octyl-2,2''-bithiophen-5-yl)-2,2':6',2''-terpyridine-6,6''-dicarbonitrile (**15**)

To a solution of 4'-(5-bromothiophen-2-yl)-2,2':6',2''-terpyridine-6,6''-dicarbonitrile (200 mg, 0.45 mmol) in anhydrous DMF (10 mL) under argon was added trimethyl(5-octylthiophen-2-yl)stannane (195 mg, 0.543 mmol) obtained as above and tetrakis(triphenylphosphine)palladium catalyst (26 mg, 5% mol) suspended in anhydrous DMF (1 mL). The reaction mixture was stirred at 90°C under argon atmosphere for 18 h, then the solvent was evaporated under reduced pressure and methanol was added to the oil to give a yellow precipitate, which was filtered, washed with methanol and dried under vacuum to give 210 mg (83%) yellow powder.

^{1}H NMR (200 MHz, $CDCl_3$): δ ppm 8.78 (dd, *J* = 8.1, 1.1 Hz, 2H), 8.59 (s, 2H), 7.98 (dd, *J* = 7.7 Hz, 7.7 Hz, 2H), 7.72 (dd, *J* = 7.6, 1.1 Hz, 2H), 7.66 (d, *J* = 3.9 Hz, 1H), 7.14 (d, *J* = 3.7 Hz, 1H), 7.13 (d, *J* = 3.3 Hz, 1H), 6.75 (d, *J* = 3.6 Hz, 1H), 2.83 (t, *J* = 7.5, 7.5 Hz, 2H), 1.79-1.64 (m, 2H), 1.58 (s, 2H), 1.44-1.26 (m, 8H), 0.89 (t, *J* = 6.7 Hz, 6.7 Hz, 3H)

^{13}C NMR (50 MHz, $CDCl_3$): δ ppm 156.88, 153.76, 146.66, 143.48, 140.54, 138.05, 137.74, 133.94, 133.08, 128.31, 127.13, 125.08, 124.33, 124.13, 123.83, 117.36, 117.28, 31.85, 31.57, 30.23, 29.32, 29.22, 29.10, 22.66, 14.11.

4'-(5''-octyl-2,2''-bithiophen-5-yl)-6,6''-bis-(1H-tetrazol-5-yl)-2,2':6',2''-terpyridine (**L6**)

A mixture of 4'-(5''-octyl-2,2''-bithiophen-5-yl)-2,2':6',2''-terpyridine-6,6''-dicarbonitrile (0.190 g, 0.34 mmol), sodium azide (0.091 g, 1.7 mmol) and ammonium chloride (0.110 g, 1.7 mmol) in anhydrous DMF (25 mL) was stirred under argon at 120°C for 60h. After cooling, the inorganic salts were filtrated and the solvent removed under reduced pressure. Addition of dilute HCl (0.1 M) resulted in a dark-red suspension which was stirred for 1h, refrigerated and then filtered. The precipitate was washed with a water-ethanol mixture and dried under vacuum to give 214 mg (98%) dark-red powder.

^{1}H NMR (200 MHz, dmso-d_6): δ ppm 8.97 (s, 2H), 8.86 (dd, *J* = 7.0, 1.0 Hz, 2H), 8.35-8.23 (m, 4H), 8.10 (d, *J* = 3.8 Hz, 1H), 7.45 (d, *J* = 3.7 Hz, 1H), 7.32 (d, *J* = 3.5 Hz, 1H), 6.88 (d, *J* = 3.5 Hz, 1H), 2.82 (t, *J* = 7.2, 7.2 Hz, 2H), 1.70-1.60 (m, 2H), 1.35-1.26 (m, 10H), 0.86 (t, *J* = 6.5 Hz, 6.5 Hz, 3H)

^{13}C NMR (50 MHz, dmso-d_6): δ ppm 155.06, 154.49, 154.32, 145.82, 143.04, 142.95, 139.49, 139.20, 138.23, 133.33, 128.42, 125.70, 124.58, 124.28, 122.78, 122.80, 116.81, 31.22, 30.95, 29.31, 28.65, 28.61, 28.43, 22.04, 13.90.

Elemental analysis calcd (%) for $C_{33}H_{31}N_{11}S_2 \cdot 1.3\ H_2O$: C 59.23, H 5.06, N 23.02; found: C 59.53, H 4.93, N 22.68.

g) Synthesis of 6,2':6',2''-terpyridine-2-carboxylic acid (**L12**)

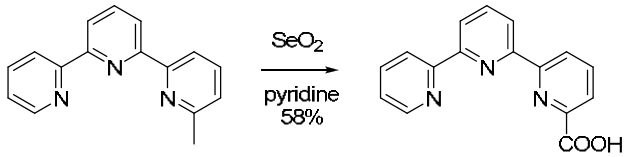

45 L12

The ligand **L12** was synthesized according to the reported procedure,[120] by oxidation of the 6-methyl-2,2':6'-2"-terpyridine precursor **45** with selenium dioxide in pyridine.

^{1}H NMR (200 MHz, dmso-d_6): δ ppm 13.28 (s, 1H), 8.85 (dd, *J* = 7.3, 1.7 Hz, 1H), 8.74 (ddd, *J* = 4.7, 1.6, 0.9 Hz, 1H), 8.64 (td, *J* = 8.4, 1 Hz, 1H), 8.61 (dd, *J* = 7.8, 0.9 Hz, 1H), 8.49 (dd, *J* = 7.8, 0.9 Hz, 1H), 8.20 (t, *J* = 7.6, 7.6 Hz, 1H), 8.15 (t+d, 2H), 8.03 (dt, *J* = 7.8, 7.8, 1.8 Hz, 1H), 7.52 (ddd, *J* = 7.4, 4.8, 1.1 Hz, 1H).

h) Synthesis of 4'-(4''-(4-allylhepta-1,6-dien-4-yl)biphenyl-4-yl)-6,6''-bis-(1H-tetrazol-5-yl)-2,2':6',2''-terpyridine (**L13**)

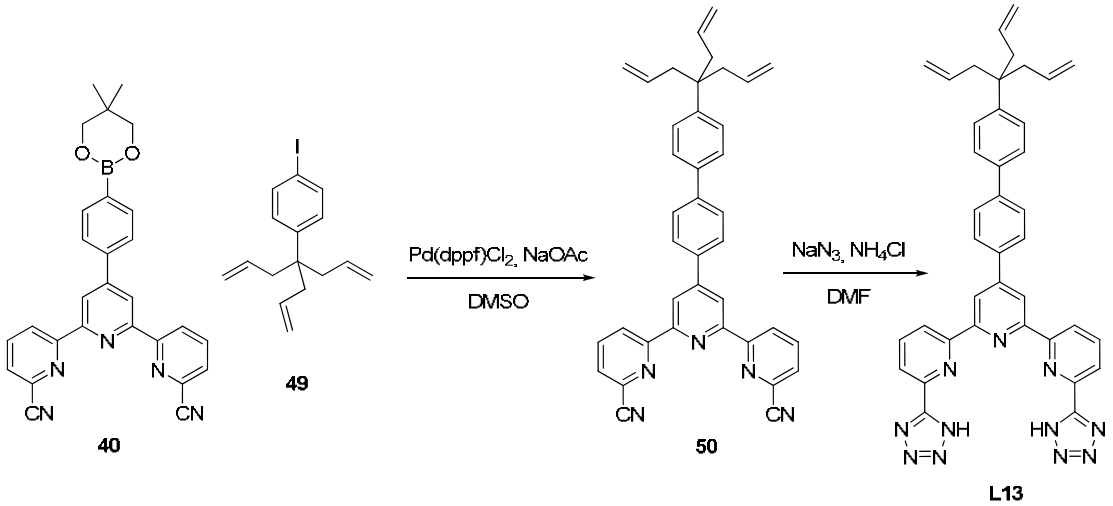

4'-(4''-(4-allylhepta-1,6-dien-4-yl)biphenyl-4-yl)-2,2':6',2''-terpyridine-6,6''-dicarbonitrile (**50**)

The product was synthetized by the Suzuki coupling of the boronic ester **40** and the previously described[179] allylic tripod **49**.

To a mixture of the allylic tripod **49** (132 mg, 0.39 mmol) and the boronic ester **40** (200 mg, 0.425 mmol) in a toluene-water-ethanol solvent mixture (45 ml of toluene, 10 mL of water, and 10 mL of ethanol) under argon was added an aqueous solution (2M) of Na_2CO_3 (10 mL) and the resulting mixture was vigorously stirred for 10min. Then the $Pd(PPh_3)_4$ catalyst (46 mg, 10% molar) was added and the reaction mixture was stirred at 95°C overnight under argon. After cooling, the mixture was washed with water, the organic phase was dried with magnesium sulphate and the solvent was evaporated. The crude product was purified by column chromatography (silica gel; hexane : ethyl acetate 2 : 1) to yield 118 mg (53 %) of white solid. Using a modified procedure (replacing the solvent mixture by DMF and using 5% catalyst) the target product was obtained in 80% yield.

^{1}H NMR (200 MHz, $CDCl_3$): δ ppm 8.87 (s, 2H), 8.87 (dd, *J* = 8.1, 1.0 Hz, 2H), 8.03 (t, *J* = 8.0, 8.0 Hz, 2H), 8.00 (dd, *J* = 8.2, 2.1 Hz, 2H), 7.82 (d, *J* = 8.5 Hz, 2H), 7.77 (dd, *J* = 7.6, 1.0 Hz, 2H), 7.67 (d, *J* = 8.4 Hz, 2H), 7.45 (d, *J* = 8.5 Hz, 2H), 5.74-5.53 (m, 3H), 5.09 (dd, *J* = 9.0, 2.2 Hz, 3H), 5.02 (s, 3H), 2.53 (d, *J* = 7.1 Hz, 6H).

^{13}C NMR (50 MHz, $CDCl_3$): δ ppm 157.34, 154.02, 150.45, 145.58, 142.03, 137.88, 137.28, 135.95, 134.40, 133.28, 128.36, 127.60, 127.58, 127.31, 126.64, 124.32, 119.95, 117.78, 117.34, 43.27, 41.85.

Elemental analysis calcd. (%) for $C_{39}H_{31}N_5 \cdot 0.25$ DMF: C 81.20, H 5.61, N 12.51; found: C 80.96, H 5.26, N 12.75.

4'-(4''-(4-allylhepta-1,6-dien-4-yl)biphenyl-4-yl)-6,6''-bis-(1H-tetrazol-5-yl)-2,2':6',2''-terpyridine (**L13**)

A mixture of dicarbonitrile **50** (146 mg, 0.26 mmol), sodium azide (85 mg, 1.25 mmol) and ammonium chloride (70 mg, 1.25 mmol) in anhydrous DMF (3 ml) was stirred under argon at 125-130ºC for 20 h. After cooling, the white precipitate formed was filtered, washed with ethanol, water and acidified water (pH ~ 2-3), then suspended in methanol and acidified with HCl 1M. The resulting yellowish suspension was sonicated, stirred for 1 h and filtered. The precipitate was thoroughly washed with methanol-water and finally water, then dried under vacuum to afford 150 mg (88%) pale yellow powder.

^{1}H NMR (200 MHz, dmso-d_6): δ ppm 9.25 (s, 2H), 8.92 (dd, J = 6.9, 2.0 Hz, 2H), 8.37-8.25 (m, 6H), 8.00 (d, J = 8.3 Hz, 2H), 7.79 (d, J = 8.3 Hz, 2H), 7.52 (d, J = 8.4 Hz, 2H), 5.70-5.49 (m, 3H), 5.09 (dd, J = 10.3, 2.2 Hz, 3H), 5.02 (s, 3H), 2.53 (underneath the solvent peak, 6H).

^{13}C NMR (50 MHz, dmso-d_6): δ ppm 155.28, 154.87, 154.34, 149.31, 145.25, 143.45, 140.67, 139.15, 136.40, 135.90, 134.26, 129.01, 127.87, 127.26, 127.00, 126.20, 122.59, 118.85, 117.85, 42.94, 41.20.

Elemental analysis calcd. (%) for $C_{39}H_{33}N_{11} \cdot 2.2\ H_2O$: C 67.36, H 5.42, N 22.16;
found: C 67.28, H 5.13, N 22.16.

VI.2.2. Ligands based on bipyridine

a) Synthesis of 6,6'-bis-(1H-tetrazol-5-yl)-2,2'-bipyridine (**L7**)

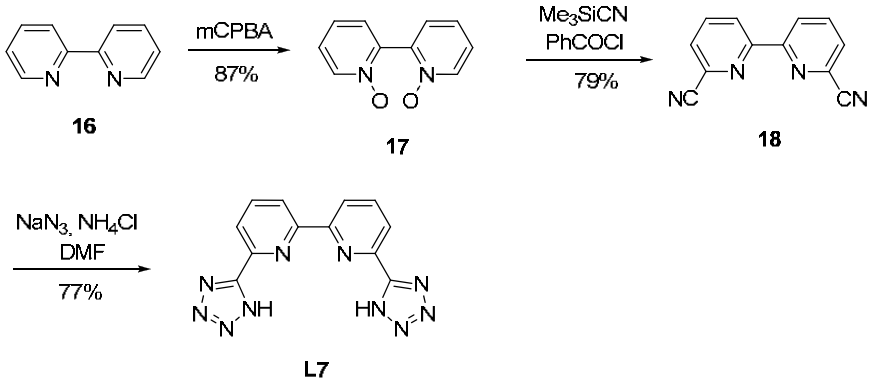

2,2'-bipyridine-6,6'-dicarbonitrile (**18**)

The compound was prepared according to a described protocol[52] similar to that employed for the terpyridine analogue **7**, starting with the initial activation of the bipyridine **16** by N-oxidation with chloroperbenzoic acid to give **17**, followed by the introduction of cyanide via a modified Reissert-Henze reaction employing trimethylsilane-carbonitrile and benzoyl chloride.

^{1}H NMR (200 MHz, $CDCl_3$): δ ppm 8.72 (d, *J* = 8.1 Hz, 2H), 8.02 (t, *J* = 7.9, 7.9 Hz, 2H), 7.78 (d, *J* = 7.7 Hz, 2H).

^{13}C NMR (50 MHz, $CDCl_3$): δ ppm 155.49, 138.39, 133.37, 129.07, 124.64, 117.01.

6,6'-bis-(1H-tetrazol-5-yl)-2,2'-bipyridine (**L7**)

A mixture of 2,2'-bipyridine-6,6'-dicarbonitrile (0.412 g, 2 mmol), sodium azide (0.65 g, 10 mmol) and ammonium chloride (0.535 g, 10 mmol) in anhydrous DMF (18 ml) was stirred under Ar at 125-130ºC for 22 h. After cooling, the inorganic salts were filtrated and the solvent removed under reduced pressure. After addition of dilute chlorhydric acid (0.1 M, 10 ml, pH ~ 2-3), the resulting suspension was stirred for 1h. The final product was filtered, washed thoroughly with cold water and dried under vacuum, to yield 0.449 g of white powder (yield: 77%).

^{1}H NMR (200 MHz, dmso-d_6): δ ppm 9.00 (p, *J* = 4.0, 4.0, 4.0, 4.0 Hz, 2H), 8.33-8.31 (m, 4H)

^{13}C NMR (50 MHz, dmso-d_6): δ ppm 154.61, 143.15, 139.45, 123.12, 123.03.

Elemental analysis calcd. (%) for $C_{12}H_8N_{10} \cdot 0.2\ H_2O$: C 48.72, H 2.86, N 47.34; found: C 48.82, H 2.91, N 47.16.

b) Synthesis of 6'-(1H-tetrazol-5-yl)-2,2'-bipyridine-6-carboxylic acid (**L8**)

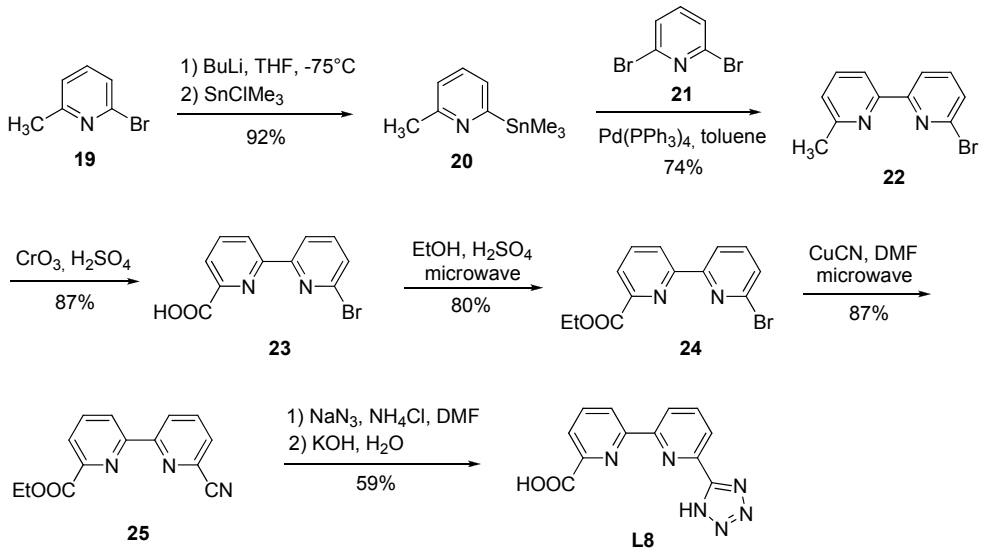

6-bromo-6'-methyl-2,2'-bipyridine (**22**)

The compound was prepared as previously described[158] by the Stille coupling of 2-methyl-6-trimethylstannylpyridine **20** with 2,6-dibromopyridine **21** in toluene using [$Pd(PPh_3)_4$] as a catalyst.

^{1}H NMR (200 MHz, $CDCl_3$): δ ppm 8.40 (td, *J* = 7.7, 0.8, 0.8 Hz, 1H), 8.19 (d, *J* = 7.8 Hz, 1H), 7.69 (t, *J* = 7.7, 7.7 Hz, 1H), 7.65 (dt, *J* = 7.8, 7.8, 0.8 Hz, 1H), 7.46 (td, *J* = 7.8, 0.8, 0.8 Hz, 1H), 7.18 (d, *J* = 7.7 Hz, 1H), 2.62 (s, 3H).

^{13}C NMR (50 MHz, $CDCl_3$): δ ppm 157.99, 157.61, 153.81, 141.49, 139.12, 137.16, 127.74, 123.86, 119.75, 118.51, 24.58.

6'-bromo-2,2'-bipyridine-6-carboxylic acid (**23**)

6-bromo-6'-methyl-2,2'-bipyridine (0.775 g, 3.10 mmol) was carefully added to concentrated sulfuric acid (5 mL) at 0°C (in an ice bath) under stirring. Chromium (VI) oxide (1 g, 10 mmol) was then added in small portions as to keep the temperature below 4°C. The viscous green mixture was stirred for 20 h while allowed to reach room

temperature. The mixture was then poured over crushed ice under stirring. The precipitate obtained was filtered, washed with cold water and dried, giving 0.764 g (87%) white product.

^{1}H NMR (200 MHz, dmso-d_6): δ ppm 8.55 (dd, *J* = 7.7, 0.5 Hz, 1H), 8.47 (dd, *J* = 6.3, 2.7 Hz, 1H), 8.20-8.11 (m, 2H), 7.96 (t, *J* = 7.8, 7.8 Hz, 1H), 7.76 (d, *J* = 0.6 Hz, 1H).

^{13}C NMR (50 MHz, dmso-d_6): δ ppm 165.82, 155.75, 153.36, 148.47, 141.00, 140.77, 138.99, 128.78, 125.29, 123.54, 120.31.

ES$^-$-MS m/z: 277.0 $[M-H]^-$

Ethyl 6'-bromo-2,2'-bipyridine-6-carboxylate (**24**)

A mixture of 6'-bromo-2,2'-bipyridine-6-carboxylic acid (0.746 g, 2.67 mmol), ethanol (10 mL) and concentrated sulfuric acid (1 mL) was heated in a microwave owen at 78°C (80W) for 80 minutes, and then left at room temperature overnight. The mixture was poured into cold water (100 mL) and the resulting precipitate filtered, washed with water and dried. Column chromatography on silica using dichloromethane:methanol (9:1) as eluent afforded finally 0.654 g (80%) white product.

^{1}H NMR (200 MHz, $CDCl_3$): δ ppm 8.60 (dd, *J* = 7.9, 1.2 Hz, 1H), 8.54 (dd, *J* = 7.7, 0.9 Hz, 1H), 8.13 (dd, *J* = 7.7, 1.2 Hz, 1H), 7.96 (t, *J* = 7.8, 7.8 Hz, 1H), 7.70 (t, *J* = 7.8, 7.8 Hz, 1H), 7.52 (dd, *J* = 7.9, 0.9 Hz, 1H), 4.49 (q, *J* = 7.1, 7.1, 7.1 Hz, 1H), 1.47 (t, *J* = 7.1, 7.1 Hz, 1H).

^{13}C NMR (50 MHz, $CDCl_3$): δ ppm 165.03, 156.29, 154.62, 147.79, 141.46, 139.30, 137.93, 128.46, 125.35, 124.36, 120.31, 61.88, 14.27.

Elemental analysis calcd. (%) for $C_{13}H_{11}BrN_2O_2$: C 50.84, H 3.61, N 9.12;
found: C 50.72, H 3.41, N 9.29.

Ethyl 6'-cyano-2,2'-bipyridine-6-carboxylate (**25**)

To a solution of ethyl 6'-bromo-2,2'-bipyridine-6-carboxylate (1.669 g, 5.43 mmol) in DMF (10 mL) was added cuprous cyanide (0.680 g, 7.61 mmol). The dark-red suspension was heated in a microwave oven for 10 min at 160°C (150W), then at 153°C (150W) for another 30 min. The end of the reaction was verified by TLC. A hot solution of potassium

cyanide (1.4 g in 10 mL water) was then poured over the reaction mixture, leading to the formation of a white precipitate. The suspension was stirred at room temperature for 1h, then extracted with 350 mL ether. The organic phase was dried over sodium sulfate, evaporated and purified by column chromatography on silica using dichloromethane as eluent, giving finally 1.190 g (87%) white product.

^{1}H NMR (200 MHz, $CDCl_3$): δ ppm 8.83 (dd, *J* = 8.1, 1.1 Hz, 1H), 8.66 (dd, *J* = 7.9, 1.1 Hz, 1H), 8.18 (dd, *J* = 7.7, 1.1 Hz, 1H), 8.01 (t, *J* = 7.8, 7.8 Hz, 1H), 7.99 (t, *J* = 7.9, 7.9 Hz, 1H), 7.74 (dd, *J* = 7.6, 1.0 Hz, 1H), 4.50 (q, *J* = 7.1, 7.1, 7.1 Hz, 2H), 1.47 (t, *J* = 7.1, 7.1 Hz, 3H).

^{13}C NMR (50 MHz, $CDCl_3$): δ ppm 164.23, 155.80, 153.39, 147.55, 139.58, 139.25, 132.32, 129.59, 125.88, 124.62, 124.16, 117.34, 61.41, 14.11.

Elemental analysis calcd. (%) for $C_{14}H_{11}N_3O_2$: C 66.4, H 4.38, N 16.59;
found: C 66.37, H 4.24, N 16.46.

6'-(1H-tetrazol-5-yl)-2,2'-bipyridine-6-carboxylic acid (**L8**)

A mixture of ethyl 6'-cyano-2,2'-bipyridine-6-carboxylate (0.682 g, 2.69 mmol), sodium azide (0.875 g, 13.45 mmol) and ammonium chloride (0.720 g, 13.45 mmol) in anhydrous DMF (25 mL) was stirred under argon for 44h at 135°C. After cooling, the inorganic salts were filtered and the solvent removed under reduced pressure. After addition of dilute chlorhydric acid, the resulting suspension was stirred for 1h, then the precipitate was filtered, washed with cold water and dried, giving 0.483 g intermediate. The product was dissolved in an aqueous molar solution of potassium hydroxide (10 mL, 6 equivalents) and heated at reflux overnight. After addition of dilute chlorhydric acid (down to pH ≈ 2), the resulting suspension was stirred for 1h, filtered and the precipitate washed with cold water and dried under vacuum to give 0.425 mg (59%) white product.

^{1}H NMR (200 MHz, dmso-d_6): δ ppm 9.04 (d, *J* = 7.3 Hz, 1H), 8.74 (dd, *J* = 6.7, 2.0 Hz, 1H), 8.32-8.15 (m, 4H).

^{13}C NMR (50 MHz, dmso-d_6): δ ppm 165.81, 154.85, 154.09, 147.95, 143.13, 139.56, 138.82, 125.36, 124.39, 122.92, 122.79.

ES^{+}-MS m/z: 646.3 **L8**

Elemental analysis calcd. (%) for $C_{12}H_8N_6O_2 \cdot 1.2\ H_2O$: C 49.73, H 3.62, N 28.99; found: C 49.81, H 3.48, N 28.69.

c) Synthesis of 2,2'-bipyridine-6,6'-dicarboxylic acid (**L9**)

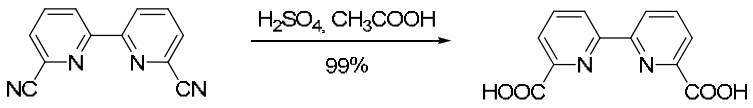

18 **L9**

Over 2,2'-bipyridine-6,6'-dicarbonitrile (0.497 g, 2.4 mmol) were added, in this order, acetic acid (9 mL), water (2.5 mL) and sulfuric acid (9 mL). The yellow solution obtained was stirred at room temperature for 30h, after which the mixture was poured over crushed ice (60 mL). The resulting precipitate was filtered, washed with water and ethanol and dried to give 0.578 g (99%) white powder.

^{1}H NMR (200 MHz, dmso-d_6): δ ppm 8.75 (dd, J = 7.0, 1.9 Hz, 2H), 8.23-8.12 (m, 4H).

^{13}C NMR (50 MHz, dmso-d_6): δ ppm 165.83, 154.35, 147.95, 138.85, 125.19, 124.04.

VI.2.3. Ligands based on pyridine

a) Synthesis of 2,6-bis(1H-tetrazol-5-yl)pyridine (**L10**)

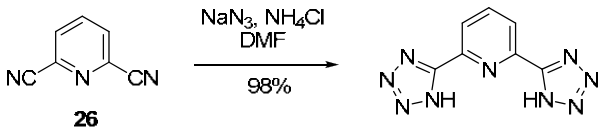

26 **L10**

A mixture of pyridine-2,6-dicarbonitrile (0.664 g, 5.0 mmol), sodium azide (1.625 g, 25 mmol) and ammonium chloride (1.337 g, 25 mmol) in anhydrous DMF (20 ml) was stirred under argon at 125ºC for 24 h. After cooling, the inorganic salts were filtrated and the solvent removed under reduced pressure. After addition of dilute HCl (0.1 M, pH ~ 2-3), the resulting suspension was stirred for 1h and refrigerated. The precipitate was filtered, washed with cold water and dried under vacuum, affording 1.087 g (98%) of white powder. The compound was recrystallized from water/ethanol.

^{1}H NMR (200 MHz, dmso-d_6): δ ppm 8.34 (sbr, 3H).

^{13}C NMR (50 MHz, dmso-d_6): δ ppm 155.02, 144.34, 140.23, 124.42.

Elemental analysis calcd. (%) for $C_7H_5N_9 \cdot 0.3\ H_2O \cdot 0.1$ EtOH: C 38.40, H 2.78, N 55.98; found: C 38.57, H 2.74, N 55.73.

b) Synthesis of 6-(1H-tetrazol-5-yl)picolinic acid (**L11**)

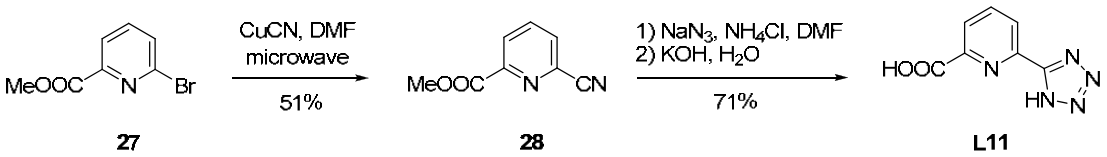

27 **28** **L11**

methyl 6-cyanopicolinate (**28**)

To a solution of methyl 6-bromopicolinate **27** (1.900 g, 8.82 mmol) in DMF (6 mL) was added cuprous cyanide (1.106 g, 12.35 mmol). The orange suspension was heated in a microwave oven for 5 min at 150°C (150W). The end of the reaction was verified by TLC. A hot solution of potassium cyanide (2.3 g in 10 mL water) was then poured over the reaction mixture, leading to the formation of a white precipitate. The suspension was stirred at room temperature for 1h, then extracted with chloroform (150 mL). The organic phase was washed with a HCl solution (50 mL 2N), then with a NaOH solution (20 mL 5%) and finally with water. The extract was dried over sodium sulfate, evaporated and purified by column chromatography on silica using a mixture dichloromethane : ethyl acetate : methanol (2:1:0.05) as eluent, giving after solvent evaporation 0.727 g (51%) white crystalline product.

^{1}H NMR (200 MHz, $CDCl_3$): δ ppm 8.34 (dd, J = 7.9, 1.2 Hz, 1H), 8.04 (t, J = 7.8, 7.8 Hz, 1H), 7.88 (dd, J = 7.7, 1.2 Hz, 1H), 4.04 (s, 3H).

^{13}C NMR (50 MHz, $CDCl_3$): δ ppm 163.94, 162.45, 149.30, 138.52, 133.85, 131.25, 127.91, 116.22.

Elemental analysis calcd. (%) for $C_8H_6N_2O_2 \cdot 0.1\ H_2O$: C 58.61, H 3.81, N 17.09;
found: C 58.78, H 3.50, N 16.98.

6-(1H-tetrazol-5-yl)picolinic acid (**L11**)

A mixture of methyl 6-cyanopicolinate (0.638 g, 3.9 mmol), sodium azide (1.279 g, 20 mmol) and ammonium chloride (1.052 g, 20 mmol) in anhydrous DMF (30 ml) was stirred under argon at 130ºC for 20 h. After cooling, the inorganic salts were filtrated, washed with hot DMF and the filtrate evaporated under reduced pressure. After addition of a HCl solution (3.5 mL 2M), the resulting suspension was stirred for 1h and refrigerated. The precipitate was filtered, washed with cold water and dried under vacuum, affording 0.605 g of white powder. The product was dissolved in an aqueous molar solution of potassium hydroxide (20 mL, 6 equivalents) and heated at reflux overnight. After addition of dilute chlorhydric acid (down to pH ~ 2), the resulting suspension was stirred for 1h, filtered and the precipitate washed with cold water and dried under vacuum to give 0.532 g (71%) white product.

^{1}H NMR (200 MHz, dmso-d_6): δ ppm 8.37 (dd, *J* = 6.9, 1.7 Hz, 1H), 8.24-8.14 (m, 2H).

^{13}C NMR (50 MHz, dmso-d_6): δ ppm 165.25, 154.66, 148.57, 143.92, 139.72, 126.21, 125.59.

Elemental analysis calcd. (%) for $C_7H_5N_5O_2 \cdot 1.1\ H_2O \cdot 0.1$ HCl: C 39.18, H 3.43, N 32.63; found: C 39.21, H 3.07, N 32.33.

VI.3. Synthesis of iridium complexes

VI.3.1. Iridium μ-chloro-bridged dimer complexes

a) Synthesis of tetrakis(2-(2,4-difluorophenyl)pyridine)bis(μ-ch1oro)diiridium (**31**)

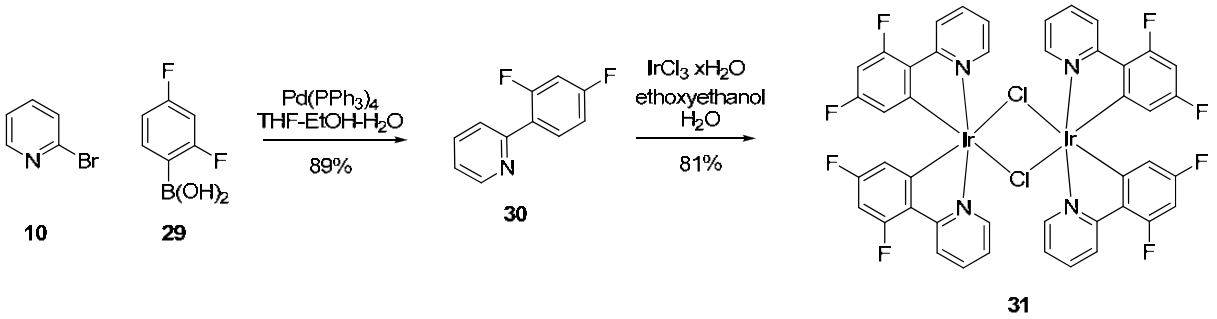

10 **29** **30** **31**

2-(2,4-difluorophenyl)pyridine (**30**) was prepared according to the literature.[81]

^{1}H NMR (200 MHz, $CDCl_3$): δ ppm 8.71 (d, *J* = 8 Hz, 1H); 8.00 (dd, *J* = 8, 2Hz, 1H); 7.72-7.75 (m, 2H); 7.25 (dd, *J* = 8, 2Hz, 1H); 7.01 (dd, *J* = 8, 2Hz, 1H); 6.92 (dd, *J* = 8, 2Hz, 1H).

tetrakis(2-(2,4-difluorophenyl)pyridine)bis(μ-ch1oro)diiridium (**31**) was synthesized according to the literature procedure.[81]

^{1}H NMR (200 MHz, $CDCl_3$): δ ppm 9.12 (dd, *J* = 5.9, 1.0 Hz, 4H), 8.31 (d, *J* = 8.4 Hz, 4H), 7.83 (dt, *J* = 7.6, 7.6, 1.2 Hz, 4H), 6.83 (ddd, *J* = 7.3, 5.9, 1.3 Hz, 4H), 6.34 (ddd, *J* = 12.4, 9.1, 2.3 Hz, 4H), 5.29 (dd, *J* = 9.0, 2.3 Hz, 4H).

b) Synthesis of tetrakis(2-phenylpyridine)bis(μ-ch1oro)diiridium (**44**)

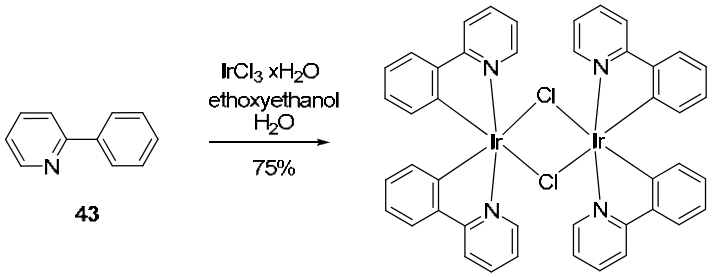

43 44

The complex was synthesized following the described procedure.[212]

^{1}H NMR (200 MHz, $CDCl_3$): δ ppm 9.24 (d, *J* = 5.1 Hz, 4H), 7.87 (d, *J* = 7.8 Hz, 4H), 7.48 (dd, *J* = 7.7, 1.1 Hz, 4H), 7.74 (t, *J* = 7.7, 7.7 Hz, 4H), 6.77 (dt, *J* = 5.8, 5.8, 1.3 Hz, 4H), 6.74 (dt, *J* = 7.6, 7.6, 1.1 Hz, 4H), 6.56 (dt, *J* = 7.6, 7.6, 1.3 Hz, 4H), 5.93 (dd, *J* = 7.7, 0.9 Hz, 4H)

VI.3.2. Iridium heteroleptic cyclometallated complexes

a) Synthesis of bis(2-(2,4-difluorophenyl)pyridine))(2-picolinic acid)iridium complex (**33**, FIrpic)

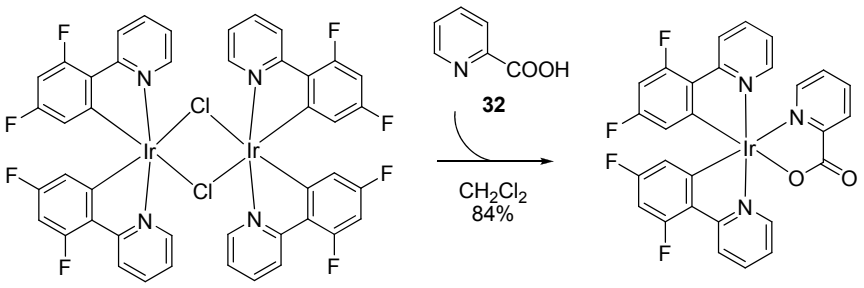

31 **33** FIrpic

The previously described[228] compound **33** was prepared adapting an existing procedure.[218]

The μ-chloro-bridged diiridium precursor **31** (82 mg, 0.068 mmol) and 2-picolinic acid **32** (23 mg, 0.187 mmol, 2.75 equivalents) were dissolved in CH_2Cl_2 (5 mL) and heated under argon at reflux for 16h. The reaction mixture was cooled at room temperature, washed with water to eliminate the unreacted picolinic acid, then the solvent was partially removed and the precipitate formed filtered, washed with water and dried under vacuum to give 79 mg (84%) of the pure product as a yellow powder.

^{1}H NMR (200 MHz, $CDCl_3$): δ ppm 8.74 (d, *J* = 5.8 Hz, 1H), 8.39-8.18 (m, 3H), 7.95 (dt, *J* = 7.7, 7.7, 1.6 Hz, 1H), 7.85-7.70 (m, 3H), 7.50-7.36 (m, 2H), 7.19 (ddd, *J* = 7.3, 5.8, 1.3 Hz, 1H), 6.97 (ddd, *J* = 7.3, 5.9, 1.3 Hz, 1H), 6.57-6.31 (m, 2H), 5.82 (dd, *J* = 8.7, 2.4 Hz, 1H), 5.57 (dd, *J* = 8.7, 2.4 Hz, 1H).

b) Synthesis of bis(2-(2,4-difluorophenyl)pyridine))(6-bromo-2-picolinic acid)iridium complex (**Ir1a**)

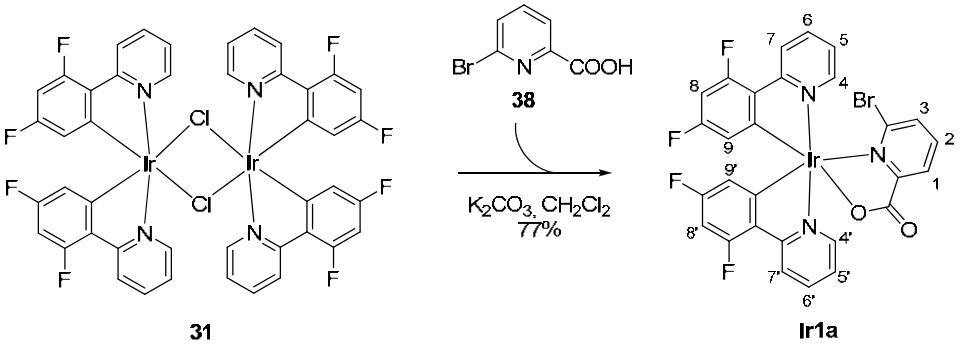

31 **Ir1a**

The μ-chloro-bridged diiridium precursor **31** (109 mg, 0.090 mmol) and 6-bromopicolinic acid **38** (50 mg, 0.246 mmol, 2.75 equivalents) were dissolved in CH_2Cl_2 (10 mL). Potassium carbonate anhydrous (125 mg, 10 equivalents) was added and the mixture heated under argon at reflux for 16h. The reaction mixture was cooled at room temperature and washed with water to eliminate the inorganic salts and the unreacted 6-bromopicolinic acid. Water was again added and the chlorinated solvent was removed by distillation under reduced pressure. The precipitate obtained was filtered, washed with water and dried to afford 107 mg (77%) of the pure product as a yellow powder.

^{1}H NMR (400 MHz, $CDCl_3$): δ ppm 8.62 (d, *J* = 5.7 Hz, H_4), 8.43 (dd, *J* = 7.6, 1.1 Hz, H_1), 8.32-8.25 (m, H_7 and $H_{7'}$), 7.87-7.74 (m, H_2, $H_{4'}$, H_6 and $H_{6'}$), 7.68 (dd, *J* = 7.9, 1.1 Hz, H_3), 7.16 (ddd, *J* = 7.2, 5.9, 1.1 Hz, H_5), 7.04 (ddd, *J* = 7.2, 5.8, 1.1 Hz, $H_{5'}$), 6.44-6.34 (m, H_8 and $H_{8'}$), 5.75 (dd, *J* = 8.9, 2.3 Hz, H_9), 5.37 (dd, *J* = 8.8, 2.3 Hz, $H_{9'}$)

Elemental analysis calcd. (%) for $C_{28}H_{15}BrF_4IrN_3O_2 \cdot 0.4\ CH_2Cl_2$: C 42.24, H 1.97, N 5.20; found: C 42.39, H 2.15, N 5.36.

c) Synthesis of bis(2-(2,4-difluorophenyl)pyridine))(5-bromo-2-picolinic acid)iridium complex (**Ir1**)

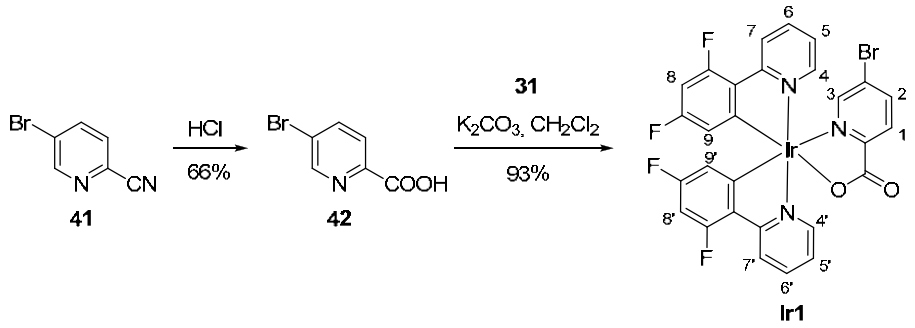

5-bromopicolinic acid (**42**) was synthesized according to the reported procedure.[227]

^{1}H NMR (200 MHz, d_6-dmso): δ ppm 13.46 (s, 1H), 8.84 (d, *J* = 1.9 Hz, 1H), 8.25 (dd, *J* = 8.4, 2.3 Hz, 1H), 7.97 (d, *J* = 8.4 Hz, 1H).

bis(2-(2,4-difluorophenyl)pyridine))(5-bromo-2-picolinic acid)iridium (**Ir1**)

The μ-chloro-bridged diiridium precursor **31** (725 mg, 0.596 mmol) and 5-bromopicolinic acid **42** (331 mg, 1.639 mmol, 2.75 equivalents) were dissolved in CH_2Cl_2 (75 mL).

Potassium carbonate anhydrous (825 mg, 10 equivalents) was added and the mixture heated under argon at reflux for 16h. The reaction mixture was cooled at room temperature and washed with water to eliminate the inorganic salts and the unreacted 5-bromopicolinic acid. Water was again added and the chlorinated solvent was removed by distillation under reduced pressure. The precipitate obtained was filtered, washed with water and dried to afford 853 mg (93%) of the pure **Ir1** as a yellow powder.

^{1}H NMR (400 MHz, $CDCl_3$): δ ppm 8.70 (d, *J* = 5.7 Hz, H_4), 8.28 (t, *J* = 9.1, 9.1 Hz, H_7 and $H_{7'}$), 8.21 (d, *J* = 8.3 Hz, H_1), 8.07 (dd, *J* = 8.3, 2.0 Hz, H_2), 7.84-7.75 (m, H_3, H_6 and $H_{6'}$), 7.45 (d, *J* = 5.7 Hz, $H_{4'}$), 7.20 (t, *J* = 6.6, 6.6 Hz, H_5), 7.01 (t, *J* = 6.6, 6.6 Hz, $H_{5'}$), 6.50 (ddd, *J* = 11.6, 9.3, 2.1 Hz, H_8), 6.40 (ddd, *J* = 11.6, 9.3, 2.1 Hz, $H_{8'}$), 5.81 (dd, *J* = 8.5, 2.0 Hz, H_9), 5.50 (dd, *J* = 8.6, 2.0 Hz, $H_{9'}$).

^{13}C NMR (50 MHz, $CDCl_3$): δ ppm 171.75, 164.77 (dd, *J* (C,F) = 64.2, 6.8 Hz), 150.60 (dd, *J* (C,F) = 59.5, 6.9 Hz), 150.45, 149.04, 148.57, 147.83, 141.21, 138.42, 129.59, 127.89, 125.42, 123.15 (dd, *J* (C,F) = 22.2, 19.8 Hz), 122.58, 122.42, 114.45 (ddd, *J* (C,F) = 20.4, 17.6, 2.8 Hz), 98.18 (dt, *J* (C,F) = 26.8, 26.8, 10.3 Hz).

Elemental analysis calcd. (%) for $C_{28}H_{15}BrF_4IrN_3O_2 \cdot 0.2\ CH_2Cl_2$: C 42.85, H 1.96, N 5.32; found: C 42.80, H 1.99, N 5.44.

d) Synthesis of bis(2-(2,4-difluorophenyl)pyridine))(6-(4-(6,6"-dicyano-terpyridin-4'-yl)phenyl)picolinic acid)iridium complex (**Ir2a**)

4'-(4-(6-methylpyridin-2-yl)phenyl)terpyridine-6,6"-dicarbonitrile (**36**)

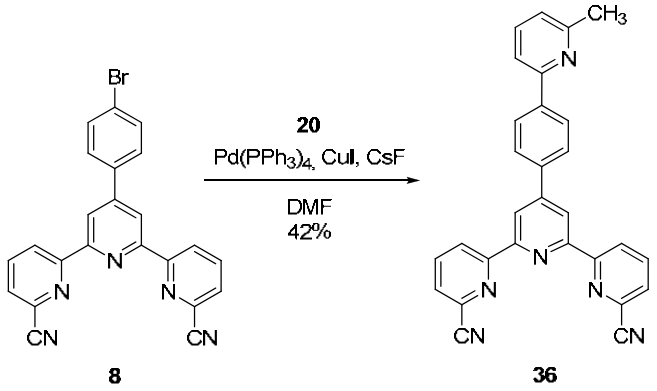

To a solution of 4'-(p-bromophenyl)-2,2':6',2"-terpyridine-6,6"-dicarbonitrile **8** (976 mg, 2.23 mmol) in anhydrous DMF (50 mL) under argon was added methyl-trimethylstannyl-pyridine **20** (570 mg) obtained as previously described, tetrakis-(triphenylphosphine)-palladium catalyst (127 mg, 5% mol), cuprous iodide (41.9 mg, 0.22 mmol) and cesium fluoride (677 mg, 4.46 mmol). The reaction mixture was stirred at 70°C under argon atmosphere for 24 h, then the solvent was evaporated under reduced pressure. Purification by column chromatography (alumina, dichloromethane) afforded after solvent evaporation 420 mg (42%) white powder.

^{1}H NMR (200 MHz, $CDCl_3$): δ ppm 8.86 (s, 2H), 8.87 (dd, *J* = 8.1, 1.0 Hz, 2H), 8.20 (d, *J* = 8.5 Hz, 2H), 8.03 (app. t, *J* = 7.9, 7.9 Hz, 4H), 7.77 (dd, *J* = 7.6, 1.0 Hz, 2H), 7.69 (d, *J* = 7.3 Hz, 1H), 7.63 (d, *J* = 6.7 Hz, 1H), 7.16 (d, *J* = 7.2 Hz, 1H), 2.68 (s, 3H).

Elemental analysis calcd. (%) for $C_{29}H_{18}N_6 \cdot 1.2\ H_2O$: C 73.78, H 4.36, N 17.80;
found: C 73.71, H 4.08, N 17.70.

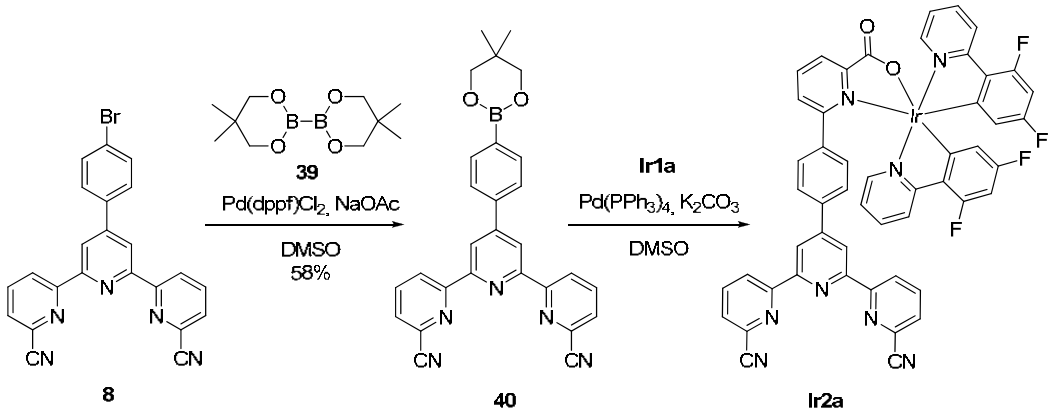

4'-(4-(Neopentyl-glycolatoboron)phenyl)terpyridine-6,6"-dicarbonitrile (**40**)

The product was prepared by adapting a literature procedure on a similar compound.[225]

To a solution of **8** synthesized as described before (1500 mg, 3.4 mmol) in anhydrous DMSO (30 mL) under argon were added bis(neopentyl glycolato)diboron **39** (965 mg, 4.1 mmol, 1.2 equivalents), NaOAc (840 mg, 3 equivalents) and $Pd(dppf)Cl_2 \cdot CH_2Cl_2$ (145 mg, 5% mol). After stirring at 80°C under argon for 7 h, the reaction mixture was diluted with CH_2Cl_2 (250 mL) and the resulting solution washed with water (300 mL). The organic phase was dried over Na_2SO_4, evaporated and purified by column chromatography (silica,

CH_2Cl_2 then CH_2Cl_2-ether 1:1). The product was obtained after recrystallization from CH_2Cl_2-MeOH (932 mg, 58%).

^{1}H NMR (200 MHz, $CDCl_3$): δ ppm 8.84 (dd, *J* = 8.3, 1.0 Hz, 2H), 8.83 (s, 2H), 8.02 (t, *J* = 7.9, 7.9 Hz, 2H), 8.01 (d, *J* = 7.9, 2H), 7.88 (d, *J* = 8.2 Hz, 2H), 7.76 (dd, *J* = 7.6, 0.9 Hz, 2H), 3.83 (s, 4H), 1.07 (s, 6H).

^{13}C NMR (50 MHz, $CDCl_3$): δ ppm 160.30, 157.08, 154.04, 142.45, 141.18, 137.82, 136.09, 131.65, 129.50, 129.46, 127.71, 123.34, 75.45, 34.93, 25.05.

ES$^+$-MS m/z: 1053.1 **40**H^+

Elemental analysis calcd. (%) for $C_{28}H_{22}BN_5O_2 \cdot 0.4\ CH_2Cl_2$: C 67.51, H 4.55, N 13.86; found: C 67.29, H 4.41, N 13.67.

bis(2-(2,4-difluorophenyl)pyridine))(6-(4-(6,6"-dicyano-terpyridin-4'-yl)phenyl)picolinic acid)iridium complex (**Ir2a**)

To a solution of **Ir1a** (400 mg, 0.516 mmol) in anhydrous DMSO (30 mL) under argon were added the boronic ester **40** (256 mg, 1.05 equivalents), anhydrous potassium carbonate (215 mg, 3 equivalents) and $Pd(PPh_3)_4$ catalyst (60 mg, 10% mol). After stirring at 80ºC for 20 h, the reaction mixture was diluted with CH_2Cl_2 and washed with water to remove DMSO and the inorganic salts. The organic phase was dried over Na_2SO_4, evaporated and separated by column chromatography on silica using a dietheylether-dichloromethane gradient for the elution of unreacted or deboronated starting material **40**, followed by a dichloromethane-acetone-ethanol gradient for the elution of the iridium complexes. Further separation of the fractions containing the desired coupling product (as checked by MS) was done by column chromatography on alumina, using a toluene-acetonitrile (3:1) solvent mixture. The resulting fractions were purified by crystallization from chloroform, affording the pure product as yellow crystals (6 mg, 1%).

^{1}H NMR (200 MHz, $CDCl_3$): δ ppm 8.89 (dd, *J* = 8.1, 0.8 Hz, 2H), 8.77 (br, 3H), 8.55 (dd, *J* = 7.7, 1.4 Hz, 1H), 8.23 (d, *J* = 8.0 Hz, 2H), 8.08 (dd, *J* = 8.6, 6.6 Hz, 1H), 8.03 (d, *J* = 7.9 Hz, 2H), 7.88 (t, *J* = 7.3, 7.3 Hz, 1H), 7.80 (t, *J* = 8.0, 8.0 Hz, 1H), 7.79 (dd, *J* = 7.6, 0.8 Hz, 2H),

7.60 (d, *J* = 5.5 Hz, 1H), 7.46 (dd, *J* = 7.6, 1.5 Hz, 1H), 7.45 (d, *J* = 8.4 Hz, 2H), 7.21 (ddd, *J* = 7.2, 5.8, 1.1 Hz, 1H), 7.07 (ddd, *J* = 7.2, 5.9, 1.2 Hz, 1H), 6.79 (br, 2H), 6.30 (ddd, *J* = 12.5, 9.3, 2.4 Hz, 1H), 5.94 (ddd, *J* = 12.2, 9.2, 2.3 Hz, 1H), 5.24 (ddd, *J* = 8.9, 5.0, 2.3 Hz, 2H)

e) Synthesis of bis(2-(2,4-difluorophenyl)pyridine))(5-(4-(6,6"-dicyano-terpyridin-4'-yl)phenyl)picolinic acid)iridium complex (**Ir2**)

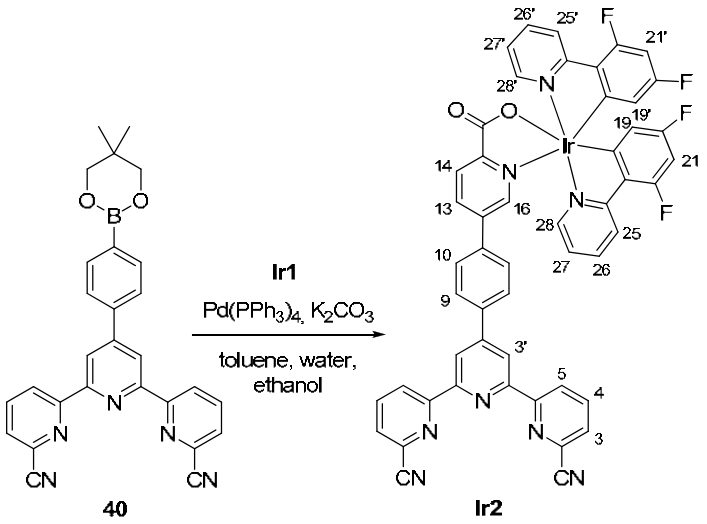

To a solution of **Ir1** (250 mg, 0.323 mmol) in degassed toluene (50 mL) under argon were added the boronic ester **40** (168 mg, 1.1 equivalents), anhydrous potassium carbonate (112 mg, 2.5 equivalents) in degassed water-ethanol (15 mL, 2:1) and $Pd(PPh_3)_4$ catalyst (26 mg, 7% mol). After stirring at 80ºC for 48 h, the heterogeneous reaction mixture was separated and the yellow precipitate was extracted in dichloromethane. The resulting organic phase was dried over Na_2SO_4 and the microcrystalline product was obtained by addition of toluene and evaporation of the chlorinated solvent, affording 226 mg (67%).

^{1}H NMR (400 MHz, $CDCl_3$): δ ppm 8.86 (dd, *J* = 8.1, 0.9 Hz, 2H, H_5), 8.83 (s, 2H, $H_{3'}$), 8.80 (d, *J* = 5.7 Hz, 1H, H_{25}), 8.43 (d, *J* = 8.1 Hz, 1H, H_{14}), 8.30 (t, *J* = 9.7, 9.7 Hz, 2H, $H_{25'}$ and H_{28}), 8.23 (dd, *J* = 8.2, 2.1 Hz, 1H, H_{13}), 8.05 (t, *J* = 7.7, 7.7 Hz, 2H, H_4), 8.05 (d, *J* = 2.2 Hz, 1H, H_{16}), 8.01 (d, *J* = 8.4 Hz, 2H, H_9), 7.80 (t, *J* = 7.7, 7.7 Hz, 2H, $H_{26'}$ and H_{27}), 7.78 (dd, *J* = 7.6, 0.9 Hz, 2H, H_3), 7.55 (d, *J* = 8.3 Hz, 2H, H_{10}), 7.56 (t, *J* = 4.9, 4.9 Hz, 1H, $H_{28'}$), 7.23 (ddd, *J* = 7.3, 6.0, 1.2 Hz, 1H, H_{26}), 7.02 (ddd, *J* = 7.3, 5.9, 1.3 Hz, 1H, $H_{27'}$), 6.55 (ddd, *J* =

11.7, 9.2, 2.3 Hz, 1H, H_{21}), 6.41 (ddd, *J* = 11.7, 9.2, 2.3 Hz, 1H, $H_{21'}$), 5.89 (dd, *J* = 8.5, 2.3 Hz, 1H, H_{19}), 5.59 (dd, *J* = 8.7, 2.3 Hz, 1H, $H_{19'}$).

^{13}C NMR (50 MHz, $CDCl_3$): δ ppm 172.53, 164.91 (dd, *J* (C,F) = 70.2, 7.0 Hz), 157.00, 154.24, 151.71 (dd, *J* = 63.8, 6.8 Hz), 150.36, 149.42, 148.72, 148.02, 145.97, 140.46, 138.74, 138.32, 138.05, 136.33, 135.91, 133.25, 128.65, 128.52, 128.38, 128.00, 127.69, 124.37, 123.15 (dd, *J* (C,F) = 22.2, 19.8 Hz), 122.59, 122.41, 119.96, 117.27, 114.48 (ddd, *J* (C,F) = 16.0, 13.0, 2.8 Hz), 98.03 (dt, *J* (C,F) = 27.1, 26.9, 9.6 Hz).

ES$^+$-MS m/z: 1053.1 **Ir2**H^+

Elemental analysis calcd. (%) for $C_{51}H_{27}F_4IrN_8O_2 \cdot 0.2\ CH_2Cl_2$: C 57.53, H 2.58, N 10.48; found: C 57.70, H 2.61, N 10.43.

f) Synthesis of bis(2-(2,4-difluorophenyl)pyridine))(5-(4-(6,6"-bis-(1H-tetrazol-5-yl)-terpyridin-4'-yl)phenyl)picolinic acid)iridium complex (**Ir3**)

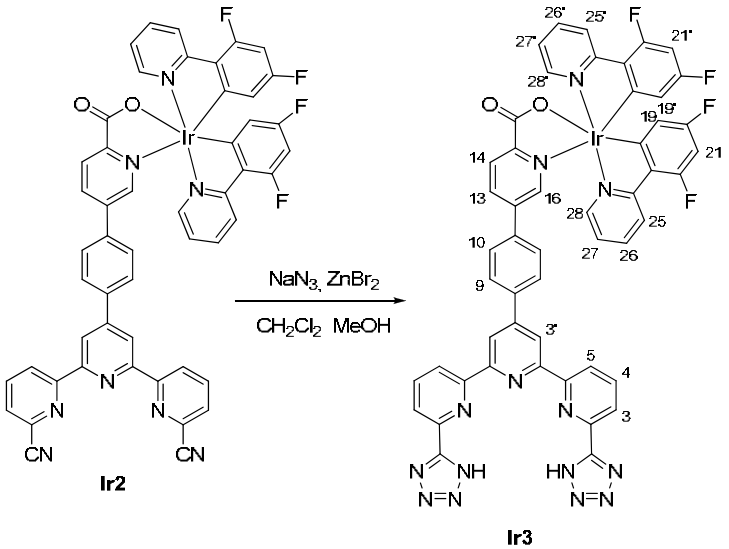

To a solution of **Ir2** (227 mg, 0.216 mmol) in CH_2Cl_2 (7 mL) under argon were added NaN_3 (140 mg, 2.16 mmol) and $ZnBr_2$ (97 mg, 0.432 mmol) dissolved in water (0.5 mL). Methanol (2 mL) was then added dropwise until a homogeneous, clear solution formed, which was stirred under argon at 35ºC for 24h. The resulting yellow precipitate was filtered, washed with methanol and water, and suspended in methanol. A solution of KOH in methanol (1N) was added until pH = 10, then the remaining insoluble products were filtered. The resulting clear yellow solution was treated with HCl in methanol (1N)

and the suspension obtained was stirred at room temperature for 1h and then refrigerated. The yellow precipitate was filtered, washed thoroughly with water and dried to afford 127 mg (62%) of product.

^{1}H NMR (200 MHz, dmso-D_6): δ ppm 9.16 (s, 2H, $H_{3'}$), 8.87 (d, *J* = 7.6 Hz, 2H, H_5), 8.61 (d, *J* = 5.7 Hz, 1H, H_{25}), 8.56 (dd, *J* = 8.1, 2.0 Hz, 1H, H_{13}), 8.33-8.25 (m, 9H, H_3, H_4, H_9, H_{14}, $H_{25'}$, H_{28}), 8.10 (t, *J* = 7.6, 7.6 Hz, 1H, $H_{26'}$), 8.25 (t, *J* = 7.6, 7.6 Hz, 1H, H_{27}), 7.99 (d, *J* = 1.8 Hz, 1H, H_{16}), 7.95 (d, *J* = 5.7 Hz, 1H, $H_{28'}$), 7.74 (d, *J* = 8.3 Hz, 2H, H_{10}), 7.54 (ddd, *J* = 7.1, 5.9, 0.9 Hz, 1H, H_{26}), 7.36 (ddd, *J* = 7.1, 5.9, 0.9 Hz, 1H, $H_{27'}$), 6.97 (ddd, *J* = 12.1, 9.5, 2.2 Hz, 1H, H_{21}), 6.81 (ddd, *J* = 12.1, 9.5, 2.2 Hz, 1H, $H_{21'}$), 5.87 (dd, *J* = 8.5, 2.3 Hz, 1H, H_{19}), 5.50 (dd, *J* = 8.5, 2.3 Hz, 1H, $H_{19'}$).

ES$^+$-MS m/z: 1139.1 **Ir3**H^+

Elemental analysis calcd. (%) for $C_{51}H_{29}F_4IrN_{14}O_2 \cdot 1\ CH_2Cl_2 \cdot 2\ H_2O$: C 49.61, H 2.80, N 15.57; found: C 49.69, H 2.87, N 15.81.

VI.3.3. Terpyridine dicarboxylate-diiridium complexes

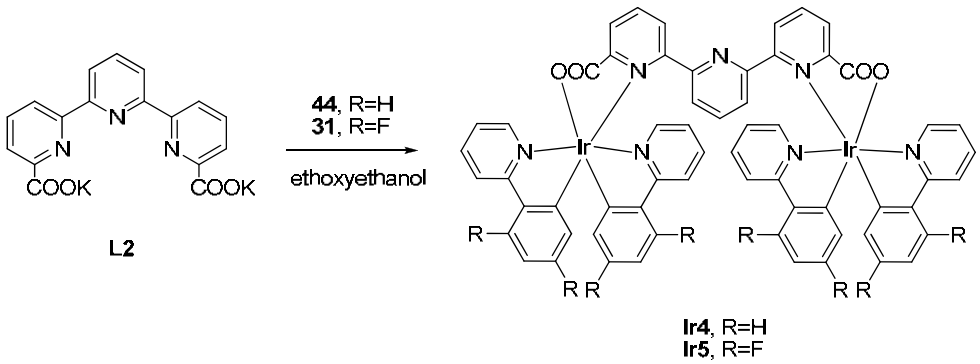

a) Synthesis of tetrakis(2-phenylpyridine)μ-(2,2':6',2''-terpyridine-6,6''-dicarboxylic acid)diiridium complex (**Ir4**)

Ligand **L2** (14.9 mg, 0.046 mmol) was suspended in methanol (10 mL) and reacted with a KOH solution 1N in methanol (92 μL, 0.092 mmol). The solvent was evaporated under vacuum and the resulting salt was suspended in ethoxyethanol (5 mL) under argon. The μ-chloro-bridged diiridium precursor **44** (49.6 mg, 0.046 mmol) was added and the mixture was stirred under argon at 60°C for 20h. The resulting precipitate was filtered, washed

with chloroform and recrystallized from dichloromethane-chloroform to afford 52.4 mg (86%) yellow product.

^{1}H NMR (200 MHz, $C_2D_2Cl_4$): δ ppm 8.68 (d, *J* = 4.3 Hz, 2H), 8.40 (d, *J* = 4.3 Hz, 2H), 8.34 (d, *J* = 7.4 Hz, 2H), 7.75 (t, *J* = 7.3, 7.3 Hz, 2H), 7.68-7.60 (m, 8H), 7.48-7.45 (m, 4H), 7.17 (d, *J* = 7.2 Hz, 2H), 7.07 (d, *J* = 7.1 Hz, 2H), 6.98 (dd, *J* = 5.7, 4.9 Hz, 2H), 6.81 (t, *J* = 6.8, 6.8 Hz, 2H), 6.61 (t, *J* = 6.7, 6.7 Hz, 2H), 6.41 (t, *J* = 6.6, 6.6 Hz, 2H), 6.30 (tbr, 1H), 6.24 (tbr, 2H), 6.07 (t, *J* = 6.9, 6.9 Hz, 2H), 5.71 (d, *J* = 7.3 Hz, 2H), 5.35 (d, *J* = 6.5 Hz, 2H).

ES$^+$-MS m/z: 1319.9 **Ir4**H^+

Elemental analysis calcd. (%) for $C_{61}H_{41}Ir_2N_7O_4 \cdot 1.5\ CHCl_3$: C 50.06, H 2.86, N 6.54; found: C 49.95, H 2.89, N 6.78.

b) Synthesis of tetrakis(2-(2,4-difluorophenyl)pyridine))μ-(2,2':6',2''-terpyridine-6,6''-dicarboxylic acid)diiridium complex (**Ir5**)

Ligand **L2** (17.3 mg, 0.054 mmol) was suspended in methanol (10 mL) and reacted with a KOH solution 1N in methanol (108 μL, 0.108 mmol). The solvent was evaporated under vacuum and the resulting salt was suspended in ethoxyethanol (5 mL) under argon. The μ-chloro-bridged diiridium precursor **31** (65.7 mg, 0.054 mmol) was added and the mixture was stirred under argon at 60°C for 20h. The resulting suspension was filtered, then the filtrate evaporated and separated by column chromatography on alumina using chloroform and chloroform-ethylacetate-ethanol (20:5:1). The product was finally obtained after recrystallization from dichloromethane-chloroform as 19.4 mg (25%) yellow powder.

^{1}H NMR (200 MHz, CD_2Cl_2): δ ppm 8.95 (dd, *J* = 5.7, 0.9 Hz, 2H), 8.46 (dd, *J* = 7.7, 1.3 Hz, 2H), 8.42 (dbr, 2H), 8.13 (d, *J* = 8.2 Hz, 4H), 7.85 (t, *J* = 7.7, 7.7 Hz, 2H), 7.76 (t, *J* = 7.8, 7.8 Hz, 2H), 7.59 (t, *J* = 7.7, 7.7 Hz, 2H), 7.27 (td, *J* = 7.6, 1.2, 1.2 Hz, 2H), 7.15 (ddd, *J* = 7.2, 5.9, 1.3 Hz, 2H), 6.85 (t, *J* = 7.7, 7.7 Hz, 1H), 6.38 (d, *J* = 7.7 Hz, 2H), 6.36 (ddd, *J* = 12.2, 9.6, 2.3 Hz, 2H), 6.25 (ddd, *J* = 7.2, 5.9, 1.2 Hz, 2H), 6.11 (ddd, *J* = 12.2, 9.6, 2.3 Hz, 2H), 5.24 (dd, *J* = 8.7, 2.3 Hz, 2H), 4.81 (dd, *J* = 8.3, 2.3 Hz, 2H).

ES$^+$-MS m/z: 1465.8 **Ir5**H^+

Elemental analysis calcd. (%) for $C_{61}H_{33}F_8Ir_2N_7O_4 \cdot 0.6\ CHCl_3$: C 48.17, H 2.20, N 6.38; found: C 48.19, H 2.47, N 6.55.

VI.4. Synthesis of lanthanide complexes

VI.4.1. Lanthanide complexes based on terpyridine ligands

a) Synthesis of the [Ln(**L1**)$_2$]NHEt$_3$ complexes (Ln = Eu, Tb, Nd)

A suspension of ligand **L1** (92.33 mg, 0.25 mmol) in methanol (6 mL) was reacted with triethylamine (69.69 µL, 0.5 mmol) to afford a colourless solution. After addition of a solution of Ln(OTf)$_3$ (0.12 mmol) in methanol (2 mL), the resulting slightly yellow solution was left standing at room temperature for 12 hours. The [Ln(**L1**)$_2$]NHEt$_3$ complexes were obtained as white crystals, filtered, washed with a little methanol and ether and dried in air (yield: 41-52%).

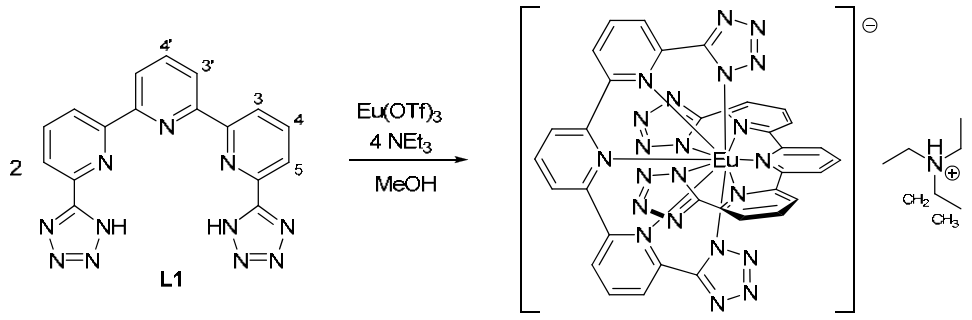

*[Eu(**L1**)$_2$]NHEt$_3$*

^{1}H NMR (400 MHz, MeOD): δ ppm 15.51 (d, *J* = 8.1 Hz, 4H, H$_5$), 12.20 (t, *J* = 7.8, 7.83 Hz, 4H, H$_4$), 5.33 (d, *J* = 7.8 Hz, 4H, H$_3$), 3.10 (q, *J* = 7.3, 7.3, 7.3 Hz, 6H, CH$_2$), 1.21 (t, *J* = 7.3, 7.3 Hz, 9H, CH$_3$) 0.72 (t, *J* = 7.5, 7.5 Hz, 2H, H$_{4'}$), -0.50 (d, *J* = 7.6 Hz, 4H, H$_{3'}$)

ES$^+$-MS m/z: 933.0 [(Eu**L1**$_2$)Na$_2$]$^+$

Elemental analysis calcd (%) for [Eu(C$_{17}$H$_9$N$_{11}$)$_2$]NHEt$_3$ · 1.25 MeOH · 1.5 H$_2$O: C 46.92, H 4.01, N 30.51; found: C 46.96, H 3.86, N 30.21.

*[Tb(**L1**)$_2$]NHEt$_3$*

^{1}H NMR (400 MHz, MeOD): δ ppm 95.43 (br, 4H), 91.87 (br, 2H, H$_{4'}$), 4.22 (q, *J* = 7.0, 7.0, 7.0 Hz, 6H, CH$_2$), 2.20 (t, *J* = 7.0, 7.0 Hz, 9H, CH$_3$), -4.58 (br, 4H), -67.59 (br, 4H), -140.08 (br, 4H). Due to the extreme paramagnetic effect of terbium, the multiplicities of the signals cannot be determined.

Elemental analysis calcd (%) for [Tb(C$_{17}$H$_9$N$_{11}$)$_2$]NHEt$_3$ · 5 H$_2$O · 0.5 CH$_3$OH: C 44.15, H 4.21, N 29.24; found: C 44.22, H 3.83, N 28.89.

*[Nd(**L1**)$_2$]NHEt$_3$*

^{1}H NMR (400 MHz, MeOD): δ ppm 16.18 (d, *J* = 6.3 Hz, 4H, H$_{3'}$), 14.99 (tbr, 2H, H$_{4'}$), 11.37 (d, *J* = 7.1 Hz, 4H, H$_3$), 5.84 (tbr, 4H, H$_4$), 3.11 (q, *J* = 7.3, 7.3, 7.3 Hz, 6H, CH$_2$), 2.06 (d, *J* = 6.4 Hz, 4H, H$_5$), 1.22 (t, *J* = 7.3, 7.3 Hz, 9H, CH$_3$)

Elemental analysis calcd (%) for [Nd(C$_{17}$H$_9$N$_{11}$)$_2$]NHEt$_3$ · 5 H$_2$O · 0.5 CH$_3$OH: C 44.72, H 4.26, N 29.63; found: C 44.74, H 3.95, N 29.36.

b) Synthesis of the [Ln(**L2**)$_2$]NHEt$_3$ complexes (Ln = Eu, Tb, Nd)

A suspension of ligand **L2** (76.36 mg, 0.24 mmol) in methanol (3 mL) was reacted with triethylamine (67 μL, 0.48 mmol) to give a clear solution. After adding a solution of Ln(OTf)$_3$ (0.12 mmol) in methanol (1 mL), a white precipitate formed, which completely redissolved in about 3 min upon heating. The solution was filtered and left at room temperature overnight. The [Ln(**L2**)$_2$]NHEt$_3$ complexes were obtained as white crystals, filtered, washed with a little methanol and dried in air (yield: 51-72%).

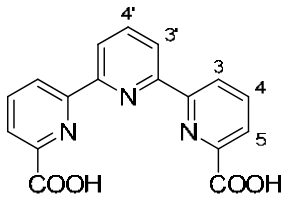

*[Eu(**L2**)$_2$]NHEt$_3$*

^{1}H NMR (400 MHz, MeOD): δ ppm 11.30 (d, *J* = 7.2 Hz, 4H, H$_5$), 9.81 (t, *J* = 7.7, 7.7 Hz, 4H, H$_4$), 7.10 (d, *J* = 7.8 Hz, 4H, H$_3$), 5.46 (t, *J* = 7.6, 7.6 Hz, 2H, H$_{4'}$), 5.01 (d, *J* = 7.7 Hz, 4H, H$_{3'}$), 3.06 (q, *J* = 7.3, 7.3, 7.3 Hz, 6H, CH$_2$), 1.20 (t, *J* = 7.3, 7.3 Hz, 9H, CH$_3$).

ES⁺-MS m/z: 793.3 $[Eu(\mathbf{L2})_2]H^+$

Elemental analysis calcd (%) for $C_{40}H_{34}EuN_7O_8 \cdot 3.75\ H_2O$: C 50.03, H 4.36, N 10.21; found: C 50.05, H 4.15, N 10.26.

*[Tb(**L2**)₂]NHEt₃*

¹H NMR (400 MHz, MeOD): δ ppm 13.23 (br, 6H, CH_2), 12.51 (br, 2H, $H_{4'}$), 9.50 (br, 9H, CH_3), -2.72 (br, 4H), -51,73 (br, 4H), -58.75 (br, 4H), -90.18 (br, 4H). Due to the extreme paramagnetic effect of terbium, the multiplicities of the signals cannot be determined.

Elemental analysis calcd (%) for $C_{40}H_{34}TbN_7O_8 \cdot 0.7\ MeOH \cdot 1.6\ H_2O$: C 51.48, H 4.24, N 10.31; found: C 51.38, H 4.06, N 10.30.

*[Nd(**L2**)₂]NHEt₃*

¹H NMR (400 MHz, MeOD): δ ppm 11.37 (d, J = 7.9 Hz, 4H, $H_{3'}$), 10.61 (t, J = 7.5, 7.5 Hz, 2H, $H_{4'}$), 9.90 (d, J = 7.8 Hz, 4H, H_3), 7.28 (t, J = 7.4, 7.4 Hz, 4H, H_4), 5.22 (d, J = 7.2 Hz, 4H, H_5), 3.20 (q, J = 7.3, 7.3, 7.3 Hz, 6H, CH_2), 1.29 (t, J = 7.3, 7.3 Hz, 9H, CH_3).

Elemental analysis calcd (%) for $C_{40}H_{34}NdN_7O_8 \cdot 3\ H_2O$: C 51.16, H 4.29, N 10.44; found: C 51.22, H 4.12, N 10.37.

c) Synthesis of the $[Ln(\mathbf{L3})_2]NHEt_3$ complexes (Ln = Eu, Tb)

A suspension of ligand **L3** (90.96 mg, 0.174 mmol) in methanol (5 mL) was reacted with triethylamine (48.36 µL, 0.347 mmol) to obtain a clear solution. After adding a solution of the appropriate lanthanide triflate (0.087 mmol) in methanol (1.5 mL) the resulting yellowish opalescent solution was heated until the opalescence disappeared and a fine crystalline precipitate started to form. The solution was left at room temperature overnight for crystallization. The crystals obtained was filtered, washed with a little methanol and dried in air to give a white-yellowish product (yield: 67-78%).

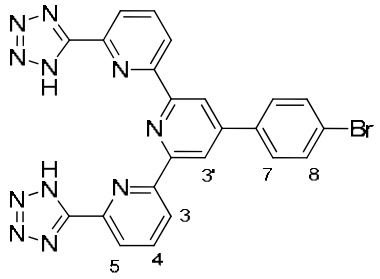

*[Eu(**L3**)$_2$]NHEt$_3$*

^{1}H NMR (400 MHz, MeOD): δ ppm 15.70 (d, *J* = 8.0 Hz, 4H, H$_5$), 12.27 (t, *J* = 7.9, 7.9 Hz, 4H, H$_4$), 6.06 (d, *J* = 8.9 Hz, 4H, H$_8$), 5.40 (d, *J* = 7.8 Hz, 4H, H$_3$), 4.08 (d, *J* = 9.0 Hz, 4H, H$_7$), 3.17 (q, *J* = 7.3, 7.3, 7.3 Hz, 6H, CH$_2$), 1.28 (t, *J* = 7.3, 7.3 Hz, 9H, CH$_3$), -0.30 (s, 4H, H$_{3'}$).

Elemental analysis calcd (%) for C$_{52}$H$_{40}$Br$_2$EuN$_{23}$· 1 MeOH · 3 H$_2$O: C 45.97, H 3.64, N 23.26; found: C 46.03, H 3.26, N 23.15.

*[Tb(**L3**)$_2$]NHEt$_3$*

^{1}H NMR (200 MHz, MeOD): δ ppm 104.63 (sbr, 4H), 61.31 (dbr, *J* = 24 Hz, 4H), 32.87 (dbr, *J* = 11 Hz, 4H), 3.50 (q, *J* = 7, 7, 7 Hz, 6H, CH$_2$), 1.57 (t, *J* = 7, 7 Hz, 9H, CH$_3$), -1.39 (sbr, 4H), -69.75 (dbr, *J* = 29 Hz, 4H), -146.42 (dbr, *J* = 81 Hz, 4H).

Elemental analysis calcd (%) for C$_{52}$H$_{40}$Br$_2$N$_{23}$Tb · 4.3 H$_2$O: C 45.15, H 3.54, N 23.29; found: C 45.08, H 3.25, N 23.11.

d) Synthesis of the [Ln(**L4**)$_2$]NHEt$_3$ complexes (Ln = Eu, Nd)

A suspension of ligand **L4** (98.03 mg, 0.185 mmol) in methanol (5 mL) was reacted with triethylamine (55 μL, 0.4 mmol) to give a clear yellow solution. After adding a solution of the appropriate lanthanide triflate (0.093 mmol) in methanol (2 mL), a yellow-orange precipitate formed, which completely redissolved in about 3 min upon heating. The solution was filtered and left at room temperature overnight. The crystals obtained was filtered, washed with a little methanol and dried in air to give a yellow product (yield: 58-64%).

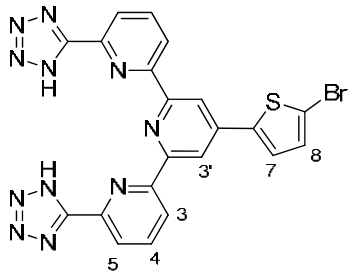

*[Eu(**L4**)$_2$]NHEt$_3$*

^{1}H NMR (400 MHz, MeOD): δ ppm 15.74 (d, *J* = 8.2 Hz, 4H, H$_5$), 12.29 (t, *J* = 8.0, 8.0 Hz, 4H, H$_4$), 5.62 (d, *J* = 4.4 Hz, 2H, H$_8$), 5.39 (d, *J* = 7.8 Hz, 4H, H$_3$), 4.20 (d, *J* = 4.3 Hz, 2H, H$_7$), 3.16 (q, *J* = 7.3, 7.3, 7.3 Hz, 6H, CH$_2$), 1.27 (t, *J* = 7.3, 7.3 Hz, 9H, CH$_3$), -0.38 (s, 4H, H$_{3'}$).

Elemental analysis calcd (%) for C$_{48}$H$_{36}$Br$_2$EuN$_{23}$S$_2$ · 1 MeOH · 1.5 H$_2$O: C 42.96, H 3.16, N 23.52; found: C 42.83, H 2.99, N 23.46.

*[Nd(**L4**)$_2$]NHEt$_3$*

^{1}H NMR (400 MHz, MeOD): δ ppm 16.51 (s, 4H, H$_{3'}$), 11.70 (d, *J* = 7.5 Hz, 4H, H$_3$ or H$_5$), 11.53 (d, *J* = 3.2 Hz, 2H, H$_7$), 8.97 (d, *J* = 3.2 Hz, 2H, H$_8$), 5.83 (t, *J* = 6.1, 6.1 Hz, 4H, H$_4$), 3.16 (q, *J* = 7.3, 7.3, 7.3 Hz, 6H, CH$_2$), 1.91 (d, *J* = 6.5 Hz, 4H, H$_5$ or H$_3$), 1.26 (t, *J* = 7.3, 7.3 Hz, 9H, CH$_3$).

Elemental analysis calcd (%) for C$_{48}$H$_{36}$Br$_2$NdN$_{23}$S$_2$ · 1 MeOH: C 44.08, H 3.02, N 24.13; found: C 44.18, H 2.96, N 24.11.

e) Synthesis of the [Eu(**L5**)$_2$]NHEt$_3$ complex

A suspension of ligand **L5** (48.31 mg, 0.092 mmol) in methanol (2 mL) was reacted with triethylamine (25 μL, 0.184 mmol) to give a clear solution. After adding a solution of europium triflate (27.7 mg, 0.046 mmol) in methanol (1 mL), a white precipitate formed, which completely redissolved in about 2 min upon heating. The solution was filtered and left at room temperature for slow evaporation. The precipitate obtained was filtered, washed with a little methanol and dried under vacuum to give 38 mg (64%) cream-white powder.

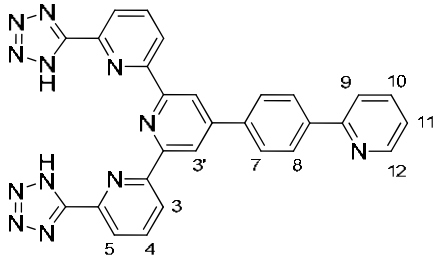

^{1}H NMR (400 MHz, MeOD): δ ppm 15.75 (d, *J* = 7.2 Hz, 4H, H_5), 12.30 (t, *J* = 7.5, 7.5 Hz, 4H, H_4), 8.03 (d, *J* = 4.2 Hz, 2H, H_{12}), 7.34 (t, *J* = 8.8, 8.8 Hz, 2H, H_{10}), 6.90 (d, *J* = 8.4 Hz, 2H, H_9), 6.87 (d, *J* = 7.3 Hz, 2H, H_{11}), 6.50 (d, *J* = 8.7 Hz, 4H, H_8), 5.42 (d, *J* = 7.8 Hz, 4H, H_3), 4.28 (d, *J* = 8.8 Hz, 4H, H_7), 3.17 (q, *J* = 7.3, 7.3, 7.3 Hz, 6H, CH_2), 1.28 (t, *J* = 7.3, 7.3 Hz, 9H, CH_3), -0.29 (s, 4H, $H_{3'}$)

Elemental analysis calcd (%) for $C_{62}H_{48}EuN_{25} \cdot 1.3\ CH_3OH \cdot 2\ H_2O$: C 55.38, H 4.20, N 25.51; found: C 55.46, H 4.13, N 25.32.

f) Synthesis of the [Nd(**L6**)$_2$]NHEt$_3$ complex

A suspension of ligand **L6** (52.71 mg, 0.082 mmol) in methanol (2 mL) was reacted with triethylamine (23 μL, 0.16 mmol) to give a clear yellow solution. A solution of neodymium triflate (24.14 mg, 0.041 mmol) in methanol (2 mL) was added, and the reaction mixture stirred at room temperature for 10 min, then acetonitrile (8 mL) was added and the methanol evaporated under reduced pressure. The resulting precipitate was filtered, washed with acetonitrile and dried, giving 57 mg (91%) yellow-orange powder.

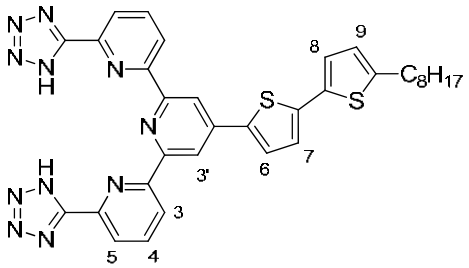

^{1}H NMR (400 MHz, MeOD): δ ppm 16.82 (s, 4H, $H_{3'}$), 11.80 (sbr, 6H, H_3 and H_6), 9.06 (d, *J* = 2.5 Hz, 2H, H_7), 8.51 (d, *J* = 3.1 Hz, 2H, H_8), 7.46 (d, *J* = 3.1 Hz, 2H, H_9), 5.78 (tbr, 4H, H_4), 3.34 (t, *J* = 7.8 Hz, 7.8 Hz, 4H, H_{C1}), 3.16 (q, *J* = 7.3, 7.3, 7.3 Hz, 6H, CH_2), 2.25-2.18 (m, 4H, H_{C2}), 1.88-1.80 (m, 4H, H_{C3}), 1.78 (dbr, 4H, H_5), 1.74-1.68 (m, 4H, H_{C4}), 1.66-1.62

(m, 4H, H_{C5}), 1.57-1.55 (m, 8H, H_{C6} and H_{C7}), 1.26 (t, *J* = 7.3, 7.3 Hz, 9H, CH_3), 1.11 (t, *J* = 7.1, 7.1 Hz, 6H, H_{C8})

Elemental analysis calcd (%) for $C_{72}H_{74}N_{23}NdS_4 \cdot 0.6$ MeOH $\cdot$ 2.6 H_2O: C 54.50, H 5.14, N 20.13; found: C 54.27, H 4.89, N 20.00.

g) Synthesis of the [Eu(**L1**)(TTA)] complex

A suspension of ligand **L1** (34.3 mg, 0.093 mmol) in methanol (7 mL) was reacted with triethylamine (26 µL, 0.19 mmol) to give a clear solution, followed by addition of europium triflate (55.71 mg, 0.093 mmol) in methanol (3 mL). To the resulting solution was added 2-thenoyltrifluoroacetone (TTA, 20.7 mg, 0.093 mmol) in methanol (2 mL) and in the presence of triethylamine (13 µL, 0.093 mmol). The resulting reaction mixture was left at room temperature for crystallization. The microcrystalline yellowish product obtained was filtered, washed with methanol and dried under vacuum to afford 51.1 mg (75%) complex.

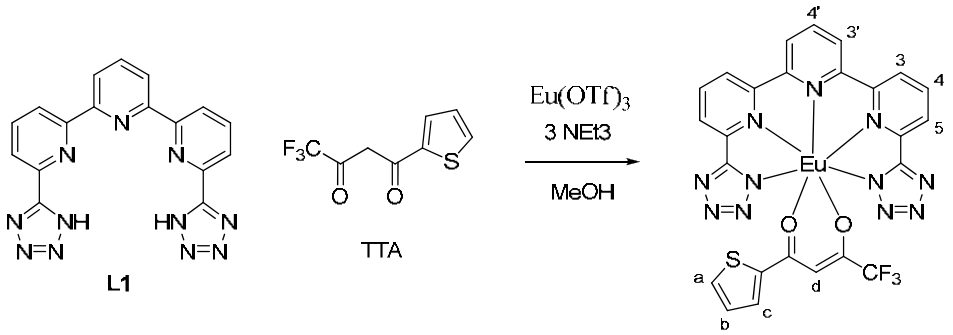

^{1}H NMR (200 MHz, dmso-D_6): δ ppm 9.07 (t, *J* = 7.6, 7.6 Hz, 1H, $H_{4'}$), 8.74 (t, *J* = 7.6, 7.6 Hz, 2H, H_4), 8.53 (d, *J* = 7.6 Hz, 2H, $H_{3'}$), 8.45 (d, *J* = 7.5 Hz, 2H, H_5), 7.65 (d, *J* = 7.7 Hz, 2H, H_3), 7.38 (d, *J* = 4.7 Hz, 1H, H_a), 6.41 (dd, *J* = 4.7, 3.4 Hz, 1H, H_b), 6.08 (d, *J* = 3.4 Hz, 1H, H_c), 4.46 (s, 1H, H_d)

Elemental analysis calcd (%) for $C_{25}H_{13}EuF_3N_{11}O_2S \cdot 1.6$ $CH_3OH \cdot 2.4$ H_2O_2: C 38.26, H 2.92, N 18.45; found: C 38.26, H 2.72, N 18.35.

h) Synthesis of the [Eu(**L12**)$(TTA)_2$] complex

A suspension of ligand **L12** (120.3 mg, 0.435 mmol) in methanol (2 mL) was reacted with a KOH solution (1N) in methanol (0.435 mL, 0.435 mmol) to give a clear solution, followed

by addition of europium triflate (260.0 mg, 0.435 mmol) in methanol (2 mL). To the resulting yellow solution, was added 2-thenoyltrifluoroacetone (TTA, 192.9 mg, 0.87 mmol) in methanol (2 mL) and in the presence of KOH (0.87 mL, 0.87 mmol, as 1N solution in methanol). The resulting reaction mixture was stirred at room temperature for 1h, then the solvent was evaporated and the complex extracted in dichloromethane. The organic phase was washed with water, dried over Na_2SO_4 and evaporated to give 367 mg white-cream powder (97%).

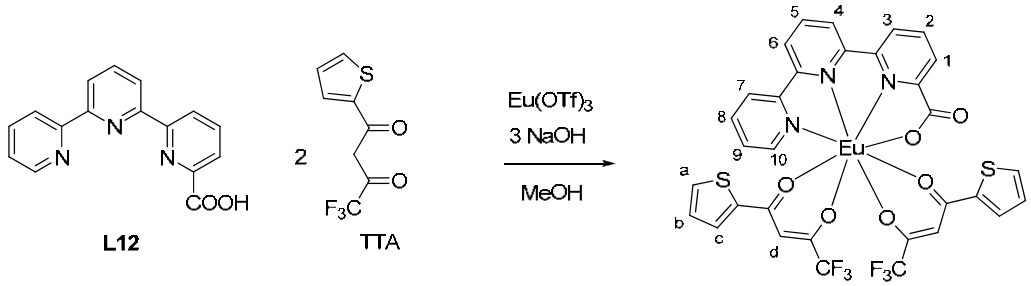

^{1}H NMR (400 MHz, MeOD, 268K): δ ppm 13.59 (br, 1H, H_{10}), 9.49 (br, 1H, H_5), 9.32 (br, 1H, H_6), 9.09 (br, 1H, H_4), 8.82 (br, 1H, H_8), 8.62 (br, 1H, H_7), 8.19 (br, 1H, H_2), 7.95 (br, 1H, H_9), 7.85 (br, 1H, H_3), 7.66 (br, 1H, H_1), 6.69 (br, 2H, H_a), 5.87 (br, 2H, H_b), 4.67 (br, 2H, H_c), 1.42 (br, 2H, H_d).

ES$^+$-MS m/z: 909.9 [Eu(**L12**)(TTA)$_2$]K$^+$

Elemental analysis calcd (%) for $C_{32}H_{18}EuF_6N_3O_6S_2 \cdot 1\ CH_2Cl_2$: C 41.48, H 2.11, N 4.40; found: C 41.63, H 2.22, N 4.52.

i) Synthesis of the [Tb(**L12**)(TFAC)$_2$] complex

A suspension of ligand **L12** (140.0 mg, 0.500 mmol) in methanol (3 mL) was reacted with a KOH solution (1N) in methanol (0.500 mL, 0.500 mmol) to give a clear solution, followed by addition of terbium triflate (306.2 mg, 0.500 mmol) in methanol (2 mL). To the resulting yellowish solution, was added trifluoroacetylacetone (TFAC, 122 µL, 1.000 mmol) in the presence of KOH (1.000 mL, as 1N solution in methanol). The resulting reaction mixture was left at room temperature overnight, then the precipitate obtained was filtered, washed with methanol and dried to afford 196 mg micro-crystalline product. The remaining filtrate was evaporated and the complex extracted in dichloromethane.

The organic phase was washed with water, dried over Na_2SO_4 and evaporated to give another 96 mg white powder (overall yield 292 mg, 78%).

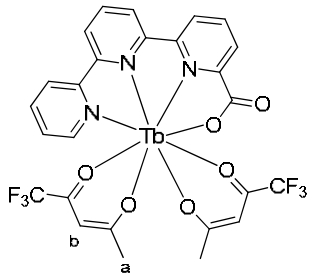

^{1}H NMR (400 MHz, $CDCl_3$, 298K): δ ppm 117.16 (br, 2H, H_b), 13.58 (br, 6H, H_a), -4.07 (br, 1H), -8.29 (br, 1H), -14.05 (br, 1H), -16.04 (br, 1H), -21.02 (br, 1H), -24.98 (br, 1H), -30.09 (br, 1H), -49.59 (br, 1H), -52.37 (br, 1H), -116.7 (br, 1H).

Elemental analysis calcd (%) for $C_{26}H_{18}F_6N_3O_6Tb \cdot 0.5\ CH_2Cl_2$: C 40.61, H 2.44, N 5.36; found: C 40.52, H 2.26, N 5.61.

VI.4.2. Lanthanide complexes based on bipyridine ligands

a) Synthesis of the [Ln(**L7**)$_2$]NHEt$_3$ complexes (Ln = Eu, Tb)

A suspension of ligand **L7** (69.80 mg, 0.24 mmol) in methanol (2 mL) was reacted with triethylamine (66.5 µL, 0.48 mmol) to obtain a colourless solution, followed by the addition of the appropriate lanthanide triflate (0.12 mmol) in 1 mL methanol. Acetonitrile (5 mL) was then added, and the solution was refrigerated for 12 hours. The [Ln(**L7**)$_2$]NHEt$_3$ complexes were obtained as white crystals, filtered, washed with a little methanol and acetonitrile and dried in air (yield: 76-88%).

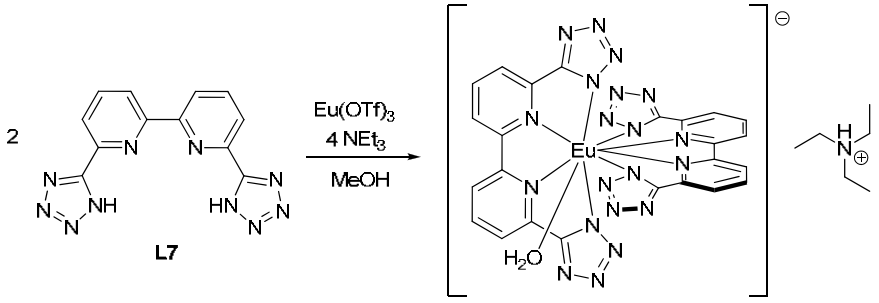

*[Eu(**L7**)$_2$]NHEt$_3$*

^{1}H NMR (200 MHz, MeOD): δ ppm 7.61 (t, *J* = 7.9, 7.9 Hz, 4H), 6.54 (d, *J* = 8.0 Hz, 4H), 5.37 (d, *J* = 7.8 Hz, 4H), 3.19 (q, *J* = 7.3, 7.3, 7.3 Hz, 6H, CH_2), 1.29 (t, *J* = 7.3, 7.3 Hz, 9H, CH_3).

Elemental analysis calcd. (%) for $C_{30}H_{28}EuN_{21} \cdot 4.3\ H_2O$: C 39.50, H 4.04, N 32.25; found: C 39.27, H 3.76, N 32.52.

*[Tb(**L7**)$_2$]NHEt$_3$*

^{1}H NMR (200 MHz, MeOD): δ ppm 17.75 (br, 4H), 4.07 (q, *J* = 6.6, 6.6, 6.6 Hz, 6H, CH_2), 2.10 (t, *J* = 6.5, 6.5 Hz, 9H, CH_3), -1.22 (br, 4H), -27.52 (br, 4H). Due to the extreme paramagnetic effect of terbium, the multiplicities of the signals cannot be determined.

Elemental analysis calcd. (%) for $C_{30}H_{28}N_{21}Tb \cdot 3.8\ H_2O$: C 39.59, H 3.94, N 32.32; found: C 39.30, H 3.56, N 32.60.

b) Synthesis of the [Ln(**L8**)$_2$]NHEt$_3$ complexes (Ln = Eu, Tb)

A suspension of ligand **L8** (53.02 mg, 0.20 mmol) in methanol (2 mL) was reacted with triethylamine (55.1 μL, 0.40 mmol) to obtain a colourless solution, followed by the addition of the appropriate lanthanide triflate (0.10 mmol) in methanol (1 mL). The solution is slowly evaporated to half, giving the [Ln(**L8**)$_2$]NHEt$_3$ complexes as white crystals, which are filtered, washed with a little methanol and dried in air (yield: 43-56%).

*[Eu(**L8**)$_2$]NHEt$_3$*

^{1}H NMR (200 MHz, MeOD): δ ppm 9.13 (t, *J* = 7.9, 7.9 Hz, 2H), 8.39 (d, *J* = 8.1 Hz, 2H), 7.39 (d, *J* = 7.8 Hz, 2H), 6.81 (d, *J* = 8.1 Hz, 2H), 6.63 (t, *J* = 7.8, 7.8 Hz, 2H), 4.00 (d, *J* = 7.6 Hz, 2H), 3.11 (q, *J* = 7.3, 7.3, 7.3 Hz, 6H), 1.21 (t, *J* = 7.3, 7.3 Hz, 9H)

Elemental analysis calcd. (%) for $C_{30}H_{28}EuN_{13}O_4 \cdot 2\ H_2O$: C 43.80, H 3.92, N 22.13; found: C 43.75, H 3.86, N 22.09.

*[Tb(**L8**)$_2$]NHEt$_3$*

^{1}H NMR (400 MHz, MeOD): δ ppm 60.46 (br, 2H), 26.95 (br, 2H), 3.23 (br, 6H, CH_2), 1.389 (br, 9H, CH_3), -3.54 (br, 2H), -24.11 (br, 2H), -28.35 (br, 2H), -32.38 (br, 2H). Due to the paramagnetic effect of terbium, the multiplicities of the signals cannot be determined.

Elemental analysis calcd. (%) for $C_{30}H_{28}N_{13}O_4Tb \cdot 2.5\ H_2O$: C 42.97, H 3.97, N 21.71; found: C 42.99, H 3.63, N 21.72.

c) Synthesis of the [Eu(**L9**)$_2$]NHEt$_3$ complex

A suspension of ligand **L9** (104.3 mg, 0.43 mmol) in methanol (20 mL) was treated with europium triflate (128.8 mg, 0.215 mmol). The mixture was heated at reflux for 15 min, under stirring, before triethylamine (120 µL, 0.86 mmol) was added. The solution is heated for complete solubilization, then evaporated to half. Diisopropylether is added, and the [Eu(**L9**)$_2$]NHEt$_3$ complex is obtained after a few days as a white powder, which is recrystallized from methanol to give finally 77.8 mg (49%) white crystals.

^{1}H NMR (200 MHz, MeOD): δ ppm 9.80 (d, J = 7.8 Hz, 4H), 8.86 (t, J = 7.8, 7.8 Hz, 4H), 6.97 (d, J = 7.5 Hz, 4H), 3.12 (q, J = 7.3, 7.3, 7.3 Hz, 6H, CH_2), 1.22 (t, J = 7.3, 7.3 Hz, 9H, CH_3)

Elemental analysis calcd. (%) for $C_{30}H_{28}EuN_5O_8 \cdot 2\ H_2O$: C 46.52, H 4.16, N 9.04; found: C 46.48, H 4.02, N 9.33.

VI.4.3. Lanthanide complexes based on pyridine ligands

a) Synthesis of the [Ln(**L10**)$_3$](NHEt$_3$)$_3$ complexes (Ln = Eu, Tb, Nd)

A suspension of ligand **L10** (81.49 mg, 0.38 mmol) in methanol (1.5 mL) was reacted with triethylamine (110 µL, 0.8 mmol) to give a colourless solution. After addition of a solution of Ln(OTf)$_3$ (0.1 mmol) in methanol (1 mL), the resulting solution was filtrated and left standing at room temperature for 12 hours. The complex was obtained as white crystals, filtered, washed with acetonitrile and dried in air. A second crop of crystals is obtained by adding acetonitrile to the filtrate and slow evaporation of the solution (final yield: 61-88%).

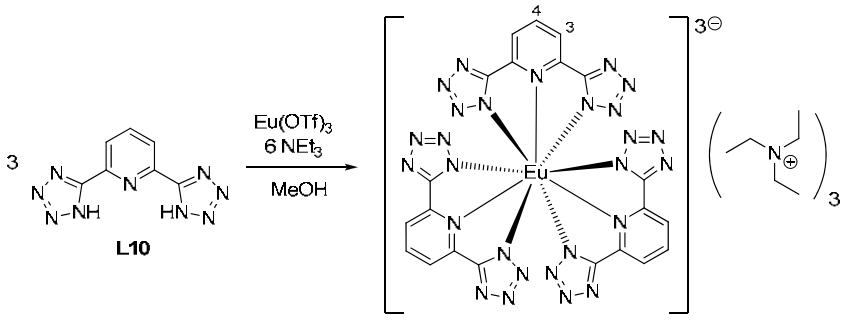

*[Eu(**L10**)$_3$](NHEt$_3$)$_3$*

^{1}H NMR (400 MHz, MeOD): δ ppm 6.29 (t, *J* = 7.9, 7.9 Hz, 3H, H$_4$), 5.04 (d, *J* = 7.9 Hz, 6H, H$_3$), 3.43 (q, *J* = 7.3, 7.3, 7.3 Hz, 18H, CH$_2$), 1.46 (t, *J* = 7.3, 7.3 Hz, 27H, CH$_3$).

ES$^+$-MS m/z: 997.6 [EuL$_3$](NHEt$_3$)$_2$H$_2^+$

Elemental analysis calcd. (%) for C$_{39}$H$_{57}$EuN$_{30}$ · H$_2$O: C 41.97, H 5.33, N 37.65; found: C 41.87, H 5.24, N 37.58.

*[Tb(**L10**)$_3$](NHEt$_3$)$_3$*

^{1}H NMR (200 MHz, MeOD): δ ppm 7.13 (br, 3H, H$_4$), 4.68 (br, 6H, H$_3$), 0.45 (br, 18H, CH$_2$), -0.74 (br, 27H, CH$_3$). Due to the extreme paramagnetic effect of terbium, the multiplicities of the signals cannot be determined.

Elemental analysis calcd. (%) for C$_{39}$H$_{57}$N$_{30}$Tb · 1.8 H$_2$O: C 41.18, H 5.37, N 36.94; found: C 41.15, H 5.15, N 36.80.

*[Nd(**L10**)$_3$](NHEt$_3$)$_3$*

^{1}H NMR (200 MHz, MeOD): δ ppm 10.33 (d, *J* = 7.8 Hz, 6H, H$_3$), 9.85 (t, *J* = 7.7, 7.7 Hz, 3H, H$_4$), 2.61 (q, *J* = 7.3, 7.3, 7.3 Hz, 18H, CH$_2$), 0.86 (t, *J* = 7.3, 7.3 Hz, 27H, CH$_3$).

Elemental analysis calcd. (%) for C$_{39}$H$_{57}$N$_{30}$Nd · 0.7 H$_2$O: C 42.47, H 5.34, N 38.10; found: C 42.73, H 5.30, N 37.83.

b) Synthesis of the [Eu(**L10**)$_3$](NHOct$_3$)$_3$ complex

A suspension of ligand **L10** (142.84 mg, 0.66 mmol) in methanol (4 mL) was reacted with trioctylamine (580 µL, 1.33 mmol) in chloroform (1.5 mL) to give a colourless solution. After addition of a solution of europium triflate (0.17 mmol) in methanol (4 mL), the

resulting solution was filtrated and the solvent evaporated. Separation by size-exclusion chromatography using Sephadex LH-20 in methanol afforded the complex as a highly-viscous transparent oil (228 mg, 74%).

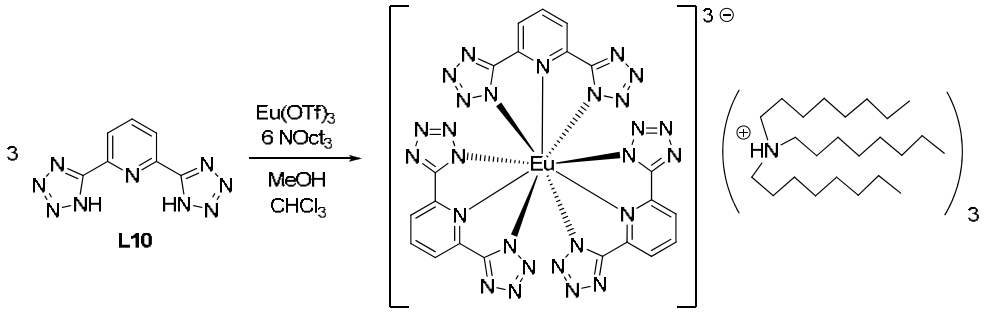

^{1}H NMR (200 MHz, MeOD): δ ppm 6.29 (t, *J* = 7.9, 7.9 Hz, 3H, H_4), 5.08 (d, *J* = 7.9 Hz, 6H, H_3), 3.31 (t, *J* = 8.4, 8.4 Hz, 18H, H_{1oct}), 1.80 (m, 18H, H_{2oct}), 1.40-1.29 (m, 90H, $H_{3oct-7oct}$), 0.90 (t, *J* = 6.5, 6.5 Hz, 27H, H_{8oct})

Elemental analysis calcd. (%) for $C_{93}H_{165}EuN_{30} \cdot 2H_2O$: C 59.05, H 9.01, N 22.22; found: C 58.80, H 8.90, N 22.13.

c) Synthesis of the [Eu(**L11**)$_3$](NHEt$_3$)$_3$ complex

A suspension of ligand **L11** (78.24 mg, 0.41 mmol) in methanol (1.5 mL) was reacted with triethylamine (125 µL, 0.9 mmol) to give a colourless solution. After addition of a solution of europium triflate (61.3 mg, 0.1 mmol) in methanol (1 mL), the resulting solution was filtrated, acetonitrile (5 mL) was added and the solution slowly evaporated. The white crystals obtained were filtered, washed with acetonitrile and dried in air (65.9 mg, 63%).

^{1}H NMR (200 MHz, MeOD): δ ppm 10.69 (d, *J* = 7.8 Hz, 1H), 9.47 (d, *J* = 7.9 Hz, 1H), 8.23 (t, *J* = 7.7, 7.7 Hz, 1H), 5.83 (t, *J* = 7.8, 7.8 Hz, 1H), 5.81 (d, *J* = 7.7 Hz, 1H), 5.47 (t, *J* = 7.7, 7.7 Hz, 1H^{sym}), 4.72 (d, *J* = 7.7 Hz, 1H^{sym}), 4.38 (d, *J* = 7.8 Hz, 1H^{sym}), 3.90 (q, *J* = 7.3, 7.3, 7.2 Hz, 24H, CH_2), 3.28 (t, *J* = 7.7, 7.7 Hz, 1H), 3.15 (d, *J* = 7.9 Hz, 1H), 1.60 (t, *J* = 7.3, 7.3 Hz, 36H, CH_3), 0.47 (d, *J* = 7.6 Hz, 1H), -0.61 (d, *J* = 7.6 Hz, 1H).

Elemental analysis calcd. (%) for $C_{39}H_{57}EuN_{18}O_6 \cdot 2\ H_2O$: C 44.11, H 5.79, N 23.74; found: C 44.29, H 5.68, N 23.89.

VI.4.4. Heterometallic iridium-lanthanide complexes

a) Synthesis of the [Eu(**Ir3**)$_2$](NHOct)$_3$ complex

A suspension of ligand **Ir3** (35.5 mg, 0.031 mmol) in dichloromethane (1.5 mL) was reacted with trioctylamine (30 μL, 0.07 mmol) to give a clear yellow solution. Then, a solution of europium triflate in methanol (1.56 mL, 10^{-2}M, 0.015 mmol) was added dropwise under stirring. The resulting mixture was separated by size-exclusion chromatography using Sephadex LH-20 and a methanol-dichloromethane (1:1) mobile phase, affording the complex as a yellow powder (5 mg, 14%) after solvent evaporation.

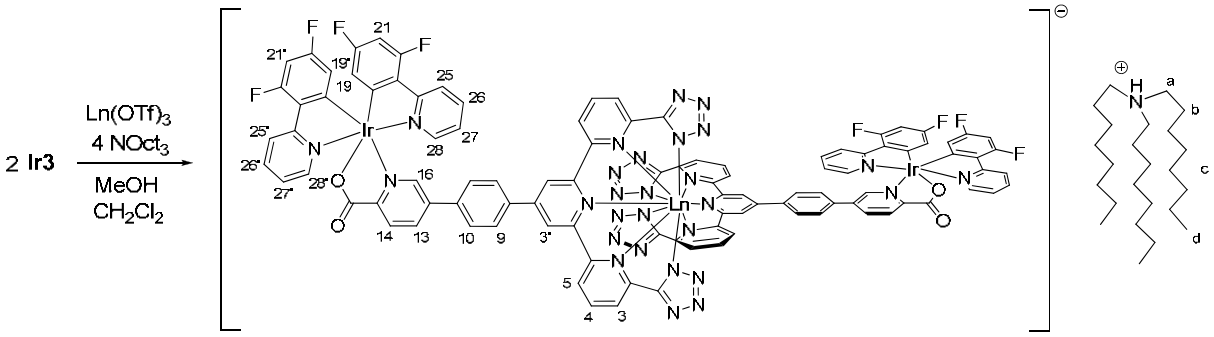

^{1}H NMR (400 MHz, MeOD-CD_2Cl_4): δ ppm 15.68 (d, *J* = 7.0 Hz, 4H, H_3), 12.22 (t, *J* = 7.5, 7.5 Hz, 4H, H_4), 8.24 (d, *J* = 5.3 Hz, 2H, H_{25}), 8.10 (d, *J* = 8.7 Hz, 2H, $H_{25'}$), 7.86 (t, *J* = 8.0, 8.0 Hz, 2H, H_{28}), 7.75 (d, *J* = 8.6 Hz, 2H, H_{14}), 7.65 (t, *J* = 7.8, 7.8 Hz, 2H, $H_{26'}$), 7.56 (dd, *J* = 12.0, 7.5 Hz, 2H, H_{27}), 7.37 (dd, *J* = 8.7, 1.4 Hz, 2H, H_{13}), 7.06 (d, *J* = 5.5 Hz, 2H, $H_{28'}$), 7.00 (t, *J* = 6.6, 6.6 Hz, 2H, H_{26}), 7.00 (s, 2H, H_{16}), 6.74 (t, *J* = 6.6, 6.6 Hz, 2H, $H_{27'}$), 6.35-6.28 (m, 2H, $H_{21'}$), 6.14-6.07 (m, 2H, H_{21}), 5.94 (d, *J* = 8.5 Hz, 4H, H_{10}), 5.34-5.28 (m, 8H, H_5, H_{19}, $H_{19'}$), 4.23 (d, *J* = 8.5 Hz, 4H, H_9), 3.04-3.00 (m, 6H, H_a), 1.66-1.58 (m, 6H, H_b), 1.34-1.27 (m, 30H, H_c), 0.87 (t, *J* = 6.8, 6.8 Hz, 9H, H_d), -0.29 (s, 4H, $H_{3'}$).

VI.5. Analytical techniques

Spectrophotometric titrations

UV titrations for the determination of conditional stability constants were performed on a Cary 50 Probe UV-vis spectrophotometer using 2 mm quartz cells, by titration of the

ligand with $Eu(OTf)_3$ in methanol solutions with ionic strength μ = 0.1 M (Me_4NCl), in either continuous or batch procedures. In the continuous experiments, solutions of high metal concentration ($2 \cdot 10^{-2}$ M compared to $2 \cdot 10^{-4}$ M for the ligand) were used in order to minimize dilution effects. Aliquots of 0.1 metal equivalents were added until reaching a M:L ratio of 3:1. In the batch experiments, 20 ligand solutions ($2 \cdot 10^{-4}$ M) were triturated with the corresponding metal solution and thermodynamically equilibrated at 45°C for 60h before being measured. Factor analysis[244] and mathematical treatment of the spectrophotometric data were performed with the SPECFIT program.[245, 246]

Luminescence measurements

Absorption spectra were recorded in 0.2 or 1 cm quartz cells on a Cary 50 Probe UV-vis spectrophotometer. Degassed samples of iridium complexes in solution were obtained by the freeze-pump-thaw technique (3 cycles), followed by equilibration with argon. Low-resolution visible luminescence measurements in solution (spectra, lifetimes, triplet states, quantum yields) were recorded on a Perkin-Elmer LS-50B spectrometer at 298K. For spectra and triplet state measurements in solid state or methanol glass, the spectrometer was fitted with a solid state adaptor equipped with a liquid nitrogen cooling system. Quartz cells with an optical path of 1 cm were used for room temperature spectra, while 77K measurements were carried out in quartz capillaries 3 mm in diameter. The singlet state was measured in methanol solutions at room temperature, while the triplet state was determined in solid state at 77K after a 0.2 ms delay. In solid state, the measurements were also done on a Fluorolog FL 3-22 spectrometer from Spex-Jobin-Yvon-Horiba with double grating emission and excitation monochromators, and a R928P photomultiplier. For measurements in the NIR spectral range, the spectrometer was fitted with a second measuring channel equipped with a FL-1004 single grating monochromator and light intensity was measured by two Jobin-Yvon solid state InGaAs detectors (i) DSS-IGA020L, cooled to 77 K (range 800-1600 nm) and (ii) DSS-IGA020A (range 800-1700 nm) working at room temperature and inserted into a LN2 housing including an elliptical mirror (90° beam path) and coupled to a Jobin Yvon SpectrAcq2 data acquisition system. All spectra

were corrected for the instrumental functions. The phosphorescence lifetimes were measured by recording the decay at the maximum of the emission spectra. The signals were analyzed as monoexponential decays in Origin® 8, and the values reported are the average of three independent determinations. Solutions for quantum yield measurements, with an absorbance usually kept under A = 0.2 in 2 mm quartz cells, were prepared by dissolution of the isolated complexes in spectrophotometric grade methanol. Quantum yields, Φ, have been calculated using the equation

$$\Phi_x/\Phi_r = A_r(\lambda)\, n_x^2\, D_x / A_s(\lambda)\, n_r^2\, D_r \qquad \text{(VI.1)}$$

where *x* refers to the sample, *r* refers to the reference, *A* is the absorbance at the excitation wavelength, *n* is the refractive index and *D* is the integrated, corrected emitted intensity over the spectral domain. The tris(dipicolinate) complexes $[Eu(dpa)_3]^{3-}$ (Φ = 24%, $7.5\cdot10^{-5}$ M in Tris buffer 0.1 M) and $[Tb(dpa)_3]^{3-}$ (Φ = 22%, $6.5\cdot10^{-5}$ M in Tris buffer 0.1 M) were used as references for the determination of solution quantum yields of the Eu and Tb containing samples, respectively[39]. The error for this type of measurements is usually taken as 15%. Absolute quantum yields in solid state were determined using the Fluorolog FL 3-22 with a home-modified integrating sphere from Oriel and the procedure is described elsewhere[247]. Emission and excitation spectra were corrected for the source intensity and emission spectral response.

DFT Calculations

The molecular geometry optimizations and electronic structures of the Ir complexes were explored by quantum chemistry in the framework of Kohn-Sham DFT (Density Functional Theory), using the Amsterdam Density Functional (ADF 2006) software package.[248,249] Basis sets were made of Slater type orbital double zeta functions including one polarization for H, N, C, O, F (1s) and Br (1s-3p), and triple zeta including one polarization function for Ir (1s-4d) metal. Becke 86 - Perdew 88 General Gradient Approximation (GGA) functional[250] has been used for all calculations. The solvent was taken into account through a Polarizable Continuum Model within ADF using the default parameters of the program.

Crystallography

All diffraction data, except for crystals of the complexes **Ir1** and **Ir2**, were collected using a Bruker SMART CCD area detector three-circle diffractometer (Mo-Kα radiation, graphite monochromator, λ = 0.71073 Å), controlled by the Bruker SMART software[251]. To prevent evaporation of co-crystallized solvent molecules, the crystals were coated with a light hydrocarbon oil and quickly transferred on the diffractometer into a stream of cold (223K) nitrogen. At the end of data collection, the first 50 frames were recollected to verify that crystal decay had not taken place during the experiment. Unique intensities with I > 10σ (I) detected on all frames using the Bruker SAINT program[252] were used to refine the values of the cell parameters. The substantial redundancy in data allows empirical absorption corrections to be applied using multiple measurements of equivalent reflections with the Bruker SADABS program[253]. Space groups were determined from systematic absences, and they were confirmed by the successful resolution of the structures. The structures were solved by direct methods using the Bruker SHELXTL 6.14 package[254] and all the atoms, including hydrogen atoms, were found by difference Fourier syntheses. All non-hydrogen atoms were anisotropically refined on *F*, whereas hydrogen atoms were refined isotropically.

For crystals of the complexes **Ir1** and **Ir2**, all diffraction data were collected using an Oxford Diffraction XCalibur S area detector four-circle diffractometer (Mo-Kα radiation, graphite monochromator, λ = 0.71073 Å), controlled by the Oxford Diffraction CrysAlis CCD software. Unique intensities with I > 10σ (I) were detected on all frames using the Oxford Diffraction CrysAlis RED software. Empirical absorption corrections were applied using multiple measurements of equivalent reflections with the Oxford Diffraction ABSPACK software and the structures were solved by direct methods using the SHELXS-97 package.

Bibliography

1. COTTON, S., *Lanthanide and Actinide Chemistry*. John Wiley: Chichester, 2006.

2. BUNZLI, J.C.; MILICIC-TANG, A., Solvation and anion interaction in organic solvents. In *Handbook on the Physics and Chemistry of Rare Earths*, Karl A. Gschneidner; Eyring, L., Eds. Elsevier: Amsterdam, 1995; Vol. 21, pp 305-366.

3. CARAVAN, P.; ELLISON, J.J.; MCMURRY, T.J.; LAUFFER, R.B., Gadolinium(III) Chelates as MRI Contrast Agents: Structure, Dynamics, and Applications. *Chemical Reviews* **1999,** *99* (9), 2293-352.

4. BRUCE, J.I.; LOWE, M.P.; PARKER, D., Photophysical Aspects of Lanthanide(III) Complexes. In *The Chemistry of Constrast Agents in Medical Magnetic Resonance Imaging*, Merbach, A.E.; Toth, E., Eds. John Willey & Sons: 2001; pp 437-460.

5. BUNZLI, J.C.; ELISEEVA, S.V., Basics of Lanthanide Photophysics. In *Lanthanide Spectroscopy, Materials and Bio-Applications*, Hanninen, P.; Harma, H., Eds. Springer: 2009; Vol. 7.

6. BUNZLI, J.C.G.; COMBY, S.; CHAUVIN, A.S.; VANDEVYVER, C.D.B., New opportunities for lanthanide luminescence. *Journal of Rare Earths* **2007,** *25* (3), 257-274.

7. BUNZLI, J.-C.G., Lanthanide Luminescent Bioprobes (LLBs). *Chemistry Letters* **2009,** *38* (2), 104-109.

8. COMBY, S.; BÜNZLI, J.-C.G., Lanthanide Near-Infrared Luminescence in Molecular Probes and Devices. In *Handbook on the Physics and Chemistry of Rare Earths*, Karl A. Gschneidner, J.J.-C.B.; Vitalij, K.P., Eds. Elsevier: Amsterdam, 2007; Vol. Volume 37, pp 217-470.

9. WEISSMAN, S.I., Intramolecular Energy Transfer The Fluorescence of Complexes of Europium. *The Journal of Chemical Physics* **1942,** *10* (4), 214-217.

10. BUNZLI, J.C.G., Lanthanide-containing luminescent molecular edifices. *Journal of Alloys and Compounds* **2006,** *408*, 934-944.

11. DOSSING, A., Luminescence from lanthanide(3+) ions in solution. *European Journal of Inorganic Chemistry* **2005,** (8), 1425-1434.

12. BUNZLI, J.C.G.; PIGUET, C., Taking advantage of luminescent lanthanide ions. *Chemical Society Reviews* **2005,** *34* (12), 1048-1077.

13. DE SILVA, A.P.; FOX, D.B.; HUXLEY, A.J.M.; MCCLENAGHAN, N.D.; ROIRON, J., Metal complexes as components of luminescent signalling systems. *Coordination Chemistry Reviews* **1999,** *186*, 297-306.

14. DE SA, G.F.; MALTA, O.L.; DONEGA, C.D.; SIMAS, A.M.; LONGO, R.L.; SANTA-CRUZ, P.A.; DA SILVA, E.F., Spectroscopic properties and design of highly luminescent lanthanide coordination complexes. *Coordination Chemistry Reviews* **2000,** *196*, 165-195.

15. GONCALVES E SILVA, F.R.; MALTA, O.L.; REINHARD, C.; GUDEL, H.-U.; PIGUET, C.; MOSER, J.E.; BUNZLI, J.-C.G., Visible and Near-Infrared Luminescence of Lanthanide-Containing Dimetallic Triple-Stranded Helicates: Energy Transfer Mechanisms in the Sm(III) and Yb(III) Molecular Edifices. *The Journal of Physical Chemistry A* **2002,** *106* (9), 1670-1677.

16. LATVA, M.; TAKALO, H.; MUKKALA, V.M.; MATACHESCU, C.; RODRIGUEZUBIS, J.C.; KANKARE, J., Correlation between the lowest triplet state energy level of the ligand and lanthanide(III) luminescence quantum yield. *Journal of Luminescence* **1997,** *75* (2), 149-169.

17. SATO, S.; WADA, M., Relations between Intramolecular Energy Transfer Efficiencies and Trplet State Energies in Rare Earth Beta-Diketone Chelates. *Bulletin of the Chemical Society of Japan* **1970,** *43* (7), 1955-1962.

18. ARNAUD, N.; GEORGES, J., Comprehensive study of the luminescent properties and lifetimes of Eu3+ and Tb3+ chelated with various ligands in aqueous solutions: influence of the synergic agent, the surfactant and the energy level of the ligand triplet. *Spectrochimica Acta Part A - Molecular and Biomolecular Spectroscopy* **2003,** *59* (8), 1829-1840.

19. ARCHER, R.D.; CHEN, H.; THOMPSON, L.C., Synthesis, Characterization, and Luminescence of Europium(III) Schiff Base Complexes. *Inorganic Chemistry* **1998,** *37* (8), 2089-2095.

20. GUILLAUMONT, D.; BAZIN, H.; BENECH, J.M.; BOYER, M.; MATHIS, G., Luminescent Eu(III) and Gd(III) trisbipyridine cryptates: Experimental and theoretical study of the substituent effects. *Chemphyschem* **2007,** *8* (3), 480-488.

21. SAMUEL, A.P.S.; XU, J.; RAYMOND, K.N., Predicting Efficient Antenna Ligands for Tb(III) Emission. *Inorganic Chemistry* **2009,** *48* (2), 687-698.

22. HANSCH, C.; LEO, A.; TAFT, R.W., A Survey of Hammett Substituent Constants and Resonance and Field Parameters. *Chemical Reviews* **1991,** *91* (2), 165-195.

23. DE SILVA, C.R.; LI, J.; ZHENG, Z.P.; CORRALES, L.R., Correlation of calculated excited-state energies and experimental quantum yields of luminescent Tb(III) beta-diketonates. *Journal of Physical Chemistry A* **2008,** *112* (20), 4527-4530.

24. SENEGAS, J.-M.; BERNARDINELLI, G.; IMBERT, D.; BUNZLI, J.-C.G.; MORGANTINI, P.-Y.; WEBER, J.; PIGUET, C., Connecting Terminal Carboxylate Groups in Nine-Coordinate Lanthanide Podates: Consequences on the Thermodynamic, Structural, Electronic, and Photophysical Properties. *Inorganic Chemistry* **2003,** *42* (15), 4680-4695.

25. STEEMERS, F.J.; VERBOOM, W.; REINHOUDT, D.N.; VANDERTOL, E.B.; VERHOEVEN, J.W., New Sensitizer-Modified Calix[4]Arenes Enabling Near-UV Excitation of Complexed Luminescent Lanthanide Ions. *Journal of the American Chemical Society* **1995,** *117* (37), 9408-9414.

26. SABBATINI, N.; GUARDIGLI, M.; LEHN, J.M., Luminescent Lanthanide Complexes as Photochemical Supramolecular Devices. *Coordination Chemistry Reviews* **1993,** *123* (1-2), 201-228.

27. BUNZLI, J.C.G., Benefiting from the unique properties of lanthanide ions. *Accounts of Chemical Research* **2006,** *39* (1), 53-61.

28. BINNEMANS, K., Rare-earth beta-diketonates. In *Handbook on the Physics and Chemistry of Rare Earths*, Gschneidner, K.A.; Bunzli, J.-C.G.; Pecharsky, V.K., Eds. Elsevier: Amsterdam, 2005; Vol. 35, pp 107-252.

29. COMBY, S.; IMBERT, D.; CHAUVIN, A.S.; BUNZLI, J.C.G., Stable 8-hydroxyquinolinate-based podates as efficient sensitizers of lanthanide near-infrared luminescence. *Inorganic Chemistry* **2006,** *45* (2), 732-743.

30. BETTENCOURT-DIAS, A.D., Small Molecule Luminescent Lanthanide Ion Complexes - Photophysical Characterization and Recent Developments. *Current Organic Chemistry* **2007,** *11*, 1460-1480.

31. ALEXANDER, V., Design and Synthesis of Macrocyclic Ligands and Their Complexes of Lanthanides and Actinides. *Chemical Reviews* **1995,** *95* (2), 273-342.

32. SAKAMOTO, M.; MANSEKI, K.; OKAWA, H., d-f Heteronuclear complexes: synthesis, structures and physicochemical aspects. *Coordination Chemistry Reviews* **2001,** *219*, 379-414.

33. WARD, M.D., Transition-metal sensitised near-infrared luminescence from lanthanides in d-f heteronuclear arrays. *Coordination Chemistry Reviews* **2007,** *251* (13-14), 1663-1677.

34. GRENTHE, I., Stability Relationships among Rare Earth Dipicolinates. *Journal of the American Chemical Society* **1961,** *83* (2), 360-364.

35. HORROCKS, W.D.; SUDNICK, D.R., Time-Resolved Europium(III) Excitation Spectroscopy - Luminescence Probe of Metal-Ion Binding-Sites. *Science* **1979,** *206* (4423), 1194-1196.

36. ALBERTSSON, J., Structural Studies on Rare-Earth Carboxylates.10. The Crystal and Molecular Structure of Monoclinic Trisodium Tris(pyridine-2,6-dicarboxylato)ytterbate(III) 13-Hydrate. *Acta Chemica Scandinavica* **1972,** *26* (3), 985-1004.

37. BRAYSHAW, P.A.; BUNZLI, J.C.G.; FROIDEVAUX, P.; HARROWFIELD, J.M.; KIM, Y.; SOBOLEV, A.N., Synthetic, Structural, and Spectroscopic Studies on Solids Containing Tris(Dipicolinato) Rare-Earth Anions and Transition or Main-Group Metal-Cations. *Inorganic Chemistry* **1995,** *34* (8), 2068-2076.

38. CHAUVIN, A.S.; GUMY, F.; IMBERT, D.; BUNZLI, J.C.G., Europium and terbium tris(dipicolinates) as secondary standards for quantum yield determination. *Spectroscopy Letters* **2004,** *37* (5), 517-532.

39. CHAUVIN, A.S.; GUMY, F.; IMBERT, D.; BUNZLI, J.C.G., Europium and terbium tris (dipicolinates) as secondary standards for quantum yield determination. *Spectroscopy Letters* **2007,** *40* (1), 193.

40. CHATTERTON, N.; BRETONNIERE, Y.; PECAUT, J.; MAZZANTI, M., An efficient design for the rigid assembly of four bidentate chromophores in water-stable highly luminescent lanthanide complexes. *Angewandte Chemie-International Edition* **2005,** *44* (46), 7595-7598.

41. ALPHA, B.; LEHN, J.M.; MATHIS, G., Energy-Transfer Luminescence of Europium(III) and Terbium(III) Cryptates of Macrobicyclic Polypyridine Ligands. *Angewandte Chemie-International Edition* **1987,** *26* (3), 266-267.

42. COMBY, S.; IMBERT, D.; CHAUVIN, A.S.; BUNZLI, J.C.G.; CHARBONNIERE, L.J.; ZIESSEL, R.F., Influence of anionic functions on the coordination and photophysical properties of lanthanide(III) complexes with tridentate bipyridines. *Inorganic Chemistry* **2004,** *43* (23), 7369-7379.

43. KOTTAS, G.S.; MEHLSTAUBL, M.; FROEHLICH, R.; DE COLA, L., Highly luminescent, neutral, nine-coordinate lanthanide(III) complexes. *European Journal of Inorganic Chemistry* **2007,** (22), 3465-3468.

44. CHARBONNIERE, L.J.; WEIBEL, N.; RETAILLEAU, P.; ZIESSEL, R., Relationship between the ligand structure and the luminescent properties of water-soluble lanthanide complexes containing bis(bipyridine) anionic arms. *Chemistry-a European Journal* **2007,** *13* (1), 346-358.

45. CHARBONNIERE, L.J.; WEIBEL, N.; ZIESSEL, R.F., Synthesis of mono-, bis- and tris-tridentate ligands based on 5'-substituted-2,2'-bipyridine-6-carboxylic acid. *Tetrahedron Letters* **2001,** *42* (4), 659-662.

46. MURNER, H.R.; CHASSAT, E.; THUMMEL, R.P.; BUNZLI, J.C.G., Strong enhancement of the lanthanide-centred luminescence in complexes with 4-alkylated 2,2':6',2''-terpyridines. *Journal of the Chemical Society-Dalton Transactions* **2000,** (16), 2809-2816.

47. PETOUD, S.; BUNZLI, J.C.G.; SCHENK, K.J.; PIGUET, C., Luminescent properties of lanthanide nitrate complexes with substituted bis(benzimidazolyl)pyridines. *Inorganic Chemistry* **1997,** *36* (7), 1345-1353.

48. PIGUET, C.; WILLIAMS, A.F.; BERNARDINELLI, G.; BUNZLI, J.C.G., Structural and Photophysical Properties of Lanthanide Complexes with Planar Aromatic Tridentate Nitrogen Ligands as Luminescent Building-Blocks for Triple-Helical Structures. *Inorganic Chemistry* **1993,** *32* (19), 4139-4149.

49. MARTIN, N.; BUNZLI, J.C.G.; MCKEE, V.; PIGUET, C.; HOPFGARTNER, G., Self-assembled dinuclear lanthanide helicates: Substantial luminescence enhancement upon replacing terminal benzimidazole groups by carboxamide binding units. *Inorganic Chemistry* **1998,** *37* (3), 577-589.

50. KADJANE, P.; CHARBONNIERE, L.; CAMEREL, F.; LAINE, P.P.; ZIESSEL, R., Improving visible light sensitization of luminescent europium complexes. *Journal of Fluorescence* **2008,** *18* (1), 119-129.

51. MUKKALA, V.M.; SUND, C.; KWIATKOWSKI, M.; PASANEN, P.; HOGBERG, M.; KANKARE, J.; TAKALO, H., New Heteroaromatic Complexing Agents and Luminescence of Their Europium(III) and Terbium(III) Chelates. *Helvetica Chimica Acta* **1992,** *75* (5), 1621-1632.

52. MUKKALA, V.M.; KWIATKOWSKI, M.; KANKARE, J.; TAKALO, H., Influence of Chelating Groups on the Luminescence Properties of Europium(III) and Terbium(III) Chelates in the 2,2'-Bipyridine Series. *Helvetica Chimica Acta* **1993,** *76* (2), 893-899.

53. NASSO, I.; GALAUP, C.; HAVAS, F.; TISNES, P.; PICARD, C.; LAURENT, S.; ELST, L.V.; MULLER, R.N., Bimodal system (luminophore and paramagnetic contrastophore) derived from Ln(III) complexes based on a bipyridine-containing macrocyclic ligand. *Inorganic Chemistry* **2005,** *44* (23), 8293-8305.

54. GALAUP, C.; COUCHET, J.M.; PICARD, C.; TISNES, P., Novel terpyridine macrocyclic complexing agent and luminescence of its neutral Ln(III) complexes (Ln=Eu, Tb, Sm, Dy) in aqueous solution. *Tetrahedron Letters* **2001,** *42* (36), 6275-6278.

55. DE SILVA, A.P.; GUNARATNE, H.Q.N.; RICE, T.E.; STEWART, S., Switching 'on' the luminescence of one metal ion with another: selectivity characteristics with respect to the emitting and triggering metal. *Chemical Communications* **1997,** (19), 1891-1892.

56. KOZHEVNIKOV, V.N.; KOZHEVNIKOV, D.N.; RUSINOV, V.L.; CHUPAKHIN, O.N.; KONIG, B., Synthesis of functionalized fluorescent europium(III) terpyridyl chelates. *Synthesis-Stuttgart* **2003,** (15), 2400-2404.

57. COPPO, P.; DUATI, M.; KOZHEVNIKOV, V.N.; HOFSTRAAT, J.W.; DE COLA, L., White-light emission from an assembly comprising luminescent iridium and europium complexes. *Angewandte Chemie-International Edition* **2005,** *44* (12), 1806-1810.

58. CHARBONNIERE, L.J.; MAMERI, S.; FLOT, D.; WALTZ, F.; ZANDANEL, C.; ZIESSEL, R.F., A disymmetric terpyridine based ligand for the formation of luminescent di-aquo lanthanide complexes. *Dalton Transactions* **2007,** (22), 2245-2253.

59. FREY, S.T.; GONG, M.L.; HORROCKS, W.D., Synergistic Coordination in Ternary Complexes of Eu3+ with Aromatic Beta-Diketone Ligands and 1,10-Phenanthroline. *Inorganic Chemistry* **1994,** *33* (15), 3229-3234.

60. KIDO, J.; OKAMOTO, Y., Organo lanthanide metal complexes for electroluminescent materials. *Chemical Reviews* **2002,** *102* (6), 2357-2368.

61. DE BETTENCOURT-DIAS, A., Lanthanide-based emitting materials in light-emitting diodes. *Dalton Transactions* **2007,** (22), 2229-2241.

62. VAN DER TOL, E.B.; VAN RAMESDONK, H.J.; VERHOEVEN, J.W.; STEEMERS, F.J.; KERVER, E.G.; VERBOOM, W.; REINHOUDT, D.N., Tetraazatriphenylenes as extremely efficient antenna chromophores for luminescent lanthanide ions. *Chemistry-a European Journal* **1998,** *4* (11), 2315-2323.

63. QUICI, S.; CAVAZZINI, M.; MARZANNI, G.; ACCORSI, G.; ARMAROLI, N.; VENTURA, B.; BARIGELLETTI, F., Visible and near-infrared intense luminescence from water-soluble lanthanide [Tb(III), Eu(III), Sm(III), Dy(III), Pr(III), Ho(III), Yb(III), Nd(III), Er(III)] complexes. *Inorganic Chemistry* **2005,** *44* (3), 529-537.

64. ATKINSON, P.; FINDLAY, K.S.; KIELAR, F.; PAL, R.; PARKER, D.; POOLE, R.A.; PUSCHMANN, H.; RICHARDSON, S.L.; STENSON, P.A.; THOMPSON, A.L.; YU, J.H., Azaxanthones and azathioxanthones are effective sensitisers for europium and terbium luminescence. *Organic & Biomolecular Chemistry* **2006,** *4* (9), 1707-1722.

65. MONTGOMERY, C.P.; PARKER, D.; LAMARQUE, L., Effective and efficient sensitisation of terbium luminescence at 355 nm with cell permeable pyrazoyl-1-azaxanthone macrocyclic complexes. *Chemical Communications* **2007,** (37), 3841-3843.

66. ALBRECHT, M.; OSETSKA, O.; KLANKERMAYER, J.; FROHLICH, R.; GUMY, F.; BUNZLI, J.C.G., Enhancement of near-IR emission by bromine substitution in lanthanide complexes with 2-carboxamide-8-hydroxyquinoline. *Chemical Communications* **2007,** (18), 1834-1836.

67. COMBY, S.; IMBERT, D.; VANDEVYVER, C.; BUNZLI, J.C.G., A novel strategy for the design of 8-hydroxyquinolinate-based lanthanide bioprobes that emit in the near infrared range. *Chemistry-a European Journal* **2007,** *13* (3), 936-944.

68. ZHANG, J.; PETOUD, S., Azulene-moiety-based ligand for the efficient Sensitization of four near-infrared luminescent lanthanide cations: Nd3+, Er3+, Tm3+, and Yb3+. *Chemistry-a European Journal* **2008,** *14* (4), 1264-1272.

69. EDDER, C.; PIGUET, C.; BERNARDINELLI, G.; MAREDA, J.; BOCHET, C.G.; BUNZLI, J.C.G.; HOPFGARTNER, G., Unusual electronic effects of electron-withdrawing sulfonamide groups in optically and magnetically active self-assembled noncovalent heterodimetallic d-f podates. *Inorganic Chemistry* **2000,** *39* (22), 5059-5073.

70. BUNZLI, J.C.G.; PIGUET, C., Lanthanide-containing molecular and supramolecular polymetallic functional assemblies. *Chemical Reviews* **2002,** *102* (6), 1897-1928.

71. KLINK, S.I.; KEIZER, H.; VAN VEGGEL, F.C.J.M., Transition metal complexes as photosensitizers for near-infrared lanthanide luminescence. *Angewandte Chemie-International Edition* **2000,** *39* (23), 4319-+.

72. POPE, S.J.A.; COE, B.J.; FAULKNER, S., Re(I) sensitised near-infrared lanthanide luminescence from a hetero-trinuclear Re(2)Ln array. *Chemical Communications* **2004,** (13), 1550-1551.

73. POPE, S.J.A.; COE, B.J.; FAULKNER, S.; LAYE, R.H., Metal-to-ligand charge-transfer sensitisation of near-infrared emitting lanthanides in trimetallic arrays M(2)Ln (M = Ru, Re or Os; Ln = Nd, Er or Yb). *Dalton Transactions* **2005,** (8), 1482-1490.

74. GLOVER, P.B.; ASHTON, P.R.; CHILDS, L.J.; RODGER, A.; KERCHER, M.; WILLIAMS, R.M.; DE COLA, L.; PIKRAMENOU, Z., Hairpin-shaped heterometallic luminescent lanthanide complexes for DNA intercalative recognition. *Journal of the American Chemical Society* **2003,** *125* (33), 9918-9919.

75. GUO, D.; DUAN, C.Y.; LU, F.; HASEGAWA, Y.; MENG, Q.J.; YANAGIDA, S., Lanthanide heterometallic molecular squares Ru-2-Ln(2) exhibiting sensitized near-infrared emission. *Chemical Communications* **2004,** (13), 1486-1487.

76. XU, H.B.; SHI, L.X.; MA, E.; ZHANG, L.Y.; WEI, Q.H.; CHEN, Z.N., Diplatinum alkynyl chromophores as sensitisers for lanthanide luminescence in Pt(2)Ln(2) and Pt(2)Ln(4) (Ln = Eu, Nd, Yb) arrays with acetylide-functionalized bipyridine/phenanthroline. *Chemical Communications* **2006,** (15), 1601-1603.

77. SHAVALEEV, N.M.; BELL, Z.R.; WARD, M.D., A simple, general synthesis of mixed d-f complexes containing both {Re(CO)(3)Cl(diimine)} and lanthanide-tris(beta-diketonate) luminophores linked by bis-diimine bridging ligands. *Journal of the Chemical Society-Dalton Transactions* **2002,** (21), 3925-3927.

78. KENNEDY, F.; SHAVALEEV, N.M.; KOULLOUROU, T.; BELL, Z.R.; JEFFERY, J.C.; FAULKNER, S.; WARD, M.D., Sensitised near-infrared luminescence from lanthanide(III) centres using Re(I) and Pt(II) diimine complexes as energy donors in d-f dinuclear complexes based on 2,3-bis(2-pyridyl)pyrazine. *Dalton Transactions* **2007,** (15), 1492-1499.

79. IMBERT, D.; CANTUEL, M.; BUNZLI, J.C.G.; BERNARDINELLI, G.; PIGUET, C., Extending lifetimes of lanthanide-based near-infrared emitters (Nd, Yb) in the millisecond range through Cr(III) sensitization in discrete bimetallic edifices. *Journal of the American Chemical Society* **2003,** *125* (51), 15698-15699.

80. TORELLI, S.; IMBERT, D.; CANTUEL, M.; BERNARDINELLI, G.; DELAHAYE, S.; HAUSER, A.; BUNZLI, J.C.G.; PIGUET, C., Tuning the decay time of lanthanide-based near infrared luminescence from micro- to milliseconds through d -> f energy transfer in discrete heterobimetallic complexes. *Chemistry-a European Journal* **2005,** *11* (11), 3228-3242.

81. COPPO, P.; PLUMMER, E.A.; DE COLA, L., Tuning iridium(III) phenylpyridine complexes in the "almost blue" region. *Chemical Communications* **2004,** (15), 1774-1775.

82. FAULKNER, S.; POPE, S.J.A., Lanthanide-sensitized lanthanide luminescence: Terbium-sensitized ytterbium luminescence in a trinuclear complex. *Journal of the American Chemical Society* **2003,** *125* (35), 10526-10527.

83. BINNEMANS, K.; GORLLER-WALRAND, C., Lanthanide-containing liquid crystals and surfactants. *Chemical Reviews* **2002,** *102* (6), 2303-2345.

84. BINNEMANS, K., Ionic liquid crystals. *Chemical Reviews* **2005,** *105* (11), 4148-4204.

85. KURIKI, K.; KOIKE, Y.; OKAMOTO, Y., Plastic optical fiber lasers and amplifiers containing lanthanide complexes. *Chemical Reviews* **2002,** *102* (6), 2347-2356.

86. PARKER, D.; DICKINS, R.S.; PUSCHMANN, H.; CROSSLAND, C.; HOWARD, J.A.K., Being excited by lanthanide coordination complexes: Aqua species, chirality, excited-state chemistry, and exchange dynamics. *Chemical Reviews* **2002,** *102* (6), 1977-2010.

87. TANG, C.W.; VANSLYKE, S.A., Organic Electroluminescent Diodes. *Applied Physics Letters* **1987,** *51* (12), 913-915.

88. BURROUGHES, J.H.; BRADLEY, D.D.C.; BROWN, A.R.; MARKS, R.N.; MACKAY, K.; FRIEND, R.H.; BURNS, P.L.; HOLMES, A.B., Light-Emitting-Diodes Based on Conjugated Polymers. *Nature* **1990,** *347* (6293), 539-541.

89. EVANS, R.C.; DOUGLAS, P.; WINSCOM, C.J., Coordination complexes exhibiting room-temperature phosphorescence: Evaluation of their suitability as triplet emitters in organic light emitting diodes. *Coordination Chemistry Reviews* **2006,** *250* (15-16), 2093-2126.

90. YERSIN, H., Triplet Emitters for OLED Applications. Mechanisms of Exciton Trapping and Control of Emission Properties. In *Transition Metal and Rare Earth Compounds*, 2004; pp 1-26.

91. YERSIN, H.; FINKENZELLER, W.J., Triplet Emitters for Organic Light - Emitting Diodes: Basic Properties. In *Highly Efficient OLEDs with Phosphorescent Materials*, Yersin, H., Ed. Wiley-VCH: 2008; pp 1-97.

92. KIDO, J.; NAGAI, K.; OHASHI, Y., Electroluminescence in a Terbium Complex. *Chemistry Letters* **1990,** (4), 657-660.

93. KIDO, J.; NAGAI, K.; OKAMOTO, Y.; SKOTHEIM, T., Electroluminescence from Polysilane Film Doped with Europium Complex. *Chemistry Letters* **1991,** (7), 1267-1270.

94. KIDO, J.; HAYASE, H.; HONGAWA, K.; NAGAI, K.; OKUYAMA, K., Bright Red Light-Emitting Organic Electroluminescent Devices Having a Europium Complex as an Emitter. *Applied Physics Letters* **1994,** *65* (17), 2124-2126.

95. YU, G.; LIU, Y.; WU, X.; ZHU, D.; LI, H.; JIN, L.; WANG, M., Soluble Europium Complexes for Light-Emitting Diodes. *Chemistry of Materials* **2000,** *12* (9), 2537-2541.

96. BIAN, Z.Q.; HUANG, C.H., Progress in Electroluminescence Based on Lanthanide Complexes. In *Highly Efficient OLEDs with Phosphorescent Materials*, Yersin, H., Ed. Wiley-VCH: 2008; pp 391-419.

97. HASEGAWA, Y.; WADA, Y.; YANAGIDA, S., Strategies for the design of luminescent lanthanide(III) complexes and their photonic applications. *Journal of Photochemistry and Photobiology C-Photochemistry Reviews* **2004,** *5* (3), 183-202.

98. HASEGAWA, Y.; SOGABE, K.; WADA, Y.; YANAGIDA, S., Low-vibrational luminescent polymers including tris(bis-perfluoromethane and ethanesulfonylaminate)neodymium(III) with 8 coordinated DMSO-d6. *Journal of Luminescence* **2003,** *101* (3), 235-242.

99. MOYNIHAN, S.; VAN DEUN, R.; BINNEMANS, K.; REDMOND, G., Optical properties of planar polymer waveguides doped with organo-lanthanide complexes. *Optical Materials* **2007,** *29* (12), 1821-1830.

100. OSTROVSKII, V.A.; KOLDOBSKII, G.I.; TRIFONOV, R.E.; ALAN, R.K.; CHRISTOPHER, A.R.; ERIC, F.V.S.; RICHARD, J.K.T., Tetrazoles. In *Comprehensive Heterocyclic Chemistry III*, Elsevier: Oxford, 2008; pp 257-423.

101. HERR, R.J., 5-substituted-1H-tetrazoles as carboxylic acid isosteres: Medicinal chemistry and synthetic methods. *Bioorganic & Medicinal Chemistry* **2002,** *10* (11), 3379-3393.

102. JULIUS V. BRAUN, W.K., Synthese von Tetrazol-Verbindungen aus Säurenitrilen. *Berichte der deutschen chemischen Gesellschaft (A and B Series)* **1932,** *65* (10), 1677-1680.

103. FINNEGAN, W.G.; HENRY, R.A.; LOFQUIST, R., An Improved Synthesis of 5-Substituted Tetrazoles. *Journal of the American Chemical Society* **1958,** *80* (15), 3908-3911.

104. DUNCIA, J.V.; PIERCE, M.E.; SANTELLA, J.B., Three synthetic routes to a sterically hindered tetrazole. A new one-step mild conversion of an amide into a tetrazole. *The Journal of Organic Chemistry* **1991,** *56* (7), 2395-2400.

105. DEMKO, Z.P.; SHARPLESS, K.B., Preparation of 5-substituted 1H-tetrazoles from nitriles in water. *Journal of Organic Chemistry* **2001,** *66* (24), 7945-7950.

106. HIMO, F.; DEMKO, Z.P.; NOODLEMAN, L.; SHARPLESS, K.B., Why is tetrazole formation by addition of azide to organic nitriles catalyzed by zinc(II) salts? *Journal of the American Chemical Society* **2003,** *125* (33), 9983-9987.

107. HIMO, F.; DEMKO, Z.P.; NOODLEMAN, L.; SHARPLESS, K.B., Mechanisms of tetrazole formation by addition of azide to nitriles. *Journal of the American Chemical Society* **2002,** *124* (41), 12210-12216.

108. PATANI, G.A.; LAVOIE, E.J., Bioisosterism: A Rational Approach in Drug Design. *Chemical Reviews* **1996,** *96* (8), 3147-3176.

109. BROAN, C.J.; COLE, E.; JANKOWSKI, K.J.; PARKER, D.; PULUKKODY, K.; BOYCE, B.A.; BEELEY, N.R.A.; MILLAR, K.; MILLICAN, A.T., Synthesis of New Macrocyclic Amino-Phosphinic Acid Complexing Agents and Their C-and P-Functionalised Derivatives for Protein Linkage. *Synthesis* **1992,** (01-02), 63-68.

110. ZHAO, H.; QU, Z.R.; YE, H.Y.; XIONG, R.G., In situ hydrothermal synthesis of tetrazole coordination polymers with interesting physical properties. *Chemical Society Reviews* **2008,** *37* (1), 84-100.

111. DINCA, M.; YU, A.F.; LONG, J.R., Microporous metal-organic frameworks incorporating 1,4-benzeneditetrazolate: Syntheses, structures, and hydrogen storage properties. *Journal of the American Chemical Society* **2006,** *128* (27), 8904-8913.

112. YEH, S.J.; WU, M.F.; CHEN, C.T.; SONG, Y.H.; CHI, Y.; HO, M.H.; HSU, S.F.; CHEN, C.H., New dopant and host materials for blue-light-emitting phosphorescent organic electroluminescent devices. *Advanced Materials* **2005,** *17* (3), 285-+.

113. STAGNI, S.; PALAZZI, A.; ZACCHINI, S.; BALLARIN, B.; BRUNO, C.; MARCACCIO, M.; PAOLUCCI, F.; MONARI, M.; CARANO, M.; BARD, A.J., A new family of ruthenium(II) polypyridine

complexes bearing 5-aryltetrazolate ligands as systems for electrochemiluminescent devices. *Inorganic Chemistry* **2006,** *45* (2), 695-709.

114. AIME, S.; CRAVOTTO, G.; CRICH, S.G.; GIOVENZANA, G.B.; FERRARI, M.; PALMISANO, G.; SISTI, M., Synthesis of the Gd(III) complex with a tetrazole-armed macrocyclic ligand as a potential MRI contrast agent. *Tetrahedron Letters* **2002,** *43* (5), 783-786.

115. FACCHETTI, A.; ABBOTTO, A.; BEVERINA, L.; BRADAMANTE, S.; MARIANI, P.; STERN, C.L.; MARKS, T.J.; VACCA, A.; PAGANI, G.A., Novel coordinating motifs for lanthanide(III) ions based on 5-(2-pyridyl)tetrazole and 5-(2-pyridyl-1-oxide)tetrazole. Potential new contrast agents. *Chemical Communications* **2004,** (15), 1770-1771.

116. ANDREWS, P.C.; JUNK, P.C.; MASSI, M.; SILBERSTEIN, M., Gelation of La(III) cations promoted by 5-(2-pyridyl) tetrazolate and water. *Chemical Communications* **2006,** (31), 3317-3319.

117. ANDREWS, P.C.; BECK, T.; FRASER, B.H.; JUNK, P.C.; MASSI, M., Synthesis and structural characterisation of cationic, neutral and hydroxo-bridged lanthanoid (La, Gd, Ho, Yb, Y) bis 5-(2-pyridyl)tetrazolate complexes. *Polyhedron* **2007,** *26* (18), 5406-5413.

118. GIRAUD, M.; ANDREIADIS, E.S.; FISYUK, A.S.; DEMADRILLE, R.; PECAUT, J.; IMBERT, D.; MAZZANTI, M., Efficient sensitization of lanthanide luminescence by tetrazole-based polydentate ligands. *Inorganic Chemistry* **2008,** *47* (10), 3952-3954.

119. GATEAU, C.; MAZZANTI, M.; PECAUT, J.; DUNAND, F.A.; HELM, L., Solid-state and solution properties of the lanthanide complexes of a new tripodal ligand derived from 1,4,7-triazacyclononane. *Dalton Transactions* **2003,** (12), 2428-2433.

120. BRETONNIERE, Y.; MAZZANTI, M.; PECAUT, J.; OLMSTEAD, M.M., Cation-controlled self-assembly of a hexameric europium wheel. *Journal of the American Chemical Society* **2002,** *124* (31), 9012-9013.

121. DE BETTENCOURT-DIAS, A.; VISWANATHAN, S.; ROLLETT, A., Thiophene-derivatized Pybox and its highly luminescent lanthanide ion complexes. *Journal of the American Chemical Society* **2007,** *129* (50), 15436-15437.

122. MORGAN, G.; BURSTALL, F.H., Researches on residual affinity and co-ordination. Part XXXVII. Complex metallic salts containing 2:6-di-2'-pyridylpyridine (2:2':2"-tripyridyl). *Journal of the Chemical Society* **1937,** *1937*, 1649-1655.

123. THOMPSON, A.M.W.C., The synthesis of 2,2':6',2''-terpyridine ligands - versatile building blocks for supramolecular chemistry. *Coordination Chemistry Reviews* **1997,** *160*, 1-52.

124. BADGER, G.M.; SASSE, W.H.F., Synthetic applications of activated metal catalysts. 2. The formation of heterocyclic diaryls. *Journal of the Chemical Society* **1956**, 616-620.

125. UENISHI, J.; TANAKA, T.; WAKABAYASHI, S.; OAE, S.; TSUKUBE, H., Ipso substitution of 2-alkylsulfinylpyridine by 2-pyridyllithium - a new preparation of oligopyridine and their bromomethyl derivatives. *Tetrahedron Letters* **1990,** *31* (32), 4625-4628.

126. JAMESON, D.L.; GUISE, L.E., An Improved, 2-Step Synthesis of 2,2'-6',2''-Terpyridine. *Tetrahedron Letters* **1991,** *32* (18), 1999-2002.

127. KROHNKE, F., Synthesis using pyridinium salts. 5. Specific synthesis of pyridines and oligopyridines. *Synthesis-Stuttgart* **1976,** (1), 1-24.

128. NEWKOME, G.R.; HAGER, D.C.; KIEFER, G.E., Synthesis of Halogenated Terpyridines and Incorporation of the Terpyridine Nucleus into a Polyethereal Macrocycle. *Journal of Organic Chemistry* **1986,** *51* (6), 850-853.

129. CONSTABLE, E.C.; LEWIS, J., The preparation and coordination chemistry of 2,2'-6',2''-terpyridine macrocycles. *Polyhedron* **1982,** *1* (3), 303-306.

130. SAUVAGE, J.P.; WARD, M., A bis(terpyridine)ruthenium(II) catenate. *Inorganic Chemistry* **1991,** *30* (20), 3869-3874.

131. GALAUP, C.; COUCHET, J.M.; BEDEL, S.; TISENS, P.; PICARD, C., Direct access to terpyridine-containing polyazamacrocycles as photosensitizing ligands for Eu(III) luminescence in aqueous media. *Journal of Organic Chemistry* **2005,** *70* (6), 2274-2284.

132. HAN, F.S.; HIGUCHI, M.; KURTH, D.G., Diverse synthesis of novel bisterpyridines via Suzuki-type cross-coupling. *Organic Letters* **2007,** *9* (4), 559-562.

133. MUTAI, T.; ARITA, S.; ARAKI, K., Phenyl-substituted 2,2':6',2''-terpyridine as a new series of fluorescent compounds - their photophysical properties and fluorescence tuning. *Journal of the Chemical Society-Perkin Transactions 2* **2001,** (7), 1045-1050.

134. KORALL, P.; BORJE, A.; NORRBY, P.O.; AKERMARK, B., High yield preparation of 4'-(4-bromophenyl)-2,2':6',2''-terpyridine by a condensation reaction. Determination of the stereochemistry of two complex by-products by a combination of molecular mechanics and NMR spectroscopy. *Acta Chemica Scandinavica* **1997,** *51* (6-7), 760-766.

135. LOPEZ, R.; VILLAGRA, D.; FERRAUDI, G.; MOYA, S.A.; GUERRERO, J., Preparation and photophysical properties of precursors of inorganic macromolecules. Mono and binuclear complexes of Ru(II) and terpyridine derivatized with thiophene and 4 '-(5-bromothiophene) groups. *Inorganica Chimica Acta* **2004,** *357* (12), 3525-3531.

136. THUMMEL, R.P.; JAHNG, Y., N-Oxides of 2,2'-6',2''-Terpyridine. *Journal of Organic Chemistry* **1985,** *50* (19), 3635-3636.

137. FIFE, W.K., Regioselective Cyanation of Pyridine 1-Oxides with Trimethylsilanecarbonitrile - a Modified Reissert-Henze Reaction. *Journal of Organic Chemistry* **1983,** *48* (8), 1375-1377.

138. STILLE, J.K., The Palladium-Catalyzed Cross-Coupling Reactions of Organotin Reagents with Organic Electrophiles. *Angewandte Chemie-International Edition in English* **1986,** *25* (6), 508-523.

139. SCHWAB, P.F.H.; FLEISCHER, F.; MICHL, J., Preparation of 5-brominated and 5,5'-dibrominated 2,2'-bipyridines and 2,2'-bipyrimidines. *Journal of Organic Chemistry* **2002,** *67* (2), 443-449.

140. NAKAMOTO, K., Ultraviolet Spectra and Structures of 2,2'-Bipyridine and 2,2',2''-Terpyridine in Aqueous Solution. *Journal of Physical Chemistry* **1960,** *64* (10), 1420-1425.

141. CHARBONNIERE, L.; MAMERI, S.; KADJANE, P.; PLATAS-IGLESIAS, C.; ZIESSEL, R., Tuning the coordination sphere around highly luminescent lanthanide complexes. *Inorganic Chemistry* **2008,** *47* (9), 3748-3762.

142. CONSTABLE, E.C.; LEWIS, J.; LIPTROT, M.C.; RAITHBY, P.R., The coordination chemistry of 4'-phenyl-2,2':6', 2"-terpyridine; the synthesis, crystal and molecular structures of 4'-phenyl-2,2':6',2"-terpyridine and bis(4'-phenyl-2,2':6',2"-terpyridine)nickel(II) chloride decahydrate. *Inorganica Chimica Acta* **1990,** *178* (1), 47-54.

143. FALLAHPOUR, R.-A.; NEUBURGER, M.; ZEHNDER, M., Ruthenium(II) complexes of novel 4'-ethoxy- and 4'-hydroxy-5,5"-dimethyl-2,2':6',2"-terpyridines: X-ray crystal structures of 4'-ethoxy-5,5"-dimethyl-2,2":6',2"-terpyridine and the ruthenium(II) complex of 4'-ethoxy-5,5"-dimethyl-2,2':6',2"-terpyridine with 4'-chloro-2,2':6',2"-terpyridine. *Polyhedron* **1999,** *18* (18), 2445-2454.

144. GODDARD, R.; HEINEMANN, O.; KRUGER, C., alpha-1H-1,2,3,4-tetrazole. *Acta Crystallographica Section C-Crystal Structure Communications* **1997,** *53*, 590-592.

145. SHANNON, R.D., Revised Effective Ionic-Radii and Systematic Studies of Interatomic Distances in Halides and Chalcogenides. *Acta Crystallographica Section A* **1976,** *32*, 751-767.

146. LYAKHOV, A.S.; GRIGORIEV, Y.V.; IVASHKEVICH, L.S.; GAPONIK, P.N., 2-(1H-tetrazol-1-yl)ethanol. *Acta Crystallographica Section E-Structure Reports Online* **2007,** *63*, O1573-O1574.

147. OUALI, N.; BOCQUET, B.; RIGAULT, S.; MORGANTINI, P.Y.; WEBER, J.; PIGUET, C., Analysis of paramagnetic NMR spectra of triple-helical lanthanide complexes with 2,6-dipicolinic acid

revisited: A new assignment of structural changes and crystal-field effects 25 years later. *Inorganic Chemistry* **2002,** *41* (6), 1436-1445.

148. PETOUD, S.; BUNZLI, J.C.G.; RENAUD, F.; PIGUET, C.; SCHENK, K.J.; HOPFGARTNER, G., Stability and size-discriminating effects in mononuclear lanthanide triple-helical building blocks with tridentate aromatic ligands. *Inorganic Chemistry* **1997,** *36* (25), 5750-5760.

149. LOWE, M.P.; CARAVAN, P.; RETTIG, S.J.; ORVIG, C., Tightening the hydrophobic belt: Effects of backbone and donor group variation on podand ligand complexes of the lanthanides. *Inorganic Chemistry* **1998,** *37* (7), 1637-1647.

150. WIETZKE, R.; MAZZANTI, M.; LATOUR, J.M.; PECAUT, J., Strong intramolecular pi-pi interactions favor the formation of 2 : 1 (L : M) lanthanide complexes of tris(2-benzimidazolylmethyl)amine. *Chemical Communications* **1999,** (2), 209-210.

151. LIDDLE, B.J.; SILVA, R.M.; MORIN, T.J.; MACEDO, F.P.; SHUKLA, R.; LINDEMAN, S.V.; GARDINIER, J.R., BORAZANs: Tunable Fluorophores Based on 2-(Pyrazolyl)aniline Chelates of Diphenylboron. *The Journal of Organic Chemistry* **2007,** *72* (15), 5637-5646.

152. HOLZ, R.C.; CHANG, C.A.; HORROCKS, W.D., Spectroscopic Characterization of the Europium(III) Complexes of a Series of N,N'-Bis(Carboxymethyl) Macrocyclic Ether Bis(Lactones). *Inorganic Chemistry* **1991,** *30* (17), 3270-3275.

153. VOGTLE, F.; GORKA, M.; VICINELLI, V.; CERONI, P.; MAESTRI, M.; BALZANI, V., A dendritic antenna for near-infrared emission of Nd3+ ions. *Chemphyschem* **2001,** *2* (12), 769-773.

154. KOROVIN, Y.; RUSAKOVA, N., Near-infrared luminescence of Yb3+Nd3+ and Er3+ in complexes with organic dyes. *Journal of Alloys and Compounds* **2004,** *374* (1-2), 311-314.

155. IMBERT, D.; COMBY, S.; CHAUVIN, A.S.; BUNZLI, J.C.G., Lanthanide 8-hydroxyquinoline-based podates with efficient emission in the NIR range. *Chemical Communications* **2005,** (11), 1432-1434.

156. HEBBINK, G.A.; GRAVE, L.; WOLDERING, L.A.; REINHOUDT, D.N.; VAN VEGGEL, F.C.J.M., Unexpected sensitization efficiency of the near-infrared Nd3+, Er3+, and Yb3+ emission by fluorescein compared to eosin and erythrosin. *Journal of Physical Chemistry A* **2003,** *107* (14), 2483-2491.

157. BUNZLI, J.C.G.; CHARBONIERE, L.J.; ZIESSEL, R.F., Structural and photophysical properties of Ln(III) complexes with 2,2 '-bipyridine-6,6 '-dicarboxylic acid: surprising formation of a H-bonded network of bimetallic entities. *Journal of the Chemical Society-Dalton Transactions* **2000,** (12), 1917-1923.

158. PATRONIAK, V.; KUBICKI, M.; STEFANKIEWICZ, A.R.; GROCHOWSKA, A.M., Preparation of new heterotopic ligands. *Tetrahedron* **2005,** *61* (23), 5475-5480.

159. CAMEREL, F.; BARBERA, J.; OTSUKI, J.; TOKIMOTO, T.; SHIMAZAKI, Y.; CHEN, L.Y.; LIU, S.H.; LIN, M.S.; WU, C.C.; ZIESSEL, R., Solution-processable liquid crystals of luminescent aluminum(8-hydroxyquinoline-5-sulfonato) complexes. *Advanced Materials* **2008,** *20* (18), 3462-3467.

160. ROBINSON, M.R.; O'REGAN, M.B.; BAZAN, G.C., Synthesis, morphology and optoelectronic properties of tris[(N-ethylcarbazolyl)(3 ',5 '-hexyloxybenzoyl)methane](phenanthroline)-europium. *Chemical Communications* **2000,** (17), 1645-1646.

161. YU, J.B.; ZHOU, L.; ZHANG, H.J.; ZHENG, Y.X.; LI, H.R.; DENG, R.P.; PENG, Z.P.; LI, Z.F., Efficient electroluminescence from new lanthanide (Eu3+, Sm3+) complexes. *Inorganic Chemistry* **2005,** *44* (5), 1611-1618.

162. NOCKEMANN, P.; BEURER, E.; DRIESEN, K.; VAN DEUN, R.; VAN HECKE, K.; VAN MEERVELT, L.; BINNEMANS, K., Photostability of a highly luminescent europium beta-diketonate complex in imidazolium ionic liquids. *Chemical Communications* **2005,** (34), 4354-4356.

163. OYAMADA, T.; KAWAMURA, Y.; KOYAMA, T.; SASABE, H.; ADACHI, C., Formation of europium chelate complexes by vacuum co-deposition and their application in organic light-emitting diodes. *Advanced Materials* **2004,** *16* (13), 1082-1086.

164. CHEN, X.Y.; BRETONNIERE, Y.; PECAUT, J.; IMBERT, D.; BUNZLI, J.C.; MAZZANTI, M., Selective self-assembly of hexameric homo- and heteropolymetallic lanthanide wheels: Synthesis, structure, and photophysical studies. *Inorganic Chemistry* **2007,** *46* (3), 625-637.

165. KIM, H.J.; LEE, J.E.; KIM, Y.S.; PARK, N.G., Ligand effect on the electroluminescence mechanism in lanthanide (III) complexes. *Optical Materials* **2003,** *21* (1-3), 181-186.

166. ZHENG, Y.X.; LIN, J.; LIANG, Y.J.; LIN, Q.; YU, Y.N.; MENG, Q.G.; ZHOU, Y.H.; WANG, S.B.; WANG, H.Y.; ZHANG, H.J., A comparative study on the electroluminescence properties of some terbium beta-diketonate complexes. *Journal of Materials Chemistry* **2001,** *11* (10), 2615-2619.

167. CHEN, X.F.; ZHU, X.H.; XU, Y.H.; RAJ, S.S.S.; OZTURK, S.; FUN, H.K.; MA, J.; YOU, X.Z., Triboluminescence and crystal structures of non-ionic europium complexes. *Journal of Materials Chemistry* **1999,** *9* (11), 2919-2922.

168. CHOWDHURY, P.S.; SAHA, S.; PATRA, A., The role of semiconducting hosts on photoluminescence efficiency of Eu-complex. *Chemical Physics Letters* **2005,** *405* (4-6), 393-397.

169. WALTENBURG, H.N.; YATES, J.T., Surface-Chemistry of Silicon. *Chemical Reviews* **1995,** *95* (5), 1589-1673.

170. SAILOR, M.J.; LEE, E.J., Surface chemistry of luminescent silicon nanocrystallites. *Advanced Materials* **1997,** *9* (10), 783-&.

171. LI, H.R.; YU, J.B.; LIU, F.Y.; ZHANG, H.J.; FU, L.S.; MENG, Q.G.; PENG, C.Y.; LIN, J., Preparation and luminescence properties of in situ formed lanthanide complexes covalently grafted to a silica network. *New Journal of Chemistry* **2004,** *28* (9), 1137-1141.

172. TONG, B.H.; WANG, S.J.; MENG, Y.Z.; WANG, B., Near-infrared luminescent lanthanide (Er, Nd) complexes covalently bonded to a terpyridine-functionalized silica matrix. *Photochemical & Photobiological Sciences* **2007,** *6* (5), 519-520.

173. ZHANG, L.; LIU, H.G.; ZHANG, R.J.; MU, Y.D.; QIAN, D.J.; FENG, X.S., Fabrication and characterization of luminescent self-assembled thin films of europium complex. *Colloids and Surfaces a-Physicochemical and Engineering Aspects* **2005,** *257-58*, 401-404.

174. GAO, X.; LIU, H.G.; ZHANG, R.J.; YANG, K.Z., Crystallization in europium complex monolayers on a composite subphase. *Thin Solid Films* **1996,** *285*, 39-42.

175. DUAN, Y.; WEN, G.A.; WEI, W.; FENG, J.C.; XU, G.Q.; HUANG, W., Covalent integration of luminescent Eu (III) complex onto composite conductors or semiconducting substrates-by grafting with organosilane. *Thin Solid Films* **2008,** *517* (2), 469-473.

176. BURIAK, J.M., Organometallic chemistry on silicon and germanium surfaces. *Chemical Reviews* **2002,** *102* (5), 1271-308.

177. CEROFOLINI, G.F.; ARENA, G.; CAMALLERI, C.M.; GALATI, C.; REINA, S.; RENNA, L.; MASCOLO, D., A hybrid approach to nanoelectronics. *Nanotechnology* **2005,** *16* (8), 1040-1047.

178. LIU, Z.; YASSERI, A.A.; LOEWE, R.S.; LYSENKO, A.B.; MALINOVSKII, V.L.; ZHAO, Q.; SURTHI, S.; LI, Q.; MISRA, V.; LINDSEY, J.S.; BOCIAN, D.F., Synthesis of Porphyrins Bearing Hydrocarbon Tethers and Facile Covalent Attachment to Si(100). *The Journal of Organic Chemistry* **2004,** *69* (17), 5568-5577.

179. PADMAJA, K.; WEI, L.; LINDSEY, J.S.; BOCIAN, D.F., A Compact All-Carbon Tripodal Tether Affords High Coverage of Porphyrins on Silicon Surfaces. *The Journal of Organic Chemistry* **2005,** *70* (20), 7972-7978.

180. WEN, S.; ZHANG, X.; HU, S.; ZHANG, L.; LIU, L., Fluorescence and Judd-Ofelt analysis of rare earth complexes with maleic anhydride and acrylic acid. *Journal of Rare Earths* **2008,** *26*, 787-791.

181. DIXON, I.M.; COLLIN, J.P.; SAUVAGE, J.P.; FLAMIGNI, L.; ENCINAS, S.; BARIGELLETTI, F., A family of luminescent coordination compounds: iridium(III) polyimine complexes. *Chemical Society Reviews* **2000,** *29* (6), 385-391.

182. FLAMIGNI, L.; BARBIERI, A.; SABATINI, C.; VENTURA, B.; BARIGELLETTI, F., Photochemistry and Photophysics of Coordination Compounds: Iridium. In *Photochemistry and Photophysics of Coordination Compounds II*, 2007; pp 143-203.

183. OHSAWA, Y.; SPROUSE, S.; KING, K.A.; DEARMOND, M.K.; HANCK, K.W.; WATTS, R.J., Electrochemistry and Spectroscopy of Ortho-Metalated Complexes of Ir(Iii) and Rh(Iii). *Journal of Physical Chemistry* **1987,** *91* (5), 1047-1054.

184. HOLDER, E.; LANGEVELD, B.M.W.; SCHUBERT, U.S., New trends in the use of transition metal-ligand complexes for applications in electroluminescent devices. *Advanced Materials* **2005,** *17* (9), 1109-1121.

185. TAMAYO, A.B.; ALLEYNE, B.D.; DJUROVICH, P.I.; LAMANSKY, S.; TSYBA, I.; HO, N.N.; BAU, R.; THOMPSON, M.E., Synthesis and characterization of facial and meridional tris-cyclometalated iridium(III) complexes. *Journal of the American Chemical Society* **2003,** *125* (24), 7377-7387.

186. LAMANSKY, S.; DJUROVICH, P.; MURPHY, D.; ABDEL-RAZZAQ, F.; KWONG, R.; TSYBA, I.; BORTZ, M.; MUI, B.; BAU, R.; THOMPSON, M.E., Synthesis and characterization of phosphorescent cyclometalated iridium complexes. *Inorganic Chemistry* **2001,** *40* (7), 1704-1711.

187. DJUROVICH, P.I.; THOMPSON, M.E., Cyclometallated Organoiridium Complexes as Emitters in Electrophosphorescent Devices In *Highly Efficient OLEDs with Phosphorescent Materials*, Yersin, H., Ed. Wiley-VCH: 2008; pp 131-161.

188. NONOYAMA, M., Benzo[H]Quinolin-10-Yl-N Iridium (III) Complexes. *Bulletin of the Chemical Society of Japan* **1974,** *47* (3), 767-768.

189. RAGNI, R.; PLUMMER, E.A.; BRUNNER, K.; HOFSTRAAT, J.W.; BABUDRI, F.; FARINOLA, G.M.; NASO, F.; DE COLA, L., Blue emitting iridium complexes: synthesis, photophysics and phosphorescent devices. *Journal of Materials Chemistry* **2006,** *16* (12), 1161-1170.

190. HUO, S.Q.; DEATON, J.C.; RAJESWARAN, M.; LENHART, W.C., Highly efficient, selective, and general method for the preparation of meridional homo- and heteroleptic tris-cyclometalated iridium complexes. *Inorganic Chemistry* **2006,** *45* (8), 3155-3157.

191. DEDEIAN, K.; DJUROVICH, P.I.; GARCES, F.O.; CARLSON, G.; WATTS, R.J., A New Synthetic Route to the Preparation of a Series of Strong Photoreducing Agents - Fac Tris-Ortho-Metalated Complexes of Iridium(III) with Substituted 2-Phenylpyridines. *Inorganic Chemistry* **1991,** *30* (8), 1685-1687.

192. RAGNI, R.; ORSELLI, E.; KOTTAS, G.S.; OMAR, O.H.; BADUDRI, F.; PEDONE, A.; NASO, F.; FARINOLA, G.M.; DE COLA, L., Iridium(III) Complexes with Sulfonyl and Fluorine Substituents: Synthesis, Stereochemistry and Effect of Functionalisation on their Photophysical Properties. *Chemistry-a European Journal* **2009,** *15* (1), 136-148.

193. MCGEE, K.A.; MANN, K.R., Selective low-temperature syntheses of facial and meridional tris-cyclometalated iridium(III) complexes. *Inorganic Chemistry* **2007,** *46* (19), 7800-7809.

194. MCDONALD, A.R.; LUTZ, M.; VON CHRZANOWSKI, L.S.; VAN KLINK, G.P.M.; SPEK, A.L.; VAN KOTEN, G., Probing the mer- to fac-isomerization of tris-cyclometallated homo- and heteroleptic (C,N)(3) iridium(III) complexes. *Inorganic Chemistry* **2008,** *47* (15), 6681-6691.

195. BARANOFF, E.; SUAREZ, S.; BUGNON, P.; BAROLO, C.; BUSCAINO, R.; SCOPELLITI, R.; ZUPPIROLI, L.; GRAETZEL, M.; NAZEERUDDIN, M.K., Sublimation not an innocent technique: A case of bis-cyclometalated iridium emitter for OLED. *Inorganic Chemistry* **2008,** *47* (15), 6575-6577.

196. GARCES, F.O.; KING, K.A.; WATTS, R.J., Synthesis, Structure, Electrochemistry, and Photophysics of Methyl-Substituted Phenylpyridine Ortho-Metalated Iridium(Iii) Complexes. *Inorganic Chemistry* **1988,** *27* (20), 3464-3471.

197. KARATSU, T.; ITO, E.; YAGAI, S.; KITAMURA, A., Radiative and nonradiative processes of meridional and facial isomers of heteroleptic irldium-trischelete complexes. *Chemical Physics Letters* **2006,** *424* (4-6), 353-357.

198. D.F. SHRIVER, P.W.A., C.H. LANGFORD, *Inorganic Chemistry*. Oxford University Press: Oxford, 1991.

199. COLOMBO, M.G.; GUDEL, H.U., Synthesis and High-Resolution Optical Spectroscopy of Bis(2-(2-Thienyl)Pyridinato-C3,N') (2,2'-Bipyridine)Iridium(III). *Inorganic Chemistry* **1993,** *32* (14), 3081-3087.

200. LAMANSKY, S.; DJUROVICH, P.; MURPHY, D.; ABDEL-RAZZAQ, F.; LEE, H.E.; ADACHI, C.; BURROWS, P.E.; FORREST, S.R.; THOMPSON, M.E., Highly phosphorescent bis-cyclometalated iridium complexes: Synthesis, photophysical characterization, and use in organic light emitting diodes. *Journal of the American Chemical Society* **2001,** *123* (18), 4304-4312.

201. CHOU, P.T.; CHI, Y., Phosphorescent dyes for organic light-emitting diodes. *Chemistry-a European Journal* **2007,** *13* (2), 380-395.

202. SAJOTO, T.; DJUROVICH, P.I.; TAMAYO, A.; YOUSUFUDDIN, M.; BAU, R.; THOMPSON, M.E.; HOLMES, R.J.; FORREST, S.R., Blue and near-UV phosphorescence from iridium complexes with cyclometalated pyrazolyl or N-heterocyclic carbene ligands. *Inorganic Chemistry* **2005,** *44* (22), 7992-8003.

203. LI, J.; DJUROVICH, P.I.; ALLEYNE, B.D.; YOUSUFUDDIN, M.; HO, N.N.; THOMAS, J.C.; PETERS, J.C.; BAU, R.; THOMPSON, M.E., Synthetic control of excited-state properties in cyclometalated Ir(III) complexes using ancillary ligands. *Inorganic Chemistry* **2005,** *44* (6), 1713-1727.

204. YOU, Y.M.; PARK, S.Y., Inter-ligand energy transfer and related emission change in the cyclometalated heteroleptic iridium complex: Facile and efficient color tuning over the whole visible range by the ancillary ligand structure. *Journal of the American Chemical Society* **2005,** *127* (36), 12438-12439.

205. LI, J.; DJUROVICH, P.I.; ALLEYNE, B.D.; TSYBA, I.; HO, N.N.; BAU, R.; THOMPSON, M.E., Synthesis and characterization of cyclometalated Ir(III) complexes with pyrazolyl ancillary ligands. *Polyhedron* **2004,** *23* (2-3), 419-428.

206. NAZEERUDDIN, M.K.; HUMPHRY-BAKER, R.; BERNER, D.; RIVIER, S.; ZUPPIROLI, L.; GRAETZEL, M., Highly phosphorescence iridium complexes and their application in organic light-emitting devices. *Journal of the American Chemical Society* **2003,** *125* (29), 8790-8797.

207. STAGNI, S.; COLELLA, S.; PALAZZI, A.; VALENTI, G.; ZACCHINI, S.; PAOLUCCI, F.; MARCACCIO, M.; ALBUQUERQUE, R.O.; DE COLA, L., Essential Role of the Ancillary Ligand in the Color Tuning of Iridium Tetrazolate Complexes. *Inorganic Chemistry* **2008,** *47* (22), 10509-10521.

208. CHEN, F.F.; BIAN, Z.Q.; LIU, Z.W.; NIE, D.B.; CHEN, Z.Q.; HUANG, C.H., Highly efficient sensitized red emission from europium (III) in Ir-Eu bimetallic complexes by 3MLCT energy transfer. *Inorganic Chemistry* **2008,** *47* (7), 2507-2513.

209. CHEN, F.F.; BIAN, Z.Q.; LOU, B.; MA, E.; LIU, Z.W.; NIE, D.B.; CHEN, Z.Q.; BIAN, J.; CHEN, Z.N.; HUANG, C.H., Sensitised near-infrared emission from lanthanides using an iridium complex as a ligand in heteronuclear Ir(2)Ln arrays. *Dalton Transactions* **2008,** (41), 5577-5583.

210. MEHLSTAUBL, M.; KOTTAS, G.S.; COLELLA, S.; DE COLA, L., Sensitized near-infrared emission from ytterbium(III) via direct energy transfer from iridium(III) in a heterometallic neutral complex. *Dalton Transactions* **2008,** (18), 2385-2388.

211. ORSELLI, E.; KOTTAS, G.S.; KONRADSSON, A.E.; COPPO, P.; FROHLICH, R.; FRTSHLICH, R.; DE COLA, L.; VAN DIJKEN, A.; BUCHEL, M.; BORNER, H., Blue-emitting iridium complexes with substituted 1,2,4-triazole ligands: Synthesis, photophysics, and devices. *Inorganic Chemistry* **2007,** *46* (26), 11082-11093.

212. SPROUSE, S.; KING, K.A.; SPELLANE, P.J.; WATTS, R.J., Photophysical Effects of Metal-Carbon Sigma-Bonds in Ortho-Metalated Complexes of Ir(III) and Rh(III). *Journal of the American Chemical Society* **1984,** *106* (22), 6647-6653.

213. MIYAURA, N.; SUZUKI, A., Palladium-Catalyzed Cross-Coupling Reactions of Organoboron Compounds. *Chemical Reviews* **1995,** *95* (7), 2457-2483.

214. LOHSE, O.; THEVENIN, P.; WALDVOGEL, E., The palladium catalysed Suzuki coupling of 2- and 4-chloropyridines. *Synlett* **1999,** (1), 45-48.

215. DEROSA, M.C.; HODGSON, D.J.; ENRIGHT, G.D.; DAWSON, B.; EVANS, C.E.B.; CRUTCHLEY, R.J., Iridium Luminophore Complexes for Unimolecular Oxygen Sensors. *Journal of the American Chemical Society* **2004,** *126* (24), 7619-7626.

216. DEDEIAN, K.; SHI, J.M.; SHEPHERD, N.; FORSYTHE, E.; MORTON, D.C., Photophysical and electrochemical properties of heteroleptic tris-cyclometalated iridium(III) complexes. *Inorganic Chemistry* **2005,** *44* (13), 4445-4447.

217. PLUMMER, E.A.; HOFSTRAAT, J.W.; DE COLA, L., Mono- and di-nuclear iridium(III) complexes. Synthesis and photophysics. *Dalton Transactions* **2003,** (10), 2080-2084.

218. LASKAR, I.R.; HSU, S.F.; CHEN, T.M., Syntheses, photoluminescence and electroluminescence of some new blue-emitting phosphorescent iridium(III)-based materials. *Polyhedron* **2005,** *24* (2), 189-200.

219. FARINA, V.; KAPADIA, S.; KRISHNAN, B.; WANG, C.J.; LIEBESKIND, L.S., On the Nature of the Copper Effect in the Stille Cross-Coupling. *Journal of Organic Chemistry* **1994,** *59* (20), 5905-5911.

220. MEE, S.P.H.; LEE, V.; BALDWIN, J.E., Stille coupling made easier - The synergic effect of copper(I) salts and the fluoride ion. *Angewandte Chemie-International Edition* **2004,** *43* (9), 1132-1136.

221. BLACK, G.; DEPP, E.; CORSON, B.B., Oxidation of Certain Methylpyridines to Pyridine Carboxylic Acids. *Journal of Organic Chemistry* **1949,** *14* (1), 14-21.

222. CHODOROWSKI-KIMMES, S.; BELEY, M.; COLLIN, J.-P.; SAUVAGE, J.-P., Construction of multicomponent systems by utilizing functionalized transition metal complexes as building blocks. *Tetrahedron Letters* **1996,** *37* (17), 2963-2966.

223. LESLIE, W.; BATSANOV, A.S.; HOWARD, J.A.K.; WILLIAMS, J.A.G., Cross-couplings in the elaboration of luminescent bis-terpyridyl iridium complexes: the effect of extended or inhibited conjugation on emission. *Dalton Transactions* **2004,** (4), 623-631.

224. WHITTLE, V.L.; WILLIAMS, J.A.G., A new class of iridium complexes suitable for stepwise incorporation into linear assemblies: Synthesis, electrochemistry, and luminescence. *Inorganic Chemistry* **2008,** *47* (15), 6596-6607.

225. ASPLEY, C.J.; WILLIAMS, J.A.G., Palladium-catalysed cross-coupling reactions of ruthenium bis-terpyridyl complexes: strategies for the incorporation and exploitation of boronic acid functionality. *New Journal of Chemistry* **2001,** *25* (9), 1136-1147.

226. ISHIYAMA, T.; MURATA, M.; MIYAURA, N., Palladium(O)-Catalyzed Cross-Coupling Reaction of Alkoxydiboron with Haloarenes - a Direct Procedure for Arylboronic Esters. *Journal of Organic Chemistry* **1995,** *60* (23), 7508-7510.

227. KULKARNIA, S.S.; NEWMAN, A.H., Design and synthesis of novel heterobiaryl amides as metabotropic glutamate receptor subtype 5 antagonists *Bioorganic & Medicinal Chemistry Letters* **2007,** *17* (7), 2074-2079

228. ADACHI, C.; KWONG, R.C.; DJUROVICH, P.; ADAMOVICH, V.; BALDO, M.A.; THOMPSON, M.E.; FORREST, S.R., Endothermic energy transfer: A mechanism for generating very efficient high-energy phosphorescent emission in organic materials. *Applied Physics Letters* **2001,** *79* (13), 2082-2084.

229. GARCES, F.O.; DEDEIAN, K.; KEDER, N.L.; WATTS, R.J., Structures of Ortho-Metalated [2-(P-Tolyl)Pyridine]Iridium(III) Complexes. *Acta Crystallographica Section C-Crystal Structure Communications* **1993,** *49*, 1117-1120.

230. ACD/C+H NMR Predictors and DB software, version 11, Advanced Chemistry Development Inc.

231. COLOMBO, M.G.; BRUNOLD, T.C.; RIEDENER, T.; GUDEL, H.U.; FORTSCH, M.; BURGI, H.B., Facial Tris Cyclometalated Rh3+ and Ir3+ Complexes - Their Synthesis, Structure, and Optical Spectroscopic Properties. *Inorganic Chemistry* **1994,** *33* (3), 545-550.

232. AVILOV, I.; MINOOFAR, P.; CORNIL, J.; DE COLA, L., Influence of substituents on the energy and nature of the lowest excited states of heteroleptic phosphorescent Ir(III) complexes: A joint theoretical and experimental study. *Journal of the American Chemical Society* **2007,** *129* (26), 8247-8258.

233. ZHAO, Q.; LI, L.; LI, F.Y.; YU, M.X.; LIU, Z.P.; YI, T.; HUANG, C.H., Aggregation-induced phosphorescent emission (AIPE) of iridium(III) complexes. *Chemical Communications* **2008,** (6), 685-687.

234. LASKAR, I.R.; HSU, S.F.; CHEN, T.M., Investigating photoluminescence and electroluminescence of iridium(III)-based blue-emitting phosphors. *Polyhedron* **2006,** *25* (5), 1167-1176.

235. YOU, Y.; KIM, K.S.; AHN, T.K.; KIM, D.; PARK, S.Y., Direct spectroscopic observation of interligand energy transfer in cyclometalated heteroleptic iridium(III) complexes: A strategy for phosphorescence color tuning and white light generation. *Journal of Physical Chemistry C* **2007,** *111* (10), 4052-4060.

236. TAMAYO, A.B.; GARON, S.; SAJOTO, T.; DJUROVICH, P.I.; TSYBA, I.M.; BAU, R.; THOMPSON, M.E., Cationic bis-cyclometalated iridium(III) diimine complexes and their use in efficient blue, green, and red electroluminescent devices. *Inorganic Chemistry* **2005,** *44* (24), 8723-8732.

237. BALZANI, V.; BERGAMINI, G.; CAMPAGNA, S.; PUNTORIERO, F., Photochemistry and photophysics of coordination compounds: Overview and general concepts. *Photochemistry and Photophysics of Coordination Compounds I* **2007,** *280*, 1-36.

238. CAMPAGNA, S.; PUNTORIERO, F.; NASTASI, F.; BERGAMINI, G.; BALZANI, V., Photochemistry and Photophysics of Coordination Compounds: Ruthenium. In *Photochemistry and Photophysics of Coordination Compounds II*, Springer-Verlag: 2007; Vol. 280, pp 117-214.

239. KUMARESAN, D.; SHANKAR, K.; VAIDYA, S.; SCHMEHL, R.H., Photochemistry and Photophysics of Coordination Compounds: Osmium. In *Photochemistry and Photophysics of Coordination Compounds Ii*, Springer-Verlag: 2007; Vol. 281, pp 101-142.

240. LAFOLET, F.; WELTER, S.; POPOVIC, Z.; DE COLA, L., Iridium complexes containing p-phenylene units. The influence of the conjugation on the excited state properties. *Journal of Materials Chemistry* **2005,** *15*, 2820 - 2828.

241. TSUBOYAMA, A.; TAKIGUCHI, T.; OKADA, S.; OSAWA, M.; HOSHINO, M.; UENO, K., A novel dinuclear cyclometalated iridium complex bridged with 1,4-bis[pyridine-2-yl]benzene: its structure and photophysical properties. *Dalton Transactions* **2004,** (8), 1115-1116.

242. AUFFRANT, A.; BARBIERI, A.; BARIGELLETTI, F.; LACOUR, J.; MOBIAN, P.; COLLIN, J.P.; SAUVAGE, J.P.; VENTURA, B., Bimetallic iridium(III) complexes consisting of Ir(ppy)(2) (ppy=2-phenylpyridine) and two laterally connected NN chelates as bridge: Synthesis, separation, and photophysical properties. *Inorganic Chemistry* **2007,** *46* (17), 6911-6919.

243. HOVINEN, J.; HAKALA, H., Versatile strategy for oligonucleotide derivatization. Introduction of lanthanide(III) chelates to oligonucleotides. *Organic Letters* **2001,** *3* (16), 2473-2476.

244. Malinowski, E. R.; Howery, D. G. Factor Analysis in Chemistry, Wiley, New York; Chichester, 1980.

245. GAMPP, H.; MAEDER, M.; MEYER, C.J.; ZUBERBUHLER, A.D., Calculation of Equilibrium-Constants from Multiwavelength Spectroscopic Data .2. Specfit - 2 User-Friendly Programs in Basic and Standard Fortran-77. *Talanta* **1985,** *32* (4), 257-264.

246. GAMPP, H.; MAEDER, M.; MEYER, C.J.; ZUBERBUHLER, A.D., Calculation of Equilibrium-Constants from Multiwavelength Spectroscopic Data .4. Model-Free Least-Squares Refinement by Use of Evolving Factor-Analysis. *Talanta* **1986,** *33* (12), 943-951.

247. DEMELLO, J.C.; WITTMANN, H.F.; FRIEND, R.H., An improved experimental determination of external photoluminescence quantum efficiency. *Advanced Materials* **1997,** *9* (3), 230-&.

248. Baerends, E. J. ADF 2006.01. SCM, Theoretical Chemistry; Vrije Universiteit: Amsterdam, The Netherlands, http://www.scm.com.

249. VeLDE, G.T.; BiCKELHAUPT, F.M.; BaERENDS, E.J.; GuERRA, C.F.; VaN GiSBERGEN, S.J.A.; SnIJDERS, J.G.; ZiEGLER, T., Chemistry with ADF. J*ournal of Computational Chemistry 2*001, 2*2* (9), 931-967.

250. BeCKE, A.D., Density-functional exchange-energy approximation with correct asymptotic-behavior. P*hysical Review A 1*988, 3*8* (6), 3098-3100.

251. SMART v. 5.628, Bruker Molecular Analysis Research Tool, Bruker AXS : Madison , WI, 2002.

252. SAINT v. 6.22, Bruker Molecular Analysis Research Tool, Bruker AXS : Madison , WI, 2002.

253. SADABS v. 2.01, An Empirical Absorption Correction Program, Bruker AXS : Madison , WI, 1995.

254. SHELXTL v. 6.14, Structure Determination Software Suite, Bruker AXS : Madison , WI, 2006.

Appendix

Table 1. Crystallographic data and structure refinement for **L1** · 2 DMSO

Empirical formula	C21 H23 N11 O2 S2
Formula weight	525.62
Temperature	223(2) K
Wavelength	0.71073 Å
Crystal system	Monoclinic
Space group	C2/c
Unit cell dimensions	a = 13.496(4) Å alpha = 90 deg.
	b = 15.144(4) Å beta = 100.303(5) deg.
	c = 12.232(3) Å gamma = 90 deg.
Volume, Z	2459.7(12) $Å^3$, 4
Density (calculated)	1.419 Mg/m^3
Absorption coefficient	0.260 mm^{-1}
F(000)	1096
Crystal size	0.35 x 0.35 x 0.35 mm
Theta range for data collection	2.04 to 24.75 deg.
Limiting indices	-14<=h<=15, -16<=k<=17, -14<=l<=14
Reflections collected	6130
Independent reflections	2094 [R(int) = 0.0185]
Absorption correction	multi-scan
Refinement method	Full-matrix least-squares on F^2
Data / restraints / parameters	2094 / 0 / 234
Goodness-of-fit on F^2	1.047
Final R indices [I>2sigma(I)]	R1 = 0.0352, wR2 = 0.0844
R indices (all data)	R1 = 0.0473, wR2 = 0.0905
Largest diff. peak and hole	0.140 and -0.264 e $Å^{-3}$

Table 2. Crystallographic data and structure refinement for **L4** · 2 DMSO

Empirical formula	C25 H24.50 Br N11 O2.25 S3
Formula weight	691.15
Temperature	223(2) K
Wavelength	0.71073 Å
Crystal system	Monoclinic
Space group	P2(1)/c
Unit cell dimensions	a = 21.825(5) Å alpha = 90 deg.
	b = 14.851(4) Å beta = 95.256(5) deg.
	c = 9.277(2) Å gamma = 90 deg.
Volume, Z	2994.2(12) $Å^3$, 4
Density (calculated)	1.533 Mg/m^3
Absorption coefficient	1.628 mm^{-1}
F(000)	1410
Crystal size	0.50 x 0.12 x 0.09 mm
Theta range for data collection	1.66 to 26.41 deg.
Limiting indices	-24<=h<=27, -18<=k<=14, -11<=l<=11
Reflections collected	16001
Independent reflections	6107 [R(int) = 0.0303]
Absorption correction	multi-scan
Max. and min. transmission	0.8740 and 0.4965
Refinement method	Full-matrix least-squares on F^2
Data / restraints / parameters	6107 / 2 / 493
Goodness-of-fit on F^2	1.079
Final R indices [I>2sigma(I)]	R1 = 0.0521, wR2 = 0.1204
R indices (all data)	R1 = 0.0762, wR2 = 0.1303
Largest diff. peak and hole	0.738 and -0.511 e $Å^{-3}$

Table 3. Crystallographic data and structure refinement for $[Eu(\mathbf{L1})_2]NHEt_3 \cdot 2H_2O$

Empirical formula	C40 H38 Eu N23 O2
Formula weight	1024.89
Temperature	293(2) K
Wavelength	0.71073 Å
Crystal system	Monoclinic
Space group	C2/c
Unit cell dimensions	a = 16.764(4) Å alpha = 90 deg.
	b = 18.295(5) Å beta = 93.207(5) deg.
	c = 14.430(4) Å gamma = 90 deg.
Volume, Z	4419(2) $Å^3$, 4
Density (calculated)	1.541 Mg/m^3
Absorption coefficient	1.485 mm^{-1}
F(000)	2072
Crystal size	0.40 x 0.20 x 0.20 mm
Theta range for data collection	2.13 to 28.27 deg.
Limiting indices	-11<=h<=21, -20<=k<=24, -18<=l<=14
Reflections collected	9808
Independent reflections	5128 [R(int) = 0.0186]
Absorption correction	multi-scan
Max. and min. transmission	0.7556 and 0.5881
Refinement method	Full-matrix least-squares on F^2
Data / restraints / parameters	5128 / 17 / 335
Goodness-of-fit on F^2	1.089
Final R indices [I>2sigma(I)]	R1 = 0.0317, wR2 = 0.0921
R indices (all data)	R1 = 0.0360, wR2 = 0.0956
Largest diff. peak and hole	1.148 and -0.509 e $Å^{-3}$

Table 4. Crystallographic data and structure refinement for [Tb(**L1**)$_2$]NHEt$_3$ · 2CH$_3$OH

Empirical formula	C41 H38 N23 O Tb
Formula weight	1027.86
Temperature	293(2) K
Wavelength	0.71073 Å
Crystal system	Monoclinic
Space group	C2/c
Unit cell dimensions	a = 16.719(4) Å alpha = 90 deg.
	b = 18.270(4) Å beta = 93.429(4) deg.
	c = 14.453(3) Å gamma = 90 deg.
Volume, Z	4406.7(17) Å^3, 4
Density (calculated)	1.549 Mg/m^3
Absorption coefficient	1.668 mm^{-1}
F(000)	2072
Crystal size	0.30 x 0.10 x 0.10 mm
Theta range for data collection	2.13 to 28.29 deg.
Limiting indices	-21<=h<=15, -24<=k<=20, -17<=l<=18
Reflections collected	13715
Independent reflections	5231 [R(int) = 0.0221]
Absorption correction	multi-scan
Max. and min. transmission	0.8509 and 0.6345
Refinement method	Full-matrix least-squares on F^2
Data / restraints / parameters	5231 / 12 / 299
Goodness-of-fit on F^2	1.064
Final R indices [I>2sigma(I)]	R1 = 0.0411, wR2 = 0.1111
R indices (all data)	R1 = 0.0488, wR2 = 0.1161
Largest diff. peak and hole	2.184 and -0.806 e Å^-3

Table 5. Crystallographic data and structure refinement for $[Nd(\mathbf{L1})_2]NHEt_3 \cdot 2H_2O$

Empirical formula	C40 H36 N23 Nd O
Formula weight	999.16
Temperature	223(2) K
Wavelength	0.71073 Å
Crystal system	Monoclinic
Space group	C2/c
Unit cell dimensions	a = 16.901(4) Å alpha = 90 deg.
	b = 18.198(5) Å beta = 93.225(6) deg.
	c = 14.395(4) Å gamma = 90 deg.
Volume, Z	4420.4(19) $Å^3$, 4
Density (calculated)	1.501 Mg/m^3
Absorption coefficient	1.237 mm^{-1}
F(000)	2020
Crystal size	0.40 x 0.20 x 0.20 mm
Theta range for data collection	1.65 to 24.73 deg.
Limiting indices	-19<=h<=19, -21<=k<=6, -16<=l<=14
Reflections collected	6124
Independent reflections	3394 [R(int) = 0.0170]
Absorption correction	multi-scan
Max. and min. transmission	0.7900 and 0.6376
Refinement method	Full-matrix least-squares on F^2
Data / restraints / parameters	3394 / 0 / 272
Goodness-of-fit on F^2	1.147
Final R indices [I>2sigma(I)]	R1 = 0.0560, wR2 = 0.1608
R indices (all data)	R1 = 0.0623, wR2 = 0.1677
Largest diff. peak and hole	1.775 and -0.857 e $Å^{-3}$

Table 6. Crystallographic data and structure refinement for [Tb(**L1**)]OTf · 4 CH_3OH · 2.5 H_2O

Empirical formula	C23.12 H32.26 F3 N11 O9.50 S Tb
Formula weight	864.28
Temperature	223(2) K
Wavelength	0.71073 Å
Crystal system	Triclinic
Space group	P-1
Unit cell dimensions	a = 9.5429(15) Å alpha = 101.217(3) deg.
	b = 13.484(2) Å beta = 105.291(2) deg.
	c = 14.456(2) Å gamma = 98.903(3) deg.
Volume, Z	1717.8(5) $Å^3$, 2
Density (calculated)	1.671 Mg/m^3
Absorption coefficient	2.200 mm^{-1}
F(000)	864
Crystal size	0.20 x 0.15 x 0.06 mm
Theta range for data collection	1.89 to 29.00 deg.
Limiting indices	-12<=h<=12, -9<=k<=18, -19<=l<=14
Reflections collected	11089
Independent reflections	7797 [R(int) = 0.0180]
Absorption correction	multi-scan
Max. and min. transmission	0.8793 and 0.6674
Refinement method	Full-matrix least-squares on F^2
Data / restraints / parameters	7797 / 2 / 548
Goodness-of-fit on F^2	1.120
Final R indices [I>2sigma(I)]	R1 = 0.0400, wR2 = 0.0972
R indices (all data)	R1 = 0.0476, wR2 = 0.1001
Largest diff. peak and hole	1.664 and -1.195 e $Å^{-3}$

Table 7. Crystallographic data and structure refinement for $[Eu(\mathbf{L2})_2]NHEt_3 \cdot 4CH_3OH$

Empirical formula	C44 H50 Eu N7 O12
Formula weight	1020.87
Temperature	293(2) K
Wavelength	0.71073 Å
Crystal system	Monoclinic
Space group	C2/c
Unit cell dimensions	a = 11.859(2) Å alpha = 90 deg.
	b = 22.762(4) Å beta = 90.856(3) deg.
	c = 16.381(3) Å gamma = 90 deg.
Volume, Z	4421.5(13) $Å^3$, 4
Density (calculated)	1.534 Mg/m^3
Absorption coefficient	1.489 mm^{-1}
F(000)	2088
Crystal size	0.50 x 0.20 x 0.20 mm
Theta range for data collection	1.94 to 28.33 deg.
Limiting indices	-10<=h<=15, -30<=k<=24, -21<=l<=21
Reflections collected	14140
Independent reflections	5239 [R(int) = 0.0140]
Absorption correction	multi-scan
Max. and min. transmission	0.7549 and 0.5230
Refinement method	Full-matrix least-squares on F^2
Data / restraints / parameters	5239 / 0 / 386
Goodness-of-fit on F^2	1.062
Final R indices [I>2sigma(I)]	R1 = 0.0212, wR2 = 0.0552
R indices (all data)	R1 = 0.0236, wR2 = 0.0564
Largest diff. peak and hole	0.460 and -0.437 e $Å^{-3}$

Table 8. Crystallographic data and structure refinement for $[Tb(\mathbf{L2})_2]NHEt_3 \cdot 2CH_3OH$

Empirical formula	C44 H50 N7 O12 Tb
Formula weight	1027.83
Temperature	293(2) K
Wavelength	0.71073 Å
Crystal system	Monoclinic
Space group	C2/c
Unit cell dimensions	a = 11.8733(18) Å alpha = 90 deg.
	b = 22.681(4) Å beta = 90.812(3) deg.
	c = 16.382(3) Å gamma = 90 deg.
Volume, Z	4411.3(12) $Å^3$, 4
Density (calculated)	1.548 Mg/m^3
Absorption coefficient	1.674 mm^{-1}
F(000)	2096
Crystal size	0.50 x 0.20 x 0.20 mm
Theta range for data collection	1.94 to 28.28 deg.
Limiting indices	-15<=h<=14, -29<=k<=24, -13<=l<=21
Reflections collected	11153
Independent reflections	5146 [R(int) = 0.0155]
Absorption correction	multi-scan
Max. and min. transmission	0.7306 and 0.4882
Refinement method	Full-matrix least-squares on F^2
Data / restraints / parameters	5146 / 0 / 386
Goodness-of-fit on F^2	1.157
Final R indices [I>2sigma(I)]	R1 = 0.0253, wR2 = 0.0621
R indices (all data)	R1 = 0.0293, wR2 = 0.0638
Largest diff. peak and hole	0.343 and -1.141 e $Å^{-3}$

Table 9. Crystallographic data and structure refinement for $[Nd(\mathbf{L2})_2]NHEt_3 \cdot 2CH_3OH$

Empirical formula	C44 H50 N7 Nd O12
Formula weight	1013.15
Temperature	293(2) K
Wavelength	0.71073 Å
Crystal system	Monoclinic
Space group	C2/c
Unit cell dimensions	a = 11.7970(15) Å alpha = 90 deg.
	b = 22.881(3) Å beta = 90.703(2) deg.
	c = 16.432(2) Å gamma = 90 deg.
Volume, Z	4435.2(10) $Å^3$, 4
Density (calculated)	1.517 Mg/m^3
Absorption coefficient	1.241 mm^{-1}
F(000)	2076
Crystal size	0.30 x 0.20 x 0.20 mm
Theta range for data collection	1.94 to 28.24 deg.
Limiting indices	-9<=h<=15, -29<=k<=30, -21<=l<=21
Reflections collected	14124
Independent reflections	5274 [R(int) = 0.0200]
Absorption correction	multi-scan
Refinement method	Full-matrix least-squares on F^2
Data / restraints / parameters	5274 / 0 / 361
Goodness-of-fit on F^2	1.076
Final R indices [I>2sigma(I)]	R1 = 0.0282, wR2 = 0.0611
R indices (all data)	R1 = 0.0342, wR2 = 0.0628
Largest diff. peak and hole	0.536 and -0.732 e $Å^{-3}$

Table 10. Crystallographic data and structure refinement for $[Eu(\mathbf{L3})_2]NHEt_3 \cdot 4CH_3OH$

Empirical formula	C56 H56 Br2 Eu N23 O4
Formula weight	1427.02
Temperature	223(2) K
Wavelength	0.71073 Å
Crystal system	Monoclinic
Space group	C2/c
Unit cell dimensions	a = 22.628(10) Å alpha = 90 deg.
	b = 19.032(8) Å beta = 107.356(7) deg.
	c = 14.977(7) Å gamma = 90 deg.
Volume, Z	6157(5) $Å^3$, 4
Density (calculated)	1.540 Mg/m^3
Absorption coefficient	2.382 mm^{-1}
F(000)	2872
Crystal size	0.50 x 0.40 x 0.40 mm
Theta range for data collection	1.81 to 23.29 deg.
Limiting indices	-25<=h<=17, -15<=k<=21, -15<=l<=16
Reflections collected	8915
Independent reflections	4377 [R(int) = 0.0418]
Absorption correction	Multi-scan
Max. and min. transmission	0.4492 and 0.3822
Refinement method	Full-matrix least-squares on F^2
Data / restraints / parameters	4377 / 0 / 392
Goodness-of-fit on F^2	1.231
Final R indices [I>2sigma(I)]	R1 = 0.0902, wR2 = 0.2002
R indices (all data)	R1 = 0.1025, wR2 = 0.2052
Largest diff. peak and hole	1.106 and -3.513 e $Å^{-3}$

Table 11. Crystallographic data and structure refinement for [Eu(**L4**)$_2$]NHEt$_3$ · 3CH$_3$OH

Empirical formula	C51 H48 Br2 Eu N23 O3 S2
Formula weight	1407.02
Temperature	223(2) K
Wavelength	0.71073 Å
Crystal system	Monoclinic
Space group	P2(1)/c
Unit cell dimensions	a = 20.964(8) Å alpha = 90 deg.
	b = 19.285(8) Å beta = 105.007(7) deg.
	c = 14.278(5) Å gamma = 90 deg.
Volume, Z	5575(4) Å^3, 4
Density (calculated)	1.676 Mg/m^3
Absorption coefficient	2.700 mm^{-1}
F(000)	2816
Crystal size	0.25 x 0.10 x 0.06 mm
Theta range for data collection	1.82 to 23.25 deg.
Limiting indices	-23<=h<=23, -6<=k<=21, -15<=l<=11
Reflections collected	15775
Independent reflections	7717 [R(int) = 0.0477]
Absorption correction	multi-scan
Max. and min. transmission	0.8548 and 0.5518
Refinement method	Full-matrix least-squares on F^2
Data / restraints / parameters	7717 / 0 / 738
Goodness-of-fit on F^2	1.207
Final R indices [I>2sigma(I)]	R1 = 0.0864, wR2 = 0.1617
R indices (all data)	R1 = 0.1103, wR2 = 0.1690
Largest diff. peak and hole	1.321 and -3.055 e Å^{-3}

Table 12. Crystallographic data and structure refinement for [Eu(**L7**)$_2$H$_2$O]NHEt$_3$ · 3CH$_3$OH

Empirical formula	C32 H38 Eu N21 O3
Formula weight	916.79
Temperature	293(2) K
Wavelength	0.71073 Å
Crystal system	Monoclinic
Space group	P2(1)/n
Unit cell dimensions	a = 18.006(4) Å alpha = 90 deg.
	b = 11.409(2) Å beta = 91.960(4) deg.
	c = 18.367(4) Å gamma = 90 deg.
Volume, Z	3770.8(14) Å^3, 4
Density (calculated)	1.615 Mg/m^3
Absorption coefficient	1.729 mm^{-1}
F(000)	1856
Crystal size	0.30 x 0.15 x 0.06 mm
Theta range for data collection	1.61 to 28.32 deg.
Limiting indices	-9<=h<=23, -14<=k<=15, -23<=l<=23
Reflections collected	23142
Independent reflections	8988 [R(int) = 0.0257]
Absorption correction	multi-scan
Refinement method	Full-matrix least-squares on F^2
Data / restraints / parameters	8988 / 0 / 666
Goodness-of-fit on F^2	1.079
Final R indices [I>2sigma(I)]	R1 = 0.0293, wR2 = 0.0640
R indices (all data)	R1 = 0.0407, wR2 = 0.0679
Largest diff. peak and hole	1.291 and -0.840 e Å^{-3}

Table 13. Crystallographic data and structure refinement for $[Eu(\mathbf{L10})_3]K_3 \cdot 8CH_3OH$

Empirical formula	C29 H41 Eu1 K3 N27 O8
Formula weight	1165.07
Temperature	293(2) K
Wavelength	0.71073 Å
Crystal system	Monoclinic
Space group	C 1 2/c 1
Unit cell dimensions	a = 19.2814(7) Å alpha = 90 deg.
	b = 10.7776(3) Å beta = 119.752(2) deg.
	c = 26.07570(10) Å gamma = 90 deg.
Volume, Z	4704.4(2) $Å^3$, 4
Density (calculated)	1.645 Mg/m^3
Absorption coefficient	1.675 mm^{-1}
F(000)	2352
Theta range for data collection	3.01 to 29.09 deg.
Limiting indices	-25<=h<=24, -14<=k<=14, -34<=l<=35
Reflections collected	22729
Independent reflections	5737 [R(int) = 0.0260]
Absorption correction	Semi-empirical from equivalents
Max. and min. transmission	1.00000 and 0.87173
Refinement method	Full-matrix least-squares on F^2
Data / restraints / parameters	5737 / 0 / 392
Goodness-of-fit on F^2	1.075
Final R indices [I>2sigma(I)]	R1 = 0.0225, wR2 = 0.0533
R indices (all data)	R1 = 0.0259, wR2 = 0.0540
Largest diff. peak and hole	0.825 and -0.376 e $Å^{-3}$

Table 14. Crystallographic data and structure refinement for $[Eu(\mathbf{L11})_3](NHEt_3)_3 \cdot 2.5CH_3OH$

Empirical formula	C39 H62 Eu N18 O8.50
Formula weight	1071.03
Temperature	293(2) K
Wavelength	0.71073 Å
Crystal system	Monoclinic
Space group	P2(1)/c
Unit cell dimensions	a = 14.335(4) Å alpha = 90 deg.
	b = 11.098(3) Å beta = 98.820(5) deg.
	c = 30.696(8) Å gamma = 90 deg.
Volume, Z	4826(2) $Å^3$, 4
Density (calculated)	1.474 Mg/m^3
Absorption coefficient	1.369 mm^{-1}
F(000)	2212
Crystal size	0.20 x 0.10 x 0.10 mm
Theta range for data collection	1.81 to 23.28 deg.
Limiting indices	-15<=h<=15, -12<=k<=12, -21<=l<=34
Reflections collected	17524
Independent reflections	6927 [R(int) = 0.0332]
Absorption correction	multi-scan
Refinement method	Full-matrix least-squares on F^2
Data / restraints / parameters	6927 / 0 / 693
Goodness-of-fit on F^2	1.146
Final R indices [I>2sigma(I)]	R1 = 0.0483, wR2 = 0.0789
R indices (all data)	R1 = 0.0639, wR2 = 0.0824
Largest diff. peak and hole	0.867 and -1.623 e $Å^{-3}$

Table 15. Crystallographic data and structure refinement for [Eu(**L12**)(TTA)]

Empirical formula	C32 H18 Eu F6 N3 O6 S2
Formula weight	870.57
Temperature	293(2) K
Wavelength	0.71073 Å
Crystal system	Monoclinic
Space group	P 1 21/n 1
Unit cell dimensions	a = 10.7907(2) Å alpha = 90 deg.
	b = 18.6444(2) Å beta = 101.3527(14) deg.
	c = 16.3804(2) Å gamma = 90 deg.
Volume, Z	3231.03(8) $Å^3$, 4
Density (calculated)	1.790 Mg/m^3
Absorption coefficient	2.155 mm^{-1}
F(000)	1712
Theta range for data collection	3.02 to 29.00 deg.
Limiting indices	-14<=h<=13, -23<=k<=24, -22<=l<=22
Reflections collected	17750
Independent reflections	7466 [R(int) = 0.0250]
Absorption correction	Semi-empirical from equivalents
Max. and min. transmission	1.00000 and 0.95783
Refinement method	Full-matrix least-squares on F^2
Data / restraints / parameters	7466 / 16 / 547
Goodness-of-fit on F^2	0.900
Final R indices [I>2sigma(I)]	R1 = 0.0224, wR2 = 0.0409
R indices (all data)	R1 = 0.0366, wR2 = 0.0423
Largest diff. peak and hole	0.667 and -0.488 e $Å^{-3}$

Table 16. Crystallographic data and structure refinement for [Tb(**L12**)(TFAC)]

Empirical formula	C27 H22 F6 N3 O7 Tb
Formula weight	773.40
Temperature	150.0(2) K
Wavelength	0.71073 Å
Crystal system	Monoclinic
Space group	P 1 21/n 1
Unit cell dimensions	a = 17.7241(5) Å alpha = 90 deg.
	b = 15.0734(3) Å beta = 104.927(3) deg.
	c = 22.6068(8) Å gamma = 90 deg.
Volume, Z	5835.9(3) $Å^3$, 8
Density (calculated)	1.760 Mg/m^3
Absorption coefficient	2.511 mm^{-1}
F(000)	3040
Crystal size	0.5 x 0.15 x 0.15 mm
Theta range for data collection	3.06 to 24.71 deg.
Limiting indices	-20<=h<=20, -17<=k<=16, -26<=l<=26
Reflections collected	26689
Independent reflections	9704 [R(int) = 0.0510]
Absorption correction	Semi-empirical from equivalents
Max. and min. transmission	1.00000 and 0.85556
Refinement method	Full-matrix least-squares on F^2
Data / restraints / parameters	9704 / 0 / 801
Goodness-of-fit on F^2	0.854
Final R indices [I>2sigma(I)]	R1 = 0.0411, wR2 = 0.0784
R indices (all data)	R1 = 0.1000, wR2 = 0.0864
Largest diff. peak and hole	1.295 and -0.959 e $Å^{-3}$

Table 17. Crystallographic data and structure refinement for **50**

Empirical formula	C39 H31 N5
Formula weight	569.69
Temperature	150(2) K
Wavelength	0.71073 Å
Crystal system	Triclinic
Space group	P-1
Unit cell dimensions	a = 8.1800(8) Å alpha = 104.925(8) deg.
	b = 13.3224(12) Å beta = 95.040(8) deg.
	c = 15.2448(14) Å gamma = 104.566(8) deg.
Volume, Z	1532.9(2) $Å^3$, 2
Density (calculated)	1.234 Mg/m^3
Absorption coefficient	0.074 mm^{-1}
F(000)	600
Crystal size	0.93 x 0.19 x 0.16 mm
Theta range for data collection	3.03 to 28.92 deg.
Limiting indices	-11<=h<=11, -18<=k<=17, -19<=l<=20
Reflections collected	27169
Independent reflections	6877 [R(int) = 0.0566]
Absorption correction	Semi-empirical from equivalents
Max. and min. transmission	0.988 and 0.983
Refinement method	Full-matrix least-squares on F^2
Data / restraints / parameters	6877 / 1 / 540
Goodness-of-fit on F^2	0.926
Final R indices [I>2sigma(I)]	R1 = 0.0448, wR2 = 0.1141
R indices (all data)	R1 = 0.0728, wR2 = 0.1225
Largest diff. peak and hole	0.284 and -0.213 e $Å^{-3}$

Table 18. Crystallographic data and structure refinement for [Eu(**L1**)(TTA)] · 3 DMSO · $2H_2O$

Empirical formula	C31 H35 Eu F3 N11 O7 S4
Formula weight	1010.90
Temperature	293(2) K
Wavelength	0.71073 Å
Crystal system	Triclinic
Space group	P-1
Unit cell dimensions	a = 11.9638(19) Å alpha = 70.788(3) deg.
	b = 12.1837(19) Å beta = 72.267(3) deg.
	c = 16.853(3) Å gamma = 62.769(2) deg.
Volume, Z	2027.7(5) $Å^3$, 2
Density (calculated)	1.656 Mg/m^3
Absorption coefficient	1.825 mm^{-1}
F(000)	1016
Crystal size	0.20 x 0.20 x 0.08 mm
Theta range for data collection	1.93 to 28.32 deg.
Limiting indices	-15<=h<=14, -15<=k<=8, -22<=l<=21
Reflections collected	13067
Independent reflections	9202 [R(int) = 0.0138]
Absorption correction	multi-scan
Refinement method	Full-matrix least-squares on F^2
Data / restraints / parameters	9202 / 8 / 702
Goodness-of-fit on F^2	1.027
Final R indices [I>2sigma(I)]	R1 = 0.0237, wR2 = 0.0519
R indices (all data)	R1 = 0.0280, wR2 = 0.0531
Largest diff. peak and hole	1.090 and -0.561 e $Å^{-3}$

Table 19. Crystallographic data and structure refinement for **31** · $3CHCl_3$

Empirical formula	C47 H27 Cl11 F8 Ir2 N4
Formula weight	1574.08
Temperature	223(2) K
Wavelength	0.71073 Å
Crystal system	Monoclinic
Space group	P2(1)/c
Unit cell dimensions	a = 12.4833(17) Å alpha = 90 deg.
	b = 19.596(3) Å beta = 97.740(3) deg.
	c = 21.318(3) Å gamma = 90 deg.
Volume, Z	5167.5(12) $Å^3$, 4
Density (calculated)	2.023 Mg/m^3
Absorption coefficient	5.783 mm^{-1}
F(000)	3000
Crystal size	0.50 x 0.35 x 0.10 mm
Theta range for data collection	1.93 to 26.42 deg.
Limiting indices	-15<=h<=10, -24<=k<=24, -10<=l<=26
Reflections collected	19565
Independent reflections	9340 [R(int) = 0.0374]
Absorption correction	multi-scan
Refinement method	Full-matrix least-squares on F^2
Data / restraints / parameters	9340 / 0 / 649
Goodness-of-fit on F^2	1.010
Final R indices [I>2sigma(I)]	R1 = 0.0402, wR2 = 0.0817
R indices (all data)	R1 = 0.0659, wR2 = 0.0889
Largest diff. peak and hole	0.972 and -0.934 e $Å^{-3}$

Table 20. Crystallographic data and structure refinement for **Ir1a** · 1.5CH_2Cl_2

Empirical formula	C59 H36 Br2 Cl6 F8 Ir2 N6 O4
Formula weight	1801.86
Temperature	223(2) K
Wavelength	0.71073 Å
Crystal system	Monoclinic
Space group	C2/c
Unit cell dimensions	a = 33.349(8) Å alpha = 90 deg.
	b = 11.305(3) Å beta = 106.581(4) deg.
	c = 16.266(4) Å gamma = 90 deg.
Volume, Z	5877(2) $Å^3$, 4
Density (calculated)	2.036 Mg/m^3
Absorption coefficient	6.236 mm^{-1}
F(000)	3448
Crystal size	0.50 x 0.20 x 0.20 mm
Theta range for data collection	2.21 to 28.32 deg.
Limiting indices	-43<=h<=44, -14<=k<=13, -20<=l<=21
Reflections collected	18269
Independent reflections	6992 [R(int) = 0.0404]
Absorption correction	multi-scan
Refinement method	Full-matrix least-squares on F^2
Data / restraints / parameters	6992 / 0 / 465
Goodness-of-fit on F^2	1.070
Final R indices [I>2sigma(I)]	R1 = 0.0442, wR2 = 0.1050
R indices (all data)	R1 = 0.0580, wR2 = 0.1102
Largest diff. peak and hole	1.838 and -4.724 e $Å^{-3}$

Table 21. Crystallographic data and structure refinement for **Ir1** · $CHCl_3$

Empirical formula	C29 H16 Br Cl3 F4 Ir N3 O2
Formula weight	892.91
Temperature	293(2) K
Wavelength	0.71073 Å
Crystal system	Monoclinic
Space group	P 1 21/c 1
Unit cell dimensions	a = 17.2952(2) Å alpha = 90 deg.
	b = 9.83830(10) Å beta = 90.0253(14) deg.
	c = 17.0381(2) Å gamma = 90 deg.
Volume, Z	2899.12(6) $Å^3$, 4
Density (calculated)	2.046 Mg/m^3
Absorption coefficient	6.320 mm^{-1}
F(000)	1704
Crystal size	0.4 x 0.2 x 0.2 mm
Theta range for data collection	3.14 to 28.96 deg.
Limiting indices	-21<=h<=23, -12<=k<=13, -22<=l<=22
Reflections collected	17217
Independent reflections	6589 [R(int) = 0.0214]
Absorption correction	Semi-empirical from equivalents
Max. and min. transmission	1.00000 and 0.42999
Refinement method	Full-matrix least-squares on F^2
Data / restraints / parameters	6589 / 0 / 480
Goodness-of-fit on F^2	0.977
Final R indices [I>2sigma(I)]	R1 = 0.0419, wR2 = 0.1005
R indices (all data)	R1 = 0.0499, wR2 = 0.1028
Largest diff. peak and hole	2.580 and -0.625 e $Å^{-3}$

Table 22. Crystallographic data and structure refinement for **Ir2** · $CHCl_3$ · C_2H_5OH

Empirical formula	C54 H34 Cl3 F4 Ir N8 O3
Formula weight	1217.44
Temperature	150(2) K
Wavelength	0.71073 Å
Crystal system	Monoclinic
Space group	I 2/a
Unit cell dimensions	a = 15.4402(8) Å alpha = 90 deg.
	b = 27.2501(14) Å beta = 92.460(5) deg.
	c = 25.5926(15) Å gamma = 90 deg.
Volume, Z	10758.1(10) $Å^3$, 8
Density (calculated)	1.503 Mg/m^3
Absorption coefficient	2.695 mm^{-1}
F(000)	4816
Crystal size	0.50 x 0.50 x 0.08 mm
Theta range for data collection	3.02 to 23.26 deg.
Limiting indices	-16<=h<=17, -29<=k<=30, -28<=l<=24
Reflections collected	19375
Independent reflections	7130 [R(int) = 0.0480]
Absorption correction	Semi-empirical from equivalents
Max. and min. transmission	0.8133 and 0.3460
Refinement method	Full-matrix least-squares on F^2
Data / restraints / parameters	7130 / 6 / 670
Goodness-of-fit on F^2	0.933
Final R indices [I>2sigma(I)]	R1 = 0.0705, wR2 = 0.1816
R indices (all data)	R1 = 0.1373, wR2 = 0.2031
Largest diff. peak and hole	1.811 and -0.920 e $Å^{-3}$

Table 23. Crystallographic data and structure refinement for **Ir5** · $3CH_2Cl_2$

Empirical formula	C64 H39 Cl6 F8 Ir2 N7 O4
Formula weight	1719.12
Temperature	223(2) K
Wavelength	0.71073 Å
Crystal system	Triclinic
Space group	P-1
Unit cell dimensions	a = 11.905(4) Å alpha = 68.398(6) deg.
	b = 15.340(5) Å beta = 73.201(6) deg.
	c = 18.726(6) Å gamma = 76.991(6) deg.
Volume, Z	3016.7(16) $Å^3$, 2
Density (calculated)	1.893 Mg/m^3
Absorption coefficient	4.754 mm^{-1}
F(000)	1664
Crystal size	0.50 x 0.35 x 0.10 mm
Theta range for data collection	1.44 to 24.74 deg.
Limiting indices	-14<=h<=8, -18<=k<=18, -22<=l<=18
Reflections collected	15265
Independent reflections	10075 [R(int) = 0.0251]
Absorption correction	multi-scan
Refinement method	Full-matrix least-squares on F^2
Data / restraints / parameters	10075 / 6 / 981
Goodness-of-fit on F^2	1.066
Final R indices [I>2sigma(I)]	R1 = 0.0442, wR2 = 0.0906
R indices (all data)	R1 = 0.0634, wR2 = 0.0988
Largest diff. peak and hole	1.184 and -1.521 e $Å^{-3}$